

# **Development and physical characterisation of polyethylene glycol glycerides-based gel formulations for macromolecule delivery**

---



**Doroty Codoni**

University of East Anglia  
School of Pharmacy

Thesis submitted for the degree of Doctor of Philosophy  
December, 2013

© This copy of the thesis has been supplied on condition that anyone who consults it is understood to recognise that its copyright rests with the author and that use of any information derived there from must be in accordance with current UK Copyright Law. In addition, any quotation or extract must include full attribution.

## Abstract

Lipid-based delivery systems offer many advantages on enhancing the bioavailability of protein/peptides. Gelucire 50/13 is a complex mixture of glycerides and PEG. It is mainly used in solid oral formulations for delivering small molecular weight drugs. The purpose of this project was to develop novel uses of Gelucire as a liquid crystalline-based gel-forming material for protein/peptide delivery. A thorough physical and mechanical characterisation of the gels (with and without lysozyme as a model protein) was conducted using a combination of analytical techniques including ATR-FTIR, DSC, relaxometry NMR, rheological and texture analyser, and imaging analyses (SEM, AFM, and cryo-TEM). The results demonstrated the sophisticated microstructures of the gels due to the formation of various liquid crystalline phases that change with the gel water content. The gels with low water contents are characterised by highly restricted diffusion of water molecules in the gels, while water-rich and lipid-rich phases are present in the gels with medium to high water contents. The ordered liquid crystalline structures with lipid-rich and water-rich domains provide excellent carrier properties for hosting proteins/peptides. The effect of water content on the microstructure, physical properties and *in vitro* performance of the gels prevails on other effects such as gel preparation method and protein incorporation. The wide range of microstructures of the gels enables the mucoadhesive properties and release profiles of lysozyme from the gels to be controlled. Highly stable disc-shaped nanoparticles were produced from the Gelucire gels using a single-step and solvent-free method without the addition of stabilisers. *In vitro* cell culture studies revealed high tolerance to and rapid uptake of the gel nanoparticles by Caco-2 cells. The good protein encapsulation efficiency and the retained biological activity of lysozyme indicates considerable potential for these nanoparticles to be a new class of safe, low-cost and effective carriers for protein/peptide delivery.

## **Acknowledgments**

I would like to thank my supervisors Dr Sheng Qi and Dr Maria O'Connell for giving me the opportunity of a PhD, for the help and support throughout my project, and for encouraging me in my research. I would also like to thank UEA for the studentship.

Mentions have to be made to many people who helped me in this project. Thanks to the late Dr Brian Hills and to Ben Piggot for their assistance with the NMR at the Institute of Food Research, to Prof Peter Belton, Dr Myles Cheesman, Dr Andrew Mayes and Dr Jonathan Moffat, to Jenna Bradley and Jonathan Cowan for the help in the biological tests. Thanks to Mr Bertrand Lezé for the help with the SEM. I am grateful to Prof Piero Baglioni and Dr Debora Berti from University of Florence and CGSI for welcoming me in their lab and for the assistance with the SAXS. Thanks to Dr Katarina Edwards and Dr Jonny Eriksson from Uppsala University for providing the cryo-TEM images.

Thanks to my housemates and friends Alberto, Fatima, Lorina, and Siok Yee (Sam) for their friendship and support and to Giulia and Marco for their friendship, patience and support especially during the writing up stage. I would like also to remember my friend Simone. Thanks also to Annalisa, Chiara, Claudia, Davide, Desiré, Francesca, Maria, Melania, Simona, Teresa, Valeria, to my lab mates, present and past, and to all the friends I have made through the years and the people I have met who have made this experience enjoyable and easier than it could have been.

A special thanks to my parents and my brother David, for their patience, love, support and encouragement and for giving me strength in the toughest moments of my PhD, and without whom I could not have achieved this goal.

---

## Table of Contents

<b>Table of Contents.....</b>	<b>i</b>
<b>List of Figures.....</b>	<b>vii</b>
<b>List of Tables.....</b>	<b>xviii</b>
<b>List of Abbreviations.....</b>	<b>xxii</b>
<b>1 Introduction.....</b>	<b>1</b>
1.1 Oral approaches for protein delivery .....	3
1.1.1 Chemical modification .....	3
1.1.2 Absorption enhancers .....	6
1.1.3 Enzyme inhibitors .....	6
1.1.4 Mucoadhesive systems.....	7
1.1.4.1 Mucoadhesion .....	8
1.1.4.1.1 Proposed mechanisms of mucoadhesion .....	10
1.1.5 Particulate carrier systems.....	13
1.1.5.1 Polymeric carriers .....	13
1.1.5.2 Lipid-based delivery systems .....	15
1.1.5.2.1 Liposomes .....	16
1.1.5.2.2 Solid Lipid Nanoparticles (SLN).....	19
1.1.5.2.3 Liquid crystalline-based delivery systems.....	22
1.2 Gelucire 50/13.....	26
1.2.1 Introduction .....	26
1.2.2 Structure of Gelucire 50/13 .....	27
1.2.3 Ageing effects .....	31
1.2.4 Water uptake .....	32
1.2.5 Pharmaceutical applications of Gelucire 50/13.....	33
1.3 Lysozyme .....	34
1.3.1 Lysozyme structure .....	35
1.3.2 Mechanism and site of action of lysozyme .....	36
1.4 Project objective .....	37
<b>2 Materials and Methods.....</b>	<b>39</b>
2.1 Introduction.....	39
2.2 Materials details.....	40
2.2.1 Stearoyl macroglycerides (Gelucire 50/13) .....	40
2.2.2 Lysozyme .....	40
2.2.3 Mucin from porcine stomach, type II.....	40

---

2.2.4	Porcine small intestine .....	40
2.2.5	Coumarin-6 .....	41
2.3	Descriptions of samples preparations.....	41
2.3.1	Preparation of lysozyme-free and lysozyme-loaded gel formulations by heating and by hydration methods .....	41
2.3.2	Preparation of lysozyme-free nanoparticles and lysozyme-loaded nanoparticles .....	42
2.3.3	Preparation of fluorescent gel nanoparticles .....	43
2.3.4	Preparation of buffer solutions.....	43
2.4	Theoretical background of physicochemical characterisation of the gels and the nanoparticles.....	44
2.4.1	Differential scanning calorimetry (DSC).....	44
2.4.2	Rheology .....	45
2.4.2.1	Oscillatory tests.....	49
2.4.2.1.1	Stress sweep test.....	51
2.4.2.1.2	Frequency sweep test.....	51
2.4.2.1.3	Temperature ramp test.....	52
2.4.2.2	Flow test in continuous ramp mode .....	52
2.4.3	Texture analysis .....	54
2.4.3.1	Texture profile analysis (TPA) test.....	54
2.4.3.2	Mucoadhesion test.....	55
2.4.4	Dynamic light scattering (DLS).....	56
2.4.4.1	Basic principles .....	56
2.4.4.2	Instrumentation .....	58
2.4.4.3	Data analysis .....	59
2.4.4.4	Methodology used in this study .....	61
2.4.5	Small angle x-ray scattering (SAXS).....	61
2.4.5.1	Basic principles .....	61
2.4.5.2	Instrumentation .....	63
2.4.5.3	Methodology used in this project.....	64
2.4.6	Relaxometry nuclear magnetic resonance (NMR).....	65
2.4.6.1	Theoretical background.....	65
2.4.6.1.1	Carr-Purcell-Meiboom-Gill (CPMG) sequence .....	69
2.4.6.1.2	Inversion Recovery pulse sequence (Inv-CPMG).....	69
2.4.6.1.3	CMPG Pulsed Gradient Spin Echo sequence (CMPG-PGSE).....	70
2.4.6.1.4	Stimulated echo diffusion sequence (PGSTE diffusion).....	71
2.4.6.2	Instrumentation and sample preparation .....	71
2.4.7	Spectroscopic techniques .....	73
2.4.7.1	Attenuated total reflectance-Fourier transform infrared (ATR-FTIR) spectroscopy.....	73
2.4.7.1.1	Basic principles .....	73
2.4.7.1.2	Structural analysis of proteins using IR .....	74
2.4.7.1.3	Methodology used in this project .....	75
2.4.7.2	Circular Dichroism (CD).....	75
2.4.8	Imaging technique.....	77
2.4.8.1	Scanning electron microscopy (SEM) .....	77
2.4.8.2	Atomic force microscopy (AFM).....	78
2.4.8.3	Cryogenic transmission electron microscopy (cryo-TEM).....	78
2.5	Drug release studies.....	79

---

2.6	Diffusion studies (Franz Cells) .....	80
2.7	Cell culture .....	81
2.7.1	Cell culture reagents and media preparation .....	81
2.7.1.1	NCI-H292.....	81
2.7.1.2	Caco-2 .....	81
2.7.2	Cell counting and viability .....	82
2.7.3	Cytotoxicity/Proliferation test.....	82
<b>3</b>	<b>Basic structure characterisation of Gelucire 50/13 gels.....</b>	<b>84</b>
3.1	Introduction.....	84
3.2	Objectives .....	85
3.3	Materials and methods.....	85
3.3.1	Attenuated Total Reflectance-Fourier Transformed Infrared spectroscopy (ATR-FTIR) .....	85
3.3.2	Small Angle X-Ray Scattering (SAXS).....	86
3.3.3	Differential Scanning Calorimetry (DSC) .....	87
3.3.4	Rheological tests .....	88
3.3.4.1	Oscillatory stress sweep test.....	89
3.3.4.2	Oscillatory frequency sweep test .....	89
3.3.4.3	Temperature ramp test.....	89
3.3.4.4	Continuous flow test .....	89
3.3.5	Texture Analysis .....	90
3.3.5.1	Textural Profile Analysis (TPA) .....	90
3.3.5.2	Adhesion test.....	90
3.3.6	Statistical analysis .....	91
3.4	Results and Discussion.....	92
3.4.1	Structural analysis of gels with ATR-FTIR spectroscopy .....	92
3.4.2	Structural analysis of the gels using SAXS .....	101
3.4.3	Thermal phase transition of the gels .....	106
3.4.3.1	DSC Thermal analysis.....	106
3.4.3.2	The temperature ramp test (Oscillation Rheometer).....	111
3.4.4	Rheological properties of gels.....	118
3.4.4.1	Determination of linear viscoelastic region (LVR): oscillation stress sweep test .....	118
3.4.4.2	The oscillation frequency sweep test .....	120
3.4.4.3	Continuous flow test .....	126
3.4.5	Mechanical properties of gels (Texture Analysis) .....	134
3.4.5.1	Texture Profile Analysis (TPA) test.....	134
3.4.6	Correlation between mechanical and rheological parameters.....	140
3.4.7	Evaluation of the mucoadhesive properties of gels.....	142
3.5	Conclusion.....	146

<b>4</b>	<b>Micro-structural analysis of water distribution in Gelucire</b>	
<b>50/13 gels</b>		<b>147</b>
4.1	Introduction.....	147
4.2	Objectives .....	148
4.3	Materials and Methods.....	148
4.3.1	Imaging analysis of freeze-dried gels .....	148
4.3.2	Differential Scanning Calorimetry (DSC) .....	149
4.3.3	Relaxometry NMR.....	149
4.3.3.1	Carr-Purcell-Meiboom-Gill (CPMG) sequence.....	150
4.3.3.2	Inversion Recovery pulse sequence (Inv-CPMG).....	150
4.3.3.3	Pulsed Field Gradient NMR.....	150
4.3.3.3.1	CMPG Pulsed Gradient Spin Echo sequence (CMPG-PGSE)....	152
4.3.3.3.2	Stimulated echo diffusion sequence (PGSTE diffusion).....	152
4.4	Results and discussion.....	153
4.4.1	Interior microstructure of freeze-dried gels .....	153
4.4.2	Determination of free water content using DSC .....	157
4.4.3	Molecular understanding of water distribution in the gels studied by Relaxometry NMR.....	163
4.4.3.1	Carr-Purcell-Meiboom-Gill (CPMG) sequence.....	164
4.4.3.2	Inversion Recovery pulse sequence (Inv-CPMG).....	169
4.4.3.3	CPMG-Pulsed Gradient Spin Echo sequence (CPMG-PGSE).....	174
4.4.4	Stimulated echo diffusion sequence (PGSTE diffusion) .....	176
4.5	Conclusions.....	178
<b>5</b>	<b>Physicochemical characterisation of lysozyme-loaded Gelucire</b>	
<b>50/13 gels</b>		<b>180</b>
5.1	Introduction.....	180
5.2	Objectives .....	181
5.3	Materials and methods.....	181
5.3.1	Attenuated Total Reflectance Infrared (ATR-FTIR) Spectroscopy.....	181
5.3.1.1	Determination of protein secondary structure.....	182
5.3.2	Small Angle X-ray Scattering (SAXS) .....	182
5.3.3	Conventional Differential Scanning Calorimetry (DSC).....	183
5.3.4	Rheology .....	183
5.3.5	Texture analyser .....	185
5.3.6	Statistical analysis .....	185
5.3.7	Lysozyme release mechanisms .....	185
5.4	Results and Discussion.....	190
5.4.1	Structural analysis of lysozyme-loaded gels using ATR-FTIR spectroscopy 190	
5.4.1.1	Secondary structure determination with ATR-FTIR spectroscopy... 191	
5.4.2	Structural analysis of Lysozyme loaded gels using SAXS .....	195

5.4.3	Thermal phase transitions of gels studied using thermal analysis and rheology.....	199
5.4.3.1	Thermal analysis .....	199
5.4.3.2	Temperature ramp test (Oscillation Rheometer).....	202
5.4.4	Rheological properties of lysozyme-loaded gels .....	205
5.4.4.1	Determination of the linear viscoelastic region: the oscillation stress sweep test .....	205
5.4.4.2	Oscillation frequency sweep test.....	207
5.4.4.3	Continuous flow test .....	213
5.4.5	Mechanical properties of gels .....	214
5.4.5.1	Texture Profile Analysis (TPA) .....	214
5.4.6	Evaluation of the mucoadhesive properties of gels.....	215
5.4.7	Lysozyme release profile .....	218
5.4.7.1	Dissolution studies .....	218
5.4.7.2	Diffusion studies .....	225
5.5	Conclusions.....	226

## 6 Development of nanoparticles based on Gelucire 50/13 gels

### 228

6.1	Introduction.....	228
6.2	Objectives .....	229
6.3	Materials and methods.....	229
6.3.1	Dynamic Light Scattering (DLS).....	230
6.3.2	Atomic force microscopy (AFM).....	230
6.3.3	Encapsulation efficiency (%EE) .....	230
6.3.4	Lysozyme activity assay .....	231
6.3.4.1	Assay procedure .....	231
6.3.4.2	Calculation of the retained biological activity (%RBA) of lysozyme	232
6.3.5	Circular Dichroism (CD).....	233
6.4	Results and discussion.....	233
6.4.1	Nanoparticles preparation method development.....	233
6.4.1.1	Physical stability .....	235
6.4.1.2	Shape analysis .....	238
6.4.1.2.1	Cryo-TEM .....	238
6.4.1.2.2	Atomic force microscopy (AFM).....	240
6.4.2	Physical characterisation of lysozyme-loaded nanoparticles.....	244
6.4.2.1	Physical stability .....	244
6.4.2.2	Shape analysis .....	246
6.4.2.3	Lysozyme Encapsulation Efficiency (%EE).....	248
6.4.2.4	Proposed molecular model of lysozyme-loaded nanoparticles.....	248
6.4.2.5	Lysozyme activity and retained biological activity (%RBA) .....	249
6.4.2.6	Assessment of the structural conformation of the lysozyme by using Circular Dichroism (CD).....	251
6.4.3	In vitro cytotoxicity study .....	252

6.4.4 Cellular uptake .....	256
6.5 Conclusions.....	259
<b>7 Conclusions and Future work.....</b>	<b>260</b>
<b>8 Appendix.....</b>	<b>266</b>
8.1 Appendix I: ATR-FTIR.....	266
8.2 Appendix II: SAXS.....	271
<b>9 References.....</b>	<b>274</b>

## List of Figures

- Figure 1.1** Schematic view of the intestinal trans-epithelial pathways: (a) transcellular active transport or receptor-mediate transport, (b) transcellular passive transport through the cells; (c) paracellular pathway through tight junctions between adjacent cells. The transcellular passive transport can be enhanced by encapsulation of active components in particulate systems which are preferably uptake by the M-cells of Payer’s patches and through which they are transported in the lymphatic circulation [9]. ..... 2
- Figure 1.2** (a) Schematic representation of a molecular structure of a mucin monomer; (b) the single units of the monomers; (c) a dimer formed by two monomeric units linked by disulphide bonds; (d) a multimer composed of multiple dimers linked by disulphide bonds [42]. ..... 10
- Figure 1.3** Mechanical bonds through interpenetrations and entanglement between bioadhesive polymer chains and mucin chains [44]. ..... 11
- Figure 1.4** Schematic view of the two phases in which the mucoadhesion process can be divided. The contact stage (I) in which the mucoadhesive polymers and the mucous membrane come into contact and the consolidation stage (II) which is characterised by the formation of non-covalent bonds and the diffusion and interpenetration of polymers and mucin chains [45]. 12
- Figure 1.5** Typical structures of lipid based delivery systems; modified from ref. [10]. ..... 16
- Figure 1.6** A) Plain liposomes with hydrophilic drug (a) encapsulated in the aqueous core or hydrophobic drug (b) incorporated in the membrane; B) immunoliposomes with antibodies covalently linked (c) or hydrophobically linked (d) to the liposomal membrane; C) Long-circulating liposomes with grafted polymers (e), such as PEG, which shelter the liposomes from the recognition from the opsonins (f); D) long-circulating immunoliposomes combining both polymers and antibody, which can be attached to the liposomal membrane (g) or to the polymeric chain (h); E) new generation liposomes with the surface of which can undergo different modifications: (i) polymer, (j) polymer-ligand conjugate, (k) attachment of diagnostic label, (l) incorporation of positively charged liposomes suitable for DNA complexation (m), (n) incorporation of stimuli-sensitive lipids, (o) incorporation of stimuli-sensitive polymers; (p) attachment of cell penetrating peptide; (q) incorporation of viral component. In addition, magnetic (s) or colloidal particles (r) may also be loaded [59]. ..... 18
- Figure 1.7** Liposomes-cell interactions of drug-loaded liposomes (A) and modified liposomes with viral components (B) [59]. ..... 19
- Figure 1.8** Illustration of the proposed possible drug absorption mechanisms when delivered using SLN. Nanoparticles can directly adhere to the mucosal wall of the intestine and deliver the drug into the site of absorption. They can also be degraded by lipase and co-lipase which leads to the formation of mono and diglycerides which are responsible for the solubilisation of the drug. Bile salts can interact with micelles forming mixed micelle which leads finally to the uptake of both lipid and drug [76]. ..... 22

<b>Figure 1.9</b> Hypothetical lipid/water phase diagram in which the phase transition depends on the water content. The regions indicated with a, b, c and d represent the intermediate phases, many of which are cubic [79]. .....	23
<b>Figure 1.10</b> (a) Different liquid crystalline phases with the corresponding packing parameter, $P$ ( $P=V/al$ ). Cryo-TEM images of dispersed reversed hexagonal phase (b); dispersed bicontinuous cubic phase, Im3m (c); vesicle obtained from dispersed lamellar phase (d); and micelle (e) [80]. .....	24
<b>Figure 1.11</b> Schematic view of the conformations of PEG: (a) helical (TTG) <sub>7</sub> , (b) zig-zag Type I (T <sub>5</sub> GT <sub>5</sub> G) and (c) zig-zag Type II (TG <sub>2</sub> TG <sub>2</sub> ), where T stands for trans and G for gauche [113]. .....	29
<b>Figure 1.12</b> Schematic view of the molecular conformation of MPEG and DPEG with the PEG chains in helical conformation and one or two acyl chains in the end [109]. .....	30
<b>Figure 1.13</b> Primary structure of hen egg-white lysozyme with four disulphide bonds between two groups of cysteine (CYS) (in dark boxes). The residues involved in $\alpha$ -helical conformations are highlighted with continuous black lines and the residues involved in binding sites are underlined [142]. .....	35
<b>Figure 1.14</b> Schematic representation of the 3D conformation of the main chain of lysozyme; $\alpha$ -helices (red), $\beta$ -sheet (blue) and the irregular loops or unordered structure (grey) [143]. .....	35
<b>Figure 2.1</b> Chemical structure of coumarin-6 .....	41
<b>Figure 2.2</b> Emulsiflex C-5 high-pressure homogeniser (adapted from AVESTIN brochure). ..	43
<b>Figure 2.3</b> Schematic representation of heat flux DSC (a) and power compensation DSC (b). A= furnaces; B=termocouples; C=sample and reference platinum resistance thermometers [149]. .....	45
<b>Figure 2.4</b> Shear stress applied to hypothetical layers of a fluid; the upper layer is sliding laterally relatively to the lower part. ....	46
<b>Figure 2.5</b> Schematic view of the mechanical models for an ideal solid (a), an ideal liquid (b) and viscoelastic materials represented in two different models: (c) and (d). .....	47
<b>Figure 2.6</b> Flow curves of non-Newtonian and Newtonian liquid. (a) Shear stress versus shear rate, and (b) viscosity versus shear rate in logarithmic scale. ....	47
<b>Figure 2.7</b> Representation of an oscillatory test with plate-plate geometry. A sinusoidal oscillation of a maximum strain, $\gamma_0$ (red line wave) is applied at an oscillatory frequency, $\omega$ . A resulting stress wave is obtained (black-line wave). For ideal elastic solid, the two waves are in phase ( $\delta=0$ ); for ideal viscous liquid, the stress and the strain are $\pi/2$ out of phase; for viscoelastic materials they lag by an angle $\delta$ ( $0 < \delta < \pi/2$ ). The elastic ( $G'$ ) and the viscous ( $G''$ ) components can be separated and the plots of frequency versus moduli can be obtained. ....	49
<b>Figure 2.8</b> Schematic view of the AR series rheometer technology and of the geometry details (TA Instruments, AR series and Peltier plate brochure). .....	50

<b>Figure 2.9</b> Viscoelastic behaviour of Non-Newtonian liquids over a broad range of frequency (adapted from reference [155]).	51
<b>Figure 2.10</b> Schematic representation of a Standard Peltier plate and cover used to prevent water loss (TA Instrument, Peltier plate brochure).	52
<b>Figure 2.11</b> Diagram of an ideal flow curve.	53
<b>Figure 2.12</b> Typical force-time plot for a TPA test. H indicates the hardness; $A_1$ is the compressibility; $A_3$ the adhesiveness and $A_2/A_1$ is the cohesiveness. The graph was obtained from a TPA test performed on the Gelucire 50/13 gel with 65 % water content prepared with hydration method.	55
<b>Figure 2.13</b> Typical force-distance plot obtained from an adhesive test using a texture analyser. The height of the peak is the maximum detachment force (N), the area under the curve is the work of adhesion or the total amount of forces involved in the probe withdrawal. The graph is a result of the adhesion test of the gel with 60% of water prepared by heating method and the mucin tablet.	56
<b>Figure 2.14</b> Scheme of scattering geometry. $k_0$ is the wave vector of the incident light, $k_s$ and $I_s$ are the wave vector and the intensity of the scattered light. The angle $\varphi$ is assumed to be $90^\circ$ [169].	57
<b>Figure 2.15</b> Illustration of scattering geometry interpretation [176].	61
<b>Figure 2.16</b> Schematic representation of the components of a SAXS instrument [177].	64
<b>Figure 2.17</b> SAXS set up used in this project.	64
<b>Figure 2.18</b> Spin $\frac{1}{2}$ at equilibrium, prior application of the magnetic field $B_1$ (left) and soon after the application of the magnetic field $B_1$ (right) [187].	66
<b>Figure 2.19</b> A typical CPMG pulse sequence	69
<b>Figure 2.20</b> A typical Inversion Recovery CPMG sequence	70
<b>Figure 2.21</b> A typical CPMG-PGSE sequence, where $\tau_1$ is the CPMG value, $\tau_2$ is the PGSE tau, $\Delta$ is the diffusion time or pulse gradient separation, $\delta$ is the pulse gradient duration and $G$ is the pulse gradient strength.	70
<b>Figure 2.22</b> A typical PGSTE diffusion sequence, where $\Delta$ is the diffusion time or pulse gradient separation, $\delta$ is the pulse gradient duration and $G$ is the pulse gradient strength. $t_1$ is the pre-gradient delay and $t_2$ the pulse gap.	71
<b>Figure 2.23</b> 23.4 MHz NMR (Maran Ultra) interfaced to a DRX console (on the left).	72
<b>Figure 2.24</b> Detail of the bottom part of a NMR sample tube loaded with gel 50% of water or below (a) and sample tube loaded with gel with 70% of water or above.	73

- Figure 2.25** (a) Left (L) and right (R) circularly polarised component of the light: when the two components have the same amplitude they recombine in the original plane (I), if they have different magnitude they combine in a elliptical (dashed line) polarised plane (II). (b) The diagram compares the absorption and the CD spectra: band 1 is from an achiral sample, which produces no CD band; band 2 generates a positive CD band (L absorbs more than R); band 3 has a negative CD spectrum (R absorbs more than L) [206]. ..... 76
- Figure 2.26** Plastic gel sample holder for dissolution test equipped with a metal plate and filled with gel with 60% water. .... 80
- Figure 2.27** Illustration of the setup of Franz cells (PermeGear). .... 80
- Figure 3.1** (a) cell for pastes used to perform the experiments in this work open, the sample is spread in the central part (identified by the black ring) on the top of the kapton® polyimide tape (brown line). (b) View of the cell closed after having loaded the sample. .... 86
- Figure 3.2** ATR-FTIR spectrum of dry Gelucire 50/13 powder (n=4). .... 93
- Figure 3.3** Partial IR spectra in the region between 4000 and 2000  $\text{cm}^{-1}$  of the gels prepared with ultrapure water by using heating method (analysed at room temperature). The spectrum of the dry Gelucire 50/13 powder is also shown for comparison (black line). .... 95
- Figure 3.4** Partial IR spectra between 1800 and 800  $\text{cm}^{-1}$  of the gels prepared with ultrapure water by using heating method, analysed at room temperature. The spectrum of the dry Gelucire 50/13 powder is also shown for comparison (black line). .... 96
- Figure 3.5** Partial IR spectra of the gels prepared with ultrapure water by using heating method, analysed at 37 °C between 1800 and 800  $\text{cm}^{-1}$ . The IR spectrum of Gelucire 50/13 powder is also shown for comparison (black line). .... 97
- Figure 3.6** Partial IR spectra (3800-2000  $\text{cm}^{-1}$ ) of the gels prepared with D<sub>2</sub>O by using heating method, analysed at room temperature. The Gelucire 50/13 powder is also shown for comparison (black line). .... 98
- Figure 3.7** Partial IR spectra of the gels prepared with D<sub>2</sub>O by using heating method, analysed at room temperature. The spectrum of the dry Gelucire 50/13 powder is also shown for comparison (black line). The arrow indicates the peak at 1205  $\text{cm}^{-1}$ . .... 99
- Figure 3.8** Partial IR spectra of the gels prepared with D<sub>2</sub>O by using hydration method, analysed at room temperature. The spectrum of the dry Gelucire 50/13 powder is also shown for comparison (brown line). The arrow indicates the peak at 1205  $\text{cm}^{-1}$ . .... 100
- Figure 3.9** IR spectra (3800-2000  $\text{cm}^{-1}$ ) of the gels prepared with D<sub>2</sub>O by using hydration method. The Gelucire 50/13 powder is also shown for comparison (black line). .... 100
- Figure 3.10** SAXS spectrum of the intensity versus  $q$  ( $\text{\AA}^{-1}$ ) of the gel with 10% water prepared by hydration and corresponding peaks position (25 °C). The peak position framed corresponds to a second lamellar phase. .... 101

---

<b>Figure 3.11</b> SAXS spectrum of the intensity versus $q$ ( $\text{\AA}^{-1}$ ) of the gel with 40% water prepared by hydration and corresponding peaks position (25 °C). The peak position framed corresponds to a second lamellar phase. ....	102
<b>Figure 3.12</b> SAXS spectrum of the intensity versus $q$ ( $\text{\AA}^{-1}$ ) of the gel with 60% water prepared by hydration (25 °C) and corresponding peaks position. The peak position framed corresponds to a second lamellar phase. ....	103
<b>Figure 3.13</b> Variable temperature SAXS spectra of the gel with 50% water content prepared by hydration upon heating from 25 °C to 37 °C and cooling back to 25 °C (indicated by the arrow ). ....	103
<b>Figure 3.14</b> Variable temperature SAXS spectra of the gel with 70% water prepared by hydration upon heating from 25 °C to 37 °C and cooling back to 25 °C (indicated by the arrow). ....	104
<b>Figure 3.15</b> DSC results of the gels prepared by heating method upon heating from 20 to 80°C. The inset shows an enlarged view of the boxed region (dashed rectangle) between 37 and 65 °C. ....	106
<b>Figure 3.16</b> DSC results of the gels prepared by heating method upon cooling from 80 to 0°C. The inset shows an enlarged view of the boxed region (dashed rectangle) between 25 and 55 °C. ....	107
<b>Figure 3.17</b> DSC results of the gels prepared by hydration method upon heating from 20 to 80°C. The inset shows the enlarged view of the boxed region (dashed rectangle) between 37 and 75 °C. ....	108
<b>Figure 3.18</b> DSC results of the gels prepared by hydration method upon cooling back from 80 to 0°C. The inset shows an enlarged view of the boxed region (dashed rectangle) between 25 and 55 °C. ....	109
<b>Figure 3.19</b> DSC results of the second heating cycle of the gel with 10% water content prepared by heating method. ....	110
<b>Figure 3.20</b> Temperature influence on the elastic modulus ( $G'$ ) for the gels prepared by heating method. ....	112
<b>Figure 3.21</b> Elastic modulus ( $G'$ ) response to the decreasing of temperature from 80° to 25 °C in the gels prepared by heating. ....	113
<b>Figure 3.22</b> Comparison between the thermogram (black line) and the rheogram (-■-) of the gel with 10% water content prepared by heating method obtained during the heating cycle. ....	113
<b>Figure 3.23</b> Comparison the thermogram (black line) and the rheogram (-■-) of the gel with 10% water content prepared by heating method and obtained during the cooling cycle. ....	114
<b>Figure 3.24</b> Comparison the thermogram (black line) and the rheogram (-■-) of the gel with 80% water prepared by heating method and obtained during the heating cycle. ....	115

---

<b>Figure 3.25</b> Comparison the thermogram (black line) and the rheogram (-■-) of the gel with 80% water prepared by heating method and obtained during the cooling cycle.....	115
<b>Figure 3.26</b> Temperature influence on the $G'$ for the gels prepared by hydration.....	116
<b>Figure 3.27</b> Elastic modulus ( $G'$ ) response to the decreasing of temperature from 80° to 25 °C in the gels prepared by hydration.....	117
<b>Figure 3.28</b> Complex modulus ( $ G^* $ ) versus oscillation stress plot of the gels prepared by heating method measured at 37 °C. ....	118
<b>Figure 3.29</b> Complex modulus ( $ G^* $ ) versus oscillation stress plot of the gels prepared by hydration measured at 37 °C.....	119
<b>Figure 3.30</b> Phase angle (delta) versus oscillation stress plot of the gels prepared by hydration method. The test was performed at 37 °C.....	119
<b>Figure 3.31</b> Phase angle (delta) versus oscillation stress plot of the gels prepared by heating method. The test was performed at 37 °C.....	120
<b>Figure 3.32</b> Plots of elastic modulus ( $G'$ ) and viscous modulus ( $G''$ ) versus frequency (Hz) for the gels prepared by hydration method (measured at 37 °C). ....	121
<b>Figure 3.33</b> Effects of the frequency (Hz) on the loss tangent ( $\tan\delta$ ) for the gels prepared by hydration (measured at 37 °C). ....	122
<b>Figure 3.34</b> Plot of elastic modulus ( $G'$ ) and viscous modulus ( $G''$ ) versus frequency (Hz) for the selected gels prepared by heating method and measured at 25 °C.....	122
<b>Figure 3.35</b> Plots of elastic modulus ( $G'$ ) and viscous modulus ( $G''$ ) versus frequency (Hz) for the gels prepared by heating method (measured at 37 °C). ....	123
<b>Figure 3.36</b> Effects of the frequency (Hz) on the loss tangent ( $\tan\delta$ ) for gels prepared by heating measured at 37 °C. ....	124
<b>Figure 3.37</b> Dynamic viscosity ( $\eta'$ , Pa.s) versus frequency (Hz) for gels prepared by heating (measured at 37 °C). ....	124
<b>Figure 3.38</b> Dynamic viscosity ( $\eta'$ , Pa.s) versus frequency (Hz) for gels prepared by hydration (measured at 37 °C). ....	125
<b>Figure 3.39</b> Flow index plot for gels prepared by heating determined with continuous flow test at 25 °C, 37 °C, 50 °C and 80 °C.....	127
<b>Figure 3.40</b> Flow index plots of the gels prepared by hydration (measured using continuous flow test at 25 °C, 37 °C, 50 °C and 80 °C).....	130
<b>Figure 3.41</b> Consistency index of gels prepared by heating (-■-) and hydration (-■-) method determined at different temperatures (25 °C, 37 °C, 50 °C and 80 °C). ....	133

---

<b>Figure 3.42</b> Comparison of the TPA parameters of gels prepared by heating method compressed twice at the depth of 5 and 10 mm. ....	135
<b>Figure 3.43</b> Adhesiveness (N.s), hardness (N) and compressibility (N.s) of gels prepared by heating. The data are presented as mean ( $\pm$ SD) $n \geq 4$ . ....	138
<b>Figure 3.44</b> Adhesiveness (N.s), hardness (N) and compressibility (N.s) of gels prepared by hydration. The data are presented as mean ( $\pm$ SD) $n \geq 4$ . ....	138
<b>Figure 3.45</b> Maximum detachment force of the gels prepared by heating method and by hydration from mucin tablets (tested at room temperature). ....	143
<b>Figure 3.46</b> Total work of adhesion of the gels prepared by heating method and by hydration from mucin tablets (tested at room temperature). ....	143
<b>Figure 3.47</b> (a) Comparison of the work of adhesion (N.s) determined by adhesive test performed on the gels prepared by heating and hydration methods with mucin tablets and porcine small intestine tissue. (b) The adhesiveness obtained from TPA test for the purpose of comparison of the adhesion of the gels towards biological and non-biological surfaces. ....	144
<b>Figure 4.1</b> SEM images of the freeze-dried gels originally prepared by heating method with 10% to 90% water content (w/w). ....	154
<b>Figure 4.2</b> SEM images of freeze-dried gels originally prepared by hydration with 10-90% water content. ....	156
<b>Figure 4.3</b> DSC results of the gels prepared by heating method at a scanning rate of 5 °C/min. An enlarge view of the peaks inside the dashed rectangle is shown in the inset. ....	158
<b>Figure 4.4</b> DSC results of the gels prepared by heating method determined at the scanning rate of 2°C/min. An enlarge view of the peaks inside the dashed rectangle is shown in the inset. .	159
<b>Figure 4.5</b> DSC results of the gels prepared by hydration method determined at the scanning rate of 5 °C/min. ....	160
<b>Figure 4.6</b> DSC results of the gels prepared by hydration method, determined by DSC at 2°C/min. ....	160
<b>Figure 4.7</b> Free water ( $W_F$ ) calculated at 5°C/min. ....	162
<b>Figure 4.8</b> Free water ( $W_F$ ) calculated at 2°C/min. ....	162
<b>Figure 4.9</b> 1-D $T_2$ proton spectra obtained by inverse Laplace transformation of the CPMG echo decay for the gels between 10%-90% water contents. ....	165
<b>Figure 4.10</b> Slowest ( $T_s$ ) and faster ( $T_f$ ) relaxation time versus water content of the gels. ....	168
<b>Figure 4.11</b> Weighted populations $P_s$ and $P_f$ versus water content. $P_{H_2O}$ is the calculated relative populations of water protons in the gels. ....	168

- Figure 4.12** 2D  $T_1$ - $T_2$  relaxation maps of the gels with 10% to 90% water contents. The dashed rectangles identify the reliable values set by the pulse sequence. The diagonal lines indicates the condition where  $T_1 = T_2$ . ..... 171
- Figure 4.13** Relaxation time ( $T_2$ ) versus diffusion coefficient plot for the gels with 70% water (a) and 80% water (b). The dashed line identify the limits of reliability of the experiment. .... 175
- Figure 4.14** Plots of echo amplitudes ( $\ln S$ ) attenuation as a function of  $q^2\Delta$  measured at the diffusion time of 56.4 ms for gels prepared by heating with water contents of 10% to 90%. The values were normalised to the signal amplitude at  $q=0$  ( $n=3$ ). ..... 176
- Figure 4.15** Plots of echo amplitudes ( $\ln S$ ) attenuation as a function of  $q^2\Delta$  measured at the diffusion time of 241.6 ms for gels prepared by heating with 10% to 90% water contents. The values were normalised to the signal amplitude at  $q=0$  ( $n=3$ ). ..... 177
- Figure 5.1** UV calibration plots of lysozyme in pH 7.4 phosphate buffer (a) and HCl, 0.1 M (b), for dissolution studies. The adjusted R-square and the slope values ( $\pm$ SE) are also listed in the tables for each plot. .... 189
- Figure 5.2** UV calibration curve of lysozyme in phosphate buffer for diffusion study. The adjusted R-squared and the slope values ( $\pm$ SE) are also listed in the tables for each plot. .... 190
- Figure 5.3** Partial ATR-FTIR spectrum of the Amide I region of lysozyme in  $D_2O$  (black line) and fitted curves (bottom). The second derivative of this section of the spectra is also shown on the top. .... 192
- Figure 5.4** Second derivative of the 10% lysozyme in  $D_2O$  with the assignment of the secondary structure conformation. .... 193
- Figure 5.5** Second derivative of the lysozyme-loaded gels prepared by hydration with  $D_2O$ . 193
- Figure 5.6** SAXS spectrum of the lysozyme-loaded gel with 40% water prepared by hydration (measured at 25 °C). ..... 196
- Figure 5.7** Variable temperature SAXS spectrum of the lysozyme-loaded gel with 50% water prepared by hydration upon heating from 25 °C to 37 °C and cooling back to 25 °C. The direction of the arrow indicate the direction of the heating-cooling process. .... 196
- Figure 5.8** SAXS spectrum of the intensity versus  $q$  ( $\text{\AA}^{-1}$ ) of the lysozyme-loaded gel at 25 °C with 70% water prepared by hydration. .... 198
- Figure 5.9** SAXS spectrum of the intensity versus  $q$  ( $\text{\AA}^{-1}$ ) of the lysozyme-loaded gel at 37 °C with 70% water prepared by hydration. .... 198
- Figure 5.10** DSC results for the lysozyme-loaded gels prepared by hydration method upon heating from 20 to 80°C. The profile of dry Gelucire powder is also shown for comparison. . 200
- Figure 5.11** DSC results of the lysozyme-loaded gels prepared by hydration method during cooling from 80 °C to 0 °C. The profile of Gelucire powder is also shown for comparison.... 201

<b>Figure 5.12</b> Temperature influence on the elastic modulus ( $G'$ ) of the lysozyme-loaded gels prepared by hydration during heating (25 °C to 80 °C) (n = 3).....	203
<b>Figure 5.13</b> Temperature influence on the elastic modulus ( $G'$ ) of the lysozyme-loaded gels prepared by hydration during cooling (80 °C to 25 °C) (n = 3).....	204
<b>Figure 5.14</b> Complex moduli ( $ G^* $ , Pa) versus oscillation stress plot of the lysozyme-loaded gels prepared by hydration method (n = 3).....	205
<b>Figure 5.15</b> Phase angle ( $\delta$ ) (degrees) versus oscillation stress plot of the lysozyme-loaded gels prepared by hydration (n = 3). .....	206
<b>Figure 5.16</b> Comparison of phase angle ( $\delta$ ) versus oscillation stress plots of the lysozyme-loaded gels with 40% and 60% water content prepared by heating and by hydration (n = 3)..	207
<b>Figure 5.17</b> Elastic modulus ( $G'$ ) and viscous modulus ( $G''$ ) versus frequency (Hz) plots for the lysozyme-loaded gels prepared by hydration method (n = 3).....	208
<b>Figure 5.18</b> Effects of the frequency (Hz) on the loss tangent ( $\tan\delta$ ) for the lysozyme-loaded gels prepared by hydration method (n = 3).....	209
<b>Figure 5.19</b> Dynamic viscosity ( $\eta'$ , Pa.s) versus frequency (Hz) plots for the lysozyme-loaded gels prepared by hydration (n = 3).....	210
<b>Figure 5.20</b> Comparison of $G'$ (Pa) and $G''$ (Pa) versus frequency (Hz) plots ( $\pm$ SD) for the lysozyme-loaded gels with 40% and 60% water contents prepared by heating (filled symbols) and by hydration methods (open symbols) (n $\geq$ 3). .....	211
<b>Figure 5.21</b> Adhesiveness (N.s), hardness (N) and compressibility (N.s) of the lysozyme-loaded gels prepared by hydration. The data are presented as mean ( $\pm$ SD) (n = 3). .....	215
<b>Figure 5.22</b> (a) Comparison of the work of adhesion (N.s) determined by adhesive test performed on the lysozyme-loaded gels and unloaded gels prepared by hydration with mucin tablets. (b) Comparison of the adhesiveness obtained from TPA performed on the lysozyme-loaded and unloaded gels prepared by hydration.....	217
<b>Figure 5.23</b> Percentage of lysozyme released from the gels with 30%, 40%, 50%, 60% and 65% water contents prepared by heating method in phosphate buffer (pH=7.4) at 37 °C (n = 3, $\pm$ SD). .....	218
<b>Figure 5.24</b> Lysozyme released from the gels with 30%, and 60% water contents prepared by hydration method in phosphate buffer (pH=7.4) at 37 °C (n = 3, $\pm$ SD). .....	219
<b>Figure 5.25</b> Percentage of lysozyme released from the gels with 30%, 40%, 50%, 60% and 65% water content prepared by heating method in HCl 0.1 M at 37 °C (n = 3, $\pm$ SD).....	222
<b>Figure 5.26</b> Percent released of lysozyme from the gels with 30% and 50% water prepared by heating method in phosphate buffer (pH=7.4) at 37 °C tested using Franz diffusion cells (n = 6, $\pm$ SD).....	225

---

<b>Figure 5.27</b> Percent released of lysozyme from the gel with 50% water prepared by hydration method in phosphate buffer (pH=7.4) at 37 °C tested with Franz diffusion cells (n = 6, ± SD). .....	226
<b>Figure 6.1</b> Calibration plot of lysozyme in Milli-Q water. The adjusted R-squared and the slope values (±SE) are also listed in the tables.....	231
<b>Figure 6.2</b> Changes of size distribution (d.nm) of the nanoparticle formulations F2, F3 and F4 prepared by being passed through the high-pressure homogeniser with different number of cycles (n = 3).....	234
<b>Figure 6.3</b> Mean particle size (d.nm) of the main population of formulations F2, F3 and F4 by varying the number of cycles with the high pressure homogeniser (n = 3, ± SD). ....	235
<b>Figure 6.4</b> Correlation function of the nanoparticle formulations analysed at day 1 at 37 °C.	236
<b>Figure 6.5</b> Size distribution (d.nm) of freshly prepared nanoparticle formulations (n = 3). ....	237
<b>Figure 6.6</b> (a) Cryo-TEM image of the nanoparticles of the formulation F2. (b) Histogram chart of the particle size of F2 formulation, measured from cryo-TEM images (plotted using frequency versus size interval). The upper part is the probability plot. ....	239
<b>Figure 6.7</b> (a) Cryo-TEM image of the nanoparticles of the formulation F2. (b) Histogram chart of the particle size of F2 formulation, measured from cryo-TEM images (plotted using frequency versus size interval). The upper part is the probability plot. ....	240
<b>Figure 6.8</b> AFM images of the nanoparticles formulations: a) F1; b) F2; c) F3; d) F4 and e) F5. .....	242
<b>Figure 6.9</b> Schematic view of the 3D-dimensions disc-like shape nanoparticles. ....	242
<b>Figure 6.10</b> Correlation function of the formulations analysed at day 1 at 37 °C.....	244
<b>Figure 6.11</b> Tapping mode AFM images and the topographic analysis of the lysozyme-loaded nanoparticles: a) F2; b) F4; c) F5.....	247
<b>Figure 6.12</b> Proposed model of disc-shape nanoparticle with lysozyme molecules encapsulated (a). A legend with the species present in the nanoparticles is also shown (b). ....	249
<b>Figure 6.13</b> Decrease in absorbance versus time of micrococcus lysodeikticus incubated with lysozyme solution and lysozyme-loaded nanoparticle formulations. ....	250
<b>Figure 6.14</b> Near UV CD spectra of lysozyme solution and lysozyme-loaded nanoparticles. Lysozyme aqueous solution was prepared at room temperature as control. ....	252
<b>Figure 6.15</b> Microscopy images of H292 cells incubated with the dilutions of F2 nanoparticle suspension for 24 hours at 37°C and treated with trypan blue. a) Control (cells without nanoparticles); b) stock solution, 600µg/ml; c) D1; d) D2; e) D3; f) D4; g) D5; h) D3 (after 48hrs incubation). ....	254

---

<b>Figure 6.16</b> In vitro cell viability of cells H292 incubated with different concentrations of nanoparticles at 37°C for 24 hours or 48 hours and determined microscopically by counting the blue stained cells (non-viable) by using trypan blue dye.....	255
<b>Figure 6.17</b> Cell viability (% $\pm$ SD) of H292 model cell line determined using MTS assay (n=3). .....	255
<b>Figure 6.18</b> Cell viability of Caco-2 model cell line incubated with F2 nanoparticle suspensions determined with MTS assay. The percentage was calculated relatively to the control (n=3)...	256
<b>Figure 6.19</b> <i>In vitro</i> Caco-2 cellular uptake of the F2 nanoparticles from dilutions D1 (a) and D4 (b) after 15 minutes of incubation. The images were taken under fluorescent light (upper row) and normal light (lower row).....	257
<b>Figure 6.20</b> <i>In vitro</i> Caco-2 cellular uptake of the F2 nanoparticles from dilutions D4 after 120 minutes of incubation (overlay image). .....	257
<b>Figure 6.21</b> <i>In vitro</i> Caco-2 cellular uptake of the dilution D2 of the unloaded F2 nanoparticles from dilutions (200 $\mu$ g/ml) after 30 minutes (a), 240 minutes (b) and after 24 hours (c) of incubation. The images were taken under fluorescent light (upper row) and normal light (lower row).....	258
<b>Figure 7.1</b> TEWL results for gel with 70% water content prepared by heating at time 0 and after 1 hour of application of the gel on the inner forearm of the volunteer. ....	263
<b>Figure 7.2</b> SEM image of spray-freeze dried nanoparticles.....	264

---

## List of Tables

<b>Table 1.1</b> List of the PEGylated macromolecules in the market (adaptated from reference [10]). .....	5
<b>Table 1.2</b> Composition of Gelucire 50/13 with the structure and the long spacing of each individual component [109].	28
<b>Table 2.1</b> List of gel and the nanoparticles formulations studied in this project.	42
<b>Table 2.2</b> Buffer solutions used in this project.	44
<b>Table 2.3</b> List of the rheological properties that can be obtained by performing an oscillatory test.	50
<b>Table 2.4</b> Light scattering theories.	58
<b>Table 2.5</b> Peak spacing ratio (Bragg peaks) and corresponding Miller indices for lamellar ( $L_n$ ), hexagonal ( $H_{I/II}$ ), Gyroid cubic (Ia3d), Diamond cubic (Pn3m) and Primitive cubic (Im3m) [179-181].	63
<b>Table 2.6</b> Assignment for the Amide I bands in the FTIR.	75
<b>Table 2.7</b> Dilutions with sterile water and corresponding final lipid concentrations in each dilution.	82
<b>Table 3.1</b> List of samples and experimental conditions adopted for the ATR-FTIR tests.	86
<b>Table 3.2</b> Experimental details adopted for the gels with 10%, 40% and 60% water prepared by hydration and gel with 60% water prepared by heating. The tests were performed at 25 °C. The duration time of the test for each sample is also described.	87
<b>Table 3.3</b> Temperature ramp performed on the gels with 50% and 70% water prepared by hydration and heating methods. The temperature and the duration time of the test (in seconds) per cycle are also listed.	87
<b>Table 3.4</b> IR band position and assignments for dry Gelucire 50/13 powder.	94
<b>Table 3.5</b> Assignment of the peaks for the gel with 50% water prepared by heating method analysed with varying the temperature. The $q$ ( $\text{\AA}^{-1}$ ) and $d$ ( $\text{\AA}$ ) values as well as the peak positioning at Bragg values are listed.	105
<b>Table 3.6</b> Mean of the onset temperature ( $T_h$ ), the peak temperature ( $T_p$ ) and the enthalpy of the main peak ( $\Delta H$ ) $\pm$ SD of the samples prepared by heating determined in a heating and cooling cycle (n=3).	108

<b>Table 3.7</b> Mean of the onset temperature ( $T_h$ ), the peak temperature ( $T_p$ ) and the enthalpy of the main peak ( $\Delta H$ ) $\pm$ SD of the samples prepared by hydration determined in a heating and cooling cycle (n=3). .....	110
<b>Table 3.8</b> Mean values of consistency ( $\pm$ SE) and flow ( $\pm$ SE) indexes for the gels prepared by heating method (measured at 25 °C, 37 °C, 50 °C and 80 °C). Measurements were performed in triplicate or quintuplicate . .....	129
<b>Table 3.9</b> Mean values of consistency ( $\pm$ SE) and flow ( $\pm$ SE) indices for the samples prepared by hydration method (measured at 25 °C, 37 °C, 50 °C and 80 °C). Measurements were performed in triplicate or quintuplicate. ....	132
<b>Table 3.10</b> Effect of the probe withdrawal speed on the hardness (N), compressibility (N.s) and adhesiveness (N.s) of the gel with 30% water prepared by heating. The values are presented as the mean ( $\pm$ SD) of at least three repetitions.....	135
<b>Table 3.11</b> Summary table of variance analysis for the compressibility, hardness and adhesiveness of the gels. ....	136
<b>Table 3.12</b> Effects of penetration distance of the probe within each level of concentration based on a linearly independent pairwise comparison among the estimated marginal means.....	137
<b>Table 3.13</b> Summary table of the two-way ANOVA test for the compressibility, hardness and adhesiveness.....	139
<b>Table 3.14</b> Effects of method of preparation within each level of water concentration based on a linearly independent pairwise comparison among the estimated marginal means. ....	140
<b>Table 3.15</b> Spearman's rho correlation coefficients between rheological and mechanical/textural properties for gels prepared by heating. The rheological values have been obtained at different frequencies (1 Hz and 99.9 Hz). ....	141
<b>Table 3.16</b> Spearman's rho correlation coefficients between rheological and mechanical/textural properties for gels prepared by hydration. The rheological values have been obtained at different frequencies (1 Hz and 99.9 Hz). ....	141
<b>Table 4.1</b> Free water contents ( $W_F$ , %) calculated for the gels prepared by heating and hydration methods (n=3). .....	161
<b>Table 4.2</b> Relaxation Time ( $T_2$ ) and relative amplitude of the peaks for the gels. ....	166
<b>Table 4.3</b> List of the total number of protons in the gels and the fraction of water protons. ...	167
<b>Table 4.4</b> List of the $T_2$ relaxation times of the peaks and the relative populations. The numbers (T1, P1....T4, P4) are in accord to the number of the peaks listed in Table 4.2. The subscripts $s$ and $f$ indicate the slowest peak and the weighted average of the faster peaks, respectively.....	167
<b>Table 4.5</b> The integrated volume of the peaks and the relaxation time $T_1$ and $T_2$ of the gels with 10% to 90% water contents.....	173

---

<b>Table 4.6</b> Comparison of the relaxation times ( $T_2$ ), determined with the three different sequences. ....	175
<b>Table 4.7</b> Self-diffusion coefficients of gels between 50% and 90% water and adjusted R-square values of the fitting. ....	178
<b>Table 5.1</b> List of the samples and experimental conditions adopted in the ATR-FTIR experiments. ....	182
<b>Table 5.2</b> Experimental details adopted in the SAXS experiments for the gels with, 40%, 50% and 70% water prepared by hydration method. ....	183
<b>Table 5.3</b> Experimental details adopted for the gels with, 40%, 50% and 70% water prepared by hydration and heating methods. ....	184
<b>Table 5.4</b> Diffusion exponent ( $n$ ) and drug release mechanisms (of matrices with different geometries) identified with Korsmeyer-Peppas model [246, 247]. ....	187
<b>Table 5.5</b> Secondary structural conformation of lysozyme in D <sub>2</sub> O and incorporated into the gels with 20%, 40%, 60%, 70% D <sub>2</sub> O content prepared by hydration method measured using ATR-FTIR. ....	194
<b>Table 5.6</b> Secondary structural conformation of lysozyme-loaded gels prepared by heating method measured using ATR-FTIR. ....	195
<b>Table 5.7</b> Assignments of the peaks for the lysozyme-loaded gel with 50% water prepared by heating method analysed using temperature scan. The $q$ ( $\text{\AA}^{-1}$ ) and $d$ ( $\text{\AA}$ ) values as well as the peak positioning at Bragg values are listed. ....	197
<b>Table 5.8</b> Mean values of the onset temperature ( $T_h$ ), the peak temperature ( $T_p$ ) and the enthalpy of the peak ( $\Delta H$ ) $\pm$ SD of the lysozyme-loaded gels determined in the heating cycle (n=3). ....	201
<b>Table 5.9</b> Mean values of the onset temperature ( $T_c$ ), the peak temperature ( $T_p$ ) and the enthalpy of the peak ( $\Delta H$ ) $\pm$ SD of the lysozyme-loaded gels determined in the cooling cycle (n=3). ....	202
<b>Table 5.10</b> Mean values of the consistency ( $\pm$ SE) and flow ( $\pm$ SE) indices for the lysozyme-loaded gels prepared by hydration method at 25 °C, 37 °C, 50 °C and 80 °C. Measurements were performed at least in triplicate (n $\geq$ 3). ....	213
<b>Table 5.11</b> Statistical parameters obtained for the model fitting of the release profile of lysozyme to different models. The results refer to the gels prepared by heating and hydration methods tested in phosphate buffer (pH=7.4) at 37 °C. $k$ refers to the release kinetic constant. The adjusted R-squared (adj. $r^2$ ) is also shown as prove of the quality of fitting. ....	221
<b>Table 5.12</b> Statistical parameters obtained for the model fitting the release profile of lysozyme. The results refer to the gels prepared by heating and tested in HCl 0.1 M at 37 °C. $k$ refers to the release kinetic constant. The adjusted R-squared (adj. $r^2$ ) is also shown as prove of the quality of fitting. ....	223
<b>Table 6.1</b> List of the nanoparticles formulations with the corresponding bulk gels. ....	229

---

<b>Table 6.2</b> Lysozyme concentrations of the original and diluted nanoparticle formulations used in the activity tests. ....	232
<b>Table 6.3</b> Mean particle size (d.nm) of the nanoparticles stored at room temperature and monitored overtime using DLS (n=3). ....	238
<b>Table 6.4</b> Size distribution (d.nm) of the nanoparticle stored at 4°C and monitored overtime using DLS (n=3; NA= Not Analysed). ....	238
<b>Table 6.5</b> Dimensions (d.nm) of the unloaded nanoparticles determined using AFM. ....	243
<b>Table 6.6</b> Mean particle size (d.nm) of the lysozyme-loaded nanoparticles stored at room temperature and monitored overtime using DLS (n=3; NA= Not Analysed). ....	244
<b>Table 6.7</b> Mean particle size (d.nm) of the lysozyme-loaded nanoparticles stored at 4 °C and monitored overtime using DLS (n=3; NA= Not Analysed). ....	245
<b>Table 6.8</b> Particle dimensions of lysozyme-loaded nanoaprticles (d.nm) determined with AFM. ....	247
<b>Table 6.9</b> Percentage of lysozyme encapsulated in the formulation (EE %) (n = 3, ± SD) ....	248
<b>Table 6.10</b> Lysozyme activity in units per ml and units per mg of protein. ....	250
<b>Table 6.11</b> Final concentrations of the dilutions of the nanoparticles formulation F2 used in the cytotoxicity study. ....	253

---

**List of Abbreviations**

Adj. $r^2$	Adjusted R square
AFM	Atomic force microscopy
ATR-FTIR	Attenuated total reflectance-Fourier infrared spectroscopy
BP	British Pharmacopoeia
CD	Circular Dichroism
CPMG	Carr-Purcell-Meiboom-Gill
CPMG-PGSE	CPMG-Pulsed Gradient Spin Echo
Cryo-TEM	cryogenic-transmission electron microscopy
D	diffusion coefficient
df	degree of freedom
D <sub>2</sub> O	Deuterium water
DLS	Dynamic light scattering
DMEM	Dulbecco's Modified Eagles Medium
DMSO	Dimethyl sulfoxide
DPEG	diacyl-polyethylene glycol
DSC	Differential Scanning Calorimetry
EDTA	Ethylenediaminetetraacetic acid
EE	Encapsulation Efficiency
F	F-ratio
FCS	Foetal calf serum
$\Delta$	Diffusion time
$\Delta H$	Transition enthalpy
G	Gradient
G'	Elastic modulus
G''	Viscous modulus
$ G^* $	Complex modulus
GI	Gastrointestinal tract
GMO	Glyceryl monooleate
HCl	Hydrochloric acid
HLB	Hydrophilic-lipophilic balance
Inv-CPMG	Inversion recovery-CPMG
k	consistency index
LVR	Linear viscoelastic region

LYS	Lysozyme
MPEG	monoacyl-polyethylene glycol
MTS	3-(4,5-dimethylthiazol-2-yl)-5-(3-carboxymethoxyphenyl)-2-(4-sulfoophenyl)-2H tetrazolium
n	Flow index
$\eta'$	Dynamic viscosity
$\eta^2$	partial eta squared
NMR	Nuclear magnetic resonance
PBS	Phosphate Buffer Saline
PEG	Polyethylene glycol
PGSTE	Pulsed Gradient-Stimulated Echo
PLM	Polarised Light Microscopy
RH	Relative humidity
SAXS	Small Angle X-ray Scattering
SD	Standard deviation
SE	Standard error
SEM	Scanning Electron Microscopy
SLN	Solid lipid nanoparticles
$\tan\delta$	Loss tangent
$T_1$	spin lattice relaxation time
$T_2$	spin-spin relaxation time
$T_c$	Crystallisation temperature
$T_h$	Melting temperature in the heating cycle
$T_m$	Melting temperature
$T_p$	Peak temperature
TPA	Texture Profile Analysis
UV-vis	Ultraviolet-visible spectroscopy
$W_F$	Free water content

## 1 Introduction

In the last two decades, the number of commercially available therapeutic proteins and peptides has increased considerably due to the development of the advanced technologies made in the biotechnology field. In general, biological medicines are considered to have fewer side effects, to be less toxic and to have a more predictable behaviour *in vivo* [1]. However, one of the major challenges faced by the commercialisation of protein-based drugs is the instability of proteins since they may encounter enzymatic degradation and the poor penetration across the biological membranes due to the high molecular weight and the polar charges of the surfaces [2]. One of the possible strategies to overcome these issues is the development of an effective delivery system that is stable over shelf-life and facilitates the absorption of the protein after administration. In order to obtain a stable formulation, it is essential to understand the physicochemical and biological properties of the proteins together with the physical and chemical stability, immunogenicity and pharmacokinetics of the formulation. The designed delivery systems need to ensure the stability of the proteins considering that their activity is directly related to the conformational structure [1].

Traditionally, the parental route (i.e. subcutaneous, s.c. and intravenous, i.v.) is the most commonly used route of administration for therapeutic proteins [3]. Many injectable proteins have short half-lives in the bloodstream, and after administration, unwanted proteins deposition may occur, thus frequent administration of high doses may be required resulting in possible toxic side effects and low patient compliance. Therefore, alternative non-parental routes have been explored over the years, such as mucosal absorption through mucous surfaces i.e. nasal, ophthalmic, buccal, rectal, vaginal, transdermal and pulmonary [3-5]. For example, the pulmonary route has advantages such as the low local enzymatic activity, the high absorptive surface area ( $\sim 75 \text{ m}^2$ , which is larger than the nasal cavity,  $\sim 180 \text{ cm}^2$ ), the extensive vascularisation, and the thin layer of alveolar epithelium (0.1-0.5  $\mu\text{m}$  thick) [3]. These advantages lead to enhanced absorption for some protein drugs delivery via pulmonary route. The advantage of a mucosal absorption is due to the fact that these mucous surfaces are more penetrable for the macromolecule than the skin and the GI tract. More importantly, it allows bypassing the hepato-gastrointestinal first-pass elimination which is associated with the oral route [4]. Moreover, the physicochemical properties of many proteins make them unsuitable for absorption in the GI tract, since they encounter degradation by the harsh acidic gastric environment and by GI enzymes such as proteases [4]. However, the oral route remains the most appealing because of its simplicity and practicability [6]. Therefore, great efforts have

been made in the development of oral protein delivery, despite it is the most challenging route for the delivery of macromolecules such as proteins and peptides [1].

The oral absorption of proteins and peptides from the intestinal lumen to the bloodstream can take place mainly via three trans-epithelial pathways. The transcellular passive transport is suitable for lipophilic molecules capable of penetrating the cell membrane by endocytosis. The transcellular active transport or facilitate pathway is a receptor-mediated transport which modulate the penetration of small molecules (e.g. sugars and amino acids) by using specific receptors exposed on the apical cell membrane. The paracellular transport occurs through the tight junctions between adjacent cells [7]. A further pathway of absorption is through the M cells of the Peyer's patches and further into the lymphatic circulation. This pathway has been reported to be responsible for some of the micro- and nanoparticles uptake [2]. They have been proved to be the effective target for oral vaccines [8]. The Peyer's patches are lymphoid follicles, highly present in the ileum and overlaid by specialised epithelium which is composed of M cells [8]. A schematic view of the main routes of absorption for oral delivery is shown in Figure 1.1.

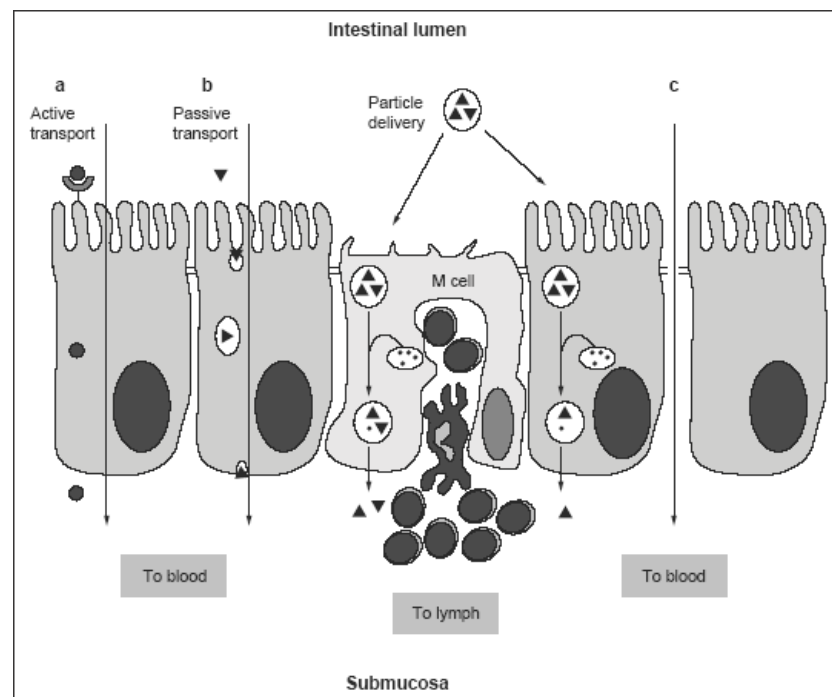


**Figure 1.1** Schematic view of the intestinal trans-epithelial pathways: (a) transcellular active transport or receptor-mediated transport, (b) transcellular passive transport through the cells; (c) paracellular pathway through tight junctions between adjacent cells. The transcellular passive transport can be enhanced by encapsulation of active components in particulate systems which are preferably uptake by the M-cells of Peyer's patches and through which they are transported in the lymphatic circulation [9].

Despite the difficulties in the oral protein delivery, the field has made significant progress and many promising case studies have been reported. This project took on the challenge of developing effective oral delivery system for proteins and peptides. During this project, a series of structured gel and nanoparticle formulations made from a lipid-based material, Gelucire 50/13, were developed and characterised for their potential to be used as delivery carriers for macromolecules such as proteins. This chapter offer a detailed discussion on the oral approaches adopted in protein/peptide delivery. An overview of the structure of Gelucire 50/13 and lysozyme which is the chosen model protein in this work is also given. Finally, the key objectives and the design of the project are presented.

## **1.1 Oral approaches for protein delivery**

In order to improve the oral bioavailability of the proteins, many physical and chemical approaches have been studied. The most commonly used approaches include structural modification of the protein in order to optimise the physicochemical properties of the drug, the use of absorption enhancers and enzyme inhibitors and the development of sophisticated delivery system to protect the proteins from enzymatic degradation and denaturation and improve bioavailability [6]. Each of these approaches is discussed as below.

### **1.1.1 Chemical modification**

The modification of the physicochemical structure of the proteins can improve the membrane permeability and the stability against enzymatic degradation [2]. The structure modification can be carried out by producing analogues (which consists in modifying one or more amino acids) or by hyperglycosylation [10], acylation and PEGylation [2]. The chemical modifications can be achieved via covalent or non-covalent modifications. The insulin analogue is an example of the approach [11]. Another approach consists in attaching small molecules to the protein as anchors. This will allow the recognition of the modified protein by specific transporters/receptors at the surfaces of cell membranes, which can further induce the endocytosis of the macromolecules. Several cellular transporters or receptors have been used as targets for enhancing the oral absorption of macromolecules, such as the glucose transporter [12], the di/tripeptide transporter [13], which have already proved to be able to transport peptidomimetics such as  $\beta$ -lactam antibiotics, ACE inhibitors and renin inhibitors [14]. Other transporters used in peptide oral delivery include the bile acids transporter [15, 16] and the vitamin B<sub>12</sub> transporter [17, 18].

Chemical modification with fatty acids (called also lipidization [2]) has also been reported to improve the stability and permeability of certain proteins and peptides. In some cases this type

of modification can increase the binding affinity of the proteins to serum albumin, which leads to the extension of the circulation time in the blood. The acylation of the insulin is an example of this kind of modification [19]. In order to overcome the issue of reduced bioactivity of lipidized proteins, the reversible lipidization has been proposed for polypeptides such as salmon calcitonin [20]. The reversible aqueous lipidization (REAL) technique consists of conjugating fatty acids to polypeptides through reversible disulphide linkages regenerate the original polypeptide in tissues or blood, due to the reversible and biodegradable nature of the disulphide bonds [21, 22].

The PEGylation process is another commonly used method for modifying proteins and peptides. The basic principle of the process is to conjugate poly(ethylene glycol) (PEG) to the targeted molecule. The technique has improved in the past decades and it remains the most successful techniques in order to improve the residence time of the proteins in the bloodstream [4]. In the evolution of the PEGylation technique, selective modification at certain amino acids was carried out which improved the purification and characterisation of the proteins. It also leads to an improved preservation of the native activity of the proteins. Thiol PEGylation is the specific modification of only the thiol group of cysteine residues not involved in disulphide bonds. This is the most difficult site to carry out the PEGylation process due to the fact that the cysteines are rarely present in proteins. Moreover, the high hydrophobicity of the cysteine makes these residues to be buried within the proteins structure. Improvements in the genetic engineering allowed the development of a method by which it is possible to introduce cysteine residues anywhere in the protein molecule making these residues more accessible. Specific PEGylation targeting amino residues (i.e. amine groups of glutamine or hydroxyl groups of serines and threonines) has been performed by using enzymes capable of recognising specific amino acids, [23] such as the transglutaminase (Tgase) which is able to recognise the glutamine residue [10].

Conjugation with PEG (PEGylation) can induce several changes in the protein molecules, such as increased molecular size and weight, changes in conformation, steric hindrance of intermolecular interactions, increased solubility and changes in electrostatic binding properties. These changes influence the physical and biological behaviour of the conjugates. The main effect of PEGylation is the prolonged circulation time, due to the decreased rate of clearance from the kidney or to a reduced proteolysis or opsonisation. Due to the presence of PEG, the conjugates are highly hydrated, which increases the hydrodynamic radius, improve the solubility and decreases the glomerular filtration of the macromolecules. Furthermore, the PEG moieties can exert a sheltering effect on the proteins. As a result, the uptake of proteins and the clearance by reticulo-endothelial cells is reduced. After PEGylation, the antigenic sites on the protein molecules are covered, which can prevent the formation of neutralising antibodies and

protect the proteins from the degradation of proteolytic enzymes (trypsin, chymotrypsin, and proteases) [10]. PEGylation has also been shown to increase the stability of the proteins by covering the hydrophobic sites of the proteins surfaces involved in non-covalent interactions that are responsible for protein aggregation, loss of activity and increase immunogenicity [23].

However, there are also disadvantages associated with the PEGylation. For example as a result of excessive PEGylation, the protein/peptide drug may reduce its activity compared to the native structure and reduce binding affinity [10]. In some cases, the prolonged residence time of the conjugates in the body may compensate the reduced activity as a result of the increased stability and higher hydrodynamic volume [23]. Some studies have reported an increase of aggregation of the PEG conjugates of proteins. PEG is a polydisperse synthetic polymer characterised by a range of molecular weights. This leads to polydisperse PEG-conjugates proteins, which may have high tendency of aggregation. Despite the disadvantages, many PEGylated polypeptides and macromolecules have been developed and some of them were approved for human use and currently on the market, others are at different stages of clinical trial [10]. The PEGylated macromolecules currently in the market are listed in Table 1.1.

**Table 1.1** List of the PEGylated macromolecules in the market (adaptated from reference [10]).

<i>Brand name</i>	<i>Drug name</i>	<i>Drug</i>	<i>Indication</i>	<i>Approval year</i>
Antigen®	Pegadamase	Adenosine deaminase	Severe combined immunodeficiency	1990
Oncaspar®	Pegaspargase	Asparaginase	leukemia	1994
PEG-INTRON®	Peginterferon-a2b	IFN-a2b	Hepatitis C	2000
PEGASYS®	Peginterferon-a2a	IFN-a21	Hepatitis C	2001
Neulasta®	Pegfilgrastim	Granulocyte-colony stimulating factor (GCSF)	Neutropenia	2002
Somavert®	Pegvisomant	Growth hormone antagonist	Agromegaly	2003
Macugen®	Pegaptanib	Anti-VEGF aptamer	age-related macular degeneration	2004
Mircera®	Epoetin $\beta$ -methoxy polyethylene glycol	Erythropoietin (EPO)	anemia associate with kidney disease	2007
Cimzia®	PEG-certolizumab pegol	Anti-TNF Fab	rheumatoid arthritis and Crohn's disease	2008

Glycosylation has also been extensively studied as a method for structural modification of macromolecules. Glycosylation consists of attaching carbohydrates to the proteins, which can induce similar effects to PEGylation. After glycosylation, the conjugated proteins show increased circulation time and reduced immunogenicity due to the reduced clearance and interaction with antigens presenting cells. Glycosylation has advantages over PEGylation as the modification uses endogenous, native and biodegradable carbohydrates, while PEG used in PEGylation is an exogenous material. The glycosylation may be carried out by specific chemical reaction *in situ* or by site directed mutagenesis, which may occur in N-linked or O-linked oligosaccharides. Polysialic acid (PSA) is an endogenous oligosaccharide, available in different size. It consists of repeating hydrophilic units, which can be covalently linked to  $\epsilon$  amino group of lysine. PSA derivatives have been used to create conjugates with therapeutic proteins. Several companies have been commercialising hyperglycosylated therapeutic proteins, such as darbepoetin alpha (hyperglycosylated EPO) which is approved in USA and marketed by Amgen [10].

### 1.1.2 Absorption enhancers

The permeation of proteins through the intestinal epithelium can be increased by the use of absorption enhancers, such as surfactants, bile salts and chelating agents, which operate with different mechanisms. Surfactants or detergents are responsible for disruption of the lipid bilayer of the cell membrane [24]. As a result the cell membrane becomes more permeable. The chelating agents, such as the  $\text{Ca}^{2+}$ -chelators, improve the paracellular transport of proteins by forming complexes with  $\text{Ca}^{2+}$  ions, which induce the rupture of tight junctions [25, 26]. Similar effects can be achieved by using long-chain enhancers, such as fatty acids sodium caprate and acyl carnitines [6]. Other approaches have been explored in order to modulate the permeability of the tight junctions. For instance, the Zonula Occludens toxin is proved to enhance the absorption of proteins, e.g. insulin, by altering the intestinal tight junctions [7]. The Pz-peptide showed also effects on improving the paracellular penetration of hydrophilic macromolecules [27]. However, the enhanced permeability through the paracellular route can expose the cells to the penetration of unwanted or potentially toxic molecules located in the intestine [28].

### 1.1.3 Enzyme inhibitors

One of the main issues for oral protein/peptide delivery is that the proteins or peptides may be degraded by several proteolytic enzymes in the GI tract [6]. The phenomenon is particularly evident in the stomach and in duodenum, and reduced in the ileum and colon. This problem could be overcome by using appropriate encapsulations or coatings with gastro resistant materials and targeting the colon and ileum region [28]. Enteric coatings that are able to delay

the drug release have been used to target the ileum and colon, e.g. polymeric coatings degradable by the human colonic flora have been proposed to target the large intestine [29]. However, the delay in the drug release and absorption, and the lack of control of the absorption due to the variability in intestinal motility of each patient may affect the overall therapeutic outcome of the formulation. Therefore, one possible approach by co-administration of enzyme inhibitors with the therapeutic protein was developed. In combination with absorption enhancers, this approach has demonstrated improved bioavailability of proteins drugs after oral administration [28]. Several trypsin or  $\alpha$ -chymotrypsin inhibitors have been studied for this purpose, such as pancreatic inhibitor, soybean trypsin inhibitor, FK-448, camostat mesylate and aprotinin [6]. Moreover, chicken and duck ovomucoids have been studied and found capable of protecting the insulin against the trypsin or  $\alpha$ -chymotrypsin degradation [30]. However, the main drawback of this approach is due to the fact that the enzyme inhibitors may facilitate the absorption of other proteins and macromolecules potentially toxic or harmful, especially during chronic drug therapies [6].

#### 1.1.4 Mucoadhesive systems

Mucoadhesive delivery systems can adhere to the mucous gel layer that covers the mucosal surface and prolong the residence time of the drugs in the site of action. Furthermore, certain mucoadhesive systems can induce changes in the normal network structure and in the swelling behaviour of the mucous layer in response to changes of the surrounding environment, such as pH, temperature, enzymes, electric field or ionic strength. For those reasons mucoadhesive systems may be considered as suitable carriers for protein/peptide delivery [6]. These environment-sensitive materials have also been called smart polymers [31]. Several smart polymers have been studied in order to improve the bioavailability of protein/peptide drugs. Chitosan coated nanocarriers showed high load efficiency and ability to deliver macromolecules [32]. Furthermore, chitosan is shown to be able to modify the transepithelial resistance and reduce the integrity of tight junctions, which leads to improve the uptake by the Caco-2 cell line [32]. New generation of mucoadhesive thiolated polymers (thiomers) have been used for the oral delivery of macromolecule, e.g. insulin [33, 34] and salmon calcitonin [20]. The studies on the use of mucoadhesive polystyrene nanoparticles with hydrophilic polymeric chains have shown that the nanoparticles improve the permeability of calcitonin and a positive correlation between mucoadhesion and permeability was concluded [20, 35]. However, mucoadhesive polymers alone may not be able to protect the proteins against enzymatic degradation, therefore conjugating the mucoadhesive polymers with protease inhibitors have been developed in order to achieve an adequate protection of the protein drug [6]. For instance, chitosan conjugated with EDTA exhibited strong inhibition effect towards zinc-dependent proteases. Additionally,

mucoadhesive polymers, such as poly(acrylate) derivatives (e.g. poly(acrylic acid) and polycarboxiphil) showed enzyme inhibiting effects on luminal proteases. It has been proposed that the inhibiting effect of the conjugated polymers is due to the ability of forming complexes with divalent cations such as  $\text{Ca}^{2+}$  and  $\text{Zn}^{2+}$  [36].

#### **1.1.4.1 Mucoadhesion**

The word bioadhesion describes the adhesion established between two biological surfaces or between a biological and a synthetic surface. In pharmaceutical field for bioadhesive drug delivery systems, bioadhesion refers to the bond between biological surfaces and polymers. Most bioadhesive formulations are natural or synthetic polymer-based systems. In many cases the adhesion to the biological surfaces involves soft tissue cell layer, or mucous layer or a combination of both. If the attachment is to a mucous layer, the phenomenon is known with the word mucoadhesion [37]. Mucoadhesion has become a subject of interest in the past decades for its potential to improve drug targeting and absorption via increasing the time of contact of the formulations to the targeted biological membrane. The use of mucoadhesive systems can improve the contact between the dosage form and the drug absorption tissue, which leads to a high drug concentration and high drug flux in the area of interest. The intimate contact established via mucoadhesion can be particularly useful for the delivery of high molecular weight drugs such as proteins and peptides [38]. Mucoadhesive drug delivery systems use the ability of certain water-soluble polymers to become adhesive on hydration. Mucoadhesion allows the dosage form to target the release of the drug in a particular site for an extent period. Several regions of the body can be potential sites for bioadhesive systems: gastrointestinal tract, urogenital tract, the airways, the nose, the ear and the eye. The mucoadhesive delivery systems can be useful for delivering drug at particular sites of the body, such as buccal and sublingual, vaginal and rectal, nasal, ocular, and gastrointestinal regions.

In case of oral delivery system, the extent of drug absorption is often limited by the residence time of the drug on the absorption site and by the transit time of the dosage form in the gastrointestinal tract. Therefore, mucoadhesion is considered as one of the strategies for improving oral absorption of the drugs. The mucoadhesive drug delivery systems should be durable but degradable when necessary and non-toxic [38]. The mucoadhesion is a complex process and not yet fully understood. The occurrence and degree of mucoadhesion depend on many factors concerning the nature of the polymer (molecular weight, concentration of the polymer, flexibility of polymer chains, spatial conformation of the molecule), the biological surface and the surrounding environment [39].

The mucosae or mucous membranes are moist surfaces which covers the wall of body cavities such as GI tract or respiratory tract [40]. The epithelia can be monolayered (such as in stomach, intestine and bronchi) or multilayered (e.g. oesophagus, vagina and cornea). The single layer epithelium contains goblet cells, which secrete mucus on to the epithelial surface. The multilayered epithelium contains specialised glands or it is adjacent to tissues containing specialised glands, which secrete mucus in the epithelia. Mucus can exist as a gel layer stratified on the mucosae or it can exist in soluble or suspended form in the lumen [40].

Mucin is the major component of the mucus. It is responsible of the gel-forming properties of the mucus. Mucins are high molecular weight glycoproteins with a molecular weight ranging between 1000 and 40000 kDa. Mucins can be divided in two classes, membrane bound mucins and secretory mucins [37]. The membrane bound mucins contain a hydrophobic-spanning domain which helps the molecules to be attached to the cell surfaces, whereas the secretory mucins are secreted from mucosal absorptive epithelial cells and specialised goblet cells. Mucins are responsible of the viscous gel formation due to the high molecular weight and to the presence of disulphide bonds [37, 41]. The physical and chemical structure of mucins has been extensively studied. They are complex and highly glycosylated molecules composed of ~80% of carbohydrates (mainly N-acetylglucosamine, fucose, galactose, sialic acid, or known also as N-acetylneuraminic acid) linked through O-glycosidic bonds to the hydroxyl groups of serine and threonines [41, 42]. The peptide core of mucin has a central glycosylated region composed of repeated sequence rich in serine, threonine and proline (STP repeats). It represents the ~20% of the molecular weight of mucins. Arranged to the STP repeats are amino acids region with little O-glycosylation and N-glycosylation sites, but with high proportion of cysteine (CYS domain). The cysteine region has domains with sequence similar to von Willebrand factor (vWF) C and D domains and C-terminal cysteine knot domains. This region is involved in the disulphide bonds formation, dimerisation and polymerisation in multimers [42]. A schematic representation of the molecular structure of the pig gastric mucin is shown in Figure 1.2. The concentration of mucin in the mucus layer varies accordingly to the region. It has been reported to be ~50, ~40, ~30 and ~20 mg/mL in the stomach, duodenum, jejunum, ileum, and colon respectively [43].

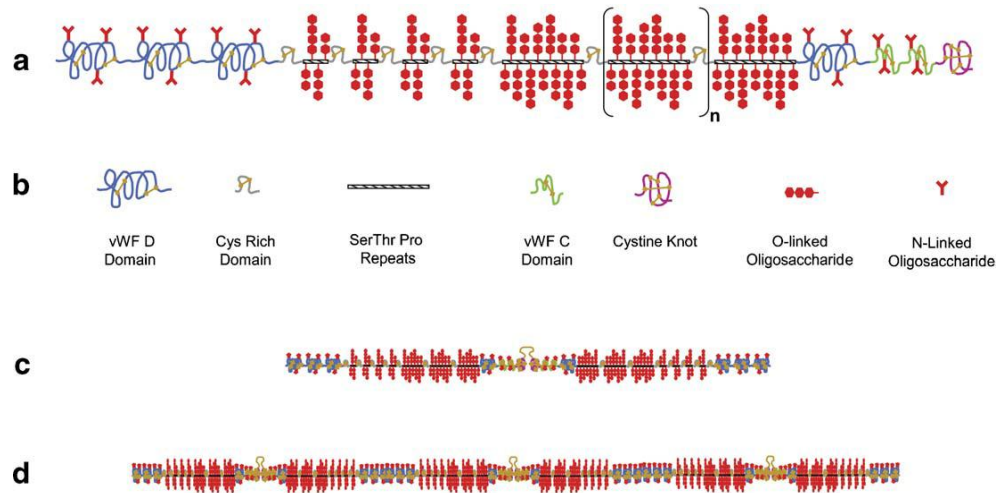


**Figure 1.2** (a) Schematic representation of a molecular structure of a mucin monomer; (b) the single units of the monomers; (c) a dimer formed by two monomeric units linked by disulphide bonds; (d) a multimer composed of multiple dimers linked by disulphide bonds [42].

#### 1.1.4.1.1 Proposed mechanisms of mucoadhesion

Different theories have been proposed to describe the mechanisms of the bioadhesion/mucoadhesion. These are electronic, adsorption, wetting, diffusion, fracture and mechanical theories [40, 44].

##### 1) Electronic theory

This theory is based on the hypothesis that the biological and the bioadhesive materials have different electronic structure. Consequently electron transfer occurs and an electrical double layer is formed at the contact interface. The attractive forces established across the double layer is responsible for the adhesion between the biological surface and the material [37].

##### 2) Wetting theory

This theory is related to liquid based bio/mucoadhesive systems. It analyses the ability of the delivery systems to spread over a biological surface. The work of adhesion ( $W_A$ ) is the measure of the energy required to separate the two surfaces and can be described by Equation 1.1.

$$W_A = \gamma_A + \gamma_B - \gamma_{AB} \quad \text{Equation 1.1}$$

Where  $\gamma_A$  is the surface tension of the liquid system A,  $\gamma_B$  is the surface tension of the biological surface B and  $\gamma_{AB}$  is the interfacial tension between the liquid system and the biological surface. The spreading coefficient ( $S_{AB}$ ) can be calculated from the surface energies of the liquid and

biological surface by using the Equation 1.2. The spreading coefficient should be positive for liquid that spreads spontaneously over the biological surface [40].

$$S_{AB} = \gamma_B - \gamma_A - \gamma_{AB} \quad \text{Equation 1.2}$$

### 3) Diffusion theory

According to the diffusion theory, the polymer chains and the mucus interpenetrate to a sufficient depth to create semi-permanent adhesive bonds (mechanical bonds) as it is shown in Figure 1.3 [44]. The diffusion process is driven by the concentration gradients. It can be significantly affected by the length and the mobility of the available molecular chains [40]. The penetration depth ( $l$ ) can be calculated by Equation 1.3:

$$l = (tD_b)^{1/2} \quad \text{Equation 1.3}$$

where  $t$  is the contact time and  $D_b$  is the diffusion coefficient of the bioadhesive material in the mucus [44].

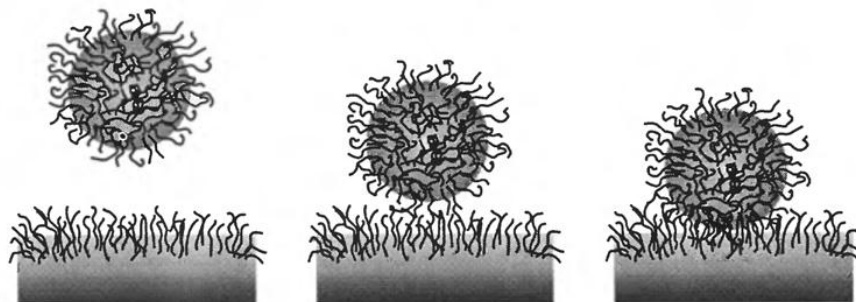


**Figure 1.3** Mechanical bonds through interpenetrations and entanglement between bioadhesive polymer chains and mucin chains [44].

### 4) Adsorption theory

The adsorption theory states that the bioadhesive bonds between the two surfaces (formulation and the biological membrane) are mainly due to van der Waals forces and hydrogen bonding. These bonds are usually weak, but the high number of interactions formed between the adhesive substrate and the mucosa makes the overall adhesion stronger. This theory is one of the most widely accepted theories for describing the mechanism of mucoadhesion [37].

### 5) Mechanical theory

The mechanical theory takes into consideration the roughness of the surface, which facilitate the intercalation of mucoadhesive formulations in the irregularities of rough area. The roughness of

the surface increases the contact area available for the adhesion [40]. This theory is particularly valid for porous and rough materials [45]

#### 6) Fracture theory

This is the most applicable theory to study the bioadhesion through mechanical measurements. This theory is divergent from the previous theories, in the sense that it relates the strength of adhesion to the force required to detach two surfaces after bio/mucoadhesion occurs. The force,  $s_m$ , calculated through tensile tests, is given by the ratio of the maximum detachment force,  $F_m$ , and the total surface area involved in the interactions between the surfaces,  $A_0$  [44] according to the following equation

$$s_m = \frac{F_m}{A_0} \quad \text{Equation 1.4}$$

However, none of these theories alone can explain the phenomenon of the mucoadhesion. It is more likely that the mucoadhesion is the result of the combination of different mechanisms. Generally, mucoadhesion process can be divided in two stages, the contact and consolidation stages as shown in Figure 1.4 [40]. These two stages can be described as three steps: (1) an intimate contact between the surfaces (wetting) and the swelling of polymers to achieve an intimate contact with the biological surface; (2) interpenetration of the mucoadhesive polymer chains into the mucous network and entanglement of polymer and mucous chains; (3) formation of weak chemical bonds between the chains [46].

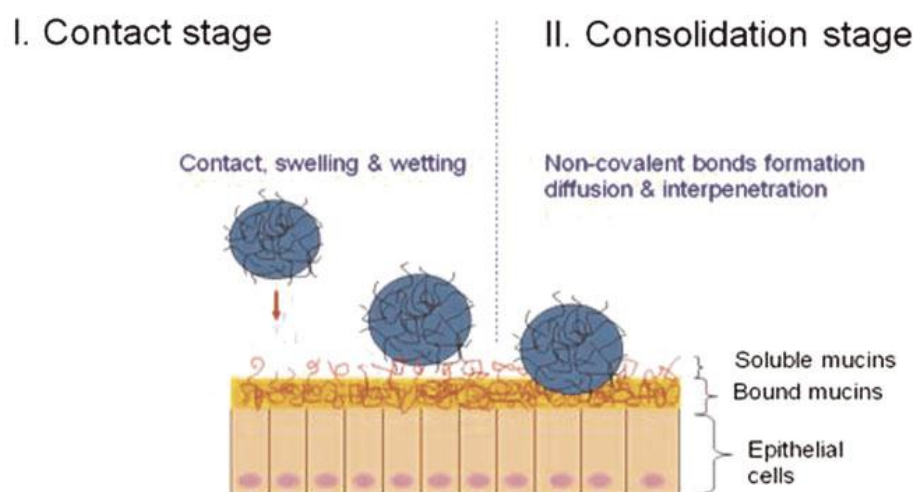


**Figure 1.4** Schematic view of the two phases in which the mucoadhesion process can be divided. The contact stage (I) in which the mucoadhesive polymers and the mucous membrane come into contact and the consolidation stage (II) which is characterised by the formation of non-covalent bonds and the diffusion and interpenetration of polymers and mucin chains [45].

The degree of adhesion of the polymers used in the formulations to the targeted tissue surface is dependent on the nature of bonds established which may be mechanical or physical bounds, secondary chemical bounds and ionic, primary or covalent bounds. The chemical bonds may be strong covalent bonds or weaker bonds, such as ionic bonds, the hydrogen bonds, the Van der Waals interactions [40]. The physical or mechanical bonds involve the inclusion of materials into the imperfections of the tissue, which involve the entanglement of mucins chains with polymeric chains and the interpenetration of mucin chains within a porous polymer substrate [44].

### 1.1.5 Particulate carrier systems

A well-established strategy for improving the administration of macromolecules is the development of suitable particulate delivery systems, which are capable to protect the proteins from enzymatic degradation and improve the absorption across the epithelium mucosa [2]. Two types of protein incorporation may be followed in the design of the formulations, the entrapment and the encapsulation [1]. In the case of being attached/encapsulated into appropriate particulate systems, the *in vivo* bioavailability of the therapeutic proteins depends not only on their own physicochemical properties, but also on the characteristics of the carriers used (such as size and surface properties) [6]. The oral absorption of the proteins is regulated by the particle size, surface charge, ligands, and dynamic nature of the particulate delivery systems used after ingested into the GI tract [6]. Examples of protein delivery systems are polymeric hydrogels, nanoparticles, microspheres and lipid-based drug delivery systems e.g. fat emulsions, liposomes and solid lipid nanoparticles (SLN) [4]. In the case of nanocarriers, the nanoparticles may be absorbed by the epithelial cells or the lymphoid tissues through the Peyer's patches without adding any absorption enhancers [2]. Drawbacks of the particulate formulations are the low incorporation efficiency of the drugs, low precision of controlled release and prevention of proteins aggregation. Additionally, the accumulation of nanoparticles (even for degradable particles but given in high dose) in local tissues may cause toxic effects [2].

#### 1.1.5.1 Polymeric carriers

Polymeric delivery systems have been studied over the years. Depending on the preparation methods nanospheres or nanocapsules can be formed. Nanospheres are polymeric matrix in which the drug is uniformly dispersed, whereas nanocapsules are vesicles with a polymeric shell and inner core in which the drug is encapsulated [47, 48]. The nature of the polymeric materials used for the formulation defines the size and the release profile of the nanoparticulate systems. Synthetic and natural polymers can be used to form different types of formulations including polymeric micelles, self-regulated delivery systems [49], porous membranes and dendrimers

[10]. Hydrogels are formed by swellable cross-linked hydrophilic polymers which are able to form three dimensional networks. These polymers can be engineered to degrade at a certain rate or respond to certain physiological stimuli from the surrounding environment such as pH, ionic strength, temperature. Hydrogels can be formulated as microspheres or as solid delivery systems which only form gel *in situ* after administration. The advantages of having *in situ* forming systems are related to a simple administration and less elaborated formulation manufacturing, which may be useful for formulating sensitive macromolecules [1].

Polymeric micelles have recently become increasingly attractive as functional nanomaterials. They are formed by amphiphilic block copolymers which self-assemble in aqueous solution. They are characterised by a hydrophobic core in which hydrophobic drugs can be encapsulated. Particularly, polyion complexes micelles have been proved to be suitable for entrapping enzymes and DNA, and improving their stability against biological environmental conditions [2]. Moreover, recently the ability of self-assembled polymer micelles crossing the intestinal barriers has been reported, which makes them suitable as oral delivery systems [50].

The most studied and recognised biocompatible material for micro/nanoparticles encapsulation is poly(D,L-lactic-co-glycolic-acid) (PLGA). This polymer is composed of lactic and glycolic acids esterified together, which are endogenous and easily metabolised through the Krebs cycle [51]. Thus, it is biocompatible and with a minimal toxicity. Once in the body, the ester bond is hydrolysed by blood esterases releasing the drugs and allowing the degradation and the clearance of the polymers and subsequently releasing the drugs. It is a class of material approved by US FDA and European Medicine Agency (EMA) for the preparation of several drug delivery systems. It can exist in different molecular weight and in different copolymer composition [52]. The most common PLGA composition is 50:50, which has the fastest degradation rate of the polymers. Other co-polymer combinations have been studied in the preclinical settings (e.g. 65:35, 70:30, 75:25 lactic acid:glycolic acid, respectively) with improved half-lives of the nanoparticles as the proportion of lactic acid increases [48].

Micro- and nanoparticles made of PLGA have been used for drug delivery. PLGA microspheres can be produced by spray-drying, double emulsions and phase-separation coacervation [53]. Encapsulation of proteins by double emulsion or phase separation may lead to aggregation, denaturation, oxidation and cleavage of the proteins which may cause the loss of activity [52, 54]. However, the stability of the proteins may be improved by the addition of stabiliser, surfactants during the preparation or modifying PLGA polymers [10]. The transport of the PLGA particles through the epithelium membranes is influenced by the size. It was reported by Desai et al. [55] that 100 nm PLGA nanoparticles can diffuse across the submucosal layers and

they are localised in the cytoplasm after uptake, mostly in the endosomes, while for 10  $\mu\text{m}$  particles the uptake is in less extent and they are mainly adsorbed at the cell surface [55].

Due to the degradation nature of PLGA, PLGA based particulate delivery systems are often used as controlled release carriers and administered via injection. Generally, microspheres are administered via subcutaneous or intramuscular routes, whereas nanoparticles can be administered intravenously. Many preclinical studies have shown the improvement in the bioavailability of certain protein drugs after being encapsulated in the PLGA or PLGA-based particulate delivery systems. For instance, the anti-angiogenic peptide, Endostar, used for solid tumors showed an increase in half-life when loaded into PEG-PLGA nanoparticles compared to the free drug. Human granulocyte colony-stimulating factor (rh-G-CSF) was successfully loaded in PLGA nanoparticles and showed sustained release over an extended period of time [56]. The pulmonary administration of calcitonin incorporated in PLGA/chitosan nanoparticles improved the delivery thanks to the mucoadhesive properties of the chitosan. Moreover it enhances the absorption by opening the tight junctions in the lung epithelium. The encapsulation of human growth factor (hGH) in PGLA microspheres resulted in increased serum level of recombinant human growth factor (rhGH), insulin-like growth factor-I (IGF-I) and its binding protein (IGFBP-3) after injection administration compared to the un-encapsulated rhGH [57]. Although the PLGA is considered to be generally safe and accepted by the regulatory authorities, the PLGA nanoparticles encounter some safety issues in some cases. This is mainly due to the fact that the nanoparticles can be phagocytosed by the cells which may undergo degradation and therefore they cause cytotoxic effects. Moreover, scale-up the preparation method of such nanoparticles is still an issue [58].

### **1.1.5.2 Lipid-based delivery systems**

Lipid based delivery systems have demonstrated promising outcomes in the delivery of proteins and peptides [58]. According to the nature of the lipid component, different types of lipid carriers can be formed. The commonly used lipid delivery systems include liposomes, solid lipid nanoparticles, oily suspensions, submicron lipid emulsions, lipid implants, lipid microbubbles, inverse lipid micelles, cochlear liposomes, lipid microtubules and microcylinders. Natural or synthetic phospholipids tend to form a bilayer structure (liposomes), whilst high melting point fats (natural or synthetic ones) tend to form a hydrophobic solid core with a monolayer of lipids, thus they are denominated solid lipid nanoparticles. Cochleates are formed by negatively charged phospholipids combined with divalent counter ion packed in spiral-shape structure without aqueous phase. Oily suspensions can be formed by suspending the drugs in natural or synthetic oils, whereas the microtubules/microcylinders and lipid micelles can be

formed by crystallizing surfactants into the lipid. An overview of the different types of lipid delivery systems is shown in Figure 1.5 [10].

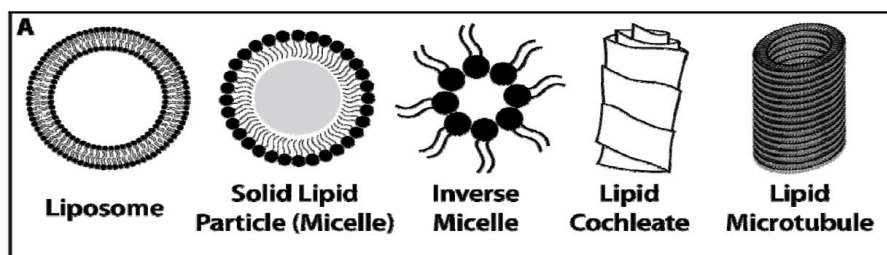


**Figure 1.5** Typical structures of lipid based delivery systems; modified from ref. [10].

Microemulsions are thermodynamically stable dispersions with low viscosity. A microemulsion formulation consists of an oil phase and a water phase, stabilised by surfactants and sometimes also co-surfactants. The inner core that can be oil (o/w) or water (w/o) has a size ranging between 5 and 100 nm. Hydrophilic drugs can be incorporated in the aqueous phase of w/o microemulsions and they have been proved to enhance the bioavailability of drugs including peptides. A commercial example of the microemulsion formulation for cyclosporine is Neoral® and Sandimmune® (Novartis, UK) [58]. Lipid nanoemulsions are fine oil in water (o/w) dispersions consisting in droplets of size ranging between 50 and 200 nm. They are often formed by triacylglycerols (10%-20%) and other ingredients, such as phospholipids and glycerol. They can be used as carriers for lipophilic drugs. They are safe to use and the production using high pressure homogeniser can be easily scaled up. However, they are characterised by rapid release and controlled release could not be achieved. Examples of nanoemulsions are self-emulsifying drug delivery systems (SEDDS), which are described as physically stable, isotropic mixtures of oil, surfactants and co-surfactants. These formulations in aqueous solution and under moderate agitation are able to form fine o/w nanoemulsions [58].

#### 1.1.5.2.1 Liposomes

Liposomes have been extensively used in biological, biochemical and medicinal fields. Due to their amphiphilic character, being biocompatible and the ease of surface modification, liposomes are suitable systems for protein/peptide delivery [58]. Liposomes are spherical vesicles composed of natural or synthetic phospholipids bilayers, and a hydrophilic core. Drugs of lipophilic and hydrophilic nature can be incorporated in the liposomes. Lipophilic drugs are usually incorporated in the phospholipid bilayers while the hydrophilic ones are solubilised in the inner core. The bioavailability and the stability of the loaded drug depend on the size, charge, surface hydrophobicity and membrane fluidity of the liposomes. Membrane permeability of the liposomes can be modified by selecting appropriate phospholipids and by

incorporating additives, such as cholesterol. Furthermore, the *in vivo* circulation time of the liposomes can be delayed by incorporating natural compounds (e.g. gangliosides) or by using PEGylation [58]. Liposomes can be prepared using different methods, though the most common method is through hydration of dried lipid films in aqueous buffer solution [10]. Liposomes differ in size, surface charge and number of layers. According to the adopted methodology of preparation multi-, oligo-, or unilamellar vesicles containing many, few or one phospholipid bilayer can be formed [58]. However, the main classification considers small unilamellar vesicles (SUV) with single lipid bilayer having a size of about 100 nm, large unilamellar vesicles (LUV) of 200-800 nm surrounded by several lipid bilayers separated by aqueous layer, giant unilamellar vesicles (GUV) [58] with a mean diameter of 1-2  $\mu\text{m}$  [10] and multilamellar vesicles consisting of multiple bilayers with a mean diameter ranging between 500 nm and 5  $\mu\text{m}$ . Multivesicular vesicles are liposomes with several vesicles inside each liposome [58]. The surface charge is governed by the phospholipids which compose the liposomes [10].

One of the disadvantages in using liposomes was the rapid clearance from the blood and capture by the cells of the reticulo-endothelial system in the liver. To overcome these issues many developments have been made [59]. One of these solutions consists of forming conjugation with ligands on the surface of the liposomes. This allows the liposomes to be recognised by the targeted cells. The most frequently used ligands are immunoglobulins (Ig) of the IgG class. The liposomes-antibodies conjugates are called immunoliposomes [60]. However, the immunoliposomes were uptake rapidly in the liver because of the short permanence time which prevented the liposomes to target the desired site of action [61]. Long-circulating liposomes have been obtained by coating with biocompatible polymers, such as PEG. The steric coating prevent the identification from the opsonins and therefore prolong the residence time of the liposomes [62, 63]. The PEG is the most widely used polymer, although other materials have also been studied for liposome surface modification [64], e.g. poly[N-(2-hydroxypropyl)methacrylamide] [65], poly-N-vinylpyrrolidones [66], L-amino-acid-based biodegradable polymer-lipid conjugates [67] and polyvinylalcohol [68]. Long-circulating immunoliposomes have also been formulated by combining the long-circulating liposomes with immunoliposomes in one formulation [59].

Therapeutic proteins can be encapsulated in the liposomes or conjugated to the surfaces of liposomes. Passive encapsulation can be obtained by incubating the proteins at or slightly below the transition temperature of the lipids. Active loading, also called triggered loading, can be achieved by heating up the liposomes in the presence of proteins in ethanolic buffer under gentle stirring. It is usually expected that the proteins are located in the aqueous core of the liposomes. However, the exposed hydrophobic regions of proteins may interact with the lipid

bilayers. Proteins can also be conjugated to the surface of liposomes. The methodologies used for the conjugation are based on three different reactions: reaction between the activated carboxyl groups and the amino groups for the formation of amide bonds, reactions between pyridyldithiols and thiols for the formation of disulphide bonds and the formation of thioether bonds by reaction between maleimide derivatives with thiols [10]. The possible location of the proteins in the liposomes and examples of surface modification are shown in Figure 1.6.

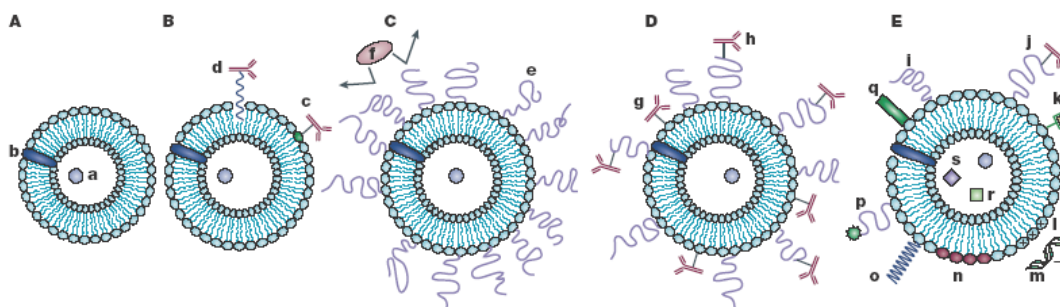


**Figure 1.6** A) Plain liposomes with hydrophilic drug (a) encapsulated in the aqueous core or hydrophobic drug (b) incorporated in the membrane; B) immunoliposomes with antibodies covalently linked (c) or hydrophobically linked (d) to the liposomal membrane; C) Long-circulating liposomes with grafted polymers (e), such as PEG, which shelter the liposomes from the recognition from the opsonins (f); D) long-circulating immunoliposomes combining both polymers and antibody, which can be attached to the liposomal membrane (g) or to the polymeric chain (h); E) new generation liposomes with the surface of which can undergo different modifications: (i) polymer, (j) polymer-ligand conjugate, (k) attachment of diagnostic label, (l) incorporation of positively charged liposomes suitable for DNA complexation (m), (n) incorporation of stimuli-sensitive lipids, (o) incorporation of stimuli-sensitive polymers; (p) attachment of cell penetrating peptide; (q) incorporation of viral component. In addition, magnetic (s) or colloidal particles (r) may also be loaded [59].

The use of liposomes for protein/peptide delivery offers several advantages. They are biocompatible since they are formed by physiological compounds for which several metabolic pathways exist which lead to a reduced toxicity [58]. They can encapsulate proteins/peptides without requiring covalent attachments or any modification on the proteins/peptides structure, which may lead to a partial loss of activity. Liposomes can protect the encapsulated proteins and peptides from inactivation or aggregations during storage. Moreover, the liposomes can deliver the biomolecules directly in the cells. The liposome-cell interactions depend on the size, charge, surface, composition and presence of targeting additives. Figure 1.7 shows the possible liposomes-cells interactions of drug loaded liposomes (A) or modified liposomes with viral components (B).

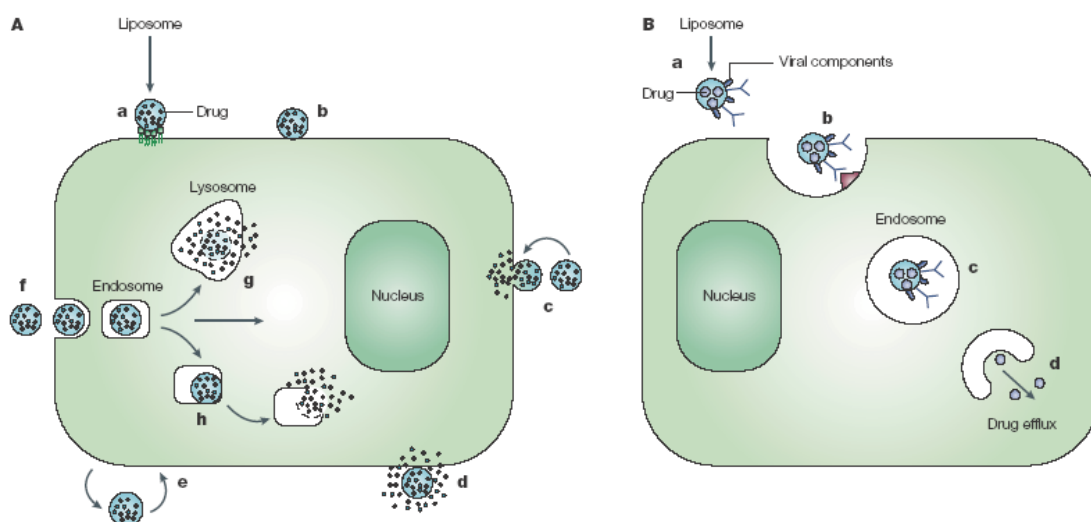


**Figure 1.7** Liposomes-cell interactions of drug-loaded liposomes (A) and modified liposomes with viral components (B) [59].

Figure 1.7A shows the possible interactions between drug-loaded liposomes and the targeted cells. Liposomes can be specifically (a) or non-specifically (b) adsorb on the cell surfaces. They can also fuse with the membrane and release the content into the cytoplasm (c). They can be destabilised by certain membrane components (d) and induce the release of the drugs, which can enter the cell via micropinocytosis. Another possible interaction involves the exchange of the lipid between liposomes and the cell membrane (e). Finally they can be internalised by endocytosis (f) and delivered from the endosomes to the lysosomes (g), in which they are degraded with subsequent release of the drugs. Alternatively, the liposomes can induce destabilisation of the endosomes resulting in the liberation of the content (h). Figure 1.7B shows the potential interactions between cell membrane and modified liposomes with viral components (viroosomes) and drug loaded (a). The viroosomes can actively interact with the cells and induce endocytosis. The interaction between the viral components and the inner membrane of the endosomes allows the drug to be released in the cytoplasm. The viroosomes were proposed for drugs or DNA intracellular delivery, lately they have been found suitable for vaccines therapy [59].

#### 1.1.5.2.2 Solid Lipid Nanoparticles (SLN)

SLN are made from solid lipid and water in the presence of emulsifier. SLN normally have a mean size range between 50 and 1000 nm [69]. They have several advantages, such as the possibility of controlled and targeted drug release, the low toxicity by using physiological lipids or lipid molecules usually used as safe excipients, possibility to incorporate and stabilise hydrophilic and lipophilic drugs, no organic solvents in the preparation and ease of sterility or

scale up [4, 70]. Despite the hydrophobic nature of the lipids and the tendency of the hydrophilic molecules to partition in the aqueous phase, several studies over the years explored the possibility of using SLN for protein/peptide delivery [4].

Two main preparation methods may be used to prepare SLN, high pressure homogenisation (by hot or cold dispersion of the drugs) and microemulsion-based technique. In both hot and cold homogenisation technique, the drug is dispersed in the molten lipid previously melted at 5 or 10 degrees above the lipid melting point. In hot homogenisation, the melted lipid containing the drug is mixed with the hot aqueous surfactant heated up to the same temperature as the molten lipid. The pre-emulsion formed is then homogenised and left to cool. The cooling allows the lipid to recrystallise which lead to the formation of SLN. In the cold homogenisation, the melted lipid containing the drug is cooled, grounded to microparticles and mixed within cold aqueous surfactant solution. This procedure minimises the melting of the lipid and therefore, reduce the partition of hydrophilic drugs to the aqueous phase, making this procedure suitable for hydrophilic drugs [69]. Microemulsion-based technique for the preparation of SLN was developed by Gasco in 1995 [71]. Microemulsions are composed of lipids, water, surfactants and in most of the cases also co-surfactants. A warm microemulsions is prepared by adding the hot aqueous solution of surfactants and co-surfactants to the molten lipid and stir gently. The microemulsion formed is then dispersed in an excess of cold water (2-3 °C) under stirring. As a consequence of the addition to water, the lipid phase precipitates as fine particles. Other reported preparation methods are solvent emulsification-evaporation, solvent emulsification-diffusion and supercritical fluid technology [4].

Cold high-pressure homogenisation has been used to incorporate lysozyme in the SLN [72]. The homogenisation conditions such as temperature, pressure and number of cycles of homogenisation have been found fundamental for the encapsulation of lysozyme. Due to its hydrophilic nature, lysozyme tends to partition into the aqueous phase. Therefore the encapsulation is only up to 59%, which lead to a poor final protein concentration in SLN (0.03%, w/w). However, the amount of lysozyme solubilised depends also on the composition of the lipid mixture. Despite the harsh homogenisation conditions, lysozyme retained its activity in the SLN formulation [72]. The high-pressure homogenisation technique has also been used for the encapsulations of Cyclosporin A (CyA), which retained their stability after the homogenisation process [73] and BSA (bovine serum albumin), whose structure was affected after homogenisation [4].

Many proteins and macromolecular drugs such as bovine serum albumin (BSA), calcitonin, cyclosporine A (CyA), insulin, human serum albumin (HSA), lysozyme, and ovalbumin have

been encapsulated in SLN systems with variable incorporation efficiency [4]. Drug incorporation may induce changes in some of the properties of SLN, such as particle size, zeta potential, lipid modification, etc. The suitability of a material as a valid drug carrier system is measured by the loading capacity, which is affected by many parameters. One of the prerequisites is the solubility of the drug in the melted lipid. Highly lipophilic drugs are more likely to be incorporated in the lipid matrix of SLN. In order to increase the drug solubility, stabiliser can be added. The use of mono- and diglycerides enhance the solubilisation of the drugs in the lipid. The crystallisation behaviour of the lipid matrix can also influence the drug encapsulation. Highly crystalline lipid particles, which form perfect lattice structure upon solidification, lead to drug expulsion. Mixtures of mono-, di- and triglycerides and fatty acids of different chain length are the preferable lipid species for SLN preparation as they form less perfect crystals, which can better accommodate the drugs. Finally, the polymorphic nature of the lipid often also plays an important role in the loading capacity of SLN. Crystallisation behaviours of the lipids in the nanoparticles differ from the ones of the bulk lipids. In the SLN nanoparticles, lipids partially recrystallise into their  $\alpha$ -form, while the bulk lipids tend to crystallise into the  $\beta'$ -modification which lead to a more stable  $\beta$ -form on aging. Increasing the presence of a more stable polymorphic form of the lipid, the imperfections in the matrix reduces and encourages drug expulsion [69]. An alternative protein loading method to encapsulation is the adsorption method. Proteins are known to have high tendency of adsorption on surfaces and accumulation at the solid-liquid interfaces. It has been reported the ability of antigens to adsorb on the surface of SLN proving the efficacy of these nanoparticles as vaccine delivery systems [4, 69].

SLN can enhance the bioavailability of drugs when used as carriers for drug delivery through different routes, such as oral, transdermal, pulmonary, ocular, rectal and parental [69, 74]. The enhancement has been attributed to the small size of the SLN particles (50-1000 nm) and biocompatible nature of the composition of SLNs, which ease the absorption of SLN through the biological barriers. The adhesion properties of the SLN nanoparticles play an important role in enhancing the bioavailability of the drugs delivered by SLN. For oral SLNs, the exposed lipid moieties allow them to adhere to the gut wall. The bioadhesion of oral SLNs increases the residence time in the GI tract, which enhances the oral absorption via prolonging the contact with epithelial membranes. The lipid absorption varies with the lipid composition, for instance medium chain lipids ( $C_8$ - $C_{12}$ ) are absorbed more effectively than long chain lipids ( $C_{16}$ - $C_{22}$ ). Digestion of triglyceride lipids based SLNs by lipase may enhance drug solubilisation and dissolution by inducing the secretion of endogenous bile salt and phospholipid in the intestinal lumen which lead to the formation of mixed micelles [74, 75]. Lipids can promote the formation of lipoprotein and stimulate the intestinal lymphatic lipid flux, which promotes the lymphatic

drug transport. A further uptake mechanism is through the M-cells and lymphatic transport of intact SLN particles. Figure 1.8 shows an overview of the proposed possible drug absorption mechanisms when delivered using SLN.

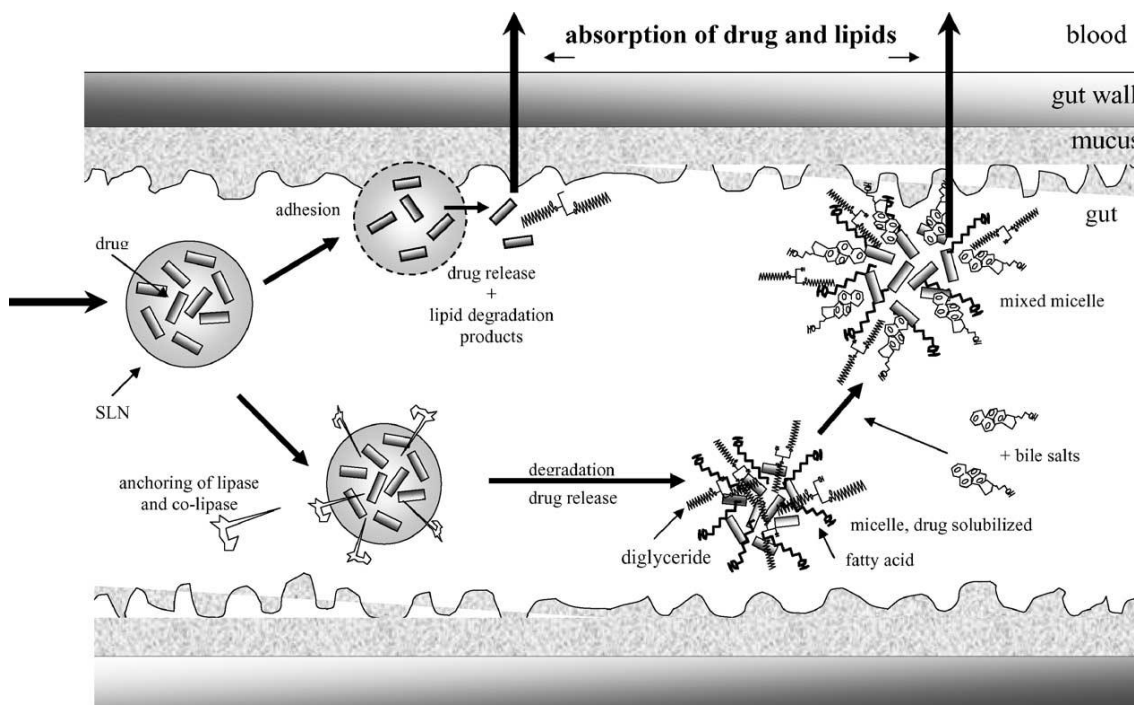


**Figure 1.8** Illustration of the proposed possible drug absorption mechanisms when delivered using SLN. Nanoparticles can directly adhere to the mucosal wall of the intestine and deliver the drug into the site of absorption. They can also be degraded by lipase and co-lipase which leads to the formation of mono and diglycerides which are responsible for the solubilisation of the drug. Bile salts can interact with micelles forming mixed micelle which leads finally to the uptake of both lipid and drug [76].

However, most SLN formulations show limitations mainly in low drug loading capacity, and physical instabilities. The complexity of the lipid behaviours, such as crystallisation or polymorphic transformation and gelation, is often the cause of stability problems (i.e. increased particle size and drug expulsion) during administration and storage [70]. In order to overcome these limitations, a second generation of solid lipid-based nanoparticles (nanostructured lipid carriers, NLC) have been proposed. NLCs are characterised by the mixture of spatially different lipid molecules which form a lipid matrix with imperfect crystalline structure [77]. The imperfections in the nanostructure improve the loading capacity and give more flexibility in modulating the release profile from NLCs. [76].

#### 1.1.5.2.3 Liquid crystalline-based delivery systems

Lipids have been extensively studied as suitable materials for drug delivery with the examples of liposomes and SLN/NLCs discussed earlier in the chapter. Spontaneous reorganisation of

certain amphiphilic lipids in aqueous environment can lead to the formation of liquid crystals with different kind of three-dimensional structures, such as lamellar, hexagonal and cubic phase [78]. A hypothetical sequence is shown in Figure 1.9. It can be seen that by varying water content and temperature, different mesophases may form in which the order of the structure formed depends on the lipid used [79].

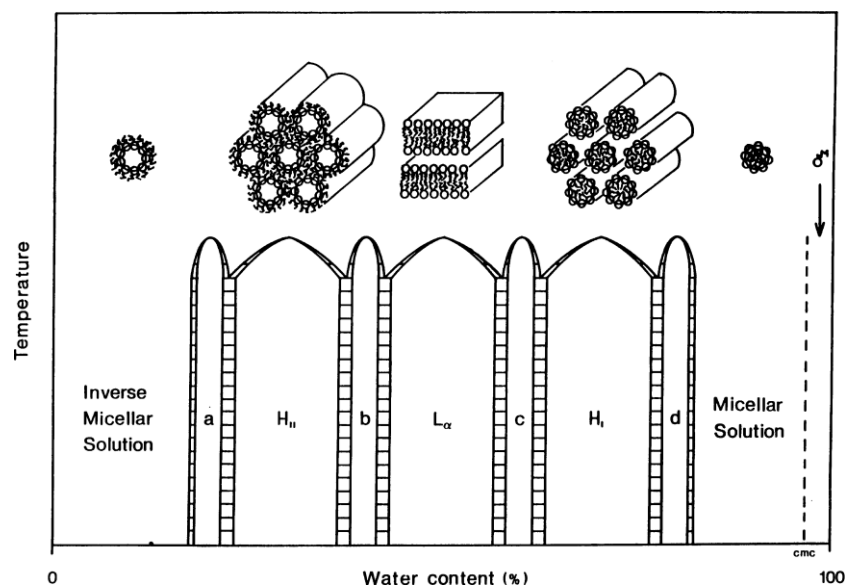


**Figure 1.9** Hypothetical lipid/water phase diagram in which the phase transition depends on the water content. The regions indicated with a, b, c and d represent the intermediate phases, many of which are cubic [79].

Figure 1.10 shows some of the possible liquid crystalline phases that can be formed by lipid materials with the corresponding packing parameters,  $P$ , which is equal to  $v/al$ , where  $v$  is the molecular volume,  $l$  is the molecular length and  $a$  is the cross sectional area of the polar head of the lipid used [80]. The lamellar phase ( $L_\alpha$ ) is characterised by a linear arrangement of alternating lipids bilayers and water channels [78], with zero mean curvature ( $P=1$ ) [80]. The reversed hexagonal phase ( $H_{II}$ ) consists in cylindrical micelles each of which surrounded by six cylindrical micelles. The order of the cylindrical micelles is two-dimensional and they are separated by lipid bilayers. In the reverse hexagonal phase, the polar head of the amphiphilic lipids point towards the inner part of the micelles, whereas in the normal hexagonal phase ( $H_I$ ), the polar heads are on the outside [79]. Materials such as hydrophilic emulsifiers can form oil-in-water self-assembly structures like normal micelles and hexagonal ( $1/3 < P < 1/2$ ) depending on the concentration, while hydrophobic emulsifiers often form reversed self-assembly structure ( $P > 1$ ) [80]. Finally, the bicontinuous cubic phase has curved three-dimensional bicontinuous lipid bilayers separated by two similar networks of water channels [78].

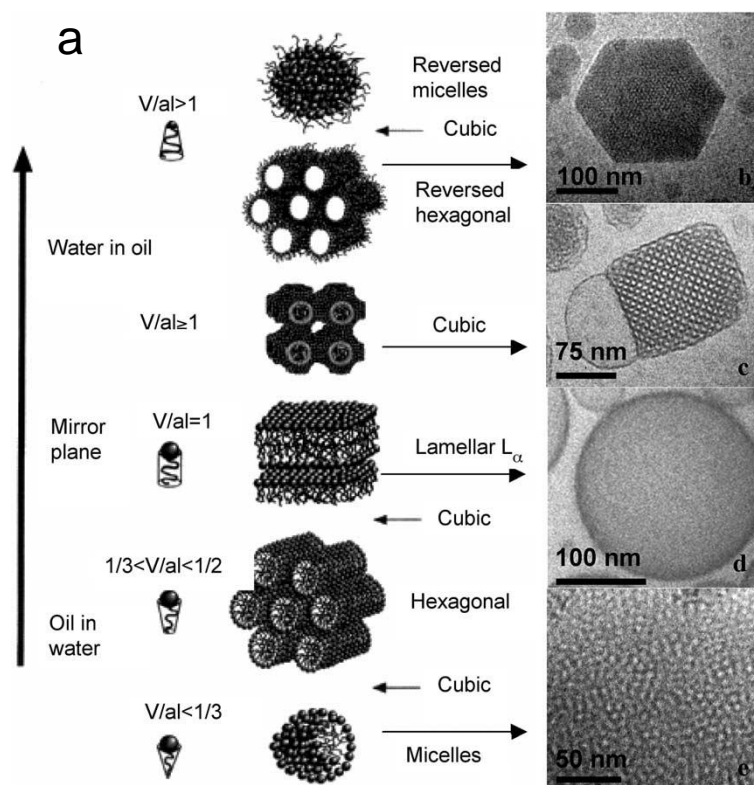


**Figure 1.10** (a) Different liquid crystalline phases with the corresponding packing parameter,  $P$  ( $P=V/al$ ). Cryo-TEM images of dispersed reversed hexagonal phase (b); dispersed bicontinuous cubic phase,  $Im3m$  (c); vesicle obtained from dispersed lamellar phase (d); and micelle (e) [80].

Cubic phase, in particular has been object of interest for its potential to be used as drugs and protein/peptide delivery systems [78, 81-84]. Cubic phase may exist in different forms. Most of the studies on the cubic phase used glyceryl monooleate (GMO) or monoolein as the material of interest, which can form a wide range of cubic phases depending on the water content and temperature. Three cubic phases with different structural features have been identified. They can be described as the periodical minimal surface as primitive (P), gyroid (G) and diamond (D), with corresponding space groups of  $Im3m$ ,  $Ia3d$  and  $Pn3m$ , respectively [80, 85]. Due to the bicontinuous structure, the assembly of cubic phase is close to the natural lipid membrane bilayer. Many proteins can interact with biological lipid membranes in their native state. Therefore, delivery systems with cubic phase structure may represent a class of suitable carrier for protein delivery.

Bicontinuous cubic phase formed by GMO has proved to be able to form sustained-release carrier for the delivery of small molecules and protein drugs via different routes (oral, parenteral, and local delivery). More importantly the protein drugs incorporated within the bilayer cubic phase appear to retain their native conformation and biological activity [78]. Many proteins have been incorporated in the cubic phase. For example, bovine haemoglobin (BHb) was been encapsulated in monoolein cubic phase with high loading efficiency (95%). The study

also reported that the BHB retained its native conformation and biological activity after incorporated into the cubic phase [86]. Moreover, cubic phase was shown to be able to increase the activation of protein kinase C (PKC) in comparison to being loaded in liposomes [87]. Bacteriorhodopsin was shown to be able to retain the native conformation when encapsulated in the cubic phase [88, 89]. The ability of cubic phase to enhance the stability of insulin against aggregation has been demonstrated by Sadhale et al. [90]. Furthermore, insulin retained its biological activity after loaded in the cubic phase [90, 91].

Cubic phase offers many advantages as potential drug delivery system. Its amphiphilic nature allows the incorporation of hydrophilic and lipophilic drugs. Due to the high curvature and complex network of water channels present in cubic phase structure, it offers the potential to be used for sustained-release of drugs, protecting proteins and peptides from acidic and enzymatic degradation. Cubic phase also shows mucoadhesive properties [92], which makes the cubic phase a good candidate for controlled oral delivery. The main disadvantage of using cubic phase as drug carriers is the high viscosity of the bulk phase, which may complicate the direct application of cubic phase formulations [78]. This issue may be obviated by formulating the bulk cubic phase into aqueous dispersion cubic particles [93]. Aqueous dispersions of nanostructured self-assembly liquid crystals have received much attention as potential carriers for drug delivery. Cubosomes and hexosomes are examples of dispersed nanoparticles with cubic and hexagonal phase structures. The production and use of these liquid crystalline nanoparticles were first proposed by Larsson and co-workers [94-96]. Inverted micellar cubic phase was also identified [97]. Cubosomes and hexosomes are formed from hydrated inverted bicontinuous cubic phase and inverse hexagonal phase, which self-assemble in excess of water under high-energy and in presence of stabilisers [94-96]. Usually amphiphilic block copolymers (e.g. Poloxamer 407) are used as stabilisers to provide steric coating of the nanoparticles. The stabilisers have the hydrophobic part anchored on the surface of the lipid and the hydrophilic ends extended in the surrounding environment [96].

Cubosomes are dispersed particles of bulk (non-dispersed) cubic phase and they share some of the advantages of the bulk cubic phase when used as drugs carriers. A range of drugs have been attempted to be incorporated in the Cubosomes, but just for few of them the *in vitro* release and *in vivo* bioavailability were tested [85]. For instance, rifampicin has been incorporated and the sustained release from Cubosomes over a period of 10 to 12 days has been reported [98]. Engström et al. reported the *in vivo* sustained release of somatostatin over a period of 6 hours on rabbits after i.v. injection [99]. The authors attributed the long circulation time of the somatostatin *in vivo* to the exposed polyoxyethylene chains of the stabiliser (Poloxamer 407) on the surface of the nanoparticles, which prevented the uptake by the reticulo-endothelial system (RES). The

efficiency of oral administration of insulin incorporated in “nanocubicles” has also been studied [100]. Nanocubicles are GMO-based cubosomes which are prepared at room temperature without heating the GMO. This formulation allowed a sustained hypoglycaemic effect over 6 hours, which was not achieved by the oral administration of insulin solution. Chung et al. suggest that this result could be attributed to the mucoadhesive properties of the cubic nanoparticles and the protection of insulin by the cubic phase from the enzymatic degradation [100].

In vitro and in vivo toxicity of Cubosomes was evaluated by incubating Caco-2 cells with various concentrations of Cubosomes (Monoolein/Poloxamer 407/Pyrene) [101]. It was found that the cubic nanoparticles were toxic at concentrations equal and greater than 500 µg of total lipid in 1 ml culture medium [101]. However, when the Cubosomes dispersions were incubated with rat jejunum tissue, no damages in the tissue cells were observed [85]. The oral uptake of cubosomes is still not well understood. In the gastrointestinal tract, lipid-based formulations are solubilised by bile salts and digested by several intestinal enzymes. Since the main component of Cubosomes is monoolein, it is reasonable to predict that the nanoparticles may be digested in the GI tract and absorbed by the absorptive cells in the small intestine in the form of mixed micelles with GI components such as bile salts and cholesterol [101].

## **1.2 Gelucire 50/13**

### **1.2.1 Introduction**

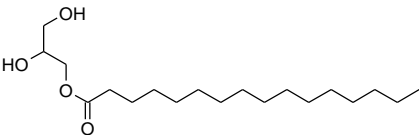
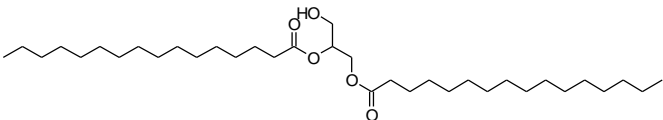
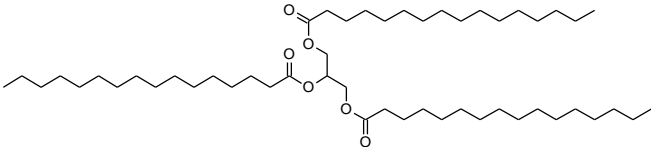
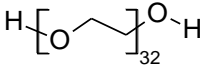
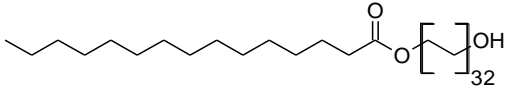
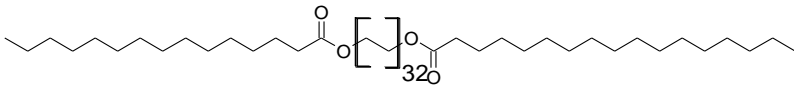
Gelucires are a family of glyceride-based excipients, which are mixtures of polyethylene glycol glycerides composed of mono-, di- and triglycerides and mono- and diesters of polyethylene glycol (PEG). They are distinguished by two numbers, the approximate melting point and the HLB value (hydrophilic-lipophilic balance) [102]. The HLB values of Gelucire may range from 1 to 18 according to the ratio of the lipophilic part (glycerides) to the polar part (polyethylene glycol esters) [103]. Their applications may vary depending on the individual Gelucire composition. It has been reported that Gelucire with low HLB values (<7) usually are suitable for slow drug release and the main release mechanism involved is the diffusion-controlled release. On the contrary, Gelucire with high HLB values are characterised by a faster release and the rate of release is governed by both diffusion and erosion [102]. Furthermore, the Gelucires with high melting points and bigger proportions of lipophilic components have been used as coating and matrices agents for sustained release, while the Gelucires with a high proportion of hydrophilic components have been used as bioavailability enhancers [104]. These lipid bases have been used for the preparation of liquid-filled hard gelatin capsules [104, 105],

pellets produced by extrusion-spheronisation and melt-solidification [106], and microspheres prepared by spray chilling [107]. In this project, we focused on using Gelucire 50/13 to develop a series of bulk gel and nanoparticle formulations for protein delivery. A discussion on the structure and properties of Gelucire 50/13 as well as its potential to be used in the protein drug delivery will be provided.

### 1.2.2 Structure of Gelucire 50/13

Gelucire 50/13 is a non-ionic water dispersible surfactant-like material [108]. It is manufactured by alcoholysis-esterification reaction from hydrogenated palm oil and PEG 1500, which is composed of 32 monomer units of  $-\text{CH}_2-\text{CH}_2-\text{O}-$ . It is a mixture of mono-, di- and triglycerides of palmitic acid and stearic acid as fatty acid chains ( $\text{C}_{16}$  and  $\text{C}_{18}$ , respectively). The glycerides represent 20% in weight of the whole material. 72% of Gelucire 50/13 is composed of mono- and diacyl polyoxyethylene glycols with one or two acyl chains of  $\text{C}_{16}$  or  $\text{C}_{18}$ . In particular, the monoacyl PEG (MPEG) and the diacyl PEG (DPEG) constitute the 29% the 43% (w/w) of the total weight of the material. The remaining 8% is free PEG 1500 [109]. Its amphiphilic nature allows the incorporation of hydrophobic and hydrophilic drugs [104]. In order to explore the potential use as drug carriers, it is important to have a thorough understanding of the structure of the material. As Gelucire 50/13 is largely crystallised material, it can undergo structural changes upon thermal treatment. Thermal and structural characterisation of untreated dry Gelucire 50/13 solid has been studied in detail by Brubach et al. [109]. The crystalline structure and the long spacings of each individual component in Gelucire 50/13 are listed in Table 1.2.

**Table 1.2** Composition of Gelucire 50/13 with the structure and the long spacing of each individual component [109].

<i>Structural Model</i>	<i>Long spacing</i>	<i>Composition</i>
 <p>Monoglycerides from palmitic or stearic acid (C<sub>16</sub> or C<sub>18</sub>)</p>		
 <p>Diglycerides from palmitic or stearic acids (C<sub>16</sub> or C<sub>18</sub>)</p>	d <sub>16</sub> =45.5 Å d <sub>18</sub> =50.7 Å	20%
 <p>Triglycerides from palmitic or stearic acids (C<sub>16</sub> or C<sub>18</sub>)</p>		
 <p>PEG 1500</p>	94 Å*	8%
 <p>Monoacyl PEG (MPEG) with acyl chains of C<sub>16</sub> or C<sub>18</sub></p>	120 Å*	29%
 <p>Diacyl PEG (DPEG) with acyl chains of C<sub>16</sub> or C<sub>18</sub></p>	145 Å*	43%

\* Theoretical values calculated by summation of the long period of the PEG 1500 with the long period of one and two acyl chains C<sub>18</sub>, respectively [109].

As free PEG and PEG esters with one or two acyclic chains are the main components of Gelucire 50/13, it is important to first gain knowledge of the structure of PEG. Polyethylene glycol (PEG) is a synthetic polymer formed by repeating units of  $[-O-CH_2-CH_2-]$  and ending with  $-OH$  group in each chain, or with  $-OCH_3$  end group, in which case it is named poly(ethylene oxide) PEO. It has both lipophilic and hydrophilic parts (carbon atoms and oxygen atoms, respectively), resulting in being soluble in water and organic solvents. The characteristics of PEG depend on the molecular weights of PEG [110]. The unit cell of crystalline PEG is monoclinic with  $a = 0.805$ ;  $b = 1.304$ ;  $c = 1.948$  nm (fibre axis) and the angle  $\beta$  equals to  $125.4^\circ$  [111]. There are four PEG chains in each unit cell [111], each of which has a distorted structure

with seven monomer units  $-\text{O}-\text{CH}_2-\text{CH}_2-$  forming two helical turns per fibre identity period of  $19.30 \text{ \AA}$  [112]. This conformation is called  $7_2$  helix [110]. Besides the helical conformation, two more conformations exist zig-zag Type I and zig-zag Type II, as represented in Figure 1.11 [113]. In the helical structure, the sequence  $-\text{O}-\text{CH}_2-\text{CH}_2-\text{O}-$  has a gauche (G) conformation in the  $-\text{C}-\text{C}-$  bond and a trans (T) conformation related to the  $-\text{C}-\text{O}-$  bond, thus the conformation of the sequence is  $(\text{TTG})_7$  [110]. The zig-zag Type I conformation has a  $(\text{T}_5\text{GT}_5\text{G})$  notation and the zig-zag Type II has a  $(\text{TG}_2\text{TG}_2)$  notation [113]. The most common conformation is the helical structure and its characteristic IR bands are the bands related to the rocking modes of the methylene groups of the sequence  $-\text{O}-\text{CH}_2-\text{CH}_2-\text{O}-$  are observed [109]. Structural analysis on PEG 1500 confirmed that the chains adopt a helical conformation under orthorhombic subcell ( $\alpha=\beta=\gamma=90^\circ$ ), which is in disagreement with structural studies conducted in PEG with higher molecular weight. Furthermore, Small angle X-ray scattering (SAXS) tests confirmed the formation of a lamellar phase with d-spacing equals to  $96.7 \text{ \AA}$  [109].

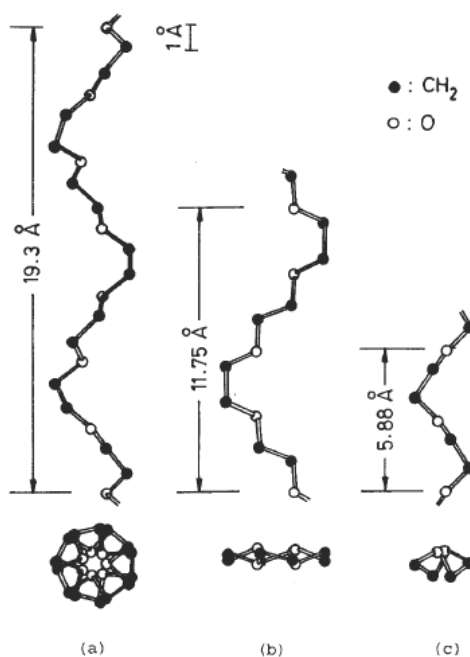


**Figure 1.11** Schematic view of the conformations of PEG: (a) helical  $(\text{TTG})_7$ , (b) zig-zag Type I  $(\text{T}_5\text{GT}_5\text{G})$  and (c) zig-zag Type II  $(\text{TG}_2\text{TG}_2)$ , where T stands for trans and G for gauche [113].

Structural studies of the untreated dry Gelucire 50/13 revealed its complex structure that is thermal history dependent. At  $20^\circ\text{C}$ , SAXS studies revealed the coexistence of three lamellar phases with different long spacing. The first lamellar phase observed has a Bragg's reflection ratio of 1:2:3 corresponding to  $q$  ( $\text{\AA}^{-1}$ ) values of  $0.051 \text{ \AA}^{-1}$ ,  $0.10 \text{ \AA}^{-1}$  and  $0.152 \text{ \AA}^{-1}$  (which correspond to  $d$  ( $\text{\AA}$ ) values of  $121$ ,  $62.5$  and  $41.3 \text{ \AA}$ , respectively). The second lamellar structure is characterised by the Bragg's reflection ratio of 1:2 with  $q$  ( $\text{\AA}^{-1}$ ) values of  $0.07 \text{ \AA}^{-1}$  and  $0.14 \text{ \AA}^{-1}$  (with  $d$  ( $\text{\AA}$ ) values of  $90$  and  $45 \text{ \AA}$ , respectively). Finally, the last lamellar phase has  $q$  value

equals to  $0.127 \text{ \AA}^{-1}$  ( $49.5 \text{ \AA}$ ). The first two lamellar phases do not encounter changes until the temperature reaches  $35 \text{ }^\circ\text{C}$ , after which the lamellar phase with  $121 \text{ \AA}$  spacing increases in intensity whilst the lamellar phase with  $90 \text{ \AA}$  spacing decreases in intensity. At about  $42 \text{ }^\circ\text{C}$ , the lamellar phase with  $121 \text{ \AA}$  spacing melts. On the contrary, the third lamellar phase with  $49.5 \text{ \AA}$  spacing does not show any temperature dependence and melts at a higher temperature ( $50 \text{ }^\circ\text{C}$ ). Furthermore, on cooling after melting, the crystallisation of the third lamellar phase occurs at  $47 \text{ }^\circ\text{C}$ , while the first two lamellar phases ( $121$  and  $90 \text{ \AA}$ ) crystallise at a lower temperature ( $29 \text{ }^\circ\text{C}$ ). The differences seen in the crystallisation and melting temperatures of the lamellar phases are likely to be related to the metastability of the various structures formed upon crystallisation during cooling.

In conclusion, the presence of the first two lamellar phases ( $121$  and  $90 \text{ \AA}$ ) is thermal history dependent, while the third structure is not. Coupling the SAXS experiments with the WAXS (wide angle X-ray scattering) it is possible to associate the components in dry Gelucire 50/13 to each lamellar phase [109]. By observing the response of the WAXS scattering peaks to the thermal treatment, it was concluded that the lamellar phases with  $121$  and  $90 \text{ \AA}$  spacings are associated with the MPEG and DPEG, respectively. The third lamellar phase ( $49.5 \text{ \AA}$ ) is associated with the glycerides part of the material. Furthermore, IR experiments confirm that in Gelucire 50/13, the free PEG chains and PEG in the mono- and diacyl polyoxyethylene glycols adopt the helical conformation, which is stable until the melting of the bulk. However, the long spacing obtained with SAXS ( $121 \text{ \AA}$ ) corresponds to the only MPEG, which has theoretical value equals to  $120 \text{ \AA}$ , while the theoretical value of the DPEG is  $145 \text{ \AA}$ , which is not found in any of the studies (see Table 1.2). The explanation from Brubach et al is that the acyl chains of the MPEG and DPEG molecules interpenetrate, resulting in a shorter spacing ( $120 \text{ \AA}$ ) as it is shown in Figure 1.12 [109].

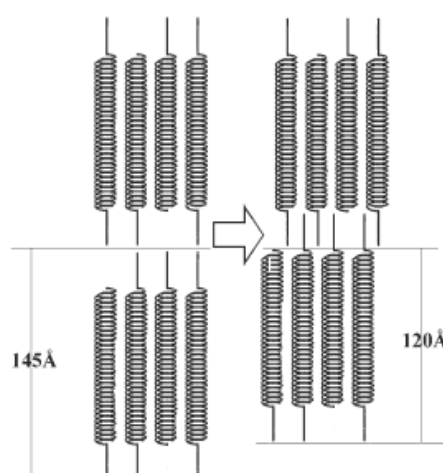


**Figure 1.12** Schematic view of the molecular conformation of MPEG and DPEG with the PEG chains in helical conformation and one or two acyl chains in the end [109].

A small part of Gelucire 50/13 (20% w/w) is composed of a mixture of glycerides [109]. It has been known that the glycerides may exist in different polymorphic structures, which have been classified as  $\alpha$ ,  $\beta'$  and  $\beta$ , depending on the composition and length of the aliphatic chains of the molecules [114, 115]. The relationship between polymorphic forms and the long spacing and the number of carbons in the acyl chain has been determined. In the Gelucire 50/13, the aliphatic chains have 50%  $C_{16}$  or 50%  $C_{18}$ . Therefore, their long spacings can be calculated using Equations 1.5 and 1.6. The calculated spacings are 45.5 Å and 50.7 Å, respectively

$$d_{16}=2.59*16+4.10=45.5 \text{ \AA} \quad \text{Equation 1.5}$$

$$d_{18}=2.59*18+4.10=50.7 \text{ \AA} \quad \text{Equation 1.6}$$

where 2.59 is the distance between every other carbon. Considering that the aliphatic chains with  $C_{16}$  and  $C_{18}$  are present in the same proportion, for steric reasons, the stearic chain ( $C_{18}$ ) with the longer chain length should be responsible for the overall packing of the glycerides in the Gelucire 50/13. Therefore, the glycerides form a lamellar phase with spacing of 49.5 Å and a hexagonal subcell indicated as  $\alpha$ , which corresponds to the third lamellar phase ( $0.127 \text{ \AA}^{-1}$ ) identified by SAXS [109].

In conclusion, Gelucire 50/13 is a non-ionic amphiphilic compound composed of a mixture of mono-, di- and triglycerides and esters of PEG with acyclic chains ( $C_{16}$  or  $C_{18}$ ) with a small amount of free PEG. Structural and thermal studies confirm the coexistence of several lamellar phases depending on the thermal history and the crystallisation rate of the sample.

### 1.2.3 Ageing effects

Many studies have reported the effect of ageing under different storage conditions on the properties and performance of Gelucire as a pharmaceutical excipient. Studies have been conducted over the years to investigate structural and behavioural differences in Gelucire 50/13 over ageing [116-118]. It has been suggested that one of the key reasons for the physical instability of processed Gelucire 50/13 is due to the changes in polymorphic forms of the glycerides present in the material. For instance, the effect of storage on triglycerides has been extensively studied when used to prepare formulations such as suppositories. Ageing resulted in an increase of the melting point of the lipid. Saito et al. attributed this increase to the polymorphic transitions of the triglycerides components [119]. Sutananta et al. studied the effect of ageing and preparation conditions on the structure of the Gelucire 50/13 [103, 120]. The authors reported the cooling rate effect on the thermal profile of aged Gelucire 50/13. The effect of crystallisation rate on the structure of the lipid was also investigated by Brubach et al. [109].

The formations of intermediate lamellar phases were observed depending on the cooling rate used. A slower cooling rate leads to the formation of the more stable lamellar phase with 120 Å spacing. On the contrary, a faster cooling rate promotes the formation of the polymorphic forms with shorter spacing (90 and 74 Å). However, in this study the authors concluded that the cooling rate did not affect the structure of the glycerides in Gelucire 50/13, confirming the formation of the lamellar phase with 50 Å spacing with hexagonal subcell.

The effects of storage conditions at 20 and 37 °C of Gelucire 50/13 dispersions alone and containing caffeine and paracetamol were investigated by Khan et al. [121]. The incorporation of paracetamol influenced the melting profile of the lipid. Changes were found in the thermal, morphological and dissolution behaviour of the Gelucire based dispersion formulations after ageing. Higher storage temperature (37 °C) showed stronger effect on the thermal DSC results of the dispersion than the effect of 20 °C storage temperature. For the Gelucire based tablet formulations, a change in the microstructure of the tablets surface was revealed after ageing. The increase in drug dissolution rate of the aged tablets has been argued to be a result of this morphological changes of the surface of the tablets [121].

#### 1.2.4 Water uptake

Due to the amphiphilic nature of Gelucire 50/13, it can absorb water (from environment or bulk water when submerged) and swell to some extent before disintegration/erosion. More recently, the environmental water uptake behaviour of solid dispersions of Gelucire 50/13 was investigated [122]. It was concluded that the temperature and the relative humidity (RH) affects the moisture uptake of the systems. Little water sorption was observed under ambient conditions (at 25 °C and RH of 40%-70%). However, by increasing the RH above 75%, the moisture sorption dramatically increased. During the moisture sorption process, it was proposed that the dissolution of free PEG and glycerides occurs first followed by the swelling of the PEG esters. The temperature is also important in the moisture uptake process of Gelucire 50/13. It has been reported that at the temperature above the onset of the melting point, the moisture uptake significantly increase. Therefore cautions should be taken when prepare and store Gelucire 50/13. In summary, an environmental relative humidity below 40% should be maintained, if melting and cooling are involved in the preparation using Gelucire 50/13. The storage temperature should be controlled at below 35°C in order to minimise the instability of Gelucire 50/13-based dispersions [122].

Little has been done in order to understand the behaviour of the Gelucire 50/13 in the presence of water. However, some studies were carried out in order to understand the swelling behaviour

and the water uptake of Gelucire 50/13 matrices by Sutananta et al [102]. In presence of water, Gelucire 50/13 matrices undergo swelling with further water uptake, which is followed by weight loss of the matrices. The reason for this behaviour is due to the fact that the matrices disintegrate at the surfaces because they are not able to accommodate the continuous water uptake during swelling. This study identified the erosion as the main mechanism of release of drugs from Gelucire 50/13 matrices. Hydration studies of Gelucire 50/13 were conducted by Qi et al. [123]. The hydrated Gelucire 50/13 is gel-like material characterised by high viscosity and absence of birefringence under polarised light microscopy. All these features fit with typical liquid crystals cubic phases. The preliminary SAXS experiments confirmed the lamellar phase which is observed in the untreated Gelucire in combination with less well defined liquid crystalline structure which is close to the diffraction pattern of a cubic phase [123]. This leads to the hypothesis of the formation of different ordered microstructure in the hydrated forms of Gelucire 50/13 by varying the water content. This hypothesis was tested in this project.

### **1.2.5 Pharmaceutical applications of Gelucire 50/13**

The pharmaceutical applications of Gelucire 50/13 mainly lie in oral formulations, either in the form of bulk capsules/tablets or micro-/nanoparticles. The potential of Gelucire 50/13 solid dispersions to improve the dissolution and the oral bioavailability of poorly soluble drugs has been extensively studied. It has been reported to improve the solubility and thus the dissolution rate of many poorly soluble small molecular drugs, such as carbamazepine [124], diclofenac [125, 126] and praziquantel [127], indomethacin [128] and etoricoxib [129]. It has been concluded that the reason for the improved release is mainly due to the increasing wettability of the drug and in particular by increasing the wettability of the drug, reducing the particle size and decreasing the crystallinity of the drug [128]. Gelucire 50/13 not only can be used to prepare filled hard capsule formulations, but also to form stable spherical-shape microparticles by using the spray chilling technique. The spray chilling method was successfully used to produce microparticles for incorporation of piroxicam and caffeine [107]. Furthermore, melt-granulation technique has been proved to be a valid method to prepare Gelucire 50/13 based microparticle formulations. Gelucire 50/13 was also used as an absorption enhancer for atazanavir, which is characterised by low oral bioavailability [130]. It has reported to enhance the release of lysozyme when incorporated in glyceryl palmitostearate (GPS) pellets [106]. However, it seems to be responsible for a reduced activity of lysozyme due to the binding of lysozyme to the dispersed Gelucire after dissolution [131]. Gelucire 50/13 has also been used as a stabiliser for lipid nanocarriers such as SLNs and NLCs. The nanoparticle formulations containing Gelucire 50/13 can improve the oral delivery of hydrophobic model drug, repaglinide [132].

### 1.3 Lysozyme

Lysozyme is an enzyme widely present in nature. It can be found in hen and other bird egg-whites, in human secretion and tissues in bacteria, phages and plants as well as in other vertebrate and invertebrate organisms [133]. However, hen egg white is the most important source of lysozyme. Therefore, an extensive amount of studies on the hen-egg white lysozyme has been accumulated [134]. Lysozyme is a relatively stable protein which retains its structure over a wide range of pH (between 6 and 9) and temperature [135]. At pH 6.2 the maximal activity is reported over a wider range of ionic strength (0.02-0.1 M), whilst at pH 9, the activity is limited to a smaller range of ionic strength (0.01-0.06 M). Furthermore, it has an isoelectric point of 11, which makes it stable in electrostatic solvents. The denaturation temperature of the lysozyme is 76 °C and it retains its biological activity in both its native and partially denatured state [135]. Considering the relatively good physical stability and the extensive knowledge existing in the literature on lysozyme, it was chosen as the model protein for this study in order to study the feasibility and efficacy of using Gelucire 50/13 gels and gels-based nanoparticles as carrier systems for protein delivery.

Lysozyme has been often used as a model compound for protein delivery studies. For instance, the incorporation of lysozyme in the water channels of monoolein cubic phase can induce transitions from a Pn3m to an Im3m structure [83]. This may be due to the frustration derived by the confinement of the enzyme in narrow water channels. Physical properties and structural behaviour of lysozyme entrapped in reverse hexagonal phases of monoolein were also investigated in order to assess the potential of using this mesophases for protein drug delivery [136]. It has been postulated that lysozyme is embedded in the outer interface of the reverse hexagonal phase in order to fit in the narrow water channels. In addition, it was supposed that lysozyme interacts with hydroxyl groups of monoolein resulting in a stabilising effect of the secondary structure towards pH, denaturing agent (urea) [136] and temperature [137]. Drawbacks in the use of reverse hexagonal phase was the low solubilisation ability of lysozyme in the water channels (3%) compared to the cubic phase (5%-8%) [84]. It can be concluded that the cubic and reverse hexagonal mesophases of monoolein stabilise lysozyme structure, although the incorporation of the enzyme induce structural changes in the monoolein. Glyceryl palmitostearate (GPS) pellets were studied as potential protein delivery systems. The addition of Gelucire 50/13 in the GPS pellets leads to increase lysozyme release from the formulation, but a decrease of lysozyme activity was also reported [131]. SLNs prepared from different lipids were evaluated as potential protein delivery using lysozyme as model protein. Low encapsulation efficiency was achieved due to the hydrophilic nature of the lysozyme; however, the lysozyme retained its activity. The SLNs can stabilise and protect lysozyme from the harsh conditions used in the preparation of the nanoparticles (cold high pressure homogeniser) [72]. More

recently, the ability of lysozyme to improve the dispersions of single-walled carbon nanotubes (SWNT) in aqueous solution was studied [138, 139]. High level of retained activity of lysozyme was reported when interacts with SWNT [139].

### 1.3.1 Lysozyme structure

The molecule of lysozyme is ellipsoidal with dimensions equal to 45 x 30 x 30 Å and a molecular weight of about 14.3 kDa. The primary structure of the lysozyme was defined in the 1960s by several groups [140, 141]. It is composed of a single chain of 129 amino-acid residues cross-linked in four places by disulphide (-S-S) bonds [133] as it is shown in Figure 1.13.

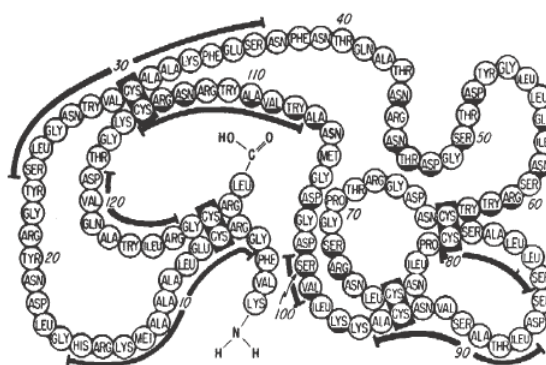


**Figure 1.13** Primary structure of hen egg-white lysozyme with four disulphide bonds between two groups of cysteine (CYS) (in dark boxes). The residues involved in  $\alpha$ -helical conformations are highlighted with continuous black lines and the residues involved in binding sites are underlined [142].

The three-dimensional conformation of the hen egg-white lysozyme has been resolved by X-ray analysis at 2 Å resolution. By comparing the information obtained with the electron density distribution at 2 Å resolution with the X-ray determined primary structure, it was possible to spatially locate each of the 129 amino acid residues [142]. A schematic view of the conformational structure of lysozyme molecule is shown in Figure 1.14.

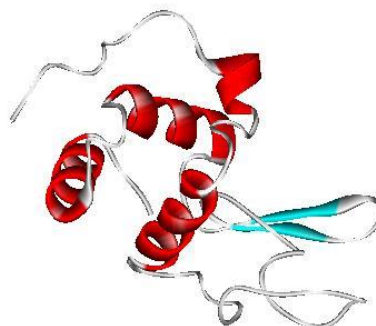


**Figure 1.14** Schematic representation of the 3D conformation of the main chain of lysozyme;  $\alpha$ -helices (red),  $\beta$ -sheet (blue) and the irregular loops or unordered structure (grey) [143].

The molecule can be divided in two parts. The first 40 amino acids (from the N-terminal end of the molecule) fold in  $\alpha$ -helix structure, which represents about the 40% of the molecule. About six lengths of the helices have been identified. As it can be seen in the Figure 1.13 (sequences underlined with continuous lines) some of them are very short and three of them are with about 10 residues length each [142]. In this part of the molecule, a number of hydrophobic side chains can be distinguished and some of them are positioned in a way to give the helices a partially hydrophobic surface. In the three-dimensional conformation, this part of the sequence forms a globular unit with hydrophobic side chains between two  $\alpha$ -helices [144]. The following fourteen residues (41-54), which include hydrophilic groups [144], double back on itself and form anti-parallel pleated sheet in the three-dimensional structure [133, 142]. In an aqueous environment these hydrophilic residues fold on themselves to protect the hydrophobic residues 55 and 56 [144]. Residues from 61 to 87 form a third segment [145] and residues from 88 to 100 fold in an irregular  $\alpha$ -helix. The last 20 residues fold around the globular unit formed by the first 40 residues. In this way the amino ends has to fold in front of the carboxyl end [144]. Generally, the hydrophobic side of the chain is included inside the molecule, while the polar side is distributed on the surface of the molecule along with the acidic (Asp and Glu) and basic (Lys, Arg and His) side chains and the terminal groups [133]. However, some of the hydrophobic residues are on the surface, such as the Trp 62, Trp 63, Ile 98, Val 109, and Trp 123. The remaining polar side chains are on the surface with the exception of the Gln 57 and Ser 91, which are protected from the surrounding liquid [144]. It can be concluded that the lysozyme has a hydrophobic core and a polar surface [133] which gives the water soluble nature of the protein. X-ray studies identified the position of the four disulphide bridges. All of them have at least one helix on one side and the bridge between residue 30 and 115 is the only bridge having helices on both sides [142].

### 1.3.2 Mechanism and site of action of lysozyme

Lysozyme promotes the dissolution of bacterial cell walls by catalysing the hydrolysis of polysaccharides that constitute the protective cell walls of some species of bacteria. For its degradation action towards bacteria, it is considered as a natural bactericidal agent [146]. The main component of bacterial cell wall is the peptidoglycan, which is formed by an alternation of N-acetylglucosamine (NAG) and N-acetylmuramic acid (NAM) residues linked together by glycosidic bonds between carbons 1 and 4 of two consecutive sugar molecules. The polysaccharides chains are cross-linked together through polypeptides of different length and nature depending on the type of bacteria. Lysozyme acts by breaking the  $\beta$  (1 $\rightarrow$ 4) linkage between carbon 1 in NAM and carbon 4 in NAG [147] The activity of cleavage of the lysozyme between the NAG residues in chitodextrin has also been reported [133, 144]. Studies from

Phillips et al [147] identified the active site of the lysozyme. It was observed that one of the glycosidic bonds between the NAM residue in position D and NAG residue in position E in the proteoglycan structure can be cleaved by lysozyme. Moreover, the most active amino acid residues in the proximity of this bond are the Asp 52 and Glu 35. The mechanism of action was proposed by Phillips et al [147]. It was proposed that the NAG residue dissociate to form a glycosidic intermediate, which is stabilised by the interaction with the negative charge of Asp 52. Finally water molecule attacks the carbonium ion completing the hydrolysis [147]. However, lately a new mechanism has been proposed by Vocadlo et al [148]. According to this study, the Asp 52 residue attacks the carbon C<sub>1</sub> of the NAM residue inducing the detachment of the NAG. The Glu 35 residue protonates the dissociated NAG residue. Finally water molecule detaches the Asp 52 residue and give the final product [148]. This recently proposed mechanism seems to be more supported by experimental data.

#### 1.4 Project objective

Advances in biotechnology and recombinant techniques have resulted in a significant increase in the number of therapeutic macromolecules such as proteins, vaccines, and hormones [6]. These macromolecules offer valid additions to the treatment options for many therapeutic areas [28]. However, the delivery of such macromolecules can be extremely challenging especially for oral administration. Many attempts have been made in order to improve the bioavailability of therapeutics macromolecules, as reviewed in this chapter. Several types of lipid-based delivery systems have been demonstrated as suitable carriers for oral protein delivery. Gelucire 50/13 is a FDA approved complex lipid excipient. Up to now it has been only used as dry excipient in the preparation of various solid dosage forms [109]. However, some preliminary studies on the physicochemical properties of hydrated forms of Gelucire 50/13 revealed some unique features of these gel-like matrices, which make worthwhile to consider Gelucire 50/13 as suitable carrier for protein/peptide delivery [102, 122, 123]. For instance, it has been suggested the possibility of forming cubic liquid crystalline phases [123] which has been considered valuable carriers for protein/peptide delivery [81]. Moreover, it has been proved to act as stabiliser in lipid-based nanoparticles [132].

The main focus of this project is the development and characterisation of Gelucire 50/13-based gels formulations as potential carriers for oral protein/peptide delivery. The work will also explore the ability of these gels to form stables nanoparticles and evaluate the performance of these nanoparticles to deliver the model protein. Throughout the thesis, a thorough characterisation of the mechanical and physical properties of unloaded and lysozyme-loaded gels will be studied by using numerous characterisation techniques. The theoretical background

of the characterisation techniques is also provided (see Chapter 2). The objectives will be listed in details in every chapter, however the main aims are summarised below.

- Physical and mechanical characterisation of Gelucire 50/13-based gels prepared over a range of water content from 10% to 90% and by using two different methods, in order to evaluate the best formulation for protein/peptide delivery (Chapter 3). The characterisation of the microstructure of the gels with a particular concern to the water distribution within the gels is also studied in order to have a better understanding of the internal structure of the gels and further insight on the gels performance as carrier for protein/peptide delivery (Chapter 4).
- Encapsulation of a model protein (lysozyme) into Gelucire 50/13-based gels previously characterised. Physical characterisation of the lysozyme-loaded gels with special attention paid on the investigation into the structural conformation changes of lysozyme after being incorporated into the gels, and *in vitro* performance of lysozyme-loaded gel formulations (Chapter 5).
- Nanoparticles formulations from Gelucire-based gels which can be potentially used for protein delivery. The characterisation of lysozyme-loaded nanoparticles as well as the encapsulation efficiency and retained biological activity of the lysozyme is also explained in Chapter 6.

## 2 Materials and Methods

### 2.1 Introduction

This project is mainly focused on the development and the characterisation of polyethylene glycol glycerides-based gels formulations for the delivery of proteins and peptides drugs. This chapter provides the general information of the source of material used through the project, the sample preparation procedures and theoretical background and methodology development of the characterisation methods used. The gels were prepared over a range of water contents 10-90% (w/w) by following two different preparation procedures, heating and hydration based methods. A model enzyme, lysozyme, was incorporated in the gel formulations. The physico-chemical characterisation of the gel formulations with and without lysozyme was assessed by using a wide range of analytical techniques including attenuated total reflectance-Fourier transform infrared (ATR-FTIR), differential scanning calorimetry (DSC), small angle X-ray scattering (SAXS), texture analyser, rheometer, relaxometry NMR. The release profile of lysozyme from the bulk gel formulations was tested with *in vitro* release studies using BP paddles dissolution method and Franz diffusion cells.

The hydrated forms of Gelucire 50/13 in excess of water can be fragmented and form stable nanoparticle suspension formulations. The potential of using these nanoparticles as oral delivery systems for protein/peptide was investigated during this project. The aqueous dispersions of Gelucire 50/13 gel nanoparticles were characterised by their sizes and shapes with dynamic light scattering (DLS) and imaging techniques including cryogenic transmission electron microscopy (cryo-TEM) and atomic force microscopy (AFM). The cytotoxicity and the cell uptake of the nanoparticles were studied using two model cell lines, human lung mucoepidermoid carcinoma-derived H292 cell line and the human intestinal Caco-2 cell line. The encapsulation efficiency and the retained biological activity of the lysozyme were quantified for the lysozyme-loaded nanoparticles. The retaining of the tertiary structure of the lysozyme after encapsulation into the nanoparticles was studied by using circular dichroism spectroscopy (CD).

## **2.2 Materials details**

### **2.2.1 Stearoyl macroglycerides (Gelucire 50/13)**

In this study, a single batch of Gelucire 50/13 donated by Gattefossé SAS, St Priest, France was used through the project. Gelucire 50/13, also known as stearoyl macrogol-32 glycerides EP or stearoyl polyoxyl-32 glycerides NF, is a mixture of mono-, di- and triglycerides and mono- and diacyl polyoxyethylene glycols. The two numbers 50 and 13 indicate the dropping point and the hydrophilic-lipophilic balance (HLB), respectively.

### **2.2.2 Lysozyme**

In this work, hen egg-white lysozyme was purchased from Sigma Aldrich (Gillingham, UK) was the chosen model protein loaded in the gels and the nanoparticles; the activity of lysozyme after formulated into the nanoparticles suspensions was tested by using the *Micrococcus lysodeikticus* cells as substrate (Sigma Aldrich, Gillingham, UK). The activity of the lysozyme loaded in the gels could not be assessed because of the design of the assay and the stickiness of the gels.

### **2.2.3 Mucin from porcine stomach, type II**

Purified mucin powder from porcine stomach (type II) containing ~1% of bound sialic acid was purchased from Sigma Aldrich (Gillingham, UK). The compressed mucin tablets were used to assess the mucoadhesive properties of the gel formulations by using a Texture Analyser, as described in section 2.4.3.2. The structure of the mucin and the mechanism of the mucoadhesion are introduced in Chapter 1 (section 1.1.4.1).

### **2.2.4 Porcine small intestine**

The porcine small intestine was obtained from the local abattoir immediately after the sacrifice of the animal. It was washed with PBS (phosphate buffer saline, pH 7.3) several times until the liquid passing through the intestine was clear. The washing process was performed as gentle as possible to ensure that the mucus layer on the lumen surface was not affected. The tissue was then cut into pieces of about 10 cm long, and frozen with liquid nitrogen. The pieces were packed in plastic specimen tubes and stored at -20°C freezer for later use. The frozen intestine segments were defrosted in the fridge over night before use.

### 2.2.5 Coumarin-6

Coumarin 6 (3-(2'-Benzothiazolyl)-7-diethylaminocoumarin) is a lipophilic fluorescent dye. It is insoluble in water and soluble in methanol and ethanol. Coumarin-6 with 98 % purity and laser grade was purchased from Acros Organics (New Jersey USA). The chemical structure is illustrated in Figure 2.1. It was used as a labelling agent in this project to study the cell penetration ability of the nanoparticles.

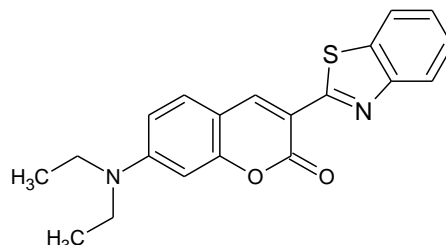


**Figure 2.1** Chemical structure of coumarin-6

## 2.3 Descriptions of samples preparations

### 2.3.1 Preparation of lysozyme-free and lysozyme-loaded gel formulations by heating and by hydration methods

A range of Gelucire 50/13 gel with water contents from 10% to 90% (w/w) was prepared following two procedures: heating and hydration method. In this work, ultrapure, type I, water (Milli-Q grade, 18 M $\Omega$ .cm at 25 °C) produced by Barnstead Nanopure, Thermo Scientific, UK) was used for all sample preparations. For the heating method, Gelucire 50/13 was melted using a hot plate at  $62 \pm 2$  °C. The appropriate amount of water, heated to the same temperature, was added to the melted lipid. A hand-held disperser (Ultra-Turrax T10 basic, IKA, Germany) was used at 8000 rpm for 2-3 minutes. For the hydration method, room temperature water was added to the melted lipid cooled down to room temperature and the system was left to hydrate at room temperature for a week.

Lysozyme was incorporated into the gels with 40% to 70% (w/w) water contents. For the samples prepared by hydration method, the lysozyme solution was added to the melted lipid and left to hydrate at room temperature. The lysozyme concentration in the gel formulation was fixed at 3% (w/w) for all the formulations. The lysozyme-loaded gels prepared by hydration were analysed one week after the preparation. Some lysozyme-loaded formulations were prepared by following the heating method as described above. The exact water content of the lysozyme-loaded gels is specified for each experiment in the corresponding chapters. The samples prepared by the heating method were characterised 24 hours after the preparation.

### 2.3.2 Preparation of lysozyme-free nanoparticles and lysozyme-loaded nanoparticles

The aqueous dispersions of the nanoparticles were prepared by fragmenting Gelucire 50/13 bulk gels. The bulk gels were prepared with the heating method following the procedure described in section 2.3.1. Fragmentation was performed by vortexing the gel using a hand-held disperser (Ultra-Turrax T10 basic, IKA, Germany) at 30000 rpm for 5 minutes in Milli-Q water. The nanoparticle dispersion with a final concentration of 2% w/w gel and 98% w/w water was homogenised by passing five times through a high-pressure homogeniser (EmulsiFlex-C5, Avestin, Ottawa, Canada) at the pressure of about 12000 psi at room temperature. The bulk gels with 30%, 40%, 50%, 60% and 65% water contents were prepared using the heating method without adding any stabiliser. They were labelled as F1 to F5, respectively (as seen in Table 2.1). The formulations were stored at 4 °C and at room temperature for the physical stability study.

The preparation of the nanoparticles loaded with lysozyme followed the same procedure used to prepare the lysozyme-free nanoparticles. The bulk gels were prepared using the heating method as described in section 2.3.1. The final concentration of the lysozyme in the nanoparticle dispersion is 0.06 mg/ml. The components of the formulations are listed in Table 2.1.

**Table 2.1** List of gel and the nanoparticles formulations studied in this project.

<i>Protein-free bulk gel formulations</i> (% water, w/w)	<i>Gel nanoparticles</i>	<i>Lysozyme-loaded bulk gel formulations</i> (% water, w/w)	<i>Gel nanoparticles</i>
30	F1	30	F1-LYS
40	F2	40	F2-LYS
50	F3	50	F3-LYS
60	F4	60	F4-LYS
65	F5	65	F5-LYS

High-pressure homogenisers have been used for several biological and pharmaceutical applications, such as cell and bacteria rupture, formulation of emulsions, liposomes and nanoparticles. The equipment used in this work is shown in It consists of a sample cylinder for sample loading, a single acting high pressure pump which is air/gas driven and a dynamic homogenizing valve. In this work, the high pressure pump operated under nitrogen gas at a pressure 240 times less than the hydraulic pressure required for the product (12500 psi). When the pump starts to cycle, the sample is sucked into the pump body through the inlet valve and pushed into the homogenizing valve through the outlet valve.

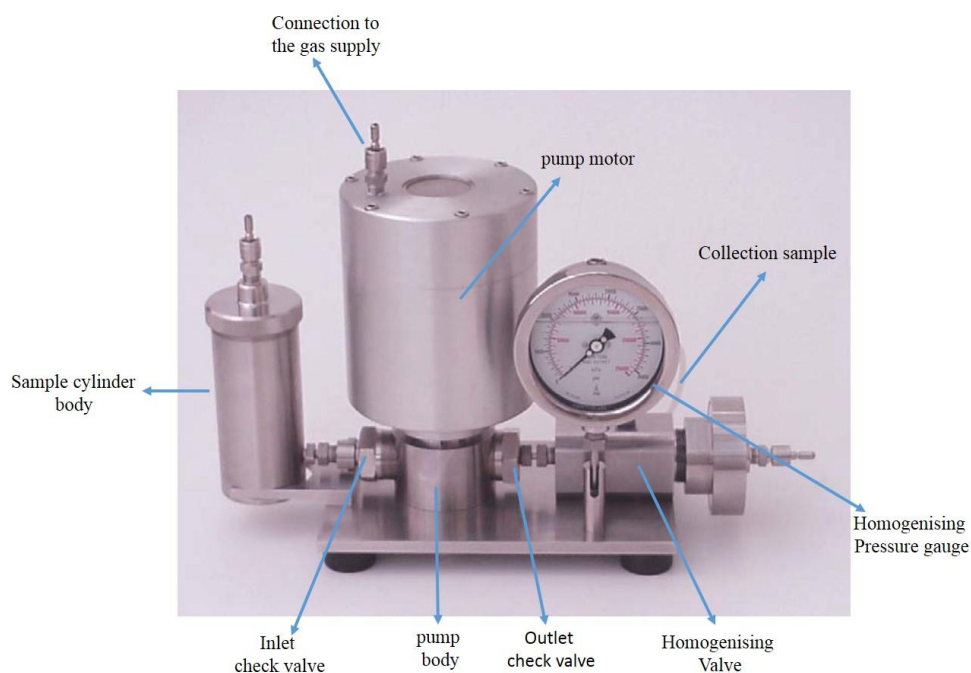


**Figure 2.2** Emulsiflex C-5 high-pressure homogeniser (adapted from AVESTIN brochure).

### 2.3.3 Preparation of fluorescent gel nanoparticles

The fluorescent labelled Gelucire 50/13 nanoparticles were prepared using the heating method. The fluorescent dye (coumarin-6) was added to the melted lipid and mixed by using a magnetic stirrer. When the dye was completely dissolved in the melted lipid, the hot water (with the same temperature of the melted lipid) was added and mixed well. The concentration of coumarin-6 in the gels is 0.001% w/w. The fluorescent labelled nanoparticles were prepared by following the same procedure described in the section 2.3.2.

### 2.3.4 Preparation of buffer solutions

Phosphate buffer solution (pH 7.4) and 0.1 M HCl solution (pH 1.2) were prepared for the drug release studies. Phosphate buffer saline (PBS) solution (pH 7.3) was prepared to treat the porcine small intestinal tissue. For all buffers, the components were dissolved in the minimum amount of water, the volume was then adjusted and the pH was checked with a bench-top pH meter (SevenEasy, Mettler Toledo, Schwerzenbach, Switzerland). The preparation and the components of the buffer used are listed in Table 2.2.

**Table 2.2** Buffer solutions used in this project.

<i>Buffers</i>	<i>Components</i>	<i>Amount added per litre</i>	<i>Concentration</i>
pH 7.4	KH <sub>2</sub> PO <sub>4</sub>	0.6 g	4.4 mM
	Na <sub>2</sub> HPO <sub>4</sub> ·12H <sub>2</sub> O	6.4 g	17.9 mM
	NaCl	5.85 g	100.1 mM
PBS pH 7.3	KCl	0.2 g	2.7 mM
	KH <sub>2</sub> PO <sub>4</sub>	0.2 g	1.47 mM
	NaCl	8 g	136.9 mM
	Na <sub>2</sub> HPO <sub>4</sub> (anhydrous)	1.15 g	8.1 mM
0.1 M HCl	HCl 12 M	8.33 ml	
Potassium Phosphate	KH <sub>2</sub> PO <sub>4</sub>	8.98 g	66 mM
	KOH	(to adjust the pH)	1 M

## 2.4 Theoretical background of physicochemical characterisation of the gels and the nanoparticles

### 2.4.1 Differential scanning calorimetry (DSC)

Differential scanning calorimetry (DSC) is the most commonly used thermal technique to evaluate the thermal transitions of a material. The thermal response of a sample to a thermal treatment is measured in terms of energy transfer and temperature. A sample subjected to a thermal programme, heating, cooling or isothermal, can experience different transitions such as melting, crystallisation, glass transitions and decomposition.

The basic working principle of a DSC is to place the sample in a furnace along with an empty reference pan and heated or cooled at a controlled rate. When a thermally related transition occurs in the sample, the temperature and the energy related to the event are measured. There are two kinds of DSC instruments, heat flux DSC and power compensation DSC. In the heat flux, one furnace is used for both sample and reference pans. The furnace heats equally the two crucibles and the difference in temperature is measured by the thermocouples placed beneath the pans. The heat flow from the furnace is calculated by using the following equation

$$\frac{dQ}{dt} = \frac{\Delta T}{R} \quad \text{Equation 2.1}$$

where  $Q$  is the heat,  $t$  the time,  $\Delta T$  the temperature difference between the furnace and the crucible and  $R$  is the thermal resistance of the heat between the furnace and the crucible. The difference in temperatures measured for the sample and reference pan is connected to one of the thermal events occurring to the sample during the run.

The power compensation DSC is more complex. Two separate furnaces are present, a sample and a reference furnace. Both of them undergo to the same temperature profile, the difference of electrical power supplied to the crucibles for each furnace is recorded. A schematic view of the heat flux DSC and power compensation DSC is shown in Figure 2.3.

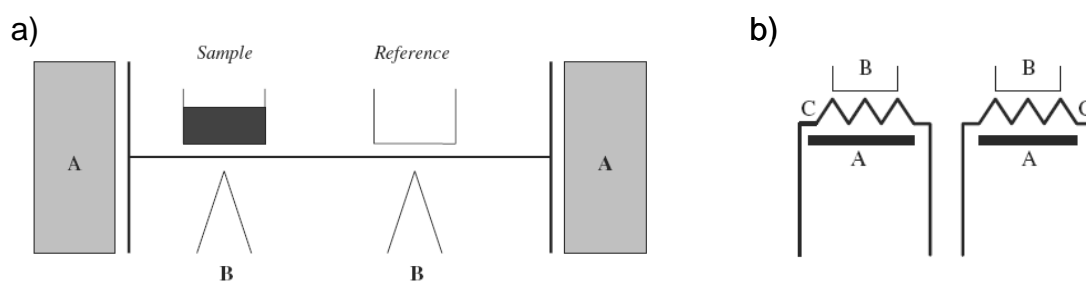


**Figure 2.3** Schematic representation of heat flux DSC (a) and power compensation DSC (b). A= furnaces; B=termocouples; C=sample and reference platinum resistance thermometers [149].

### 2.4.2 Rheology

Rheology is the study of the deformation and the flow of the matter. This technique can be used to characterise materials used in different scientific disciplines such as engineering and fabrication field, pharmaceutical formulations and formulations of detergents and paints [150]. Their mechanical and rheological properties often can influence the performance of the materials. For instance in pharmaceutical and biomedical fields, understanding the rheological behaviour of polymers and any other vehicle material provides useful information on formulations development. Some of the rheological properties can be directly related to the spreadability and the injectability of the material, the ease of removal from containers and retention on a specific site of action [151-154].

Rheology studies the relationship existing between the stress, the deformation (also called strain) and the time. The Hooke and Newton laws describe the linear relationship between the

stress and the strain for ideal elastic solid and viscous liquid, respectively. A liquid can be considered as a pack of hypothetical layers separated by an infinitesimal distance and sliding over each other as shown in Figure 2.4.

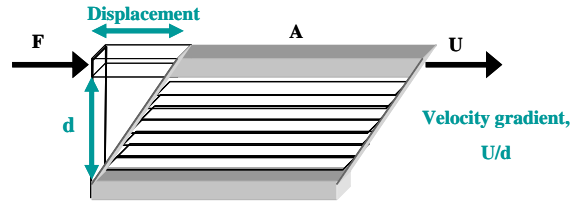


**Figure 2.4** Shear stress applied to hypothetical layers of a fluid; the upper layer is sliding laterally relative to the lower part.

When a force,  $F$ , is applied, the upper layer flows with a relative velocity,  $U$ , and it transmits part of the movement to the lower layer with a decreasing in velocity. The delay in the flow is called viscosity, which is an “internal friction” due to the resistance to flow. The difference of velocity between the two layers is called “velocity gradient” or shear rate,  $\dot{\gamma}$  ( $s^{-1}$ ), and the force  $F$  per unit of area,  $A$ , is called shear stress,  $\sigma$  (Pa). The constant of proportionality between the shear rate and the shear stress is called coefficient of viscosity,  $\eta$  (Pa.s) [150, 155]. For an ideal elastic (Hookean) solid, the strain ( $\gamma$ , dimensionless) is proportional to the applied stress ( $\sigma$ ). The constant of proportionality is the elastic modulus,  $G$  (Pa), (Equation 2.2). If a deformation is applied to an ideal solid, a stress occurs and if the strain is removed the stress falls to zero, therefore ideal solids present a no-time dependent behaviour.

$$\sigma = G\gamma \quad \text{Equation 2.2}$$

For a Newtonian liquid, the applied stress,  $\sigma$ , is proportional to the rate of strain,  $\dot{\gamma}$ . The constant of proportionality is the viscosity,  $\eta$  (Equation 2.3)

$$\sigma = \eta\dot{\gamma} \quad \text{Equation 2.3}$$

When a stress is applied, a deformation occurs and the liquid will deform indefinitely until the stress is removed. After the removal of the stress, the liquid will not go back to its original form. Again, the behaviour is not time dependent. The laws of Hooke and Newton are linear laws, but most of the real materials do not obey them. In fact, they display a combination of elastic and viscous properties and they are referred to as viscoelastic materials. The ideal liquids and solids also can be represented by mechanical models. The Hookean solid can be described as a spring, whereas the Newtonian liquid is described by a dashpot. Connecting a spring with a dashpot in

series we have a mechanical representation of a viscoelastic liquid according to the Maxwell model, if they are connected in parallel, a representation of a viscoelastic solid is obtained (Kelvin-Voigt model). A schematic representation of the mechanical model is shown in Figure 2.5 [150, 155, 156].

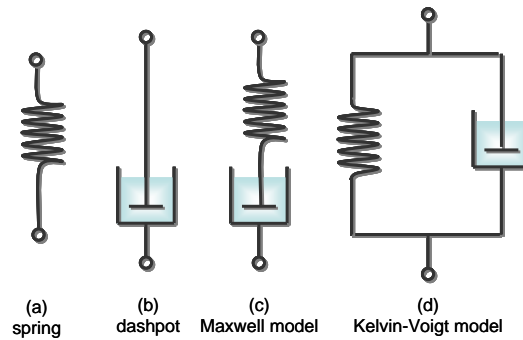


**Figure 2.5** Schematic view of the mechanical models for an ideal solid (a), an ideal liquid (b) and viscoelastic materials represented in two different models: (c) and (d).

The flows shown in Figure 2.4 are a simplified view of the real situation that is more complex due to the coexistence of shear and extensional flows. In shear flows the particles flow over or past each other; in the extensional, they flow away or towards each other [155]. Viscosity of real materials can be affected by shear rate, temperature, pressure and time of shearing. For a Newtonian liquid at constant temperature and pressure, the only stress generated is the shear stress,  $\sigma$ . The shear viscosity does not vary with the shear rate, and it is constant with respect to the time of shearing. The shear stress falls to zero after the shearing is stopped. Materials with behaviour different from the one just described are known as non-Newtonian fluids, and they are generally classified as shear-thinning (also known as pseudoplastic), shear thickening (also known as dilatant), and plastic (also known as Bingham). Figure 2.6 shows the flow curves of the non-Newtonian fluids in comparison with an ideal liquid (Newtonian).

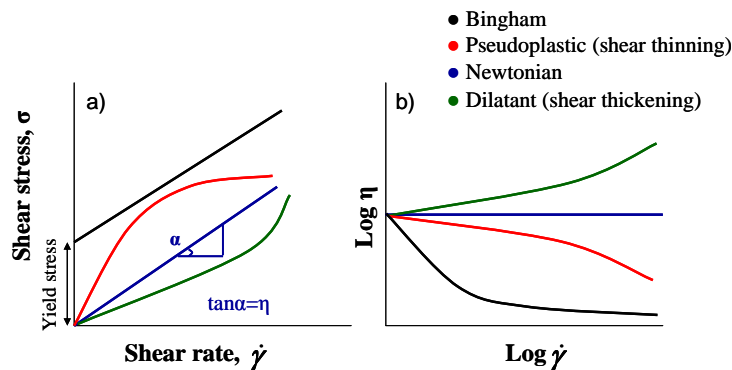


**Figure 2.6** Flow curves of non-Newtonian and Newtonian liquid. (a) Shear stress versus shear rate, and (b) viscosity versus shear rate in logarithmic scale.

In many materials, a deformation occurs in response to the applied force and the viscosity drops with the increase of the shear rate. This behaviour is typical of shear-thinning materials. When the viscosity increases with the shear rate, they are called shear-thickening or dilatants. The Bingham or plastic materials are a kind of shear-thinning fluids, but they do not flow until a critical yield stress is overcome. In this case, the viscosity is infinite at zero shear rate (Figure 2.6b). As previously discussed, the shear stress and the viscosity can be affected by the time of shearing. According to the time dependence, the materials can be classified as thixotropic if the viscosity gradually decreases under shear stress, followed by gradual recovery after the removal of the stress. For anti-thixotropic materials, the viscosity gradually increases under stress and recovers. Thixotropy is generally associated with a shear-thinning behaviour, while anti-thixotropy is typical of shear-thickening materials.

For a viscoelastic material, its viscoelasticity can be classified as linear and non-linear, but only the linear one can be mathematically characterised [157]. The characterisation of the linear viscoelastic region (LVR) of the materials can be useful for many reasons. It allows the molecular structure of the materials to be determined, which is often useful information to assess certain physical properties of the materials (which can be used for quality control). The LVR can be characterised by relatively simple mathematical approaches [150]. The linear viscoelastic parameters do not depend on the magnitude of the stress or on the time in which the stress acts. On the contrary, non-linear viscoelastic parameters depend on the magnitude of the stress and the strain. The theory of the linear viscoelasticity is based on the Boltzmann superposition principle, which states that the mechanical behaviour of the systems depends on the stress history of the sample. In other words, it assumes that the effect of the deformation is independent of other deformations, thus the behaviour of the samples can be calculated by adding the effects of the deformations that take place singularly [157]. Two different methods can be used to measure the LVR region, static method, such as creep test at constant stress or relaxation tests at constant strain, and dynamic method, such as oscillatory tests. These are introduced in detail in the following sections.

### 2.4.2.1 Oscillatory tests

In an oscillatory test a sinusoidal oscillation maximum strain  $\gamma_o$  [158] is applied to the sample at an oscillatory frequency (expressed in radians per second,  $\omega$  [157]). As a result, a stress wave is obtained. For purely elastic materials, the output stress wave is in phase with the input strain wave, whilst for purely viscous systems the two waves are  $\pi/2$  out of phase. Viscoelastic systems have both elastic and viscous components, and the stress wave intervals from the strain wave by an angle  $\delta$ , which is between zero and  $\pi/2$ , as seen in Figure 2.7.

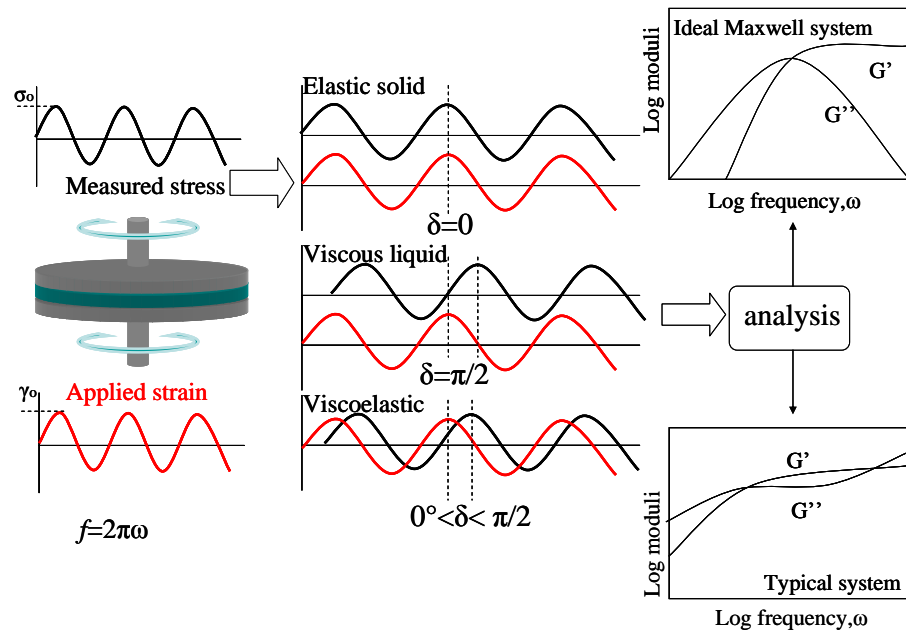


**Figure 2.7** Representation of an oscillatory test with plate-plate geometry. A sinusoidal oscillation of a maximum strain,  $\gamma_o$  (red line wave) is applied at an oscillatory frequency,  $\omega$ . A resulting stress wave is obtained (black-line wave). For ideal elastic solid, the two waves are in phase ( $\delta=0$ ); for ideal viscous liquid, the stress and the strain are  $\pi/2$  out of phase; for viscoelastic materials they lag by an angle  $\delta$  ( $0 < \delta < \pi/2$ ). The elastic ( $G'$ ) and the viscous ( $G''$ ) components can be separated and the plots of frequency versus moduli can be obtained.

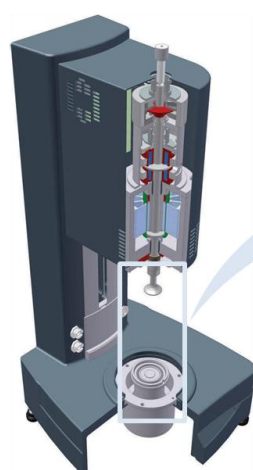
The ratio between the maximum value of stress ( $\sigma_o$ ) and the maximum value of strain ( $\gamma_o$ ) is called the complex dynamic modulus,  $|G^*|$ . This is resolved in a real component, elastic modulus ( $G'$ ) and an imaginary component, the viscous modulus ( $G''$ ). The elastic modulus is connected to the elastic deformation, which is restored following the removal of the stress. Thus it is also called the storage modulus. The viscous deformation does not recover, but the energy can be dissipated, so it is often called loss modulus [150, 157]. The rheological parameters that can be obtained with an oscillatory analysis are listed in Table 2.3.

**Table 2.3** List of the rheological properties that can be obtained by performing an oscillatory test.

Parameters	Symbols	Units	Descriptions
Complex dynamic modulus	$ G^* $	Pa	$G^* = \sqrt{G'^2 + G''^2}$
Elastic modulus	$G'$	Pa	$G' =  G^*  \cos \delta$
Viscous modulus	$G''$	Pa	$G'' =  G^*  \sin \delta$
Dynamic viscosity	$\eta'$	Pa.s	$\eta' = \frac{G''}{\omega}$
Loss tangent	$\tan \delta$	—	$\tan \delta = \frac{G''}{G'}$

A schematic view of the rheometer used in this project is represented in Figure 2.8. Plate-plate geometry was adopted. For the upper part, a stainless steel solvent trap plate was used with a diameter varying between 20, 40 and 60 mm according to the viscosity of the gels. The smaller plate was used for gels with higher viscosity (the samples with higher Gelucire content). In the lower part is a standard Peltier plate and the temperature can be controlled within a range between -10 and 99 °C.

AR series technology



Geometry detail

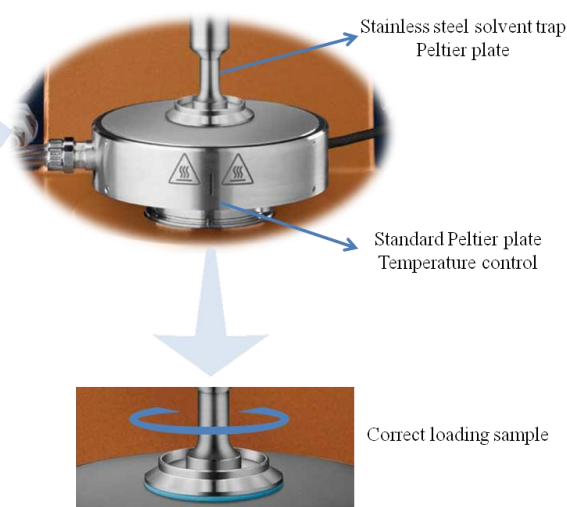


**Figure 2.8** Schematic view of the AR series rheometer technology and of the geometry details (TA Instruments, AR series and Peltier plate brochure).

In this work, oscillation and flow tests were performed on the lysozyme-free gels (with 10% to 90% water content) prepared by heating and hydration methods and the selected lysozyme-loaded gels by using a rheometer (AR 1000-N Rheolyst, TA Instruments, New Castle, USA) connected to a water bath for plate temperature control. Three types of oscillation tests were performed in this study. The stress sweep test (section 2.4.2.1.1) was first performed to assess the linear viscoelastic region (LVR) of the samples, followed by a frequency sweep test (section 2.4.2.1.2) and a temperature ramp test (section 2.4.2.1.3). All tests were performed at least in

triplicate. Flow tests were also performed at fixed selected temperature in order to study the effect of testing temperature on the flow properties of the gels (section 2.4.2.2).

#### 2.4.2.1.1 Stress sweep test

This test is one of the most frequently used tests to determine the LVR of a material. It is usually the starting step to establish the appropriate stress (within the LVR region) applied to the sample for subsequent oscillatory tests. The stress sweep test consists in applying a range of stresses or displacements in which the structure of the sample is stretched, but not destroyed. After the application of the stress/strain at a fixed frequency and temperature, the resulting oscillatory strain/stress is monitored [155]. The sample structure is stretched over increasing stresses until it broke and it results in a drop of the elastic modulus.

#### 2.4.2.1.2 Frequency sweep test

The oscillatory frequency curves give a fingerprint of the state of the microstructure of the materials. Several types of behaviours of a material can be retrieved from a viscoelastic spectrum. A general view of the viscoelastic response of non-Newtonian liquids is shown in Figure 2.9.

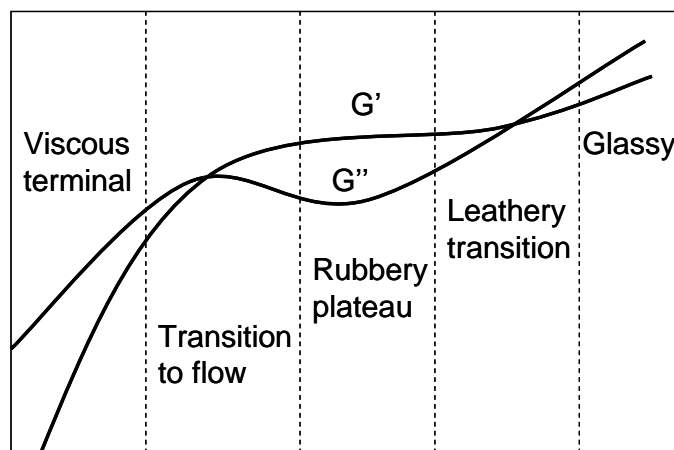


**Figure 2.9** Viscoelastic behaviour of Non-Newtonian liquids over a broad range of frequency (adapted from reference [155]).

At low frequency  $G''$  prevails on  $G'$ , which means that the viscous behaviour is predominant (viscous terminal region). As the frequency increase,  $G'$  and  $G''$  increase and sometimes the two moduli cross over at certain frequency. The inverse of the frequency where the crossover takes place gives the longest relaxation time of the material,  $\tau_{max}$  ( $\sim 1/\omega$ ) [155]. The longest relaxation time describes the time at which the fluid relaxes to the equilibrium state after being perturbed by a shear oscillation. At frequency values close to the crossover point ( $1/\tau_{max}$ ), the

fluid is viscous, while above this point the elastic behaviour prevails [159]. In many cases a plateau occurs and the elastic behaviour always predominates ( $G' > G''$ ). At higher frequency, a leathery transition is observed.  $G''$  increases faster than  $G'$  due to the high-frequency relaxation and the dissipation mechanism. In this region, a second crossover may take place from which another characteristic relaxation time may be calculated. Finally, at the highest frequencies usually a glassy region is observed where  $G''$  continues to rise faster than  $G'$ . A typical range of frequencies between  $10^{-2}$  and  $10^2$  rad/s is usually applied in oscillatory frequency tests and just two of the regions described above can be observed. The type of regions observed depends on the materials and their longest relaxation times. In fact, for the material with  $\omega\tau_{max} \sim 1$  the viscous and the transition to flow regions are observed. For the material with  $\omega\tau_{max} > 1$ , the plateau region is often seen. For many dilute polymers solution  $\omega\tau_{max} < 1$ , therefore  $G''$  always predominated [155].

#### 2.4.2.1.3 Temperature ramp test

A temperature ramp test was also performed by heating the samples from 25°C to 80°C and cooling back to 25°C at a fixed frequency of 1 Hz and with the same stress value chosen for the frequency sweep test. The change of the storage moduli ( $G'$ ) with the temperature was plotted. A standard Peltier plate solvent trap geometry equipped with a solvent cover filled up with water was used to prevent water loss from the sample during the experiments, a schematic view of the geometry is shown in Figure 2.10.

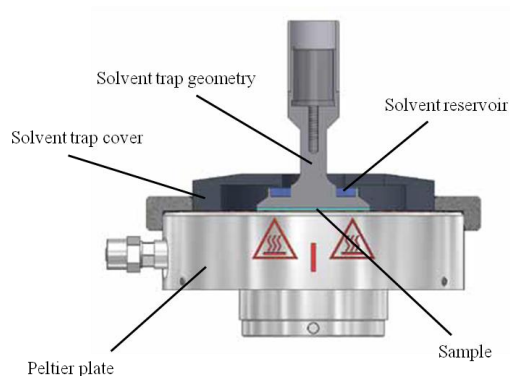


**Figure 2.10** Schematic representation of a Standard Peltier plate and cover used to prevent water loss (TA Instrument, Peltier plate brochure).

#### 2.4.2.2 Flow test in continuous ramp mode

The flow behaviour of a material is highly related to its rheological properties. An ideal complete flow curve is represented in Figure 2.11. The viscosity is constant at low values of shear rates (or stress) (first Newtonian plateau). At a certain point the viscosity decreases into a

linear region which is called power law. In the end, the viscosity becomes constant again (second Newtonian plateau). Hence, from a flow curve, two extreme Newtonian viscosities  $\eta_0$  and  $\eta_\infty$  separated by a power law region can be obtained, as seen in Figure 2.11.

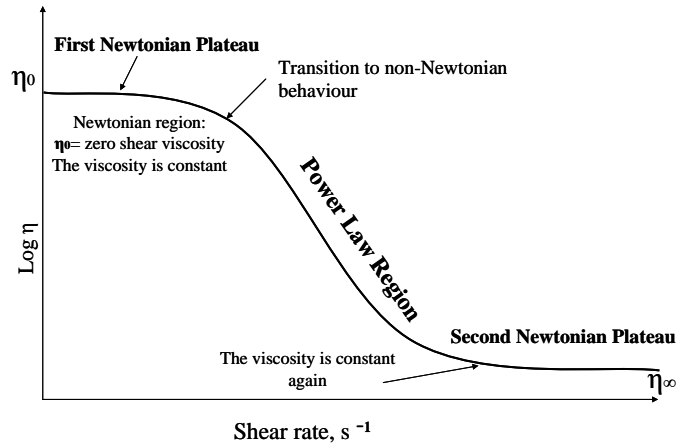


**Figure 2.11** Diagram of an ideal flow curve.

Flow curves can be defined mathematically. The whole curve can be described by the Cross model with the following equation

$$\frac{\eta_0 - \eta}{\eta - \eta_\infty} = (K\dot{\gamma})^m \quad \text{Equation 2.4}$$

where  $\eta_0$  and  $\eta_\infty$  represents the asymptotic values of viscosity at very low and very high shear rates respectively,  $K$  is a constant parameter with the dimension of time and  $m$  is a dimensionless parameter that describes the degree of shear thinning. If  $m$  it is close to zero describes more Newtonian liquids and if it is close to 1, it is a typical shear thinning behaviour. With appropriate assumptions, Equation 2.4 can be reduced to power law (Equation 2.5), Sisko (Equation 2.7), or other Newtonian behaviour. If  $\eta_0 \gg \eta_\infty$ ,  $K\dot{\gamma} \gg 1$  and  $\eta_\infty$  is small, the power law or the Ostwald de Waele equation is obtained (Equation 2.5)

$$\sigma = k\dot{\gamma}^n \quad \text{Equation 2.5}$$

or in terms of viscosity

$$\eta = k\dot{\gamma}^{n-1} \quad \text{Equation 2.6}$$

where  $\sigma$  is shear stress (Pa),  $k$  is consistency index,  $\dot{\gamma}$  is shear rate ( $s^{-1}$ ) and  $n$  is flow index (dimensionless). For a Newtonian liquid, the flow index is equal to 1. If it is greater than 1, the

system is shear thickening; otherwise, it is shear thinning. The Sisko equation describes the flows of most of the structured fluids, such as emulsions and suspensions. In this case, the viscosity occurs in the region after the power law and it plateaus towards  $\eta_{\infty}$ . This mathematical model adds a Newtonian contribution to the power-law description of the viscosity (Equation 2.7)

$$\eta = k\dot{\gamma}^{n-1} + \eta_{\infty} \quad \text{Equation 2.7}$$

or in terms of shear stress, [155]

$$\sigma = k\dot{\gamma}^n + \eta_{\infty}\dot{\gamma} \quad \text{Equation 2.8}$$

In this study, continuous flow tests were performed on the gels using a parallel steel plate geometry (20 mm diameter and a gap of 1000  $\mu\text{m}$ ) over a range of different stress and at selected temperatures of 25  $^{\circ}\text{C}$ , 37  $^{\circ}\text{C}$ , 50  $^{\circ}\text{C}$  and 80  $^{\circ}\text{C}$ . The testing conditions were selected according to the consistency of the samples. The stress grew over a period of 60 seconds. The tests were performed at least in triplicate and the curves were fitted with a power law equation.

### 2.4.3 Texture analysis

Texture analyser is a useful technique for measuring the internal properties and the texture of a material. It consists of a movable upper arm where the load cell is located. The upper arm can move vertically up and down. Different kind of tests can be performed in compression or in tension mode, and probes of different materials and shapes can be used. This technique has been widely used in the food industry for product development and quality control [160]. Texture analyser has also been used in pharmaceutical field for the characterisation of the mechanical properties and mucoadhesive behaviour of formulations [151, 161, 162]. One of the methods used to characterise pharmaceutical systems is the texture profile analysis (TPA), and several other tests can be performed such as the compression and the adhesion tests.

#### 2.4.3.1 Texture profile analysis (TPA) test

The texture profile analysis (TPA) is one of the tests used to characterise the mechanical and textural properties of the pharmaceutical formulations [162] and food materials [163]. It can be also used to assess the adhesiveness of a material without using artificial or biological surfaces. The test consists in compressing twice the samples at a defined rate and depth, allowing a recovering time between the two compressing cycles. From the force-distance or force-time

plots, several mechanical parameters can be determined. Some of them are directly determined such as hardness, cohesiveness, adhesiveness and elasticity. These parameters can be used to determine some characteristics of pharmaceutical semi-solid systems, i.e. the spreadability of the system on a surface which can be skin or mucosa, and the mucoadhesion potentials [153]. Others parameters such as fracturability, chewiness, gumminess can be derived from the measurements. The hardness (units of Force, N) is the force required to get a deformation. The compressibility (units of work, N.s) is the work necessary to compress the sample through a fixed distance [162]. In practice, it is the amount of force required to deform the product during the first cycle of compression. The adhesiveness (unit of works, N.s) describes the work required to overcome the attractive forces between the surface of the samples and the surface of the probe with which the samples is in contact (unit of work, N.s) [153]. The cohesiveness (dimensionless) represents the work required to overcome the internal bonds of the materials [164] and indicates the extent of deformation of the materials. It is the ratio of the area under the force-time curve of the second compression cycle to the area under the curve of the first compression cycle after a recovery period occurs [165] (see Figure 2.12). The elasticity (dimensionless) is a measure of the rate at which the deformed sample recovers from the deformation after the removal of the deforming force [163]. Practically it is the ratio of the time required to reach the maximum structural deformation during the second compression cycle to that on the time of the first compression cycle separated by a determined period of recovery [166]. A typical TPA force-time curve is shown in Figure 2.12.

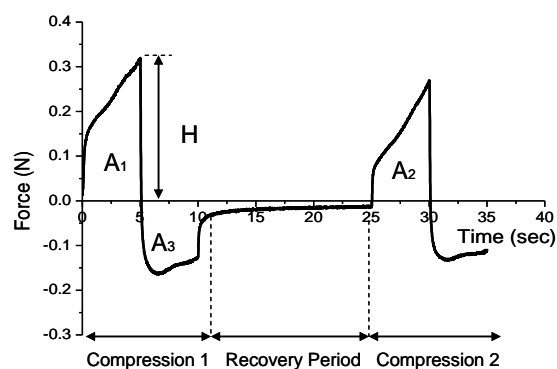


**Figure 2.12** Typical force-time plot for a TPA test. H indicates the hardness;  $A_1$  is the compressibility;  $A_3$  the adhesiveness and  $A_2/A_1$  is the cohesiveness. The graph was obtained from a TPA test performed on the Gelucire 50/13 gel with 65 % water content prepared with hydration method.

#### 2.4.3.2 Mucoadhesion test

The texture analyser was also used to evaluate the adhesion of pharmaceutical systems to biological surfaces (such as mucin tablets or tissues) [161, 162, 167] or non-biological (such as the probe surface, for instance using the TPA test). The mucoadhesion can be evaluated through

several *in-vitro* and *in-vivo* methods. Most of the *in-vitro* methods measure the tensile strength or the shear strength. Methods using the tensile strength consist on measuring the force necessary to detach two surfaces after the establishment of the mucoadhesive bond [168]. The shear strength examines the force that makes the adhesive polymer slides on the mucous layer in the parallel direction of their plane of contact. The texture analyser is an example of tensile strength method. The adhesive properties are evaluated by measuring the maximum force needed to separate the dosage form from an artificial or biological surface after being in contact for a certain time under a constant applied force. The work of adhesion, which is the total amount of forces involved in the detachment of the two surfaces, can be also measured [161]. A typical force-distance plot of such test is shown in Figure 2.13.

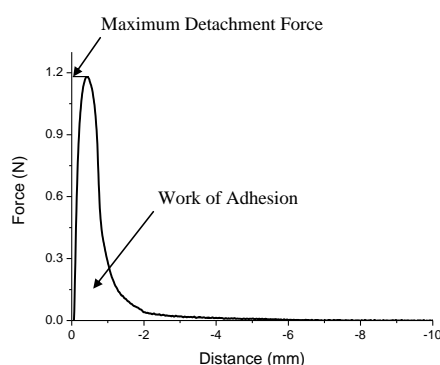


**Figure 2.13** Typical force-distance plot obtained from an adhesive test using a texture analyser. The height of the peak is the maximum detachment force (N), the area under the curve is the work of adhesion or the total amount of forces involved in the probe withdrawal. The graph is a result of the adhesion test of the gel with 60% of water prepared by heating method and the mucin tablet.

## 2.4.4 Dynamic light scattering (DLS)

### 2.4.4.1 Basic principles

Dynamic light scattering (DLS) or also known as Photon Correlation Spectroscopy (PCS) or Quasi-Elastic Light Scattering (QELS) is a valuable technique to measure the diffusion properties (e.g. diffusion coefficient) of the particulate materials in solution or in suspension. By knowing the diffusion coefficient, parameters such as the size of the particles, the molecular weight, the conformation of the macromolecular chains and various interactions among the components may be assessed [169]. The basic principle underpinning this technique is that a monochromatic beam of a laser light collides on a sample and is scattered to a detector allocated at an angle  $\theta$  with respect to the incident beam direction. Because the particles undergo Brownian motions, the intensity of the scattered light at the detector will fluctuate with time [170]. Light is an electromagnetic radiation. When a light beam hits a molecule with different dielectric constant from the medium, it can be scattered or absorbed or both, depending on the

optics properties of the molecule. Both scattering and absorption remove part of the beam energy. As a result the beam is attenuated, this phenomenon is known as extinction [171]. Scattering is possible only in materials heterogeneous in itself, which might be due either to local density fluctuations in pure material or because of different polarization of the dispersed particles in the medium. In a homogeneous material, the radiation scattered from the individual particle negatively interferes and therefore, no scattering can be observed [169].

A schematic representation of the scattering geometry is shown in Figure 2.14. The incident light with wavelength  $\lambda$  propagates through the  $x$  direction. The magnitude of the wave vector,  $k_0$ , is equal to  $2\pi/\lambda$  and is randomly oriented in non-polarised light. For polarised light it is oriented in particular directions. It can be vertically polarised ( $E_v$ ) or horizontally polarised ( $E_h$ ). Most of the incident lights pass through the scattering volume and it can be scattered at the direction specified by the angle  $\theta$  (also called the scattering angle). The plane formed by the incident, the transmitted and the scattered light beams is called the scattering plane.

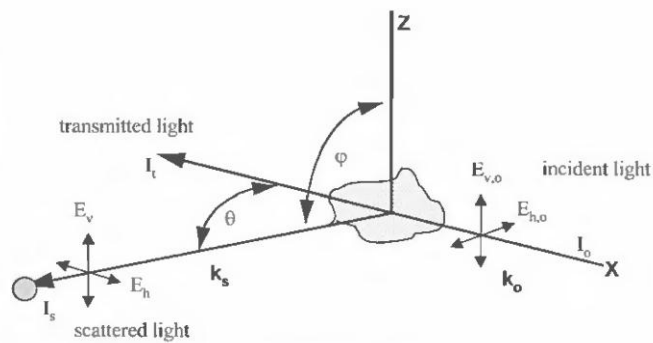


**Figure 2.14** Scheme of scattering geometry.  $k_0$  is the wave vector of the incident light,  $k_s$  and  $I_s$  are the wave vector and the intensity of the scattered light. The angle  $\varphi$  is assumed to be  $90^\circ$  [169].

Many theoretical approaches may be used to describe the scattering of particles. They are the rigorous solution or Mie theory and three theories derived from it, which are approximations of the scattering from particles with size smaller or larger compared to the wavelength of light. These theories are listed in Table 2.4.

**Table 2.4** Light scattering theories.

Theory	Assumption	Description	Formula
Mie theory	None	For spherical, homogeneous, isotropic and non-magnetic particle of any diameter	
Rayleigh Scattering	$size \ll k_0^{-1}$ $ m  \cdot size \ll k_0^{-1}$	For particle much smaller than the wavelength	$I = (1 + \cos^2\theta)k_0^4 \alpha ^2 \frac{I_0}{2r^2}$
Rayleigh-Debye-Gans Scattering	$ m - 1  \cdot size \ll k_0^{-1}$ $ m - 1  \ll 1$	Size of particles are larger that treatable as single dipole	
Fraunhofer Diffraction	$size \gg k_0^{-1}$	Size of particles larger than the wavelength of the light	
Numerical Approach	None	For particles of arbitrary shape with size comparable to the wavelength range	

“m” is the refractive index;  $\alpha$  is the polarizability

The intensity of the scattered light is correlated to the direction of the incident light, scattering angle, the refractive index ratio between the molecules and the medium along with other solution parameters. For the molecules of size much smaller than the wavelength of the light, the Rayleigh approximation applies [172]. According to the Rayleigh approximation, the scattering intensity,  $I_s$ , is inversely proportional to the fourth power of the wavelength ( $\lambda$ ) and directly proportional to the sixth power of the particle dimension ( $d$ )

$$I_s \propto I_0 / \lambda^4 \quad \text{Equation 2.9}$$

$$I_s \propto d^6 \quad \text{Equation 2.10}$$

The inverse dependence indicates that the intensity of the scattering increases with the decrease of the wavelength (Equation 2.9) and it is more intense for larger particles (Equation 2.10). For the particles which sizes are larger and almost equivalent to the wavelength, the Mie solution can be applied. The theory is valid for spherical, homogeneous, isotropic and non-magnetic particle dispersed in a non-absorbing medium [169].

#### 2.4.4.2 Instrumentation

Modern DLS instrumentations consist in several parts. A coherent light beam generates from a light source, such as the He-Ne laser. The light is transmitted and delivered to the scattering volume in the sample module by optics devices. The scattered light from a defined volume and at a scattered angle is collected by collecting optics and detected by the detector, which can be a photomultiplier or photodiodes. A series of digitized numbers (counts) is created in the

correlator by counting number of photon events, which occur in the defined time interval,  $\Delta t$ , in the photon-counting mode, or the event frequency at fixed sample time if used in the current mode. These counts are used to produce the autocorrelation function [169].

### 2.4.4.3 Data analysis

The correlation function determines in which extend two dynamical properties are correlated over a period of time. In the autocorrelation function, either the electric field or the light intensity can be the variable in the autocorrelation function. In the first case, it is called the electric field-electric field autocorrelation function (or first-order autocorrelation function,  $G^{(1)}(\tau)$ ), and in the second case it is called the intensity-intensity autocorrelation function (or second-order autocorrelation function,  $G^{(2)}(\tau)$ ). The normalised functions of  $G^{(1)}(\tau)$  and  $G^{(2)}(\tau)$  are denoted as  $g^{(1)}(\tau)$  and  $g^{(2)}(\tau)$ . Usually  $G^{(1)}(\tau)$  and  $G^{(2)}(\tau)$  are not related, but in particular situations when e.g. the scattered electric field of the particles undergo Brownian motions, these two functions are connected by the Siegert relation (Equation 2.11)

$$G_s^{(2)}(\tau) = A \left( 1 + \beta \left| g_s^{(1)}(\tau) \right|^2 \right) \quad \text{Equation 2.11}$$

or

$$g_s^{(2)}(\tau) = 1 + \beta \left| g_s^{(1)}(\tau) \right|^2 \quad \text{Equation 2.12}$$

where  $A$  is the baseline and  $\beta$  is an instrument efficiency parameter, which is always less than the unity [169]. For monodisperse and spherical molecules, the electric field autocorrelation function,  $g^{(1)}$ , can be described by a simple exponential decay  $g^{(1)} = \exp(-\Gamma\tau)$ , where  $\Gamma$  is the decay constant. For polydispersed particulate systems,  $g^{(1)}$  is equal to the summation of the single exponential decays characterised by a different decay constant (see Equation 2.13)

$$\left| g^{(1)}(\tau, q) \right| = \sum q(\Gamma_i) \exp(-\Gamma_i\tau) = \int_0^{\infty} q(\Gamma) \exp(-\Gamma\tau) d\Gamma \quad \text{Equation 2.13}$$

where  $i$  represents a population of particles  $q(\Gamma_i)$  with the same characteristic decay constant,  $\Gamma_i$ , and  $q$  is the scattering vector. The decay constant ( $\Gamma$ ) distribution is related to the translational and rotational motions of the particles. It can be determined by using several algorithms, including the Cumulants analysis, the inversion of Laplace Integral equation, the regularised

Non-Negative Least-Squares method and CONTIN, according to the specific case. The decay constant,  $\Gamma$ , is related to the diffusion coefficient  $D_T$  at any angle through the following equation

$$\Gamma = D_T q^2 \quad \text{Equation 2.14}$$

where  $q$  is the scattering vector, which is equal to

$$q = \frac{4\pi \cdot n}{\lambda_0} \sin(\theta/2) \quad \text{Equation 2.15}$$

$n$  is the refractive index of the suspensions. The diffusion coefficient,  $D_T$  is the variable measured by DLS instrument.

The dependence of the diffusion coefficient ( $D_T$ ) on the concentration ( $c$ ) of the particles can be expressed by the equation

$$D_T = D_T^0 (1 + k_d c) \quad \text{Equation 2.16}$$

where  $k_d$  is a virial coefficient, which takes into account of the particle-particle interactions and of the multiple scattering [169]. For spherical particles, the size can be determined by relating the diffusion coefficient to the hydrodynamic diameter,  $d_h$ , through the Stokes-Einstein equation (Equation 2.17)

$$D_T = \frac{k_B T}{3\pi\eta_0 d_h} \quad \text{Equation 2.17}$$

Where  $k_B$  is the Boltzman constant;  $T$ , the absolute temperature and  $\eta_0$ , the solvent viscosity [173]. It has been noticed that the  $d_h$  values determined by DLS technique are usually larger than the ones obtained using direct imaging methods such as the TEM (transmission electron microscopy). The reason for that has been explained by Xu [174]. It has been found that the  $d_h$  monotonically increases as the conductivity reduces, this is due to the fact that when the particles undergo Brownian motion, a layer of medium which is part of the electrical double layer moves with them, resulting in a larger diameter determined by DLS [174].

#### 2.4.4.4 Methodology used in this study

In this study, the particle sizes of the nanoparticle dispersions prepared by following the procedures described in section 2.3.2 and stored at room temperature and at 4 °C were measured using DLS (Zetasizer Nano, Malvern Instruments, Worcestershire, UK) at 37 °C. The detector was positioned at a fixed angle of 173°. The data were analysed using the instrument software provided. It was found that the cumulant analysis is not appropriate to determine the particles size possibly due to the high polydispersity of the systems, and therefore the distribution analysis was used.

### 2.4.5 Small angle x-ray scattering (SAXS)

#### 2.4.5.1 Basic principles

SAXS is one of the X-ray techniques for the determination of the structure of the matter of different nature (polymers, biological macromolecules in solution, emulsions, porous materials, nanoparticles, etc [175]) and provides information on the structural features of the material such as shape, size, mass and intermolecular spacing. SAXS is also one of the most powerful techniques for the determination of the liquid crystal phases. All scattering techniques are described by a reciprocity law, which relates the scattering angle to the particle size. For colloidal materials with dimensions larger than the x-ray wavelength, the observable scattering angle is small. Considering that the x-rays are scattered by the electrons, the small angle x-ray scattering method observes the elastic (or coherent) scatterings of x-rays induced by samples with inhomogeneities in the electron densities. Incoherent scatterings (Compton scatterings) may exist, but they are too weak at small angles that they can be neglected [176]. In coherent scattering, electrons oscillate as consequence of the electric field of the x-ray beam and produce secondary waves with the same wavelength of the x-ray beam but 180° out of phase. The measured scattering at the angle of  $2\theta$  is proportional to  $(1+\cos^2 2\theta)$  and reaches a maximum when  $2\theta$  is equal to zero. It decreases at large angles.

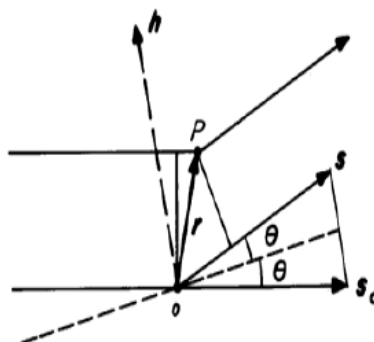


**Figure 2.15** Illustration of scattering geometry interpretation [176].

A geometrical interpretation of the scattering is shown in Figure 2.15, where  $s_0$  is the unit vector of the incident beam and  $s$  is the vector of the scattered beam. The path difference between the point P and the origin O (given by the point vector  $r$ ) is equal to  $r(s-s_0)$  [176]. The phase difference ( $\varphi$ ) is the difference between the incident and the scattered waves which is given by the scattering vector multiplied by  $2\pi$ . It is also related to the distance between the scatterers ( $\Delta$ ) by the relation of  $\varphi = q \Delta$  [177]. The wavevector,  $q$  (sometimes also called  $h$  or  $s$ ) has a magnitude equal to  $4\pi \sin\theta/\lambda$ , where  $2\theta$  is the scattering angle and  $\lambda$  is the wavelength of the incident beam. Compared to the Bragg's law in x-ray crystallography, the wavevector  $q$  is related to the lattice spacing ( $d$ ) by  $q=2\pi/d$ . The limit of the resolution which is the minimum distance at which two objects can be detected is defined by one the properties of the x-rays:  $d_{min}=\lambda/2$  [178]. Each point generates a secondary wave with amplitude defined by the term  $e^{iqr}$  and the sum of amplitudes derived by  $N$  number of electrons is described by the Fourier distribution (Equation 2.18)

$$F_q = \sum_{i=1}^N f_e e^{iqr} \quad \text{Equation 2.18}$$

where  $f_e$  is the scattering amplitude (or scattering factor). However, considering the huge number of electrons, it is more convenient to consider the electron density. The electron density is defined as the number of electrons per unit volume and it is indicated by  $\rho(q)$  [176]. Therefore, for a small volume  $dV$ , at a position  $r$ , there will be  $\rho(q)dV$  electrons. The summation can be replaced by the integration of the volume  $V$  irradiated by the incident beam (Equation 21), so the amplitude  $F$  is

$$F(q) = \iiint dV \cdot \rho(q) e^{iqr} \quad \text{Equation 2.19}$$

In the cases of lyotropic liquid crystals, the position of the peaks of the plot  $I(q)$  vs  $q$ , can be used to characterise the structure (space groups) and the unit cell dimensions of the single liquid crystal phases. The space groups are obtained by comparing the Bragg peaks and the Miller indices (h, k, l) for different phases. Usually, three or more peaks are necessary for an unequivocal identification. The relationship between the Bragg peaks and the Miller indices is summarised in Table 2.5 [179].

**Table 2.5** Peak spacing ratio (Bragg peaks) and corresponding Miller indices for lamellar ( $L_a$ ), hexagonal ( $H_{111}$ ), Gyroid cubic (Ia3d), Diamond cubic (Pn3m) and Primitive cubic (Im3m) [179-181].

Liquid crystal phases	Symmetry (dimensionality) [182]	Peaks spacing ratio	Miller indices (h, k, l)	Lattice parameter	
Lamellar	Smectic (1D)	1	110	$q(h,k,l) = \frac{2\pi}{a} \left( \frac{2}{\sqrt{3}} \right) (h^2 + k^2 - hk)^{1/2}$	
		$\sqrt{4}$	220		
		$\sqrt{9}$	300		
Hexagonal 1	2D	1	10		
		$\sqrt{3}$	11		
		$\sqrt{4}$	20		
		$\sqrt{7}$	21		
		$\sqrt{9}$	30		
Cubic	Gyroid, Ia3d (3D)	$\sqrt{6}$	221		$q(h,k,l) = \frac{2\pi}{a} (h^2 + k^2 + l^2)^{1/2}$
		$\sqrt{8}$	220		
	Diamond, Pn3m (3D)	$\sqrt{2}$	110		
		$\sqrt{3}$	111		
		$\sqrt{4}$	200		
		$\sqrt{6}$	211		
		$\sqrt{8}$	220		
		$\sqrt{9}$	221		
		$\sqrt{10}$	300		
		Primitive, Im3m (3D)	$\sqrt{2}$	110	
$\sqrt{4}$	200				
$\sqrt{6}$	211				
$\sqrt{8}$	220				
		$\sqrt{9}$	221		

### 2.4.5.2 Instrumentation

The basic components of the SAXS instrument are shown in Figure 2.16. It consists of a source, a collimation system, the sample, the beam stop and the detector. The source can be an x-ray tube or tube with rotating anode, but synchrotrons can also be used. The advantage of synchrotrons is the production of highly collimated, low-divergent, focused x-ray beam. The collimation system is required to reduce the divergence of the incoming beam before hitting the sample. The collimation system constitutes of a series of slits or pinholes, which reduce the

intensity of the beam and produce parasitic scattering [176]. The beam stop prevents the beam to hit the detector [183].

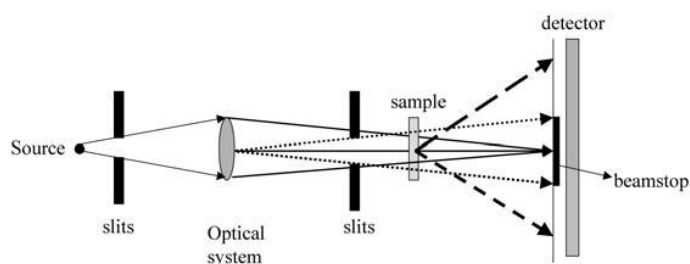


**Figure 2.16** Schematic representation of the components of a SAXS instrument [177].

### 2.4.5.3 Methodology used in this project

The structural conformation of the gels were detected with a SAXS instrument (S3-micro from Hecus X-ray Systems GmbH, Graz, Austria) provided with a point microfocus source GemixFox 3D (Xenoxs, Grenoble, France), as shown in Figure 2.17.



**Figure 2.17** SAXS set up used in this project.

A two-dimensional position sensitive detector was used with a sample-to-detector distance of 268 mm. The samples were loaded in the cell for pastes between two windows of kapton®, which absorbs at  $4e^{-1}\text{Å}$  (or 700 number of channel). The experiments were performed using an X-ray source power of 50W (5kV, 1mA). The acquisition time was 2 hours at the temperature of 25°C. The gel with 50% and 70% water contents prepared by heating and hydration methods were also analysed with a temperature scan from 25 to 37 °C and back down to 25 °C. The liquid crystalline phases were identified using the software 3D-view (Hecus, Graz).

### 2.4.6 Relaxometry nuclear magnetic resonance (NMR)

The nuclear magnetic resonance (NMR) spectroscopy is a useful technique to characterise the physical, chemical and biological properties of the matter. Several kind of NMR techniques have been developed, such as one-dimensional, two-dimensional, solid state NMR, NMR imaging and relaxometry NMR for the characterisation of complex materials [184].

Relaxometry NMR can be used to qualitatively and quantitatively study the behaviour of water in complex samples. In particular, it is a non-invasive technique, which can be useful to understand the structure and the water compartment size in the materials [185].

#### 2.4.6.1 Theoretical background

The nuclear magnetic resonance is a phenomenon occurring to nuclei of atoms when they are immersed in a static magnetic field and they are exposed to a second oscillating magnetic field [184]. The ability of the nuclei to respond to a magnetic field depends on the spin angular momentum. This spin angular momentum gives a magnetic moment on a nucleus. The nuclear spin quantum number ( $I$ ) can have the values of 0, 1/2, 1, 3/2 and so on in increments of 1/2 [186]. When the atomic number and the atomic mass are even, the nucleus has no magnetic properties and its spin is zero. The non-spinning nuclei are not detectable in the NMR spectroscopy, for example  $^{12}\text{C}$  or  $^{16}\text{O}$  [187]. The nuclear spin quantum number ( $I$ ) is a fixed quantity which characterises a nucleus in its stable ground state [188]. In absence of a magnetic field  $B_0$ , all the nuclei have the same energy, but when they are exposed to a magnetic field, their energies are affected. For instance, for nuclei with spin equals to 1/2, two levels of energy are formed and the magnetic moments align in parallel or anti-parallel directions to the magnetic field. The energy difference between the two spin states is described by the following equation [187]

$$\Delta E = \gamma \hbar B_0 \quad \text{Equation 2.20}$$

where  $\Delta E$  is the energy difference between the spin state,  $\hbar$  is the Planck's constant  $h$  divided by  $2\pi$  and  $\gamma$  the gyromagnetic ratio [187]. The magnetic moments precess around  $B_0$  with angular frequency  $\omega_0$  called Larmor frequency ( $\text{rad}\cdot\text{s}^{-1}$ ).

$$\omega_0 = \gamma B_0 \quad \text{Equation 2.21}$$

Where  $\gamma$  is the gyromagnetic ratio, and in the case of protons it is equal to  $2.675 \times 10^8 \text{ rad}\cdot\text{s}^{-1}\cdot\text{T}^{-1}$  [188]. In a sample with an ensemble of spins having the same Larmor frequency, the parallel

orientation of the  $z$  component of each spin along the  $B_0$  direction has a lower energy compared to the antiparallel one. Thus, at the thermal equilibrium, there is a net magnetisation along the  $z$ -axis. All the spins have some components precessing in the  $xy$  plane, but because they all have the same energy, the precession is random. In summary, there is no magnetisation in the  $xy$  plane and the total magnetisation is along the  $z$  axis, as seen in Figure 2.18 [186].

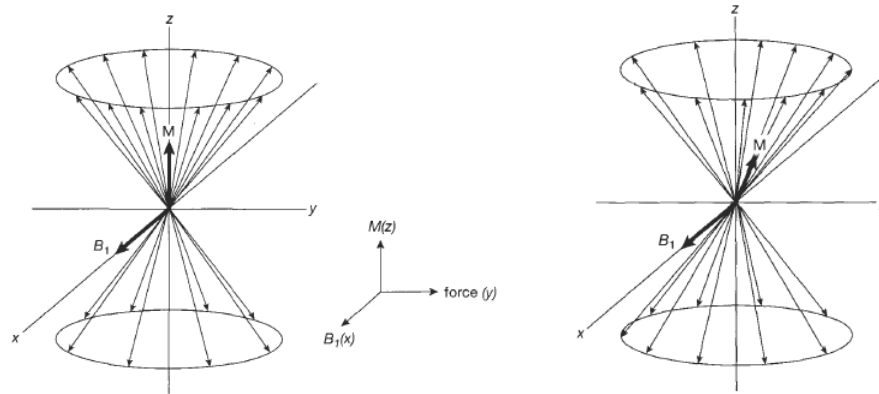


**Figure 2.18** Spin  $1/2$  at equilibrium, prior application of the magnetic field  $B_1$  (left) and soon after the application of the magnetic field  $B_1$  (right) [187].

When an oscillating magnetic field  $B_1$  (also known as the radio frequency, r.f., pulse) is applied transverse to the spin system in a thermal equilibrium in a longitudinal field  $B_0$ , a disturbance in the spins equilibrium state occurs and the magnetisation  $M$  is driven off the  $z$  axis towards the  $y$  axis. As a result, a group of spins moves towards the  $y$  axis. The phases of the spins are no longer random, but they are in coherence. Therefore some  $xy$  components of the magnetisation exist. The  $xy$  components of magnetisation is the signal detected electronically as resonance [187].

As long as the r.f. pulse  $B_1$  is on, the magnetisation continues to precess around  $B_1$  at Larmor frequency equals to  $\omega = \gamma B_1$ . The precession occurs more frequently around the  $y$  axis than on the natural  $z$  direction. The angle  $\theta$  of rotation increases as long as the r.f. pulse is applied, thus  $\theta$  is determined by the time of duration, and it is expressed in Equation 2.22

$$\theta = \gamma B_1 t \quad \text{Equation 2.22}$$

A pulse of  $90^\circ$  (or  $\pi/2$  pulse) aligns the magnetisation along the  $y$ -axis, the magnetisation can be restored by applying a pulse double the duration ( $180^\circ$  or  $\pi$  pulse). The magnetisation following the  $90^\circ$  pulse stays in the  $xy$  plane and it decays exponentially with time. The reduction of the magnetisation along the  $y$  axis is called free induction decay (FID) [187]. As a consequence of the application of a magnetic field,  $B_1$ , the disturbance of the thermal equilibrium occurs. The

process that returns the  $z$  magnetisation to the thermal equilibrium is called spin-lattice relaxation or longitudinal relaxation time ( $T_1$ ) [187]. This process consists in the exchange of energy between the spin systems and the surrounding space (also known as lattice) with which is in equilibrium. At room temperature, usually  $T_1$  ranges between 0.1 and 10 seconds. The description of this process is given by the following equation

$$\frac{dM_z}{dt} = \frac{-(M_z - M_0)}{T_1} \quad \text{Equation 2.23}$$

with solution

$$M_z = M_0 \left(1 - e^{(-t/T_1)}\right) \quad \text{Equation 2.24}$$

The transverse relaxation ( $T_2$ ) is the process that returns the equilibrium in the  $xy$  plane, that is the spins come to the thermal equilibrium among themselves. Thus it is also referred to as the spin-spin relaxation time [188]. The spin-spin relaxation consists in a state of phase coherence between the spins. This means that  $T_2$  relaxation depends on the interactions that cause the nuclear spins to dephase. For this reason,  $T_2$  relaxation may be more rapid than  $T_1$  in samples where the interactions between the nuclear spins are very slow, i.e. solids or rigid macromolecules. Usually  $T_2$  range between 10  $\mu$ s and 10 seconds. The description of the transverse relaxation is given by

$$\frac{dM_{x,y}}{dt} = \frac{-M_{x,y}}{T_2} \quad \text{Equation 2.25}$$

with solution

$$M_z = M_{x,y} \left(1 - e^{(-t/T_2)}\right) \quad \text{Equation 2.26}$$

In order to guarantee the same chemical environment to the nuclei, inhomogeneities in the magnetic field need to be removed. However, sometime external inhomogeneities might be introduced. In order to measure the diffusion, external magnetic field gradients are introduced to the magnetic field  $B_0$  [185]. Pulse field gradients cause temporary distortion in the samples and as a result, the magnetic field differs in every part within the sample. Because the gradient fields are much smaller than the polarising field  $B_0$ , only the parallel components to  $B_0$  affect the Larmor frequency, thus the local Larmor frequency is defined by the following equation

$$\omega(r) = \gamma B_0 + \gamma Gr \quad \text{Equation 2.27}$$

where  $r$  is the nuclei spins position and  $G$  is the pulse field gradient component parallel to  $B_0$  [188]. Magnetic field gradients can be used to locate the position of the nuclei through the Larmor frequency. For example, the relationship between the Larmor frequency  $\omega$  and the position  $r$  is fundamental for the NMR imaging. The pulse gradient field methods are very advantageous techniques to study diffusion. They allow the restricted and anisotropic diffusion to be determined. Both diffusion phenomena are characterising of heterogeneous systems such as porous and biological materials and provide useful information on the structure of the systems [185]. Translational diffusion is one of the most important molecular motion modes [185] and it is influenced by boundaries [188]. The self-diffusion is the result of random motion of molecules due to their thermal energy, which means that no net forces are applied on the molecules [185]. In NMR, it is not possible to detect signal from individual spins, instead the signal is the superposition of signals from an ensemble of spins. As a result, the diffusion can be determined as the probability  $P(r_0, r, t_d)$  of finding any spins that has displacement in a certain position  $r$  at a time  $t_d$ , according to the following equation

$$P(r_0, r, t_d) = (4\pi Dt_d)^{-3/2} \exp\left(-\frac{(r-r_0)^2}{4Dt_d}\right) \quad \text{Equation 2.28}$$

where  $D$  is the self-diffusion coefficient. In non-restricted systems, the free diffusion is a Gaussian curve, which enlarges with time. Under this condition, the mean displacement of particles in the three dimensions is zero. However, for a three dimensional diffusion, the root mean square  $(\langle X^2 \rangle)^{1/2}$  of a molecule moved in a time  $t$  with a diffusion coefficient  $D$  is equal to

$$(\langle X^2 \rangle)^{1/2} = (6Dt_d)^{1/2} \quad \text{Equation 2.29}$$

In free diffusion, the mean displacement increases linearly with the square root of the diffusion time. Furthermore, through the Stokes-Einstein equation, the diffusion coefficients is related to the structural characteristics of a molecule, such as size, shape, weigh and molecular interactions. Restricted diffusion might be more complicated but it has been resolved with analytical equations at least for pore of defined geometries (i.e. spherical, planar and cylindrical) [189-191]. There are many pulse sequences can be used in modern relaxometry NMR. Among

them, there are the Carr-Purcell Meiboom-Gill (CPMG) sequence (section 2.4.6.1.1), the inversion recovery sequence (section 2.4.6.1.2), the pulsed gradient spin echo (PGSE) sequence (section 2.4.6.1.3) and the stimulated echo (section 2.4.6.1.4). The attenuation of the spin echo, which arises from the dephasing under application of a steady gradient, can be used to measure molecular self-diffusion. A typical pulse sequence is the PGSE experiment. However, there is a limitation in the measurement of the self-diffusion using PGSE, which is the loss of the phase coherence due to the transverse relaxation. A way to overcome this limitation is to apply a second  $90^\circ$  pulse. The magnetisation is restored at later time and rephased in a stimulated echo, this is also referred to as PGSTE, section 2.4.6.1.4. Another way to intervene is to use a CPMG echo train with two pulse gradients inserted at a certain time distance between the r.f.  $180^\circ$  pulse (section 2.4.6.1.3) [188]. Both these techniques are non-destructive and do not require a chemical tracker in the material [192].

#### 2.4.6.1.1 Carr-Purcell-Meiboom-Gill (CPMG) sequence

The CPMG pulse sequence is widely used to measure spin-spin relaxation time ( $T_2$ ). According to the sequence, a  $90^\circ$  pulse is applied to the sample, the magnetic field ( $M$ ) rotates down the  $xy$  plane and it begins to dephase. After a certain time, a  $180^\circ$  pulse is applied which rotates the magnetization by  $180^\circ$  from the  $x$  axis which cause  $M$  to partially rephase (Figure 2.19). Following this sequence, a signal, called echo, is produced [184].

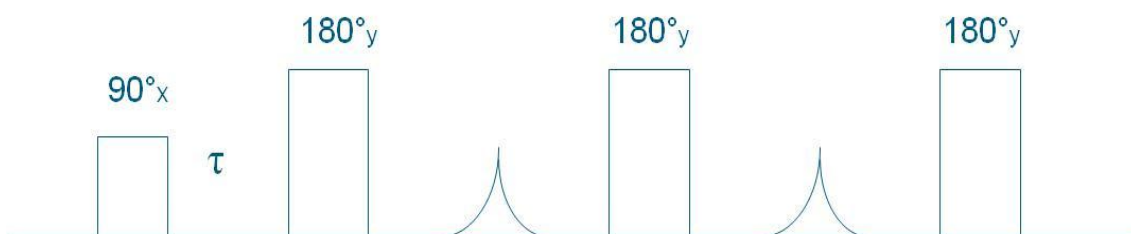


**Figure 2.19** A typical CPMG pulse sequence

#### 2.4.6.1.2 Inversion Recovery pulse sequence (Inv-CPMG)

To confirm the assignment of the protons, the inversion recovery pulse sequence (Inv-CPMG) and the CPMG-pulsed gradient spin echo sequence (CPMG-PGSE) were performed. In the Inv-CPMG test, the inversion recovery step [ $180^\circ$ - $T_1$ -] is inserted prior to the CPMG sequence. The data is then acquired and the sequence is repeated. The inversion recovery step is used to measure the  $T_1$  relaxation time. The  $180^\circ$  pulse inverts the magnetisation vector so that the system is subject to a severe disturbance. The  $T_1$  relaxation proceeds for a time  $t$ , after which a  $90^\circ$  pulse is applied. The independent variables are the recovery time,  $T_1$  and the CPMG

acquisition time  $T_2$ , which is equal to  $2n\tau$  with  $n > 1$  and  $\tau$  is the  $90^\circ$ - $180^\circ$  pulse gap ( $\mu\text{s}$ ) in the CPMG sequence. The  $T_2$  dimension is acquired with any  $\tau$  spacing as seen in Figure 2.20).

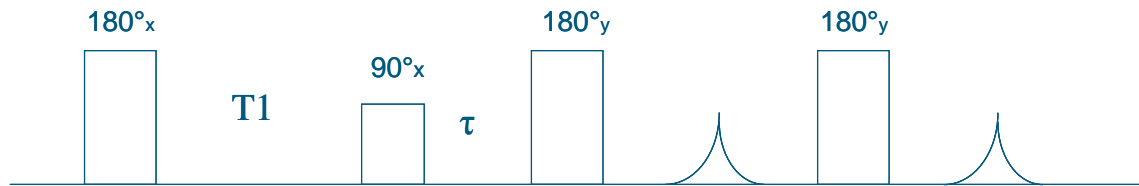


**Figure 2.20** A typical Inversion Recovery CPMG sequence

#### 2.4.6.1.3 CPMG Pulsed Gradient Spin Echo sequence (CPMG-PGSE)

The CPMG-pulsed gradient spin echo sequence (CPMG-PGSE) was performed on the gels with selected water contents (70% and 80%). A CPMG sequence,  $90^\circ [-\tau-180^\circ]_n$ , is inserted prior to the PGSE sequence [ $90^\circ$ -gradient- $180^\circ$ -gradient]. The independent variables are CPMG time  $T_2$ , which is given by  $2n\tau$ , the diffusion time  $\Delta$ , and the pulsed gradient area, which is defined by the following equation

$$q = (2\pi)^{-1} \gamma \delta G \quad \text{Equation 2.30}$$

where  $\gamma$  is the gyromagnetic ratio,  $\delta$  is the pulsed gradient duration and  $G$  is the gradient strength. The CPMG-PGSE sequence is shown in Figure 2.21.

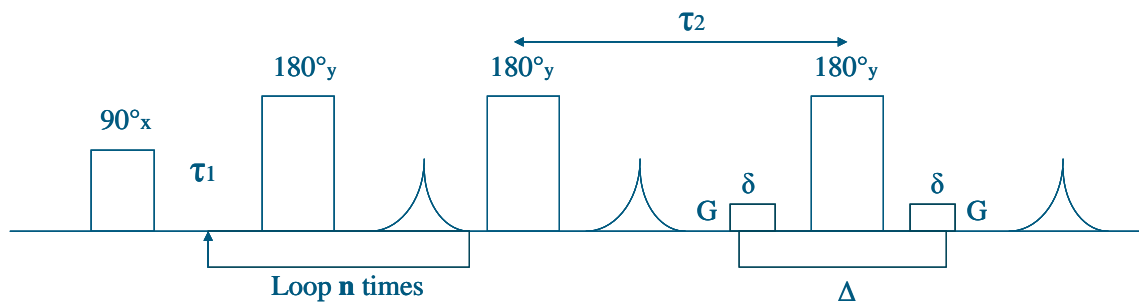


**Figure 2.21** A typical CPMG-PGSE sequence, where  $\tau_1$  is the CPMG value,  $\tau_2$  is the PGSE tau,  $\Delta$  is the diffusion time or pulse gradient separation,  $\delta$  is the pulse gradient duration and  $G$  is the pulse gradient strength.

In a PGSE sequence, the echo attenuation is measured as a function of the gradient wavevector  $q$  ( $\text{m}^{-1}$ ) and the diffusion time  $\Delta$ . The relaxation response and the  $q$ -vector response can be separate by using two different sequences with which the relaxation and the diffusive effects are determined by two different variables. Therefore, a CPMG pulse sequence is performed. During this sequence, the time over which the transverse relaxation time occurs is varied and followed by the PGSE sequence in which the  $q$ -vector is changed [191].

## 2.4.6.1.4 Stimulated echo diffusion sequence (PGSTE diffusion)

The PGSTE diffusion is a modified sequence of a typical PGSE. The advantage of using this sequence is that the magnetisation is protected from the  $T_2$  relaxation. Furthermore, it is exposed to reduced precessional dephasing due to residual gradients [188]. The sequence contains three  $90^\circ$  pulses and an echo after the third pulse is called stimulated echo (Figure 2.22) [185].

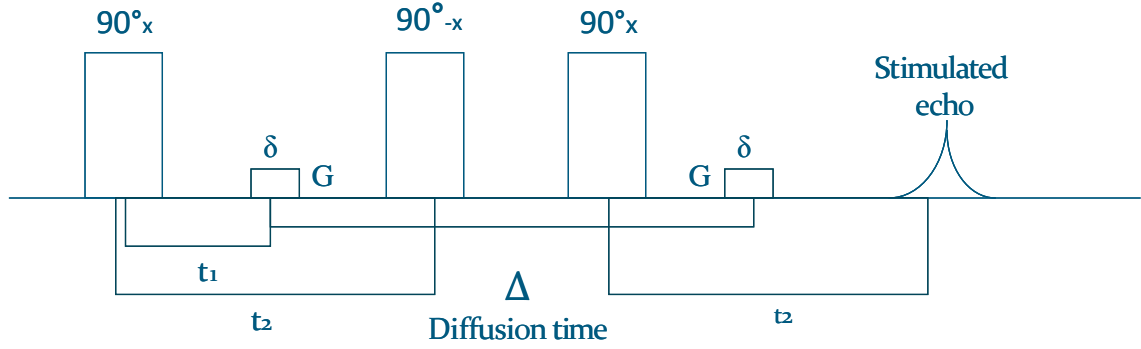


**Figure 2.22** A typical PGSTE diffusion sequence, where  $\Delta$  is the diffusion time or pulse gradient separation,  $\delta$  is the pulse gradient duration and  $G$  is the pulse gradient strength.  $t_1$  is the pre-gradient delay and  $t_2$  the pulse gap.

The spins positions are localised at time  $t = 0$  in a given direction ( $O_i$ ) by applying a pulse gradient along this direction. A second pulse gradient is applied after a diffusion time  $\Delta$ . The second gradient will remove the effect of the previous one, unless the spins have moved during time  $\Delta$  along the same direction ( $O_i$ ). As a result, the second gradient cannot refocus the signal of all the spins. This leads to the amplitude of the echo,  $E(q, \Delta)$ , decreases, according to the following equation

$$E(q, \Delta) = \frac{I(q, \Delta)}{I(0, \Delta)} = \exp\left[-4\pi^2 q^2 e_i^T D e_i (\Delta - \delta/3)\right] \quad \text{Equation 2.31}$$

where  $q = (2\pi)^{-1} \gamma \delta G$ ,  $G$  the intensity of the pulsed field gradient,  $\delta$  the duration of the gradient,  $e_i$  the unitary vector along the defined direction ( $O_i$ ),  $e_i^T$  the transposed vector,  $\Delta$  the diffusion time and  $\gamma$  the gyromagnetic ratio of the proton and  $D$  is the diffusion coefficient.  $I(q, \Delta)$  and  $I(0, \Delta)$  are the echo intensities measured with and without applying a pulse field gradient, respectively [192].

## 2.4.6.2 Instrumentation and sample preparation

Two-dimensional NMR relaxation studies were performed on Gelucire 50/13 gels with a range of water contents (10%-90%) and prepared by heating method. A pulse field gradient was also applied. In the presence of a pulse gradient, which is a distortion of the magnetic field, the

magnetic field is different in every part of the sample. The pulsed field gradient (PFG) NMR is particularly useful for imaging and studying molecular mobility. The tests were carried out at room temperature, using a bench-top NMR (23.4 MHz, Maran Ultra, Resonance, Oxford Instruments) equipped with a DRX console, which generates the pulse gradient (Figure 2.23).



**Figure 2.23** 23.4 MHz NMR (Maran Ultra) interfaced to a DRX console (on the left)

The parameters analysed in the tests are the spin-lattice relaxation time ( $T_1$ ) or longitudinal relaxation, which is the decay constant for the recovery of the  $z$  component of the magnetization ( $M_z$ ) and the spin-spin relaxation time ( $T_2$ ) or transverse relaxation, which is the time constant, which describes the return to equilibrium of the transverse magnetization ( $M_{xy}$ ). The samples were loaded in different way according to their viscosity. The thicker samples (from 10% to 60% water content) were loaded into a small glass tube (7 mm in diameter) and then the tube was put inside a sample tube (10 mm in diameter) as shown in Figure 2.24a. The samples with higher water content and lower viscosity (between 70 and 90% water contents) were directly put inside the sample tube (Figure 2.24b). A PTFE piston is placed against the sample and the tube was sealed with Parafilm® to avoid evaporation of water during the test. Several sequences were performed on the samples including CPMG, Inv-CPMG, CPMG-PGSE, PGSTE diffusion test. All the data were analysed using MatLab.

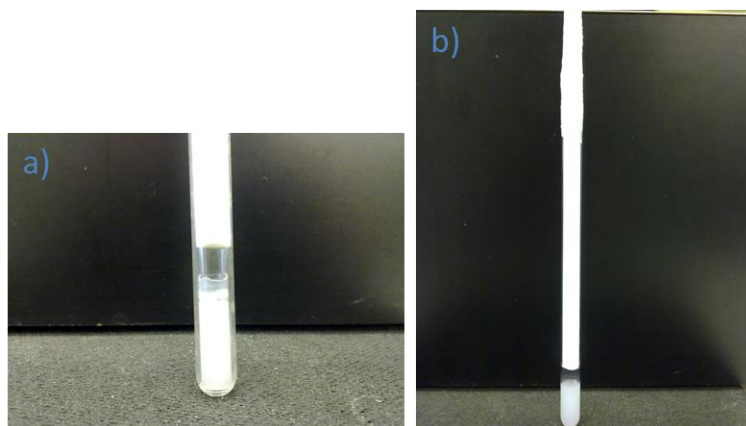


**Figure 2.24** Detail of the bottom part of a NMR sample tube loaded with gel 50% of water or below (a) and sample tube loaded with gel with 70% of water or above.

## 2.4.7 Spectroscopic techniques

### 2.4.7.1 Attenuated total reflectance-Fourier transform infrared (ATR-FTIR) spectroscopy

#### 2.4.7.1.1 Basic principles

IR spectroscopy is one of the most widely used analytical techniques to characterise the molecular structure of compounds. When an IR radiation passes through a molecule, part of the energy is absorbed and the molecular vibrations are enhanced to higher energetic levels. In order for a molecule to respond to the IR radiation, it is necessary that a change in the dipole moment occurs with the vibrations. A compound can undergo to different motions including symmetric and asymmetric stretching, in-plane bendings (such as rocking and scissoring) and out-of plane bendings (such as wagging and twisting). Nowadays the most used IR spectrometers are Fourier-transformed based instruments. The FTIR spectrometers have improved the quality of the spectra and decreased the time of acquisition the data. The main principle is based on the idea of interference of radiation by using an interferometer. The interferogram obtained is then converted into a spectrum mathematically by using the Fourier transformation.

Reflectance techniques can be useful to study complex samples, which are difficult to analyse with conventional IR. They exist several reflectance methods, and the most used one is the attenuated total reflectance (ATR) which consists in internal reflectance of the beam when the angle of incidence at the interface between sample and the diamond cell is greater than the critical angle, which is a measure of the refractive indexes of the two surfaces [193].

#### 2.4.7.1.2 Structural analysis of proteins using IR

The Fourier Transform Infrared (FTIR) spectroscopy like nuclear magnetic resonance (NMR), circular dichroism (CD) and X-Ray diffraction is a useful technique for the characterisation of proteins, peptides and polypeptides. Particularly for the determination of the secondary structure [194]. NMR spectroscopy and X-Ray crystallography are the best way to get information on proteins structure, but it is not always practicable. Proteins can form complex and dynamic systems within the biological environment that can lead to difficult interpretations. For instance, in crystallographic techniques high quality single crystals are required which is not always possible for each protein species. Also the “static” conformation that proteins assume in the crystal is far from the real conformation in the biological environment of cells. On the contrary, NMR spectroscopy is able to analyse proteins in their biological environment, but complicated spectra of larger proteins (over 20 kDa) can make the interpretation extremely difficult. For these limitations “low-resolution” studies such as the circular dichroism and vibrational spectroscopy are preferred in some cases [195]. The IR spectroscopy is one of the most powerful methods to detect hydrogen bonds and the changes in the surrounding environment. It is also a valuable way to analyse the dynamics of hydrogen atoms in hydrogen bonds [196].

In the mid-IR region, the proteins and polypeptides present nine characteristic bands of absorbance called amide A, amide B and amide I-VII [197] which are correlated to the vibrations of the peptide groups [195]. The use of FTIR led to improvements in the quantitative analysis on the conformations of proteins. The NH stretch is a localized mode and it is usually a doublet called Amide A (about  $3500\text{ cm}^{-1}$ ) and Amide B (about  $3100\text{ cm}^{-1}$ ). In samples that are in solution, this band can be overlapped with the OH stretch of water. The main modes studied are the Amide I and the Amide II. The Amide I ( $1600\text{-}1700\text{ cm}^{-1}$  [198]) mainly refers to the C=O stretch vibration of the polypeptide backbone [194], but it may consider also the CN stretch and the CCN deformation and from the NH in-phase bending [199]. The Amide II mode ( $1500\text{-}1600\text{ cm}^{-1}$ ) depends on the out-of-phase combination of the NH in-plane bending and CN stretching and to some extent depends on the C=O in-plane bending and CN stretching [196]. The amide III in the  $1200\text{-}1400\text{ cm}^{-1}$  region [199]. The amide I band is observed at  $1620\text{-}1680\text{ cm}^{-1}$  [200] and it is the result of the overlapping of several components corresponding to the  $\alpha$ -helix, anti-parallel and parallel  $\beta$ -sheet,  $\beta$ -turns and random coil structures [201]. The assignments of the conformations studied using IR are listed in Table 2.6.

**Table 2.6** Assignment for the Amide I bands in the FTIR.

<i>Position (cm<sup>-1</sup>)</i>	<i>Assignment</i>	<i>References</i>
1620-1640	$\beta$ -sheet	[200]
1640-1645	random coil	[193]
1648 -1658	$\alpha$ -helix	[193, 200]
1659-1666	“3-turn” helix	[193]
1670-1695	$\beta$ -turn	[193, 196, 202]
1680-1690	antiparallel $\beta$ -sheets at high wave number	[202]
1620-1640	antiparallel $\beta$ -sheets at low wave number	[202]

#### 2.4.7.1.3 Methodology used in this project

ATR-FTIR was used to obtain information on the structure of the gels and to determine the secondary structure of the lysozyme incorporated in the gels. For this purpose the Amide I peak, which absorbs between 1620 and 1680 cm<sup>-1</sup> was analysed as described in Chapter 5. As the O-H bending of water (present in each gel) occurs in the same range, deuterium oxide (D<sub>2</sub>O) was used to replace water and prepare the gels.

The ATR-FTIR tests were performed on two series of Gelucire/D<sub>2</sub>O gels with 10% to 90% (w/w) water contents prepared by heating and by hydration methods. In general, four main regions can be observed the X-H stretching region (4000-2500 cm<sup>-1</sup>), the triple bond region (2500-2000 cm<sup>-1</sup>), the double bond region (2000-1500 cm<sup>-1</sup>) and the fingerprint region (1500-600 cm<sup>-1</sup>) [193]. The gels prepared by heating method using ultrapure water (Milli-Q grade) were also analysed to assess whether D<sub>2</sub>O may change the structure of the gels. Lysozyme-loaded gels prepared by hydration method were also analysed with four D<sub>2</sub>O concentrations: 20%, 40%, 60% and 70% (w/w). Lysozyme-loaded gels prepared by heating method with D<sub>2</sub>O concentrations of 40%, 50% and 60% (w/w) were also analysed. A 10% (w/w) LSZ/D<sub>2</sub>O solutions and was also analysed. The analyses were performed with an ATR-FTIR spectrometer (Bruker IFS66/S, Coventry, UK). The tests conditions are described in details in Chapter 3 (section 3.3.1) for the lysozyme-free gels and in Chapter 5 (section 5.3.1) for the lysozyme-loaded gels. All the data were analysed with the software OPUS.

#### 2.4.7.2 Circular Dichroism (CD)

Circular dichroism (CD) spectroscopy is a commonly used technique to perform structural studies on proteins, especially suitable to determine their secondary structures, folding and binding properties [203]. However, information on the tertiary structure can also be obtained. Unlike X-ray cristallography and NMR, CD is a low resolution structural technique, but less

demanding in sample requirements and non-destructive [204]. A CD spectrometer consists of a light source, monochromator to disperse the light in several wavelengths, a sample compartment and a detector (photomultiplier) [205]. When the light reaches the photomultiplier, a current is produced. Most CD instruments keep the current constant by increasing the voltage as the amount of light decreases. At low wavelengths, the absorbance increases leading to an increase in voltage. When the voltage is above 500 volts the data become noisy and less reliable [203]. A CD spectrometer is equipped with a linear polarised light and a quarter wave retarder which convert the linear polarised light into a circular polarised light (left-handed (L) and right-handed (R)). CD measures the difference in intensity of these two lights [205]. If they are not absorbed or they are absorbed in the same extent, the two lights recombine in the original plane (Figure 2.25a I). If an asymmetric sample partially absorbs the light, the result is an elliptically polarised light (Figure 2.25a II) [204].

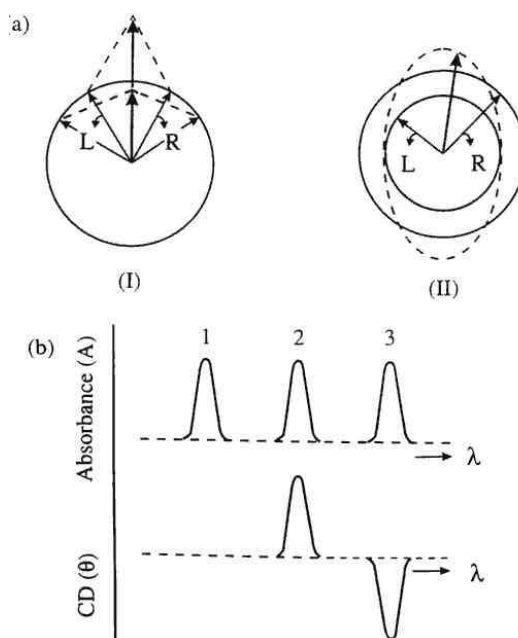


**Figure 2.25** (a) Left (L) and right (R) circularly polarised component of the light: when the two components have the same amplitude they recombine in the original plane (I), if they have different magnitude they combine in a elliptical (dashed line) polarised plane (II). (b) The diagram compares the absorption and the CD spectra: band 1 is from an achiral sample, which produces no CD band; band 2 generates a positive CD band (L absorbs more than R); band 3 has a negative CD spectrum (R absorbs more than L) [206].

As a normal absorption technique, in a CD the Lambert-Beer law can be applied. For the CD results of a molecule, the extinction coefficients for the two parts of the circular polarised light are defined as described by the relation below

$$A_L(\lambda) - A_R(\lambda) = \Delta A(\lambda) = [\varepsilon_L(\lambda) - \varepsilon_R(\lambda)] \cdot l \cdot c = \Delta \varepsilon(\lambda) \cdot l \cdot c \quad \text{Equation 2.32}$$

Where  $A$  is the absorbance and the subscripts  $L$  and  $R$  stand for “left” and “right”;  $\epsilon$  is the extinction coefficient which varies with the wavelength  $\lambda$ ;  $l$  the pathlength of the cell and  $c$  the concentration of the material.

Therefore, CD absorption bands can be positive or negative according to which type of light is absorbed. It differentiates from zero for asymmetric molecules. The difference in absorbance is reported more often in terms of ellipticity ( $\theta$ ) in degrees (deg), which is related to the absorbance by  $\Delta A = \theta/32.98$  [205]. Usually the observed CD signals are small and the ellipticity is in the range of 10 mdeg corresponding to a difference in absorbance of the order of  $3 \times 10^{-4}$  between the left ( $L$ ) and the right ( $R$ ) circularly polarised components [204].

Every spectral band produced can be associated to a structural conformation of the studied protein. Two types of information can be obtained, the secondary structure conformation and the tertiary structure. The bands in the far UV region (below 240 nm) principally arise from the peptide bond region. These data analysed with a number of algorithms provide information on the secondary structure of proteins. The near UV region (between 260 and 320 nm) spectrum reflects the aromatic amino acids chains, each of which have a specific wavelength profile. The magnitude and the shape of the near UV spectrum depend on the number of each of the aromatic side chains of the protein molecule, their mobility, their environment and their special positions. This region contains also information of the tertiary structure of the proteins [204, 206].

## 2.4.8 Imaging technique

### 2.4.8.1 Scanning electron microscopy (SEM)

SEM is an electronic microscope that is used to produce high-resolution images of samples of different nature and shape. The signals produced by the electrons-sample interactions are collected to provide images of the surface [207]. In most of the cases, the samples are scanned at room temperature and under high vacuum conditions. The samples is normally pre-coated with a conducting material, i.e. gold, to prevent an accumulation of charges from the electric beam [208].

In this study, SEM images were used to determine the interior structure of the freeze-dried gels (prepared both hydration and heating methods following the procedure described in paragraph 2.3.1). The samples were fixed on the sample stubs by using double-side tape and coated with gold using Polaron High Resolution SC7640 gold coater (Quorum Technologies, Newhaven,

UK). Imaging process was carried out with a JEOL JSM 5900 LV SEM (Tokyo, Japan), operating at an acceleration voltage of 5-20 kV.

#### **2.4.8.2 Atomic force microscopy (AFM)**

Atomic force microscopy (AFM) is a valuable technique for imaging samples at atomic resolution. It has been used for the determination of the structure of biological molecules such as proteins and DNA [209] and to image nanomaterial and colloidal dispersions such as liquid crystalline cubosomes and hexosomes structure [210]. An AFM consists of a cantilever equipped with a tip (probe) at the end and a detector to measure any deflection of the cantilever. The deflections are determined through an optical laser beam. The sample is located on piezoelectric elements, which are able to move the sample in three directions (x, y and z). The imaging acquisition can be performed principally in two modes, the contact mode and the tapping mode. Contact mode imaging is used for solid and hard surfaces since the tip remains in contact with the sample throughout the scanning and for the same reason it is not suitable for soft matter or biological structures. Therefore a non-contact or tapping mode can be adopted to acquire the images for soft surfaces. Compared to the contact mode, in the tapping mode (or intermittent contact) the tip oscillates at a constant amplitude and at a frequency near or at the cantilever resonance and when it comes into contact with the surface the probe intermittently “taps” the sample [209].

Tapping mode AFM (Caliber, Veeco, USA) was used to characterise the shape and to determine the size of the nanoparticles. The measurements were carried out with TESP cantilever (Bruker, CA, USA), calibrated before each scan. The nanoparticles were diluted 1:10 with ultrapure type I water. 3 µl of the dilutions were dropped on a mica film and left to dry for 15 minutes. The film was then rinsed with ultrapure water and dried with compressed air. Five to ten sites of each formulation were scanned to assess the shape and the size of the particles and the homogeneity of the samples.

#### **2.4.8.3. Cryogenic transmission electron microscopy (cryo-TEM)**

Cryo-TEM is a transmission electron microscopy used on thin vitrified aqueous films held at nitrogen temperature. This technique has contributed over the years to a better understanding of the complex structure of amphiphilic molecules in aqueous solution. Particularly it has been successfully employed to better characterise the structure of liposomes and liquid crystals. The advantage of this microscopic technique is to visualise the samples in solution without dehydration thanks to the rapid vitrification, which means no structural rearrangements take place during the procedure. The size range for suitable observation with the cryo-TEM is

between 4-5 nm and 500 nm, bigger size means slow rate of vitrification and larger scattering of the electrons by the surrounding water. The contrast can be a limiting factor. It is given by the difference of electron density between the atoms of the amphiphile sample and the water [211]. It has been also stated that the PEG polymer is invisible to the cryo-TEM beam for the poor contrast with the surrounding vitrified water [212]. This may explain the low contrast of the cryo-TEM images obtained on the nanoparticles (see Chapter 6).

The cryo-TEM was used to assess the size and shape of the nanoparticle formulations F2 and F4. The nanoparticles were placed on the microscope copper grid (coated with a perforated polymer film) in order to form a thin aqueous film. The excess of liquid was removed by blotting with a filter paper. The film was then immersed in a cooling medium (ethane) held at the temperature just above the freezing point. The film rapidly vitrified without crystallisation. The grid with the vitrified film was transferred under a Zeiss EM 902 A transmission electron microscope (Oberkochen, Germany). The sample was held at liquid nitrogen temperature and at a controlled humidity environment during the test. All observations were made in zero-loss bright-field mode and at an accelerating voltage of 80 kV. The nanoparticles suspensions were analysed non-diluted and at a maximum magnification of 50000x.

## 2.5 Drug release studies

*In vitro* dissolution studies can help to design and select the appropriate dosage forms, and represent a valuable way to correlate the performance *in vivo* of the drug [213]. In this work, the *in vitro* dissolution tests were used to assess the release profile of lysozyme encapsulated in the gels. It was also used to determine whether and how the gels structure and the percentage of water content in the gel can affect the release, and if the pH of media plays a role in the release profile.

The dissolution studies on the lysozyme-loaded gels prepared by both heating and hydration methods were performed using BP paddle method with a dissolution apparatus (Caleva 8ST, Dorset, UK) with two different dissolution media, phosphate buffer solution (pH 7.4 prepared according to the British Pharmacopoeia 2012) and 0.1 M HCl (pH 1.2). The amount of gels used for the test was calculated in order to keep constant the amount of solid Gelucire in all the gels, which was equal to 1 g. The gels were weight inside plastic gel sample holder equipped with metal plate and immersed in the vessels filled with 500 mL of the medium. The container used to place the gels for the dissolution studies is illustrated in Figure 2.26.



**Figure 2.26** Plastic gel sample holder for dissolution test equipped with a metal plate and filled with gel with 60% water.

The temperature was set at  $37.0 \pm 0.5$  °C and the rotation speed of the paddles at 100 rpm. At fixed sampling points, 5 mL of the sample was collected each time with a syringe and filtered by using a 0.45  $\mu\text{m}$  pore size membrane filters (Minisart NML single use syringe, Sartorius, UK) and replaced with the exact volume of fresh medium, which was pre-heated at the same temperature. The absorbance of lysozyme was measured through a UV-Vis spectrophotometer (Perkin-Elmer lambda 35, USA) at the wavelength of 280 nm. The lysozyme-free gels were tested in the same conditions and the absorbance measured with the UV spectrophotometer as controls. The UV spectra of the lysozyme-free gels were subtracted to the spectra of the lysozyme-loaded gels in order to remove any contributions of the Gelucire to the spectra.

## 2.6 Diffusion studies (Franz Cells)

Diffusion cells are widely used to perform *in vitro* permeation or transport studies, especially for topical formulation development. The diffusion cells have been used in this study to assess the drug release properties of the gels across model membranes. It is also used for assessing the potential of the gel formulations for transdermal drug delivery systems. The diffusion tests were performed on a vertical glass Franz diffusion cells (PermeGear, Inc., Hellertown, USA). A schematic view of the cell is shown in Figure 2.27.

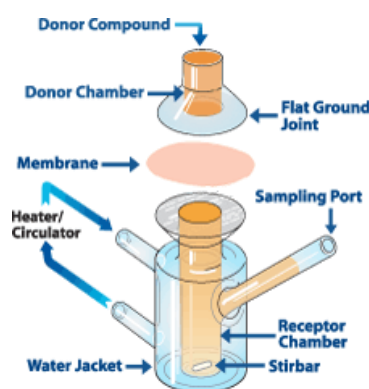


**Figure 2.27** Illustration of the setup of Franz cells (PermeGear).

A Franz diffusion cell is composed of a donor chamber where the sample is located and the receptor chamber containing the medium. The two compartments are separated by a synthetic or biological membrane. The receptor chamber has a maximum capacity of 5 ml and it is kept under stirring (at speed of 500 rpm) for the all duration of the experiments. Six jacketed cells are installed in stirrer equipment (V6A stirrer) to stir the receptor fluid inside the cells. The jacketed cells are connected to a thermostat (HAAKE SC100, Thermo Scientific) to keep the temperature of the cells at 37 °C.

## **2.7 Cell culture**

### **2.7.1 Cell culture reagents and media preparation**

Foetal calf serum (FCS) was purchased from Biosera (East Sussex, UK). Trypan blue 0.4% was purchased from Sigma Aldrich (UK). DMEM (Dulbecco's Modified Eagles Medium with glucose and glutamine), 10,000 U/ml penicillin and 10,000 µg/ml streptomycin, 0.25% trypsin-EDTA were purchased from Invitrogen (Paisley, UK). Non-essential amino acids and sodium pyruvate were purchased from Thermo Fisher Scientific (Loughborough, UK).

#### **2.7.1.1 NCI-H292**

NCI-H292 cell line were purchased from the European Collection of Cell Cultures (ECACC). They derive from a cervical node metastasis of a pulmonary mucoepidermoid carcinoma from a 32-year-old female. The cells retain mucoepidermoid characteristics in culture, and some of them contain numerous small mucin-containing granules (ECACC). NCI-H292 cells were cultured in RPMI-1640 (Roswell Park Memorial Institute) media containing 100 U/ml penicillin, 100 µg/ml streptomycin, 2 mM L-glutamine and 10% FCS. When the confluence was about 80-90%, the cells were passaged by washing with PBS (phosphate buffer saline) followed by adding 0.25% trypsin-EDTA 1x solution for 30 seconds. The cells were removed and incubated at 37 °C for 3-5 minutes to allow the cell detachment. Afterwards the cells were re-suspended in 5 ml fresh media. The cells were maintained between  $3 \times 10^5$  and  $1 \times 10^6$  cells/ml in 75 cm<sup>2</sup> at 37 °C and 5% CO<sub>2</sub> and they were routinely passaged every 3-4 days. They were used between passage numbers 11-30.

#### **2.7.1.2 Caco-2**

The Caco-2 cells were kindly provided by the Institute of Food Research (IFR). Caco-2 cells are isolated from a primary colonic tumour in a 72-year-old Caucasian male by using explant culture technique. The cells were cultured in DMEM (Dulbecco's Modified Eagles Medium)

with glucose and glutamine, containing 10% FCS, 100 U/ml penicillin and 100 µg/ml streptomycin solution, 1% non-essential amino acids and sodium pyruvate. The sub-confluent cells (70-80%) were passaged by washing with PBS followed by addition of 0.25% trypsin-EDTA 1x solution for 30 seconds and then removed. The cells were placed in the incubator at 37 °C, 5% CO<sub>2</sub> for cell detachment. Subsequently, the cells were re-suspended in 5 ml fresh media. The cells were maintained at a concentration of 3 x 10<sup>5</sup> and 1 x 10<sup>6</sup> cells/ml in 75 cm<sup>2</sup> at 37 °C and 5% CO<sub>2</sub> and they were routinely passaged every 3-4 days. The cells were used at passage 58 and with a concentration of 1 x 10<sup>5</sup> cells/ml.

### 2.7.2 Cell counting and viability

The cells H292 and Caco-2 cells were diluted 1:2 with 0.4% trypan blue solution. 10 µl of the solution is added on the Neubauer haemocytometer (Thermofisher Scientific) and visualised with a light microscope. Trypan blue dye is used to calculate the cell viability. The dye is able to penetrate the cells in which the membrane is not intact and therefore non-viable. In order to enumerate the viable cells, the number of blue stained cells (non-viable) is divided by the total number of cells and multiplied by 100.

### 2.7.3 Cytotoxicity/Proliferation test

*In vitro* cytotoxicity of the aqueous dispersions of the nanoparticles was tested using H292 and Caco-2 cells (grown as previously described) by performing the MTS assay (CellTiter96® AQueous One Solution, Promega). The assay tests the reduction in viability of cells stimulated with the presence of the nanoparticles by using a solution of MTS tetrazolium compound (3-(4,5-dimethylthiazol-2-yl)-5-(3-carboxymethoxyphenyl)-2-(4-sulfophenyl)-2H tetrazolium) and an electron coupling reagent (phenazine ethosulfate, PES). The MTS compound is reduced by the cells in a formazan compound, which is soluble in the cell medium. The formation of the formazan was measured at 490 nm and it is directly proportional to the number of living cells.

**Table 2.7** Dilutions with sterile water and corresponding final lipid concentrations in each dilution.

<i>Dilutions</i>	<i>Final concentration (µg/ml)</i>
Stock	600
D1	300
D2	200
D3	150
D4	120
D5	100

The cells were incubated with diluted nanoparticles suspensions prepared from the bulk gel with 40% (w/w) of water. The concentrations of the nanoparticles in the dilutions are listed in Table 2.7. For the H292 cells, only the stock solution and the dilutions D1 and D2 were used, while the Caco-2 cells were incubated with all the dilutions listed in Table 2.7.

The tests were performed in triplicate using a 96 well-plates. Five  $\mu\text{l}$  of dilutions were added to 100  $\mu\text{l}$  media in each well. The cells were incubated at 37 °C for 24 hours, after incubation 10  $\mu\text{l}$  of MTS (CellTiter96® AQueous One Solution reagent) was added to each well and left to incubate for 150 minutes. The absorbance at 490 nm was recorded using a POLARstar OPTIMA microplate reader. The reading of cells in DMSO was taken as control and it represents the 100% cell proliferation.

## **3 Basic structure characterisation of Gelucire 50/13 gels**

### **3.1 Introduction**

The general aim of this work is to investigate the potential of stearyl macroglycerides (Gelucire 50/13) as a suitable material to develop formulations for protein/peptide drug delivery. As discussed in Chapter 1, the delivery of proteins and peptides, especially via oral route, can be very challenging as the proteins may undergo denaturation or deactivation as a consequence of enzymatic processes in the body. Therefore, the design of appropriate formulations that are able to protect the structure of the proteins and preserve their activity is crucial for the development of protein delivery systems. For this project, in order to better understand the behaviour and to explore the potential use of Gelucire 50/13 based carrier systems, it is important to fully characterise the properties of the vehicle materials. Although very little is known on the physical properties of hydrated forms of Gelucire 50/13, the results from previous study has indicated the presence of possible liquid crystalline phases in the hydrated forms of Gelucire 50/13 [107]. These finding encourage us to hypothesise that the structure of liquid crystalline phases of the hydrated Gelucire 50/13 may vary with the water content.

This chapter mainly focuses on the physicochemical characterisation of Gelucire 50/13 gels prepared with two different procedures (heating and hydration methods) using a combination of spectroscopic, thermal and mechanical tests, which allowed a clear understanding of the basic structure of the gels formed. The structural information of the gels was obtained by coupling small angle x-ray scattering (SAXS) technique with infrared spectroscopy (ATR-FTIR). The phase transitions of the gels upon thermal treatment were investigated with a conventional differential scanning calorimeter (DSC). Rheological and mechanical properties of the gels were determined by using rheometer and texture analyser. The mucoadhesive properties of the gels were also evaluated using texture analyser with mucin tablet and porcine small intestine tissues. The knowledge gained from the studies described in this chapter forms the foundation for the development of Gelucire 50/13 gels as potential carriers for oral protein delivery.

## **3.2 Objectives**

The main purpose of the chapter is to characterise the hydrated Gelucire 50/13 gels prepared over a range of water contents by using both heating and hydration methods. The detailed aims achieved in this part of the project are:

- Identification of the structure changes of the gels with changing the water content and temperature (SAXS and ATR-FTIR)
- Investigation of the phase transitions of the gels upon thermal treatment using DSC
- Characterisation of the rheological and mechanical properties of the gels and correlates the results with the structural changes with water content and temperature observed with thermal and spectroscopic methods
- Evaluation of the mucoadhesive properties of the gels

## **3.3 Materials and methods**

Stearoyl macrogolglycerides (Gelucire 50/13) were kindly donated by Gattefossé SAS, St Priest, France. The Gelucire 50/13 gels were prepared using Milli-Q water (18 M $\Omega$ .cm, Barnstead Nanopure, Thermo Scientific, UK) following the procedure described in Chapter 2, section 2.3.1. Deuterium water (D<sub>2</sub>O, > 99.92 atoms % D, Apollo Scientific Limited, Stockport, UK) was used for the ATR-FTIR spectroscopic measurements. Mucin powder from porcine stomach type II (Sigma Aldrich, Gillingham, UK) and porcine small intestine (obtained from the local abattoir) were used to assess the mucoadhesion of the Gelucire 50/13 gels with the Texture Analyser (TA-XTplus, Stable Micro System Ltd, Godalming, UK).

### **3.3.1 Attenuated Total Reflectance-Fourier Transformed Infrared spectroscopy (ATR-FTIR)**

The ATR-FTIR was used to characterise the structural conformations (mainly PEG and PEG esters proportions) of the gels and to assess whether and how the structure can be affected by the water content. The tests were performed on the gels with 10% to 90% (w/w) D<sub>2</sub>O prepared by heating and by hydration method in mid-IR region (4000 and 400 cm<sup>-1</sup> wavenumber). The gels prepared by heating method using ultrapure water (Milli-Q grade) were also analysed. The analyses were performed with an FTIR spectrometer (Bruker IFS66/S, Coventry, UK) equipped with a single reflection diamond ATR cell (SPECAC, Orpington, UK). The gel with each water concentration was tested at least in triplicate. The average spectrum was calculated after baseline corrections and presented in section 3.4.1. The testing conditions applied on the gels are listed in Table 3.1.

**Table 3.1** List of samples and experimental conditions adopted for the ATR-FTIR tests.

<i>Samples</i>	<i>Preparation procedure</i>	<i>Temperature</i>	<i>Resolution</i>	<i>Number of scans</i>	<i>Notes</i>
Gelucire powder	—	Room temperature	2 cm <sup>-1</sup>	64	
Gelucire /H <sub>2</sub> O	Heating method (see section 2.3.1)	Room temperature	4 cm <sup>-1</sup>	32	
		37 °C	4 cm <sup>-1</sup>	32	Left to equilibrate for 5 minutes
Gelucire /D <sub>2</sub> O	Heating method (see section 2.3.1)	Room temperature	2 cm <sup>-1</sup>	64	
		37 °C	2 cm <sup>-1</sup>	64	Left to equilibrate for 5 minutes
Gelucire /D <sub>2</sub> O	Hydration method (see section 2.3.1)	Room temperature	2 cm <sup>-1</sup>	64	

### 3.3.2 Small Angle X-Ray Scattering (SAXS)

The identification of the liquid crystalline phases of the gels was carried out using SAXS (S3-micro from Hecus X-ray Systems GmbH, Graz, Austria) with a point microfocus source GemixFox 3D (Xenoxs, Grenoble, France). A two-dimensional position sensitive detector with a sample-to-detector distance of 268 mm was used to detect the scattered X-rays. The experiments were performed using an X-ray source power of 50W (5kV, 1mA). The samples were loaded in a cell for pastes between two windows of kapton® (polyimide tape), which absorbs at  $4e^{-1}\text{Å}$  (or 700 number of channel) (Figure 3.1).

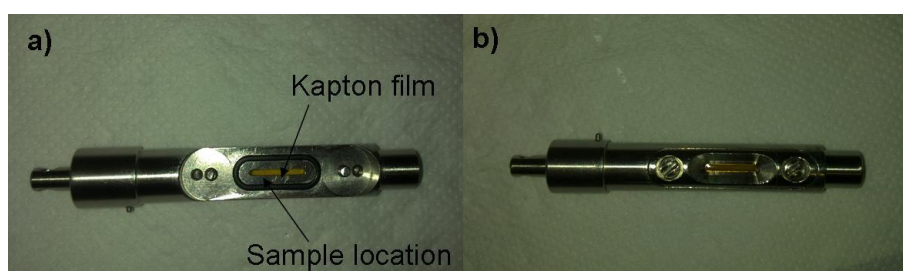


**Figure 3.1** (a) cell for pastes used to perform the experiments in this work open, the sample is spread in the central part (identified by the black ring) on the top of the kapton® polyimide tape (brown line). (b) View of the cell closed after having loaded the sample.

The gels were previously visualised with a polarised light microscope (PLM), by which the formation of lamellar or cubic phases could be hypothesised (data not shown). According to the results of the PLM studies, the gels with selected water contents prepared by heating and hydration methods (according to the procedure described in section 2.3.1) were analysed with SAXS. The details of the experimental conditions applied and the samples analysed are listed in Table 3.2.

**Table 3.2** Experimental details adopted for the gels with 10%, 40% and 60% water prepared by hydration and gel with 60% water prepared by heating. The tests were performed at 25 °C. The duration time of the test for each sample is also described.

<i>Samples (%, water content)</i>	<i>Preparation procedure</i>	<i>Temperature (°C)</i>	<i>Time (s)</i>
10	Hydration method	25	6112
40			4797
60			7200
60	Heating method	25	7200

In addition, the gels with 50% and 70% water contents prepared by heating and hydration methods were analysed in temperature ramp mode, as described in Table 3.3.

**Table 3.3** Temperature ramp performed on the gels with 50% and 70% water prepared by hydration and heating methods. The temperature and the duration time of the test (in seconds) per cycle are also listed.

<i>Samples (%, water content)</i>	<i>Preparation procedure</i>	<i>Temperature (°C)</i>	<i>Time (s)</i>	<i>Preparation procedure</i>	<i>Temperature (°C)</i>	<i>Time (s)</i>
50 and 70	Heating method (see section 2.3.1)	25	7200	Hydration method (see section 2.3.1)	25	3600
			25		3600	
		30	1800		25	3600
		25	3600		25	3600
		35	1800		25	3600
		30	3600		30	3600
		37	3600		37	3600
		37	3600		37	3600
		37	3600		37	3600
		35	600		37	3600
		35	3600		35	3600
		30	600		30	3600
		25	1800		25	3600
		25	1800		25	3600

### 3.3.3 Differential Scanning Calorimetry (DSC)

The phase transitions of the gels upon thermal treatment were studied by using a conventional DSC (Q series, TA Instruments, New Castle, USA). DSC tests were performed under nitrogen flux with purge rate of 50 ml/min. A full calibration was performed prior to the experiments. This consisted of performing the cell resistance and capacitance calibration (Tzero and baseline) with empty cells and sapphire disks, respectively. The temperature range of calibration was from -150 °C to 400 °C at 20 °C/min. Secondly, the enthalpy and temperature calibrations were performed. For the enthalpy calibration, indium standard was used having a  $T_m$  of 156.6 °C and heat of fusion of 28.6 J/g. Finally, a temperature calibration was performed using benzoic acid ( $T_m=123$  °C, heat of fusion of 147.3 J/g) and n-octadecane ( $T_m=28.2$  °C). The enthalpy and

temperature calibration were performed at the same temperature as planned for the sample analysis, which was 5 °C/min. Aluminium hermetic pans (Perkin Elmer, Massachusetts, USA) were used and the sample weights range between 2 and 5 mg. The samples were equilibrated at 20 °C for 2 minutes and heated up to 80 °C and then cooled down to 0 °C at 5°C/min. The gels with 10% water prepared by heating and by hydration methods underwent a different temperature programme: after equilibrating at 20 °C, it was heated to 80 °C, cooled down to 0 °C and re-heated to 80 °C, at the scanning rate of 5 °C/min. All experiments were performed in triplicate.

### **3.3.4 Rheological tests**

Rheological tests were used to obtain information on the viscoelastic properties of the gels. In particular, it was possible to determine whether the method of preparation can influence the rheological properties of the gels and how these properties change with applied stress, frequency and temperature.

The rheological tests were performed on the gels prepared by hydration and heating methods using a rheometer (AR 1000-N Rheolyst, TA Instruments, New Castle, USA) connected to a water bath. Plate-plate geometry was used for all the experiments. The diameter of the upper plate changed from 20 to 40 mm depending on the viscosity of the gels. The smaller the diameter, the larger the shear rate. Thus, the 20 mm plate was used for more viscous gels, (the gels with 10% and 20% water concentration) and the plate with 40 mm was used for the gels with medium to low viscosity. The gap between the upper and the lower plates was set at 1000 µm. The inertia of each geometry was calculated through the TA rheology software.

Rheological tests were performed on the gels prepared by heating over the water concentration from 10% to 80% and on the gels prepared by hydration method with water contents between 30% and 80% (w/w). The gels with 10% and 20% water contents prepared by hydration were not analysed because of difficulties in the sample preparation due to the high viscosity and lack of homogeneity. The gel with 90% water content was too liquid to be tested.

Three types of oscillatory tests were performed. The stress sweep test was used to assess the linear viscoelastic region (LVR), while the frequency sweep test was used to assess the change in the viscoelastic properties upon change in frequency. The temperature ramp test allows the determination of the viscoelastic change of the gels with the temperature. Flow tests were also performed. The theory behind these tests has been discussed in Chapter 2, sections 2.4.2.1 and

2.4.2.2. The details on the parameters and experimental conditions applied in this study are described in the following sections (3.3.4.1-3.3.4.4).

#### **3.3.4.1 Oscillatory stress sweep test**

The region where the complex modulus,  $|G^*|$ , and the phase angle,  $\delta$ , are not influenced by the applied stress is called linear viscoelastic region (LVR). Performing tests at a stress value within the LVR means that the structure of the system is not disrupted. The linear viscoelastic region was determined by an oscillation stress sweep test performed at 37 °C and at a constant frequency of 1 Hz with a stress value from 10 to 1000  $\mu\text{Nm}$ . Selected gels with water contents of 40%, 50% and 60% prepared by heating were also tested at 25 °C. The complex modulus  $|G^*|$  (Pa) and the phase angle,  $\delta$ , were plotted against the oscillatory stress (Pa) to identify the LVR for each gel. All samples tests were analysed at least in triplicate.

#### **3.3.4.2 Oscillatory frequency sweep test**

To determine the elastic and viscous behaviour of the samples oscillation frequency tests were performed at 37 °C in a range of frequency from 1 to 100 Hz at a fixed stress value chosen within the LVR. This fixed stress value varied with the samples. Selected gels with water contents of 40%, 50% and 60% prepared by heating were also tested at the temperature of 25 °C in the same frequency range (Hz). The elastic modulus ( $G'$ , Pa), the viscous modulus ( $G''$ , Pa), the loss tangent ( $\tan\delta$ ,  $G'/G''$ ) and the dynamic viscosity ( $\eta'$ , Pa.s) were plotted against the frequency (Hz). All samples were analysed at least in triplicate.

#### **3.3.4.3 Temperature ramp test**

Temperature ramp tests were also performed on the gels prepared by heating and by hydration methods. The gels were heated from 25 °C to 80 °C and cooled down to 25 °C at a scanning rate of 1 °C/min with a fixed frequency of 1 Hz. For each samples the stress applied was chosen within the LVR which was the same stress used for the frequency sweep test. The results show the change of the storage modulus ( $G'$ ) over the range of tested temperature.

#### **3.3.4.4 Continuous flow test**

Continuous flow tests were performed on the gels prepared by heating and by hydration methods, using parallel steel plate geometry (20 or 40 mm diameter and a gap distance between the plates of 1000  $\mu\text{m}$ ) over a range of different stress and at the selected temperatures of 25 °C, 37 °C, 50 °C and 80 °C. The stress grew over a period of 60 seconds. All samples were analysed

at least in triplicate and the curves were fitted with a power law equation (Equation 3.1, section 3.4.4.3).

### **3.3.5 Texture Analysis**

The mechanical properties of the gels prepared by both hydration and heating methods were analysed by using a texture analyser (TA-XTplus, Stable Micro System, Surrey, UK). Two kinds of tests were performed, the textural profile analysis (TPA) and the adhesion test which was performed to study the adhesive properties of the gels.

#### **3.3.5.1 Textural Profile Analysis (TPA)**

The TPA test can provide extensive information on the mechanical and textural properties of the gels. The vials were fixed on the lower plate of the Texture Analyser. A cylindrical Perspex probe (11.6 mm diameter) was lowered at 1 mm/s and compressed twice at the depth of 5 mm, and a delay period of 15 seconds was applied between the two compressions. The parameters analysed from the force-time plots were the adhesiveness, the hardness and the compressibility using the TPA macro supplied in the software Texture Exponent 32. The experiments were performed at least in triplicate.

#### **3.3.5.2 Adhesion test**

In this work, adhesive tests were performed on the Gelucire 50/13 gels prepared by heating and by hydration methods to assess the adhesive properties of the gels with mucin tablets and porcine small intestine tissues (internal lumen surface). Mucin tablets were prepared by compressing 300 mg of mucin powder (from porcine stomach, type II) with a manual hydraulic press (SPECAC, Orpington, UK) using a 13 mm die applying a force of 5 tons for 60 seconds. The tablets were attached to the cylindrical probe (Perspex, 11.6 mm diameter) of the texture analyser with a double-sided adhesive tape. The vials containing the gels, prepared following the same methods described in section 2.3.1, were fixed on the lower plate of the texture analyser. Prior the adhesion tests, the mucin tablets were submerged in a 5% mucin suspension in 0.1 M HCl solution for 30 seconds. Afterwards, the probe was lowered at the speed of 1 mm/s until they come into contact. The contact was held for 30 seconds applying a force equals to 10 g (0.1 N) [151]. The probe was moved up at a constant speed of 2 mm/s. From the force-distance plot, two parameters were determined the force maxima ( $F_{\max}$ ), which is the maximum force required to separate the mucin discs to the gels and the work of adhesion ( $W_{\text{ad}}$ ), which is the amount of forces involved in the detachment. Both values were calculated from the force-distance plots by using the software Texture Exponent 32.

Mucoadhesive tests with porcine small intestine tissues were carried following the same procedure described above. The small intestine tissues of about 5 cm were cut lengthwise and fixed to the perspex probe using rubber bands. The tissue was wrapped around the probe exposing the lumen part to the gels and ensuring to avoid the contact with the walls of the vials.

### **3.3.6 Statistical analysis**

The significant effect of the water content in the gels on the TPA parameters (compressibility, hardness and adhesiveness) was determined statistically using IBM SPSS statistics software 20.0. One-way ANOVA test was performed on the mechanical parameters calculated for the gels prepared by hydration. To perform this test, the data need to meet the requirement of homogeneity of variances that is the assumption according to which the variances of the populations are equal. This condition does not apply to any of the parameters, but considering that the experiments are a balanced design (i.e. the samples have the same size) the results from ANOVA test may be considered reliable. This is the case for the gels prepared by hydration since the number of repetitions was the same. On the contrary, the experiment conducted on the gels prepared by heating method was not a balanced design, since the number of repetitions for the gels with 20% and 30% water content differs from the repetitions used for the rest of the concentrations. Due to the non-balanced design, the ANOVA test cannot be reliably applied and a non-parametric test should be used. However, the data can be transformed (i.e in the logarithmic scale) and the homogeneity of the variances of the transformed data can be tested. In the case that the homogeneity is proved, the ANOVA test can be successfully performed. The logarithm of the compressibility and hardness values show homogeneity in variances, but the requirement was not met for the adhesiveness. Post-hoc comparisons of the means of the individual groups were performed using Scheffé test. The gels prepared by heating were analysed by performing a one-way ANOVA test on the data transformed into the logarithmic scale. Nevertheless, in order to further test the statistical significance of the results, non-parametric tests (Kruskal-Wallis), followed by Mann-Whitney U test with Bonferroni correction or by Dunn test, were performed.

The water content and the method of preparation may both affect the physical and mechanical properties of the gels. In order to test which of these two parameters has more significant impact on the resulting gels, two-way ANOVA was performed. A parameter obtained with the two-way ANOVA is the interaction. It can be stated that there is interaction between hypothetical two factors A and B (in this case water content and method of preparation) when the sample means depend on the factor A differently for different values of factor B, and viceversa. On the other

hand, there is no interaction if the samples means depend on factor A in the same way for all the values of factor B.

For both series of gels prepared by heating and hydration methods, the effect of the water content in the gels on the rheological parameters ( $G'$ ,  $G''$ ,  $\tan\delta$  and  $n'$ ) at fixed frequencies (1, 9.942, 25.13, 50.26 and 99.9 Hz) was investigated by performing a one-way ANOVA. Statistical analyses were also performed on the flow rheological parameters (consistency index,  $k$  and flow index,  $n$ ). In all cases, post-hoc comparisons of the means were performed using a Scheffé test and the significance of the statistical tests was denoted by the significance level of  $p < 0.05$  or  $p < 0.001$ . A correlation between the rheological and textural/mechanical parameters was investigated by using a Spearman's rho correlation test (see section 3.4.6), with significance level of  $p < 0.01$  or  $p < 0.05$ .

## 3.4 Results and Discussion

### 3.4.1 Structural analysis of gels with ATR-FTIR spectroscopy

The tests were performed on the gels with 10% to 90% (w/w) water content, prepared by heating and hydration methods with D<sub>2</sub>O. The ATR-FTIR studies were carried out in the mid-IR region, in which the spectrum extends between 4000 and 400 cm<sup>-1</sup> wavenumber. Generally, this region can be divided in four main regions: the X-H stretching region (4000-2500 cm<sup>-1</sup>), the triple bond region (2500-2000 cm<sup>-1</sup>), the double bond region (2000-1500 cm<sup>-1</sup>) and the fingerprint region (1500-600 cm<sup>-1</sup>) [193]. Since PEG and its esters are the major component in Gelucire 50/13, the IR spectra of the gels have been compared to the IR spectra of pure PEO or PEG from the literature.

The structure of the PEG and the conformation adopted by the chains has been discussed in Chapter 1, section 1.3.2. The most common conformation of PEG is the helical conformation. Its characteristic bands are the bands related to the rocking modes of the methylene groups of the sequence  $-\text{O}-\text{CH}_2-\text{CH}_2-\text{O}-$ . As demonstrated by previous works [109, 113, 214], these bands are 842 cm<sup>-1</sup>, 947 cm<sup>-1</sup>, 954 cm<sup>-1</sup>, 1061 cm<sup>-1</sup>, 1280 cm<sup>-1</sup>, and 1360 cm<sup>-1</sup>. A broad and intense band between 2800 and 3200 cm<sup>-1</sup>, centred at 2890 cm<sup>-1</sup>, can also be observed. This band is associated to the symmetric and asymmetric stretching of the methylene group [109]. A planar zig-zag conformation has an all-trans conformation and it is represented by bands at 837, 1337 or 1500 cm<sup>-1</sup>. More complicated structures with alternate trans and gauche conformations give strong band at 1012 cm<sup>-1</sup>, due to the stretching of the methylene moiety of the trans  $-\text{O}-\text{CH}_2-\text{CH}_2-\text{O}-$  sequence and a band at 1322 cm<sup>-1</sup> which is associated to the combination of rocking and stretching of the  $-\text{CH}_2-$  group [109].

Dry Gelucire 50/13 powder (the raw material used for preparing the gels) was analysed by using the ATR-FTIR spectroscopy. This information was used as reference later to compare with the spectra of the Gelucire gels. The peak assignments of the dry Gelucire spectrum are listed in Table 3.4. The PEG, MPEG and DPEG are the main components of Gelucire 50/13. In the IR spectrum, the bands related to the helical conformation of the PEG can be observed at  $842\text{ cm}^{-1}$ ,  $1061\text{ cm}^{-1}$ ,  $1280\text{ cm}^{-1}$ , and  $1359\text{ cm}^{-1}$  and they are in agreement with the literature values [109] (Figure 3.2).

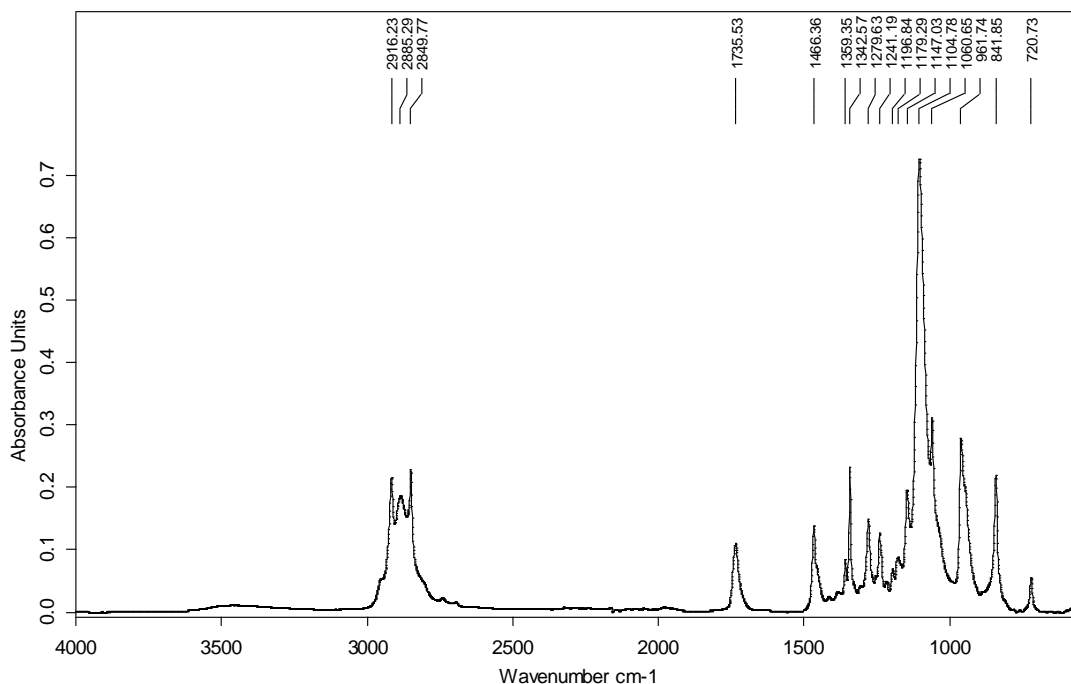


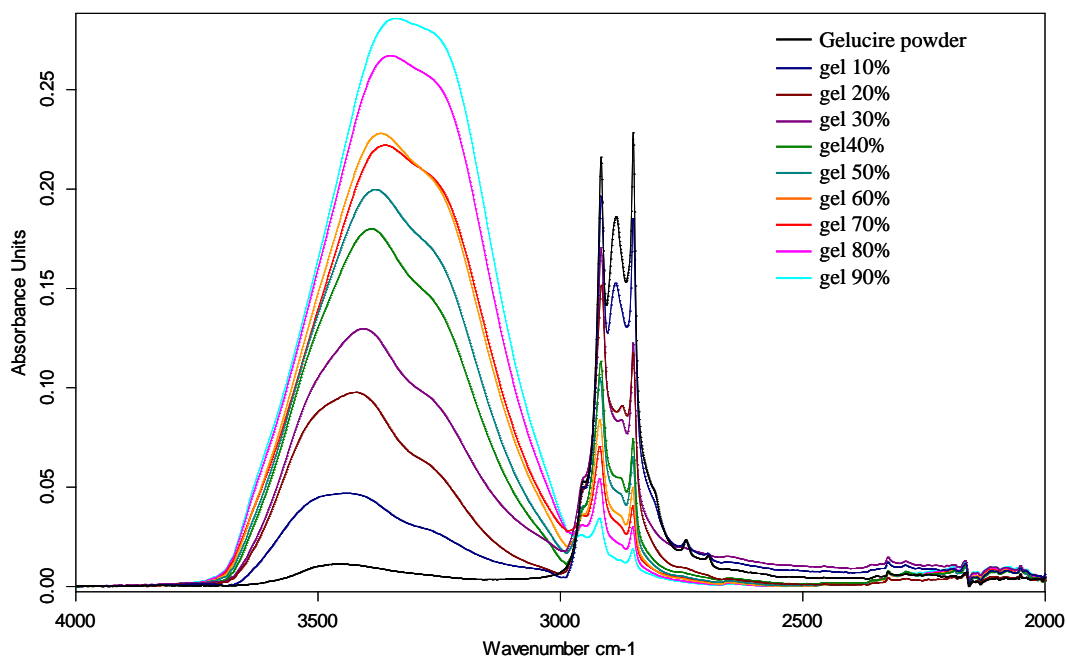
Figure 3.2 ATR-FTIR spectrum of dry Gelucire 50/13 powder (n=4).

**Table 3.4** IR band position and assignments for dry Gelucire 50/13 powder.

<i>Gelucire 50/13</i> Wavenumber ( $\text{cm}^{-1}$ )	<i>PEG [109, 214]</i> Wavenumber ( $\text{cm}^{-1}$ )	<i>Assignment</i>
2916		$\nu(\text{CH}_2)$ asymmetric
2885	2890	$\nu(\text{O-CH}_2)$ symmetric
2850		$\nu(\text{CH}_2)$ symmetric
	2735	
	2695	
1736		$\nu(\text{C=O})$
1466	1466	$\delta(\text{CH}_2)$ asymmetric
	1453	
1359	1359	$\omega(\text{CH}_2)$ symmetric
1343	1342	
1280	1283	$\tau(\text{CH}_2)$
1241	1240	$\tau(\text{CH}_2)$ asymmetric
1197		
1179		$\nu(\text{C-C}) + \nu(\text{C-O}) + \text{r}(\text{CH}_3)$
1147		$\nu(\text{C-C}) + \nu(\text{C-O}) + \text{r}(\text{CH}_3)$
1105		$\delta(\text{C-O-C})$ symmetric and asymmetric
1061	1061	$\delta(\text{C-O-C})$ asymmetric + $\text{r}(\text{CH}_2)$ symmetric
962	957	$\text{r}(\text{CH}_2)$ symmetric
842	842	$\text{r}(\text{CH}_2)$ asymmetric
721		$\text{r}(\text{CH}_2)$

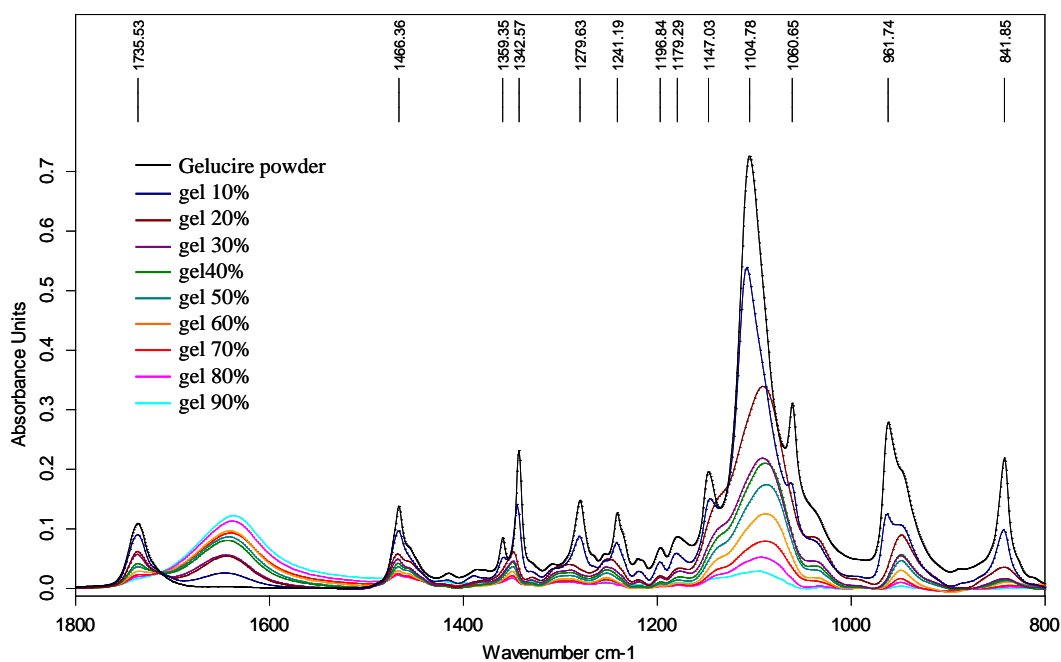
$\nu$ , vibrational band;  $\delta$ , stretching;  $\text{r}$ , bending;  $\omega$ , rocking;  $\tau$ , wagging

The PEG related peak, centred in  $2890 \text{ cm}^{-1}$ , splits into three poorly resolved peaks, at 2916, 2885 and  $2850 \text{ cm}^{-1}$  with moderate intensity. This characteristic is present in many PEG or PEO intercalated compounds [113]. It is often explained as the result of the interaction of the polymer with other compounds, such as glycerides in the case of Gelucire 50/13. In the Gelucire 50/13 spectrum (Figure 3.2), the peaks associated with the helical conformation of the free PEG ( $842, 1061, 1280, 1360 \text{ cm}^{-1}$ ) are clearly visible. The peaks associated with other conformations of the PEG reported in the literature are not present. This may suggest that PEG largely retains a helical conformation in the dry Gelucire 50/13. The peak at  $1736 \text{ cm}^{-1}$  can be assigned to the triacylglycerol ester carbonyl (C=O) stretching [193].



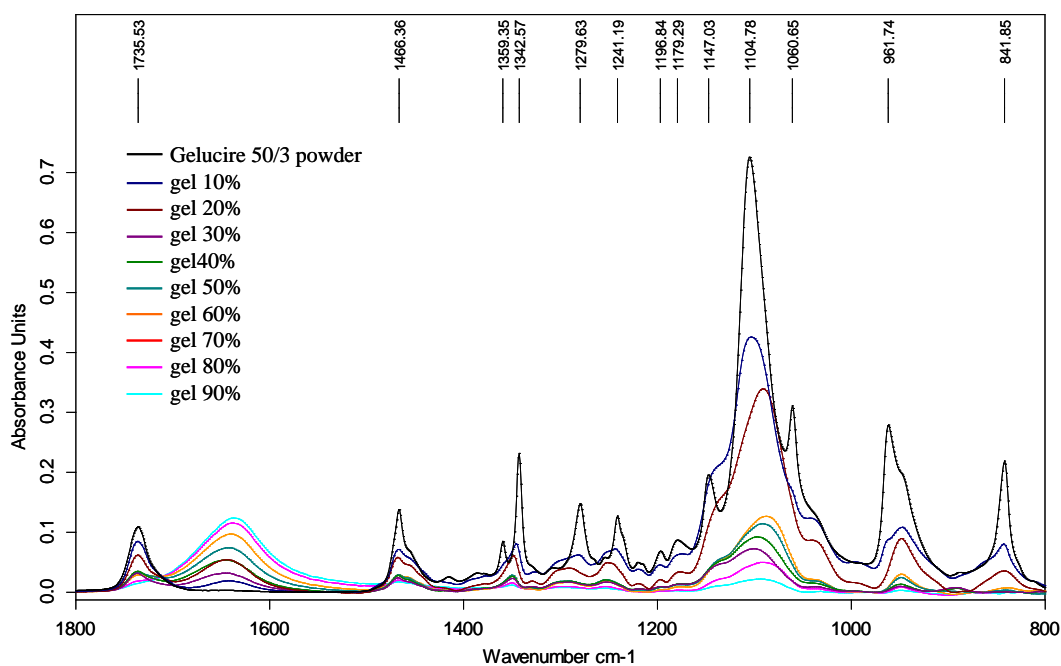
**Figure 3.3** Partial IR spectra in the region between 4000 and 2000  $\text{cm}^{-1}$  of the gels prepared with ultrapure water by using heating method (analysed at room temperature). The spectrum of the dry Gelucire 50/13 powder is also shown for comparison (black line).

The peak assignments of the full IR spectra of the gels prepared by hydration method and by heating method with ultrapure water (analysed at room temperature and at 37 °C) and  $\text{D}_2\text{O}$  are listed in Appendix I. Figure 3.3 shows the partial IR spectra of the gels prepared by heating with ultrapure water. The typical peak related to water is evident at  $\sim 3000 \text{ cm}^{-1}$ , which increases in intensity with increasing the water content in the gel formulation. As expected, the three peaks associated to the pure Gelucire 50/13, which are centred at 2916, 2885 and  $2850 \text{ cm}^{-1}$  wavenumber, decrease in intensity as the water content increase. However, the peak centred at  $2885 \text{ cm}^{-1}$  gradually diminished in the gels with water content above 10% (Figure 3.3).



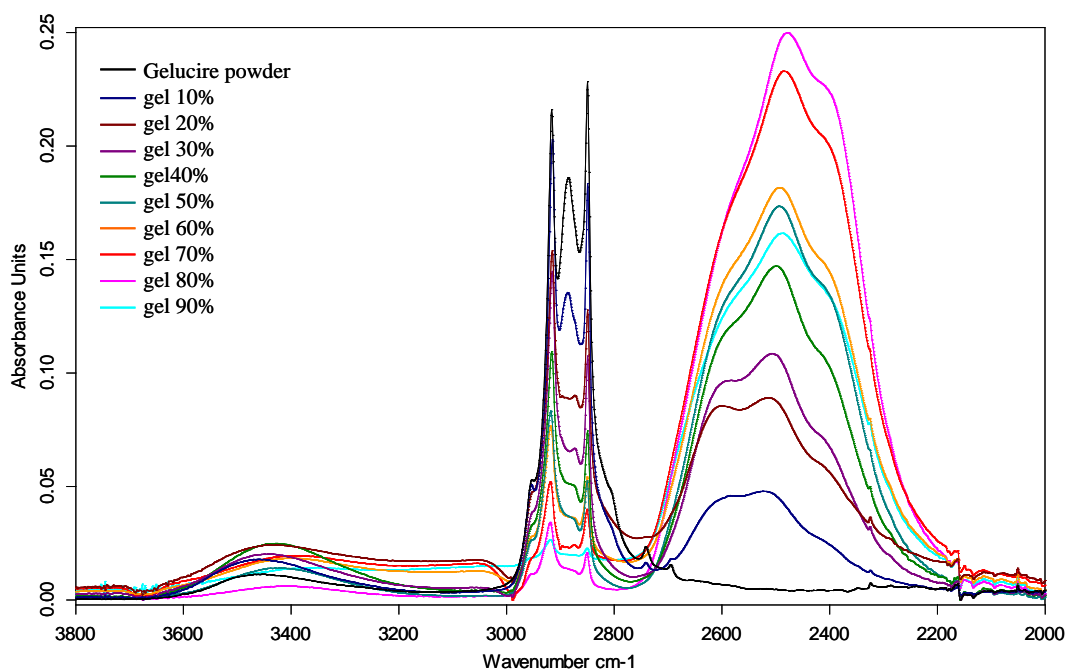
**Figure 3.4** Partial IR spectra between 1800 and 800  $\text{cm}^{-1}$  of the gels prepared with ultrapure water by using heating method, analysed at room temperature. The spectrum of the dry Gelucire 50/13 powder is also shown for comparison (black line).

Figure 3.4 shows the partial IR spectra of the gels in the IR region between 1800 and 800  $\text{cm}^{-1}$  obtained at room temperature. The peak centred at 1650  $\text{cm}^{-1}$  is associated with the O-H of the water. As it can be seen in the spectra, the gel with 10% water content retains the characteristic peaks of the pure Gelucire 50/13 within this wavenumber region, while some peaks tend to disappear in gels with higher water content. Two of the peaks associated with the helical conformation of the PEG (1061 and 1360  $\text{cm}^{-1}$ ) are not present in any concentration, while the peaks at 842 and 1280  $\text{cm}^{-1}$  disappear in gels above 60% water content (Figure 3.4). This may indicate that after hydration the free PEG lost part of its original structural conformation in the dry Gelucire.



**Figure 3.5** Partial IR spectra of the gels prepared with ultrapure water by using heating method, analysed at 37 °C between 1800 and 800  $\text{cm}^{-1}$ . The IR spectrum of Gelucire 50/13 powder is also shown for comparison (black line).

The two peaks at 842 and 1280  $\text{cm}^{-1}$  disappear upon heating to 37 °C (see Figure 3.5), which is consistent with the literature [109], which states that after 39 °C the melting of the PEG 1500 is observed. Even though the peak centred at 1280  $\text{cm}^{-1}$  is still present in the gels with 10%, it shifts towards higher values (1290  $\text{cm}^{-1}$ ) in the gels with 20%, 50% and 60% water contents, indicating the possible conformation changes in the PEG proportion of Gelucire in the gels. In general, as the water content increases, more conformational features of pure Gelucire 50/13 are lost in the IR spectra of the gels.



**Figure 3.6** Partial IR spectra ( $3800\text{-}2000\text{ cm}^{-1}$ ) of the gels prepared with  $\text{D}_2\text{O}$  by using heating method, analysed at room temperature. The Gelucire 50/13 powder is also shown for comparison (black line).

Figure 3.6 shows the IR spectra (in the region between  $3800$  and  $2000\text{ cm}^{-1}$ ) of gels prepared by heating method with  $\text{D}_2\text{O}$ . By using  $\text{D}_2\text{O}$ , the broad water peak at  $\sim 3500\text{ cm}^{-1}$  disappeared, but the rest of the spectra are similar to the ones collected from the gels prepared with  $\text{H}_2\text{O}$ . This indicates that the presence of  $\text{D}_2\text{O}$  does not affect the features of the gels. Overall, the gels retain the most typical features of the dry Gelucire 50/13. The peaks at  $2916$ ,  $2885$  and  $2850\text{ cm}^{-1}$  decrease in intensity as the water content increases. The peak centred at  $2885\text{ cm}^{-1}$  is still evident in the gel with 10%, but it disappears in the spectra of the gels with water content between 50-90%. For the gels with water content between 20-40%, a weak peak at lower wavenumber can be identified. The peak centred at  $\sim 2500\text{ cm}^{-1}$  is typical of the  $\text{D}_2\text{O}$ , and the peak intensity increases with the  $\text{D}_2\text{O}$  content, exception for the gel with 90% in which the peak is less intense (below the gel with 50% water content).

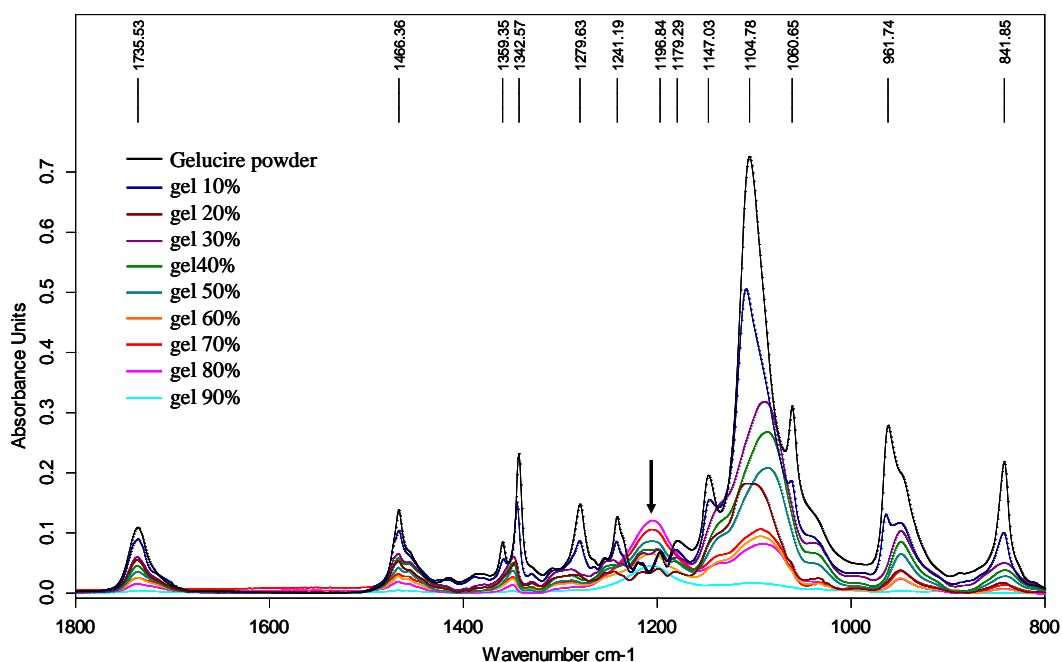


**Figure 3.7** Partial IR spectra of the gels prepared with D<sub>2</sub>O by using heating method, analysed at room temperature. The spectrum of the dry Gelucire 50/13 powder is also shown for comparison (black line). The arrow indicates the peak at 1205 cm<sup>-1</sup>.

As seen in Figure 3.7, in the 1800-800 cm<sup>-1</sup> region, some of the peaks associated with the helical conformation of the PEG are still present (842, 1280 cm<sup>-1</sup>), but not the peaks at 1061 and 1359 cm<sup>-1</sup>, which were seen in the spectrum of the dry Gelucire. The gels with lower water concentration (up to 40% water content) show a profile closer to the pure Gelucire 50/13. For gels with 50 to 90% water, the typical D<sub>2</sub>O peaks are more evident. For all gels, the main difference is visible in the peak centred at ~1200 cm<sup>-1</sup> (indicated with an arrow in Figure 3.7), which appears as a broad peak for the gels with 50% to 90% water content. This broad peak may be given by the merging of the two peaks at 1220 and 1197 cm<sup>-1</sup> which are visible in the spectra of the gels with and below 40% water content and in the dry Gelucire powder. For the gel with 90% water, much fewer peaks can be identified than other gels and the peak at 1205 cm<sup>-1</sup> is the most visible peak in this IR region (see Figure 3.7).

The gels prepared by hydration method with D<sub>2</sub>O were also studied. In the region between 1800 and 800 cm<sup>-1</sup>, the spectra look similar to the spectra of the gels prepared by heating. The peaks are less intense as the water content increases in the gels. The peak at 1205 cm<sup>-1</sup> is visible for the gels with and above 50% water content, while in the spectra of the gels with water content below 50% two peaks are identified at ~1220 and ~1197, (see Figure 3.8).

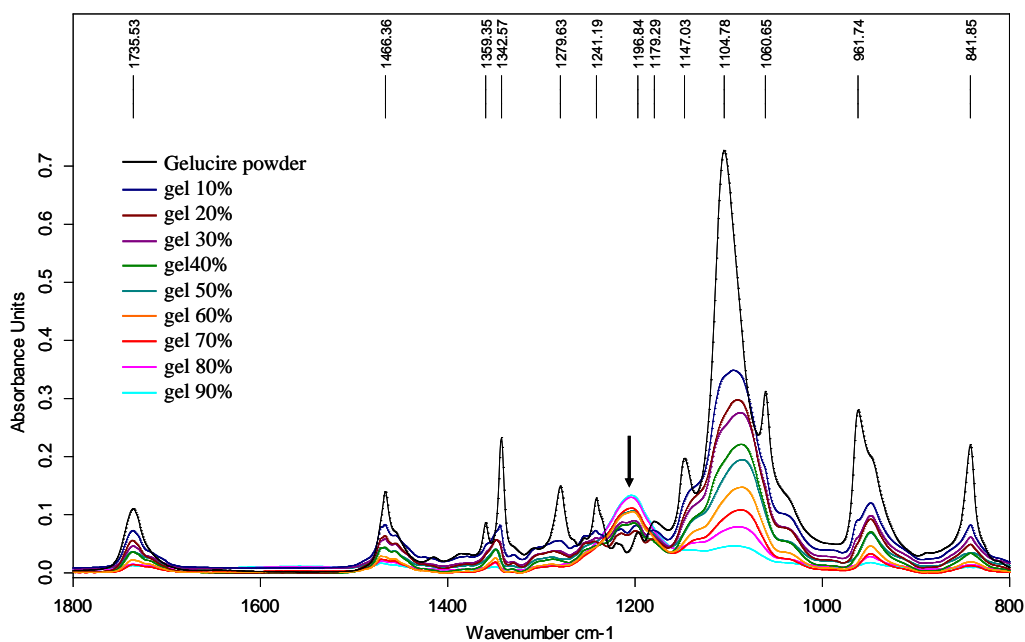


**Figure 3.8** Partial IR spectra of the gels prepared with D<sub>2</sub>O by using hydration method, analysed at room temperature. The spectrum of the dry Gelucire 50/13 powder is also shown for comparison (brown line). The arrow indicates the peak at 1205 cm<sup>-1</sup>.

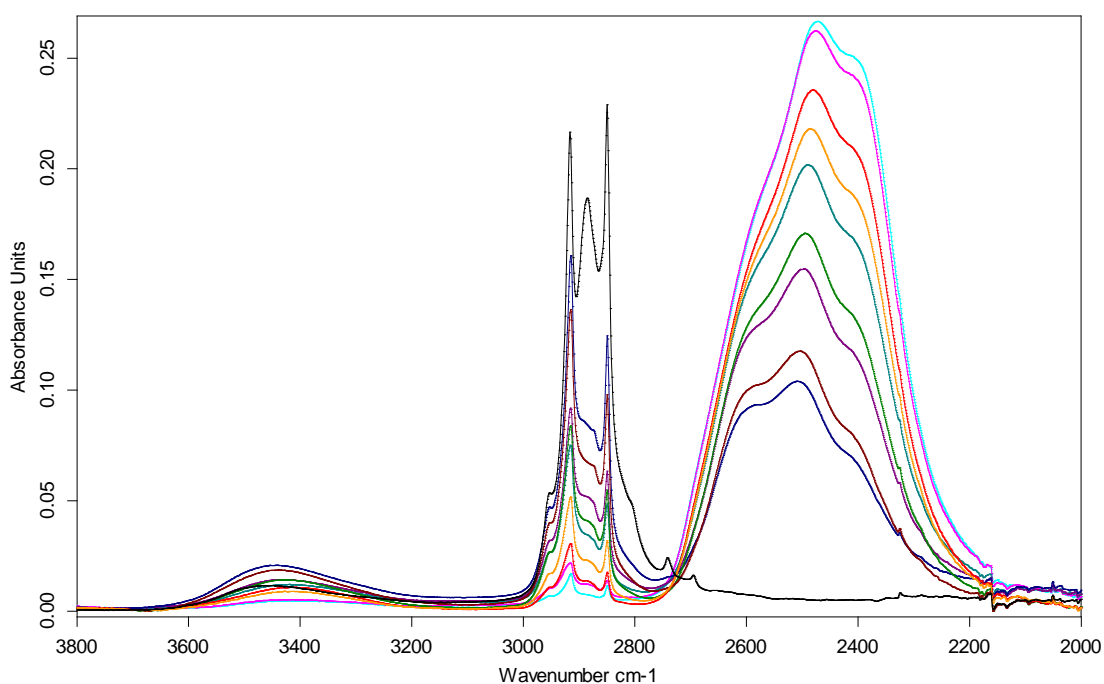


**Figure 3.9** IR spectra (3800-2000 cm<sup>-1</sup>) of the gels prepared with D<sub>2</sub>O by using hydration method. The Gelucire 50/13 powder is also shown for comparison (black line).

In the region between 3800 and 2000 cm<sup>-1</sup>, the gels prepared with D<sub>2</sub>O by hydration method show similar IR profiles to the gels prepared by heating method (Figure 3.9), exception for the

peak at  $2885\text{ cm}^{-1}$ , which is not visible in any of the gels. The peak centred at  $\sim 2500\text{ cm}^{-1}$  associated with  $\text{D}_2\text{O}$  increases with increasing the  $\text{D}_2\text{O}$  content in the gels.

In conclusion, the IR spectra showed the characteristic features of the gels. These results demonstrated that the gels retain the typical features of the dry Gelucire 50/13 powder, even though the peaks become less intense and some disappear with increasing the water content. Some changes in the peaks associated with the helical conformation of the free PEG in Gelucire can be seen in some gels. This suggests that the presence of water induced some changes in the structural conformation of the components of Gelucire 50/13. However, no significant difference was observed in the spectra prepared by different methods.

### 3.4.2 Structural analysis of the gels using SAXS

SAXS allows the characterisation of the nanostructure of the materials. In this study, the tests were performed at  $25\text{ }^\circ\text{C}$  on the gels with selected water contents prepared by hydration and by heating methods as described in Chapter 2, section 2.3.1. The gels with two water concentrations (50% and 70% w/w) were analysed by SAXS with a heat-cooling cycle. The gels were heated up to  $37\text{ }^\circ\text{C}$  and cooled down to  $25\text{ }^\circ\text{C}$ .

According to the literature, at  $20\text{ }^\circ\text{C}$  three lamellar phases were identified in untreated dry Gelucire 50/13 [109]. The first one has Bragg reflections in the positional ratio of 1:2:3, corresponding to  $q\text{ (}\text{\AA}^{-1}\text{)}$   $0.051\text{ }\text{\AA}^{-1}$ ,  $0.10\text{ }\text{\AA}^{-1}$  and  $0.152\text{ }\text{\AA}^{-1}$ . The second one has positional ratio equals to 1:2, corresponding to  $q\text{ (}\text{\AA}^{-1}\text{)}$  values at  $0.07\text{ }\text{\AA}^{-1}$  and  $0.14\text{ }\text{\AA}^{-1}$ . The third lamellar phase has value of  $0.127\text{ }\text{\AA}^{-1}$ . The existence of the first two lamellar phases depends on the thermal history of the Gelucire 50/13. Above  $35\text{ }^\circ\text{C}$ , the intensity and the position of the peaks change. The third phase shows no modification with changing temperature [109].

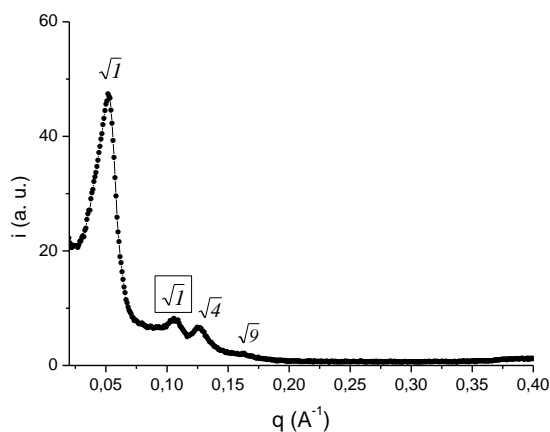


**Figure 3.10** SAXS spectrum of the intensity versus  $q\text{ (}\text{\AA}^{-1}\text{)}$  of the gel with 10% water prepared by hydration and corresponding peaks position ( $25\text{ }^\circ\text{C}$ ). The peak position framed corresponds to a second lamellar phase.

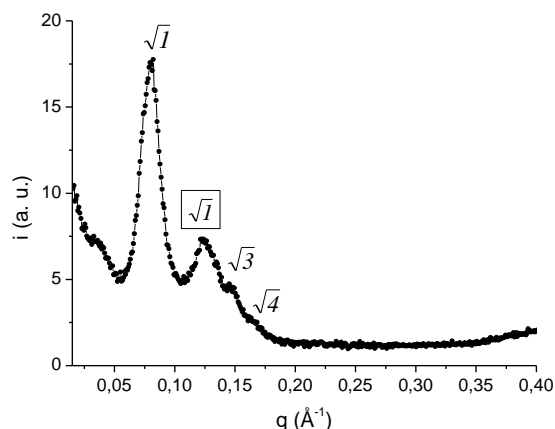


**Figure 3.11** SAXS spectrum of the intensity versus  $q$  ( $\text{\AA}^{-1}$ ) of the gel with 40% water prepared by hydration and corresponding peaks position (25 °C). The peak position framed corresponds to a second lamellar phase.

SAXS spectrum of the gels with 10% and 40% water contents prepared by hydration method are shown in Figure 3.10 and Figure 3.11. At 25 °C, the gel with 10% water prepared by hydration showed two lamellar phases at  $q$  ( $\text{\AA}^{-1}$ ) values similar to the untreated dry Gelucire 50/13 [109]. The first lamellar phase at positional ratio of 1:2 was observed at  $q$  ( $\text{\AA}^{-1}$ ) of 0.052  $\text{\AA}^{-1}$  and 0.106  $\text{\AA}^{-1}$  (corresponding to  $d$  ( $\text{\AA}^{-1}$ ) 121.5 and 59.3  $\text{\AA}$ , respectively). The second lamellar phase has a peak at 0.126  $\text{\AA}^{-1}$  (49.7  $\text{\AA}$ ). The gel with 40% water content shows the pattern of a hexagonal phase, with Bragg reflections at positional ratio of  $1:\sqrt{3}:\sqrt{4}$ , corresponding to the peaks at 0.080, 0.145 and 0.164  $\text{\AA}^{-1}$  (78.5, 44.6 and 38.5  $\text{\AA}$ , respectively). The peak at 0.125  $\text{\AA}^{-1}$  (50.3  $\text{\AA}$ ) was also observed. The SAXS spectrum of the gel with 60% water content is not as well resolved as the spectra of the gels with 10% and 40%. The peaks were identified at  $q$  values of 0.078, 0.111, 0.135 and 0.148  $\text{\AA}^{-1}$  (corresponding to 80.6, 56.3, 46.5 and 42.4  $\text{\AA}$ ) with a positional ratio of  $1:\sqrt{2}:\sqrt{3}:\sqrt{4}$ , which suggests a possible diamond cubic phase (Pn3m). However, apart from the first peak, the following three peaks are not well resolved. A further peak at 0.121  $\text{\AA}^{-1}$  (52.1  $\text{\AA}$ ) was also identified, which possibly corresponds to the third lamellar phase related to the glycerides components present in the Gelucire 50/13 as discussed in the literature [109] (Figure 3.12).

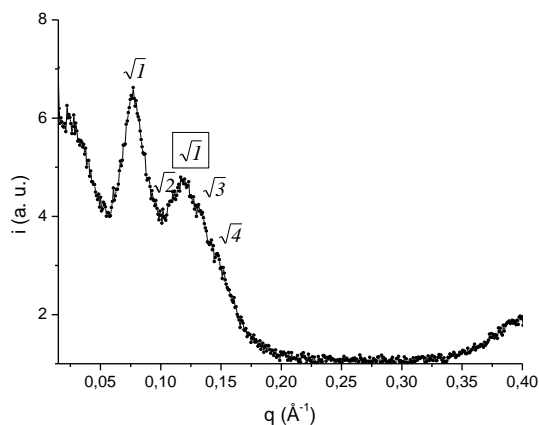


**Figure 3.12** SAXS spectrum of the intensity versus  $q$  ( $\text{\AA}^{-1}$ ) of the gel with 60% water prepared by hydration ( $25\text{ }^{\circ}\text{C}$ ) and corresponding peaks position. The peak position framed corresponds to a second lamellar phase.

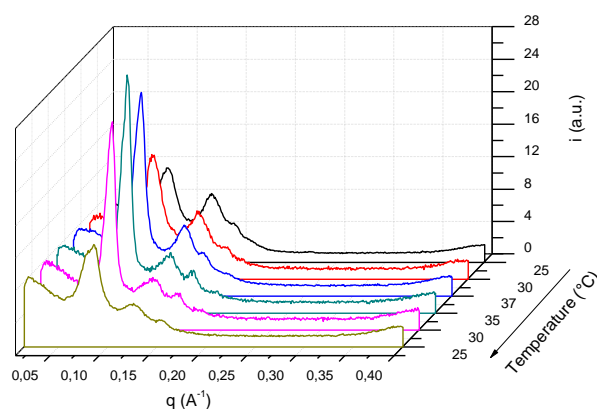


**Figure 3.13** Variable temperature SAXS spectra of the gel with 50% water content prepared by hydration upon heating from  $25\text{ }^{\circ}\text{C}$  to  $37\text{ }^{\circ}\text{C}$  and cooling back to  $25\text{ }^{\circ}\text{C}$  (indicated by the arrow).

Figure 3.13 shows the SAXS spectra of the gel with 50% water content prepared by hydration after heating up to  $37\text{ }^{\circ}\text{C}$  and cooling down to  $25\text{ }^{\circ}\text{C}$ . At  $25\text{ }^{\circ}\text{C}$ , the SAXS spectrum of the gel with 50% water content largely fits with a hexagonal phase with positional ratio equals to  $1:\sqrt{3}:\sqrt{4}$  with the peaks centred at  $q$  values of  $0.081$ ,  $0.145$  and  $0.160\text{ }^{\circ}\text{\AA}^{-1}$  ( $77.3$ ,  $43.3$  and  $39.3\text{ }^{\circ}\text{\AA}$ ). The third peak (at  $0.160\text{ }^{\circ}\text{\AA}^{-1}$ ) is a shoulder at room temperature, but it becomes more apparent as the temperature increased to  $37\text{ }^{\circ}\text{C}$ . This peak is still visible after cooling down to  $30\text{ }^{\circ}\text{C}$ . However, the intensity of the peak decreases when cooled back at  $25\text{ }^{\circ}\text{C}$ . A further peak at  $q\ 0.125\text{ }^{\circ}\text{\AA}^{-1}$  ( $50.4\text{ }^{\circ}\text{\AA}$ ) was also identified. With increasing the temperature, the peak at  $0.125\text{ }^{\circ}\text{\AA}^{-1}$  shifts towards higher  $q$  values, reaching the values of  $0.131\text{ }^{\circ}\text{\AA}^{-1}$  (corresponding to  $d$  value of  $47.85\text{ }^{\circ}\text{\AA}$ ) at  $37\text{ }^{\circ}\text{C}$ , which implies that a transition towards a different phase occurred. Cooled from  $37\text{ }^{\circ}\text{C}$  to  $25\text{ }^{\circ}\text{C}$ , the SAXS spectrum of the gel fits more with a diamond cubic phase (Pn3m) having a sequence of positional ratio equals to  $1:\sqrt{2}:\sqrt{3}:\sqrt{4}$ . This transformation

from hexagonal at room temperature to cubic after thermal treatment demonstrates the effect of thermal history on the microstructures of the gels.

The gel with 70% water content prepared by hydration showed two main peaks (Figure 3.14). From 25 °C to 30 °C, the peaks are centred at 0.11 and 0.14 Å<sup>-1</sup>, which may be related to the two different lamellar phases identified in the untreated dry Gelucire [109]. At 37 °C, these two peaks shifted to 0.08 and 0.115 Å<sup>-1</sup> are observed. In the cooling cycle (from 37 °C to 25 °C), the peaks identified are centred at 0.07 and 0.125 Å<sup>-1</sup>, which may still be related two lamellar phases observed before the thermal treatment. However, the complexity of the pattern indicates the lack of well-defined liquid crystalline phases. It is possible that there are mixed phases in this gel.

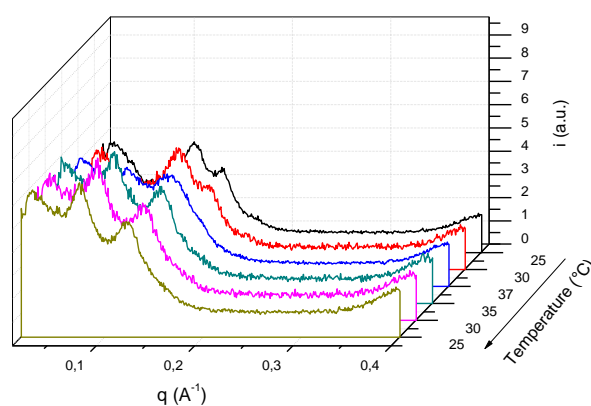


**Figure 3.14** Variable temperature SAXS spectra of the gel with 70% water prepared by hydration upon heating from 25 °C to 37 °C and cooling back to 25 °C (indicated by the arrow).

Temperature scan was also performed on the gels with 50% and 70% water contents prepared by heating. The SAXS spectra of the gel with 70% water content showed two peaks in the heating cycle from 25 °C to 37 °C, but no particular phase could be identified. In the cooling cycle, the peaks disappeared (data not shown). Therefore the exact assignment of the liquid crystalline of the gel with 70% is inconclusive. The gel with 50% water showed a better defined structure which can be approximately be assigned as cubic (Table 3.5). Although at 25 °C, the peaks do not fit exactly as cubic, they showed the ratio of a diamond cubic phase (Pn3m) which is  $1 : \sqrt{2} : \sqrt{3} : \sqrt{4} : \sqrt{6}$ , at 37 °C. After cooling down to 35 °C a further peak appeared with the positional ratio with a sequence of  $1 : \sqrt{2} : \sqrt{3} : \sqrt{4} : \sqrt{6} : \sqrt{8}$ . At 30 °C and 25 °C (in the cooling cycle), the peaks at 42.1 and 36.8 Å disappear, but the phase can still be approximately assigned as diamond cubic. The assignment on the peaks is listed in Table 3.5. The gel with 60% water content prepared by heating method and analysed at 25 °C showed two main peaks at 0.058 and 0.105 Å<sup>-1</sup> (107.8 and 59.8 Å), which cannot be associated to any known liquid crystalline phase.

This may be explained by two possibilities (1) the method of preparation, which results in an uneven mixing of Gelucire with water and (2) due to the gel being a mixture of different liquid crystalline phases.

**Table 3.5** Assignment of the peaks for the gel with 50% water prepared by heating method analysed with varying the temperature. The  $q$  ( $\text{\AA}^{-1}$ ) and  $d$  ( $\text{\AA}$ ) values as well as the peak positioning at Bragg values are listed.

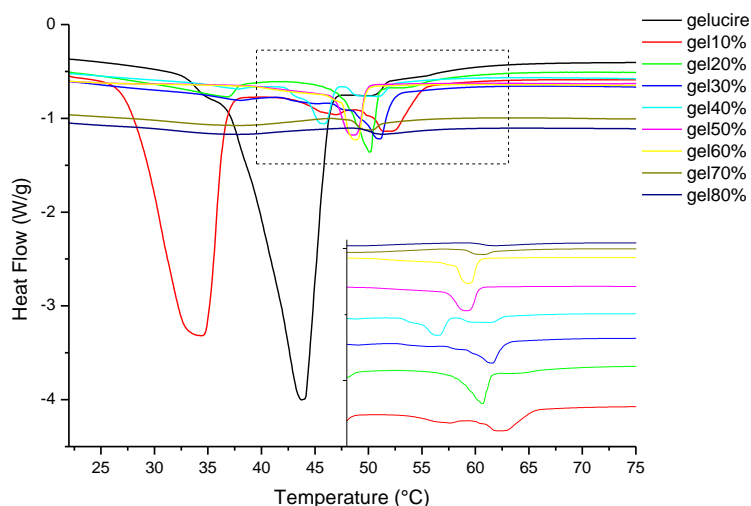
<i>Temperature</i>	$q(\text{\AA}^{-1})$	$d(\text{\AA})$	<i>Bragg's positional ratio</i>	
25°C	5.83x10 <sup>-2</sup>	<b>107.80</b>	<b>1</b>	1
	7.72x10 <sup>-2</sup>	<b>82.3</b>	<b>1.31</b>	
	1.12x10 <sup>-1</sup>	<b>55.88</b>	<b>1.93</b>	$\sqrt{4}$
	1.30x10 <sup>-1</sup>	<b>48.45</b>	<b>2.22</b>	$\sqrt{5}$
30°C	5.83x10 <sup>-2</sup>	<b>107.8</b>	<b>1</b>	1
	7.96x10 <sup>-2</sup>	<b>78.91</b>	<b>1.37</b>	$\sim\sqrt{2}$
	1.16x10 <sup>-1</sup>	<b>54.29</b>	<b>1.99</b>	$\sqrt{4}$
	1.35x10 <sup>-1</sup>	<b>46.68</b>	<b>2.31</b>	$\sim\sqrt{5}$
35°C	6.08x10 <sup>-2</sup>	<b>103.4</b>	<b>1</b>	1
	8.04x10 <sup>-2</sup>	<b>78.1</b>	<b>1.32</b>	$\sim\sqrt{2}$
	1.21x10 <sup>-1</sup>	<b>51.73</b>	<b>2</b>	$\sqrt{4}$
37°C	6.08x10 <sup>-2</sup>	<b>103.43</b>	<b>1</b>	1
	8.37x10 <sup>-2</sup>	<b>75.04</b>	<b>1.38</b>	$\sim\sqrt{2}$
	1.24x10 <sup>-1</sup>	<b>50.70</b>	<b>2.04</b>	$\sqrt{4}$
	1.48x10 <sup>-1</sup>	<b>42.54</b>	<b>2.43</b>	$\sqrt{6}$
35°C	6.08x10 <sup>-2</sup>	<b>103.43</b>	<b>1</b>	1
	8.46x10 <sup>-2</sup>	<b>74.31</b>	<b>1.39</b>	$\sqrt{2}$
	1.04x10 <sup>-1</sup>	<b>60.27</b>	<b>1.72</b>	$\sqrt{3}$
	1.21x10 <sup>-1</sup>	<b>51.73</b>	<b>2</b>	$\sqrt{4}$
	1.49x10 <sup>-1</sup>	<b>42.07</b>	<b>2.46</b>	$\sqrt{6}$
	1.71x10 <sup>-1</sup>	<b>36.82</b>	<b>2.81</b>	$\sqrt{8}$
30°C	5.99x10 <sup>-2</sup>	<b>104.8</b>	<b>1</b>	1
	8.46x10 <sup>-2</sup>	<b>74.31</b>	<b>1.41</b>	$\sqrt{2}$
	1.10x10 <sup>-1</sup>	<b>57.13</b>	<b>1.83</b>	$\sqrt{3}$
	1.22x10 <sup>-1</sup>	<b>51.38</b>	<b>2.04</b>	$\sqrt{4}$
25°C	5.75x10 <sup>-2</sup>	<b>109.3</b>	<b>1</b>	1
	8.37x10 <sup>-2</sup>	<b>75.0</b>	<b>1.46</b>	$\sqrt{2}$
	1.19x10 <sup>-1</sup>	<b>52.8</b>	<b>2.07</b>	$\sqrt{3}$
	1.39x10 <sup>-1</sup>	<b>45.3</b>	<b>2.41</b>	$\sqrt{4}$

### 3.4.3 Thermal phase transition of the gels

It has been previously reported by Brubach et al. [109] that the thermal treatment of the untreated dry Gelucire 50/13 can induce structural changes of the material. However, there is no knowledge on how the structure of the hydrated Gelucire 50/13 gels may change with temperature. Following the temperature scan SAXS experiments on the gels with 50% and 70% water content (heated up to 37 °C and cooled back to 25 °C), indications on phase changes with varying temperature were obtained. The ATR-FTIR spectra suggest a change in some features of the gels when heated up to 37 °C (see section 3.4.1). In this part of the study, DSC and temperature ramp rheometer were used to obtain a better understanding of the thermal behaviour of the gels upon thermal treatment. DSC allows the determination of the thermally related phase transitions, while the rheometer studies the change of the viscoelastic properties of the gels upon thermal treatment.

#### 3.4.3.1 DSC Thermal analysis

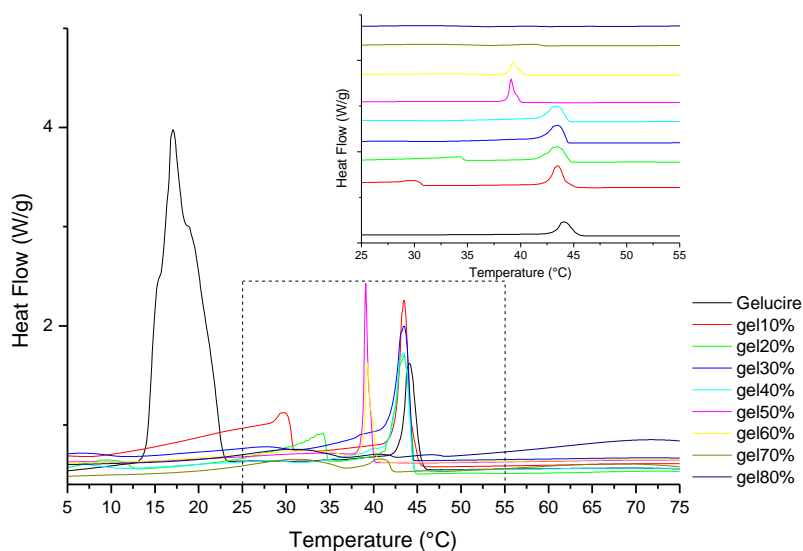
Phase transitions of the gels prepared by heating and by hydration methods with changing temperature were first investigated using DSC. The gels were treated with the same thermal programme, as described in section 3.3.3. An overview of the DSC detected phase transitions of the Gelucire 50/13 powder and of the gels prepared by heating is shown in Figure 3.15. The untreated dry Gelucire 50/13 was presented for comparison.



**Figure 3.15** DSC results of the gels prepared by heating method upon heating from 20 to 80°C. The inset shows an enlarged view of the boxed region (dashed rectangle) between 37 and 65 °C.

For the dry Gelucire 50/13, a main peak at 43.5 °C followed by a shoulder peak at 49 °C can be observed. All gels show a main endothermic transition in the same temperature range (43-51 °C). The gel with 10% water content shows a different profile from the other gels. The main

transition of this gel is at 33 °C, which is lower than the other gels and the dry Gelucire 50/13 powder. However, it also shows two small endothermic peaks at higher temperatures, 47 and 52 °C. The gel with 20% water content shows two endothermic transitions at 36 °C and 50 °C. Similar transitions are visible in the gel with 30% water (38 °C and 51 °C). The gel with 40% water content shows three endothermic transitions at 38 °C, 46 °C and 50 °C. The one at 46 °C is the main transition. In the gels with 50% and 60% water content, one main endothermic transition at 49 °C is recorded. A shoulder appears in the gel with 60% water content at lower temperature (at about 42 °C). In the gels with 70% and 80% water content, two endothermic transitions are observed at 37 °C for both and at 50-51 °C. No peak was detected for the gel with 90% water content. It is noted that the enthalpy values of the main peaks observed in the gels is much smaller, proportional-wise, in comparison to the main melting transition of the dry Gelucire 50/13. For example, the enthalpy of the endothermic peaks sharply drops from 62.30 J/g (which is less than half of enthalpy value of the main melting peaks of the dry Gelucire) for the gel with 10% water content to 16.12 J/g for the gel with 20%, and it continues to decrease with increasing the water contents. Therefore, it is reasonable to suggest that these transitions observed in the gels are more likely to be associated with liquid crystalline phase transitions than the melting of undissolved lipid in the gels.



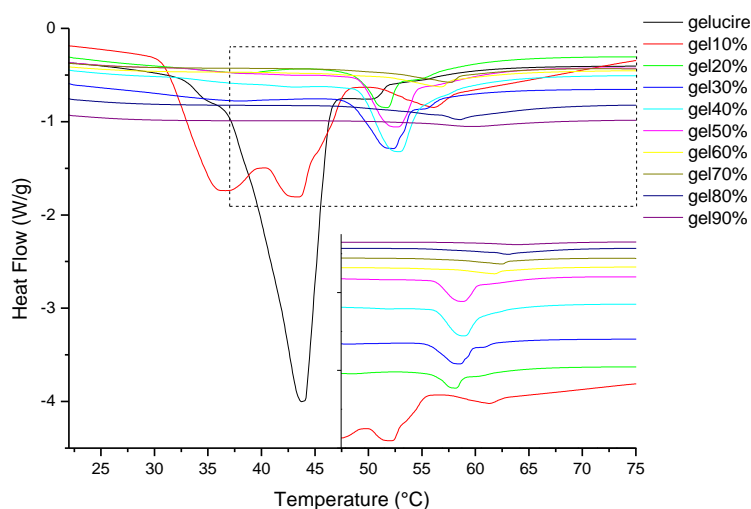
**Figure 3.16** DSC results of the gels prepared by heating method upon cooling from 80 to 0°C. The inset shows an enlarged view of the boxed region (dashed rectangle) between 25 and 55 °C.

Figure 3.16 shows the DSC profiles of the gels prepared by heating during the cooling cycle from 80 to 0 °C. The result of the dry Gelucire 50/13 is shown for comparison. For the dry Gelucire 50/13, two transitions occur at 17 °C and 44 °C. As seen in Figure 3.16, all gels show similar DSC profile during cooling. A main transition is visible in all gels between 39 °C and 44 °C and a second peak is also visible at ~30 °C, except for the gel with 50% water content in

which the second peak is not present. However, the second transition at  $\sim 30$  °C is a shoulder peak for the gels with water content at and above 30%. The enthalpy values of the exothermic peaks for gels with 10% to 40% water content are relatively close to the enthalpy value of the peak at 44 °C of the dry Gelucire powder. However, it decreases significantly with increasing the water content for the gels with 50% to 80% water content. The enthalpy of the main peak of the untreated dry Gelucire at 17 °C is much higher (92.62 J/g). This main exothermic peak may be associated to the polymorphic transitions of the glycerides components. The absence of this peak in the gels indicates that no undissolved lipid is present. Therefore, the transitions are likely to be due to the liquid crystalline phases. The onset temperatures ( $T_h$  or  $T_c$ , which stands for the temperature of the heating and the cooling cycle, respectively), the peak temperatures ( $T_p$ ) and the enthalpy values of the peaks ( $\Delta H$ ) for the transitions of the main peaks in the heating and cooling cycles were determined and summarised in Table 3.6.

**Table 3.6** Mean of the onset temperature ( $T_h$ ), the peak temperature ( $T_p$ ) and the enthalpy of the main peak ( $\Delta H$ )  $\pm$ SD of the samples prepared by heating determined in a heating and cooling cycle (n=3).

% Water	Heating			Cooling		
	$T_h$ (°C)	$T_p$ (°C)	$\Delta H$ (J/g)	$T_c$ (°C)	$T_p$ (°C)	$\Delta H$ (J/g)
0%	38 $\pm$ 0.4	44 $\pm$ 0.1	128.1 $\pm$ 1.40	45 $\pm$ 0.1	44 $\pm$ 0.1	9.73 $\pm$ 0.34
10%	28 $\pm$ 0.4	33 $\pm$ 0.6	62.30 $\pm$ 1.09	45 $\pm$ 0.1	43 $\pm$ 0.0	8.71 $\pm$ 0.20
20%	47 $\pm$ 0.6	50 $\pm$ 0.3	12.14 $\pm$ 1.39	45 $\pm$ 0.4	45 $\pm$ 0.4	8.53 $\pm$ 1.26
30%	48 $\pm$ 0.4	51 $\pm$ 0.3	5.60 $\pm$ 0.66	44 $\pm$ 0.1	44 $\pm$ 0.0	9.77 $\pm$ 0.26
40%	44 $\pm$ 0.5	46 $\pm$ 0.4	8.46 $\pm$ 0.67	45 $\pm$ 0.0	44 $\pm$ 0.2	9.61 $\pm$ 0.58
50%	47 $\pm$ 0.8	49 $\pm$ 0.8	5.54 $\pm$ 1.76	39 $\pm$ 0.5	39 $\pm$ 0.5	6.04 $\pm$ 1.39
60%	48 $\pm$ 0.7	51 $\pm$ 0.6	2.98 $\pm$ 1.50	41 $\pm$ 0.8	40 $\pm$ 0.7	2.86 $\pm$ 1.06
70%	49 $\pm$ 0.0	50 $\pm$ 0.1	1.00 $\pm$ 0.11	42 $\pm$ 0.1	41 $\pm$ 0.5	0.49 $\pm$ 0.25
80%	50 $\pm$ 0.1	51 $\pm$ 0.1	0.55 $\pm$ 0.25	43 $\pm$ 0.2	41 $\pm$ 0.8	0.45 $\pm$ 0.31



**Figure 3.17** DSC results of the gels prepared by hydration method upon heating from 20 to 80°C. The inset shows the enlarged view of the boxed region (dashed rectangle) between 37 and 75 °C.

Figure 3.17 shows the thermograms of the heating cycles of the gels prepared by hydration method, which are slightly different (in terms of the peak temperature and shape) from the DSC results of the gels prepared by heating method. The gel with 10% water content shows a different thermal profile compared to the other gels. A joint peak with two peak temperatures at 35 °C and 43 °C can be observed. A third peak at a higher temperature is also found (55 °C). For the gels with 20%, 30% and 40% water, two transitions are observed, a main one at 52 °C and a shoulder at lower temperatures ~37 °C. The shoulder peak becomes less apparent as the water increases. For the gels with water content at and above 50%, only one main endothermic transition is observed between 53 °C to 60°C.

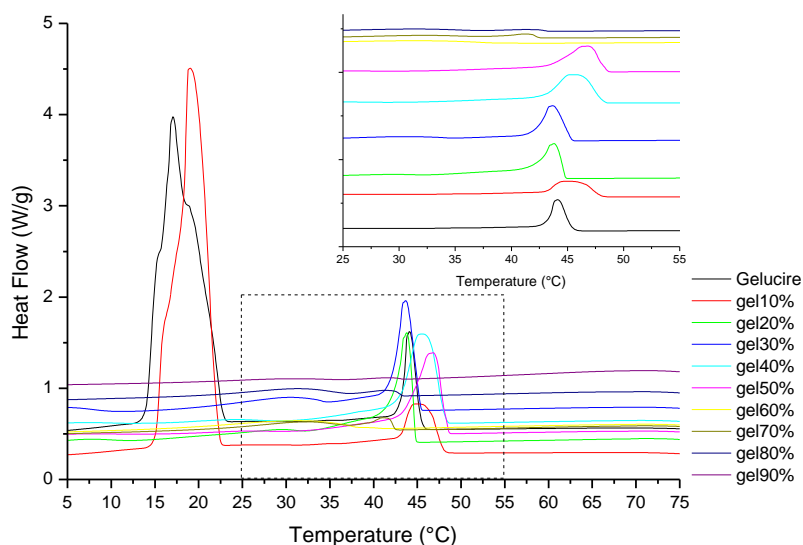


**Figure 3.18** DSC results of the gels prepared by hydration method upon cooling back from 80 to 0°C. The inset shows an enlarged view of the boxed region (dashed rectangle) between 25 and 55 °C.

In the cooling cycle, one main exothermic peak is observed in all gels prepared by hydration, except for the gel with 10% water, in which two peaks can be distinguished at 46 °C and 17 °C. The thermogram of the gel with 10% water is very similar to the one of the dry Gelucire 50/13 powder, this may be attributed to the uneven mixing of Gelucire 50/13 with water in the preparation by hydration. Concerning the gels with 20% to 50% water contents, one exothermic peak around 44 °C is observed. In the gel with 60% water content, a small broad peak is found at 31 °C. In the gels with 70% and 80% water content, a main exothermic transition at 41 and 42 °C, respectively, is found, followed by a shoulder at lower temperature. No peaks are observed for the gel with 90% water content. Again due to the similar reason (enthalpy values) explained for the gels prepared by heating method, the transitions observed in the gels are likely to the liquid crystalline phases. The transitions observed in the gels may be due to the liquid crystalline phases. The onset temperature ( $T_h$  or  $T_c$ , which stands for the temperature of the

heating and the cooling cycle, respectively), the peak temperature ( $T_p$ ) and the enthalpy of the peak ( $\Delta H$ ) for the main transitions are summarised in Table 3.7.

**Table 3.7** Mean of the onset temperature ( $T_h$ ), the peak temperature ( $T_p$ ) and the enthalpy of the main peak ( $\Delta H$ )  $\pm$ SD of the samples prepared by hydration determined in a heating and cooling cycle (n=3).

% Water	Heating			Cooling					
	$T_h$ ( $^{\circ}$ C)	$T_p$ ( $^{\circ}$ C)	$\Delta H$ (J/g)	$T_c$ ( $^{\circ}$ C)		$T_p$ ( $^{\circ}$ C)		$\Delta H$ (J/g)	
				Peak 1	Peak 2	Peak 1	Peak 2	Peak 1	Peak 2
10	30 $\pm$ 1.55	35 $\pm$ 1.74	61.31 $\pm$ 31.60	46 $\pm$ 0.77	20 $\pm$ 3.38	46 $\pm$ 0.25	17 $\pm$ 3.01	7.69 $\pm$ 0.49	73.44 $\pm$ 3.96
20	49 $\pm$ 0.54	52 $\pm$ 0.17	10.75 $\pm$ 3.54	45 $\pm$ 0.18		44 $\pm$ 0.18		12.99 $\pm$ 2.77	
30	49 $\pm$ 0.34	52 $\pm$ 0.61	5.64 $\pm$ 3.90	45 $\pm$ 0.45		44 $\pm$ 0.20		12.08 $\pm$ 1.30	
40	49 $\pm$ 0.51	52 $\pm$ 1.25	9.32 $\pm$ 6.21	46 $\pm$ 1.91		44 $\pm$ 1.17		10.56 $\pm$ 7.92	
50	50 $\pm$ 0.95	53 $\pm$ 0.51	11.35 $\pm$ 4.93	46 $\pm$ 4.45		44 $\pm$ 4.13		10.31 $\pm$ 9.97	
60	51 $\pm$ 0.58	57 $\pm$ 0.28	5.24 $\pm$ 0.48	38 $\pm$ 0.45		31 $\pm$ 0.14		5.52 $\pm$ 1.22	
70	52 $\pm$ 0.79	58 $\pm$ 0.52	5.19 $\pm$ 0.74	43 $\pm$ 0.23	37 $\pm$ 0.06	41 $\pm$ 0.28	31 $\pm$ 0.05	0.94 $\pm$ 0.65	3.25 $\pm$ 0.31
80	53 $\pm$ 1.72	59 $\pm$ 0.20	3.72 $\pm$ 0.79	43 $\pm$ 0.09	36 $\pm$ 0.34	42 $\pm$ 0.13	31 $\pm$ 0.16	0.34 $\pm$ 0.18	1.70 $\pm$ 0.55
90	53 $\pm$ 1.02	60 $\pm$ 0.34	2.40 $\pm$ 1.72						

The gel with 10% water content prepared by heating showed a different behaviour from the rest of the gels and from the Gelucire powder, though the one prepared by hydration has a more similar profile to the powder profile (especially in the cooling cycle). To better detect its behaviour a heat-cool-reheat cycle was performed, from 20 $^{\circ}$ C to 80 $^{\circ}$ C, cool back to 0 $^{\circ}$ C and heat again to 80 $^{\circ}$ C. For the gel with 10% water content prepared by heating, the peak temperature of the second heating cycle identify three main transitions at 32  $^{\circ}$ C, 37  $^{\circ}$ C and 45  $^{\circ}$ C (Figure 3.19). The gel with 10% water content prepared by hydration showed the same three transitions in the second heating cycle (33  $^{\circ}$ , 38  $^{\circ}$ C and 45  $^{\circ}$ C). It is likely that the gels were more homogeneously mixed after the first heating-cooling cycle (in the DSC pans). Therefore the DSC results of the re-heating cycle are very similar for the 10% gels prepared by different methods.

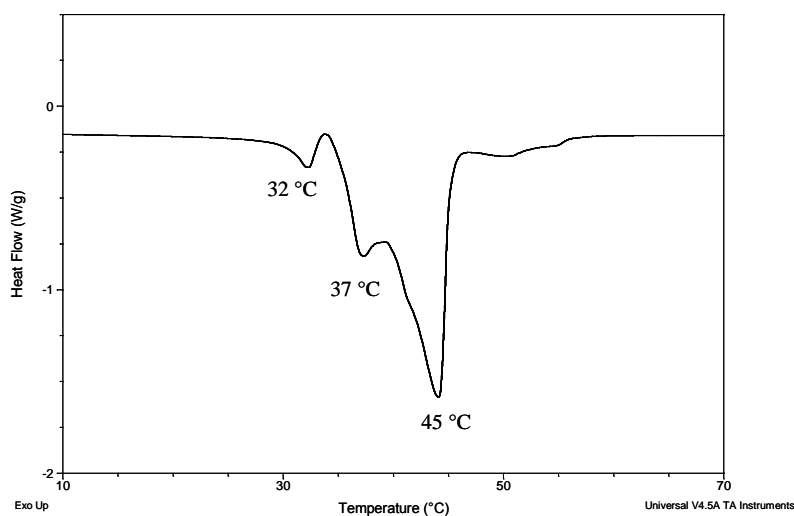


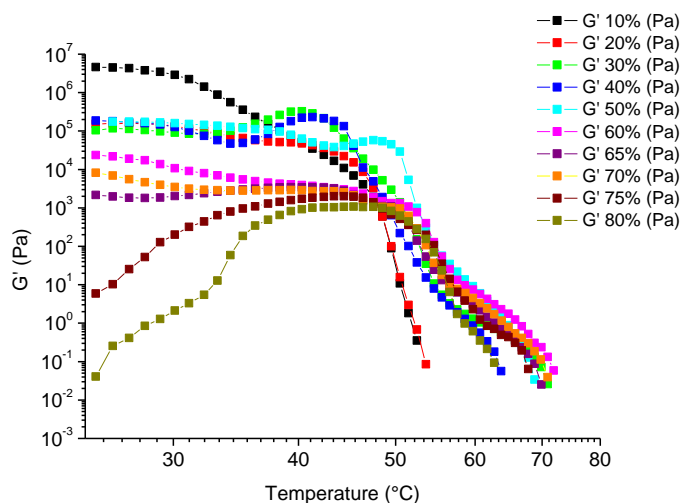
**Figure 3.19** DSC results of the second heating cycle of the gel with 10% water content prepared by heating method.

This behaviour may be due to the formation of intermediate phase as a consequence of the second fusion of the sample. This can be related to the structural/polymorphic changes of MPEG and DPEG hydrocarbon chains, which undergo structural modifications due to the tilt of the chains regarding the long and short side of the subcells. Brubach et al. [109] correlated the formation of different lamellar phases with temperature for dry Gelucire 50/13. Several lamellar phases have been identified for the MPEG and DPEG chains according to the thermal history and the crystallisation rate. The phases have long spacing of 90 Å, 94 Å, 100 Å, 105 Å, 120 Å and the transitions occurred at 30 °C, 35 °C and about 40 °C. At 35 °C, three lamellar phases (94 Å, 99 Å, 105 Å) coexist. The formation of different mesophases was observed only after the second heating cycle, while after the first cycle one transition was observed from the 90 Å to 120 Å lamellar phase and no intermediate phases were identified [109]. A comparison with the rheological technique will be discussed in the next section (3.4.3.2).

The DSC results of the gels prepared by both heating and hydration methods show little differences in transition temperatures and peak shapes during heating and cooling. The transitions observed for both set of gels within the heating cycle are likely to be related to the liquid crystalline phase transitions of the gels. The little difference in their thermal behaviour is likely to be a result of the preparation methods, which give slightly different structures of the gels. However, the effect of such little difference on the viscoelastic properties of the gel is unknown. This was further tested using rheological method as described in the following section.

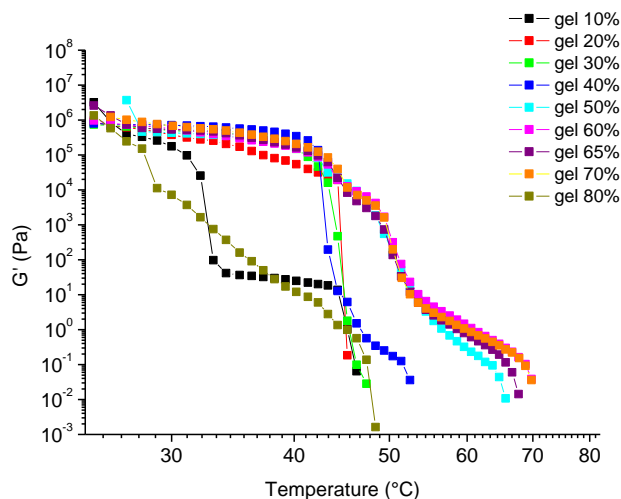
#### **3.4.3.2 The temperature ramp test (Oscillation Rheometer)**

The temperature ramp test using oscillation rheometer allows the identification of different physical properties of the systems. The determination of the storage/elastic moduli ( $G'$ ) and loss/viscous moduli ( $G''$ ) as a function of temperature lead to the identification of the main transitions that occur between different liquid crystalline phases [159]. The sol-gel temperature may be also identified when  $G'=G''$ . In this study, a temperature ramp test was performed over a range of temperature from 25 °C to 80 °C as described in section 3.3.4.3 and the  $G'$  is plotted against temperature.



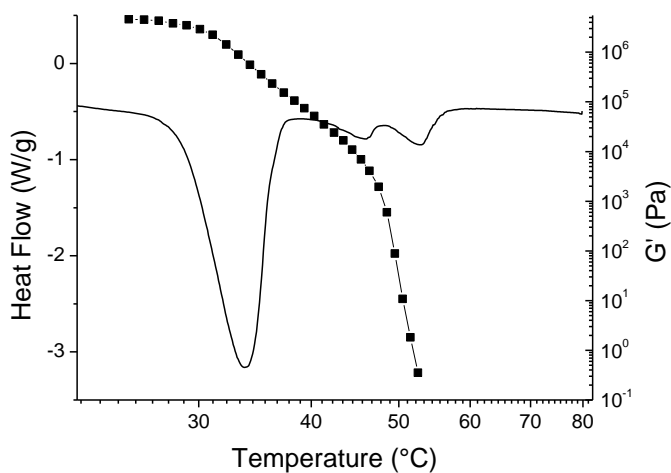
**Figure 3.20** Temperature influence on the elastic modulus ( $G'$ ) for the gels prepared by heating method.

As it can be seen in Figure 3.20, the  $G'$  values of all the gels decrease after the testing temperature increases to above 50 °C. At lower temperatures, the  $G'$  values decrease with increasing water content. In the gel with 10% water, the  $G'$  gently decreases over a broad range of temperature between 32 and 52 °C, after that it rapidly drops to below 1 Pa. Upon further increasing the testing temperature,  $G'$  is not detectable. This indicates that the gels show a pure liquid-like behaviour. In the gel with 20% water content, the  $G'$  almost plateaus up to 46 °C. After 46 °C, it sharply decreases by four orders of magnitude. The gel with 30% and 40% water contents shows a similar trend. The  $G'$  curves of these two gels have a shoulder at 32 and 34 °C followed by a maximum at 40 °C, after which the  $G'$  values decrease. The gel with 50% water content shows a shoulder at higher temperature (44 °C) and the maximum is at 47 °C. The  $G'$  values of the gels with 60%, 65% and 70% water tend to plateau before starting to decrease at ~44 °C and continuing to drop by about four order of magnitude at 70 °C. The gel with 75% and 80% water contents exhibits an unusual behaviour. The  $G'$  increases with temperature, it reaches a maximum at 43 and 50 °C, respectively. The  $G'$  decreases with further increasing the testing temperature.



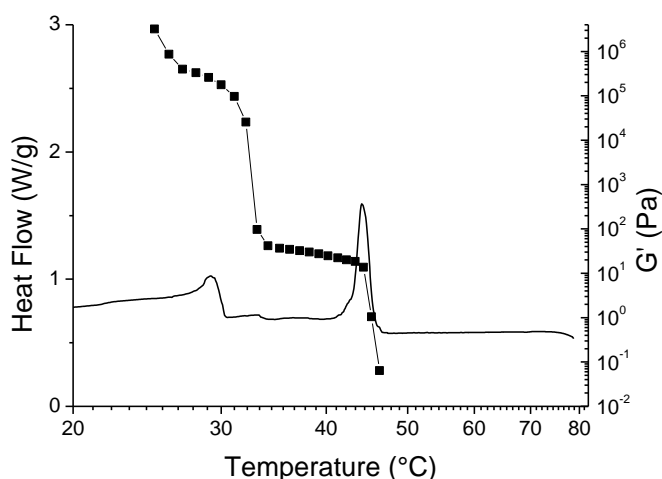
**Figure 3.21** Elastic modulus ( $G'$ ) response to the decreasing of temperature from 80° to 25 °C in the gels prepared by heating.

Figure 3.21 shows the recovery of the  $G'$  when the gels were cooled back at 25 °C. Across the gels, three types of behaviour may be distinguished. In the gels with 50% to 70% water content, the  $G'$  values gently increase below 70 °C. More rapid increase is observed at temperature below 52 °C and they continue to increase finally recover to  $1 \times 10^6$  Pa. The  $G'$  values of the gels with 20-40% water content abruptly increase at  $\sim 45$  °C and then they plateau at  $10^5$ - $10^6$  Pa. The change of the viscoelastic properties of these gels is thermo reversible. As it can be seen from the  $G'$  values which recover their original values after cooling. Finally, the gels with 10% and 80% water exhibit a different behaviour from the rest of the gels. In order to better understand the transitions that occur in the gels with 10% and 80% water content, a comparison between the DSC thermogram and the rheogram in both heating and cooling cycles was conducted.



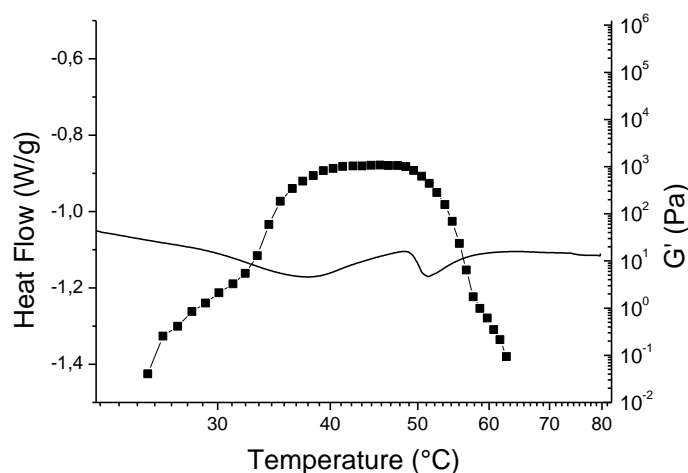
**Figure 3.22** Comparison between the thermogram (black line) and the rheogram (-■-) of the gel with 10% water content prepared by heating method obtained during the heating cycle.

Figure 3.22 shows the comparison between the DSC thermogram and the rheogram obtained by heating the gels with 10% water up to 80 °C. In the DSC result, a main transition occurs at 33 °C and two less visible at 47 and 52 °C. As previously discussed for the DSC results (see section 3.4.3.1), these thermal transitions may be related to the transition temperatures of the different lamellar phases. In the heating cycle, the transitions are identified with the DSC with three peaks. In the rheogram, after an initial plateau between 25 and 32 °C, the curve decreases by about six orders of magnitude over a temperature range between 32 and 52 °C. Thus, the different transitions found with the DSC can also be recognised from the rheometer as one progressive change. After this transitions region, the  $G'$  drops sharply from ~50 °C onwards, which temperature corresponds to the endothermic DSC transitions at 47 and 52°C of the gel. The transitions at higher temperature are related the complete breakdown of any order structure in the gel. Above these transitions, the gel turned into a liquid-like state, which corresponds well with the sharp drop of  $G'$  at high temperature.



**Figure 3.23** Comparison the thermogram (black line) and the rheogram (-■-) of the gel with 10% water content prepared by heating method and obtained during the cooling cycle.

The rheogram of the cooling cycle (Figure 3.23) shows that the process is reversible and the  $G'$  recovers the initial value. Two different transitions are identified during cooling in both DSC and  $G'$  results. The first one occurs at 44 °C, after which a plateau follows. The second transition occurs at 34 °C, a second plateau follows and the  $G'$  rises again. The gel again shows thermo-reversible properties. In summary, both techniques identified two main phase transitions at the temperature of 35 °C and 50 °C in the heating cycle and at 30 °C and 45 °C in the cooling cycle.



**Figure 3.24** Comparison the thermogram (black line) and the rheogram (-■-) of the gel with 80% water prepared by heating method and obtained during the heating cycle.

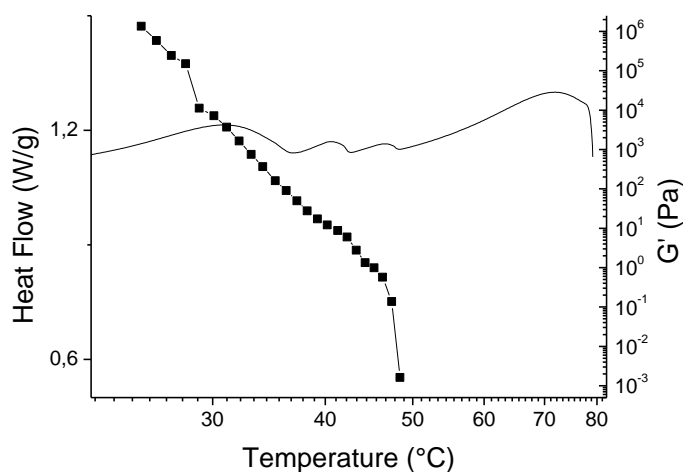


**Figure 3.25** Comparison the thermogram (black line) and the rheogram (-■-) of the gel with 80% water prepared by heating method and obtained during the cooling cycle.

The usual response to an oscillation rheometer temperature test is a decreasing in the viscoelastic properties with increasing the temperature. However, in the gel with 80% water, the  $G'$  increases upon heating and plateaus at 39 °C, which is very close to the temperature of the first thermal phase transitions identified by DSC (Figure 3.24). On heating, the  $G'$  sharply decreases at ~50 °C. This is in agreement with the second thermal phase transitions detected by DSC. The increasing of  $G'$  upon heating may be due to a change in structure in which the gel flow more slowly. At and above 50 °C, the flow of the gel increases which is associated with the complete structure breakdown of the gel. After 62 °C,  $G'$  is no longer detectable and the gel shows a pure liquid-like behaviour. During cooling, the  $G'$  sharply increases of three orders of magnitude at 50 °C and it progressively increases of six orders of magnitude (Figure 3.25). This transition temperature is consistent with the thermal phase transitions detected by DSC. The  $G'$

recovered completely when the gel was cooled to 25 °C. The final value of the  $G'$  at 25 °C is higher than the  $G'$  detected before the heating-cooling cycle. This may be related to the possible water loss occurred during the test, despite the use of the cage to prevent such a loss. This resulted in a more concentrated gel and therefore higher values of  $G'$ . In summary, the two temperature-ramp based techniques complement each other. The detected thermal transitions correspond to the rheological ones very well in the cases of both gels. These are likely to be the transitions between different liquid crystalline states of the gels.

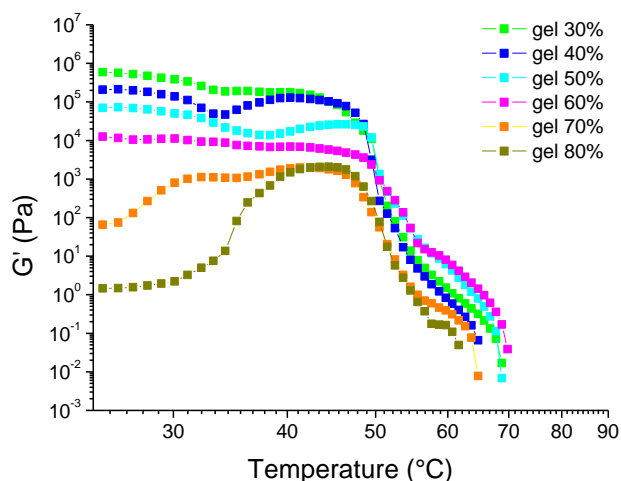


**Figure 3.26** Temperature influence on the  $G'$  for the gels prepared by hydration.

The gels prepared by hydration at room temperature show a similar behaviour to the gels prepared by heating (Figure 3.26). At low temperatures, the  $G'$  of the gels increases with increasing the lipid content in the gels. The  $G'$  values decreased dramatically at ~50 °C for all gels. In the gel with 30% water content, the  $G'$  slightly decreases up to 50 °C. With increasing the temperature, it abruptly drops to lower  $G'$  value and progressively drops up to 70 °C. In the gel with 40% water content, the  $G'$  value initially decreases, but at 34 °C the  $G'$  value increases again and reaches a maximum. Finally, at 47 °C it starts to drop. A pure liquid-like behaviour was observed when the temperature approached 70 °C. The gel with 50% water content has a similar behaviour to the gel with 40% water, though the depression happens at higher temperature value (37 °C), a small increase of  $G'$  follows. This pattern is consistent with the change in liquid crystalline phases determined with the SAXS (Figure 3.13). According to the SAXS results, at 25 °C the gel with 50% water content exhibited a hexagonal phase, which changed into a cubic phase (Pn3m) at 37 °C. This phase change may be responsible for the increase of the  $G'$  value of the gel. Above 50 °C, the  $G'$  reduces; this may suggest that the cubic structure may be destroyed with increasing temperature and as a result the gel flow more easily [215]. No change in  $G'$  was detected for the gel with 60% water content up to 49 °C, after which the  $G'$  value decreases. The gel with 70% water content shows slight increases in  $G'$  (one

order of magnitude) at lower temperature region (25-31 °C). It plateaus at about 31 °C and starts to decrease at 48 °C. The different transitions are evident in the rheogram for the gel with 70% water content but they are not supported by the DSC result, where a single peak is identified at 58 °C. However, both SAXS (Figure 3.14) and rheology tests indicate a mixture of ordered phases. The gel with 80% water has a similar behaviour to the gel with 70% water content. The  $G'$  shows significant increase from 35 °C and the value started to decrease from 50 to 55 °C onwards (Figure 3.26).

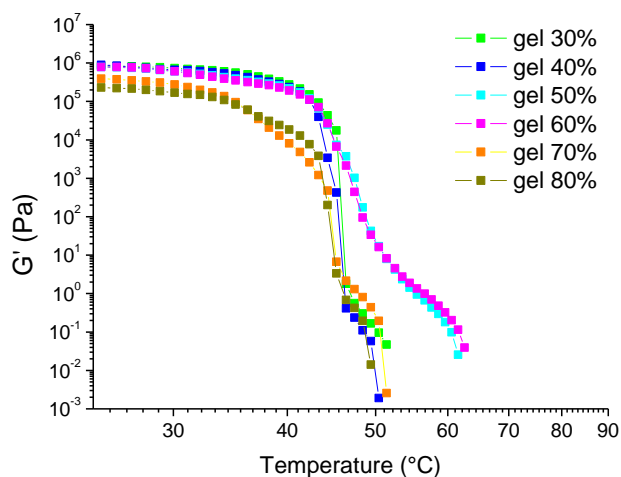


**Figure 3.27** Elastic modulus ( $G'$ ) response to the decreasing of temperature from 80° to 25 °C in the gels prepared by hydration.

During cooling (from 80 to 25 °C), all gels show sharp increases at 45-55 °C (Figure 3.27). The  $G'$  values recovered to between  $1 \times 10^5$  and  $1 \times 10^6$  Pa after cooled to 25 °C, which is higher than the original  $G'$  values of the gels before heating. The gels with 50% and 60% water content have the same trend, which is slightly different from the others. The increases of the  $G'$  values of these two gels are less sharp than the rest tested gels.

In conclusion, the coupling of different techniques such as variable temperature SAXS, DSC and rheometry allow a better understanding of the structure of the gels upon thermal treatment. Overall, the rheological results are largely consistent with the DSC and variable temperature SAXS results. The existence of different liquid crystalline phases in the gels (depending on the water content of the gels) are confirmed by the combined analyses of the results of all three techniques. The phase transition temperatures detected by DSC and rheometer may differ slightly, but this is due to the different way the two techniques analyse the samples. Furthermore, the results from both techniques showed that the gels with the same water content but prepared in the two different methods, have a similar behaviour. This suggests that the methods of preparation are likely to have little effect on the structure of the gels upon thermal

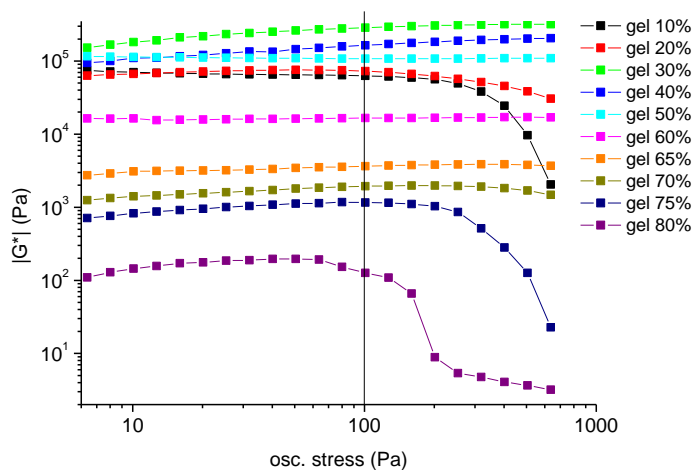
treatment. This was later confirmed in the chapter by the statistical analysis of the rheological and mechanical results of the gels.

### 3.4.4 Rheological properties of gels

The rheological behaviour of liquid crystals has been studied over the years. Several works tried to identify the liquid crystalline phases by studying the viscoelastic properties changes with frequency or with temperature [159, 216, 217]. In this work, the rheological properties of the gels were studied in the attempt to better understand the structural properties of the gels and whether the method of preparation plays a role in influencing their physical properties.

#### 3.4.4.1 Determination of linear viscoelastic region (LVR): oscillation stress sweep test

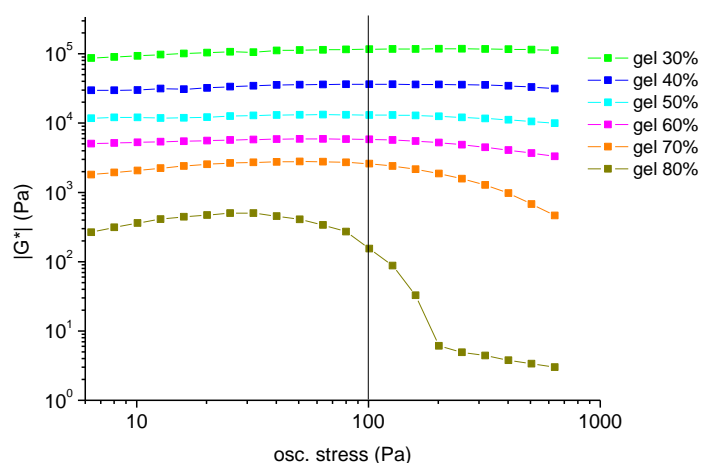
The linear viscoelastic region (LVR) is the region represented by the range of stress over which the complex modulus,  $|G^*|$ , and the phase angle,  $\delta$ , are independent of the applied stress. Performing tests at a stress value within the LVR is very important. This means that the structure of the sample is not disrupted. The LVR for each gel was determined by an oscillation stress sweep test at a constant frequency of 1 Hz and a temperature of 37 °C. The test was also performed on selected concentrations (40%, 50% and 60%) of gels prepared by heating at 25 °C (data not shown), which confirmed the same trend as the corresponding gels analysed at 37 °C. With this test the  $|G^*|$  and  $\delta$  were measured as a function of stress as seen in Figure 3.28 and Figure 3.29.



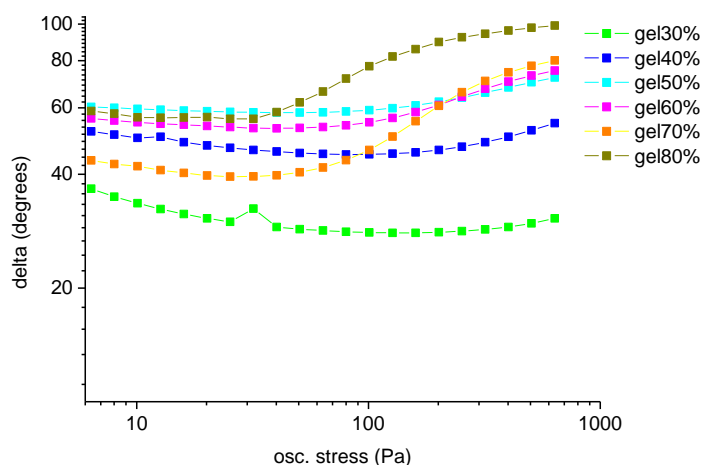
**Figure 3.28** Complex modulus ( $|G^*|$ ) versus oscillation stress plot of the gels prepared by heating method measured at 37 °C.

Figure 3.28 shows the complex modulus,  $|G^*|$ , plotted versus the oscillation stress of the gels prepared by heating method. The complex modulus generally drops at high values of stress,

except for the gel with 80% water, in which it drops after 100 Pa. This means that after the drop a disruption of the structure takes place, so a stress of 80 Pa was chosen to perform further tests (frequency sweep test and temperature ramp test) for all the gels. The LVR seems to increase with the lipid content, exception for the gels with 10% and 20% water contents. The same stress was used also for the samples prepared by hydration, except for the gel with 80% water where the  $|G^*|$  decreases at lower value. In this case a stress of 40 Pa was applied (Figure 3.29). The gels with 10% and 20% water contents prepared by hydration method were not analysed because they are too viscous and not homogeneous.



**Figure 3.29** Complex modulus ( $|G^*|$ ) versus oscillation stress plot of the gels prepared by hydration measured at 37 °C.



**Figure 3.30** Phase angle (delta) versus oscillation stress plot of the gels prepared by hydration method. The test was performed at 37 °C.

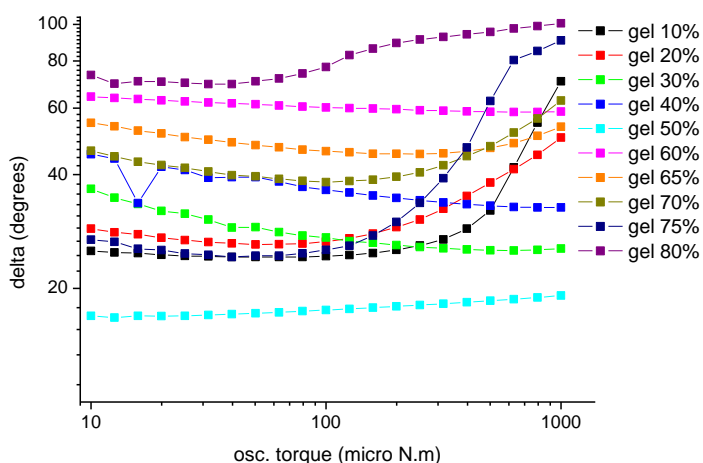


**Figure 3.31** Phase angle ( $\delta$ ) versus oscillation stress plot of the gels prepared by heating method. The test was performed at 37 °C.

A confirmation of LVR is given by plotting  $\delta$  versus oscillation stress (Figure 3.30 and Figure 3.31). The phase angle can change from the elastic region ( $\delta < 45$  degrees) to the viscous region ( $\delta > 45$  degrees) with increasing the stress. For the gel with 80% water prepared by hydration, the change occurs at around 40 Pa. For the other gels, it happens at around 100 Pa as seen in Figure 3.30 and Figure 3.31. The gels with 10%, 20% and 75% water contents prepared by heating show a change in the phase angle at 100 Pa. This change is observed at slight lower stress for the gel with 80% water content (Figure 3.31). These results are in agreement with the  $|G^*|$  plot.

In summary, in all the gels the LVR exists below 100 Pa. In order to be sure to apply a stress within the LVR, an 80 Pa stress was applied in the following experiments. Exception to this behaviour is the gel with 80% water content prepared by hydration, in which the LVR is below 40 Pa.

#### 3.4.4.2 The oscillation frequency sweep test

The oscillatory curve gives a fingerprint of the state of the microstructure of the materials [155] and it allows a better understanding of the viscoelastic behaviour of the gels. Moreover the frequency tests can be used to study the effect of the frequency on the structural properties of the gels. The frequency sweep test is a dynamic test, which measures the response of the system as a function of frequency (Hz) at a constant stress chosen within the LVR. In this way, the systems can be analysed under non-destructive conditions. The tests were performed at 37 °C at a fix stress value of 80 Pa (chosen within the LVR as discussed in section 3.4.4.1), in a range of frequency from 1 to 100 Hz.  $G'$ ,  $G''$ , the loss tangent ( $\tan\delta$ ) and the dynamic viscosity ( $\eta'$ ) were plotted against the frequency.

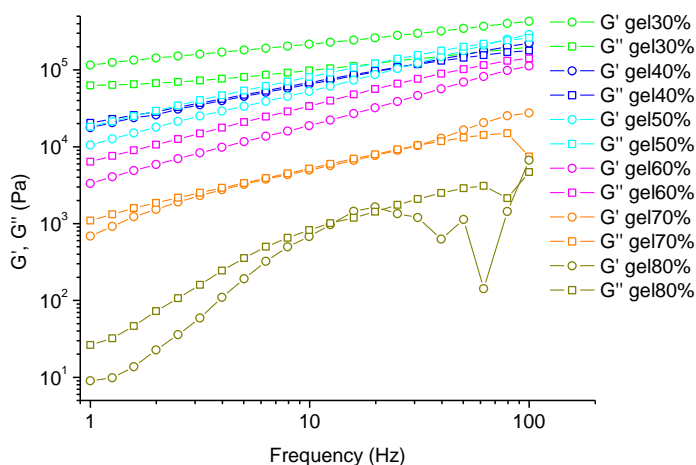


**Figure 3.32** Plots of elastic modulus ( $G'$ ) and viscous modulus ( $G''$ ) versus frequency (Hz) for the gels prepared by hydration method (measured at 37 °C).

Figure 3.32 shows the change of  $G'$  and  $G''$  with testing frequency (Hz) in the gels prepared by hydration.  $G'$  and  $G''$  values significantly increase with the lipid content ( $\chi^2 = 128.9$ ,  $df = 5$ , two tailed  $p < 0.001$  and  $\chi^2 = 128.8$ ,  $df = 5$ , two tailed  $p < 0.001$ , for  $G'$  and  $G''$  respectively). The gels with water content between 30% and 50% are statistically different from the gels with water content above 50%. The 30% water gel content presents a cross linked-like behaviour since  $G'$  is higher than  $G''$  and the two moduli are parallel (the slope of the plot approaches zero). For the gels with 40% and 50% water contents, the  $G'$  and the  $G''$  have similar values and similar trends, which is characteristic to the entangled-like network. In the gel with 40% water content, at lower frequencies,  $G'' > G'$  and they cross over at around 25 Hz. When  $G'$  and  $G''$  cross (called cross-over point),  $G' = G''$ , thus the elastic and the viscous properties of the system are equivalent. In the 50% water content, the crossover occurs at higher frequencies (at 72 Hz). The gel with 70% water content shows the entanglement network pattern and the cross-over occurs at 31 Hz. On the contrary,  $G''$  is higher than  $G'$  in the gel with 60% water content, but there is no cross-over. In this sample the  $G''$  is predominant and it behaves like a viscous fluid. A different trend was found for the gel with 80% water content. At lower frequencies,  $G'' > G'$  and at 12 Hz the two moduli cross over, but despite a slight increasing of  $G'$  compared to  $G''$ , the loss modulus grows higher than  $G'$ .

The classification of the gels is confirmed by the loss tangent value ( $\tan\delta$ ) (Figure 3.33). The loss tangent is a dimensionless parameter that describes the ratio between the  $G''$  and the  $G'$ . It is also known as the mechanical damping parameter [156]. It is less prone to theoretical considerations compared to the other dynamical parameters (such as  $G'$  and  $G''$ ) [218]. It has been stated that for covalently cross linked gels,  $\tan\delta$  never exceeds the unity, while it happens for entangled polymer networks [219]. For amorphous polymers, in the transition zone, the  $\tan\delta$

= 1. A higher contribution of  $G''$  on the viscoelastic properties leads to a larger value of loss tangent ( $\tan\delta > 1$ ). As seen in Figure 3.32, for the gel at 30% water,  $\tan\delta$  is below 1, which means  $G'' < G'$ , while it is over for the other concentrations ( $G'' > G'$ ). The gel with 60% water content has the highest value of  $\tan\delta$ , which means that viscous contribution to the overall viscoelastic properties of the sample is greater than the other gels.

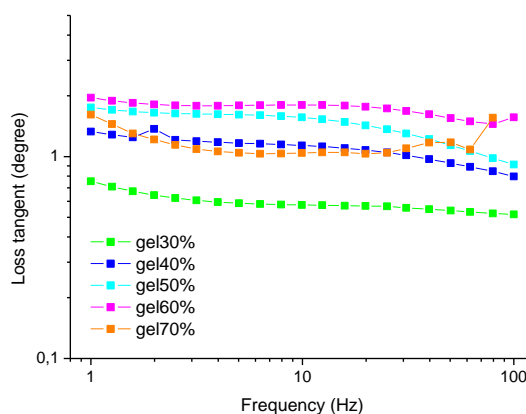


**Figure 3.33** Effects of the frequency (Hz) on the loss tangent ( $\tan\delta$ ) for the gels prepared by hydration (measured at 37 °C).

In the gels prepared by heating and analysed at 37 °C,  $G'$  and  $G''$  increase with the Gelucire content, exception for the gel with 10% and 20% water content, which values are lower than expected. Generally,  $G'$  is higher than  $G''$ , except for the gel with 60% water, where the  $G''$  is higher at lower frequencies ( $G'' > G'$ ) and they cross at 5 Hz. In the gel with 70% water content, at lower frequencies,  $G'$  is higher than the  $G''$  and they cross at 25 Hz. This is the typical behaviour of entanglement networks, and the gel behaves more as an elastic material than a viscous fluid [152]. For the gels between 10% and 50% water contents,  $G'$  is higher than  $G''$  and no crossover took place (Figure 3.35).

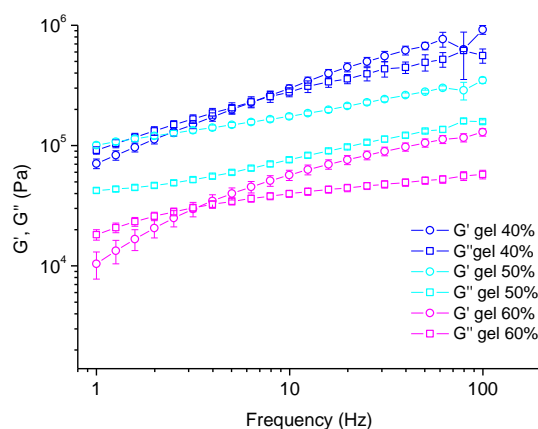


**Figure 3.34** Plot of elastic modulus ( $G'$ ) and viscous modulus ( $G''$ ) versus frequency (Hz) for the selected gels prepared by heating method and measured at 25 °C.

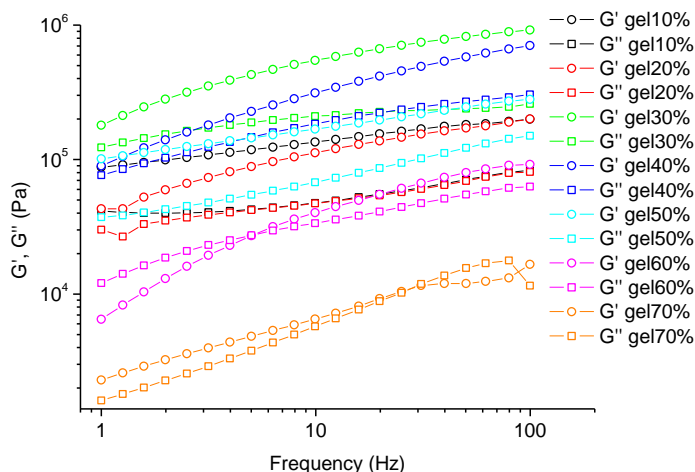


**Figure 3.35** Plots of elastic modulus ( $G'$ ) and viscous modulus ( $G''$ ) versus frequency (Hz) for the gels prepared by heating method (measured at 37 °C).

Figure 3.34 and Figure 3.35 show the variation of the viscoelastic parameters with frequency at 25 °C and 37 °C, respectively. The temperature has a slight effect on the  $G'$  and  $G''$  values in the gels with 40% and 60% water content. In the gel with 40% water, there is no crossover at 37 °C, whilst the cross-over point is evident at 25 °C. This means that at 25 °C and at low frequency values, the viscous part of the gel is more dominant than the elastic part, after the cross-over the situation reverses. However, at 37 °C, the elastic part always exceeds the viscous part. For the 60% water content, at 25 °C, the crossover happens at a slight lower frequency. Varying temperature showed no effect on the pattern of the gel with 50% water.

The non-parametric Kruskal-Wallis tests were performed separately on both the viscoelastic moduli ( $G'$  and  $G''$ ). It was found that  $G'$  and  $G''$  of the gels with different water contents are statistically significant ( $\chi^2 = 248.8$ ,  $df = 9$ , two tailed  $p < 0.001$  and  $\chi^2 = 250.8$ ,  $df = 9$ , two tailed  $p < 0.001$ , for  $G'$  and  $G''$  respectively). In particular, it was found that the behaviour of the gels with 30% and 40% water contents are statistically different from the rest of the gels. There is no difference between the gels with lower water concentration (10% and 20%) and the gels with higher water content (50% and 60% for the  $G'$ , 50%-70% for the  $G''$ ). The plot of loss tangent versus frequency confirms that the gels between 10% and 50% are below 1, presenting the same behaviour of cross-linked gels; while for the gels with 60%-75% the loss tangent is greater than 1, which is entangled-like behaviour and the system is highly viscous (Figure 3.36).

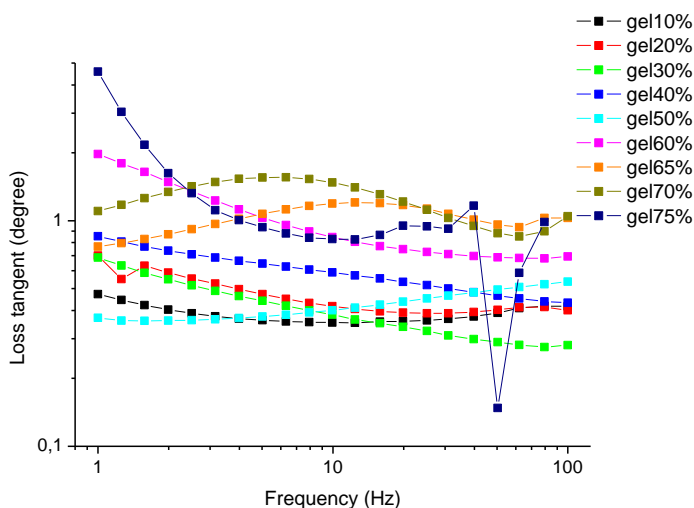


**Figure 3.36** Effects of the frequency (Hz) on the loss tangent ( $\tan\delta$ ) for gels prepared by heating measured at 37 °C.

Another viscoelastic parameter analysed as a function of frequency is the dynamic viscosity ( $\eta'$ ). The  $\eta'$  is commonly used to describe the viscoelastic character of gels. It is correlated to the loss modulus (or viscous modulus) as it is defined as the ratio of  $G''$  to the angular frequency ( $\omega$ ) [155]. In the gels prepared by heating and hydration methods, the dynamic viscosity was found to be dependent on the frequency. It decreases with increasing of frequency (Figure 3.37 and Figure 3.38), which means that at lower frequencies the viscous part of the gels is predominant, while at higher frequencies the elastic properties are more evident.

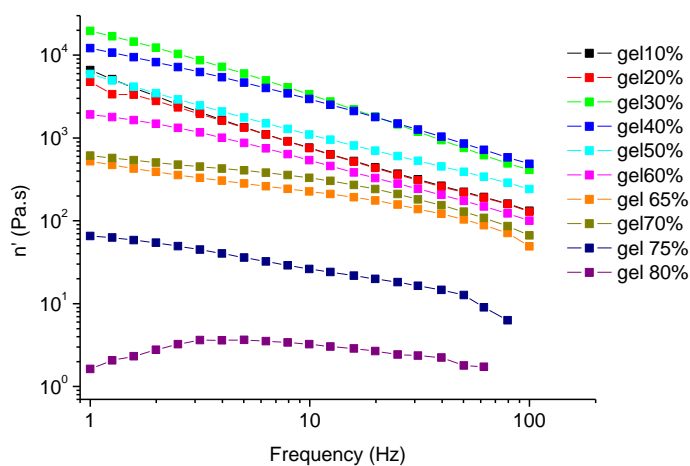


**Figure 3.37** Dynamic viscosity ( $\eta'$ , Pa.s) versus frequency (Hz) for gels prepared by heating (measured at 37 °C).

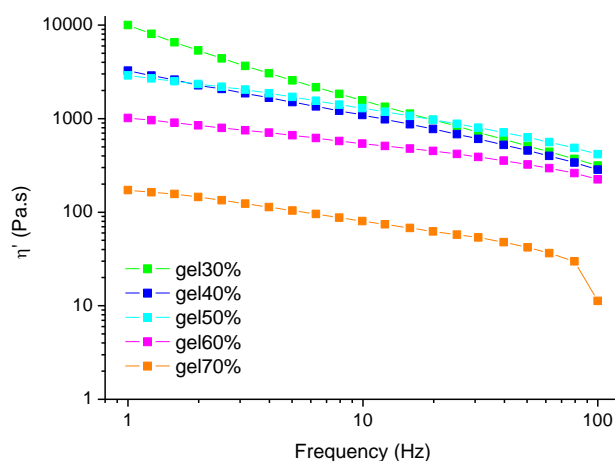


**Figure 3.38** Dynamic viscosity ( $\eta'$ , Pa.s) versus frequency (Hz) for gels prepared by hydration (measured at 37 °C).

For the gels prepared by heating, the  $\eta'$  significantly increases with the Gelucire content in the gels (Kruskal-Wallis test:  $\chi^2 = 186.9$ ,  $df = 9$ , two-tailed  $p < 0.001$ ). The gels with 75% and 80% water contents are statistically different from the rest of the gels. The gels with 10% and 20% water contents are not statistically different from gels with higher water concentration (up to 70%). The gels with 30% and 40% water are not statistically different between each other and from the gels with 10% and 20% water content, but are different from the gels with above 50% water.

For gels prepared by hydration, the Kruskal-Wallis test found that the  $\eta'$  increase significantly with the Gelucire concentration ( $\chi^2 = 138.9$ ,  $df = 5$ , two-tailed  $p < 0.001$ ). In particular, there is no significant difference between the gels at 30%, 40% and 50% water contents. The gel with 60% water is statistically different from the all the other gels, except for the gel with 40% water content.

A two-way ANOVA was performed to evaluate the effect of the water content and the method of preparation on the rheological parameters of the gels. The effect of the water content has a stronger effect on the  $G'$  and on the  $G''$  ( $F = 81.38$ ,  $p < 0.001$ ,  $\eta^2 = 0.61$  and  $F = 99.25$ ,  $p < 0.001$ ,  $\eta^2 = 0.65$ , respectively) compared to the methods of preparation ( $F = 96.92$ ,  $p < 0.001$ ,  $\eta^2 = 0.17$  and  $F = 29.93$ ,  $p < 0.01$ ,  $\eta^2 = 0.06$ , respectively). For the loss tangent ( $\tan\delta$ ), the result is not statistically significant. The dynamic viscosity is also more influenced by the water content in the gels than by the method of preparation ( $F = 16.66$ ,  $p < 0.001$ ,  $\eta^2 = 0.24$  and  $F = 15.18$ ,  $p < 0.01$ ,  $\eta^2 = 0.31$ , respectively). For  $G'$ ,  $G''$  and  $\eta'$ , the method of preparation is statistically significant just for gels with 30% and 40% water content ( $p < 0.01$  or  $p < 0.05$ ).

### 3.4.4.3 Continuous flow test

The flow test provides information concerning the variation of viscosity with applied shear stress. The study of the flow properties of pharmaceutical formulations is particularly important because it defines how easily it can be removed from a container or in case of topical formulations the spreadability on the site of application [154].

Continuous flow tests were performed for both heating and hydration methods at selected temperature of 25 °C, 37 °C, 50 °C and 80 °C, over a range of different stress according to the consistency of the samples. In each case, the stress continually increases over a period of 60 seconds. Flow tests at 25 °C were performed on gels with 60%, 70% and 80% prepared by heating and in the gels with 70% and 80% prepared by hydration. It was not possible to obtain reliable data at 25 °C for gels with lower water content, due to the high viscosity of the gels. The curves were mathematically defined with a power law equation, also called Ostwald de Waele equation (Equation 3.1) with which the consistency and the flow index were calculated.

$$\sigma = k\gamma^n \quad \text{Equation 3.1}$$

where  $\sigma$  is the shear stress (Pa),  $k$  is the consistency index (Pa.s<sup>n</sup>),  $\gamma$  is the shear rate (1/s) and  $n$  is the flow index (dimensionless). For a Newtonian liquid, the flow index is equal to 1, if it is greater than 1 the system is classified as shear thickening, if lower it is shear thinning. The consistency index is a measure of the property of the material by which it resists to the permanent change of shape [150]. The effect of the temperature and the water concentration on the flow parameters (consistency and flow index) were statistically investigated by performing a two-way ANOVA test. The level of significance was set as  $p < 0.001$ . Multi comparison post-hoc test (Scheffé test) was performed.

The consistency and flow indices for the gels prepared by heating method are listed in Table 3.8. In the gels prepared by heating, the consistency index of each concentration decreases with the temperature. However, it does not progressively change with the water content. The temperature at which the test was performed has a significant effect ( $F_{3,81} = 145.432$ ,  $p < 0.001$ ,  $\eta^2 = 0.843$ ) in the gels with 40% and 50% water contents (between 37 °C and 80 °C and between 37 °C and 50 °C), and 60% water content (between 25 °C and 37 °C and 25 °C and 50 °C). The water content has a significant effect on the consistency index ( $F_{7,81} = 91.635$ ,  $p < 0.001$ ,  $\eta^2 = 0.888$ ). It was found that the gels with 40%, 50% and 60% water content are statistically different between them and from the other concentrations, whilst there is no

significant difference between the gels with lower water content (gels between 10% and 30%) and the ones with higher water content (70% and 80%).

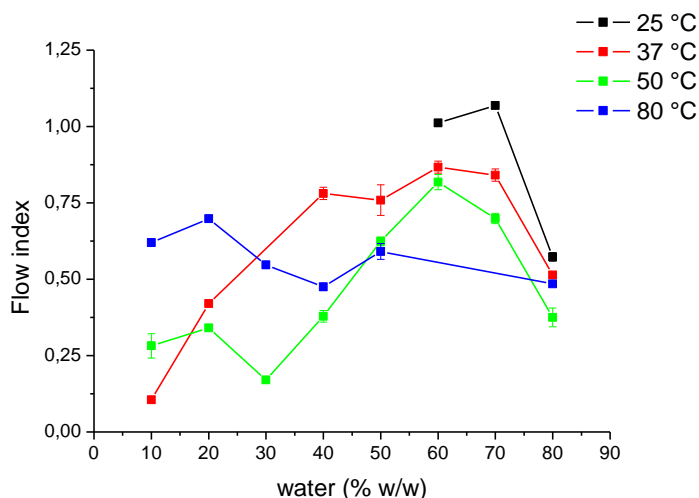


**Figure 3.39** Flow index plot for gels prepared by heating determined with continuous flow test at 25 °C, 37 °C, 50 °C and 80 °C.

The flow index ( $n$ ) of the gels prepared by heating is always smaller than one, as seen in Figure 3.39 thus the samples are shear-thinning or pseudoplastic liquids, except for the gels with 60% and 70% water contents at 25 °C, in which  $n$  approaches the unity (1.01 and 1.07, respectively), which suggests a Newtonian behaviour. At 25 °C, the gel with 80% water retains the shear thinning behaviour ( $n < 1$ ). Furthermore, the gels with 50% and 70% water show a progressive diminishing of flow index with the temperature, which is not observed in the other gels. The flow index decreases with the water concentration, which may be explained by the reduction of the entanglement of the Gelucire chains; hence the gels have high degree of flow. However, the gel with 80% water content has a different behaviour from the other gels. The flow index determined at 37 °C is higher than the one at 50 °C, except for the gel with 10% water where it is reversed. At 80 °C, the flow index is between 0.5 and 0.75 for all the gels, which may be explained by the fact that at this temperature, the gels are above the melting point and they are in the flow region, therefore no particular difference can be found in the gels.

The temperature and the water content have significant effects on the flow index of the gels ( $F_{3,81} = 18.449$ ,  $p < 0.001$ ,  $\eta^2 = 0.615$  and  $F_{7,81} = 18.970$ ,  $p < 0.001$ ,  $\eta^2 = 0.413$ , respectively). The effect of the temperature is significant in the gels with 10% water (between 37 °C and 80 °C), 40% water (between 37 °C and 50 °C) and in the gel with 80% water (between 37 °C and 50 °C and 37 °C and 80 °C). Considering the water content effect, the gel with 80% is not statistically different from the gels with lower content of water (from 10% to 50%). However, the gels with 60% and 70% water contents are not different from the gel with 50% water

content, but significantly different from the rest of the gels, though they are not different with the gel with 50%.

Overall, the gels prepared by heating with intermediate water content (40%, 50%, 60%) differ from the gels with low (below 40% water) and high water content (above 70% water). However, the gels with low and high water content do not differ from each other. Both of the flow parameters, the consistency and the flow indices do not progressively change with the water content and the testing temperature. This different responses observed in different gels may be due to the rearrangement of the gel structures that occur to each gel by varying the temperature.

**Table 3.8** Mean values of consistency ( $\pm$  SE) and flow ( $\pm$  SE) indexes for the gels prepared by heating method (measured at 25 °C, 37 °C, 50 °C and 80 °C). Measurements were performed in triplicate or quintuplicate .

Water %	Heating method											
	Consistency Index (k)				Flow Index (n)				Adj. $r^2$			
	25 °C	37 °C	50 °C	80 °C	25 °C	37 °C	50 °C	80 °C	25 °C	37 °C	50 °C	80 °C
10	NA	678.05 $\pm$ 9.12	77.44 $\pm$ 19.38	1.03 $\pm$ 0.08	NA	0.10 $\pm$ 0.01	0.28 $\pm$ 0.04	0.62 $\pm$ 0.01	NA	0.980	0.902	0.998
20	NA	1117.23 $\pm$ 6.8	71.82 $\pm$ 3.64	0.76 $\pm$ 0.05	NA	0.42 $\pm$ 0.00	0.34 $\pm$ 0.01	0.70 $\pm$ 0.01	NA	0.999	0.996	0.999
30	NA	NA	96.46 $\pm$ 2.34	2.27 $\pm$ 0.16	NA	NA	0.17 $\pm$ 0.00	0.55 $\pm$ 0.01	NA	NA	0.995	0.998
40	NA	6223.25 $\pm$ 338.36	86.64 $\pm$ 5.85	3.55 $\pm$ 0.24	NA	0.78 $\pm$ 0.02	0.38 $\pm$ 0.02	0.47 $\pm$ 0.01	NA	0.997	0.985	0.997
50	NA	14444.03 $\pm$ 3064.39	200.33 $\pm$ 4.24	1.48 $\pm$ 0.24	NA	0.76 $\pm$ 0.05	0.62 $\pm$ 0.01	0.59 $\pm$ 0.03	NA	0.972	0.997	0.990
60	13297.54 $\pm$ 491.4	1861.76 $\pm$ 65.14	229.69 $\pm$ 5.48	NA	1.01 $\pm$ 0.01	0.87 $\pm$ 0.02	0.82 $\pm$ 0.02	NA	0.999	0.997	0.996	NA
70	173.22 $\pm$ 0.89	43.81 $\pm$ 0.42	23.09 $\pm$ 0.33	NA	1.07 $\pm$ 0.00	0.84 $\pm$ 0.02	0.70 $\pm$ 0.02	NA	0.999	0.997	0.997	NA
80	1.04 $\pm$ 0.08	1.45 $\pm$ 0.09	3.88 $\pm$ 0.64	1.19 $\pm$ 0.04	0.57 $\pm$ 0.01	0.51 $\pm$ 0.01	0.37 $\pm$ 0.03	0.48 $\pm$ 0.01	0.997	0.998	0.971	0.999

NA stands for “not analysed”

For the gels prepared by hydration, the consistency index for each gel decreases with increasing temperature, but there is no progressive change with the water content (Table 3.9). The unrelated ANOVA test showed that for the consistency index, significance effects were obtained by altering water content in the gel ( $F_{5,45} = 17,226$ ,  $p < 0.001$  and  $\eta^2 = 0.657$ ) and the temperature at which the tests were performed ( $F_{2,45} = 78,635$ ,  $p < 0.001$  and  $\eta^2 = 0.778$ ). The interaction between water and temperature is statistically significant ( $F_{9,45} = 13.570$ ,  $p < 0.001$  and  $\eta^2 = 0.731$ ), which means that the flow parameters depend on the water content in different ways for different temperature values. However, according to the  $F$ -ratio value, it seems that the temperature has a greater effect on the results. The consistency index of gels with 40% and 50% water contents is not statistically different from each other, but they are significantly different from the gels with 30%, 60%, 70% and 80% water contents. Regarding the effect of the temperature, there is significant difference between the data obtained at 37 °C and the ones obtained at 50 and 80 °C. In particular, it is significantly different in the gels with 40%, 50% and 60% water contents, while it is not significant in the gels with 70% and 80% water contents. Similar pattern of behaviour considerations can be seen for the flow indices of the gels prepared by hydration, as it can be seen in Figure 3.40.

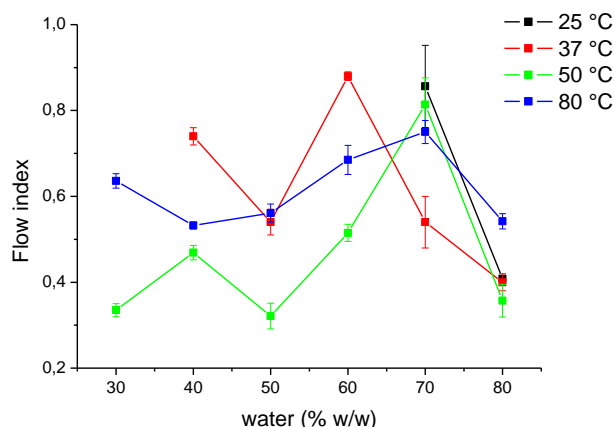


**Figure 3.40** Flow index plots of the gels prepared by hydration (measured using continuous flow test at 25 °C, 37 °C, 50 °C and 80 °C).

Flow indices determined at 25 °C for the gels with 70% and 80% water contents are similar to those determined at 37 °C, but clear changes can be observed when the testing temperature increases to 50 °C. Generally, the flow index decreases when the temperature increases from 37 °C to 50 °C, exception for the gel with 70% water content. At 80 °C, the flow indices fluctuate between 0.5 (for the gel with 40% water) and 0.74 (for the gel with 70% water). This follows the similar pattern of the flow indices of the gels prepared by heating (Figure 3.39). This confirms that the gels at this temperature are in the flow region.

The test showed that the water concentration ( $F_{5,45} = 20.006$ ,  $p < 0.001$  and  $\eta^2 = 0.690$ ), testing temperature ( $F_{2,45} = 11.565$ ,  $p < 0.001$  and  $\eta^2 = 0.339$ ) and their interaction ( $F_{9,45} = 13.292$ ,  $p < 0.001$  and  $\eta^2 = 0.727$ ) can all have a significant effect on the behaviour of the gels. The water concentration has no significant effect on the gels with 40%, 50% and 60% water contents. The gel with 80% water content is statistically different from the other gels, (except for the gel with 30% water). There is no difference for the results obtained at 50° and 80 °C water (exception for the gel with 30% water), while there is difference for the tests performed at 37 °C compared to the other two testing temperatures. For the gels with 50% and 80% water contents, the temperature has no significant effect on the flow parameters. An explanation for this behaviour may be due to the fact that above 50 °C the viscosity of gels reduces, as it could be seen from the temperature ramp test (see section 3.4.3.2), thus no difference in the flow parameters was observed. Overall, we can distinguish two groups of gels according their response on the flow tests. The gels with intermediate water content, 40% and 50%, and the gels with 30%, 60%, 70% and 80%.

**Table 3.9** Mean values of consistency ( $\pm$  SE) and flow ( $\pm$  SE) indices for the samples prepared by hydration method (measured at 25 °C, 37 °C, 50 °C and 80 °C). Measurements were performed in triplicate or quintuplicate.

Water %	<i>Hydration method</i>											
	<i>Consistency Index (k)</i>				<i>Flow Index (n)</i>				<i>Adj. r<sup>2</sup></i>			
	25 °C	37 °C	50 °C	80 °C	25 °C	37 °C	50 °C	80 °C	25 °C	37 °C	50 °C	80 °C
30	NA	NA	127.37 $\pm$ 7.63	1.64 $\pm$ 0.17	NA	NA	0.33 $\pm$ 0.01	0.64 $\pm$ 0.02	NA	NA	0.990	0.997
40	NA	3739.50 $\pm$ 223.91	484.01 $\pm$ 6.24	2.50 $\pm$ 0.12	NA	0.74 $\pm$ 0.02	0.47 $\pm$ 0.02	0.53 $\pm$ 0.01	NA	0.996	0.993	0.999
50	NA	1375.41 $\pm$ 118.16	273.44 $\pm$ 16.48	1.88 $\pm$ 0.24	NA	0.54 $\pm$ 0.03	0.32 $\pm$ 0.03	0.56 $\pm$ 0.02	NA	0.964	0.886	0.994
60	NA	2402.73 $\pm$ 55.55	456.31 $\pm$ 6.24	1.02 $\pm$ 0.21	NA	0.88 $\pm$ 0.01	0.51 $\pm$ 0.02	0.68 $\pm$ 0.03	NA	0.999	0.992	0.990
70	94.38 $\pm$ 17.18	136.99 $\pm$ 18.61	19.48 $\pm$ 4.75	0.71 $\pm$ 0.11	0.86 $\pm$ 0.10	0.54 $\pm$ 0.06	0.81 $\pm$ 0.06	0.75 $\pm$ 0.03	0.962	0.964	0.980	0.995
80	3.59 $\pm$ 0.08	5.96 $\pm$ 0.81	7.32 $\pm$ 1.64	1.39 $\pm$ 0.16	0.41 $\pm$ 0.00	0.40 $\pm$ 0.02	0.36 $\pm$ 0.04	0.54 $\pm$ 0.02	0.999	0.984	0.953	0.994

NA stands for “not analysed”

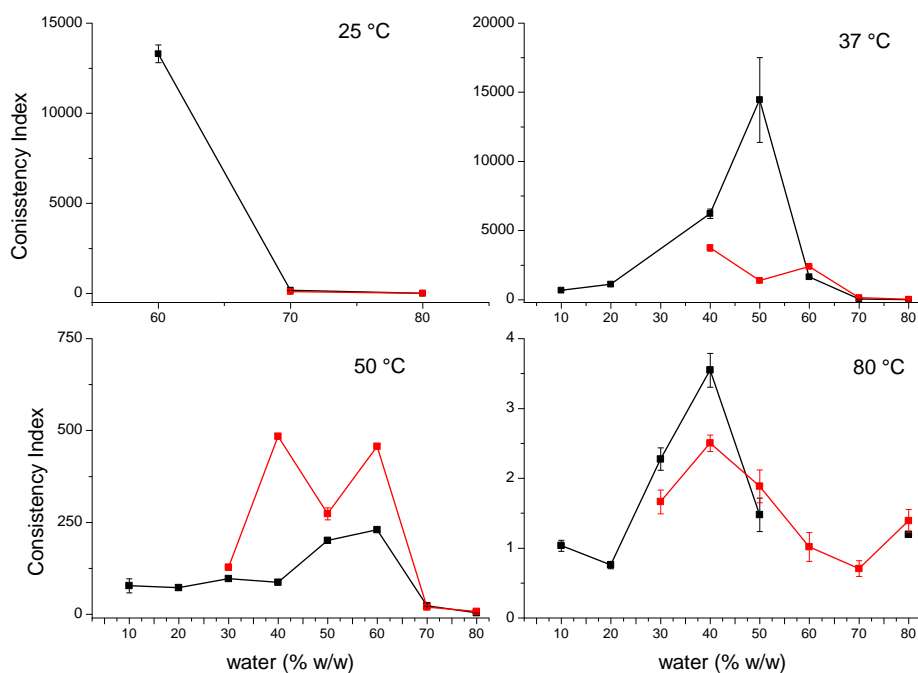


**Figure 3.41** Consistency index of gels prepared by heating (■) and hydration (■) method determined at different temperatures (25 °C, 37 °C, 50 °C and 80 °C).

Figure 3.41 shows a comparison of the consistency indices of the gels prepared by both heating and hydration methods analysed at four different temperatures, 25 °C, 37 °C, 50 °C and 80 °C. The effect of the method of preparation was further investigated. It was found that the method of preparation has a significant effect on the consistency index of the gels ( $F_{3,81} = 38.494$ ,  $p < 0.001$ ,  $\eta^2 = 0.234$ ) even though the effect is weaker in respect to the testing temperature and the water content in the gels. In particular, it has a significant effect on the gels with 40% and 50% at the temperature of 37 °C. For the other gels, the consistency indices of each gel measured at different temperature is not statistically different.

In conclusion, the gels with intermediate water content (between 40% and 60%) seem to differ in consistency from the gels with lower and higher water contents. This may be attributed to the structural difference observed by other analytical methods, such as SAXS. The gels with lower water content (between 10% and 30%) are similar to those with higher water content (70% and 80%), which is consistent with the  $G'$  and  $G''$  values obtained with the frequency test for the gels prepared by heating (Figure 3.35). The method of preparation of the gels has no substantial effect on the flow properties of the gels. Overall, the gels show shear thinning (or pseudoplastic) behaviour, which makes them suitable for topical formulations (see discussion in Chapter 7 on the further development of the topical application of Gelucire 50/13 gels).

### **3.4.5 Mechanical properties of gels (Texture Analysis)**

The mechanical properties of the gels along with the flow properties are useful to study the effects of the compressed stress on the flow of the formulations. They also can provide further information on the structure of the gels via understanding the link between the mechanical and rheological properties of the gels. For example, the increase of hardness and compressibility, which are two of the mechanical properties of a gel, may be due to an increase in the entanglement of the gels, which can lead to a reduced flow [151]. In this study, the texture profile analysis (TPA) tests were performed on the gels prepared by hydration and heating methods in order to better understand the behaviour of the gels under compressed stress. The effects of the water content in the gels and of the methods of preparation also have been evaluated using appropriate statistical analysis.

#### **3.4.5.1 Texture Profile Analysis (TPA) test**

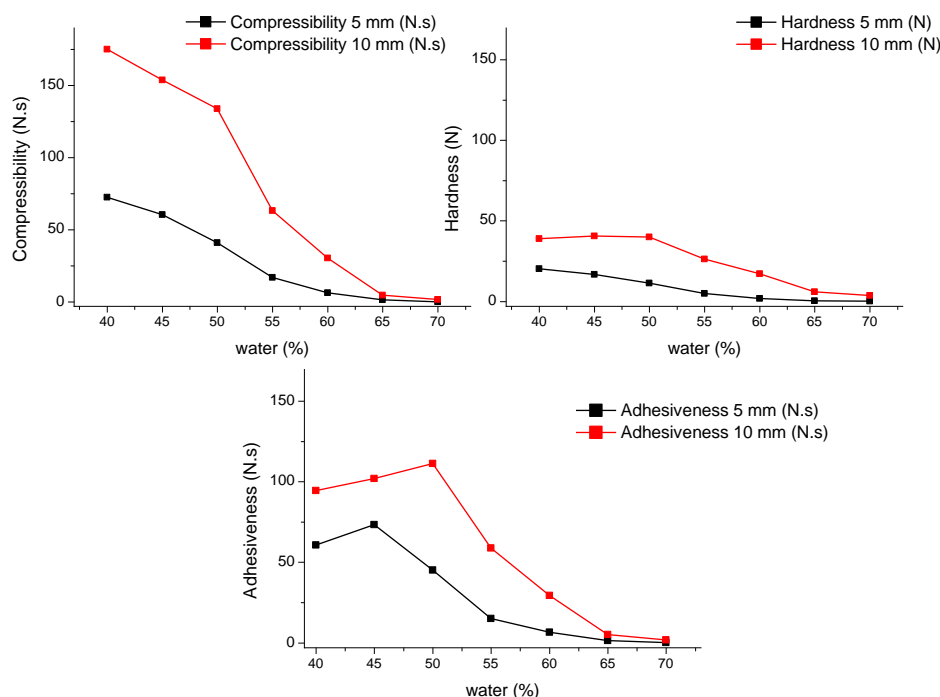
The parameters that can be obtained using the TPA test are the hardness, the compressibility and the adhesiveness. The hardness (units of Force, N) is the force required to get a deformation; the compressibility (units of work, N.s) is the amount of force required to deform the product during the first cycle of compression. In other words, it is a measure of whether the gels can retain the structure after the first cycle of compression [220]. The adhesiveness (unit of works, N.s) describes the work necessary to overcome the attractive forces between the surface of the systems and the surface of the probe with which the sample comes into contact (unit of work, N.s) [153].

The withdrawn speed of the probe was selected after performing the test on gels with 30% (w/w) water content prepared by heating method at fixed probe moving rates of 1, 3, 5 and 8 mm/s. The samples were compressed at a depth of either 5 or 10 mm. The depth of 10 mm could not be achieved for the gel with 30% water content. This might be due to the high strength of the gels, which opposed resistance to the compression and therefore the tests were only performed at the distance of 5 mm for this gel. The effects of the probe speed on the hardness, the adhesiveness and the compression of the gel with 30% water content are listed in Table 3.10.

**Table 3.10** Effect of the probe withdrawal speed on the hardness (N), compressibility (N.s) and adhesiveness (N.s) of the gel with 30% water prepared by heating. The values are presented as the mean ( $\pm$ SD) of at least three repetitions.

% water content	Probe speed $mm.s^{-1}$	Distance $mm$	Adhesiveness $N.s$	Hardness $N$	Compressibility $N.s$
30	1	5	0.047 $\pm$ 0.008	27.573 $\pm$ 6.808	74.737 $\pm$ 14.466
30	3	5	0.026 $\pm$ 0.010	47.093 $\pm$ 8.184	42.733 $\pm$ 6.194
30	5	5	0.015 $\pm$ 0.002	44.238 $\pm$ 5.928	23.190 $\pm$ 2.502
30	8	5	0.007 $\pm$ 0.002	49.079 $\pm$ 0.879	16.998 $\pm$ 1.555

From the results, we can conclude that the adhesiveness and the compressibility decreases with increasing the probe speed; whereas the hardness increases at first, but then it equalises at 3 mm/s probe speed. The effect of the probe speed on the TPA parameters was analysed statistically by performing the one-way ANOVA test. The probe speed has no effect on the hardness ( $F_{3,11}=62.03$ ,  $p=0.009$ ). However, for the adhesiveness ( $F_{3,11}=20.34$ ,  $p=0.000$ ), the effect from using the speed at 1 mm/s is statistically different from the ones obtained by using the other probe moving speeds. The ANOVA test results on the logarithm of the compressibility values show no statistical difference between the data obtained using the speed at 5 and 8 mm/s. On the other hand, the data obtained using the speed at 3 mm/s and at 1 mm/s are statistically different between each other and from the ones obtained using speeds of 5 and 8 mm/s.

**Figure 3.42** Comparison of the TPA parameters of gels prepared by heating method compressed twice at the depth of 5 and 10 mm.

As the adhesiveness values are very low at higher probe speed, a 1 mm/s probe speed was chosen to perform the TPA test. The TPA tests on the gels prepared by heating method were performed by compressing the gels twice at 5 and at 10 mm penetration depth. A comparison of the results is shown in Figure 41. Due to the extremely high viscosity, the probe could not penetrate the gel with 10% water content with the applied force. Due to the similar reason, the tests on the gels with 20% and 30% water contents were performed only by compressing at a probe distance of 5 mm. Generally, the compressibility and the hardness decrease with increasing the water content in the gel as the strength of the gels reduces with increasing the water content. On the contrary, the adhesiveness does not progressively decrease with increasing water content. The adhesiveness reaches a maximum in the gels with 45% and 50% water contents when the gels were tested by being compressed at 10 and 5 mm probe depths, respectively. The values of the TPA parameters obtained by compressing at probe depth of 10 mm are higher than the ones obtained by compressing at 5 mm. This may be explained by the fact that by forcing the probe deeper into the gels, the probe is more in contact with them, hence the forces required to compress and to withdraw are higher.

A two-way ANOVA test was performed to assess the effect of the water concentration and the distance of the probe penetration into the gel on the TPA parameters of the gels with 40-70% water contents. The Levene's test assessed the non-homogeneity of variances, thus a more conservative level of significance was adopted ( $p < 0.001$ ).

**Table 3.11** Summary table of variance analysis for the compressibility, hardness and adhesiveness of the gels.

Source of variance	Compressibility			Hardness			Adhesiveness		
	F	Sig.	$\eta^2$	F	Sig.	$\eta^2$	F	Sig.	$\eta^2$
Distance	376.354	<0.001	0.881	134.954	<0.001	0.726	80.210	<0.001	0.611
Water	207.265	<0.001	0.961	38.525	<0.001	0.819	76.985	<0.001	0.901
Distance-Water interaction	38.635	<0.001	0.820	5.995	<0.001	0.414	7.420	<0.001	0.466

Sig. stands for "significance"

From Table 3.11, it can be seen that for all the TPA parameters there is a significant effect from the distance of probe penetration and the concentration of water ( $p < 0.001$ ). The partial eta squared ( $\eta^2$ ) is the estimation of the degree of the effect and it is a measure of the proportion of the variability on the independent variable due to a specific factor. The water concentration has significant effects on all the TPA parameters, while the probe penetration distance has higher effect on the compressibility than on the hardness and the adhesiveness (as it can be seen by the partial eta squared values in Table 3.11). A follow-up pairwise comparison was performed to evaluate at which level the distance of penetration has an effect on the TPA results.

**Table 3.12** Effects of penetration distance of the probe within each level of concentration based on a linearly independent pairwise comparison among the estimated marginal means.

Water %	Compressibility			Hardness			Adhesiveness		
	<i>F</i>	<i>Sig.</i>	$\eta^2$	<i>F</i>	<i>Sig.</i>	$\eta^2$	<i>F</i>	<i>Sig.</i>	$\eta^2$
40	230.357	0.0000	0.819	26.293	0.0000	0.340	17.432	0.0002	0.255
45	142.293	0.0000	0.736	32.740	0.0000	0.391	9.425	0.0034	0.156
50	189.084	0.0000	0.788	62.388	0.0000	0.550	67.710	0.0000	0.570
55	47.093	0.0000	0.480	34.767	0.0000	0.405	29.298	0.0000	0.365
60	11.412	0.0014	0.183	15.739	0.0002	0.236	7.153	0.0100	0.123
65	0.210	0.6489	0.004	2.080	0.1554	0.039	0.190	0.6646	0.004
70	0.046	0.8306	0.001	0.864	0.3570	0.017	0.037	0.8480	0.001

*Sig.* stands for "significance"

Each *F* value tests the effect of the distance of the probe penetration on each level of water concentration. Looking at the significance (denoting significance at  $p < 0.001$ ), the distance effect is statistical significant for the gels with water concentration between 40% and 55%. It has no effect on the compressibility and adhesiveness of the gels between 60 and 70% water contents. For the hardness, the distance has no significance effect for gels with 65% and 70% water content (Table 3.12).

The effect of the water content on the TPA parameters of the gels obtained by compressing with probe depth of 5 mm was investigated by performing one-way ANOVA tests on the transformed values of the TPA parameters, which were obtained by taking the logarithm. The ANOVA test on the transformed values of the gels prepared by heating shows an overall significant effect of the concentration on the compressibility ( $F_{8,32} = 1312.12$ ;  $p < 0.001$ ). The compressibility decreases with the water concentration. Gels with 30%, 40% and 45% water are not significantly different between them, as also the gels with 45% and 50%. All the other groups are significantly different from each other. The Kruskal-Wallis test confirmed that the groups differ significantly ( $\chi^2 = 38.65$ ,  $p < 0.001$ ), but the Mann-Whitney U test with Bonferroni correction show that the rank of the groups are not statistically different. The Dunn test result shows a significance difference of the gels with 65% and 70% water from the gels with lower water content (between 20 to 45%). The effect of the water content was statistically significant for the hardness of the gels (ANOVA:  $F_{8,32} = 1356,215$ ,  $p < 0.001$ ; Kruskal-Wallis:  $F_{8,32} = 39.15$ ,  $p < 0.001$ ). The post hoc multi-comparison tests on the hardness data show the similar trend to the compressibility. Concerning the adhesiveness, significant differences can be concluded between the gels ( $\chi^2 = 36.31$ ,  $p < 0.001$ ). In particular, the group of gels with 40, 45 and 50% water content is significantly different from the gel with 70% water (high water content gel). The gel with 45% is also different from the one with 65% water content. Despite the

heterogeneity of the variances of the data and the unequal sample size of the experiment, the rest of the gels are not significantly different from each other, which was confirmed by the one-way ANOVA performed on the transformed values of adhesiveness ( $F_{8,32} = 115,657, p < 0.001$ ).

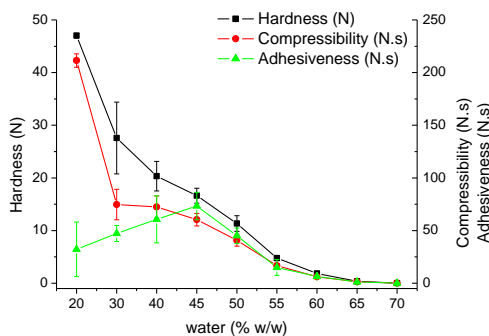


**Figure 3.43** Adhesiveness (N.s), hardness (N) and compressibility (N.s) of gels prepared by heating. The data are presented as mean ( $\pm$ SD)  $n \geq 4$ .

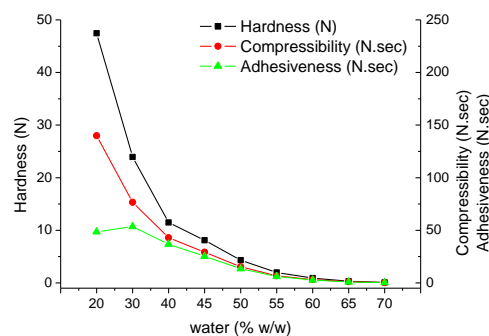


**Figure 3.44** Adhesiveness (N.s), hardness (N) and compressibility (N.s) of gels prepared by hydration. The data are presented as mean ( $\pm$ SD)  $n \geq 4$ .

The TPA tests were also performed on the gels prepared by hydration by compressing twice at 5 mm probe depth and with a withdrawal probe speed of 1 mm/s. Figure 3.43 and Figure 3.44 compare the hardness, adhesiveness and compressibility values calculated for the gels prepared by heating and gels prepared hydration methods, respectively. The hardness and compressibility values of the gels decrease with increasing Gelucire content in the gel. There is no noticeable difference between the gels prepared by hydration and by heating methods. On the contrary, the adhesiveness is different in the gels prepared by different methods. For the gels prepared with the heating method the adhesiveness increases with increasing the water content and reaches a peak maximum for the gel with 45% water content, whereas for the gels prepared by hydration a more linear pattern is registered. The gels with the highest adhesiveness are the ones with 20% and 30% water, with the 30% having a slightly higher value. For the gels with water content above 40%, the adhesiveness decreases with further increasing the water content in the gel. This may be because that when the concentration of water increases the gels become less sticky and the amount of forces required to detach the probe from the gels is low. For the gels prepared by heating method, the gel with 45% water is stickier than the gels with other water contents.

For the gels prepared by hydration, the data do not show homogeneity in the variances but since the experiment is a balanced design, the one-way ANOVA results should be considered reliable. The compressibilities of the gels with 50% to 70% water content are not significantly different between each other. The difference is significant between the gels with 20% and 30% water contents ( $F_{8,32} = 372,704, p < 0.001$ ). Kruskal-Wallis test found a statistical significance

between the gels ( $\chi^2 = 43.48, p < 0.001$ ). The follow-up test (Mann-Whitney U test with Bonferroni correction) found no statistical significance comparing the ranks of samples. The Dunn test found that the compressibility of the gels with 20 and 30% water contents differ from the ones of the gels with 70% and 65% water contents. The gel with 20% water also differs from the gels with 40%, 60% and the 70% water contents. Same results for the hardness of the gels were obtained (ANOVA:  $F_{8,32} = 1110,530, p < 0.001$ ; Kruskal-Wallis:  $\chi^2 = 43.48, p < 0.001$ ). Concerning the adhesiveness, there is no difference between the gels with 20% and 30% water contents, and the gels with water contents between 50 to 70% (ANOVA:  $F_{8,32} = 120,591, p < 0.001$ ; Kruskal-Wallis:  $\chi^2 = 42.71, p < 0.001$ ).

In conclusion, the effect of water content is statistically significant on the determination of the mechanical parameters of the gels prepared by both heating and by hydration and measured by TPA. Combining the parametric and non-parametric tests, we can conclude that there are differences between the group of gels with lower water concentration (20% and 30%) and the ones with higher water content (between 50% and 70%). For the adhesiveness of gels prepared by heating, the difference exists between the group of gels with 40-45% water and the other concentrations.

A two-way ANOVA test was performed to assess the combinational effect of both the preparation methods and the water concentration on the TPA parameters of the gels. Again, the analyses on three TPA parameters fail the Levene's test, thus a more conservative significance is applied ( $p < 0.001$ ). The test results show significant effect on the TPA parameters of the gels from both the method of preparation and the water concentration, as seen in Table 3.13.

**Table 3.13** Summary table of the two-way ANOVA test for the compressibility, hardness and adhesiveness.

Source of variance	Compressibility			Hardness			Adhesiveness		
	F	Sig.	$\eta^2$	F	Sig.	$\eta^2$	F	Sig.	$\eta^2$
Methods	220.771	<0.001	0.765	94.722	<0.001	0.582	42,339	<0.001	0.384
Water	761.033	<0.001	0.989	730.364	<0.001	0.988	71,348	<0.001	0.894
Methods-Water interaction	34.912	<0.001	0.804	12.714	<0.001	0.599	12,518	<0.001	0.596

Sig. stands for "significance"

A pairwise comparison was performed to assess at which level of water concentration in the gel the effect of the method of preparation is more significant. As shown in Table 3.14, the effect of the preparation method is statistically significant on the compressibility for the gels with water contents of 20%, 40% and 50%, while the effect on the hardness and the adhesiveness is significant for the gels with 40% and 50% water contents. This means that for these

concentrations, the method of preparation is responsible to the change of their TPA parameters and highly likely the structure of the gels as well.

**Table 3.14** Effects of method of preparation within each level of water concentration based on a linearly independent pairwise comparison among the estimated marginal means.

Water	Compressibility			Hardness			Adhesiveness		
	<i>F</i>	<i>Sig.</i>	$\eta^2$	<i>F</i>	<i>Sig.</i>	$\eta^2$	<i>F</i>	<i>Sig.</i>	$\eta^2$
20	286.459	0.000	0.808	0.122	0.728	0.002	0.880	0.351	0.013
30	0.202	0.655	0.003	9.165	0.003	0.119	1.158	0.286	0.017
40	64.976	0.000	0.489	73.058	0.000	0.518	21.569	0.000	0.241
45	72.601	0.000	0.516	67.795	0.000	0.499	86.419	0.000	0.560
50	48.825	0.000	0.418	45.675	0.000	0.402	37.584	0.000	0.356
55	7.574	0.008	0.100	7.349	0.008	0.098	2.950	0.090	0.042
60	0.683	0.411	0.010	0.826	0.367	0.012	0.539	0.466	0.008
65	0.007	0.935	0.000	0.004	0.952	0.000	0.004	0.949	0.000
70	0.003	0.544	0.000	0.003	0.958	0.000	0.001	0.976	0.000

Sig. stands for "significance"

### 3.4.6 Correlation between mechanical and rheological parameters

In order to better understand the physical behaviour and performance of the gels, the rheological properties of the gels were related to their mechanical parameters via statistical tools. It has been demonstrated by previous works that the rheological and the mechanical/textural properties can be related through a dimensionless analysis, where the TPA parameters were used to characterise the flow rheological behaviour [153] or through statistics correlation [220, 221]. In this study, the non-parametric correlation coefficients (Spearman's rho test) were calculated between the rheological and the mechanical properties of the gels prepared by hydration and heating methods with water contents from 20% and 70%. The Spearman correlation is described by a number between -1 and 1 that measure the level of correlation between two variables. The positive value describes a positive linear correlation (that is an increasing trend between two variables), whereas the negative value describes a negative relationship (which means a decreasing trend between the variables). If there is no correlation, the value is close to zero.

For the gels prepared by heating, a significant positive correlation ( $r < 0.8$ ,  $p < 0.01$ ) was found between the rheological ( $G'$ ,  $G''$  and  $\eta'$ ) and the textural properties. Particularly a strong and significant positive correlation was found between the hardness and the compressibility ( $r = 0.997$ ,  $p < 0.01$ ) and between the  $G'$  and  $G''$  ( $r = 0.990$ ,  $p < 0.01$ ) at several frequencies values. A moderate positive correlation ( $r < 0.5$ ,  $p < 0.01$ ) was found between  $\tan\delta$  and the rest of rheological parameters, while a higher positive correlation was found between  $\tan\delta$  and the TPA parameters ( $r < 0.8$ ,  $p < 0.01$ ). There is no significant correlation between the flow rheological

parameters (consistency and flow index) and the frequency rheological parameters or the textural parameters. Exception is for the consistency index determined at 37 °C and the flow index at 50 °C that have a negative significant correlation with the frequency rheological parameters and the adhesiveness, see Table 3.15.

**Table 3.15** Spearman’s rho correlation coefficients between rheological and mechanical/textural properties for gels prepared by heating. The rheological values have been obtained at different frequencies (1 Hz and 99.9 Hz).

	C	H	A	1 Hz				99.9 Hz		
				G'	G''	tanδ	n'	G'	G''	tanδ
H	0.997									
A	0.880	0.885								
1 Hz	G'	0.768	0.780	0.819						
	G''	0.847	0.855	0.849	0.921					
	tanδ	-0.390*	-0.397*	-0.427*	-0.632	-0.383*				
	n'	0.847	0.855	0.849	0.921	1.000	-0.383*			
	G'	0.767	0.772	0.800	0.910	0.938	-0.467	0.938		
99.9 Hz	G''	0.799	0.796	0.848	0.860	0.946	-0.291*	0.946	0.907	
	tanδ	-0.548	-0.553	-0.466	-0.542	-0.571	0.400	-0.571	-0.721	-0.430
	n'	0.799	0.796	0.848	0.860	0.946	-0.291*	0.946	0.907	1.000

H, hardness; C, compressibility; A, adhesiveness

\* the significance level is p<0.05; otherwise is equal to p<0.01

Similar results were obtained for the gels prepared by hydration (Table 3.16). There is a strong positive correlation between the TPA parameters and the rheological parameters obtained at the frequency of 1 Hz. The loss tangent (*tanδ*) values have a moderate negative correlation. For the rheological parameters obtained at 99.9 Hz, the correlation is less strong for the *G'* and just moderate for the *G''*, while the loss tangent has no significant correlation with all the parameters. The highest correlation is between the *G''* and the dynamic viscosity ( $r = 1$ ,  $p < 0.01$ ).

**Table 3.16** Spearman’s rho correlation coefficients between rheological and mechanical/textural properties for gels prepared by hydration. The rheological values have been obtained at different frequencies (1 Hz and 99.9 Hz).

	C	H	A	G'	G''	1 Hz		n'	G'	99.9 Hz	
						tanδ	n'			G'	G''
H	0.992										
A	0.991	0.985									
1 Hz	G'	0.951	0.955	0.959							
	G''	0.927	0.931	0.936	0.985						
	tanδ	-0.657	-0.669	-0.668	-0.690	-0.616					
	n'	0.926	0.930	0.936	0.985	1.000	-0.619				
	G'	0.819	0.819	0.819	0.819	0.921	-0.456*	0.920			
99.9 Hz	G''	0.575	0.541	0.575	0.541	0.664	>0.05	0.663	0.771		
	tanδ	>0.05	>0.05	>0.05	>0.05	>0.05	0.597	>0.05	>0.05	>0.05	
	n'	0.574	0.540	0.574	0.540	0.663	>0.05	0.664	0.770	1.000	>0.05

H, hardness; C, compressibility; A, adhesiveness

\* correlation is significant at  $p < 0.05$ ; otherwise is equal to  $p < 0.01$

### 3.4.7 Evaluation of the mucoadhesive properties of gels

Adhesive tests were performed to evaluate the adhesive properties of the gels when it is in contact with mucin tablets and porcine small intestine tissue (as model mucosa surface). In the literature, several types of mucosa have been used to perform adhesive test: rat intestine [222], rabbit stomach, bovine sublingual mucous [223], porcine buccal mucosa [224], porcine gastric mucosa [225], chicken pouch [167], and so on. Performing tests on biological surface can be challenging due to the difficulties to obtain uniform surfaces and therefore obtaining reproducible results [167, 222]. Smart et al. [222] revealed a non-uniform surface in the pig buccal mucosa, moreover the adhesion results obtained by testing the formulations with different parts of the pig gastric mucosa have been found to be non-consistent . Due to the large surface area, a more uniform surface can be obtained by using the intestinal tissue as a model biological surface, though a certain biological variability still remains [167].

The target of this work is to characterise Gelucire based gels in order to design an appropriate oral delivery formulations. For the Gelucire 50/13 gels with certain water contents, the rheological and mechanical properties of the gels, such as highly viscous and high adhesiveness, have indicated the possibility of the gel being bioadhesive. This will be beneficial for enhancing the absorption of the therapeutic agent delivered. Therefore, a porcine small intestine tissue was chosen to assess the mucoadhesive properties of the gels. The reason for choosing the porcine small intestine is that it can guarantee a uniform surface and a relatively high level mucus. The gels were prepared according to the procedures described in Chapter 2 (section 2.3.1). For the method and the parameters applied, refer to section 3.3.5.2. From the force-distance plot, the Force maxima ( $F_{max}$ ) which is the maximum force required to separate the mucin discs to the gels and the work of adhesion ( $W_{ad}$ ) which is the amount of forces involved in the detachment, were calculated by using the provided software, Texture Exponent 32.

For the gels with lower water content (below 40%), the mucin tablets were in contact just with the surface of the gels and they do not penetrate inside the gels. This was due to the high resistance of the gels to the applied force. When the water content increases, the resistance force of the gels to the penetration of the probe decreases. Therefore, the probe entered more easily into the gels.

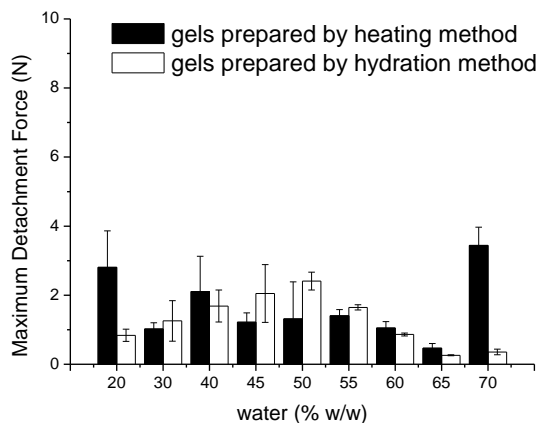


**Figure 3.45** Maximum detachment force of the gels prepared by heating method and by hydration from mucin tablets (tested at room temperature).

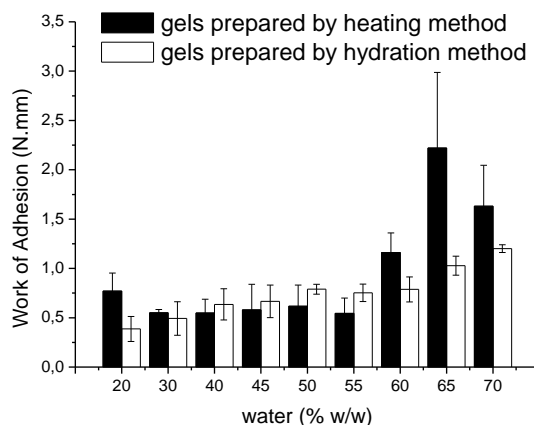


**Figure 3.46** Total work of adhesion of the gels prepared by heating method and by hydration from mucin tablets (tested at room temperature).

The results of the gels prepared by heating and hydration are compared in Figure 3.45 and Figure 3.46. As it is seen in Figure 3.45, for the gels prepared by hydration the maximum detachment force reach a maximum level with the gel with 50% water meaning this gel required the highest detachment force. For the gels prepared by heating the gel with 70% water have the highest value of detachment force. Concerning the work of adhesion, which is the total amount of force required to detach the tablet from the gels, the gels with the highest adhesiveness are the ones with higher water content, in particular the gel with 65% water prepared by heating and the gel with 70% water prepared by hydration Figure 3.46.

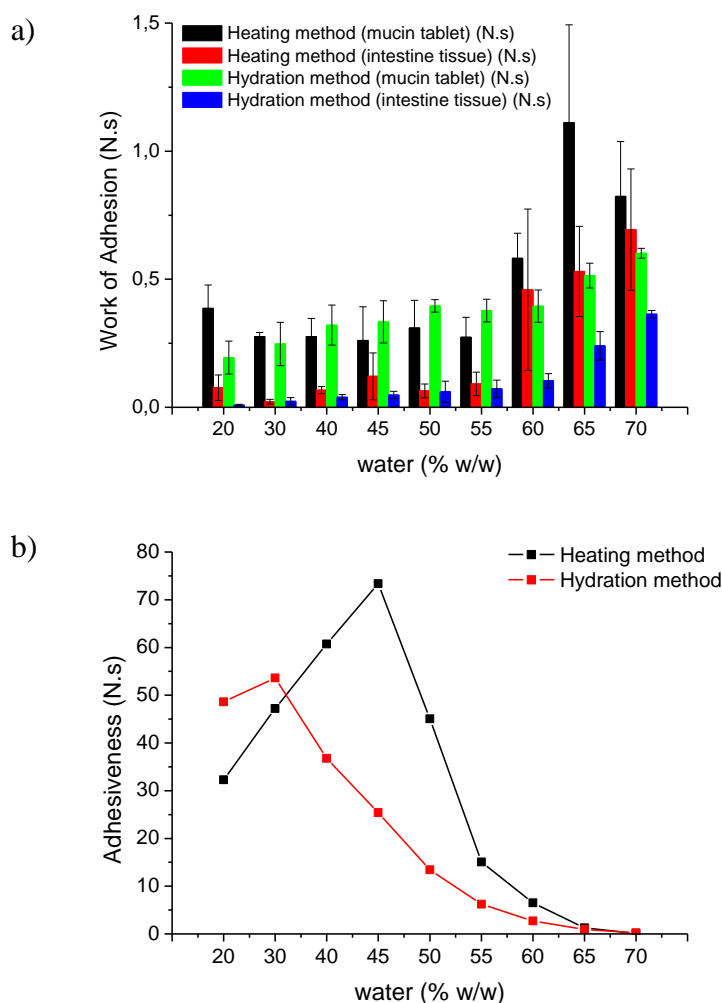


**Figure 3.47** (a) Comparison of the work of adhesion (N.s) determined by adhesive test performed on the gels prepared by heating and hydration methods with mucin tablets and porcine small intestine tissue. (b) The adhesiveness obtained from TPA test for the purpose of comparison of the adhesion of the gels towards biological and non-biological surfaces.

The same experiment performed with mucin tablets was carried out with porcine small intestine tissues. The intestine was wrapped around the probe and fixed with rubber bands. Figure 3.47a gives an overview of the work of adhesion of the gels when put in contact with mucin tablets and intestine tissue (a). The data are compared to the adhesiveness calculated with the TPA test, Figure 3.47b (as described in section 3.4.5.1). Concerning the total amount of force involved in the detachment of the probe from the mucin tablet, the gel with lowest Gelucire content exhibited the highest work of adhesion. For the samples prepared by heating, the gel with 65% water show the higher adhesion to the mucin tablets, followed by the gels with 70% and the 60% water contents. For the gels prepared by hydration, the adhesion increases with increasing water content in the gels and reaches the maximum by the gel with 70% water content. This pattern is the opposite of the one that describes the adhesiveness calculated with the TPA test

(Figure 3.47.b). According to the TPA test, the adhesion to the probe surface is higher in gels with higher content of Gelucire, which may be due because of the stickiness of these gels. The mucoadhesion results suggest that there is an actual interaction between the gels and the mucin, encouraging the statement that the lowest Gelucire concentrations show mucoadhesive properties.

The extent of the bioadhesion of the gels (measured by work of adhesion) drops to lower values when the tests were performed using porcine small intestinal tissue. This may be explained by the composition of the mucus at the surface of the intestinal tissue. Mucus is mainly composed of water (90-98%) and the mucin content is the 2-5% weight [226], This is a much lower concentration of mucin compared to the mucin tablets, which leads to higher level of adhesion when the gels interact with the mucin tablets.

In order to evaluate the extent of the mucoadhesive properties of the Gelucire 50/13, comparison with reported mucoadhesive materials is necessary. However, discrepancy may be found in the literature considering the high variety of in vitro and in vivo tests used to assess the mucoadhesion [227, 228]. The use of different experimental conditions may also lead the different results. For instance, the contact time [162] and the applying force may affect the mucoadhesive properties of the gels [161, 162]. In addition, the interaction between dry materials (i.e. tablets) and the mucosa may differ from the interaction between aqueous formulations (i.e. gels) with mucin tablets as different mechanisms may be involved.

As it was suggested by previous works [45, 229], the maximum force of detachment alone does not provide all the information relatively to the bioadhesion properties of the samples. The mucoadhesion is a more complex phenomenon, which involve not only the adhesiveness but also the deformation and the mechanical properties of the systems. However, it can be used in combination with the work of adhesion or with the detachment profile of the samples. Some researchers suggested a linear correlation between the maximum detachment force and the total work of adhesion [227, 230], however not always a linear relationship can describe the complexity of the adhesiveness. In this work, the linear correlation between the maximum detachment force and the total work of adhesion calculated for the mucin and the intestine tissue was evaluated by performing a Pearson correlation test. A positive linear relationship was obtained by comparing the mean of the total work of adhesion calculated with mucin tablets and the total work of adhesion for the intestine tissues ( $r = 0.977$ ,  $df = 7$ ,  $p < 0.001$ ). However, no significant correlation was found between the maximum detachment force for mucin tablet and for intestine tissue, nor between maximum detachment forces and total work of adhesion ( $p > 0.05$ ).

### **3.5 Conclusion**

The combination of spectroscopic, thermal, rheological and mechanical techniques allows the structural characterisation of the hydrated forms of Gelucire 50/13 (gels). The ATR-FTIR spectroscopic results confirmed that the key components of Gelucire 50/13, such as PEG and PEG esters, largely retain their structural conformation after being formulated into the Gelucire gels. The study demonstrated that the gels (in particular the ones with moderate to high water contents) have complex semi-crystalline/liquid crystalline structures depending on the water content of the gels. The combined SAXS and DSC analysis identified the possible co-existence of different liquid crystalline phases (including lamellar for the gels with low water contents, hexagonal and diamond cubic Pn3m for the gels with intermediate to high water contents) in these gels. The rheological and mechanical properties of the gels are highly water content dependent. The method of preparation has no statistically significant effect on most of the rheological and mechanical parameters measured. The mechanical and bioadhesion tests of gels indicate that the gels with moderate to high water contents exhibit better bioadhesion properties in comparison to the gels with low water content.

## **4 Micro-structural analysis of water distribution in Gelucire 50/13 gels**

### **4.1 Introduction**

As the Gelucire 50/13 gels are made by hydrating the lipid with water, it is important to understand the distribution and behaviour of water in the gels. This knowledge will allow better understanding of physical properties and delivery performance of the gels. The physical and chemical characteristics of water have been widely studied for a long time and many of its properties have been established [231]. Water plays an important role in biomolecular processes, such as solvation of polar groups, and has significant impacts on the structure, function, dynamics and thermodynamics of the systems [232]. The behaviour of water is influenced by the presence of adjacent interfaces with which the water is in contact and which can be inorganic (e.g ions) or organic (such as biomembranes and proteins). Thus the behaviour of water close and at these interfaces can be different from the average behaviour of bulk free water [233]. For example, the behaviour of water in the systems with restricted geometries (such as micro-, nanopores and channels in the system) is markedly different from bulk free water. The possible cause of this has been attributed to the presence of high density interfaces in the close neighbourhood micro-environment, which reduces the degrees of freedom of water molecules at the interfaces [234].

In micro-structured materials, such as microemulsions and liquid crystals, several kind of water can be identified depending on the interactions of water molecules with the interfaces present in the material. They can be roughly divided into three types: bulk free water, interfacial water and internal or bound water (chemically-bound water) [232]. One way to distinguish the different types of water is by considering their behaviour at low temperature (below the freezing point of bulk free water). The bulk free water freezes at about 0°C with a fixed heat capacity. The interfacial water is defined as the water molecules present closely at the interfaces formed by other systems molecules, such as the oleic phase of a surfactant, polymeric and macromolecular. The interfacial water melts at around -10°C [233]. The bound water is defined as the water molecules that chemically bonded to the interfaces. The behaviour of bound water is strongly influenced by the interface, which leads to different thermodynamic properties of this type of water. Generally, the bound water does not freeze at sub-zero temperature, thus is referred to as non-freezing or non-freezable water [232].

Calorimetric methods are often used to distinguish these different types of water (free and interfacial) present in a material. For instance, the study of the freezing behaviour of non-bulk

water allows the properties of water in microporous materials, gels, biological tissues or food to be determined [232].

## **4.2 Objectives**

This chapter will focus on investigating the behaviour of water in Gelucire 50/13 gels using a combination of imaging technique, thermal and relaxometry NMR analysis. This further helps the determination of the microstructure of the gels, which will provide insights into the performance of the gels as potential carrier systems for delivering proteins and peptides. The detailed aims of this part of study are listed below:

- Visualisation of the interior microstructure of the freeze-dried gels using SEM, which may give some indications of the possible interior arrangement of the gels before freeze-drying
- Investigation into the microstructure of the gels via studying the freezing behaviour of water in the gels using thermal analysis
- Further investigation into microstructure of the gels via studying the diffusion behaviour of the water molecules in the gel using NMR relaxometry

## **4.3 Materials and Methods**

Stearoyl macroglycerides (Gelucire® 50/13, Gattefossé, France) gels were prepared using Milli-Q water (ultrapure, Type I, water) following the procedure described in Chapter 2, section 2.3.1.

### **4.3.1 Imaging analysis of freeze-dried gels**

Gels prepared by heating and hydration methods as described in section 2.31 were freeze-dried using a bench-top freeze-drier (VirTis adVantage 2.0, SP Scientific, Gardiner, NY, USA). In the thermal treatment step, the shelf temperature was set at -40 °C and isothermed for 120 minutes. The primary drying phase was carried out in sequential temperature steps of 120 minutes each step, from -35 °C to 25 °C with 5 °C increment between each step at the chamber pressure of 200 millitorr. The secondary drying was set at 25 °C for 60 minutes. After freeze-drying, the gels were stored in a desiccator at 0% RH prior to the examination with SEM. The cross-sections of the freeze-dried gels were examined by SEM, as described in section 2.4.8.1. Approximately 10 different locations of each freeze-dried gel sample were examined.

### 4.3.2 Differential Scanning Calorimetry (DSC)

Conventional DSC was performed under nitrogen flux with purge rate of 50 ml/min. A full instrument calibration was performed prior to the sample runs. The cell resistance and capacity calibrations (Tzero and baseline) were performed with empty cells and sapphire disks, respectively at 20 °C/min from -150 °C to 400 °C. Furthermore, the cell constant calibration using indium as standard and temperature calibrations using Milli-Q water ( $T_m=0$  °C) and n-octadecane ( $T_m=28.2$  °C) were performed. Aluminium hermetic pans (Perkin Elmer, USA) were used for all samples and the average sample weight of 2-5 mg was used through the study.

The gels samples with 10% to 90% (w/w) water contents prepared by heating and hydration methods were equilibrated at -50 °C for 15 minutes, followed by heating up to 25 °C, after 2 minutes of isothermal at 25 °C. Two scanning rates of 5°C/min and at 2 °C/min were used in this study in order to examine the heating rate effect on the freezing behaviour of water in the gels. The heat of fusion of ultrapure water (Milli-Q grade) was experimentally determined by treating the water with the same temperature programme described above. It was found that the heat of fusion of pure water is equal to 334.07 J/g at the rate of 5 °C/min and equal to 346.47 J/g at the rate of 2 °C/min. All experiments were performed in triplicate.

### 4.3.3 Relaxometry NMR

The gels prepared by heating method were analysed using a bench-top NMR (Maran Ultra, Resonance, Oxford Instruments) equipped with a DRX console, which generates the pulse gradients as described in section 2.4.6.2. The frequency and the magnetic field strength applied are 23 MHz and 0.54 T, respectively. Prior to each experiment, the system parameters were set up using the Free Induction Decay (FID) pulse sequence. The parameters to be set up were the offset, 90° pulse length, 180° pulse length and the receiver gain. The frequency of the radio frequency pulse is described by two parameters, the spectrometer frequency and the offset. Once the correct frequency is established, the right pulse length to obtain the largest NMR signal has to be set. The signal is proportional to the  $\sin\theta$ , where  $\theta$  is proportional to the pulse length. When  $\theta = 90^\circ$  the maximum signal amplitude is achieved. The receiver gain (RG) is the amount of amplification that is applied to the NMR signal before being collected. The RG depends on the instrument and the sample. These system parameters are sample dependent [235]. For all the experiments, a relaxation delay (RD) time equals to 10 seconds has been applied, except for the stimulated echo tests. The RD is the time between consecutive scans and it should be long enough to allow the system to return to the equilibrium state. RD depends on the sample spin-lattice relaxation time ( $T_1$ ) of each sample and usually is 5 times of the  $T_1$  [235].

Four scans were performed for each sample. Once the system parameters have been set, further pulse sequences were performed.

#### **4.3.3.1 Carr-Purcell-Meiboom-Gill (CPMG) sequence**

The CPMG pulse echo sequence is widely used to measure spin-spin relaxation time ( $T_2$ ). The pulse sequence used in this study has been shown in section 2.4.6.1.1. In order to perform the CPMG sequence, further parameters were set, the number of echoes, which is the number of rephasing pulses applied, and tau ( $\tau$ ) which is the time between consecutive pulses [235]. The number of echoes varies with the sample analysed and it increases with water content from 2048 (for gels with 10% and 20% water) to 16384 (for gels between 70% and 90% water). Tau ( $\tau$ ) was fixed to 300  $\mu$ s. The CPMG echo decay data were deconvoluted with an inverse Laplace transform by using WINDPX software package.

#### **4.3.3.2 Inversion Recovery pulse sequence (Inv-CPMG)**

The Inv-CPMG sequence was performed to confirm the assignment of the protons. The Inv-CPMG sequence consists in adding the inversion recovery step [ $180^\circ - \tau_1$ ] in front of a CPMG sequence (see section 2.4.6.1.2). By adding this step, the longitudinal  $T_1$  can be determined. The independent variables are the recovery time which is the  $\tau_1$  and the CPMG acquisition time which is the spin-spin relaxation time  $T_2$  (which is equal to  $2n \cdot \tau$  with  $n > 1$ ). The  $T_1$  was acquired with 64 steps. The  $T_2$  dimension was acquired with any  $\tau$  spacing according to the sample. A CPMG sequence was performed first and then the inversion recovery sequence was applied by following a script written using MatLab (MathWorks, Massachusetts, USA). The data were analysed by using MATLAB software package, through which the peaks were identified and integrated. The integration of the peaks gives the  $T_1$  and  $T_2$  values.

#### **4.3.3.3 Pulsed Field Gradient NMR**

Through the CPMG and Inv-CPMG sequences, the  $T_1$  and  $T_2$  relaxation times of the protons have been determined in the attempt to distinguish the aliphatic from the water protons. The application of magnetic field gradients to a spin echo sequence can be used to measure the displacement of the spins through their Larmor frequency [185]. Therefore, this non invasive technique is one of the most valuable way to measure the translational motion of the molecules [185, 236]. The most used sequence is the pulsed gradient spin echo (PGSE), which is a modified version of the Hahn spin echo pulse sequence [ $90^\circ - \tau - 180^\circ - \text{echo}$ ] [188]. In the PGSE sequence, two equal gradient pulses are included into each period  $\tau$  of the spin-echo sequence

[185]. The first gradient pulse applied locate the starting position of the spins, while the second one, after a determined time  $\Delta$ , locate the final position [236].

The echo attenuation,  $E(q)$  is a function of two parameters, the diffusion time  $\Delta$ , which is the pulse gradient separation time, and the gradient pulse area, which is connected to the wavevector  $q$ , described by the following equation

$$q = (2\pi)^{-1} \gamma \delta G \quad \text{Equation 4.1}$$

where  $\gamma$  is the gyromagnetic ratio (for protons H,  $(2\pi)^{-1} \cdot \gamma = 2.675 \times 10^8 \text{ rad} \cdot \text{s}^{-1} \cdot \text{T}^{-1}$  or  $42.576 \text{ MHz} \cdot \text{T}^{-1}$ ),  $\delta$  is the pulsed gradient duration and  $G$  is the gradient strength. The value  $q$  is referred to as the wavevector, similarly to the wavevector in scattering techniques such as the neutron scattering. The magnitude of the vector is equal to  $\gamma \delta G$  and the direction is given by the gradient  $G$ . Through  $q$  it is possible to determine the probability of finding the spins displacements from the original position  $r$  to a new position  $r'$  [188]. The displacements of the nuclear spins within a diffusive material (such as the Gelucire 50/13 gels) are influenced by the collision, which can be enhanced by applying the NMR relaxation sequence (such as the PGSE). Under these circumstances, it is possible to determine the pore size of the material. Furthermore, knowing the diffusive properties of the water molecules, it enables the determination of the geometries of the barriers and can provide information on the diffusive and eventual restrictive barriers [189]. In the case of free diffusion where no barriers are involved, the echo attenuation,  $E(q)$ , is given by the following equation

$$E(q) = \exp\left(-4\pi^2 q^2 D \Delta\right) \quad \text{Equation 4.2}$$

The logarithmic plot of the attenuation of the signal is a straight line, whose slope gives the diffusion coefficient [188]. In the case of restricted diffusion, a linear plot is not obtained, but a more complex pattern is observed and the degree of attenuation of the echo tends to zero. In the case of permeable boundaries, an intermediate behaviour can be observed.

The PGSE sequence can be coupled with the CPMG spin echo (see section 4.3.3.3.1). A modified pulse sequence can also be used, consisting in applying three  $90^\circ$  pulses that produce a stimulated echo (PGSTE, see section 4.3.3.3.2).

#### 4.3.3.3.1 CPMG Pulsed Gradient Spin Echo sequence (CPMG-PGSE)

CPMG-PGSE experiments were performed on the gels with selected water contents (70% and 80% water content). The CPMG sequence ( $90^\circ [-\tau-180^\circ]_n$ ) is inserted in front of the PGSE sequence:  $[90^\circ-G-180^\circ-G]$ . The CPMG-PGSE sequence used in this work is shown in section 2.4.6.1.3. The independent variables for this sequence are CPMG time  $T_2$ , which is given by  $2n \cdot \tau_I$ , the diffusion time  $\Delta$ , and the pulsed gradient area, which is given by Equation 4.1.

The CPMG-PGSE sequence consists of performing a CPMG test (as described in section 4.3.3.1 by using the same settings) followed by a PGSE sequence. In this case, a field gradient  $G$  was applied along the  $y$ -axis. The amplitudes of the gradients vary from 0 to 20000 RI units (which is from 0 to  $2.406 \text{ T} \cdot \text{m}^{-1}$ ) in 20 steps. The number of echoes applied varies in 20 steps from 0 to the number of echoes defined in the CPMG sequence. The CPMG tau ( $\tau_I$ ) is equal to  $300 \mu\text{s}$ , the PGSE  $\tau$  is equal to  $12000 \mu\text{s}$  which is also the pulse gradient separation  $\Delta$ . The pulse gradient duration,  $\delta$ , is equal to  $1500 \mu\text{s}$ . The  $T_2$  relaxation time and the  $q$ -vector domain were analysed by performing an inverse Laplace transformation through MATLAB® software (MathWorks, Massachusetts, USA).

#### 4.3.3.3.2 Stimulated echo diffusion sequence (PGSTE diffusion)

Another technique for studying diffusion is the stimulated echo (PGSTE) [185]. The sequence contains three  $90^\circ$  pulses and the echo after the third pulse is called stimulated echo. The typical sequence used in this study is shown in section 2.4.6.1.4.

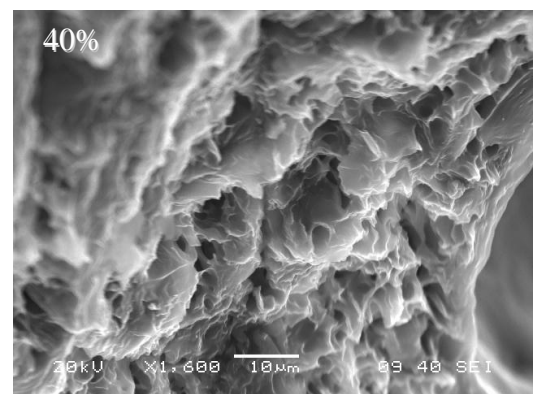
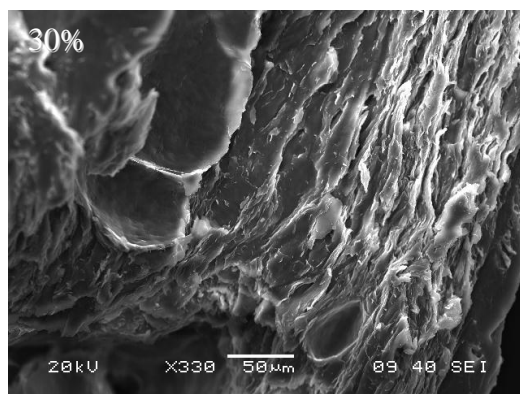
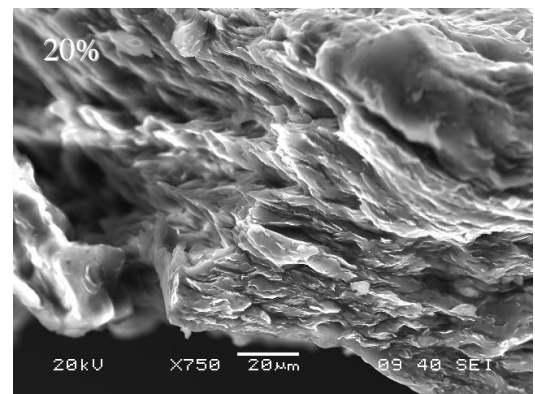
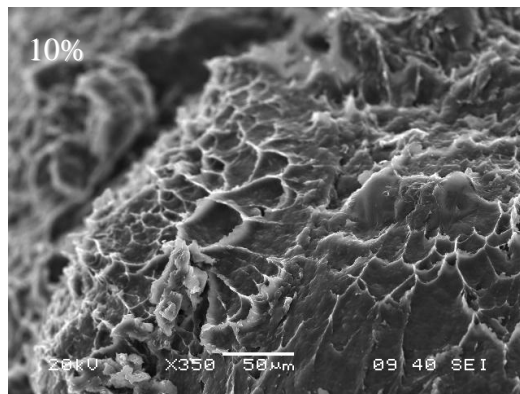
As for the CPMG-PGSE sequence, a field gradient along the  $y$ -axis was applied. The data were acquired by using a script, which used two lists of defined  $G$  amplitudes and  $\Delta$  values. For each  $G$  value, the script went through all the values of  $\Delta$ . The  $G$  values progressed in 20 steps from 0 to 20000 RI units (from 0 to  $2.406 \text{ T} \cdot \text{m}^{-1}$ ). The  $\Delta$  went from 50 ms to 500 ms. The pre-gradient delay ( $D_1$ ) was set as  $100 \mu\text{s}$ , the gap between  $90^\circ$  pulses ( $D_2$ ) should be greater than  $D_1 + \delta + Aq/2$  and it was set at 7 ms, where  $Aq$  is the acquisition time. The pulse gradient duration ( $\delta$ ) was equal to  $300 \mu\text{s}$ . The relaxation delay ( $RD$ ) time was fixed at 2 seconds and it is calculated accordingly to the following equation

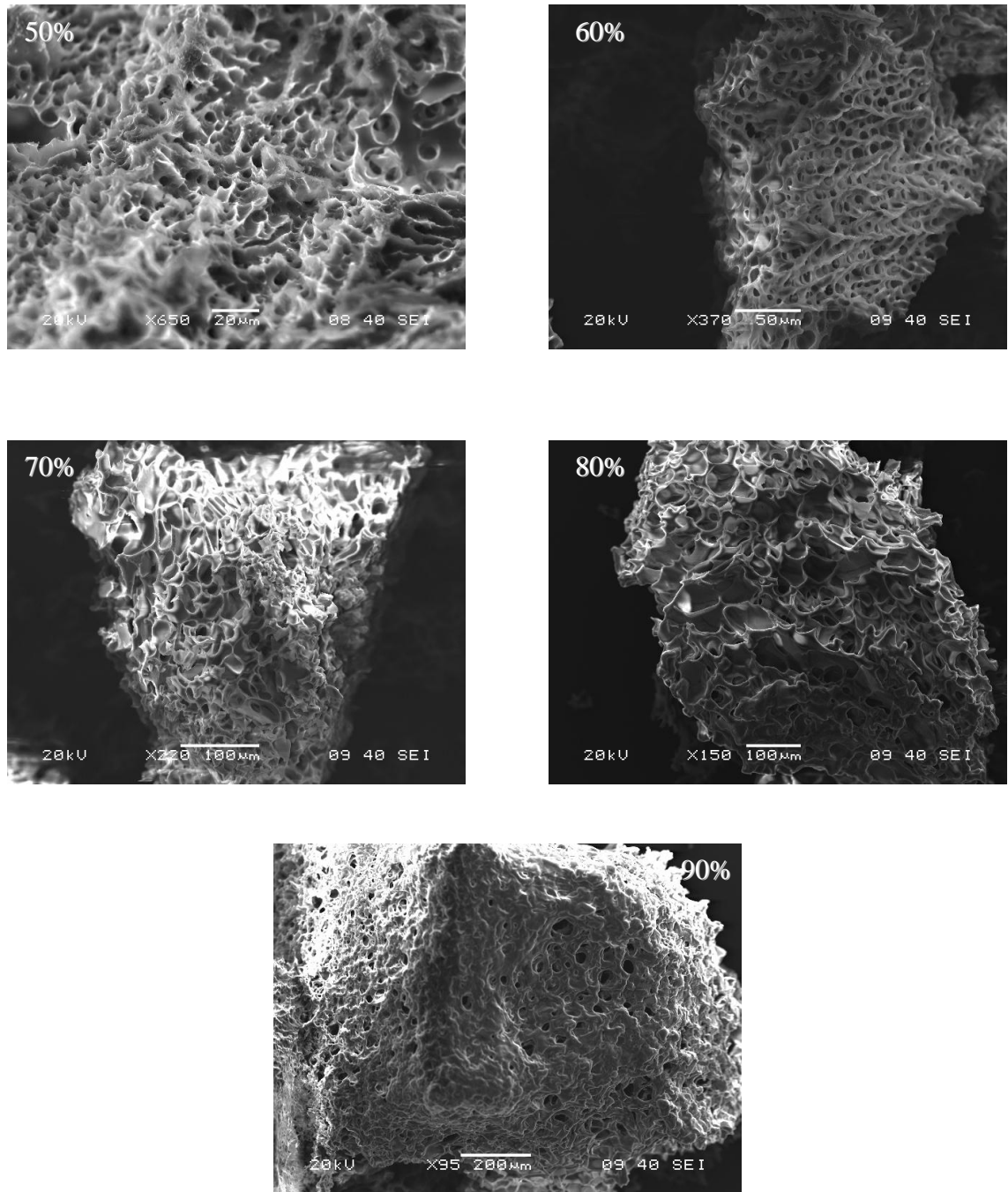
$$RD = 2 \cdot (\Delta + D_2 + Aq/2) \quad \text{Equation 4.3}$$

## 4.4 Results and discussion

### 4.4.1 Interior microstructure of freeze-dried gels

In order to visualise the microstructure of the gels prepared by heating and by hydration methods, the samples were freeze dried and examined by SEM. The freezing temperature (-40 °C) has been selected in order to be lower than the temperature where both the bulk water and the interfacial water freeze, according to the information obtained from the DSC tests. The success of the freeze-drying process was assessed by using DSC. The freeze-dried gels were tested with the same thermal programme described in section 4.3.2. In the heating cycle from -50 °C to 25 °C no peaks were detected, suggesting that the water was removed from the gels. No peaks were found in the following cooling cycle from 25 °C to -50 °C, also confirming no significant amount of residue water present in the freeze-dried gels (data not shown).

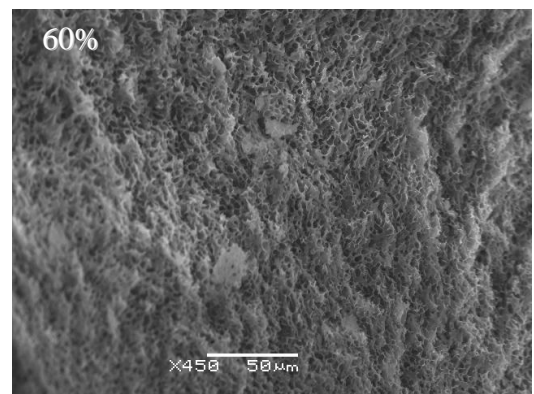
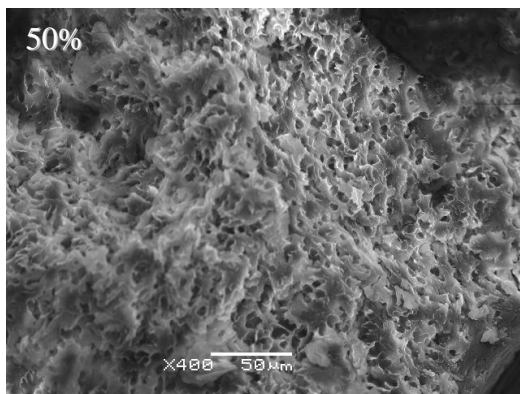
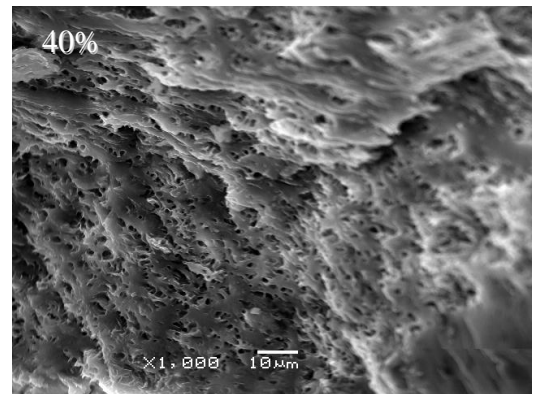
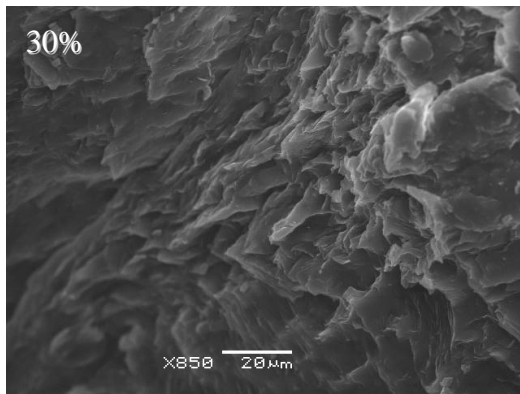
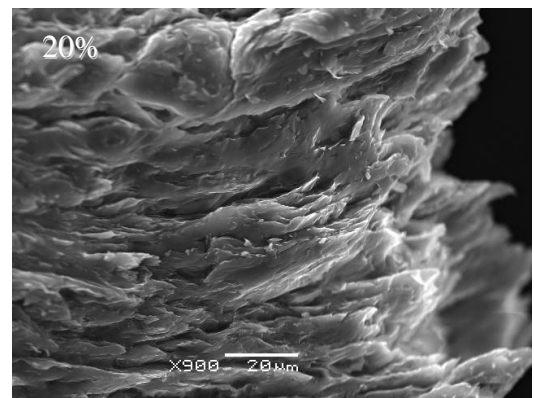
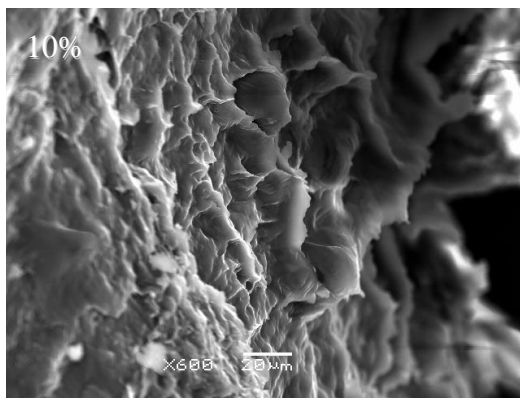




**Figure 4.1** SEM images of the freeze-dried gels originally prepared by heating method with 10% to 90% water content (w/w).

The SEM images of the freeze-dried gels prepared by heating method are shown in Figure 4.1. The images show a porous network interior structure indicating the possible presence of water channels and pockets in the gels before freeze-drying. The porous structure reflects the freeze-concentrated solution [237]. The images (Figure 4.1) show a structure with air filled voids, which correspond to the spaces occupied by the ice prior to the primary drying. The pores can be clearly seen in the gels with water contents above 50% (Figure 4.1). For the gels with lower water contents (10%, 20% and 30% water content), no uniform pores can be observed, but a layered structure can be seen. In the gel with 40% water content, both layered structure and

porous network are visible. The pore size increases with increasing the water content from 50% to 90% (as seen in Figure 4.1). For every sample, at least 10 SEM images were taken across the freeze-dried gel to evaluate the homogeneity of the samples and the average size of the pores was measured using imaging software. In the gel with 50% water content, the pore size is around 6  $\mu\text{m}$ , while in the gel with 60% water is approximately 7  $\mu\text{m}$ . The size is bigger in the gel with 70% water content (~18  $\mu\text{m}$ ). All the gels are relatively homogeneous, except for the gels with 80% and 90% water contents, which seem to form aggregates as a result of the freeze-drying process. Other sites of the gel with 90% water show collapse of the structure (image not shown). This may be due to the low lipid content in the gel, which leads to lack of ordered structure.



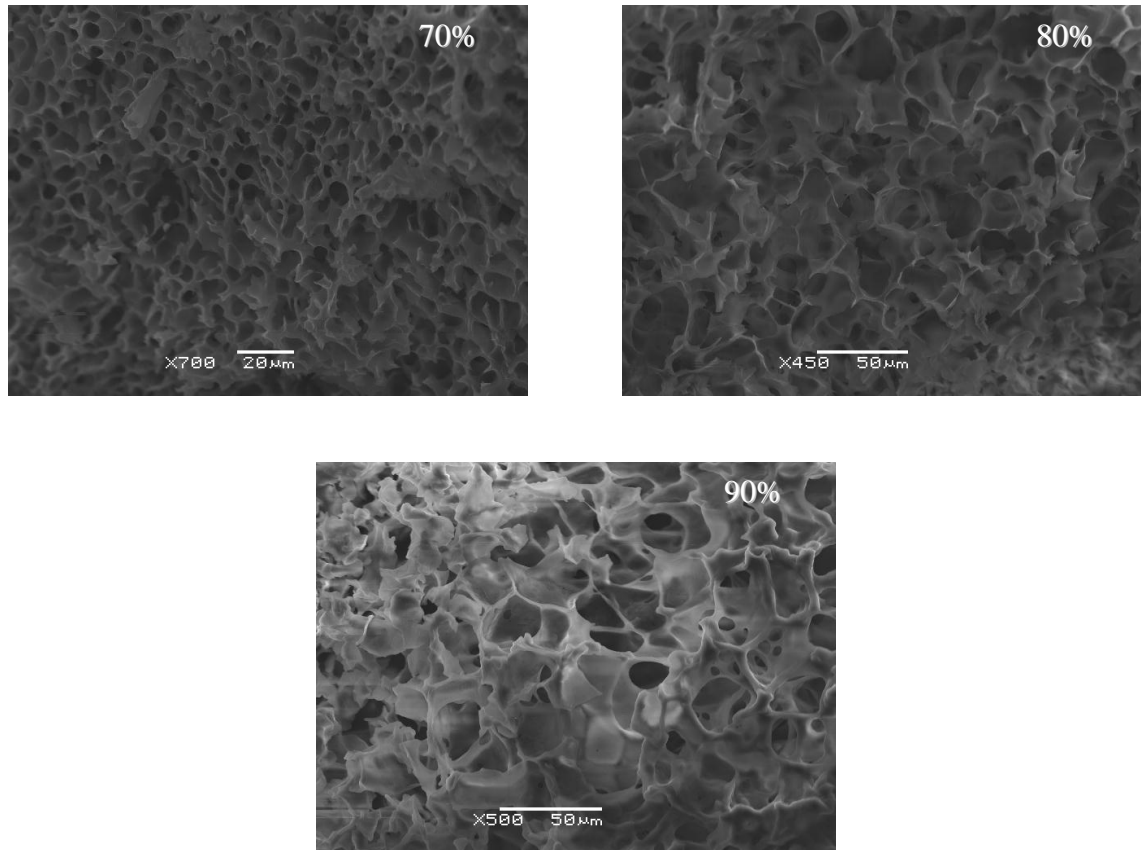


**Figure 4.2** SEM images of freeze-dried gels originally prepared by hydration with 10-90% water content.

The SEM results of the gels prepared by hydration method are largely similar to the gels prepared by heating (as seen in Figure 4.2). The gels between 10-30% water contents show a layered structure, whereas the gels with 40% water and above are characterised by a porous structure. Small pores are visualised in the gels with 40-60% (1.5  $\mu\text{m}$  for 40% gel, 3.5  $\mu\text{m}$  for 50% gel and 3  $\mu\text{m}$  for 60% gel), which are slightly smaller than the pore size determined in the gels with 50% and 60% water prepared by heating method (6 and 7  $\mu\text{m}$ , respectively). The size increases with the water content. The average pore sizes are 5  $\mu\text{m}$ , 12.5  $\mu\text{m}$  and 21  $\mu\text{m}$ , for the gels with 70%, 80% and 90% water, respectively. The gel with 70% water prepared by hydration show a smaller size compared to the one prepared by heating method (18  $\mu\text{m}$ ). The structures of gels with 80% and 90% water contents are collapsed in the majority of the domains scanned with the SEM. However, in the image shown in Figure 4.2, a porous structure with some intact plates for the gels with 80% and 90% water content is still visible. The interior is more structured for these gels with high water contents compared to the gels prepared by heating method.

#### 4.4.2 Determination of free water content using DSC

In this work, the percentage of bulk free water in the gels prepared by hydration and by heating method was determined using DSC following the procedure described in section 4.3.2. The enthalpy ( $\Delta H$ ) of the endothermic melting peaks at 0 °C ( $\pm 5$  °C) was measured and used to calculate the content of bulk free water (%) in the gels using the following equation

$$W_F = \frac{\Delta H_F(\text{exp})}{\Delta H_F} \times 100 \quad \text{Equation 4.4}$$

where  $W_F$  is the free water concentration (% w/w),  $\Delta H_F(\text{exp})$  is the measured enthalpy value of the endothermic peak at 0 °C,  $\Delta H_F$  is the heat of fusion of pure water, which was experimentally determined as described in section 4.3.2.

For the gels prepared by heating method at a scanning rate of 5 °C/min, no peaks were found in the gels with 10%, 20% and 30% water contents (data not shown). This suggests that the water in these gels is largely bound water to the interfaces within the microstructure of the gels. The gel with 40% water shows a main endothermic peak at -13 °C (peak temperature), which is likely to be associated with the presence of interfacial water. The gel with 50% water shows a main endothermic peak at -7 °C, which is lower than the one associated to the free water. Therefore it is also more likely to be considered as the interfacial water. In the gels with 60% water, the peaks at -5 °C can be seen. As this is close to 0 °C, it is likely to be largely associated with the presence of a significant amount of free water in this gel (shown in Figure 4.3). For the gels with 40% to 60% water contents a shoulder peak at temperatures between -20 to -25°C can be observed (see inset in Figure 4.3). These peaks are at much lower temperatures than the main peak for each sample. They may still be considered as interfacial water within the ordered microstructure of the gels, but clearly have different thermal behaviour from the interfacial water represented by the main endothermic transitions at higher temperatures (-5 °C to -13 °C). However, the presence of these second populations of interfacial water (with much lower melting temperatures) within these gels may indicate that they are entrapped in more restricted micro-environment and have closer contact with the Gelucire interfaces. This suggests that there may be mixed structures in these gels, such as layered planes, pore, and channels. This agrees well with the SAXS results presented in Chapter 3 and the SEM results discussed in section 4.4.1.

The gels with 70%, 80% and 90% water contents show a main endothermic peak close to 0°C. For these gels, a small broad shoulder peak at lower temperature (with peak temperatures between -20 to -10°C) can be seen in Figure 4.3. These results confirmed the presence of

significant amounts of bulk free water in these gels and small amounts of interfacial water entrapped in microstructure of the gels.

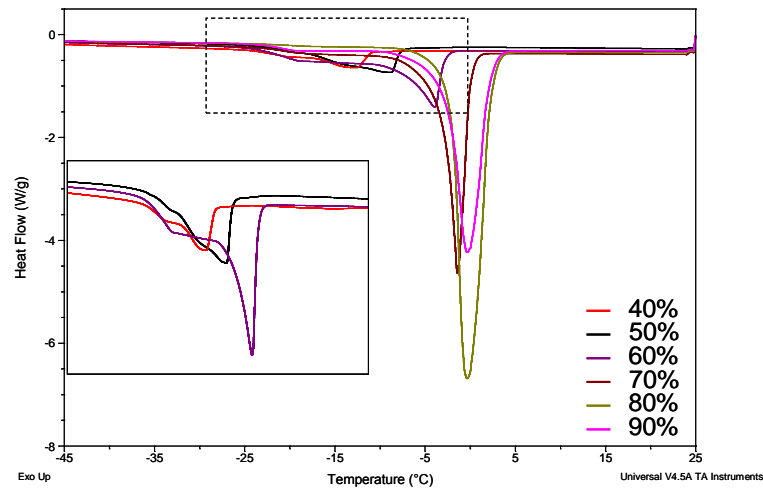


**Figure 4.3** DSC results of the gels prepared by heating method at a scanning rate of 5 °C/min. An enlarge view of the peaks inside the dashed rectangle is shown in the inset.

A lower scanning rate (2 °C/min) was also used in order to evaluate the effect of the heating rate on the temperature peak. In the tests performed at this rate, no peaks were found for gels with water content below 40% (data not shown). As seen in Figure 4.4, the gel with 40% water showed a peak at -12 °C, which can be associated with interfacial water and is consistent with the tests performed at 5 °C/min. On the contrary, the gel with 50% water shows a peak at -6.5 °C, which is very close to the one obtained performing the test at 5 °C/min. In fact, little effect of heating rate on the peak temperatures of the main transitions was observed for all gels. The main endothermic peaks shift towards 0 °C as the water content further increase to above 60%. Similar to the results obtained using 5 °C/min scanning rate, a shoulder peak at lower temperature (-20 to -10 °C) is visible in the gels with 40% to 60%. The gels with 70% to 90% water contents exhibited similar behaviour to the results obtained using 5 °C/min scanning rate. A main transition at 0 °C and a broad shoulder peak at a lower temperature can be seen in the DSC results of these samples, indicating the co-existence of bulk free water and interfacial water within the structure of these gels.

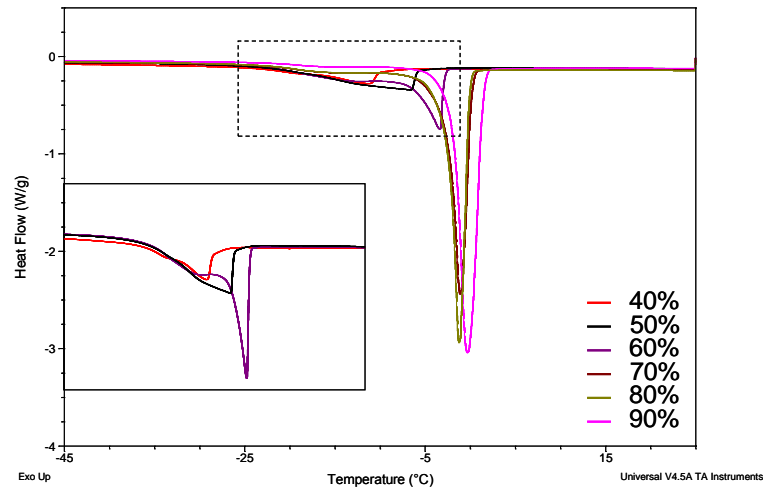


**Figure 4.4** DSC results of the gels prepared by heating method determined at the scanning rate of 2°C/min. An enlarge view of the peaks inside the dashed rectangle is shown in the inset.

Concerning the samples prepared by hydration method, the DSC results of the gels scanned at 5°C/min showed similar results to the ones obtained for the gels prepared by heating method. No peaks were found for water contents below 30% water (data not shown). The 30% and 40% gels showed a broad peak at -13 °C, which may be associated with the interfacial water. For the rest of the gels with higher water contents, the main endothermic peak temperature increases with water content, from -9.5 °C for the gel with 45% water to almost 0 °C for the gel with 90% (Figure 4.5). For the gels with water contents from 45% to 90%, a shoulder peak at lower temperature (between -18 to -10 °C) than the main endothermic peak is evident. These shoulder peaks are likely to be associated with the small amount of interfacial water entrapped in the gel microstructure. These results confirmed the microstructure of the gels prepared by hydration method is largely similar to the gels prepared by heating method. However, the presence of melting peak in the gel with 30% water content prepared by hydration method may indicate that the mixing and the homogeneity of the gels prepared by heating may be slightly higher than the gels prepared by hydration method, as the gel with 30% water prepared by heating showed no melting (Figure 4.4).

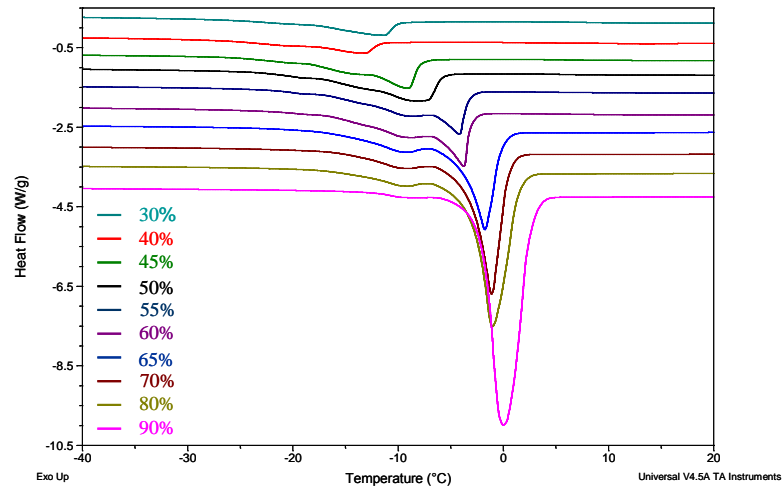


**Figure 4.5** DSC results of the gels prepared by hydration method determined at the scanning rate of 5 °C/min.

The DSC results of the gels prepared by hydration method, tested at 2 °C/min, show similar results to the ones obtained using a scanning rate of 5 °C/min. For the gels with 10% and 20% water contents, no melting peak can be observed (data not shown), while the gel with 30% water shows a peak at -16 °C. The DSC results of the gels with 40%, 45% and 50% waters content show main peaks associated with the interfacial water at temperatures of -13, -10 and -9 °C, respectively, and shoulder peaks at lower temperatures. The peak associated with the bulk free water is evident in the gels with 55% water content and above (Figure 4.6).

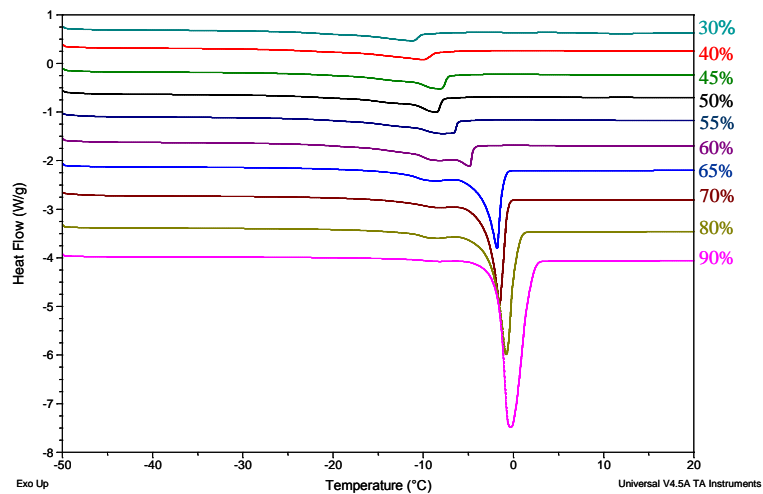


**Figure 4.6** DSC results of the gels prepared by hydration method, determined by DSC at 2 °C/min.

**Table 4.1** Free water contents ( $W_F$ , %) calculated for the gels prepared by heating and hydration methods (n=3).

Gel samples (% water)	Heating method				Hydration method			
	5°C/min		2°C/min		5°C/min		2°C/min	
	$T_p$ (°C)	$W_F$ (%)	$T_p$ (°C)	$W_F$ (%)	$T_p$ (°C)	$W_F$ (%)	$T_p$ (°C)	$W_F$ (%)
10	NF	NF	NF	NF	NF	NF	NF	NF
20	NF	NF	NF	NF	NF	NF	NF	NF
30	NF	NF	NF	NF	-12.4±1.0	NF	-16.23±5.06	NF
40	-13.4±0.6	NF	-11.9±0.6	NF	-13.2	NF	-12.77±3.85	NF
45	NA	NA	NA	NA	-9.5±1.4	NF	-10.19±2.28	NF
50	-7.0±2.1	NF	-6.5±1.2	NF	-8.3±0.4	NF	-8.63±0.69	NF
55	NA	NA	NA	NA	-4.5±0.4	27±0.8	-6.01±1.67	22±3.3
60	-4.2±1.0	26±2.4	-5.2±2.9	23±8.1	-4.9±1.6	24±4.2	-4.9±0.03	23±2.0
65	NA	NA	NA	NA	-3.0±1.4	34±10.0	-2.33±0.81	37±7.3
70	-1.4±0.2	39±4.2	-1.3±0.4	38±15.7	-1.5±0.3	44±2.2	-1.67±0.21	45±1.6
80	-0.8±0.6	48±0.8	-1.1±0.1	40±3.8	-0.5±0.5	58±2.8	-0.7±0.30	61±5.0
90	-0.5±0.1	70±4.1	-0.7±0.5	45±23.3	-0.1±0.1	73±1.6	-1.09±1.19	81±1.8

NF stands for “not found”

NA stands for “not analysed”

The content of free water ( $W_F$ ) was calculated for each gel according to the Equation 4.4. The results are summarised in Table 4.1. The data were then plotted against the water content of the gel and is shown in Figure 4.7 and Figure 4.8. The plots compare the free water content in the gels prepared by heating and hydration methods at the different scanning rates (5°C/min and 2°C/min). Overall, the amount of free water increases with the water content of the gels for the gels with 55% to 90% water in the gels prepared by hydration and for the gels with 60% to 90% water content prepared by heating method.

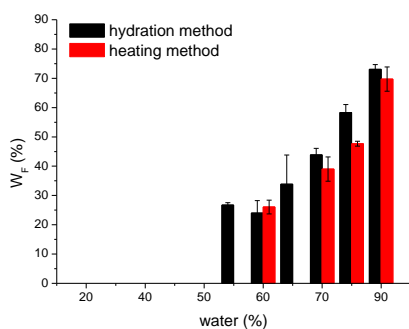


Figure 4.7 Free water ( $W_F$ ) calculated at 5°C/min.

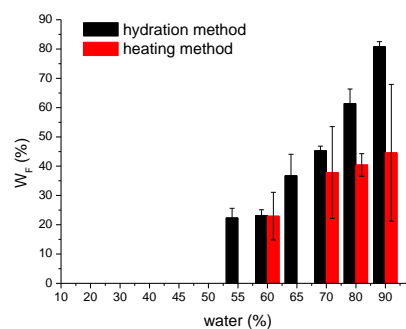


Figure 4.8 Free water ( $W_F$ ) calculated at 2°C/min.

As seen in Figure 4.7 and Figure 4.8, bulk free water is clearly evident in the gels with 55% to 90% water content prepared by both methods and analysed at both scanning rates. However, the actual amount of free water content in the gels is affected by the method of preparation and the heating rate used for the DSC test. When the gels were tested using a scanning rate of 5 °C/min, for the gels with 60% to 90% water, the calculated free water content increases with increasing the water concentration in the gel. It is 26%, 39%, 48% and 70% (w/w) for the gels with 60%, 70%, 80% and 90% prepared by heating, and 24%, 44%, 58% and 73% for the gels with 60%, 70%, 80% and 90% water prepared by hydration, respectively. It can be seen that the bulk free water contents in the gels prepared by hydration method are higher than the ones in the gels prepared by heating method. The reason why the gels prepared by hydration show higher content of free water compared to the gels prepared by heating lies in the preparation method itself. In the heating method, there is a more homogeneous mixing of the aqueous and oleic phases, which promotes a higher level of water-lipid interaction and possibly more complete formation of ordered microstructure.

When the DSC results of the gels tested at 2 °C/min were analysed, the differences in the amount of bulk free water measured for the gels prepared by hydration and heating are even more significant than the results of the tested run at 5 °C/min. At 2 °C/min, for the gels prepared by heating method with 70%, 80% and 90% water contents, the amount of bulk free water

measured is equal to 38%, 40% and 45%, respectively. These values changed to 45%, 61% and 81% for the gels prepared by hydration.

Comparing the results of the gels prepared by heating, but obtained at the two scanning rates, it is evident that the rate has more effect on the measured free water content, for the gels with high water contents (80% and 90%). At 2 °C/min, the amounts of free water measured are 40% and 45% for the gels with 80 and 90% water contents. While at 5 °C/min, the values increased to 48% and 70%, respectively. Even though it is worth mentioning that for the gel with 90% water a higher standard deviation is registered.

In summary, DSC was proven to be a useful semi-quantitative method to study the physical state of water in the Gelucire 50/13 gels. The results not only give insights on the microstructure of the gels, but also provide information on the effect of preparation methods on the microstructure of the resulted gels

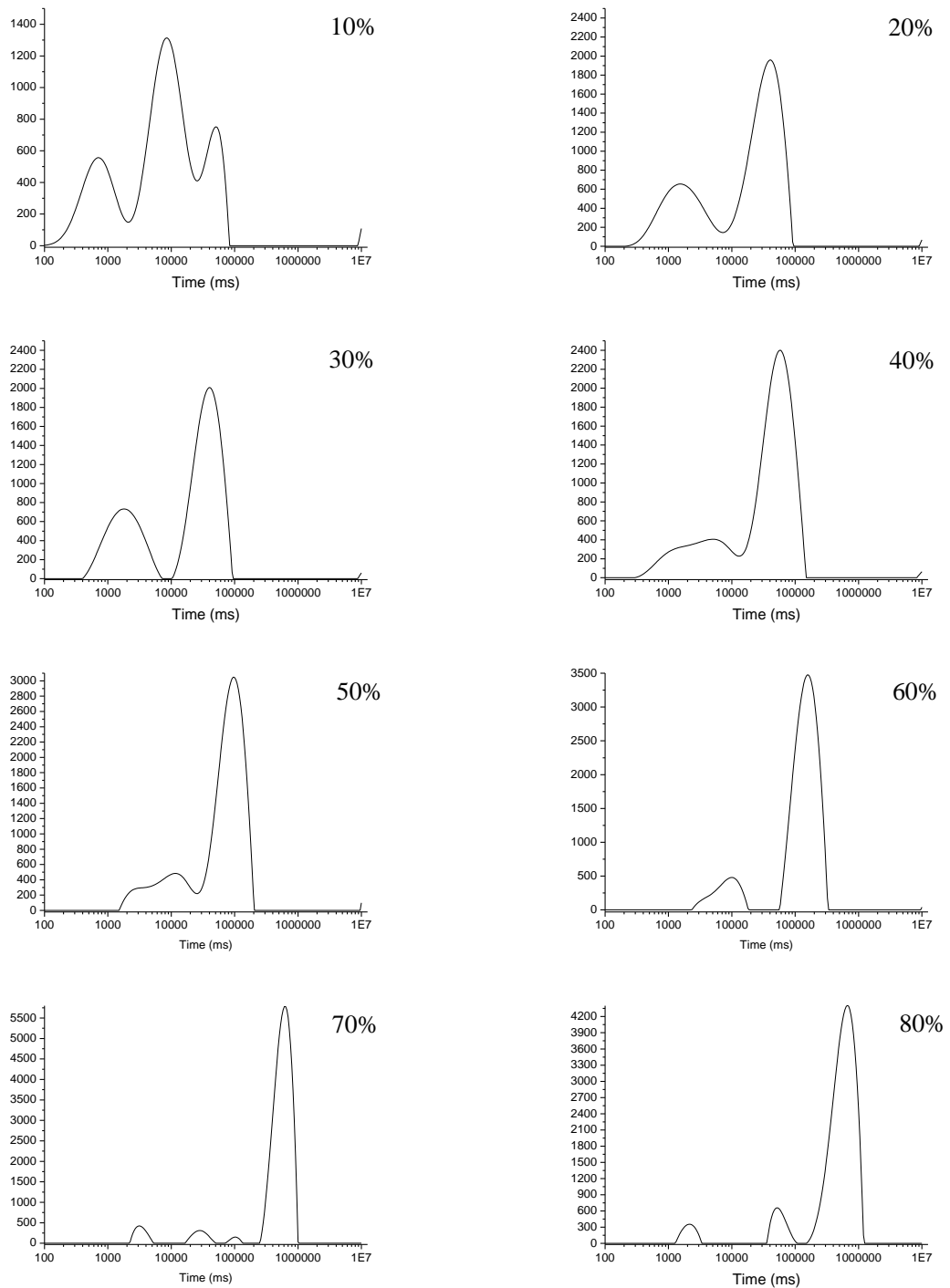
#### **4.4.3 Molecular understanding of water distribution in the gels studied by Relaxometry NMR**

An overall understanding of the microstructure of the gels can be achieved using the visual results obtained with SEM and the quantitative analysis with DSC in combination with the SAXS results discussed in Chapter 3. However, the bound water cannot be directly measured by thermal analysis as no melting can be detected [233]. Furthermore, the limit of detection of DSC is limited and low quantity of interfacial water may remain undetected [238]. In order to obtain molecular level understanding of the interactions of water with Gelucire in the gels, the more powerful NMR relaxometry was used. This method allows the detection of both the free water and the restricted water by characterising the diffusion behaviour of water in each gel.

In this study, only the gels prepared by heating method were analysed with the NMR, as with this method of preparation is expected to obtain a more homogeneous gels.

4.4.3.1 Carr-Purcell-Meiboom-Gill (CPMG) sequence

The CPMG sequence is a simple and routinely method to assess the transverse relaxation times in different kind of systems, such as water-in-oil emulsions [239, 240] and hydrogels [238]. The gels with water content between 10 and 90%, prepared by heating method were analysed according to the CPMG sequence described in section 4.3.3.1 and  $T_2$  one-dimension graphs are obtained, as seen in Figure 4.9.



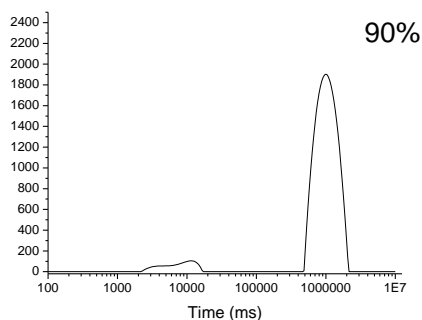


**Figure 4.9** 1-D  $T_2$  proton spectra obtained by inverse Laplace transformation of the CPMG echo decay for the gels between 10%-90% water contents.

The 1D- $T_2$  spectra of the gels obtained with the CPMG differ in peak amplitude and position as seen in Figure 4.9. The relaxation times and the amplitudes of the peaks of each concentration are listed in (Table 4.2). The gel with 10% water shows three peaks at 51, 8 and 0.7 ms. For the gels with 20% and 30% water content, two peaks are evident: one bigger in amplitude at slower relaxation time (40.54 ms for both gels), and one at faster relaxation time (1.6 and 1.8 ms, respectively). From gel with 40% to 60% water contents, the peak at faster relaxation time tends to split in two peaks, but not fully resolved. In the gels with 70% and 80% water contents, separated peaks at faster relaxation times can be distinguished. In the gel with 90% water, the peaks at faster time overlap. For the gels with 20% to 90% water contents, a main peak at slower relaxation time and with high amplitude is particular visible. The peak amplitude increases with the water content reaching the maximum of 3477 in the gel with 60% water and decreases down to 1903 in the gel with 90% water. More importantly, the  $T_2$  relaxation times shift towards slower relaxation time with increasing the water concentration. For the gels with 10-30% water, the  $T_2$  is approximately between 40-50 ms. It reaches 1 s in the gel with 90% water content, which is comparable with the relaxation time of the free water.

**Table 4.2** Relaxation Time ( $T_2$ ) and relative amplitude of the peaks for the gels.

Water Content	Peak No	$T_2$ (ms)	Amplitude
10%	1	50.80	752.41
	2	8.35	1314.04
	3	0.70	556.51
20%	1	40.54	1959.22
	2	1.57	654.68
30%	1	40.54	2009.58
	2	1.79	733
40%	1	58.17	2401.90
	2	5.31	405.94
	3	1.20	298.85
50%	1	95.59	3048.49
	2	11.98	483.67
	3	2.82	286.21
60%	1	157.06	3476.66
	2	10.00	480.15
	3	3.70	171.49
70%	1	405.36	2273.51
	2	42.41	256.78
	3	13.11	141.22
	4	2.70	173.34
80%	1	581.71	1685.45
	2	44.37	244.39
	3	2.96	220.19
90%	1	1000.00	1903.04
	2	11.98	104.32
	3	3.54	52.87

It was assumed that the peak at the slowest relaxation time (the one at higher  $T_2$  and identified as peak number 1 in Table 4.2) is associated with the OH of water and consequently the other peaks are associated with protons of CH bonds of the lipid. Further calculations were made to assess accuracy of this assumption. First, the total number of protons contained in the gels (that is the protons of both Gelucire 50/13 and water) was calculated. Considering that Gelucire 50/13 is composed by a mixture of aliphatic chains with 16 and 18 carbons, the average number of aliphatic protons was calculated. The number of protons for each gel is listed in Table 4.3. The table exhibits also the fraction of water protons ( $P_{H_2O}$ ) calculated by dividing the number of water protons to the total number.

**Table 4.3** List of the total number of protons in the gels and the fraction of water protons.

Water (%)	Average aliphatic protons	Water protons	Total protons in gels	fraction $P_{H2O}$
10	2.918E+23	3.344E+22	3.253E+23	0.103
20	2.595E+23	6.687E+22	3.263E+23	0.205
30	2.269E+23	1.003E+23	3.272E+23	0.307
40	1.945E+23	1.337E+23	3.283E+23	0.407
50	1.622E+23	1.672E+23	3.294E+23	0.508
60	1.297E+23	2.006E+23	3.303E+23	0.607
70	9.727E+22	2.341E+23	3.313E+23	0.706
80	6.485E+22	2.675E+23	3.323E+23	0.805
90	3.242E+22	3.009E+23	3.334E+23	0.903

From the amplitude of the peaks listed in Table 4.2, the fractional populations of the protons of peaks 1, 2...4 (indicated as P1, P2...P4) were determined, as shown in Table 4.4. To simplify the calculations, the peaks were divided into two groups, one at slower relaxation times,  $T_s$ , which is identified as peak 1, in Table 4.2. The second one at faster relaxation times,  $T_f$ , was calculated as the weighted average of the relaxation times of the peaks (identified as peak 2, 3 and 4, in Table 4.2).  $P_{s,f}$  are the corresponding fractional populations of the relaxation times  $T_{s,f}$ .

**Table 4.4** List of the  $T_2$  relaxation times of the peaks and the relative populations. The numbers (T1, P1...T4, P4) are in accord to the number of the peaks listed in Table 4.2. The subscripts  $s$  and  $f$  indicate the slowest peak and the weighted average of the faster peaks, respectively.

Water (%)	10	20	30	40	50	60	70	80	90
<b>T1</b>	50.800	40.540	40.54	58.170	95.590	157.060	405.360	581.710	1000
<b>P1</b>	0.287	0.750	0.733	0.733	0.789	0.842	0.799	0.894	0.924
<b>T2</b>	8.350	1.570	1.790	5.310	11.980	10.000	42.410	44.370	11.980
<b>P2</b>	0.501	0.250	0.267	0.131	0.127	0.116	0.090	0.065	0.051
<b>T3</b>	0.700			1.200	2.820	3.700	13.110	2.960	3.540
<b>P3</b>	0.212			0.096	0.075	0.042	0.050	0.041	0.026
<b>T4</b>							2.700		
<b>P4</b>							0.061		
<b>T<sub>s</sub></b>	50.800	40.540	40.54	58.170	95.590	157.060	405.360	581.710	1000
<b>T<sub>f</sub></b>	6.075	1.57	1.79	3.037	8.579	8.325	23.07	28.35	9.25
<b>P<sub>s</sub></b>	0.287	0.750	0.733	0.733	0.789	0.842	0.799	0.894	0.924
<b>P<sub>f</sub></b>	0.713	0.250	0.267	0.227	0.202	0.158	0.201	0.106	0.076

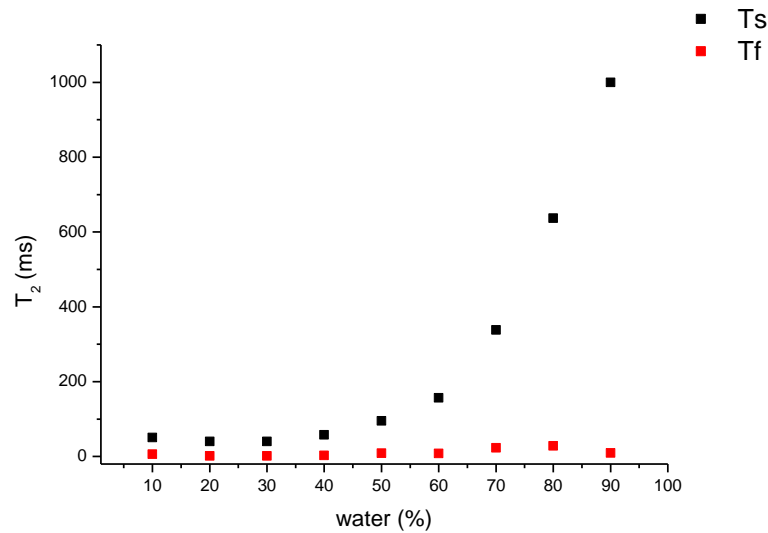


**Figure 4.10** Slowest ( $T_s$ ) and faster ( $T_f$ ) relaxation time versus water content of the gels.

The slowest relaxation times,  $T_s$  (that is the  $T_2$  times of the peaks number 1) and the faster relaxation times,  $T_f$  are plotted against the water content. As seen in Figure 4.10,  $T_s$  has a strong dependence on the water contents of the gels. It sharply increases when the water reaches and exceeds 60%. On the contrary,  $T_f$  does not show any clear dependence on the water content.

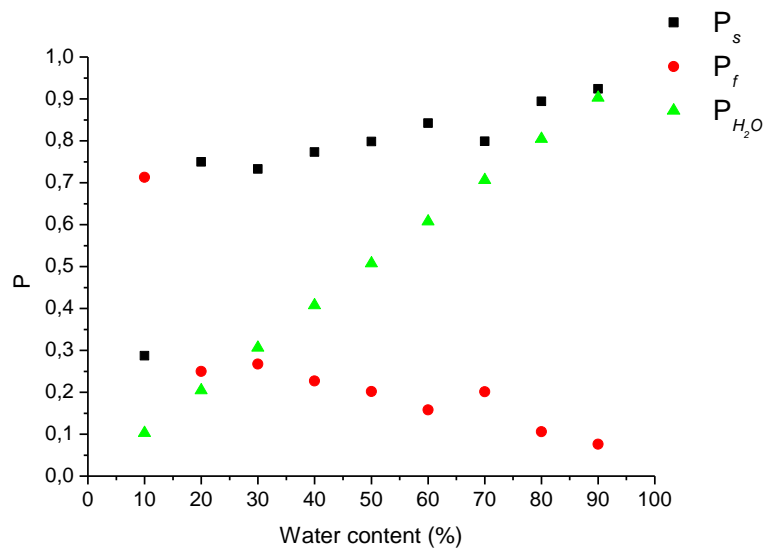


**Figure 4.11** Weighted populations  $P_s$  and  $P_f$  versus water content.  $P_{H_2O}$  is the calculated relative populations of water protons in the gels.

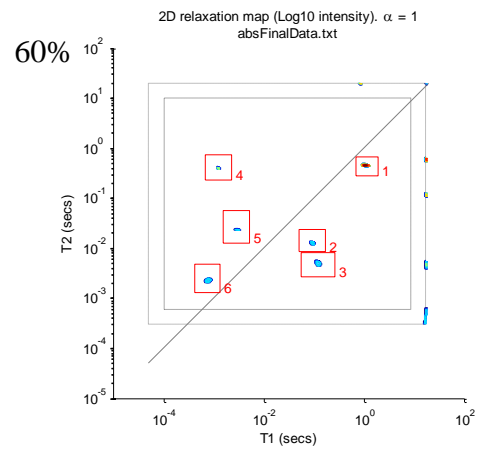
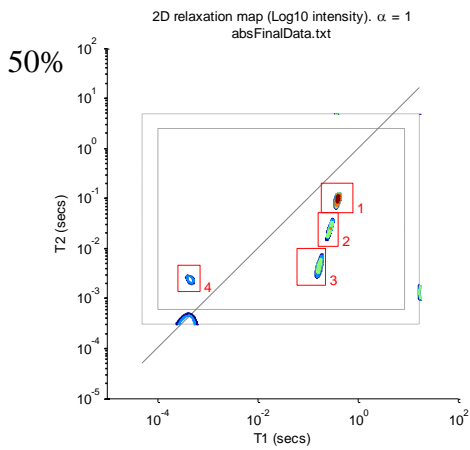
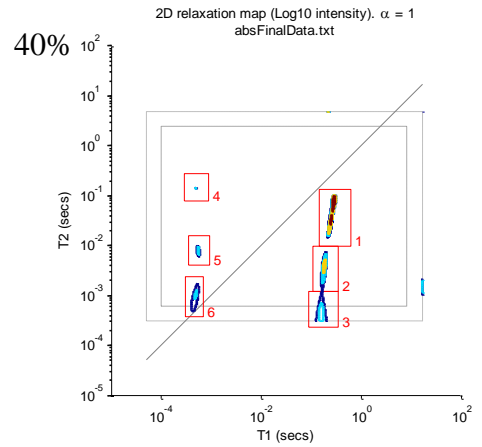
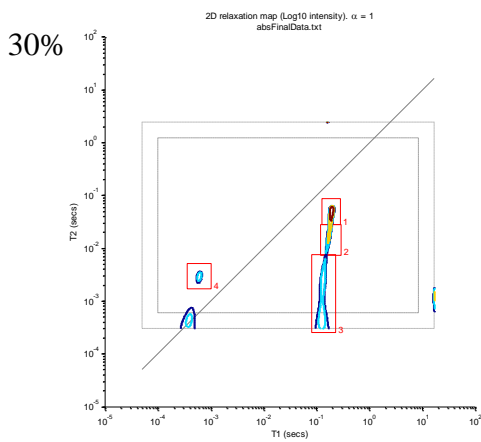
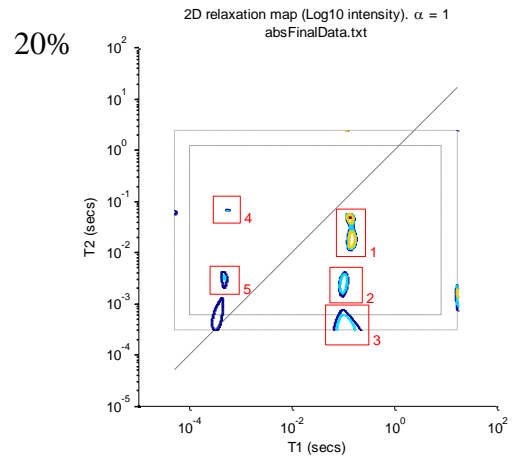
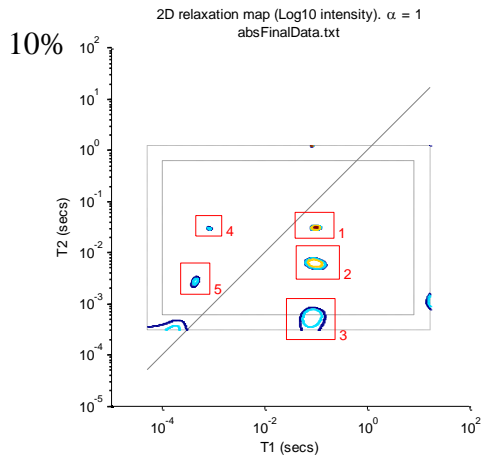
However, the corresponding population of the  $T_s$  peak does not reflect the actual population of water protons as it can be seen from Figure 4.11. The population  $P_s$ , which is the population of protons of the slowest peak ( $T_s$ ), differs from the water protons population which was theoretically calculated ( $P_{H_2O}$  in Table 4.3). The effect is particularly evident for gels between 20% and 60% water. This means that the population of protons of the slowest peak ( $P_s$ ) cannot

be associated exclusively to the water protons of these gels. In the gels with 70%, 80% and 90%, and surprisingly, in the gel with 10%, the protons population,  $P_s$ , is close to the theoretical values of the water protons ( $P_{H_2O}$ ). This suggests that the contribution to the slowest peak,  $T_s$ , does not depend only on the water protons, but also on the magnetisation of the aliphatic protons. In conclusion, at low water contents (20% and 30%) the main effect in the relaxation time,  $T_s$ , may arise from both the water and aliphatic protons. As the water content increases, the contribution to the relaxation time is mainly from water protons as the gels are richer in water.

However, this technique has encounters some limitations in characterising complex multi-component and multi-compartment systems. In some cases, oil and water transverse relaxation times are similar. As a result, the peaks may overlap, especially if the water is compartmentalised, which is likely to be the case for the gel systems studied in this project. As it could be seen in this work, the aliphatic protons have a similar relaxation time as the water protons, which makes difficult to have a clear separation of the two populations of protons [241] Therefore, more elaborated NMR sequence were applied to further study the gels.

#### ***4.4.3.2 Inversion Recovery pulse sequence (Inv-CPMG)***

The 2D  $T_1$ - $T_2$  data plots obtained by performing the Inv-CPMG sequence allow the characterisation of different populations of protons by separating the protons having the same transverse relaxation times ( $T_2$ ) but different longitudinal relaxation times ( $T_1$ ). The experiments were performed following the procedure described in section 4.3.3.2. The data were analysed using a MatLab script, which performs a 2D fast Laplace transformation. The 2D  $T_1$ - $T_2$  relaxation map were obtained for all the gels (see Figure 4.12).



(to be continued)

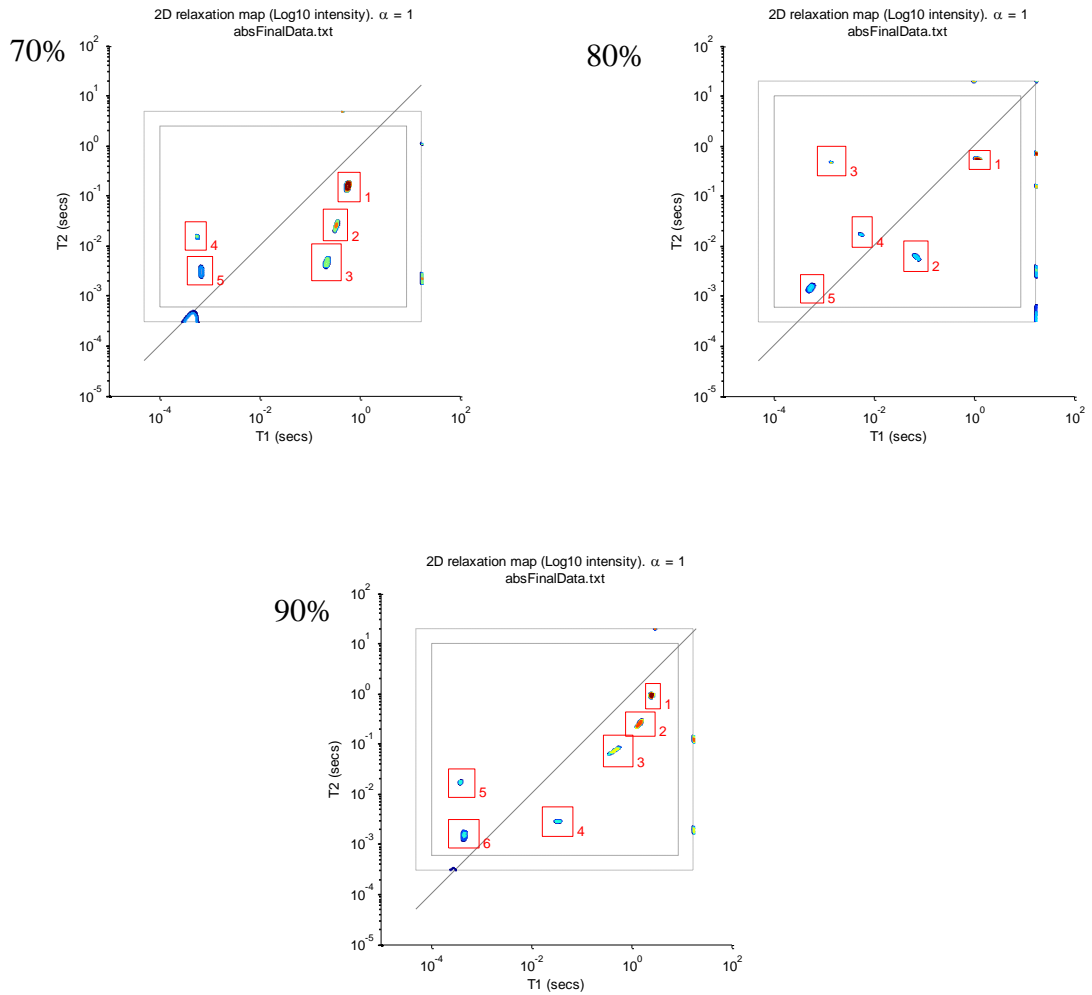


**Figure 4.12** 2D  $T_1$ - $T_2$  relaxation maps of the gels with 10% to 90% water contents. The dashed rectangles identify the reliable values set by the pulse sequence. The diagonal lines indicates the condition where  $T_1 = T_2$ .

Although the 2D inverse Laplace transformation may be numerically ill-conditioned, some important features may be retrieved from the 2D maps in Figure 4.12. The dashed rectangles identify the reliable values set by the pulse sequence and the diagonal line indicates the condition where  $T_1 = T_2$ . Above the  $T_1 = T_2$  line, there is the non-physical region with  $T_1 < T_2$ . Peaks in this region may be considered as the result of artefacts of the inverse Laplace transformation [242]. However, considering that the peaks comfortably fall in the reliable area, they can be considered as real rather than artefacts. In a material, different proton pools may be identified. They mainly can be classified as exchangeable, non-exchangeable and external water protons. The non-exchangeable protons come from nuclei covalently bound to the material, therefore are not involved in chemical exchange processes. The exchangeable protons may be largely from the groups such as NH, COOH, OH and so on. However, it has been also proposed that they arise from the water incorporated in the systems and that can exchange with the external water. The external water includes free (bulk) water and “bound” water and by the term “bound” is considered the water close to the interface which influence the water motion [243]. However, in the case of the gels with high water contents, the effects of the interface are far too

small as the water is largely present as bulk free water (as suggested by the previous DSC results). Therefore, it is more likely that there is water inside the gel phase, which has a shorter relaxation time and this water exchanges with the bulk water. Considering two proton pools, in absence of cross relaxation, two distinguished peaks are detected. But in the case of protons exchange different peaks may arise depending on the cross relaxation rate. In the fast cross relaxation, the two peaks merge in one peak, which has an averaged relaxation rate. If the cross relaxation is slow, two-well defined peaks should be observed. In the intermediate case, two peaks may be found but they may shift towards larger relaxation rates. The peaks lying above the  $T_1 = T_2$  line are associated with exchanging protons, whereas the non-exchanging peaks lie on the  $T_1 = T_2$  line or below the diagonal line, in the domain characterised by  $T_1 > T_2$  [241]. Because of the exchange effects, additional peaks may arise. The high level of information obtained with this technique can provide useful information on the characterisation of the systems, but at the same time, the assignment of protons can be complicated.

**Table 4.5** The integrated volume of the peaks and the relaxation time  $T_1$  and  $T_2$  of the gels with 10% to 90% water contents.

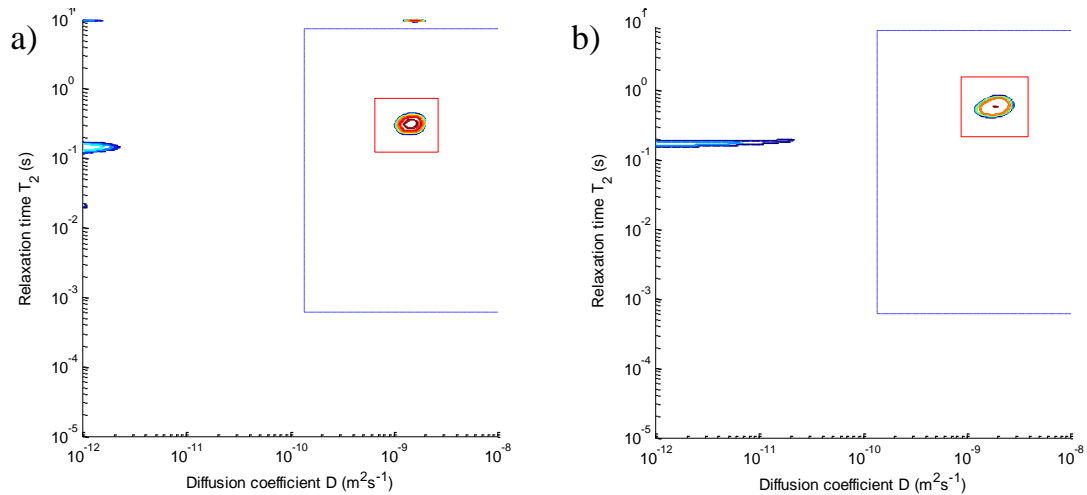
<i>Water content</i>	<i>Peak No</i>	<i>Integrated volume (%)</i>	<i>T<sub>1</sub> (ms)</i>	<i>T<sub>2</sub> (ms)</i>
10%	1	18.8	96.99	31.24
	2	38.8	92.95	6.22
	3	38.0	78.41	0.58
	4	1.1	0.79	29.55
	5	3.4	0.44	2.86
20%	1	58.1	130.62	48.87
	2	15	96.99	2.63
	3	23.8	105.60	0.39
	4	0.1	0.54	68.08
	5	2.8	0.46	3.34
30%	1	50.3	191.54	51.91
	2	14.9	175.92	27.57
	3	31.6	130.62	2.96
	4	3.2	0.59	2.96
40%	1	68.5	280.86	85.05
	2	14.9	175.92	3.90
	3	9.7	154.85	0.47
	4	0.1	0.48	142.95
	5	1.8	0.54	7.96
	6	5	0.48	1.03
50%	1	54.3	378.26	100.03
	2	10.6	269.17	24.78
	3	9.9	161.58	4.44
	4	3.3	0.44	2.47
60%	1	77.8	554.65	162.76
	2	7.4	332.95	27.31
	3	7.1	208.54	4.73
	4	0.8	0.54	15.73
	5	3.0	0.67	3.10
70%	1	86.7	1006.02	464.12
	2	2.0	89.08	13.19
	3	3.8	114.98	5.03
	4	2.1	1.21	415.24
	5	1.0	2.84	23.87
	6	4.4	0.73	2.31
80%	1	43.3	1142.93	558.69
	2	2.3	69.02	6.05
	3	0.7	1.32	481.66
	4	0.4	5.38	17.10
	5	3.0	0.52	1.48
90%	1	59.3	2355.15	939.06
	2	25.5	1413.75	266.07
	3	8.5	448.40	75.39
	4	2.0	32.10	2.88
	5	1.2	0.37	17.74
	6	3.5	0.44	1.59

Table 4.5 shows the calculated values of  $T_1$  and  $T_2$  (ms) of every peak of each sample lying within the dashed rectangle with some exception for the gels with 10%-40% water contents, for which the peaks lying outside the dashed rectangle have been considered as seen in Figure 4.12. The integrated volume of each peak is also listed. From the 2D maps in Figure 4.12 and the  $T_1$  and  $T_2$  values listed in Table 4.5, some general features of the gels can be obtained. For all gels, the presence of the peaks in the non-physical region (above the diagonal) indicates the existence of protons exchange. Furthermore, two different types of systems can be distinguished. For the gels with water contents up to 50%, the differences in  $T_1$  in the physical region (below the  $T_1=T_2$  line) is very small. The gels with 10% and 20% water show three well-defined peaks in the physical region labelled from 1 to 3 with a comparable  $T_1$  but different  $T_2$ . For the gels with 30% and 40% water, the peaks tend to be less defined and merge into one peak, though some distinction is still possible. The peaks on the edges of the reliable region (identified by the dashed rectangle) also can be seen. These peaks are measurable and they suggest rapid proton exchange. For the gels with water content above 40%, the peaks tend to separate and the  $T_1$  values are more distinct. A phase separation between rich and poor water component becomes clear between 50% and 60%. For the gels with 70% to 90% water, one peak with  $T_1$  of about 1 s appears, suggesting a component rich in water. At these water content ( $> 50\%$ ), the freezable free water appears as suggested by DSC results as well, which is consistent with systems with highly aqueous phase. Increasing the water content, the separation of peaks become more evident as a result, it is more clear the formation of distinguishable populations even though the process of proton exchange is still evident.

In conclusion, at 10% water content, the water is absorbed but in small quantity. As the amount of water increases, more components were hydrated and a more intimate mixture of all components was formed. The degree of separation between components rich and poor in water appears in the gels with concentrations between 50% and 60%. From gels with 70% to 90% water, a peak with  $T_1$  of 1 s emerges, which is consistent with the  $T_1$  value of the water. The presence of water with diffusion properties close to those of the bulk water in these gels with high water contents is confirmed by the CPMG-PGSE test (see section 4.4.3.3).

#### **4.4.3.3 CPMG-Pulsed Gradient Spin Echo sequence (CPMG-PGSE)**

The CPMG-PGSE was performed on selected gels with high water contents (70% and 80%). The data were analysed using the software MatLab and two dimensional  $T_2$ - $D$  plots were obtained. The  $T_2$ - $D$  plots assess the presence of water with diffusive properties close to the bulk water (see Figure 4.13).



**Figure 4.13** Relaxation time ( $T_2$ ) versus diffusion coefficient plot for the gels with 70% water (a) and 80% water (b). The dashed line identify the limits of reliability of the experiment.

As seen in Figure 4.13, just one peak is visible in the 2D maps for both gels. The smeared-out peaks at lower diffusivity (in the order of  $10^{-11} \text{ m}^2 \text{ s}^{-1}$ ) are outside the limit of reliability of the experiment. For the gel with 70% water, the relaxation time ( $T_2$ ) is 312.60 ms and the diffusion coefficient ( $D$ ) is equal to  $1.44 \times 10^{-9} \text{ m}^2 \text{ s}^{-1}$ . For the gel with 80% water, the  $T_2$  is equal to 596.92 ms and  $D$  is equal to  $1.84 \times 10^{-9} \text{ m}^2 \text{ s}^{-1}$ . The translational diffusion coefficients of the slowest relaxation time are in the same order as the diffusion coefficient of bulk water in aqueous solutions which has been determined as  $2.3 \times 10^{-9} \text{ m}^2 \text{ s}^{-1}$  [244], confirming that these peaks more likely belong to the OH of free water in the gels.

Comparing the relaxation time ( $T_2$ ) obtained with different tests for the gels with 70% and 80% water contents, similar values are obtained (as summarised in Table 4.6). The results confirm that the peak with high intensity and high relaxation time ( $T_2$ ) obtained with the CPMG sequence (Figure 4.9) is related to the water protons, though not entirely as the relative populations implied (Figure 4.11).

**Table 4.6** Comparison of the relaxation times ( $T_2$ ), determined with the three different sequences.

NMR Sequence	Relaxation Time ( $T_2$ ), ms	
	70%	80%
CPMG	323.45	581.71
Inv-CPMG	297.39	601.71
CPMG-PGSE	312.60	596.92

#### 4.4.4 Stimulated echo diffusion sequence (PGSTE diffusion)

The  $T_2$ - $D$  relaxation experiments assist in the peaks assignment and the determination of the relaxation times. Moreover, it provides the diffusion time of the samples. However, in many systems, such as porous materials, the longitudinal relaxation time ( $T_1$ ) of the liquid confined within the systems is greater than the transverse relaxation time ( $T_2$ ). In this case, the conventional PGSE test is not suitable for measuring self-diffusion coefficients with appropriate accuracy. This situation applies also to this work. As it is shown in Table 4.5 for all the gels,  $T_2$  is shorter than  $T_1$ . Therefore, a modified sequence of PGSE, the PGSTE sequence, can be used [192]. The stimulated echo diffusion sequence is one of the most used techniques to investigate the diffusion. The main aim of the test is to assess the effect of the gradient pulse on the echo amplitude.

The PGSTE tests were performed at least in triplicate, according to the procedure described in section 4.3.3.3.2. For most of the gels, the results were reproducible, with the exception of the gel with 10% water where some inconsistency was encountered. This may be related to the heterogeneity of the sample. The echo amplitudes in logarithmic scale ( $\ln S$ ) were plotted against the  $q^2\Delta$  values, where  $q$  is a variable and  $\Delta$  is a fixed value. Figure 4.14 and Figure 4.15 show the echo amplitude of the gels determined at the fixed diffusion times ( $\Delta$ ) of 56.4 ms and 241.6 ms, respectively. The first diffusion time was selected because is the second close to the shorter time applied, the second one is the intermediate diffusion time applied. The  $q$  values varied from 0 to  $5.122 \times 10^4 \text{ m}^{-1}$ . In order to remove the effect of the normal relaxation of the spins, the  $Sq$  signal is normalised to the intensity of the signal obtained in the same timescale but without the application of pulsed gradient field ( $q=0$ ).

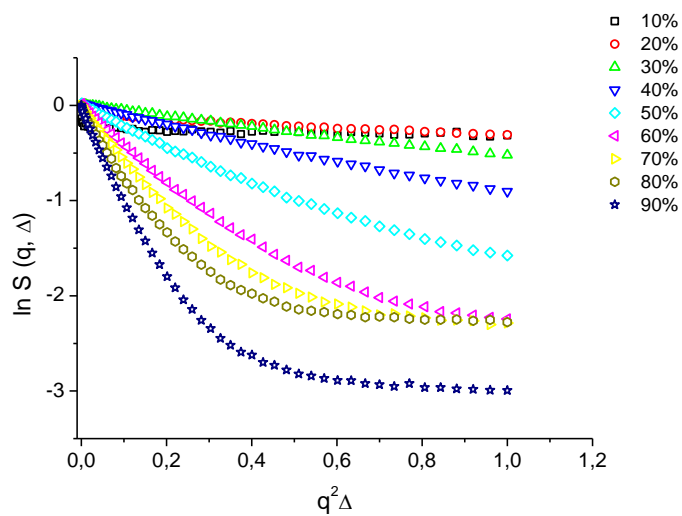


**Figure 4.14** Plots of echo amplitudes ( $\ln S$ ) attenuation as a function of  $q^2\Delta$  measured at the diffusion time of 56.4 ms for gels prepared by heating with water contents of 10% to 90%. The values were normalised to the signal amplitude at  $q=0$  ( $n=3$ ).

In Figure 4.14, three different regions are apparent. The first region with low water contents (the gels between 10% and 40% water) is characterised by low diffusion and the presence of barrier effect. For the gel with 50% water content, there is the intermediate region. A third region is detected for the gels with water contents greater than 50%, characterised by a strong change in slope. The reason for the different behaviours is that at low concentrations, a small amount of water is present and it is evenly distributed within the gels. In this case, water diffuses slowly due to the restrictions of the barriers (the interfaces present in the microstructure of the gels). As the amount of water increases in the gels, the solubility of the water in the matrix of the gels reduces and two different phases form: a rich in water phase, in which the diffusion is faster but with some restrictions, and a poor in water phase, in which the diffusion is slow.

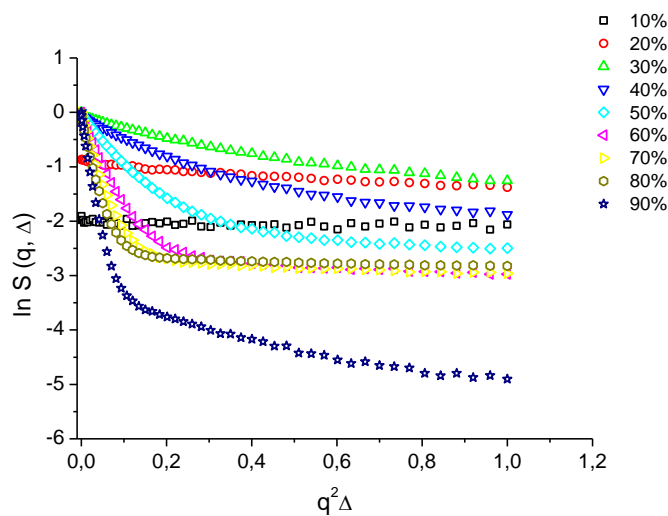


**Figure 4.15** Plots of echo amplitudes ( $\ln S$ ) attenuation as a function of  $q^2\Delta$  measured at the diffusion time of 241.6 ms for gels prepared by heating with 10% to 90% water contents. The values were normalised to the signal amplitude at  $q=0$  ( $n=3$ ).

Increasing the time of diffusion ( $\Delta$ ), a slightly different pattern is obtained (Figure 4.15). It is still possible to distinguish the different regions, although the attenuation of the echoes is sharper and more sudden, especially for the gels with water content above 50%. This may be due to a longer diffusion time as the spins experience more contacts with the barriers. The results obtained with the PGSTE test are consistent with both the 2D (CPMG-PGSE) and the 1D relaxation time (CPMG) data.

The echo attenuation,  $\ln S(q)$  was plotted against  $q^2\Delta$ , where  $\Delta$  varied from 50 ms to 500 ms and  $q$  is fixed. Several plots can be obtained at different values of  $q$ , and gradient strength  $G$  by the relationship existing between  $q$  and  $G$  (described by the Equation 4.1). From the plots, the condition of linearity was verified and the slope of the straight line gives the diffusion coefficients ( $D$ ). The gel with 10% water shows a sigmoid-like curve for increasing values of gradient strength,  $G$  (data not shown). In gels between 20% and 50% water content, a plateau at

low values of diffusion time,  $\Delta$  appears. At higher values of  $\Delta$ , the curve tends to be linear. This trend is consistent at all values of  $G$ . For the gels with water content above 50%, the linearity of the curve is more apparent at low diffusion times,  $\Delta$ , and the diffusion coefficients were calculated by linear fitting. The coefficients for the gels with water contents above 50% are within the order of  $10^{-10} \text{ m}^2 \text{ s}^{-1}$  at  $G = 0.147 \text{ T/m}$ , while increasing the gradient values, the diffusion coefficients decrease to the order of  $10^{-11} \text{ m}^2 \text{ s}^{-1}$ . The diffusion coefficients of the gels are one or two order of factor lower than the one of the free water, which is  $2.3 \times 10^{-9} \text{ m}^2 \text{ s}^{-1}$ . This is a consequence of the boundaries and the restriction encountered by the water molecules in the gel microstructures. A list of the coefficients at selected  $G$  values is shown in Table 4.7.

**Table 4.7** Self-diffusion coefficients of gels between 50% and 90% water and adjusted R-square values of the fitting.

Water (%)	$D \text{ (m}^2 \text{ s}^{-1}\text{)}$ $g=0.147 \text{ T/m}$	Adj $r^2$	$D \text{ (m}^2 \text{ s}^{-1}\text{)}$ $g=0.589 \text{ T/m}$	Adj $r^2$
50	$5.9 \times 10^{-10}$	0.955	$1.9 \times 10^{-11}$	0.971
60	$6.0 \times 10^{-11}$	0.978	$3.0 \times 10^{-11}$	0.988
70	$7.5 \times 10^{-11}$	0.992	$3.7 \times 10^{-11}$	0.992
80	$9.3 \times 10^{-11}$	0.967	$4.7 \times 10^{-11}$	0.987
90	$1.1 \times 10^{-10}$	0.997	$5.3 \times 10^{-11}$	0.980

## 4.5 Conclusions

This chapter investigated the behaviour of water within the gels using a combination of imaging, thermal and relaxometry NMR approach. It can provide insights into the internal microstructure of the gels. The gels proved to have an ordered network-like structure with water channels of different size, as indicated by the SEM images of the freeze-dried gels. The size of the pores/channels observed via SEM are not real as they are enlarged as a consequence of the freeze-dried process. In the gels prepared by both heating and hydration methods, two different microstructures of the gels can be defined. The first one includes the gels with water contents below 40%, which shows no water channels, but a structure characterised by an ensemble of different layers. The second one consists of the gels with water contents above 40%, which shows the presence of water channels increasing in size with increasing the water content in the gels. The existence of the two microstructures is consistent with the data obtained by thermal analysis and the NMR. In fact, in the DSC tests, the peaks associated with the “free” (bulk) water appear from the gels with 50% water and above. Shoulder peaks associated with the interfacial water is visible in all the gels. This trend is valid for the gels prepared by both methods (heating and hydration), though it seems that the method of preparation has a slight influence on the amount of free water in the gels with higher water contents (i.e. 90% water content). Nevertheless, there are always two type of water behaviour which defines the two

types of microstructures of the gels with water contents below 50% and between 60% and 90%. This is proved by the relaxometry NMR tests performed on the gels prepared by heating. The first type of gel (the gels between 10% and 40%) is lipid rich and is characterised by restricted diffusion of water molecules. The second type contains two phases (gels between 60 and 90%) which are water rich phase and lipid rich phase and shows a prompt diffusion with some restrictions. This result agrees well with the SAXS findings of the co-existence of mixed liquid crystalline phases in the gels.

## **5 Physicochemical characterisation of lysozyme-loaded Gelucire 50/13 gels**

### **5.1 Introduction**

Chapters 3 and 4 have described the characterisation of the structure, physical and mechanical properties of the unloaded Gelucire 50/13 gels prepared by hydration and by heating methods over a range of water content (between 10% and 90%). The results from these chapters have revealed the promising characteristics of Gelucire 50/13 as a carrier for proteins and peptides delivery. For example, the SAXS, ATR-FTIR and DSC results confirmed the presences of ordered liquid crystalline phases, such as cubic and hexagonal phases, in the gels. These order microstructures of the gels may result suitable for protein/peptide drugs. In literature, cubic and hexagonal and their corresponding nanodispersions have been used for protein delivery [78, 82, 100, 136, 137]. Chapter 3 also described the mucoadhesion properties exhibited by the Gelucire 50/13 gels. This can act as an advantage of the Gelucire gel formulations for oral delivery as it may prolong the residence time of the formulation at local site of the absorption and enhance the bioavailability of the therapeutic protein delivered.

This chapter focuses on the characterisation of protein-loaded gels using lysozyme as model protein. The effects of the incorporation of the enzyme on the properties of the gels were assessed. The selection of the gels for loading the lysozyme was carried out on the basis of the information obtained by the study of the drug-free gels. The microstructure of the lysozyme-loaded gels was studied with ATR-FTIR and SAXS. The ATR-FTIR was also used to identify the changes in the secondary structure of the lysozyme after incorporation in the gels. The phase transitions of the lysozyme-loaded gels upon thermal treatment were investigated with DSC and rheometer. Rheological and mechanical properties of lysozyme-loaded gels were determined by using rheometer and texture analyser. The texture analyser was also used to evaluate the effect of lysozyme incorporation on the mucoadhesive properties of the gels. Furthermore, investigation of the release profile of the lysozyme from the gels is performed with dissolution bath and Franz diffusion cells.

## 5.2 Objectives

The purpose of the chapter is to characterise the gels loaded with lysozyme, with particular emphasis on the assessment of whether the incorporation of lysozyme leads to a modification in the behaviour of the gels (comparing with the results of the characterisation on unloaded gels) and whether the lysozyme retains its structure. The aims achieved in this part of the project are:

- Identification of the ordered structure of the gels loaded with lysozyme in comparison to Gelucire 50/13 and drug-free gels
- Study of the phase transitions of the lysozyme-loaded gels upon thermal treatment
- Evaluation of the rheological and mechanical properties of the lysozyme-loaded gels
- Evaluation of the mucoadhesive properties of the lysozyme-loaded gels
- Assessment of the release profile of the lysozyme from the gel formulations

## 5.3 Materials and methods

The gels were prepared using Milli-Q water (18 M $\Omega$ .cm, Barnstead Nanopure, Thermo Scientific, UK) following the procedure described in Chapter 2, section 2.3.1. Deuterium water (D<sub>2</sub>O, > 99.92 atoms % D, Apollo Scientific Limited, Stockport, UK) was used for the ATR-FTIR measurements. Mucin powder from porcine stomach type II (Sigma Aldrich, USA) and porcine small intestine (obtained from the local abattoir) were used to assess the mucoadhesion of the gels with the Texture Analyser (TA-Xtplus, Stable Micro System Ltd, Godalming, UK).

### 5.3.1 Attenuated Total Reflectance Infrared (ATR-FTIR) Spectroscopy

The tests were performed on selected lysozyme-loaded gels prepared by hydration (gels with 20%, 40%, 60% and 70% water) and by heating (40%, 50% and 60%) methods, according to the procedure described in section 2.3.1. D<sub>2</sub>O water was used in both cases. Each sample was tested at least in triplicate and the average was calculated (through the software OPUS) after baseline correction and used for further analysis. The average spectra of the Gelucire/D<sub>2</sub>O unloaded gels was calculated and used for further comparison. The ATR-FTIR test conditions used in this part of the project are listed in Table 5.1.

**Table 5.1** List of the samples and experimental conditions adopted in the ATR-FTIR experiments.

<i>Samples</i>	<i>Preparation procedure</i>	<i>Temperature (°C)</i>	<i>Resolution</i>	<i>Sample scans</i>	<i>Notes</i>
Lysozyme/D <sub>2</sub> O	—	Room temperature	2 cm <sup>-1</sup>	64	—
Gelucire 50/13/LYS/D <sub>2</sub> O	Heating method (section 2.3.1)	Room temperature	2 cm <sup>-1</sup>	128	Selected gels were analysed (40, 50, 60% water)
Gelucire 50/13/LYS/D <sub>2</sub> O	Hydration method (section 2.3.1)	Room temperature	2 cm <sup>-1</sup>	64	Selected gels were analysed (20, 40, 60, 70% water)

LYS stands for lysozyme

### 5.3.1.1 Determination of protein secondary structure

Amide I peak (1620-1680 cm<sup>-1</sup>) of lysozyme was taken into consideration to determine the secondary structure of the protein. Because the Amide I peak could overlap with the Amide II peak, a wider region between 1700 and 1490 was considered. For each spectrum, a second derivative with 9 points Savitzky-Golay smoothing was calculated. The peaks found in the second derivative were directly used as input parameters for the curve fitting. The fitting was performed by using the Levenberg-Marquardt algorithm. The positions and the intensity of the peaks were left to change in order to obtain the best match of the original curve [245]. It was found that the curves have a Gaussian shape. It was possible to determine the different type of conformations of the protein molecules (in percentage, %) by using the integrated area of each peak. This is because the area under the curve of the each peak is directly proportional to the relative proportion of the different type of conformations of the protein molecule [193]. In the determination of the conformations, the following regions were used. 1620-1640 cm<sup>-1</sup> for the  $\beta$ -sheet; 1650-1658 cm<sup>-1</sup> for the  $\alpha$ -helix; the values in between these two ranges were considered as unordered conformations, and the region between 1670-1695 for the turn conformations (see Chapter 2, section 2.5.2.1, Table 6).

### 5.3.2 Small Angle X-ray Scattering (SAXS)

The existence of any ordered structure in the lysozyme-loaded gels were detected using SAXS (S3-micro from Hecus X-ray Systems GmbH, Graz, Austria) provided with a point microfocus source GemixFox 3D (Xenoxs, Grenoble, France). A two-dimensional position sensitive detector with a sample-to-detector distance of 268 mm was used to detect the scattered X-rays. The samples were loaded in cell for pastes between two windows of kapton® (polyimide tape), which absorbs at 4e<sup>-1</sup> Å (or 700 number of channel). The experiments were performed using an

X-ray source power of 50 W (5 kV, 1 mA). The composition of the analysed gels and the experimental conditions are listed in Table 5.2.

**Table 5.2** Experimental details adopted in the SAXS experiments for the gels with, 40%, 50% and 70% water prepared by hydration method.

<i>Samples</i> (%, water content)	<i>Temperature</i> (°C)	<i>Exposition Time</i> (s)
40%	25	7200
	25	6810
	25	7200
	30	7200
	35	7200
50%	37	18000
	35	3600
	30	3600
	25	7200
	25	7200
70%	37	3600
	37	3600
	37	3600

### 5.3.3 Conventional Differential Scanning Calorimetry (DSC)

Conventional DSC (Q series, TA Instruments, New Castle, USA) was used under nitrogen flux with purge rate of 50 ml/min. Hermetic pans were used for all experiments. A series of calibrations were performed prior the experiments as described in section 3.3.3. The tests were performed on selected lysozyme-loaded gels (20%, 40%, 50%, 60%, 70% water content), following the same procedure used for unloaded gels (section 3.3.3). Aluminium hermetic pans (Perkin Elmer, USA) and the sample weights range between 2 and 5 mg were used. The samples were equilibrated at 20 °C/min for 2 minutes and heated up to 80 °C/min and then cooled down to 0 °C/min at the rate of 5 °C/min.

### 5.3.4 Rheology

The tests were performed on selected lysozyme-loaded gels prepared by hydration (40%, 50%, 60% and 70%) and by heating methods (40% and 60%) as described in section 2.3.1 by using a rheometer (AR 1000-N Rheolyst, TA Instruments, New Castle, USA). Plate-plate geometry was

adopted for all the experiments. For the upper plate, stainless steel solvent trap plate with 40 mm in diameter was used. Oscillation (stress sweep, frequency sweep and temperature ramp) and flow tests were performed. The stress and the frequency sweep tests were performed in quadruplicate or in quintuplicate. The temperature ramp tests were performed in triplicate at the rate of 1 °C/min. The details of the analysed samples and the experimental parameters are listed in Table 5.3.

**Table 5.3** Experimental details adopted for the gels with, 40%, 50% and 70% water prepared by hydration and heating methods.

<i>Samples</i> (% water)	<i>Preparation procedure</i> (section 2.3.1)	<i>Parameters</i>	<i>Stress</i> <i>sweep</i>	<i>Frequency</i> <i>sweep</i>	<i>Temperature</i> <i>ramp</i>
40	Hydration	<i>Temperature</i> (°C)	37	37	1) 25 to 80 2) 80 to 25
		<i>Stress</i>	10 to 1000 µNm	80 Pa	80 Pa
		<i>Frequency</i>	1 Hz	0.02-100 Hz	1 Hz
	Heating	<i>Temperature</i> (°C)	37	37	1) 25 to 80 2) 80 to 25
		<i>Stress</i>	10 to 1000	50 Pa	50 Pa
		<i>Frequency</i>	1 Hz	1-100 Hz	1 Hz
50	Hydration	<i>Temperature</i> (°C)	37	37	1) 25 to 80 2) 80 to 25
		<i>Stress</i>	80-8000 µNm	20 Pa	20 Pa
		<i>Frequency</i>	1 Hz	0.02-100 Hz	1 Hz
60	Hydration	<i>Temperature</i> (°C)	37	37	1) 25 to 80 2) 80 to 25
		<i>Stress</i>	80-8000 µNm	25 Pa	25 Pa
		<i>Frequency</i>	1 Hz	0.02-100 Hz	1 Hz
	Heating	<i>Temperature</i> (°C)	25 and 37	25 and 37	1) 25 to 80 2) 80 to 25
		<i>Stress</i>	10 to 1000 µNm	50 Pa	50 Pa
		<i>Frequency</i>	1 Hz	1-100 Hz	1 Hz

70	Hydration	<i>Temperature (°C)</i>	37	37	1) 25 to 80 2) 80 to 25
		<i>Stress</i>	80-8000 μNm	25 Pa	25 Pa
		<i>Frequency</i>	1 Hz	0.02-100 Hz	1 Hz

Continuous flow ramp tests were performed on the gels with 60% and 70% water prepared by hydration method. The stress applied continually increased between 64 mPa to 636.6 Pa over a period of 60 seconds at a fixed temperature of either 25 °C, or 37 °C, or 50 °C. When the test was performed at 80 °C, the stress applied ranged between 64 mPa and 100 Pa. All tests were performed in triplicate.

### 5.3.5 Texture analyser

The mechanical properties of the lysozyme-loaded gels with selected water contents (with 40% to 70% water) were studied using a texture analyser. The experiments were performed using the same parameters and procedures used for the unloaded gels (see section 3.3.5). The compressibility, hardness and adhesiveness properties of the gels were analysed by performing TPA tests. About 5 g of gels were packed into a vial, which were fixed on the lower plate of the instrument. A cylindrical Perspex probe (11.6 mm diameter) was compressed twice to the depth of 5 mm, at the selected speed of 1 mm/s, and a delay period of 15 seconds was applied between the two compressions. Mucoadhesion properties of the gels were also studied using mucin tablets (see section 3.3.5.2). For the method and the parameters applied, refer to section 2.4.3.2. All samples were tested at least in triplicate.

### 5.3.6 Statistical analysis

Statistical analyses were performed on the rheological parameters and the TPA parameters (compressibility, hardness, and adhesiveness) in order to assess the effect of water content and the presence of the lysozyme on the physical performance of the gels. The analyses were performed using IBM SPSS statistics software 20.0 as described in section 3.3.5.

### 5.3.7 Lysozyme release mechanisms

As reported in the literature, Gelucires 50/13 is mainly used as sustained release matrix and may swell in the presence of water due to the high HLB values. For the swellable matrices, the drug release is often controlled by a combination of mechanisms: the water diffuses in the matrix to cause hydration; the matrix swells as a consequence of the hydration or for the relaxation of the

polymeric chains (Case II transport); the drug diffuses through the swollen matrix; dissolution or erosion of the matrices may occur during the release of the drugs [102]. The mechanism of release may depend on the property of the loaded drug (crystallinity, particle size, solubility, concentration in the formulation), the matrix material and the method of measurement, [102].

In this part of the project, the release profiles were fitted to several release kinetic models in order to identify the dominant mechanism involved in the release of the lysozyme from the gels. The fitting was performed by using the software SigmaPlot 12.5 (Systat Software Inc., California, USA) and five built-in fitting models. The mathematical models used to describe the release behaviour are:

- First order kinetics model

$$\ln\left(\frac{Q_t}{Q_0}\right) = k_1 t \quad \text{Equation 5.1}$$

where  $Q_t$  is the amount of drug release in time  $t$ ,  $Q_0$  is the initial amount of drug and  $k_1$  is the first kinetic order. According to the Equation 1, the logarithmic plot of the drug release profile vs time should give a linear correlation. This model applies to the release of water-soluble drug in porous matrices [246].

- Higuchi model

Higuchi developed several mathematical models to describe the release profile of water soluble and poorly water-soluble drugs from different matrices which may applied to different matrix with different geometries such as uniform matrix, heterogeneous matrix systems, porous systems [246, 247]. Generally, Higuchi model can be simplified as follow,

$$M_t = k_H \sqrt{t} \quad \text{Equation 5.2}$$

where  $k_H$  is the Higuchi dissolution constant and  $M_t$  is the amount of drug release at time  $t$ . Higuchi model describes the drug release as proportional to the square root time (based on the Fick's law) [246]. This model applies when the drug solubility in the media is much higher than the drug concentration in the formulation and when the pure diffusion is the rate-controlling step [248]. It can be used to describe the dissolution of drugs from modified release dosage forms, such as transdermal or matrix tablets [246].

- Hixson-Crowell model

This model introduces the concept of change in the surface area and particle size as the particles are being dissolved [249]. It assumes that the dissolution surface area is proportional to the cubic root of its volume, thus, the equation is as follow

$$W_0^{1/3} - W_t^{1/3} = k_s t \quad \text{Equation 5.3}$$

Where  $W_0$  is the initial amount of drug,  $W_t$  is the remaining amount of drug at time  $t$  and  $k_s$  is the kinetic constant. This model is only valid for particle of spherical or cubic shape in which the particles dissolve in the same manner at all sides. This model is used when the release rate is limited by the particle size, but not by the diffusion [246, 249].

- Korsmeyer-Peppas model

Korsmeyer et al. [250] developed a semi-empirical model which links exponentially the drug release to time.

$$\frac{M_t}{M_\infty} = kt^n \quad \text{Equation 5.4}$$

where  $k$  is the kinetic constant and  $n$  is the diffusional exponent, by which it is possible to determine the kind of mechanism involved in the release. In particular, for  $n = 0.5$ , a Fickian diffusion is dominant, while for  $0.5 < n < 1$  a non Fickian (anomalous) diffusion prevails,  $n = 1$  is typical of Case II transport and  $n > 1$  identifies a super Case II transport [250]. The diffusional exponent,  $n$ , changes with the geometries of the devices, i.e. slabs, cylindrical or spherical which lead to changes in the diffusional exponent (see Table 5.4). The determination of the exponent  $n$  is obtained by fitting the first 60% of the fractional release curves to the mathematical model. This model is particularly useful when the mechanism of release is unknown or when more than one mechanism is involved.

**Table 5.4** Diffusion exponent ( $n$ ) and drug release mechanisms (of matrices with different geometries) identified with Korsmeyer-Peppas model [250, 251].

<i>Diffusional release exponent (n)</i>			<i>Drug release mechanism</i>	<i>Release rate as a function of time</i>
<i>Thin film</i>	<i>Cylindrical sample</i>	<i>Spherical sample</i>		
0.5	0.45	0.43	Fickian diffusion	$t^{-0.5}$
$0.5 < n < 1$	$0.45 < n < 0.89$	$0.43 < n < 0.85$	Anomalous (non-Fickian) transport	$t^{n-1}$
1	0.89	0.85	Case II transport	Zero order release
$n > 1$			Super Case II transport	$t^{n-1}$

- Baker-Lonsdale model

This model has been developed from the Higuchi model. It often applies to the drug release from spherical matrices. A simplified form of the equation is

$$\frac{3}{2} \left[ 1 - \left( 1 - \frac{M_t}{M_\infty} \right)^{2/3} \right] - \frac{M_t}{M_\infty} = kt \quad \text{Equation 5.5}$$

where  $k$  is the release constant [246].

The release behaviour of lysozyme from the Gelucire 50/13 gels were studied using BP paddle method. The gels loaded with lysozyme were prepared by hydration and by heating methods as described in section 2.3.1. The conditions of the test were described in section 2.6. Prior to the dissolution tests, suitable calibration curves were constructed for lysozyme in each media used in the dissolution study.

The calibration curves were constructed for the lysozyme in phosphate buffer (pH=7.4) and HCl, 0.1 M (pH=1.2). The preparation of the media was described in section 2.3.4. For the dissolution bath method, a quartz cuvette, with 10 mm light path and 3.5 ml volume was used. For the drug release studies using diffusion cells, the calibration was conducted using a quartz cuvette, with 10 mm light path and 0.7 ml volume was used. The preparation of the media and calibration sets were identical in both cases. A lysozyme solution with a concentration of 0.9 mg/ml (0.09 % w/v) in each medium was prepared. When the enzyme was completely dissolved in the medium, 1, 2, 3, 4 and 5 ml aliquots of the stock solution were individually transferred in to 10 ml volumetric flasks to prepare dilutions of lysozyme concentrations of 0.09, 0.18, 0.27, 0.36 and 0.45 mg/ml, respectively. Three repetitions were performed for each calibration. Measurements were taken using a UV spectrophotometer (lambda 35, Perkin-Elmer, USA) at 280 nm  $\lambda_{\max}$  for both media.

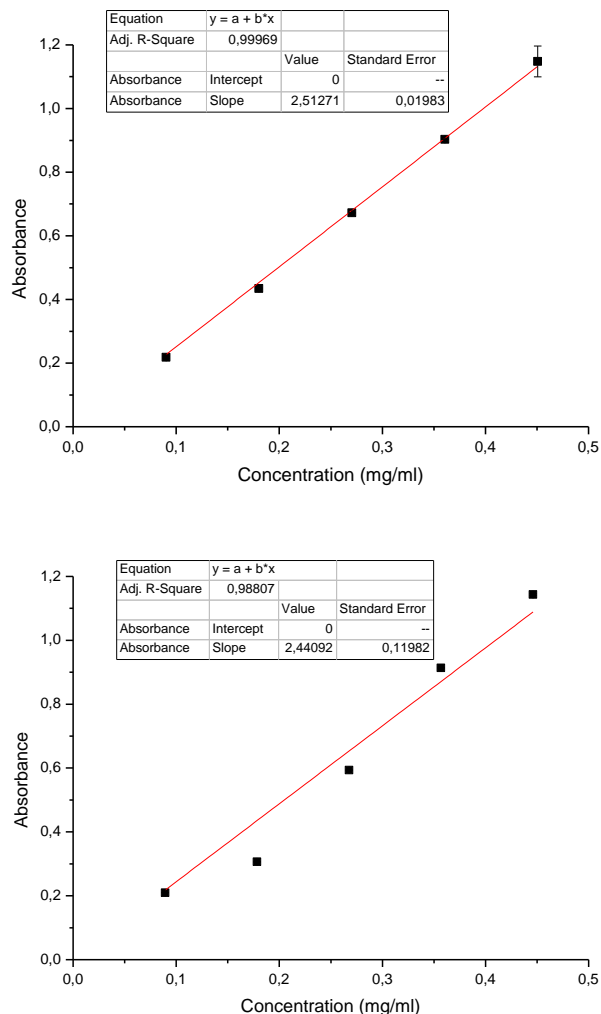


**Figure 5.1** UV calibration plots of lysozyme in pH 7.4 phosphate buffer (a) and HCl, 0.1 M (b), for dissolution studies. The adjusted R-square and the slope values ( $\pm$ SE) are also listed in the tables for each plot.

Diffusion studies using Franz cells were also carried out on selected lysozyme-loaded gels with 30% and 50% (w/w) water content prepared by both hydration and heating. All the tests were performed in six cells and in phosphate buffer (pH 7.4). About 60 mg of the gel were weighed on the membrane used for the diffusion study (mixed cellulose esters, 0.45  $\mu$ m pore size, MF Millipore, Merck, Germany). The membrane loaded with the gel was located between the receptor chamber and the donor chamber. The two chambers were clamped together and sealed with Parafilm® to prevent water loss. The receptor chambers were filled with 5 ml of phosphate buffer (pH 7.4). The prevention of the formation of air bubbles beneath the membrane was checked prior the start of each test. The temperature was fixed at  $37.0 \pm 0.5$  °C and the cells were kept under stirring throughout the experiment. At fixed sampling points, 300  $\mu$ l solution were withdrawn with a 1 ml syringe and replaced with the same volume of fresh media kept at the same temperature. No filtration has been made after withdrawing the samples due to the low volume of the samples withdrawn. The amount of lysozyme released over time was assessed by

using the UV-Vis spectrophotometer. Prior to the test, a calibration curve was constructed as described above. Figure 5.2 shows the UV calibration curve of lysozyme in phosphate buffer used for the analysis of diffusion cell results.

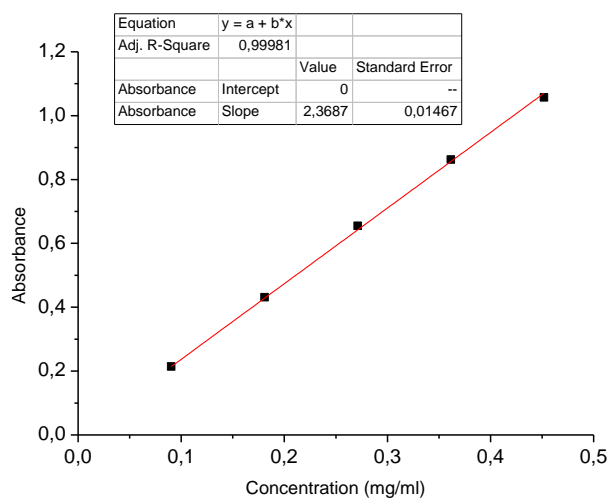


**Figure 5.2** UV calibration curve of lysozyme in phosphate buffer for diffusion study. The adjusted R-squared and the slope values ( $\pm$ SE) are also listed in the tables for each plot.

## 5.4 Results and Discussion

### 5.4.1 Structural analysis of lysozyme-loaded gels using ATR-FTIR spectroscopy

The structure of the lysozyme-loaded gels was studied using ATR-FTIR by following experimental conditions described in section 5.3.1. The gels were prepared by hydration method (see section 2.3.1) with D<sub>2</sub>O and analysed at room temperature. D<sub>2</sub>O was used instead of MilliQ water in order to avoid the overlapping of the water peak and the Amide I peak of lysozyme, which is in the region between 1600 and 1700 cm<sup>-1</sup> wavelength [198]. However, it also has been stated that the presence of D<sub>2</sub>O may lead to increased hydrophobic interactions, which may result in changes in the secondary structure of the protein [252]. Therefore, caution was taken in the analysis of the data.

The Amide I peak is associated with the C=O stretch vibration of the polypeptide backbone [194] as well as the CN stretch, the CCN deformation and the NH in-phase bending [199]. This region contains information regarding the secondary structure of proteins. This peak is the result of the overlapping of peaks associated to the  $\alpha$ -helix, anti-parallel and parallel  $\beta$ -sheet,  $\beta$ -turns and random coil (unordered) structures of the protein molecule. The Amide II band is associated to the N-H bending, with some C-N stretching. It is also possible to obtain more information on the secondary structure of proteins using this region. However, the Amide II region is sensitive to the D<sub>2</sub>O, and the peak is shifted from 1550 cm<sup>-1</sup> to lower frequencies (1450 cm<sup>-1</sup>). Moreover, the peak overlaps with the H-O-D bending. Therefore, it would be difficult to obtain valid

information on the secondary structure from the Amide II region. The deconvolution of the Amide I peak and the determination of the secondary structure of the lysozyme incorporated in the gels is discussed in the section 5.4.1.1. The list of the IR peaks detected in the ATR-FTIR spectra of the lysozyme-loaded gels is presented in the Appendix I.

The spectra of the lysozyme-loaded gels prepared by hydration show the characteristic peaks associated with the Gelucire 50/13 in the region between 2916 and 2850  $\text{cm}^{-1}$ , although the peak at 2885  $\text{cm}^{-1}$  is just noticeable and not well defined as in the spectra of the dry Gelucire powder and the unloaded gels. The peaks centred at 2500  $\text{cm}^{-1}$  are associated with  $\text{D}_2\text{O}$ . However, the most interesting region is between 1700 and 1600  $\text{cm}^{-1}$ , which corresponds to the Amide I region. The features of the spectra of the loaded gels are close to that of the lysozyme aqueous solution, especially the gels with higher water content (60% and 70%). No peaks can be found in the region between 1700 and 1600  $\text{cm}^{-1}$  of the spectra of the unloaded gels and the Gelucire 50/13 powder. This confirms that Gelucire have no contribution to the intensity of the peaks appeared in the Amide I region and the peaks within this region can be confidently assigned to the presence of lysozyme in the gels. The Amide I peak of the lysozyme solution in  $\text{D}_2\text{O}$  is centred at 1650  $\text{cm}^{-1}$  and in the gels with 60% and 70% water content is centred at 1648 and 1649  $\text{cm}^{-1}$ , respectively. In gels with lower water content (20% and 40%), the Amide I peak is centred at lower wavenumber (1637 and 1636  $\text{cm}^{-1}$ , respectively). This shift may indicate the slight difference in the conformation of the protein in the gels with different water contents. This is further discussed in section 5.4.1.1.

The lysozyme-loaded gels with 40%, 50% and 60%  $\text{D}_2\text{O}$  contents prepared by heating method with  $\text{D}_2\text{O}$  were also analysed using ATR-FTIR spectroscopy. The spectra of the lysozyme-loaded gels with 40%, 50% and 60%  $\text{D}_2\text{O}$  contents prepared by heating method are not different among them and they show the same peaks of the unloaded gels. However, the peaks associated to the Amide I region shift towards lower wavenumbers compared to the lysozyme solution. For the lysozyme-loaded gels prepared by heating, the Amide I peak is centred at 1643  $\text{cm}^{-1}$  for the gel with 40% and 50% water, and at 1641  $\text{cm}^{-1}$  in the gel with 60% water. Overall, the intensity of the Amide I peaks of the lysozyme-loaded gels prepared by heating are lower than the Amide I peaks of the lysozyme-loaded gels prepared by hydration.

#### **5.4.1.1 Secondary structure determination with ATR-FTIR spectroscopy**

The change in the secondary structure of the lysozyme can be an indication of denaturation or deactivation of lysozyme, which may be caused by the preparation procedure or the interaction with the Gelucire 50/13 in the gels. IR spectroscopy is a well-established method for the

determination of the secondary structure of proteins. The theory behind the determination of the secondary structure using IR and the procedure followed in this study were described in section 2.5.2.1 and section 5.3.1.1, respectively. All the spectra manipulation and calculation were made using the software OPUS. The aqueous solution of 10% lysozyme in D<sub>2</sub>O was analysed as reference. Figure 5.3 shows the Amide I region of the 10% lysozyme D<sub>2</sub>O solution, which is centred at 1650 cm<sup>-1</sup>. The second derivative spectrum of the Amide I region and the fitted curves are also shown in Figure 5.3.

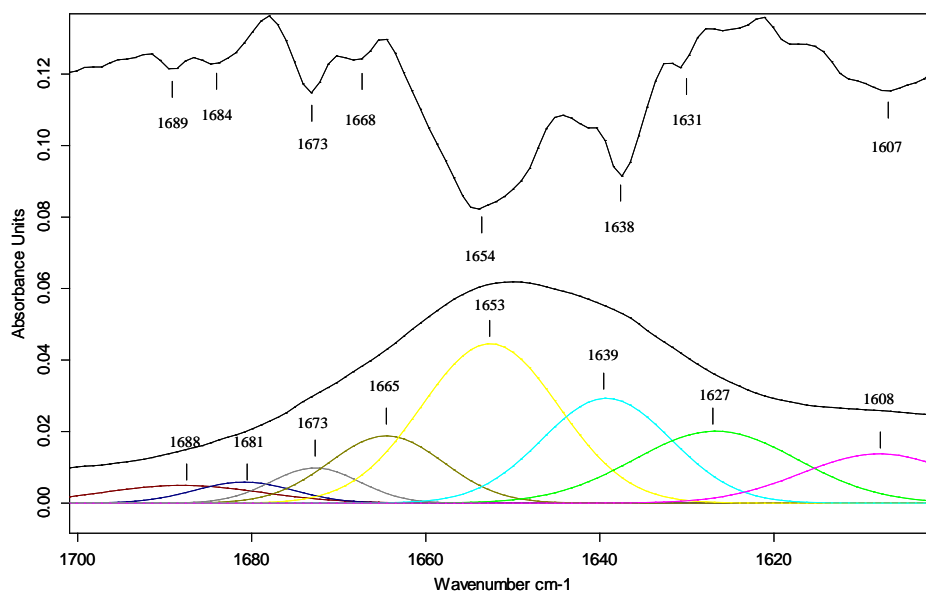


**Figure 5.3** Partial ATR-FTIR spectrum of the Amide I region of lysozyme in D<sub>2</sub>O (black line) and fitted curves (bottom). The second derivative of this section of the spectra is also shown on the top.

The second derivative of the Amide I region resolved a number of the peaks in the Amide I region. The curve fitting of the spectrum revealed seven bands of Gaussian shape at 1688, 1681, 1673, 1665, 1653, 1639 and 1627 cm<sup>-1</sup>, which are comparable with the peak positions found with the second derivative (top curve in Figure 5.3). The peak at 1608 cm<sup>-1</sup> can be associated with the arginyl side chain [193]. The peaks at 1627 cm<sup>-1</sup> is characteristic of the  $\beta$ -sheet, while the band at 1639 cm<sup>-1</sup> may be assigned to the unordered structure, also referred to as random coil. The peaks at 1673, 1684 and 1689 cm<sup>-1</sup> are characteristics of the turns and bends. Finally, the peak at 1654 and 1665 cm<sup>-1</sup> can be assigned as  $\alpha$ -helix. Normally, in IR spectra of proteins, one band associated to the  $\alpha$ -helix is visible. However, X-ray data have suggested two  $\alpha$ -helix conformations for the lysozyme [193]. These two conformations are identified as  $\alpha$ -helix and “3-turn” helix. They vibrate at two different frequencies: 1648-1657 cm<sup>-1</sup> ( $\alpha$ -helix) and 1659-1666 cm<sup>-1</sup> (“3-turn” helix) [193]. In our finding, the band at 1653 cm<sup>-1</sup> is indicative of the  $\alpha$ -helix, while the band at 1665 cm<sup>-1</sup> describes the 3-turn helix. An overview of the assignments of the lysozyme structural conformations from the second derivative of the ATR-FTIR spectra of the gels is shown in Figure 5.4.

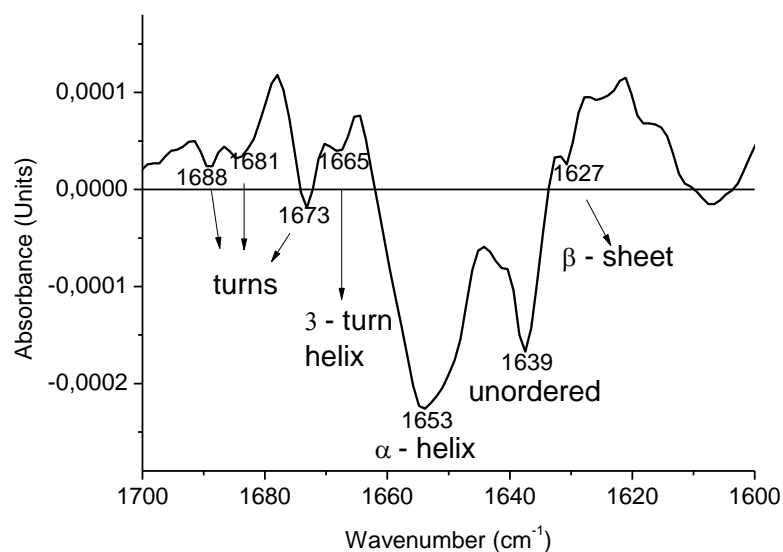


**Figure 5.4** Second derivative of the 10% lysozyme in D<sub>2</sub>O with the assignment of the secondary structure conformation.

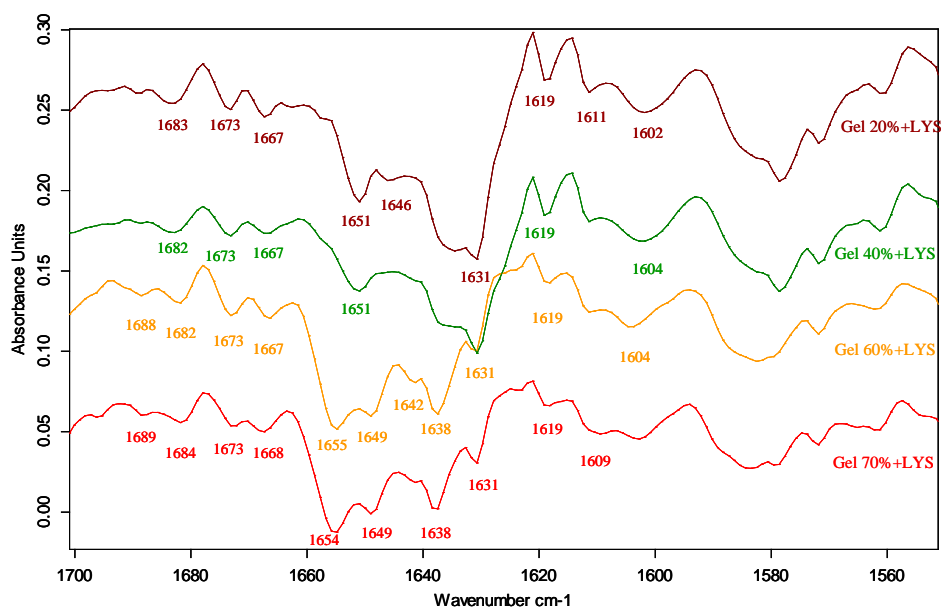


**Figure 5.5** Second derivative of the lysozyme-loaded gels prepared by hydration with D<sub>2</sub>O.

Figure 5.5 shows the second derivative results of the lysozyme-loaded gels prepared by hydration with 20%, 40%, 60% and 70% D<sub>2</sub>O water content. No particular differences were observed for the  $\beta$ -sheet and the unordered conformations, which are represented by the peaks centred at 1619 cm<sup>-1</sup> and 1631 cm<sup>-1</sup> in all the four gels. However, they are at lower wavenumbers compared to the peaks found in the spectrum of the lysozyme solution (1627 cm<sup>-1</sup> and 1639 cm<sup>-1</sup>, respectively). Concerning the turns conformation, the peak at 1673 cm<sup>-1</sup> is visible in all the gels, while the peak at ~1681 cm<sup>-1</sup> observed in the lysozyme solution shifts to 1688 and 1689 cm<sup>-1</sup> in the gel with 60 and 70% water content, but disappeared in the spectra of the gels with

20% and 40% water content. The main difference is observed in the  $\alpha$ -helix region. Two  $\alpha$ -helix conformations have been identified. In the gel with 20% and 40%, the band at  $1667\text{ cm}^{-1}$  is associated to the “3-turn”  $\alpha$ -helix, while the band at  $1651\text{ cm}^{-1}$  is associated to the  $\alpha$ -helix. In the gel with 20% a weak peak at  $1646\text{ cm}^{-1}$  is identified which is related to the  $\alpha$ -helix conformation. This peak is not visible in the spectrum of the gel with 40% water. In the gels with 60% and 70% water content, the  $\alpha$ -helix band shift towards higher frequencies values, at  $1655\text{ cm}^{-1}$  and  $1654\text{ cm}^{-1}$ , respectively. The bands associated with the “3-turn” helix  $\text{cm}^{-1}$  are visible at  $1649\text{ cm}^{-1}$  and at  $1667\text{ cm}^{-1}$ . The bands identified with the second derivatives were used to quantify the proportion of the secondary structure conformations of lysozyme present in the gels. A quantitative estimation of the conformations for lysozyme in  $\text{D}_2\text{O}$  and for the gels prepared by hydration with 20%, 40%, 60% and 70%  $\text{D}_2\text{O}$  contents is listed in Table 5.5.

**Table 5.5** Secondary structural conformation of lysozyme in  $\text{D}_2\text{O}$  and incorporated into the gels with 20%, 40%, 60%, 70%  $\text{D}_2\text{O}$  content prepared by hydration method measured using ATR-FTIR.

Samples	$\beta$ -sheet		unordered		$\alpha$ -helix		turn	
	Range ( $\text{cm}^{-1}$ )	%						
LYS- $\text{D}_2\text{O}$	1627	19	1639	21	1653-1665	47	1673-1688	13
Gel 20% water	1618-1632	29	—	—	1647	43	1676-1693	28
Gel 40% water	1632	30	1646	37	1662-1668	33	—	—
Gel 60% water	1622-1637	34	1643	12	1649-1665	44	1674-1686	10
Gel 70% water	1624-1631	20	1639	18	1648-1665	52	1674-1686	10

The secondary structure of lysozyme loaded in the gels prepared by heating method was determined using the same method described above. Table 5.6 shows the secondary structure of the lysozyme loaded in the gels prepared by heating. The gels with 50% and 60% water content have a similar conformation. The conformations of lysozyme in the gel with 40% water contain less  $\alpha$ -helix and  $\beta$ -sheet, but more turns in comparison to the other two gels. The conformation of the lysozyme differs from the conformation determined in the gels prepared by hydration. Overall, the  $\beta$ -sheet and the  $\alpha$ -helix components decrease, while the turn structure increases. This result may suggest that heating method induced changes in the structural conformation of the lysozyme, whether this change leads to reducing the biological activity of lysozyme in the gels is uncertain.

**Table 5.6** Secondary structural conformation of lysozyme-loaded gels prepared by heating method measured using ATR-FTIR.

<i>Samples</i>	<i><math>\beta</math>-sheet</i>		<i>unordered</i>		<i><math>\alpha</math>-helix</i>		<i>turn</i>	
	<i>Range</i> ( <i>cm<sup>-1</sup></i> )	<i>%</i>						
Gel 40% water	1621-1630	18	1641	16	1650-1663	25	1672-1691	42
Gel 50% water	1621-1632	25	1644	28	1650-1665	31	1678-1691	16
Gel 60% water	1622-1631	21	1643	29	1650-1663	30	1677-1695	20

Discrepancy exists in the literature regarding the peak assignments of the lysozyme. In literature, FTIR data of lysozyme in D<sub>2</sub>O was previously reported to show a conformation with 48%  $\alpha$ -helix, 23%  $\beta$ -sheet, 13% turns and 16% unordered structures [193]. This agrees well with our finding. However, in other work [253], the proportions of these conformations were reported as 19%, 40%, 27% and 14% or 21%, respectively. The proportion of 19%, 45%, 23%, 13%, respectively was reported when measured with X-ray crystallography [254]. Lysozyme buffer solution analysed with circular dichroism (CD) spectroscopy 29-45% of  $\alpha$ -helix, 11-39% of  $\beta$ -sheet, 8-26% of turn and 8-60% of unordered [255-261]. Overall, the information obtained from the literature is that the  $\alpha$ -helix structure should be the dominating conformation for active lysozyme.

#### 5.4.2 Structural analysis of Lysozyme loaded gels using SAXS

SAXS studies were performed in order to determine the nanostructure of the lysozyme-loaded gels and to assess whether the presence of the lysozyme induced any change in the gel structure. The lysozyme-loaded gels prepared by hydration method were analysed using SAXS as described in section 5.3.2. SAXS spectrum of the lysozyme-loaded gel with 40% water determined at 25 °C is shown in Figure 5.6. The scattering pattern differs from the one obtained for the unloaded gel determined in the same conditions (see section 3.5, Figure 9). The first peak was observed at  $q$  ( $\text{\AA}^{-1}$ ) of  $0.07 \text{\AA}^{-1}$  and the second peak at  $0.14 \text{\AA}^{-1}$ , which correspond to 89.8 and 44.9  $\text{\AA}$ , respectively. Thus, the gel shows a Bragg reflection of 1:2, typical of a lamellar phase, which differs from the hexagonal structure found for the unloaded gel with 40% water prepared by hydration. For the lysozyme-loaded gel, the ordered phase structure is not so clear, since only two peaks are identified and the second peak at  $0.14 \text{\AA}^{-1}$  is broad and not well defined.

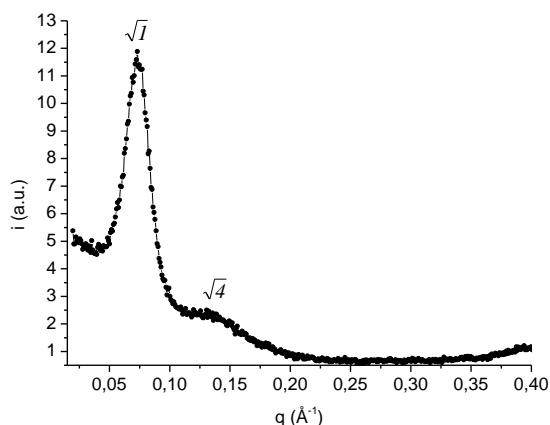


**Figure 5.6** SAXS spectrum of the lysozyme-loaded gel with 40% water prepared by hydration (measured at 25 °C).

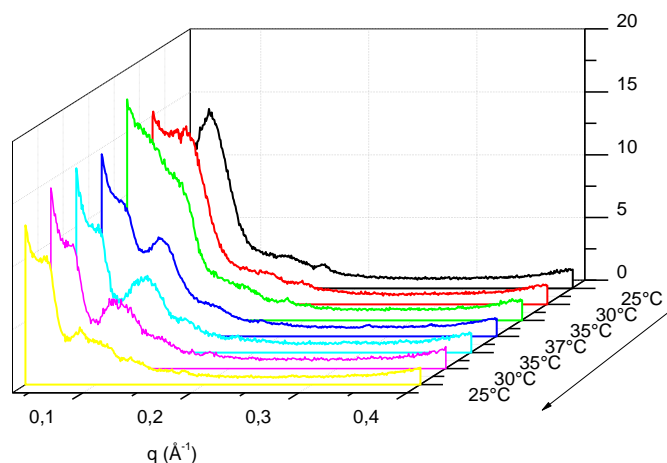


**Figure 5.7** Variable temperature SAXS spectrum of the lysozyme-loaded gel with 50% water prepared by hydration upon heating from 25 °C to 37 °C and cooling back to 25 °C. The direction of the arrow indicate the direction of the heating-cooling process.

In order to further investigate the effect of the thermal treatment on the structure of the lysozyme-loaded gels, SAXS experiments with variable temperature scan was used to study the lysozyme-loaded gel with 50% water prepared by hydration. Figure 5.7 shows the temperature scan of the gel with 50% water content. Despite the peaks are not well defined, it was possible to assign the peaks and identify the evolution of the liquid crystalline phases during the thermal treatment. At 25 °C and 30 °C, the gel is likely to be in hexagonal phase, though the second characteristic diffraction peak of hexagonal phase is not particularly evident. The result is consistent with the phase identification of the unloaded gel with 50% water content (section 3.4.2). However, upon heating and cooling, the diffraction peaks are less defined, probably because of the coexistence of mixed phases during thermal treatment. At 30 °C in the cooling cycle, the structure is close to the hexagonal phase. This finding differs from the unloaded gel, which showed a diamond (Pn3m) cubic phase when heated up to 37 °C and cooled back down

to 25 °C. Table 5.7 shows the list of the diffraction peaks with the corresponding Bragg's positional ratio.

**Table 5.7** Assignments of the peaks for the lysozyme-loaded gel with 50% water prepared by heating method analysed using temperature scan. The  $q$  ( $\text{\AA}^{-1}$ ) and  $d$  ( $\text{\AA}$ ) values as well as the peak positioning at Bragg values are listed.

Temperature (°C)	$q(\text{\AA}^{-1})$	$d(\text{\AA})$	Bragg's positional ratio		Liquid crystalline structure
25	$6.57 \times 10^{-2}$	<b>95.67</b>	<b>1</b>	1	Hexagonal
	$1.12 \times 10^{-1}$	<b>55.88</b>	<b>1.71</b>	$\sqrt{3}$	
	$1.35 \times 10^{-1}$	<b>46.68</b>	<b>2.05</b>	$\sqrt{4}$	
	$1.7 \times 10^{-1}$	<b>36.99</b>	<b>2.59</b>	$\sim \sqrt{7}$	
30	$6.73 \times 10^{-2}$	<b>93.34</b>	<b>1</b>	1	Hexagonal
	$1.21 \times 10^{-1}$	<b>52.08</b>	<b>1.79</b>	$\sqrt{3}$	
	$1.40 \times 10^{-1}$	<b>45.04</b>	<b>2.07</b>	$\sqrt{4}$	
	$1.74 \times 10^{-1}$	<b>36.12</b>	<b>2.58</b>	$\sim \sqrt{7}$	
35	$5.5 \times 10^{-2}$	<b>114.23</b>	<b>1</b>	1	Mixed phases
	$8.46 \times 10^{-2}$	<b>74.31</b>	<b>1.54</b>	—	
	$1.43 \times 10^{-1}$	<b>44.00</b>	<b>2.60</b>	$\sqrt{7}$	
	$1.83 \times 10^{-1}$	<b>34.34</b>	<b>3.33</b>	$\sim \sqrt{10}$	
37	$5.5 \times 10^{-2}$	<b>114.23</b>	<b>1</b>	1	Mixed phases
	$9.19 \times 10^{-2}$	<b>68.34</b>	<b>1.67</b>	$\sim \sqrt{3}$	
	$1.39 \times 10^{-1}$	<b>45.38</b>	<b>2.51</b>	$\sqrt{6}$	
35	$5.58 \times 10^{-2}$	<b>112.55</b>	<b>1</b>	1	Mixed phases
	$1.01 \times 10^{-1}$	<b>62.23</b>	<b>1.81</b>	$\sim \sqrt{3}$	
	$1.35 \times 10^{-1}$	<b>46.40</b>	<b>2.43</b>	$\sqrt{6}$	
30	$5.5 \times 10^{-2}$	<b>114.23</b>	<b>1</b>	1	Close to Hexagonal
	$9.36 \times 10^{-2}$	<b>67.14</b>	<b>1.70</b>	$\sim \sqrt{3}$	
	$1.05 \times 10^{-1}$	<b>59.80</b>	<b>1.91</b>	$\sim \sqrt{4}$	
	$1.41 \times 10^{-1}$	<b>44.56</b>	<b>2.56</b>	$\sim \sqrt{7}$	
25	$5.50 \times 10^{-2}$	<b>114.23</b>	<b>1</b>	1	Mixed phases
	$8.70 \times 10^{-2}$	<b>72.21</b>	<b>1.58</b>	—	
	$1.05 \times 10^{-1}$	<b>59.80</b>	<b>1.91</b>	$\sim \sqrt{4}$	
	$1.34 \times 10^{-1}$	<b>46.97</b>	<b>2.43</b>	$\sqrt{6}$	

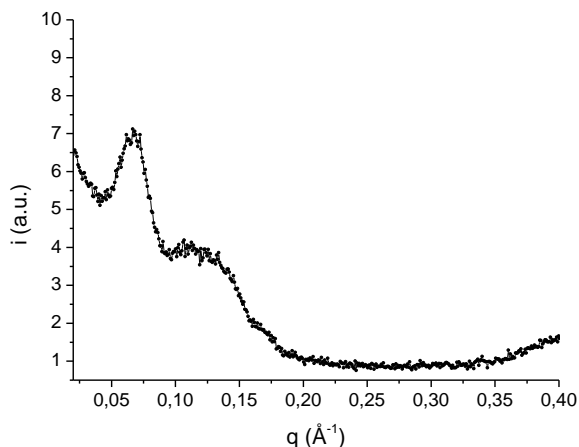


**Figure 5.8** SAXS spectrum of the intensity versus  $q$  ( $\text{\AA}^{-1}$ ) of the lysozyme-loaded gel at 25 °C with 70% water prepared by hydration.

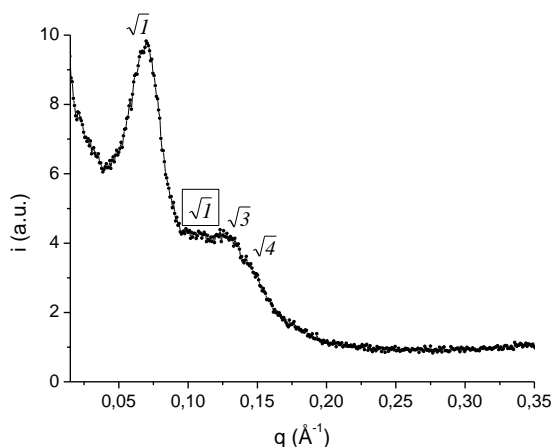


**Figure 5.9** SAXS spectrum of the intensity versus  $q$  ( $\text{\AA}^{-1}$ ) of the lysozyme-loaded gel at 37 °C with 70% water prepared by hydration.

Similar to the unloaded gels, the water content can have significant impact on the structures of the gels. Figure 5.8 shows the SAXS spectrum of the lysozyme-loaded gel with 70% water content analysed at 25 °C. The peaks are not well defined, thus it is not possible to accurately identify the structure. The first peak is centred at  $0.072 \text{ \AA}^{-1}$  ( $87.2 \text{ \AA}$ ), followed by a shoulder. This shoulder may be the submerged peak of the peaks centred at  $0.115 \text{ \AA}^{-1}$  and  $0.130 \text{ \AA}^{-1}$  ( $54.7$  and  $48.1 \text{ \AA}$ ). The three peaks may be part of the three different lamellar phases identified in a previous work on dry Gelucire 50/13 [109]. These three lamellar phases are: the first one corresponds to  $q$  ( $\text{\AA}^{-1}$ )  $0.051 \text{ \AA}^{-1}$ ,  $0.10 \text{ \AA}^{-1}$  and  $0.152 \text{ \AA}^{-1}$ . The second one corresponds to  $q$  ( $\text{\AA}^{-1}$ ) values at  $0.07 \text{ \AA}^{-1}$  and  $0.14 \text{ \AA}^{-1}$  and the third lamellar phase has value of  $0.127 \text{ \AA}^{-1}$ . A further peak at  $0.174 \text{ \AA}^{-1}$  is also identified. At 37 °C, the peaks are not well defined, but can still be assessed. It shows a Bragg's positional ratio close to a hexagonal phase  $1: \sqrt{3} : \sqrt{4}$  (Figure 5.9). The first peak remains centred at  $0.072 \text{ \AA}^{-1}$  ( $87.2 \text{ \AA}$ ), while the shoulder peak observed at 25 °C,

it is better defined as one peak at  $0.130 \text{ \AA}^{-1}$  ( $48.1 \text{ \AA}$ ). In between the two peaks, a peak at  $0.115 \text{ \AA}^{-1}$  is barely visible (see the squared  $\sqrt{I}$  in Figure 5.9). The third peak at  $0.144 \text{ \AA}^{-1}$  ( $43.5 \text{ \AA}$ ) is more like a shoulder. Therefore, it can be concluded that the lysozyme-loaded gel with 70% water prepared by hydration, at  $25 \text{ }^\circ\text{C}$  shows mixed phases as the unloaded-gel. However, at  $37 \text{ }^\circ\text{C}$  a hexagonal phase could be recognised, whilst it was not possible to determine any phase in the unloaded one (Figure 12, section 3.5).

In conclusion, the incorporation of lysozyme in the gels prepared by hydration induced changes in the gel structure. In particular, the gel with 40% water changed the structure from hexagonal to lamellar after incorporation of lysozyme. The gel with 50% water retains mainly the hexagonal phase at  $25 \text{ }^\circ\text{C}$  and  $30 \text{ }^\circ\text{C}$ . However, at  $37 \text{ }^\circ\text{C}$  and cooling back down to  $25 \text{ }^\circ\text{C}$  the unloaded gel is characterised by a diamond (Pn3m) cubic phase. As a consequence of the incorporation of lysozyme, the order of the gel structure reduce. Finally, the unloaded gel with 70% water was characterised by mixed phases. After the incorporation of the lysozyme at  $25 \text{ }^\circ\text{C}$  the gel still remains as mixed phases. However, at  $37 \text{ }^\circ\text{C}$  the hexagonal phase could be identified in the lysozyme-loaded gel with 70% water.

### **5.4.3 Thermal phase transitions of gels studied using thermal analysis and rheology**

In Chapter 3, phase transitions of the unloaded gels prepared by hydration upon thermal treatment were studied with DSC and rheometer. The same tests were performed on the lysozyme-loaded gels prepared by hydration method in order to assess whether the incorporation of lysozyme has any effect on the behaviour of the gels. The thermal behaviour of the loaded gels was studied with DSC, while the rheometer investigated the change of the viscoelastic properties of the lysozyme-loaded gels.

#### **5.4.3.1 Thermal analysis**

Thermal phase transitions of the lysozyme-loaded gels were analysed with conventional DSC. The onset temperatures ( $T_h$  or  $T_c$ , which stands for the onset temperature of the heating and the cooling cycle, respectively), the peak temperatures ( $T_p$ ) and the enthalpy of the detectable peaks ( $\Delta H$ ) were determined and summarised in Table 5.8 and Table 5.9. Untreated lysozyme was also analysed as a control. No peak was found in the temperature range studied.

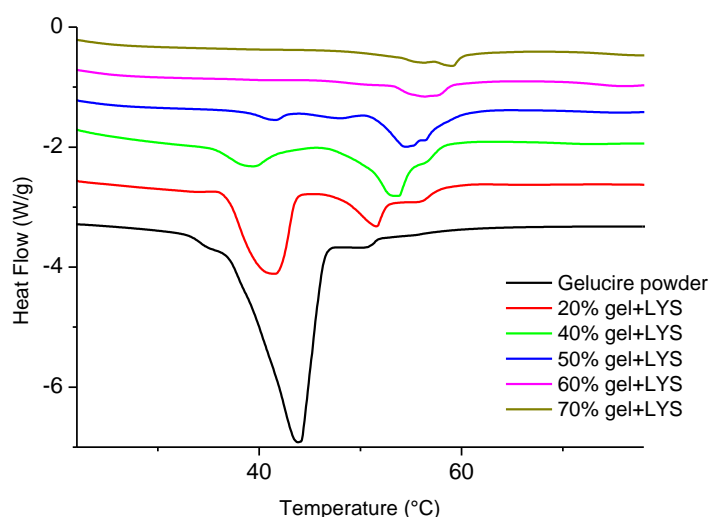


**Figure 5.10** DSC results for the lysozyme-loaded gels prepared by hydration method upon heating from 20 to 80°C. The profile of dry Gelucire powder is also shown for comparison.

The lysozyme-loaded gels with 20%, 40% and 50% water contents show two endothermic peaks in the heating cycle one at lower temperature (40-41 °C) and the other one at a higher temperature (above 50 °C). The results of the lysozyme-loaded gels with 20% and 40% water content are consistent with the thermal results of the unloaded gels with 20% and 40% water content prepared by hydration, which showed two transitions peaks at about 50 °C and 37 °C, although the second transitions at 37 °C is a shoulder peak (see Table 3.7, section 3.4.3.1). The lysozyme-loaded gel with 50% water content showed a different pattern from the unloaded gel with 50% water content prepared by hydration. One main transition at 53 °C can be seen in the DSC result of the unloaded gel. This may be explained by the different structures/phase transformation formed upon heating for the unloaded and lysozyme-loaded gels with 50% water. The SAXS results (section 5.4.2) identified in both cases a hexagonal phase up to 30 °C. Above 37 °C the phases differ, the unloaded gel show a diamond cubic phase (Pn3m), while the lysozyme-loaded is characterised by mixed phase. Therefore, in the case of the gel with 50% water, it is clear that the presence of the lysozyme induced structural changes in the gel. The peak at lower temperature, which disappears in the gels with 60% and 70% water content, was not visible in the unloaded gels.

**Table 5.8** Mean values of the onset temperature ( $T_h$ ), the peak temperature ( $T_p$ ) and the enthalpy of the peak ( $\Delta H$ )  $\pm$ SD of the lysozyme-loaded gels determined in the heating cycle (n=3).

Sample (% water)	Heating					
	$T_{h1}$ (°C)	$T_{p1}$ (°C)	$\Delta H_1$ (J/g)	$T_{h1}$ (°C)	$T_{p1}$ (°C)	$\Delta H_1$ (J/g)
0	38±0.42	44±0.14	128.07±1.40	—	—	—
20	49±0.93	52±0.35	10.33±1.52	37±0.52	41±0.21	12.68±11.14
40	49±0.72	53±0.45	9.48±4.78	36±0.81	40±1.26	2.86±2.22
50	51±0.68	54±0.51	7.67±1.40	38±1.15	41±0.26	1.05±0.149
60	53±0.19	56±1.04	5.88±2.31	—	—	—
70	54±1.77	59±0.04	5.41±1.03	—	—	—

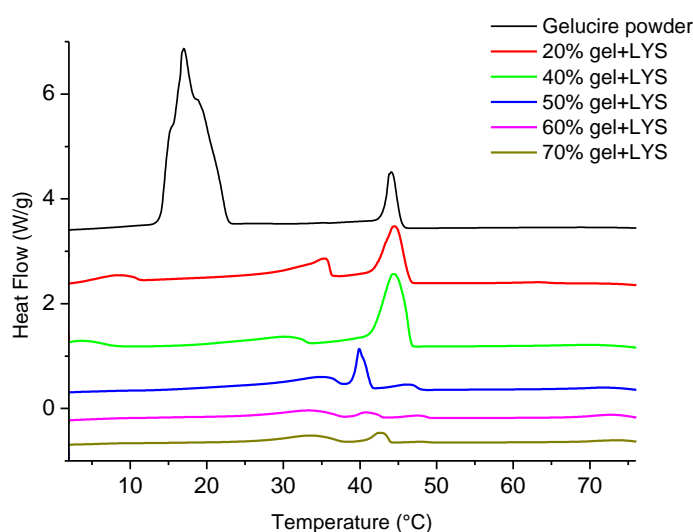


**Figure 5.11** DSC results of the lysozyme-loaded gels prepared by hydration method during cooling from 80 °C to 0 °C. The profile of Gelucire powder is also shown for comparison.

As seen in Figure 5.11, all gels with lysozyme show two exothermic peaks during the cooling cycle. The peak at lower temperature (32-36 °C) is a shoulder peak. It is more apparent in the gel with 20% water (35 °C). The second peak arises at 40-45 °C. The gels with 20% and 40% water content show the second peak at 44 °C, which is very close to the second peak in the DSC result of the dry Gelucire powder. For the lysozyme-loaded gels with 20% and 40% water content, the main peak transitions at 44 °C are consistent with the main transitions of the unloaded gels with 20% and 40% water content prepared by hydration (45 °C and 44 °C). For the lysozyme-loaded gels with 50%, 60% and 70% water contents, this peak shifts towards lower temperature (40, 41 and 43 °C, respectively) with decreasing water content. The unloaded gel with 50% water has a peak at few degrees higher (44 °C) compared to the main peak of the lysozyme-loaded gel. The unloaded gel with 60% water has a peak at 31 °C, which arises at a temperature 10 degrees lower than the lysozyme-loaded gel with the same water content.

Finally, the unloaded gel with 70% water has a peak at 41 °C, which is similar to the lysozyme-loaded gel (see section 3.4.3.1).

**Table 5.9** Mean values of the onset temperature ( $T_c$ ), the peak temperature ( $T_p$ ) and the enthalpy of the peak ( $\Delta H$ )  $\pm$ SD of the lysozyme-loaded gels determined in the cooling cycle (n=3).

Sample (% water)	Cooling					
	$T_{c1}$ (°C)	$T_{p1}$ (°C)	$\Delta H_1$ (J/g)	$T_{c1}$ (°C)	$T_{p1}$ (°C)	$\Delta H_1$ (J/g)
0	21±0.3	17±0.9	92.62±1.23	45±0.1	44±0.1	9.73±0.34
20	35±1.5	32±3.0	5.75±3.69	46±0.6	44±0.3	11.23±1.67
40	38±3.8	36±5.1	5.21±1.98	47±0.1	45±0.1	9.41±7.74
50	37±0.0	34±1.0	4.72±0.30	41±0.8	40±0.5	3.92±2.46
60	38±0.2	33±0.3	3.78±0.95	42±0.6	41±0.2	1.11±0.05
70	37±0.1	33±0.4	3.32±0.63	42±1.1	43±1.2	0.78±0.67

Considering the absence of the peaks in the DSC results of the untreated lysozyme, it is reasonable to propose that the peaks found are associated with the phase transitions of carrier gels. However, some differences were observed compared to the untreated Gelucire and to the unloaded gels, indicating the presence of the lysozyme may be responsible for the changes in the phases present in the lysozyme loaded gels.

#### 5.4.3.2 Temperature ramp test (Oscillation Rheometer)

In order to better understand the effect of lysozyme on the viscoelastic properties of the gels upon thermal treatment, the oscillation temperature ramp tests were performed with a rheometer. The lysozyme-loaded gels prepared by hydration method were heated up from 25 °C to 80 °C at rate of 1 °C/min and a frequency of 1 Hz and the changes in their viscoelastic properties were followed. The stress applied was chosen within the linear viscoelastic region (LVR) determined by the stress sweep test (see section 5.4.4). The rheograms obtained show the change of elastic moduli ( $G'$ ) with the temperature for the heating and the cooling cycles.

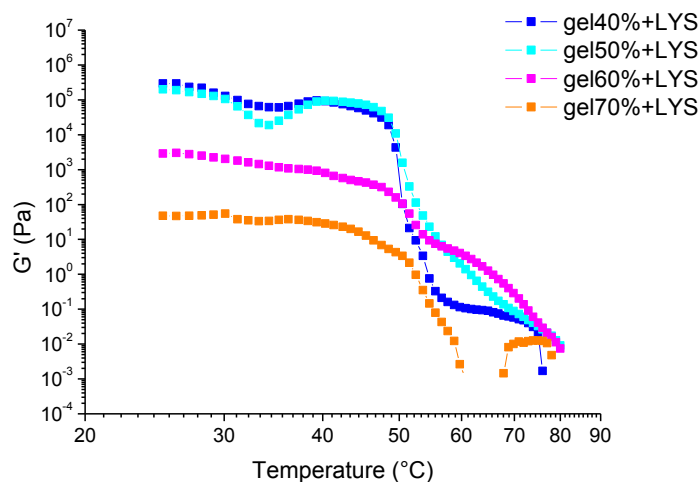


**Figure 5.12** Temperature influence on the elastic modulus ( $G'$ ) of the lysozyme-loaded gels prepared by hydration during heating (25 °C to 80 °C) ( $n = 3$ ).

Figure 5.12 shows the  $G'$  change of all studied gels upon heating from 25 °C to 80 °C. The  $G'$  of the lysozyme-loaded gel with 40% water content initially decreases until the temperature reaches 35 °C, after which  $G'$  slowly increases up to 40 °C. The  $G'$  sharply decreases 5 orders of magnitude at 48–53 °C and it finally plateaus. This means that after ~50 °C, the gel exists in a flow state. The rheogram of the lysozyme-loaded gel with 40% water content is similar to its corresponding unloaded gel, except for the final plateau region, which is not present in the unloaded gel (see Figure 23 in section 3.4.3.2). The rheogram of the lysozyme-loaded gel with 50% water is similar to the unloaded gel with 50% water. The  $G'$  initially decreases and it reaches a minimum point at 34 °C, which is at a slight lower temperature compared to the unloaded gel with 50% water (which is at 37 °C). The  $G'$  increases when heated up to 40 °C, and as the heating progresses it levels off up to 47 °C. Following that, it drops of 5 orders of magnitude until the temperature reaches 53 °C and it continues to gently decrease up to 80 °C. The transitions at 34 °C for the lysozyme-loaded gels with 40% and 50% water contents can be correlated to the first thermal transitions found with the DSC (Table 5.8, section 5.4.3.1). However, the transitions occurred at 49 and 51 °C, respectively, determined with DSC, they are likely to be associated with the breakdown of the gel structure as it is indicated by the rheogram. Furthermore, for the lysozyme-loaded gel with 50% water, the transition at 34 °C corresponds to the structural change from a hexagonal to a mixed phase identified by the SAXS experiments (Table 5.7, section 5.4.2).

For the gel with 60% water content,  $G'$  slightly decreases of one order of magnitude between 25 °C to 49 °C. The main transition occurs between 50 and 56 °C, which is in agreement with the peak recorded by DSC (56 °C peak temperature). After this main transition, the  $G'$  slowly decreases as the temperature increases up to 80 °C. The  $G'$  profile of the lysozyme-loaded gel

with 60% water is similar to the one of the corresponding unloaded gel. The  $G'$  of lysozyme-loaded gel with 70% water content is constant up to 40 °C. Gradually it decreases and finally it drops at 50 °C. This profile differs from the unloaded gel with 70% water, in which case the  $G'$  initially increases followed by a plateau and a drop at 50 °C.

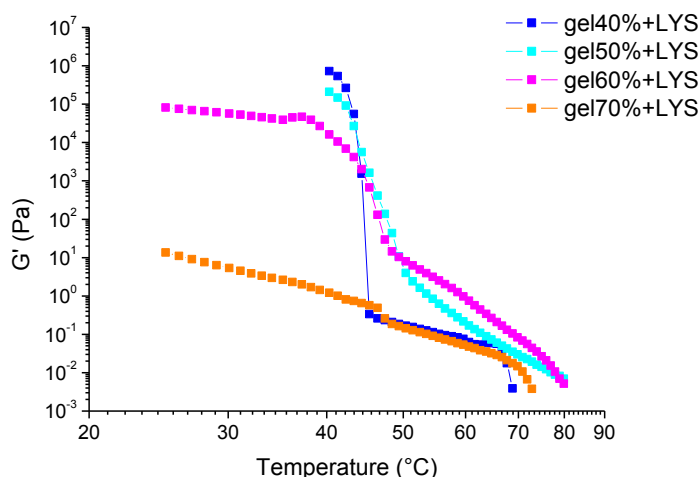


**Figure 5.13** Temperature influence on the elastic modulus ( $G'$ ) of the lysozyme-loaded gels prepared by hydration during cooling (80 °C to 25 °C) (n = 3).

For all the gels, the  $G'$  values recover when the gels were cooled down, as shown in Figure 5.13. The recovery is sharper in the lysozyme-loaded gel with 40% water, which jumps towards higher value of  $G'$  at 45 °C. In the gels with 50% and 60% water contents, the  $G'$  values gently increase with decreasing the temperature from 80 °C to ~50 °C. After that, the  $G'$  values suddenly increase reaching the original value. In the gel with 70% water content, the  $G'$  progressively increases with decreasing the temperature. This profile is completely different from the profile of the unloaded gel with 70% water content, in which a jump of four orders of magnitude in  $G'$  is visible at ~45 °C (see Figure 24, section 3.6.2). Combined with the results obtained by SAXS, ATR-FTIR and DSC, the effect of lysozyme on the gel structure seems most significant for the gel with 70% water content.

The lysozyme-loaded gels with 40% and 60% water prepared by heating method were analysed. Comparing the  $G'$ 's profiles, no particular differences were found with the lysozyme-loaded gels with 40% and 60% water content prepared by hydration method (data not shown). Thus, it may be conclude that the method of preparation has no significant effect in the response of the elastic moduli and possibly in the phase transition of the lysozyme-loaded gels upon thermal treatment.

#### 5.4.4 Rheological properties of lysozyme-loaded gels

Chapter 3, section 3.4.4, describes the investigation into the rheological properties of the unloaded gels by evaluating the viscoelastic response to the applied stress, frequency and the flow parameters. Overall, the unloaded gels demonstrate as entangled-like or cross linked-like network behaviour. In this chapter, the lysozyme-loaded gels prepared by hydration method were analysed in order to investigate the effect of the incorporation of the lysozyme on the viscoelastic properties of the gels. The lysozyme-loaded gels with 40% and 60% water content prepared by heating method were also analysed to assess whether the method of preparation plays a role in altering the rheological and structural properties of the gels.

##### 5.4.4.1 Determination of the linear viscoelastic region: the oscillation stress sweep test

The linear viscoelastic region (LVR) was identified with stress sweep tests. The tests were performed as described in section 5.3.4. As previously discussed in section 3.7.1, the determination of the LVR is very important for further carrying out valid rheological tests. It allows the identification of the range of stress within which the structure of the material does not undergo disruption. The complex modulus,  $|G^*|$ , and the phase angle,  $\delta$ , were measured as a function of stress. The oscillation stress within the linear viscoelastic region was chosen to perform further oscillation tests.

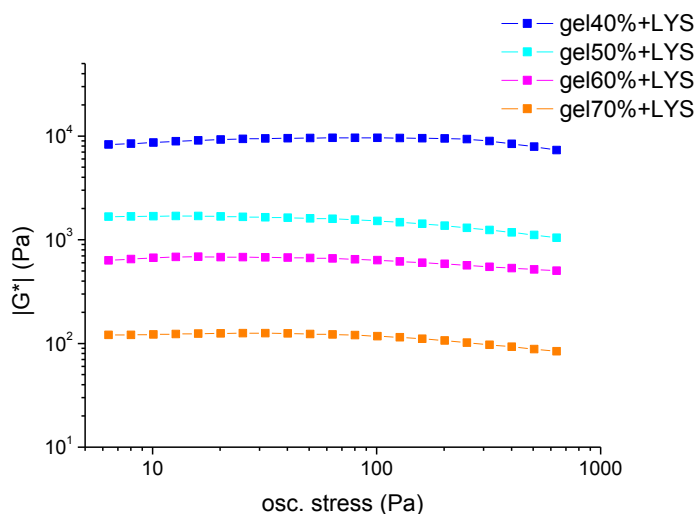


**Figure 5.14** Complex moduli ( $|G^*|$ , Pa) versus oscillation stress plot of the lysozyme-loaded gels prepared by hydration method ( $n = 3$ ).

Figure 5.14 shows the complex moduli,  $|G^*|$  (Pa) plotted against oscillation stress (Pa) for the lysozyme-loaded gels with 40%, 50%, 60% and 70% water contents prepared by hydration method. The  $|G^*|$  values decrease with increasing the water content in the gels. This reflects the similar trend of the unloaded gels prepared by hydration method (see Figure 29, section 3.4.4.1).

For the lysozyme-loaded gel with 40% water content, the  $|G^*|$  is constant throughout the oscillation stress applied. This means that the structure of the gel is not disrupted within this range. However, it can be seen a slight decrease above 200 Pa can be observed in the gel with 50% water (the  $|G^*|$  starts to decrease after 40 Pa), while in the gels with 60% and 70% water contents, the LVR is between 60 and 80 Pa.

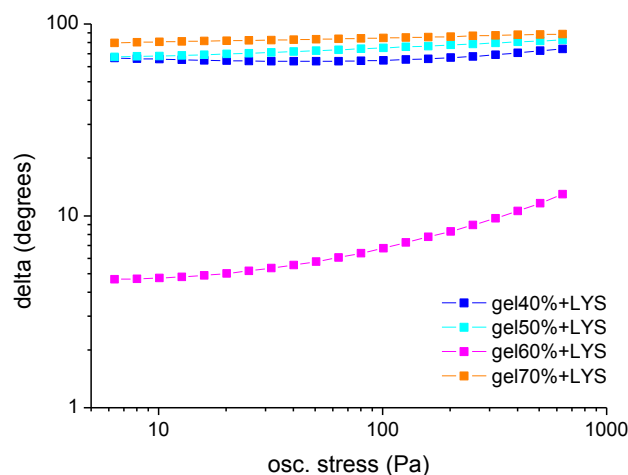


**Figure 5.15** Phase angle ( $\delta$ ) (degrees) versus oscillation stress plot of the lysozyme-loaded gels prepared by hydration ( $n = 3$ ).

In order to better identify the LVR, a second dynamic properties (phase angle,  $\delta$ ) has been considered (Figure 5.15). Figure 5.15 shows the phase angle ( $\delta$ ) plotted against oscillation stress for the lysozyme-loaded gels. The data are very different from the unloaded gels (Figure 30, section 3.4.4.1), especially for the gels with 60% and 70% water contents. The gel with 60% water has  $\delta$  smaller than  $10^\circ$ , which suggests that the elastic component prevails. For this particular gel, the angle is constant up to 30 Pa, which is in contrast with the  $|G^*|$  values. After 30 Pa, it increases with the applied stress, though the elastic component is still dominant ( $\delta < 45^\circ$ ). Therefore, a stress value of 25 Pa was chosen for further rheological experiments. The gel with 40%, 50% and 70% water contents all have  $\delta > 45^\circ$ , which suggests that the viscous component in the gels is dominant. In the gel with 40% water,  $\delta$  is constant up to 200 Pa, and then it slightly increases. Therefore, a stress of 80 Pa was applied for further experiments. In the gel with 50% water,  $\delta$  slightly increases when the stress is above 30 Pa, thus a stress of 25 Pa was chosen for further tests. Finally, the gel with 70% water content follows a trend which is completely different from the unloaded gel with 70% water, in which the  $\delta$  was slightly below  $45^\circ$  at low stress values and it increases when the stress applied is above 80 Pa. For the lysozyme-loaded gel with 70% water,  $\delta$  is  $\sim 80^\circ$ , which means that the viscous component is prevalent and it slightly increase above 50 Pa. In this case, a stress of 25 Pa was chosen for further experiments.

Comparing the parameters  $|G^*|$  and  $\delta$  (Figure 5.16) for the lysozyme-loaded gels with 40% water prepared by hydration and by heating, no particular difference has been observed. The  $\delta$  values of the lysozyme-loaded gel with 40% water prepared by heating are slightly lower than the ones of the gel prepared by hydration, but both are above  $45^\circ$ . This means that the viscous part still prevails. Overall, the LVRs for the gels prepared by different methods are in the same range. However, for the lysozyme-loaded gels with 60% water, prepared by heating and by hydration, different results in the  $\delta$  values were obtained. In the gel with 60% water prepared by hydration,  $\delta$  is about  $10^\circ$ . It decreases at 30 Pa and remains below  $45^\circ$ , which means that the elastic component is dominant. In the gel with 60% water prepared by heating,  $\delta$  is always above  $45^\circ$ , more precisely at  $83^\circ$  (Figure 5.16). Therefore, a different oscillation stress range was applied to the lysozyme-loaded gels prepared by heating for further testing.

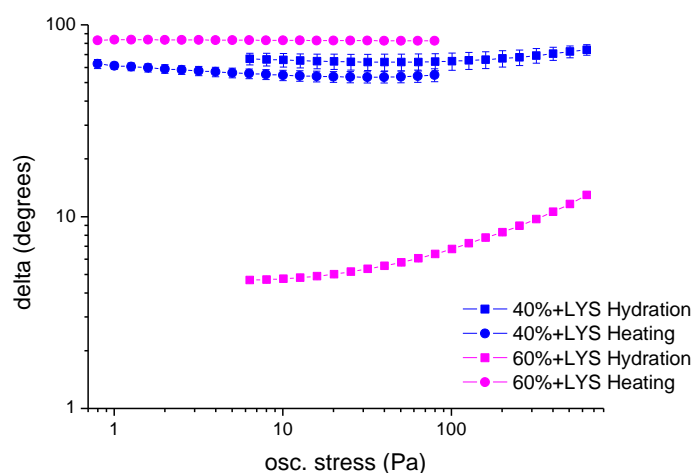


**Figure 5.16** Comparison of phase angle ( $\delta$ ) versus oscillation stress plots of the lysozyme-loaded gels with 40% and 60% water content prepared by heating and by hydration ( $n = 3$ ).

#### 5.4.4.2 Oscillation frequency sweep test

As discussed in Chapter 3, section 3.7.2, the oscillatory curves give the fingerprint of the microstructure of the gels. The frequency sweep tests were conducted on the lysozyme-loaded gels as described in section 5.3.4. The stress applied was chosen as discussed in section 3.4.4.1. In this section the studies on the viscoelastic parameters  $G'$ ,  $G''$ ,  $\tan\delta$  and  $\eta'$  are described for the lysozyme-loaded gels prepared by hydration.

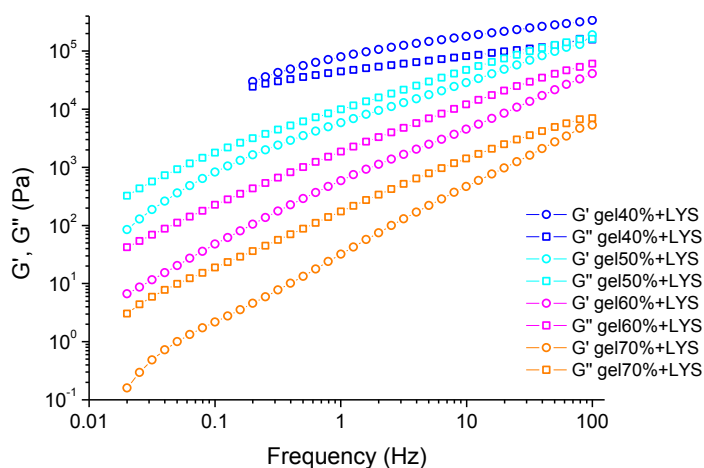


**Figure 5.17** Elastic modulus ( $G'$ ) and viscous modulus ( $G''$ ) versus frequency (Hz) plots for the lysozyme-loaded gels prepared by hydration method ( $n = 3$ ).

Figure 5.17 shows the changes of  $G'$  and  $G''$  over a range of frequency between  $10^{-2}$  and  $10^2$  Hz. Overall, the viscous component ( $G''$ ) always prevail to the elastic one ( $G'$ ), exception for the gel with 40% water where  $G'$  is predominant and it is consistent with cross linked-like behaviour. Furthermore it may be suggested a crossover at frequency below 0.2 Hz, which means that  $G'$  and  $G''$  are equivalent. This trend is different from the unloaded gel with 40% water, where  $G'$  prevails on  $G''$  at low frequency and they cross at 25 Hz. In the lysozyme-loaded gel with 50% water,  $G'' > G'$ , which is consistent with entangled-like behaviour. The two moduli cross at 88 Hz, which is slightly higher than the unloaded gel with 50% water (72 Hz). The lysozyme-loaded gels with 60% and 70% water contents also show entangled-like behaviour as  $G'' > G'$  and no crossover can be observed This is consistent with the unloaded gel with 60% water content. Similar as the other tests performed previously, the different trends of behaviour is observed for the lysozyme-loaded and unloaded gel with 70% water. For the unloaded gel,  $G'$  cross with  $G''$  at 31 Hz. This means that the lysozyme-loaded gel with 70% water is predominantly viscous throughout the range of frequency applied. Therefore, it may be concluded that the presence of the lysozyme has an impact on the viscoelastic properties and hence on the structure of the gels with 40% and 70% water contents, while for the gels with 50% and 60% water, no particular difference can be observed.

In order to statistically compare the difference in rheological behaviour of the gels, one-way ANOVA tests on  $G'$  and  $G''$  were performed at selected frequency values (0.2, 1, 4, 10, 25, 50 and 100 Hz).  $G'$  and  $G''$  significantly increase with the Gelucire content in the lysozyme-loaded gels ( $F = 45.31$ ,  $df = 3$ ,  $p < 0.001$ ;  $F = 32.35$ ,  $df = 3$ ,  $p < 0.001$ , respectively). Since the  $G'$  and  $G''$  fail the Levene's test on the homogeneity in variances, a more conservative level of significance was adopted ( $p < 0.001$ ). Furthermore in order to assess how robust the test is, the

Welch and the Brown-Forsythe tests were performed. Both tests are statistically significant at the  $p < 0.001$  level, which makes the ANOVA result reliable. A Sheffé test was performed as multicomparison test, according to which, the  $G'$  of the lysozyme-loaded gel with 40% water is statistically different from the gels with 50%, 60% and 70%. The gel with 50% water is not statistically different from the gel with 60% water, which is not statistically different from the gel with 70% water.  $G''$  of the gels with 40% and 50% water contents are statistically different from the  $G''$  of the gels with 60% and 70% water contents. In order to validate the test a non-parametric Kruskal-Wallis test was performed on both the  $G'$  and  $G''$  ( $\chi^2 = 86.90$ ,  $df = 3$ , two tailed  $p < 0.001$  and  $\chi^2 = 76.59$ ,  $df = 3$ , two tailed  $p < 0.001$ , for  $G'$  and  $G''$  respectively), followed by a multicomparison test (Dunn test). According to the test result, the gel with 40% water is statistically different from the gels with 60% and 70% water, which are not different from each other. The gel with 50% water is not statistically different from the gel with 40% water. These tests confirm the ANOVA tests result, exception for the gel with 50% water.

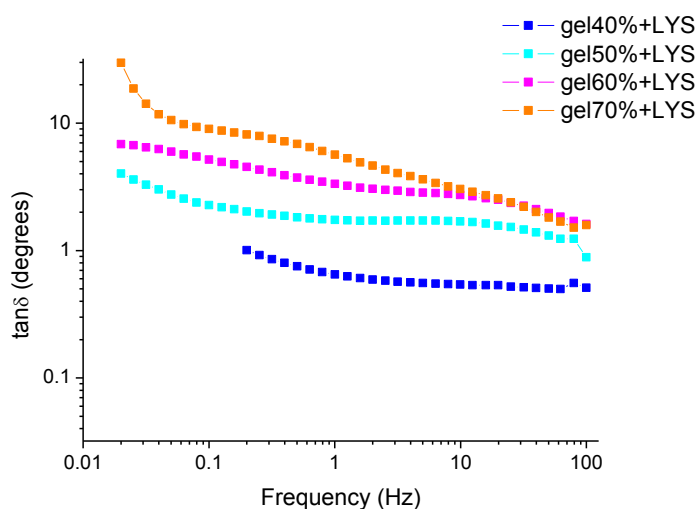


**Figure 5.18** Effects of the frequency (Hz) on the loss tangent ( $\tan\delta$ ) for the lysozyme-loaded gels prepared by hydration method ( $n = 3$ ).

The determination of the viscoelastic properties and the structure of the gels can be further confirmed by the loss tangent ( $\tan\delta$ ) plot, which is shown in Figure 5.18. The loss tangent is a dimensionless parameter that describes the ratio between the  $G''$  and the  $G'$  [156]. It has been stated that for covalently cross-linked gels,  $\tan\delta$  never exceeds the unity, while it happens for entangled polymer networks [219]. The  $\tan\delta$  increases with decreasing the Gelucire content and it decreases with the frequency. The  $\tan\delta$  of the lysozyme-loaded gel with 40% water is smaller than 1, which is consistent with cross linked-like behaviour ( $G'' < G'$ ), but it is in disagreement with the unloaded gel with 40% water prepared by hydration. The lysozyme-loaded gels with 50%, 60% and 70% have  $\tan\delta > 1$ , which is typical of entangled-like behaviour, as previously demonstrated in Figure 5.17 and it is in agreement with the unloaded gels prepared by hydration.

The ANOVA test on the  $\tan\delta$  results ( $F = 38.87$ ,  $df = 3$ ) with a level of significance set to  $p < 0.001$  confirms that the lysozyme-loaded gel with 40% water is not statistically different from the lysozyme-loaded gel with 50% water. However, it is statistically different from the lysozyme-loaded gels with 60% and 70% water content, which are not statistically different from each other. The gel with 50% water is not statistically different from the gel with 60% water, but it differs from the gel with 70% water content. The non-parametric Kruskal-Wallis test ( $\chi^2 = 92.56$ ,  $df = 3$ , two tailed  $p < 0.001$ ) confirms the ANOVA results. The results are largely in agreement with the statistical results for  $G'$  and  $G''$ , exception for the statistical difference between the gels with 50% and 70% water contents.

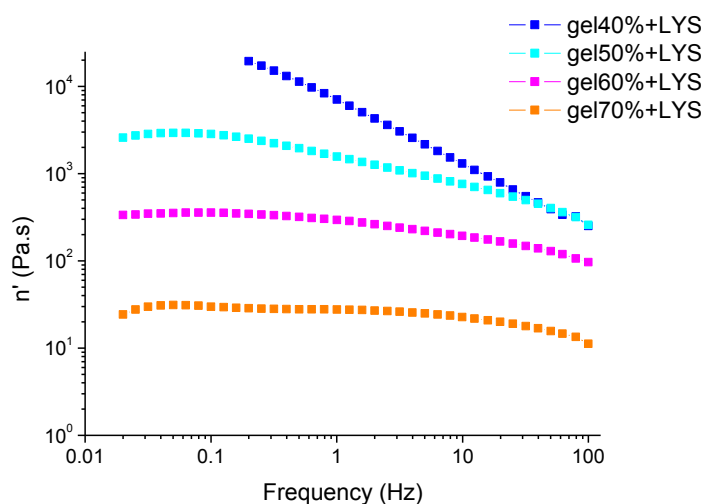


**Figure 5.19** Dynamic viscosity ( $\eta'$ , Pa.s) versus frequency (Hz) plots for the lysozyme-loaded gels prepared by hydration ( $n = 3$ ).

The dynamic viscosity ( $\eta'$ , Pa.s) is the ratio between  $G''$  (Pa) and the angular frequency,  $\omega$  (rad.s). Therefore this parameter is closely correlated to the viscous part of the gels. For most gels, the dynamic viscosity was found to be dependent on the frequency. In the lysozyme-loaded gel with 40% water content,  $\eta'$  sharply decreases with increasing the testing frequency. However, the decrease is much gradual for the lysozyme-loaded gel with 50% water content. For the gels with 60% and 70% water contents, the  $\eta'$  tends to level off, though it decreases above 20 Hz. This means that at lower frequencies the viscous part of the gels is predominant, while at higher frequencies the elastic properties are more evident.

The one-way ANOVA test performed on the dynamic viscosity data shows that the lysozyme-loaded gel with 40% water is significantly different at the  $p < 0.001$  level from the gels with 60% and 70% water contents, whereas it is not different from the lysozyme-loaded gel with 50% water ( $F = 9.66$ ,  $df = 3$ ,  $p < 0.001$ ). The gels with 50%, 60% and 70% water are not significantly different from each other. These results are in agreement with the statistical results for the other viscoelastic parameters ( $G'$ ,  $G''$  and  $\tan\delta$ ).

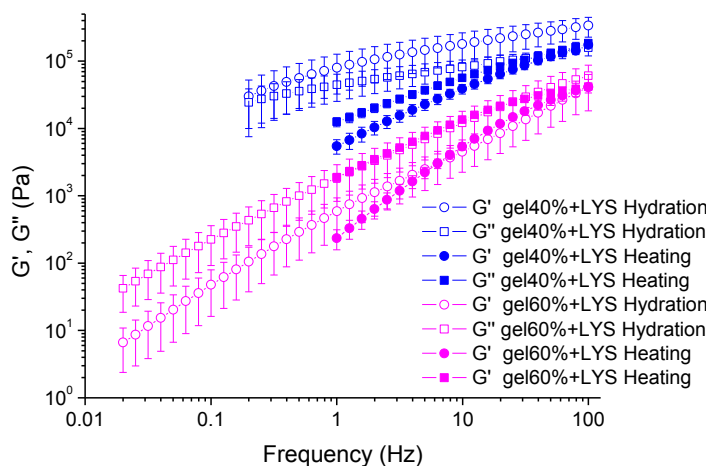


**Figure 5.20** Comparison of  $G'$  (Pa) and  $G''$  (Pa) versus frequency (Hz) plots ( $\pm$ SD) for the lysozyme-loaded gels with 40% and 60% water contents prepared by heating (filled symbols) and by hydration methods (open symbols) ( $n \geq 3$ ).

Frequency sweep tests on the lysozyme-loaded gels with 40% and 60% water contents prepared by heating method were performed, in order to investigate whether the viscoelastic properties of the lysozyme-loaded gels change with the method of preparation. Figure 5.20 shows the comparison of the  $G'$  and  $G''$  values of the lysozyme-loaded gels with 40% and 60% prepared by hydration and by heating methods. Overall, the gels prepared by heating have smaller values of standard deviation, which means the repetitions are more consistent and it can be used as a measure of the homogeneity of the samples. For the lysozyme-loaded gels with 60% water prepared by hydration and by heating, the  $G'$  and  $G''$  values are similar, even though for the gel with 60% water prepared by heating, the  $G'$  cross  $G''$  at 100 Hz, while no crossover is observed for the gel prepared by hydration. For the lysozyme-loaded gels with 40% water content, the  $G'$  and  $G''$  values are very different. For the gel prepared by hydration, the elastic component prevails on the viscous component since ( $G' > G''$ ), whereas for the gel prepared by heating the situation reverse and  $G'' > G'$ , indicating the viscous part is dominant.

In order to investigate the effect of the water content and of the method of preparation on the viscoelastic parameters of the lysozyme-loaded gels, two-way ANOVA tests were performed on the gels with 40% and 60% water content prepared by hydration and by heating. The water content has a stronger effect on the  $G'$  ( $F = 71.00$ ,  $p < 0.001$ ,  $\eta^2 = 0.37$ ) than the method of preparation ( $F = 15.97$ ,  $p < 0.001$ ,  $\eta^2 = 0.12$ ). For the lysozyme-loaded gels with 60% water content, the method of preparation has no statistically significant effect on the rheological behaviour of the lysozyme-loaded gels, but does for the lysozyme-loaded gels with 40% water content. Regarding  $G''$ , the only effect is due to the water content ( $F = 71.9$ ,  $p < 0.001$ ,  $\eta^2 = 0.37$ ), while the effect of the method of preparation is not statistically significant ( $p > 0.05$ ).

Same result was obtained for the  $\tan\delta$  and  $\eta'$ , where the main effect is due to the water content ( $F = 65.67$ ,  $p < 0.001$ ,  $\eta^2 = 0.35$  and  $F = 11.38$ ,  $p < 0.001$ ,  $\eta^2 = 0.09$ ), while the method of preparation is not statistically significant.

Finally, two-way ANOVA test was performed on the lysozyme-loaded gels and unloaded gels with 40%, 50%, 60% and 70% water content prepared by hydration to investigate the significance of the effect of the lysozyme on the rheological properties of the gels. From the results, it can be stated that the changes in the viscoelastic properties of the gels are mainly due to the water content, while the presence of the lysozyme has no statistically significant impact for most of the gels. The water content has significant effect on the  $G'$ ,  $G''$  and  $\eta'$  ( $F = 59.07$ ,  $p < 0.001$ ,  $\eta^2 = 0.43$ ;  $F = 47.34$ ,  $p < 0.001$ ,  $\eta^2 = 0.37$  and  $F = 26.32$ ,  $p < 0.001$ ,  $\eta^2 = 0.25$ , respectively), while the effect of the incorporation of lysozyme is not statistically significant ( $p > 0.001$ ), exception for the  $G'$  of the gel with 40% water. However, both water content and the incorporation of lysozyme have effect on the  $\tan\delta$  of all gels ( $F = 50.72$ ,  $p < 0.001$ ,  $\eta^2 = 0.39$  and  $F = 48.04$ ,  $p < 0.001$ ,  $\eta^2 = 0.17$ , for the water and the enzyme respectively). The water content has a stronger effect than the incorporation of lysozyme as it can be seen by the higher value of the partial eta square ( $\eta^2$ ). The effect of the incorporation of lysozyme is statistically significant for  $\tan\delta$  values of the gels with 60% and 70% water contents.

In conclusion, the lysozyme-loaded gel with 40% water prepared by hydration has cross linked-like behaviour, which differs from the unloaded gel prepared by hydration. Furthermore, it is statistically different from the gels with 60% and 70% water, while it is not different from the gel with 50% water content. The gels with 50%, 60% and 70% are entangled-like, which is consistent with the rheological properties of the unloaded gels prepared by hydration. Comparing the lysozyme-loaded gels prepared by both hydration and heating methods, it was found that the method of preparation has no significant effect on the rheological properties. Moreover the gels prepared by heating method are more homogeneous (Figure 5.20). Thus, it may be concluded that the heating method is the better option for the preparation of the protein-loaded gel formulations. Finally, the effect of the incorporation of the lysozyme in the viscoelastic properties of the gels prepared by hydration was investigated. Overall, it may be concluded that the lysozyme has no significant effect in the properties of the gels, though with some exception for the gel with 40% water (for the  $G'$ ) and the  $\tan\delta$  of the gels with 60% and 70%.

### 5.4.4.3 Continuous flow test

The flow properties of the lysozyme-loaded gels prepared by hydration were investigated by performing a continuous flow test, with which the changes of viscosity upon variation of shear stress were studied. The test provides important information on the behaviour (i.e. ease of administration) of the gels when a stress is applied. Continuous flow tests were performed on the lysozyme-loaded gels with 60% and 70% water content prepared by hydration method. The curves obtained by the average of the three repetitions were mathematically fitted with the power law (Ostwald de Waele) equation (Equation 5.6), with which the consistency index ( $k$ , Pa.s<sup>*n*</sup>) and the flow index ( $n$ , dimensionless) were calculated

$$\sigma = k\gamma^n \quad \text{Equation 5.6}$$

For a Newtonian liquid, the flow index,  $n$ , is equal to 1. If it is greater than 1, the system is classified as shear thickening, if lower it is shear thinning [150]. The effects of temperature and water content on the flow parameters (consistency and flow index) were statistically investigated by performing a two-way ANOVA test. The level of significance was set as  $p < 0.001$ . Multicomparison post-hoc test (Scheffé test) was also performed.

**Table 5.10** Mean values of the consistency ( $\pm$  SE) and flow ( $\pm$  SE) indices for the lysozyme-loaded gels prepared by hydration method at 25 °C, 37 °C, 50 °C and 80 °C. Measurements were performed at least in triplicate ( $n \geq 3$ ).

Water (%)	Temperature	Flow parameters		Adj. $r^2$
		Consistency Index, $k$	Flow Index, $n$	
60% + LYS	25 °C	251.32± 6.34	0.61±0.02	0.994
	37 °C	100.14±9.59	0.70±0.04	0.986
	50 °C	32.79±3.52	0.91±0.04	0.993
	80 °C	1.31±0.25	0.66±0.03	0.992
70% + LYS	25 °C	8.16±3.39	0.86±0.09	0.946
	37 °C	11.43±1.71	0.82±0.03	0.992
	50 °C	10.51±1.03	0.75±0.02	0.997
	80 °C	2.24±0.85	0.62±0.07	0.963

Table 5.10 summaries  $k$  and  $n$  of the lysozyme-loaded gels with 60% and 70% water content prepared by hydration. For the gel with 60% water,  $k$  decreases with increasing the temperature, while it is almost constant for the gel with 70% water content. These values are lower than the  $k$  values of their corresponding unloaded gels (Table 8, section 3.7.3). However, the lysozyme-loaded gels show shear thinning behaviour as they have flow index values below the unity, which is consistent with the behaviour of the unloaded gels.

Two-way ANOVA tests were performed on the lysozyme-loaded gels with 60% and 70% water prepared by hydration to investigate whether the water content or the temperature applied have a more significant effect on the flow properties of the gels. The results indicate that the main effect on the consistency index is due to the water content of the gels ( $F = 24.49, p < 0.001, \eta^2 = 0.48$ ), while the temperature has no statistically significant effect ( $p > 0.001$ ). However, the multicomparison test revealed that in the lysozyme-loaded gel with 60% water,  $k$  calculated at 25 °C is statistically different from the one calculated at 80 °C. No statistical significance has been observed for  $k$  determined for the lysozyme-loaded gel with 70% water at the testing temperatures.

The effect of the water content, testing temperature and incorporation of lysozyme on the  $k$  values of the lysozyme-loaded gels and on the  $k$  values of the unloaded gels has been studied with the ANOVA test. The results reveal that all the parameters mentioned above have an effect on the  $k$  of the gels. However, the water content has a slight greater impact than the other parameters on the data ( $F = 499.68, p < 0.001, \eta^2 = 0.94$ ;  $F = 415.21, p < 0.001, \eta^2 = 0.92$ ,  $F = 350.11, p < 0.001, \eta^2 = 0.95$ , for the water, enzyme and temperature respectively). The effect of the incorporation of the lysozyme on the  $k$  values of the gels is evident for the gel with 60% and 70% water contents, when 37 °C was used as the testing temperature. None of the effects of the water content, the test temperature and the incorporation of the lysozyme is statistically significant on the flow index ( $p > 0.001$ ).

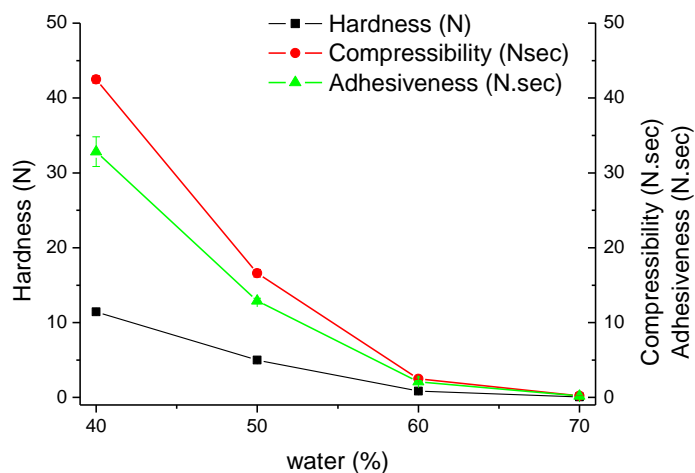
#### **5.4.5 Mechanical properties of gels**

The mechanical and the flow properties (section 5.4.4.3) can provide complementary information on the structure of the gels. Mechanical and flow tests measure the capability of the materials to response to an applied stress and evaluate the effect on the flow. Thus, they can characterise properties such as spreadability and adhesiveness of the materials [151]. Chapter 3 investigated the mechanical properties of the unloaded gels prepared by both heating and hydration methods by performing the texture profile analysis (TPA) test. In this part of the project, the TPA test was used to study the mechanical properties of lysozyme-loaded gels prepared by hydration. A comparison with the unloaded gels prepared by hydration is also presented.

##### **5.4.5.1 Texture Profile Analysis (TPA)**

TPA test was performed on the lysozyme-loaded gels with 40% to 70% water contents. The mechanical properties analysed are hardness (units of Force, N), compressibility (units of work,

N.s) and adhesiveness (unit of works, N.s). The test was performed in triplicate by following the experimental procedure described in section 5.3.5.



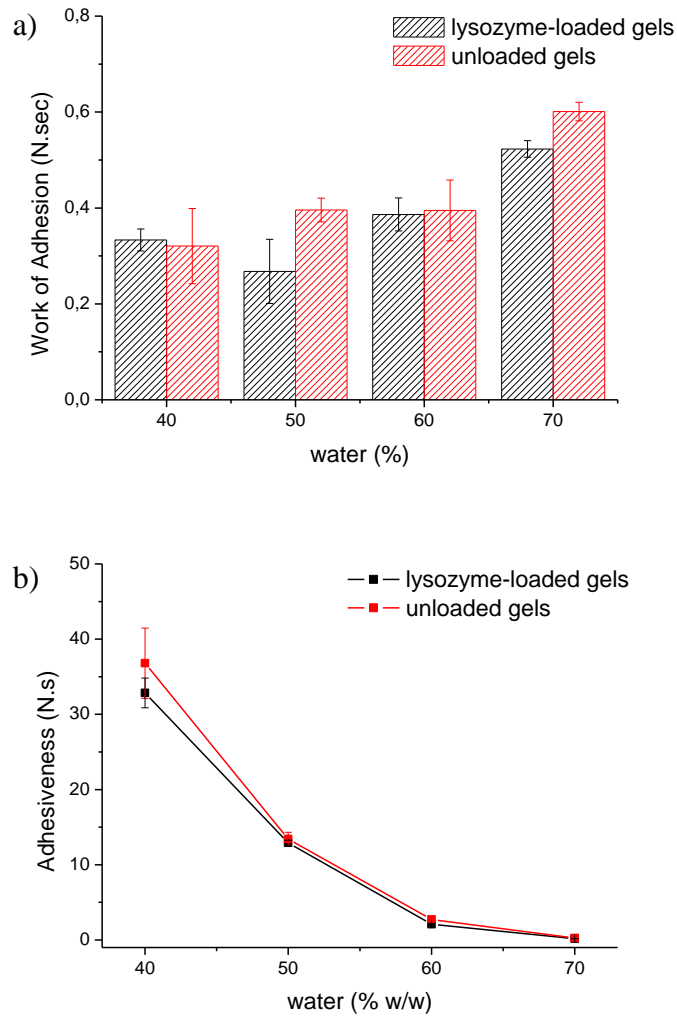
**Figure 5.21** Adhesiveness (N.s), hardness (N) and compressibility (N.s) of the lysozyme-loaded gels prepared by hydration. The data are presented as mean ( $\pm$ SD) ( $n = 3$ ).

Figure 5.21 shows the changes of the mechanical parameters for the lysozyme-loaded gels with the water contents in the gels. All measured mechanical parameters decrease with increasing the water content in the gel, which reflect the same trend as the unloaded gels prepared by hydration (Figure 3.44, section 3.4.5.1). The hardness is statistically different among the gels. For the compressibility and the adhesiveness the gels with 60% and 70% water content are not statistically different ( $p > 0.001$ ), while the gel with 40% and 50% water are statistically different. The TPA parameters of the lysozyme-loaded gels prepared by hydration are not statistically different from the parameters determined in the unloaded-gels prepared by hydration. The two-way ANOVA test results indicate that the only variable that can influence the TPA parameters is the water content of the gels ( $F = 1471.20, p < 0.001, \eta^2 = 0.99$ ;  $F = 2020.10, p < 0.001, \eta^2 = 1.00$ ;  $F = 457.76, p < 0.001, \eta^2 = 0.98$ , for the compressibility, hardness and adhesiveness respectively). The incorporation of lysozyme has no statistically significant effect on the mechanical properties studied here. In conclusion, the incorporation of the lysozyme does not affect the mechanical properties of the gels. This largely agrees with the rheological results.

#### 5.4.6 Evaluation of the mucoadhesive properties of gels

In order to evaluate the effect of the lysozyme incorporation on the mucoadhesive properties of the gels, adhesion tests with the mucin tablets were performed with a texture analyser. The tests were performed in triplicate. From the force-time plot, the Force maxima ( $F_{max}$ ) which is the maximum force required to separate the mucin discs from the gels and the work of adhesion

( $W_{ad}$ ) which is the amount of forces involved in the detachment, were calculated by using the provided software, Texture Exponent 32. Accordingly to previous works [45, 229], the work of adhesion better describes the mucoadhesion phenomenon, which involves not only the adhesiveness but also the deformation and the mechanical properties of the material. Therefore, in this work, only the work of adhesion is considered to evaluate the mucoadhesion properties of the gels. The comparison on the work of adhesion values for the lysozyme-loaded gels with the unloaded gels is shown in Figure 5.22a. The comparison on the adhesiveness obtained from the TPA tests was also conducted and is presented in Figure 5.22b. The purpose of this comparison is to identify differences in the adhesion profile of the gels when in contact with a biological and a non-biological surface. According to the results, the mucoadhesion of the lysozyme-loaded gels increase with the water content of the gel, hence the gel with 70% water has the highest mucoadhesive properties. This trend is similar to the one of the unloaded gels. For the lysozyme-loaded gel with 50% water, the work of adhesion values are significantly different from the unloaded gel with 50% water and shows a lower level of mucoadhesion (Figure 5.22a). The adhesiveness obtained with the TPA test reveals an opposite behaviour. The adhesion decreases with increases water content and as a result, the gel with 40% water shows the higher adhesion. This different trend may indicate the different type of interaction between the probe surface/mucin tablet and the gels. The results obtained with the mucin tablets also suggest that an interaction between mucin tablets and gel occurs at high water content (70%), which leads to the higher mucoadhesive properties of the lysozyme-loaded gels with higher water content. Moreover, the mucoadhesive properties of the lysozyme-loaded gels are not statistically different from the unloaded-gels.



**Figure 5.22** (a) Comparison of the work of adhesion (N.s) determined by adhesive test performed on the lysozyme-loaded gels and unloaded gels prepared by hydration with mucin tablets. (b) Comparison of the adhesiveness obtained from TPA performed on the lysozyme-loaded and unloaded gels prepared by hydration.

The two-way ANOVA test was used to evaluate the effect of the water content and the incorporation of lysozyme on the mucoadhesive parameters of the lysozyme-loaded and unloaded gels. The incorporation of lysozyme has no significant effect on the work of adhesion ( $p < 0.001$ ) tested using mucin tablets, except for the gels with 50% water, in which the presence of lysozyme is statistically significant ( $p = 0.001$ ). The main effect on the work of adhesion is due to the water content of the gels ( $F = 49.26$ ,  $p < 0.001$ ,  $\eta^2 = 0.85$ ) and in particular for the lysozyme loaded-gel with 70% water, which is statistically different from the lysozyme-loaded gels with 40%, 50% and 60% water contents. For the adhesiveness, the main effect is also due to the water content of the gels ( $F = 457.76$ ,  $p < 0.001$ ,  $\eta^2 = 0.98$ ), exception for the gels with 60% and 70% water contents, which are not statistically different between them. However, they are different from the gel with 40% and 50% water content. The

incorporation of the lysozyme has no significant effect on the adhesiveness of the gels ( $p > 0.001$ ).

#### 5.4.7 Lysozyme release profile

##### 5.4.7.1 Dissolution studies

The release profiles of the lysozyme from the lysozyme-loaded gels prepared by heating method (30%, 40%, 50%, 60% and 65% water contents) and by hydration method (30% and 60% water content) were studied using the BP paddle method. The experiments were conducted as described in section 5.3.7.

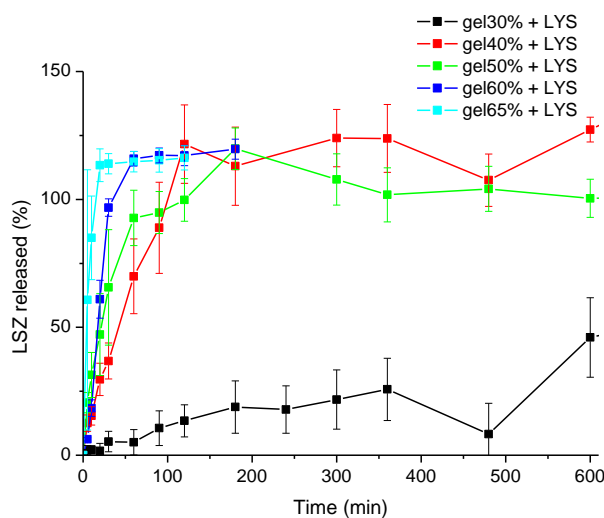


**Figure 5.23** Percentage of lysozyme released from the gels with 30%, 40%, 50%, 60% and 65% water contents prepared by heating method in phosphate buffer (pH=7.4) at 37 °C (n = 3, ± SD).

Figure 5.23 shows the release profiles of lysozyme from the gels with different water content prepared by heating method using phosphate buffer (pH=7.4) as dissolution media. For the gel with 30% water, a sustained release pattern was achieved. Less than 50% lysozyme was released within 600 minutes. The release rate of lysozyme from the gels increased dramatically by increasing the water content. The higher the water content in the gel, the faster the lysozyme was released. However, the gels with 30%, 40% and 50% water are not completely dissolved in the media after 600 minutes, suggesting that the diffusion mechanism controls the release of lysozyme instead of the erosion mechanism. For the gel with 60% water content, lysozyme was completely released after 30 minutes, while for the gel with 65% water content, the 100% release is achieved after 20 minutes. The gels with 60% and 65% water are completely dissolved in the medium, which suggests that the dominating mechanism of release for these two gels is likely to be erosion.

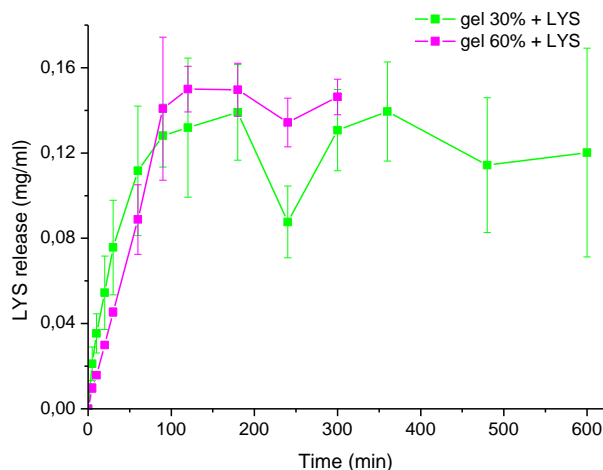


**Figure 5.24** Lysozyme released from the gels with 30%, and 60% water contents prepared by hydration method in phosphate buffer (pH=7.4) at 37 °C (n = 3, ± SD).

The gels with 30% and 60% water content prepared by hydration method were tested using the dissolution bath in the same experimental conditions as the gels prepared by heating. The release profiles of the gels are shown in Figure 5.24. For the gels prepared by hydration method, the effect of water content on the release rate is much less significant than for the gels prepared by heating method. For the gel with 30% water content, the release profile changes dramatically compared to the behaviour exhibited by the gel with 30% water prepared by heating (Figure 5.24). This may be due to the different structures of the gels prepared by hydration and heating methods. From the thermal analysis results discussed in Chapter 3 (section 3.4.3), the gel with 30% water prepared by hydration method seems to be less homogeneous compared to the one prepared by heating method. This was confirmed by the DSC results on the amount of free water (section 4.4.2). For the gel with 30% water prepared by hydration, interfacial water (-13 °C) was identified. On the contrary, the gel prepared by heating did not show any peak. This may indicate that the homogeneity of the gel with 30% water prepared by hydration is lower than the one prepared by heating and the water is less bound to Gelucire. Therefore, considering that lysozyme more likely partitions in the aqueous phase, the release of lysozyme should be faster in the gel prepared by hydration than in the one prepared by heating.

On the contrary, for the gel with 60% water prepared by hydration the release is slower than in the gel with 60% water prepared by heating. This may be due to the slightly different structures of the unloaded gels prepared by different methods as suggested by SAXS results (3.4.2) by which a cubic diamond phase was identified for the gel with 60% water prepared by hydration and mixed phases for the gel prepared by heating method. Therefore, it can be stated that the method of preparation influences the release profile of the lysozyme. Although it has to consider that the presence of lysozyme may have induced changes in the structures of the unloaded gels.

In attempt to identify the mechanism by which the lysozyme is released from the gels, the release profiles were fitted with five different models (as described in section 5.3.7): Baker and Lonsdale, Korsmeyer and Peppas, Hixon and Crowell, Higuchi square root time and first order. The fitting results are listed in Table 5.11. The fitting results indicate that the Korsmeyer-Peppas model is the most suitable model to describe the drug release kinetics of the gels. For the gels with 30%, 40% and 50% water prepared by the heating method, the diffusional exponent,  $n$ , obtained by the Korsmeyer-Peppas model, is between 0.5 and 1, indicating a non-Fickian (anomalous) behaviour [250]. The fitting of the release profile of the gel with 65% water prepared by heating could not be performed since the 60% of the release was achieved after 10 minutes. For the gel with 60% water,  $n > 1$ , suggesting a supercase II transport behaviour. For the gel with 30% water prepared by hydration a non-Fickian behaviour is observed ( $0.5 < n < 1$ ), while in the gel with 60% water  $n$  approaches 1 which indicates a Case II transport.

**Table 5.11** Statistical parameters obtained for the model fitting of the release profile of lysozyme to different models. The results refer to the gels prepared by heating and hydration methods tested in phosphate buffer (pH=7.4) at 37 °C. *k* refers to the release kinetic constant. The adjusted R-squared (adj.  $r^2$ ) is also shown as prove of the quality of fitting.

<i>Water (%)</i>	<i>Methods</i>	<i>Baker-Lonsdale</i>		<i>Korsmeyer-Peppas</i>			<i>Hixon-Crowell</i>		<i>Higuchi</i>		<i>First Order</i>	
		<i>k</i>	<i>Adj r<sup>2</sup></i>	<i>k</i>	<i>n</i>	<i>Adj r<sup>2</sup></i>	<i>k</i>	<i>Adj r<sup>2</sup></i>	<i>k</i>	<i>Adj r<sup>2</sup></i>	<i>k</i>	<i>Adj r<sup>2</sup></i>
30	Heating	0.0001	0.8403	0.4448	0.6939	0.9384	0.0005	0.9502	2.3113	0.9026	0.0016	0.9364
40		0.0012	0.817	2.5923	0.8014	0.9872	0.003	0.6916	6.9134	0.7033	0.0226	0.5022
50		—	—	6.7660	0.6625	0.9914	—	—	—	—	0.0364	0.9013
60		0.0105	0.3279	0.3682	1.7052	0.9995	0.0093	0.8684	11.2098	0.8151	0.0505	0.8821
65		0.0209	0.1253	—	—	—	0.0146	0.0268	14.9828	0.087	0.2259	0.8849
30	Hydration	—	—	0.0068	0.7069	0.9959	—	—	—	0.1894	0.0626	0.4169
60		0.0017	0.8804	0.0017	0.9619	0.9989	0.0047	0.9757	6.9978	0.8665	0.0178	0.959

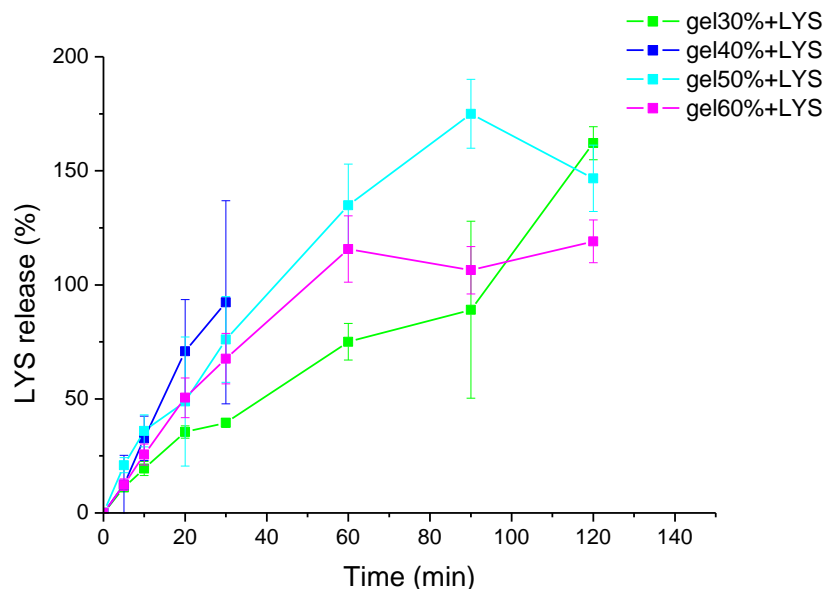


**Figure 5.25** Percentage of lysozyme released from the gels with 30%, 40%, 50%, 60% and 65% water content prepared by heating method in HCl 0.1 M at 37 °C ( $n = 3, \pm$  SD).

The dissolution tests were conducted on the gels with 30%, 40%, 50% and 60% prepared by heating method in HCl, 0.1 M. The tests were carried out in triplicate for a testing period of 120 minutes, and the release curves are shown in Figure 5.25. The release profile of the gel with 40% water exhibits a rapid release and after 30 minutes, about 90% of lysozyme is released. For the gel with 30% water, 90% of lysozyme was released after 90 minutes. While for the gels with 50% and 60% water contents, the maximum release of lysozyme was achieved after 60 minutes. The reason for the release profiles exceed 100% may be due to the lack of homogeneity of the gels. Therefore, higher amount of lysozyme than the theoretical value were in the tested gels. The release profiles of lysozyme were fitted to the five models described earlier in order to assess the dominant release mechanism. The fitting results are listed in Table 5.12. In general, the Kersmeyer-Peppas model shows a better fitting to the release profiles. The diffusional exponent value,  $n$ , determined with the Kersmeyer-Peppas model is above 0.5 for all gels. The gel with 30% exhibit non-Fickian behaviour, while for the gel with 40% water  $n$  is greater than 1 which suggests a super Case II transport behaviour. For the gels with 50% water, the parameter  $n$  is just above 0.5, suggesting Fickian diffusion with some contributions of non-Fickian diffusion. This may explain the good fitting with the Higuchi model, which is suitable for release profile driven by diffusion transport. Finally, for the gel with 60% water,  $n$  approaches 1 which indicates Case II transport behaviour. Overall, the release mechanism in HCl may be comparable to the mechanism in phosphate buffer in which non-Fickian was seen for all the gels with 30%-60% and supercase II transport was seen for the gel with 60% water.

**Table 5.12** Statistical parameters obtained for the model fitting the release profile of lysozyme. The results refer to the gels prepared by heating and tested in HCl 0.1 M at 37 °C. *k* refers to the release kinetic constant. The adjusted R-squared (adj.  $r^2$ ) is also shown as prove of the quality of fitting.

<i>Water (%)</i>	<i>Baker-Lonsdale</i>		<i>Korsmeyer-Peppas</i>			<i>Hixon-Crowell</i>		<i>Higutchi</i>		<i>First Order</i>	
	<i>k</i>	<i>Adj r<sup>2</sup></i>	<i>k</i>	<i>n</i>	<i>Adj r<sup>2</sup></i>	<i>k</i>	<i>Adj r<sup>2</sup></i>	<i>k</i>	<i>Adj r<sup>2</sup></i>	<i>k</i>	<i>Adj r<sup>2</sup></i>
30	0.0017	0.771	4.3482	0.6638	0.9414	0.0066	0.7947	10.9371	0.8439	0.0259	0.7636
40	0.0133	0.4747	1.3051	1.4036	0.9954	0.0243	0.7727	48.617	0.766	—	—
50	0.0057	0.7241	9.1268	0.5655	0.9510	0.0151	0.7753	15.246	0.9191	0.0532	0.6659
60	0.0042	0.8682	2.5464	0.9975	0.9916	0.0125	0.9636	11.6861	0.9328	0.0412	0.9245

In conclusion, in phosphate buffer, the mechanism of release of lysozyme from the gels is due to a combination of erosion and diffusion transport. This is consistent with a previous work from Sultananta et al. [102] which proposed that the drug is released from matrices of Gelucire 50/13 mainly through erosion, with some contribution of the diffusion. In this work, it has been observed that the gels with higher water contents (i.e. 60% and 65%) quickly dissolve completely in the medium. On the contrary, the dissolution is not complete for the gels with 40% and 50% water. Residue of the gels is still evident even after 24 hours and the complete dissolution of the gel is even less apparent in the gel with 30% water, although the release of lysozyme was completed. However, it has to be said that the amount of the gels accommodate in the sample holders (cap-shaped holders) was calculated in order to have the same amount of dry Gelucire 50/13 in the caps. Thus, it may be concluded that the mechanisms of release is influenced more by the different internal structure of the gels more than by the amount of Gelucire in the gels. Finally, the pH of the medium also seems to play a role in influencing the release of lysozyme. The gels with 30% and 50% water in acidic pH show non-Fickian release, whereas for the gel with 60% water approaches a zero-order release.

### 5.4.7.2 Diffusion studies

In order to assess the release of the drug where the gels may be potentially used as transdermal and transmucosal formulation, diffusion studies were carried out with Franz cells as described in section 2.6. Through the study, the diffusion profile of lysozyme from the gels with 30% and 50% water prepared by heating method and from the gel with 50% water prepared by hydration were determined. In contrast with the dissolution bath, the gels could not be dissolved in the medium but only wetted locally in the diffusion experiments. The pore size of the membrane (0.45  $\mu\text{m}$ ) was chosen in order to allow the diffusion of the lysozyme.

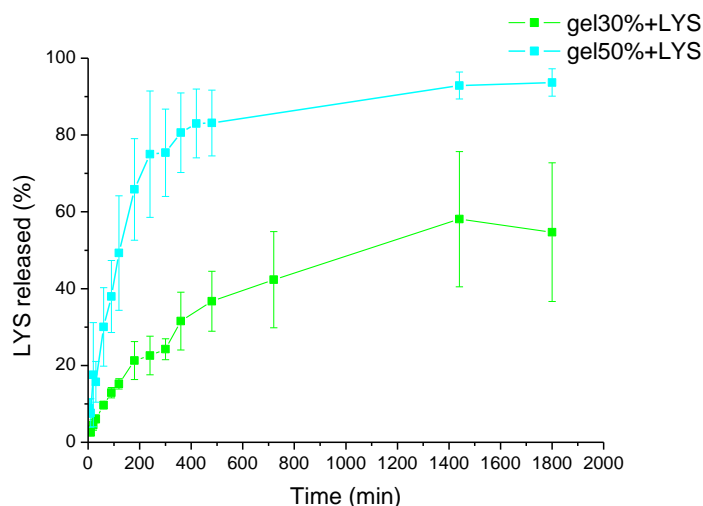


**Figure 5.26** Percent released of lysozyme from the gels with 30% and 50% water prepared by heating method in phosphate buffer (pH=7.4) at 37 °C tested using Franz diffusion cells (n = 6,  $\pm$  SD).

Figure 5.26 shows the diffusion profiles of lysozyme from the gels with 30% and 50% water prepared by heating method. From the gel with 50% water, over 80% of lysozyme was released into the receptor chamber after 6-8 hours, while from the gel with 30% water, only maximum of 58% has been released after 24 hours. Compared to the dissolution studies, the release/diffusion rate of lysozyme across the model membrane is much slower. It may be due to the effect of the cellulose membrane, through which the lysozyme needs to diffuse. Moreover, the gel may interact with the membrane and obstructs the pores.

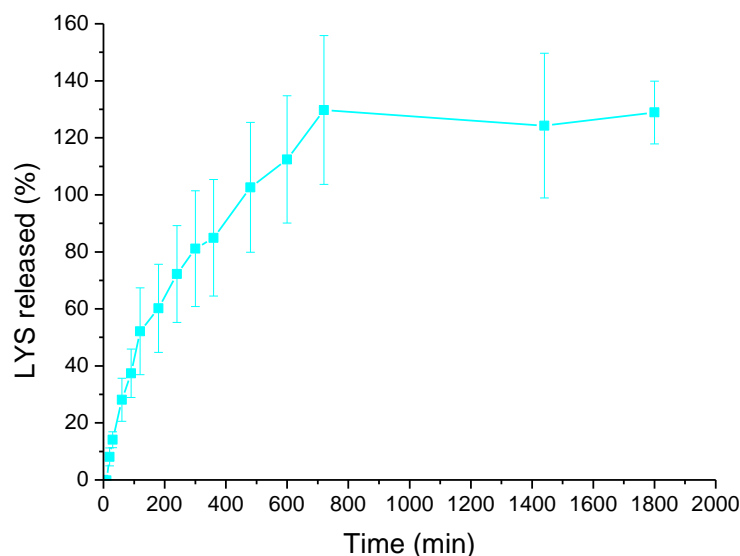


**Figure 5.27** Percent released of lysozyme from the gel with 50% water prepared by hydration method in phosphate buffer (pH=7.4) at 37 °C tested with Franz diffusion cells (n = 6,  $\pm$  SD).

For the gel with 50% water prepared by hydration, the lysozyme diffusion across the membrane profile differs from the gel prepared by heating method. For the gel prepared by hydration, the release was faster than in the gel prepared by heating. In fact, 80% of lysozyme was released after 5 hours, and a complete release is achieved after 10 hours. However, the release exceeds the 100%, which may be caused by the lack of homogeneity of the gel.

## 5.5 Conclusions

The main aim of this chapter is to investigate the structural and mechanical properties as well as the release behaviour of the lysozyme-loaded Gelucire 50/13 gels. Based on the information obtained from the characterisation of the unloaded gels in Chapter 3, lysozyme was incorporated into the Gelucire gel with selected water contents. The effects of water content, lysozyme incorporation and method of preparation on the physical and mechanical properties of the gels were studied using a range of techniques. Relating to the structure of the gels, according to the ATR-FTIR spectroscopy, the lysozyme-loaded gels do not differ from the unloaded gels. However, the incorporation of lysozyme induced a change in the microstructure of the gels (phase behaviour) as revealed by the SAXS experiments. It was found that no clear phase but the possibility of coexistence of mixed phases may present in the gels after incorporation of lysozyme. This may be confirmed by the study of the thermal phase transition using DSC, with which a second endothermic peak at  $\sim 37$  °C possibly associated with a second liquid crystalline phase was identified in the gels with 20%, 40% and 50%. On the other hand, the lysozyme-loaded and the unloaded gels prepared by hydration show similar changes of viscoelastic

properties upon thermal treatment. Except for the lysozyme-loaded gel with 70% water, which showed a completely different rheogram from the unloaded gel. Furthermore, the response of the lysozyme-loaded gels with 40% and 60% water prepared by heating to the thermal treatment did not statistically differ from the lysozyme-loaded gels with 40% and 60% prepared by hydration, suggesting that the method of preparation has no significant effect in the properties of the gels. Despite some of the rheological properties are affected by the presence of the lysozyme especially in the gel with 40% water, it may be concluded that the incorporation of the lysozyme has a little effect on the viscoelastic properties of the gels. Furthermore, it was found that the method of preparation has no significant effect on the gels. Although, the gels prepared by heating method were found to be more homogeneous. Thus, it may be concluded that the heating method is a better option for the preparation of the formulations. Overall, the water content exerts the more significant effect on the characteristics of the gels. The mechanical properties of the gels as well as the mucoadhesion properties are not affected by the incorporation of the lysozyme.

Since the method of preparation does not influence the mechanical and viscoelastic properties of the gels, the release behaviour of the gels prepared by both methods should be similar. However, different conformations of the lysozyme in the gels prepared by hydration and heating method were determined using ATR-FTIR. It is unknown whether this will have any effect on the activity of lysozyme (as the lysozyme activity in the gel is not assessable). The method of preparation (which likely leads to different microstructure) also lead to different results in the mechanisms of release of the lysozyme, especially in the gel with 30% water, characterised by a rapid release when prepared by hydration, opposite to a sustained release of the lysozyme when prepared by heating method.

## **6 Development of nanoparticles based on Gelucire 50/13 gels**

### **6.1 Introduction**

In the previous Chapters (3 and 4), Gelucire 50/13 based gel formulations were characterised in order to evaluate the potential of being used as carriers for protein/peptide drug delivery. The structure analysis of the gels showed the formation of liquid crystalline phases including lamellar, hexagonal and cubic phases. For the gels with intermediate to high water contents the structural analyses suggest the possibility of the co-existence of multiple liquid crystalline phases. The rheological studies proved the formation of cross-linked-like or entangle-like structure depending on the water content of the gels. The SEM results of the freeze-dried gels and the DSC and relaxometry NMR studies on the gels confirmed the existence of water compartments (such as water channels and domains) in the interior of the gels. The ordered network structure of the gels gives the potential of forming nanoparticles by fragmentation.

Gelucire 50/13 is a mixed glycerides based systems esterified with PEG. In the literature, the ability of glycerides based materials, such as the glycerylmonooleate (GMO), to form submicron particles has been established [95]. However in order to obtain stable nanoparticle suspension formulations, the addition of stabilisers, such as surfactants, sugars, polymers (i.e. Poloxamer) and PEG, is often required [96, 262]. Gelucire 50/13 has also been used as stabiliser in solid lipid nanoparticles (SLN) or nanostructured lipid carriers (NLC) [263]. With a stable nanoparticle formulation, the therapeutic outcome of the formulation often cannot be fully realised due to the short circulation of the nanoparticles in the body. Furthermore, to increase the protein loaded nanoparticles half-life in the bloodstream, PEGylation is considered to be the most successful approach. It has been argued that PEGylation reduces the metabolic degradation and the immunogenicity of the nanoparticles [4]. Gelucire 50/13 contains 8% free PEG 1500 which can act as the intrinsic stabiliser if the gels are made into nanoparticles. Therefore in theory, Gelucire 50/13 gels are good candidates for producing gel nanoparticles. However, to date, there is no studying exploring the ability of using Gelucire 50/13 alone to form stable nanoparticles.

The aim of this chapter is to develop a robust method for preparing the nanoparticle formulations based on Gelucire 50/13 gels alone and to perform physical characterisations on the gel nanoparticles. Finally, lysozyme was incorporated into the nanoparticles and the characterisation of the lysozyme-loaded nanoparticles as well as the encapsulation efficiency and the retained activity of lysozyme were assessed. *In vitro* cytotoxicity of the nanoparticles was assessed using two cell model lines, lung cancer cell line (H292) and human intestinal cell

line (Caco-2). The details on the cell lines are available in Chapter 2 (section 2.7). The cellular uptake of the gel nanoparticles was also evaluated using Caco-2 cells.

## 6.2 Objectives

The main purpose of this chapter is to evaluate the ability of using Gelucire 50/13 gels to produce stable nanoparticles to be used as protein/peptide delivery. The principal aims are:

- Development of a robust simple method for preparing the nanoparticles
- Size characterisation and physical stability assessment of the nanoparticles using DLS
- Morphology studies of the lysozyme-loaded and unloaded nanoparticles by using imaging techniques including AFM and cryo-TEM
- Evaluation of the encapsulation efficiency of the model enzyme (lysozyme) and the retained biological activity after encapsulation by using the *Micrococcus Lysodeikticus* assay
- *In vitro* cytotoxicity tests on two cell model lines: lung cancer cell line (H292) and human intestinal cell line (Caco-2)
- Cellular uptake of the nanoparticles by using human intestinal cell line (Caco-2)

## 6.3 Materials and methods

Stearoyl macroglycerides (Gelucire® 50/13, Gattefossé SAS, St Priest, France) gels were prepared as described in Chapter 2 (section 2.3.1), hen egg-white lysozyme from Sigma Aldrich (Gillingham, UK) was the chosen model protein. The nanoparticles were prepared as described in section 2.3.2. The compositions of the nanoparticles formulations and their corresponding names used in this chapter are listed in Table 6.1.

**Table 6.1** List of the nanoparticles formulations with the corresponding bulk gels.

<i>Protein-free bulk gel formulations</i> (% water, w/w)	<i>Gel nanoparticles</i>	<i>Lysozyme-loaded bulk gel formulations</i> (% water, w/w)	<i>Gel nanoparticles</i>
30	F1	30	F1-LYS
40	F2	40	F2-LYS
50	F3	50	F3-LYS
60	F4	60	F4-LYS
65	F5	65	F5-LYS

### 6.3.1 Dynamic Light Scattering (DLS)

The size of the nanoparticles in aqueous suspension was analysed with a DLS (Zetasizer Nano, Malvern Instruments Ltd, Malvern, UK) at the detector position of 173°. The samples were equilibrated at 37 ° C for 15 minutes and three acquisitions were taken for each sample. The samples were analysed in triplicate. The physical stability tests of the nanoparticles suspension formulations were performed on the formulations stored at room temperature and at 4 °C over a period of time up to 4 months. The distribution of the size obtained is based on the intensity calculation by the Zetasizer software, 6.20. The DLS results obtained correspond to the hydrodynamic diameters of the corresponding sphere.

### 6.3.2 Atomic force microscopy (AFM)

The sizes and shapes of the selected lysozyme-free and lysozyme-loaded nanoparticle formulations (F2, F4 and F5) were analysed using AFM. The formulations were diluted 1:10 with MilliQ water and 3 µl of the dilution were dropped on a mica film and left to dry for 15 minutes, then the film was rinsed with water and dried with compressed air. As the nanoparticles show little tendency of aggregation (see stability results), it was assumed that the dilution and drying process applied would not lead to significant changes in the sizes of the nanoparticles. Five to ten sites on each sample were analysed in order to assess the level of homogeneity of the formulations.

### 6.3.3 Encapsulation efficiency (%EE)

Centrifugation method was chosen to assess the encapsulation efficiency of lysozyme in the nanoparticle formulations. 3 ml of the nanoparticles aqueous suspensions were loaded in the centrifugal filter tubes (Amicon Ultra-4, Millipore) with regenerate cellulose membrane (MWCO 30 kDa) and centrifuged at 2000 g (Heraeus, Thermo Scientific, UK) for a period of time that allowed the collection of 2.5 ml of filtrate solution. The filtrate solutions collected after centrifugation were analysed with a UV spectrometer to assess the quantity of lysozyme. The quantification of the encapsulation efficiency was calculated using the following formula

$$EE\% = \frac{F_{lys_t} - F_{lys_c}}{F_{lys_t}} \quad \text{Equation 6.1}$$

where  $F_{lys_t}$  is the total amount of lysozyme loaded in the formulation and  $F_{lys_c}$  is the amount of free lysozyme recovered in the filtrate after centrifugation.

Prior the analysis, a calibration curve of lysozyme in aqueous solution was constructed. A lysozyme aqueous solution with a concentration of 0.9 mg/ml (0.09 % w/v) was prepared as the stock solution. 1, 2, 3, 4 and 5 and 5 ml aliquots of the stock solution were then individually transferred in 10 ml volumetric flasks to prepare dilutions of lysozyme solutions with concentrations of 0.09, 0.18, 0.27, 0.36 and 0.45 mg/ml, respectively. Three repetitions were used and the average UV absorbance values of the solutions were plotted against the protein concentrations. The measurements were taken using a UV spectrophotometer (Lambda 35, Perkin-Elmer, USA). The wavelength of maximum absorbance,  $\lambda_{\max}$ , was 280 nm. The calibration plot of lysozyme in Milli-Q water is shown in Figure 6.1.

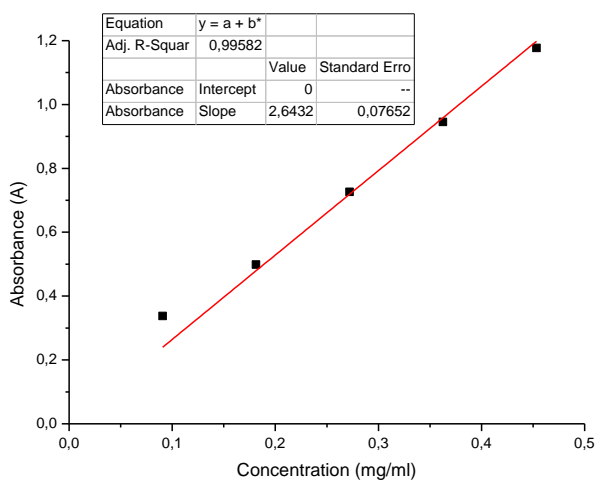


**Figure 6.1** Calibration plot of lysozyme in Milli-Q water. The adjusted R-squared and the slope values ( $\pm$ SE) are also listed in the tables.

### 6.3.4 Lysozyme activity assay

#### 6.3.4.1 Assay procedure

The biological activities of lysozyme in solution and formulations were tested by measuring the degree of lysis induced by lysozyme on *Micrococcus lysodeikticus* cells using a turbidimetry test described by Shugar [264]. The test is based on the comparison of the decrease in turbidity of the suspension and therefore the decrease of absorbance at 450 nm of a lysozyme solution with the known activity. A 0.015% (w/v) *Micrococcus lysodeikticus* cell suspension was prepared using 66 mM potassium phosphate buffer (pH=6.27) at 25 °C. Immediately before the test, a lysozyme buffer solution was prepared to contain 400 U/ml of the protein as control. The lysozyme-loaded nanoparticle formulations with a lysozyme concentration equal to 0.6 mg/ml were diluted with the phosphate buffer to get a final concentration of lysozyme equal to 0.01 mg/ml. The final lysozyme concentrations of the formulation solutions used in the activity tests are listed in Table 6.2.

**Table 6.2** Lysozyme concentrations of the original and diluted nanoparticle formulations used in the activity tests.

<i>Samples</i>	<i>Original Concentrations (mg/ml)</i>	<i>Dilutions (mg/ml)</i>
LYS solution	0.1062	0.01062
F2+LYS	0.6012	0.01004
F3+LYS	0.6008	0.01003
F4+LYS	0.6016	0.01005

The tests were performed by pipetting 2.5 ml of the substrate (*Micrococcus lysodeikticus*) into a quartz cuvette and leaving it to equilibrate at 25 °C for five minutes. 100 µl of the phosphate buffer (for the blank control) or the diluted nanoparticle formulation was then added and mixed by inversion. The absorbance of the tested solution at 450 nm was measured every 10 seconds over a period of 5 minutes. The decreases in absorbance were plotted against the time.

#### 6.3.4.2 Calculation of the retained biological activity (%RBA) of lysozyme

The biological activity of lysozyme expressed in units/ml was calculated according to the following equation

$$\text{units/ml lysozyme} = \frac{(\Delta A_{450\text{nm}}/\text{minTest} - \Delta A_{450\text{nm}}/\text{minBlank}) \times df}{(0.001) \times (0.1)} \quad \text{Equation 6.2}$$

where *df* is the dilution factor, 0.001 is the change in absorbance at  $\Delta A_{450\text{nm}}$  as per unit definition. One unit produces a  $\Delta A_{450\text{nm}}$  of 0.001 per minute at pH 6.24 at 25°C using a suspension of *Micrococcus lysodeikticus* as substrate in 2.6 ml reaction mixture. 0.1 is the volume (in millilitre) of lysozyme used in the test. The activity of lysozyme can be described in units/mg according to the following formula

$$\text{units/mg solid} = \frac{\text{units/ml lysozyme}}{\text{mg solid/ml lysozyme}} \quad \text{Equation 6.3}$$

The retained biological activity (RBA, %) of lysozyme can be calculated using Equation 4

$$\%RBA = \frac{\text{experimental activity}}{\text{theoretical activity}} \times 100 \quad \text{Equation 6.4}$$

where the theoretical activity is  $\geq 40000$  units/mg proteins according to the product information obtained from Sigma Aldrich.

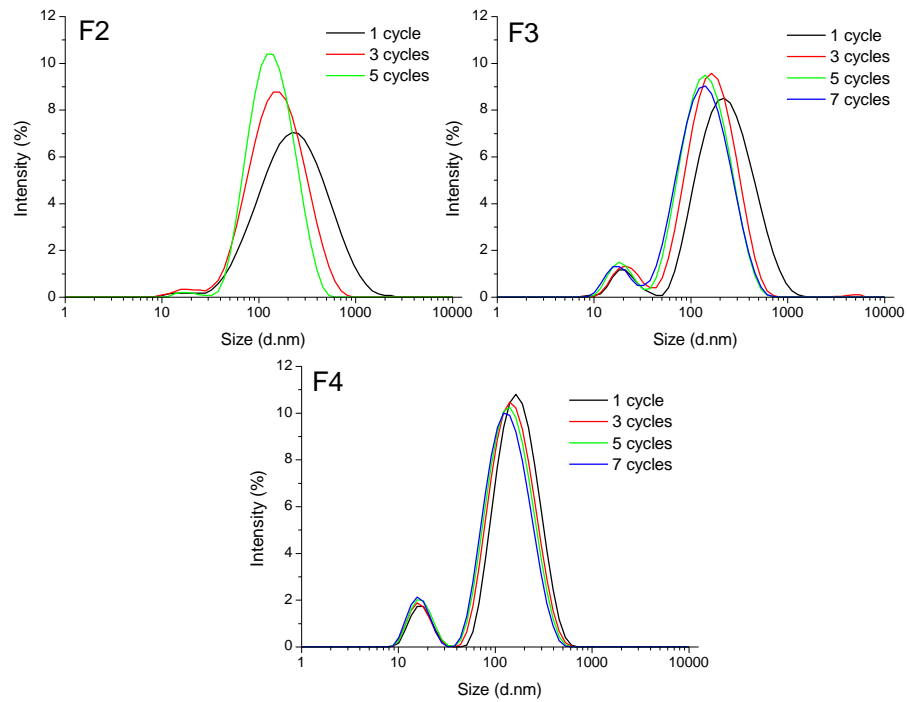
### **6.3.5 Circular Dichroism (CD)**

CD spectroscopy was used to study the changes in the lysozyme conformation after incorporated into the gel nanoparticle formulations. CD spectra were acquired in the near UV (240-500 nm) for lysozyme aqueous solution (0.6 % w/w) and for lysozyme-loaded nanoparticles dispersions (following the procedure described in section 2.3.2) with lysozyme concentration of 0.6 mg/ml (w/w). The tests were performed in triplicate by using a JASCO J-810 spectropolarimeter (Tokio, Japan). A quartz cuvette with 10 mm pathlength was used.

## **6.4 Results and discussion**

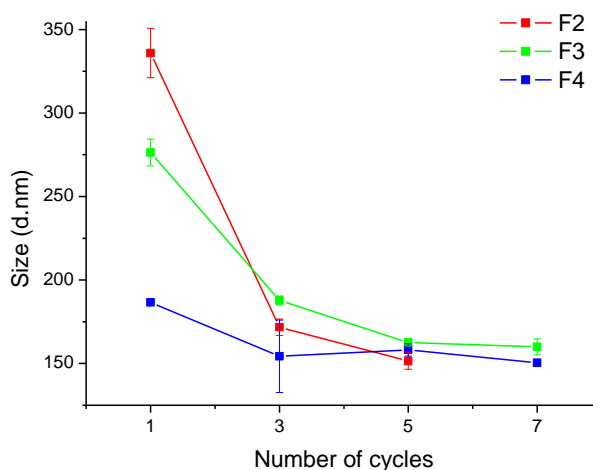
### **6.4.1 Nanoparticles preparation method development**

As some of the Gelucire 50/13 gels exhibit characteristic features of cubic liquid crystalline phase, the basic principal method for preparing cubosomes was adopted in this study to produce Gelucire gel nanoparticles [96]. Gelucire 50/13 gels nanoparticles were prepared in excess of water with a hand-held disperser. In order to further reduce the particle size and improve the homogeneity of the sample, the nanoparticle suspensions were passed through a high pressure homogeniser. In the attempt to establish the effective number of cycles required for the high-pressure homogenisation process, the size of the nanoparticles after 1, 3, 5 and 7 cycles were determined using DLS. According to the DLS results, as shown in Figure 6.2 the effect of the homogenisation is mainly on reducing particle size and producing a more homogeneous distribution of nanoparticles.



**Figure 6.2** Changes of size distribution (d.nm) of the nanoparticle formulations F2, F3 and F4 prepared by being passed through the high-pressure homogeniser with different number of cycles ( $n = 3$ ).

Figure 6.2 compares the changes of size distribution of the formulations F2, F3 and F4 prepared by being passed through high-pressure homogeniser with different numbers of cycles. The effect of the number of cycles is more evident for the formulation F2. After one cycle, a broad peak is visible, which suggest a high distribution of particle size. A second population (peak) at smaller size can also be observed for the formulation F2. The second population at smaller particle size is more visible for formulations F3 and F4. For the formulation F3, the effects of increasing the homogenisation cycles can also be seen in the reduction of particle size. However, no improvement on the polydispersity (narrowing of the size of the distribution peak) can be seen for F3 and F4. The effect of the number of cycles on the particle size and size distribution is least evident in the results of F4 nanoparticles compared to F2 and F3. The sizes of the second population with smaller particle sizes are less affected by the number of cycles of homogenisation in comparison to the population with larger particle sizes.



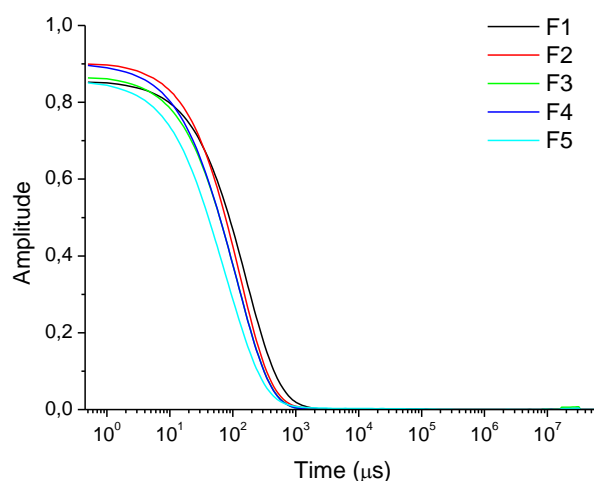
**Figure 6.3** Mean particle size (d.nm) of the main population of formulations F2, F3 and F4 by varying the number of cycles with the high pressure homogeniser ( $n = 3, \pm SD$ ).

Figure 6.3 shows the change of the mean particle size of the main population of the formulations F2, F3 and F4 as a function of the number of cycles applied during the homogenisation. It can be clearly seen that for all three formulations, the mean particle size decreases with increasing the number of homogenisation cycles and no further reduction is seen when 5 or more cycles are applied. However, this effect is more evident in the formulations F2 and F3 when the number of cycles was increased from 1 to 3. For the formulation F2, the mean particle size determined by DLS after the first cycle (336 nm) is statistically different from the ones obtained at 3 (172 nm) and 5 cycles (151 nm) (One-way ANOVA test). The mean particle sizes obtained for formulation F2 after being homogenised 3 and 5 cycles are not different at level of significance equals to  $p < 0.001$ . For F3, the mean particle sizes obtained after being homogenised 5 and 7 are not statistically different ( $p > 0.05$ ). The effect of homogenisation cycles on the particle size is less evident in the formulation F4 in comparison to F2 and F3. In fact, there is no significant difference between the particles processed using 1, 3, 5 and 7 cycles (One-way ANOVA test,  $F = 6.837, p > 0.001$ ). As a result, five cycles were considered to be appropriate in order to obtain homogeneous nanoparticles suspensions.

#### 6.4.1.1 Physical stability

The physical stabilities of the gel nanoparticle formulations were studied by monitoring the particle size of the nanoparticles using DLS during storage under different conditions (room temperature and 4 °C). The correlation functions of the freshly prepared nanoparticle formulations were obtained by plotting the amplitudes versus the time of decay ( $\mu s$ ) of the nanoparticles, as it is shown in Figure 6.4. The correlogram provides information on the quality of the sample analysed. The dropping point at which the correlation function starts to

decay is related to the mean diameter. The degree of deviation of the slope from a vertical straight line after the dropping point is a measure of the polydispersity of the sample. The level of smoothness of the baseline shows whether large particles or aggregates are present in the samples. If the baseline deviates from zero, it is an indication of the presence of large aggregates in the samples. In Figure 6.4, it is possible to see that all the formulations show a certain degree of polydispersity as the deviation of the slope after the dropping point deviates from the straight vertical line. The formulation F5 decays more rapidly than the other formulations, indicating the F5 formulation has smaller hydrodynamic diameters than the other formulations. F3 and F4 show similar correlation functions, suggesting a comparable diameter, whereas F1 and F2 have a longer decay suggesting that the particles have bigger hydrodynamic radius than F3, F4 and F5. Furthermore, given the smooth baseline of all measured samples, it may be concluded that all the formulations tested do not contain large aggregates.



**Figure 6.4** Correlation function of the nanoparticle formulations analysed at day 1 at 37 °C.

The DLS results can also be represented by using the intensity data. A bimodal distribution was observed in all the formulations when plotted using the intensity data. The main population has a larger diameter, which ranges between 120-200 nm, depending on the formulation. The second population has smaller diameter of about 20 nm. The population with smaller particle size is higher in percentage in the formulations F3, F4 and F5, which are formed using gels with higher water content, while in F1 and F2 the population with smaller particle size is not always visible. The size distribution in term of intensity is shown in Figure 6.5.

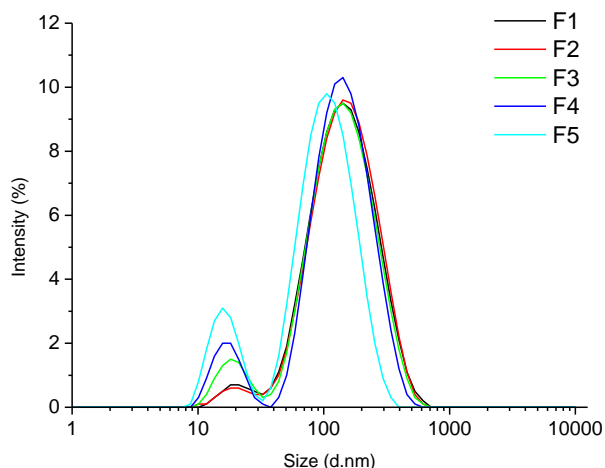


**Figure 6.5** Size distribution (d.nm) of freshly prepared nanoparticle formulations (n = 3).

In order to establish the physical stability of the nanoparticle formulations, the size distributions of the nanoparticles suspension stored at room temperature and at 4 °C were monitored over time. Table 6.3 shows the measure size diameters of the nanoparticles stored at room temperature over a period of two weeks. In general, the sizes of the nanoparticles decrease with increasing water content in the gels, from ~ 200nm for F1 (prepared from the gel with 30% water content) to ~150-160 nm for F2-F4 (prepared from the gels with 40-60% water contents) and ~120 nm for F5 (prepared from the gel with 65% water content).

Table 6.4 lists the changes of the particle sizes of the nanoparticle formulations stored at 4 °C over a period of four months. The size of nanoparticles stored at 4 °C is comparable to that of the nanoparticles stored at room temperature and little changes in the particle size can be observed on aging.

Overall, the stability data suggest that no aggregation occurred in the formulations stored at room temperature up to two weeks and up to four months in the samples stored at 4 °C. The samples stored at room temperature were not analysed after 14 days and the ones stored at 4 °C were not analysed after 4 months, due to the time limitation of the project. However, it should be mentioned that the nanoparticle formulations may be stable for longer period than the tested period in this project. A complete long-term stability study is necessary to establish the real shelf-life of these formulations (see Chapter 7 for the proposed long-term stability study).

**Table 6.3.** Mean particle size (d.nm) of the nanoparticles stored at room temperature and monitored overtime using DLS (n=3).

Formulations	Population 1				Population 2			
	Time (days)				Time (days)			
	1	2	7	14	1	2	7	14
<b>F1</b>	—	—	—	—	207±1.18	225±29	216±9.95	224±6.63
<b>F2</b>	—	—	—	—	151±4.88	154±3.92	160±5.45	162±2.82
<b>F3</b>	21±0.89	19±1.47	19±0.39	19±0.60	163±2.50	161±1.14	161±0.37	161±0.88
<b>F4</b>	17±0.47	17±0.61	17±0.35	17±0.60	158±1.79	160±0.06	157±0.27	156±0.41
<b>F5</b>	17±0.20	17±0.56	17±0.32	18±0.44	119±1.87	127±2.75	124±4.41	128±2.29

**Table 6.4** Size distribution (d.nm) of the nanoparticle stored at 4°C and monitored overtime using DLS (n=3; NA= Not Analysed).

Formulations	Time (days)				Time (days)			
	7	14	30	120	7	14	30	120
<b>F1</b>	—	—	—	—	214±7.77	204±3.26	210±1.66	NA
<b>F2</b>	—	—	—	—	163±3.15	157±2.35	153±0.94	179±35.37
<b>F3</b>	20±0.19	18±0.52	NA	19±0.68	160±1.54	159±3.18	NA	163±9.41
<b>F4</b>	17±0.43	17±0.35	NA	16±2.75	153±4.12	156±2.74	NA	152±5.81
<b>F5</b>	17±0.16	18±0.50	NA	19±0.83	120±0.98	124±14.46	NA	117±0.68

### 6.4.1.2 Shape analysis

#### 6.4.1.2.1 Cryo-TEM

Although the DLS can provide estimation of the hydrodynamic diameter of the nanoparticles, the analysis is based on the assumption of the particles being spherical. Therefore, in order to obtain more detailed information of the shape of the nanoparticles, selected formulations were analysed using cryo-TEM. The cryo-TEM images on the formulations F2 and F4 allows the direct visualisation of the shape of the nanoparticles (Figure 6.6 and Figure 6.7). The images were obtained at 50000x magnification. Different sites of each sample were analysed and the size of the nanoparticles was determined by using ImageJ 1.46r software (Wayne Rasband, National Institute of Health, USA). Histograms of the frequency (number of particles within a certain size range) versus the particle size were plotted using OriginPro 8 (Northampton, MA, USA) (Figure 6.6 b and Figure 6.7 b). The upper parts of the histograms are the probability plots, which evaluate whether the data fit with a normal distribution. The probability plots were obtained by plotting the cumulative frequencies of the observations versus particle size and then

rescaling in the probability scale type (that means a range of values between 0 and 100%). Data with normal distribution would show a straight line, otherwise, deviations from the straight line should be observed. Despite the low contrast of the images, the shape of the nanoparticles can still be observed (dash line circles were used in the images as a guide of the eyes for the readers). The reason for the low contrast is due to the poor contrast of the material such as PEG chains which are not visible to the electron beam [265]. In both formulations, the cryo-TEM images reveal the polydispersity of the size of the nanoparticles with size ranging between 50 nm to ~250 nm, which agrees well with DLS results.

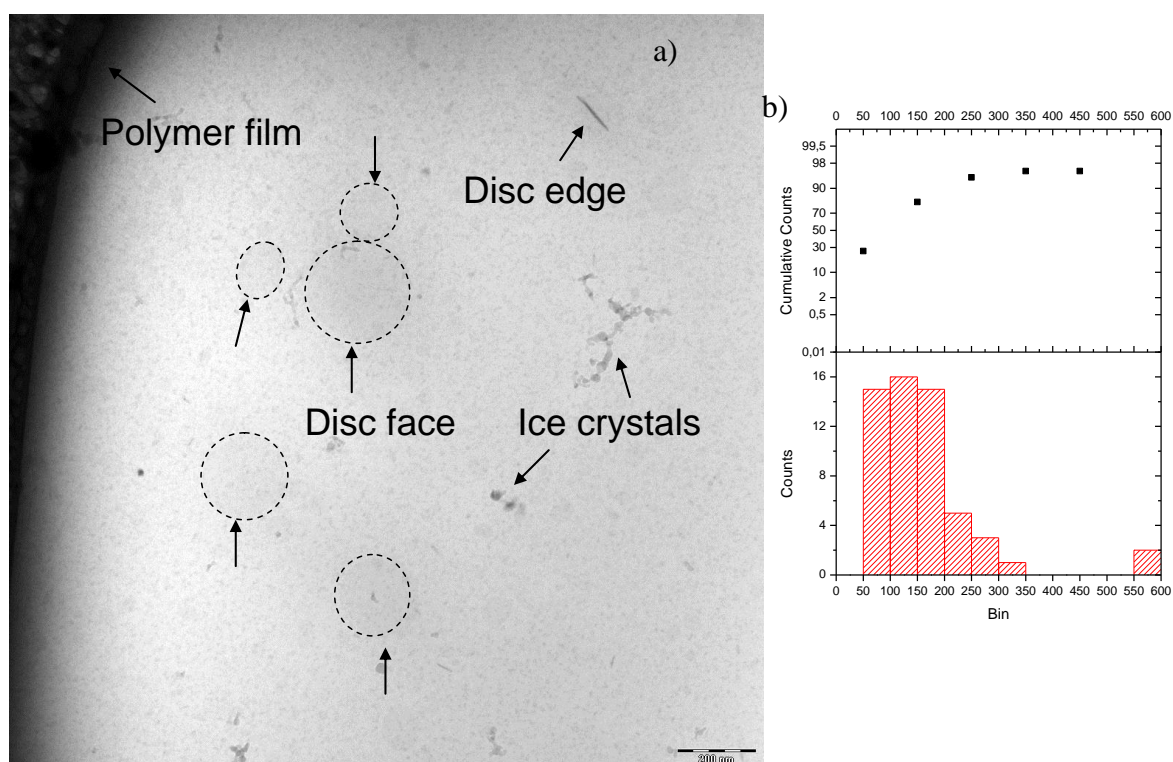


**Figure 6.6** (a) Cryo-TEM image of the nanoparticles of the formulation F2. (b) Histogram chart of the particle size of F2 formulation, measured from cryo-TEM images (plotted using frequency versus size interval). The upper part is the probability plot.

In Figure 6.6 two types of shapes can be observed, circular and rod. The presence of rod shape may be the reflection of the nanoparticle from a side-view. This suggests that the nanoparticles may have a disc-like shape and the elongated rod shape objects are associated with the disc edges of the nanoparticles, while the circular shape objects are the disc-face view of the particles. The histogram chart (Figure 6.6 b) shows that the nanoparticles in the formulation F2 have a main size range between 50 and 200 nm, few nanoparticles with higher size (between 200 and 350 nm and between 550 and 600 nm) have been identified. This result largely agrees with the DLS results.

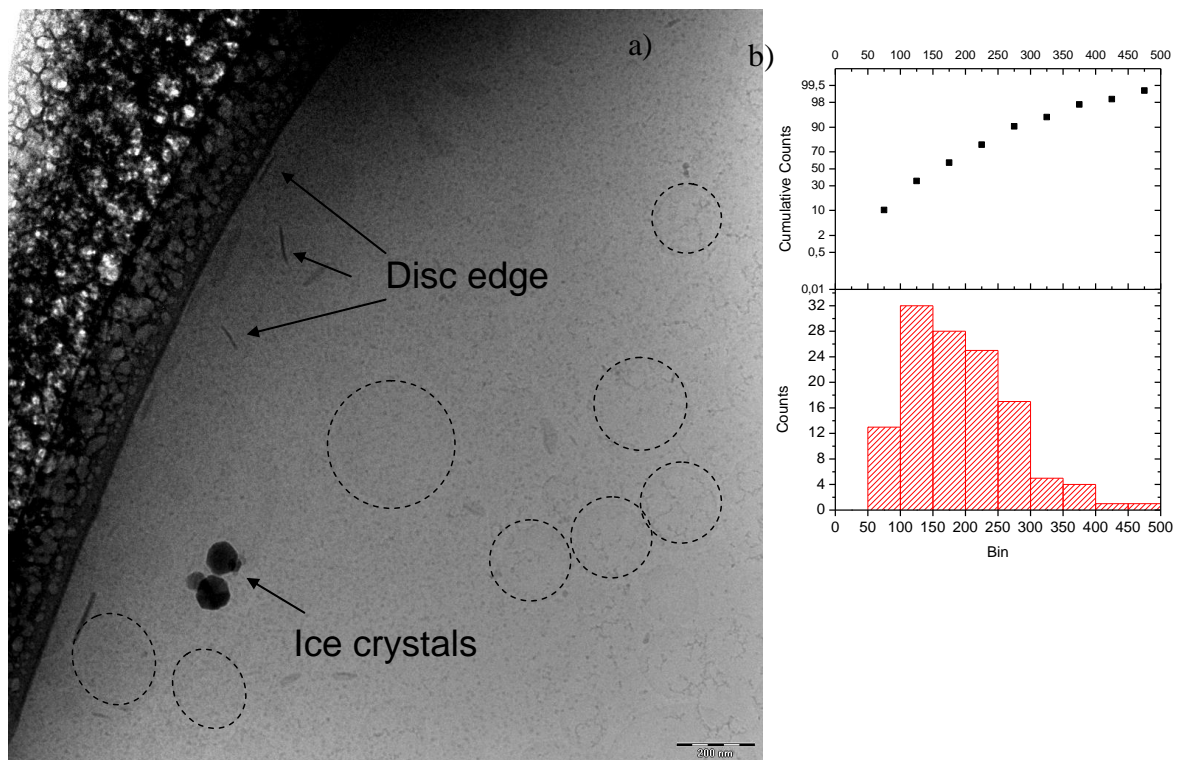
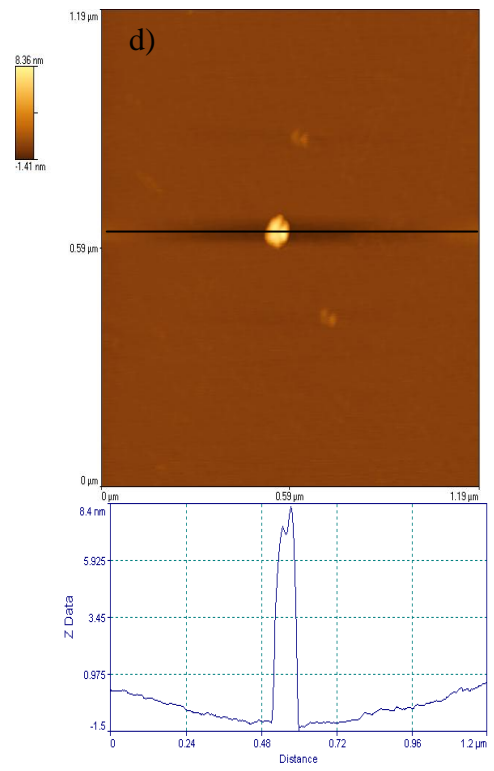
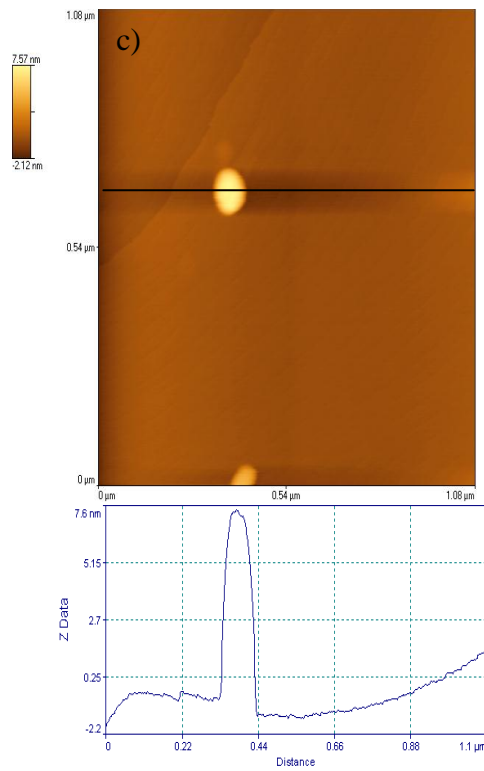
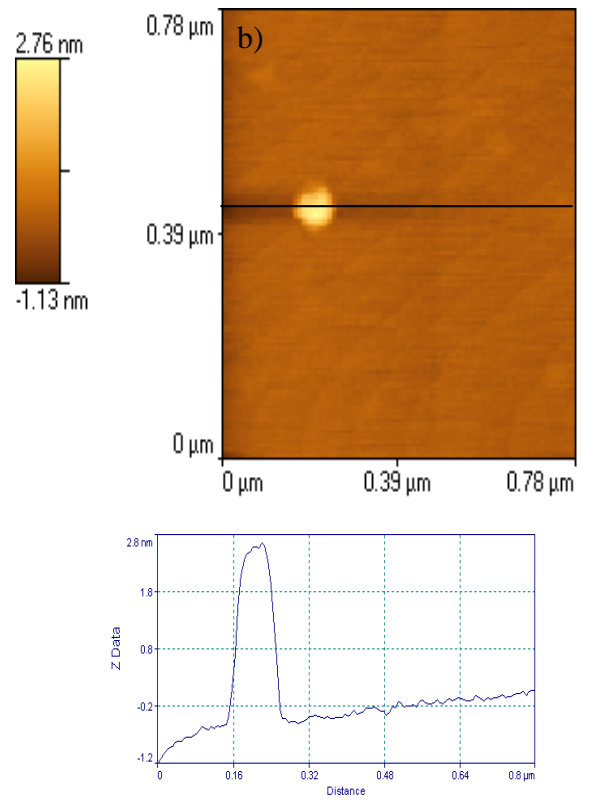
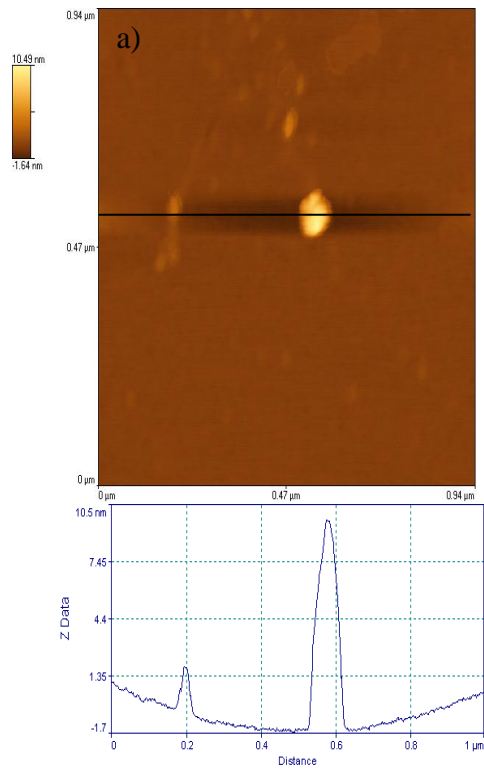


**Figure 6.7** (a) Cryo-TEM image of the nanoparticles of the formulation F2. (b) Histogram chart of the particle size of F2 formulation, measured from cryo-TEM images (plotted using frequency versus size interval). The upper part is the probability plot.

A typical cryo-TEM image of the formulation F4 is shown in Figure 6.7a. It shows similar results to the ones of the formulation F2. The nanoparticles have a disc-like shape with a slightly larger size ranging between 50 and 300 nm. Few nanoparticles with bigger diameter (between 350 and 500 nm) can also be identified. However, the nanoparticles are largely to be within average 150 nm in diameter, which is consistent with the DLS result. In both F2 and F4 formulations, the data fail to fit the normal distribution as it can be seen from the probability plots as a result of the polydispersity of the nanoparticles, which was also indicated by DLS.

#### 6.4.1.2.2 Atomic force microscopy (AFM)

AFM was used to image the nanoparticles in order to further obtain 3-D information on the shape and size of the nanoparticles *in situ*. This method can also avoid the freezing procedure required in cryo-TEM. Tapping mode AFM was used to characterise the shape and size of the gel nanoparticles. The reason of using the non-contact tapping mode is mainly due to the concern of the softness of the Gelucire 50/13 nanoparticles.



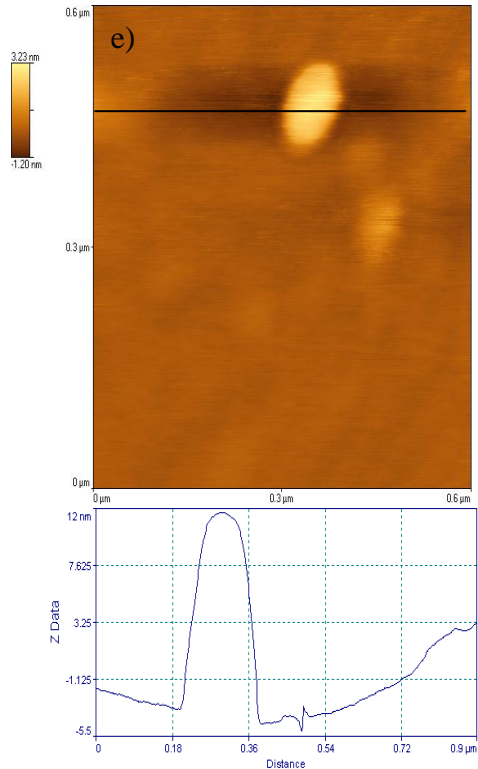


**Figure 6.8** AFM images of the nanoparticles formulations: a) F1; b) F2; c) F3; d) F4 and e) F5.

Figure 6.8 shows the tapping mode AFM images of the nanoparticles formulations F1 to F5. Individual nanoparticles were well isolated from each other and can be easily imaged. 5 to 10 sites of each sample were imaged and the results are relatively reproducible, indicating that the samples are largely homogenous. Through the topographic analysis (line analysis), 3-D dimensions of the nanoparticles can be obtained. The height of the peaks is related to the thickness of the nanoparticles ( $z$ -axis), whereas the width of the peak is a measure of the diameter of the nanoparticles. The diameter was calculated along the  $x$ -axis and the  $y$ -axis (as shown in Figure 6.9) and listed in Table 6.5. Therefore it can be concluded that the gel nanoparticles have a disc-like shape, as illustrated in Figure 6.9.

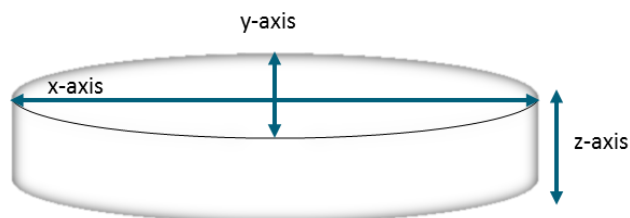


**Figure 6.9** Schematic view of the 3D-dimensions disc-like shape nanoparticles.

**Table 6.5** Dimensions (d.nm) of the unloaded nanoparticles determined using AFM.

<i>Formulations</i>	<i>Size (d.nm)</i>		
	<i>X axis</i>	<i>Y axis</i>	<i>Z axis</i>
F1	75±20.65	79±11.93	10±2.6
F2	84±4.93	62±9.29	3±0.6
F3	96±7.92	110±13.99	9±1.8
F4	77±1.41	78.5±4.95	9±0.6
F5	124±48.8	134±43.1	8±5.7

Concerning the diameters of the circular faces of the nanoparticles, they are ~75-100 nm for the formulations F1 to F4, whereas the DLS measured mean diameters of these nanoparticles are approximately 150-200 nm. For the formulation F5, the size that is determined with AFM (124-134 nm) is largely comparable with the size determined with DLS (~120 nm). Overall, the size of the nanoparticles determined with AFM is smaller than the size measured with DLS and visualised with the cryo-TEM. The reason for this difference may be due to the experimental conditions of different characterisation techniques. For example, the drying process of the nanoparticle suspensions on the mica film during the AFM sample preparation may lead to shrinkage of the nanoparticles and result in reduced particle size observed by AFM. Considering the significant differences in the z-axis and x/y axis, it is reasonable to suggest that z-axis is correlated to edge-side of the nanoparticles, thus the thickness of the nanoparticles. This also confirms the formation of disc-like shape nanoparticles, as revealed by the cryo-TEM images. The thickness values of the F1, F3, F4 and F5 nanoparticles are similar and range between 10 nm (F1) and 8 nm (F5), while F2 nanoparticles show much thinner edge-side (3 nm). The difference in dimensions of the nanoparticles may be attributed to the structure and composition of the bulk Gelucire gels used to prepare the nanoparticles.

Both imaging techniques (cryo-TEM and AFM) confirm the presence of poly-dispersity and disc-like shaped nanoparticles. The size range of the formulations determined with the cryo-TEM are consistent with the size obtained with the DLS but bigger than the size measured using AFM. It should be consider that the different principles behind each characterisation technique may contribute to the small differences in size obtained by different methods. For example, the size determined with the DLS corresponds to the hydrodynamic diameter of the equivalent sphere diameter, which is now known to be not the actual shape of the nanoparticles. Furthermore, as the PEG chains are invisible to the cryo-TEM beam, the real dimension of the nanoparticles may be slightly bigger than the one visualised using cryo-TEM.

## 6.4.2 Physical characterisation of lysozyme-loaded nanoparticles

### 6.4.2.1 Physical stability

The sizes of the lysozyme-loaded nanoparticles were monitored over time following the same method described for the unloaded nanoparticles. As seen in Figure 6.10, the presence of lysozyme increased the polydispersity and the sizes of the main population of the nanoparticles in comparison to the corresponding unloaded nanoparticles.

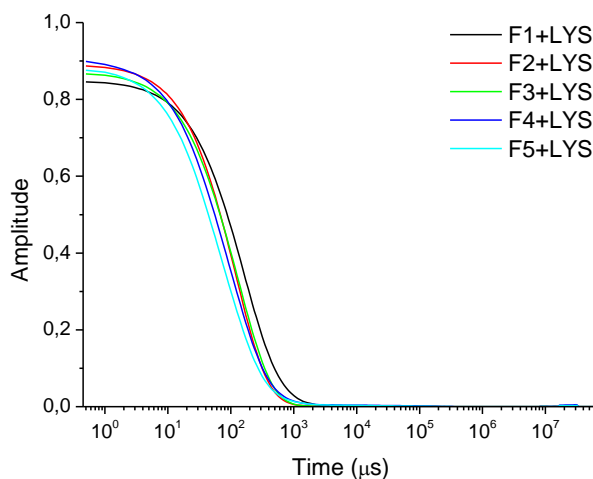


**Figure 6.10** Correlation function of the formulations analysed at day 1 at 37 °C.

Similar to the studies conducted on the unloaded nanoparticles, the change in particle size was used as a main indication of the physical stability of the formulations. Table 6.6 lists the mean diameters of the lysozyme-loaded nanoparticles of the formulations F1 to F5 stored at room temperature. For formulations F1, F2 and F5 nanoparticles stored at room temperature, a precipitate was observed from 14 days of aging, thus no more tests were performed after 14 days. F3 and F4 nanoparticle formulations were not analysed after 7 days. Among the formulations, the size of the formulation F2, F3 and F4 stored at room temperature are reasonably constant over the testing period.

**Table 6.6** Mean particle size (d.nm) of the lysozyme-loaded nanoparticles stored at room temperature and monitored overtime using DLS (n=3; NA= Not Analysed).

Samples	Population 1				Population 2			
	Time (days)				Time (days)			
	1	2	7	14	1	2	7	14
<b>F1</b>	19±0.24	—	—	18±2.79	286±30.8	246±13.9	NA	220±5.3
<b>F2</b>	—	—	—	—	147±4.28	151±1.86	148±0.91	151±1.11
<b>F3</b>	18±0.27	18±2.09	19±1.03	NA	174±7.1	178±3.97	177±1.08	NA
<b>F4</b>	17±0.55	17±0.68	17±00.26	NA	139±4.04	136±4.04	139±0.05	NA
<b>F5</b>	18±0.40	18±0.11	18±0.37	18±0.53	117±5.33	117±2.86	130±17.55	122±2.68

Two populations of nanoparticles with different size could be identified in all the tested formulations. A population with smaller particle size ranging between 17 and 19 nm is consistent with the size of the population of small particle size identified in the unloaded nanoparticles. The second population has a larger particle size than the unloaded nanoparticles for the formulations F1 and F3. For example, for the lysozyme-loaded formulation F1, the mean diameter size of the freshly prepared gel nanoparticles is 286 nm, while the unloaded F1 nanoparticles have an average size of 207 nm. For the formulation F3 the lysozyme-loaded nanoparticles have an average size of 174 nm against 163 nm of the unloaded ones. The size of the lysozyme-loaded nanoparticles in the formulations F2 and F5 (147 nm and 117 nm, respectively) are slightly bigger with the size of the unloaded nanoparticles (151 nm and 119 nm, respectively). On the contrary, lysozyme-loaded nanoparticles of formulation F4 show smaller size (139 nm) compared to the unloaded nanoparticles (158 nm).

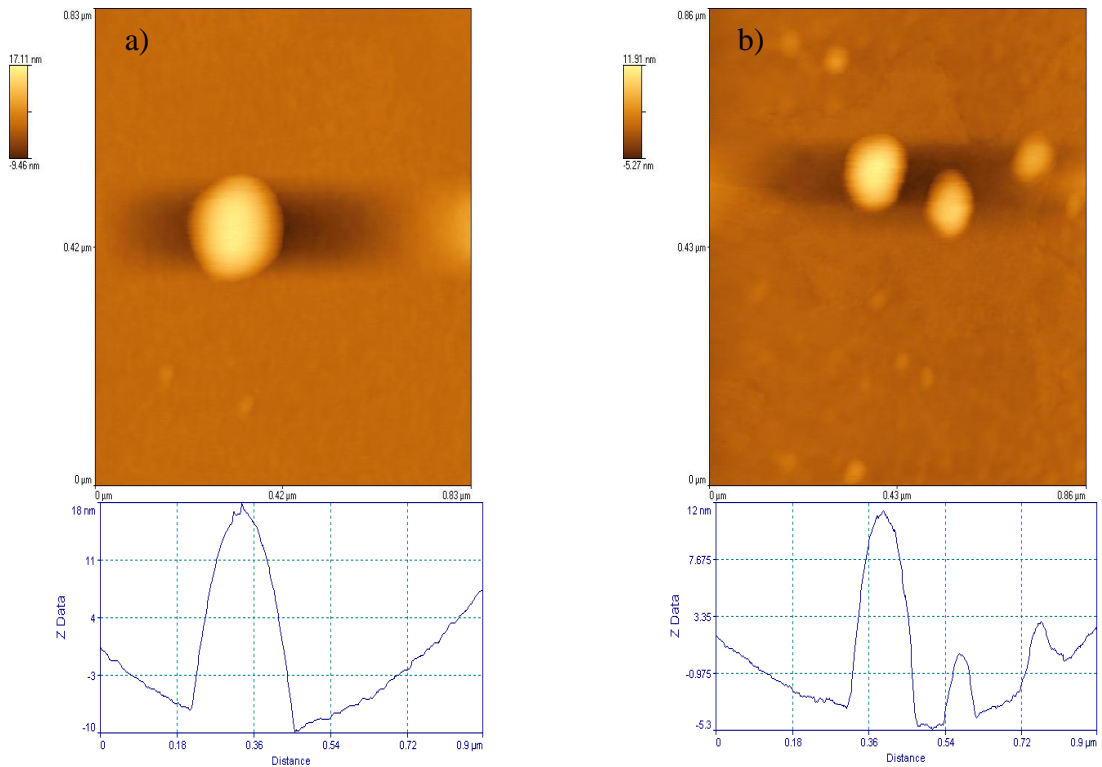
**Table 6.7** Mean particle size (d.nm) of the lysozyme-loaded nanoparticles stored at 4 °C and monitored overtime using DLS (n=3; NA= Not Analysed).

Samples	Population 1				Population 2			
	Time (days)				Time (days)			
	7	14	30	120	7	14	30	120
<b>F1</b>	—	—	NA	17±2.36	NA	232±19.2	NA	NA
<b>F2</b>	—	—	—	—	155±9.18	150±2.57	NA	NA
<b>F3</b>	18±0.27	18±2.09	19±1.03	—	183±0.74	NA	NA	179±3.70
<b>F4</b>	17±0.27	18±0.48	18±0.36	17±0.34	139±4.74	138±2.46	143±2.78	146±5.51
<b>F5</b>	17±0.73	17±0.06	NA	14±4.85	139±20.25	136±15.4	NA	156±23.18

The lysozyme-loaded nanoparticles stored at 4 °C were stable (using the particle size as the measure) over the period of 4 months. For all populations, the population of the nanoparticles with smaller size stored at 4 °C is consistent with the size of the nanoparticles stored at room temperature and remained stable over time. For the main population with larger particle size, the size determined after 7 days of aging is largely consistent with the nanoparticles stored at room temperature. For the formulations F4 and F5, the size is stable up to 14 days, after which an increase in size is observed. The lysozyme-loaded formulation F3 is stable up to 120 days. Formulations F1 and F2 were not analysed after 14 days due to the presence of precipitates. It may be concluded that formulations F3, F4 and F5 (prepared from the bulk gels with 50-65% water contents) are more stable over time than the formulations F1 and F2, which are made of the bulk gels with lower water contents (30% and 40%, respectively). From the DLS results, it can be concluded that the presence of lysozyme increases the polydispersity and the instability of the nanoparticles.

### 6.4.2.2 Shape analysis

Tapping mode AFM was used to study the shape of the lysozyme-loaded nanoparticles. About 10 sites of each sample were visualised in order to assess the homogeneity of the samples. The results revealed that the lysozyme-loaded nanoparticles are less homogeneous than the unloaded nanoparticles and aggregates were found. However, the disc-like shape of the lysozyme-loaded nanoparticles still can be confirmed from the topographic analysis of the AFM images, as seen in Figure 6.11.



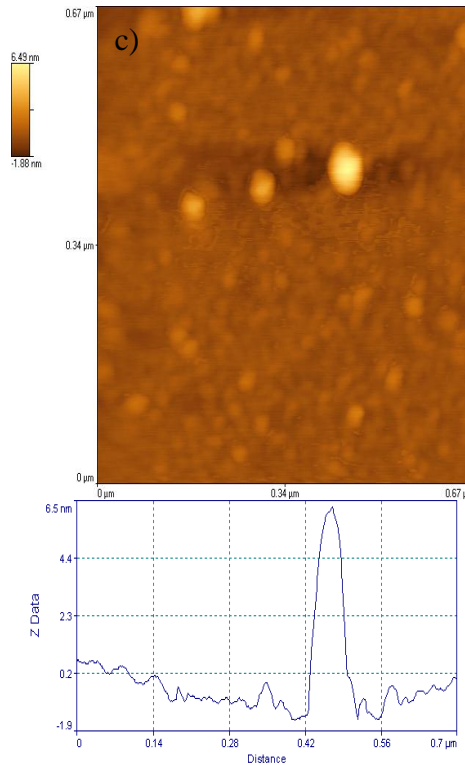


**Figure 6.11** Tapping mode AFM images and the topographic analysis of the lysozyme-loaded nanoparticles: a) F2; b) F4; c) F5.

Table 6.8 lists the dimensions of the nanoparticles imaged in Figure 6.11. Similar to the results of the unloaded nanoparticles, the diameters of the disc-face lysozyme-loaded F5 nanoparticles determined using AFM (~67) is smaller than the size measured using DLS (117 nm). On the contrary, in the formulation F2, the diameter of the disc-face is bigger than the size calculated with the DLS in which it was found to be 147 nm versus ~200 nm measured using AFM. For the formulation F4, the size calculated with AFM (~140 nm) is comparable to the one measured using DLS (139 nm).

**Table 6.8** Particle dimensions of lysozyme-loaded nanoparticles (d.nm) determined with AFM.

Formulations	LYS loaded		
	X axis	Y axis	Z axis
F2	207	184	27±0.9
F4	142	139	12
F5	66	69	6.5

### 6.4.2.3 Lysozyme Encapsulation Efficiency (%EE)

The encapsulation efficiency of lysozyme in each nanoparticle formulation was measured using the method described in section 6.3.3. The results are listed in Table 6.9. For F1 and F2 nanoparticle formulation, the lysozyme is encapsulated in higher efficiency (38% and 40%, respectively) than was in formulations F3, F4 and F5 (33%, 29% and 33%, respectively). Overall, the encapsulation efficiency of enzyme in the nanoparticle formulations decreases with increasing the water content in the bulk gel used to prepare the nanoparticles. This may indicate that the encapsulation efficiency may be related to the different nanostructure of the bulk gels containing different water concentrations. However, the encapsulation efficiency does not seem to be correlated with the particle size of the different formulations. For instance, the formulations F2 and F4 have a similar size (151 and 158 nm, respectively), but the encapsulation efficiency of F2 is 9% higher than F4. Furthermore, F5 shows the same encapsulation efficiency as F3. However, the size of the F5 nanoparticles is much lower than the size of the F3 nanoparticles (119 versus 163 nm).

**Table 6.9** Percentage of lysozyme encapsulated in the formulation (EE %) (n = 3,  $\pm$  SD)

<i>Formulations</i>	<i>EE (%)</i>
F1	40 $\pm$ 3.67
F2	38
F3	33 $\pm$ 0.96
F4	29 $\pm$ 1.97
F5	33 $\pm$ 1.49

### 6.4.2.4 Proposed molecular model of lysozyme-loaded nanoparticles

A molecular arrangement of the nanoparticles can be proposed by using the physical characterisation knowledge obtained for the unloaded and lysozyme-loaded nanoparticles. Further indications were obtained from the knowledge on the structure of the dry Gelucire 50/13 provided by Brubach et al. [109]. It can be proposed that because the nanoparticles formulations are in aqueous solution, the polar head of the glycerides and the PEG chains are located on the surface, while the hydrophobic chains (C<sub>16</sub> and C<sub>18</sub>) are hidden in the inner compartment of the nanoparticles. The presence of the PEG on the surface of the nanoparticles could also explain the good stability of the formulations. The nanoparticles were confirmed to have disc-like shape. The thickness of the nanoparticles agrees well with the length of the glycerides aliphatic chains (4.5-5 nm). As the nanoparticles are in disc-like shape, macromolecules such as lysozyme may not be able to interpenetrate within the nanoparticles, due to the restricted dimensions of the nanoparticles. It can be supposed that lysozyme may interact with the polar part of the surface of the nanoparticles. This interaction may anchor the lysozyme molecules at

the surface of the nanoparticles. As a result, a dynamic system may form which increases the size of the nanoparticles and change over time. However, low encapsulation efficiency is expected in this scenario as only the nanoparticle surfaces are used to load the protein. This may explain the relatively low encapsulation efficiency for the formulations with low values of thickness of the discs. A proposed molecular model of the disc-like gel nanoparticles loaded with lysozyme is shown in Figure 6.12.

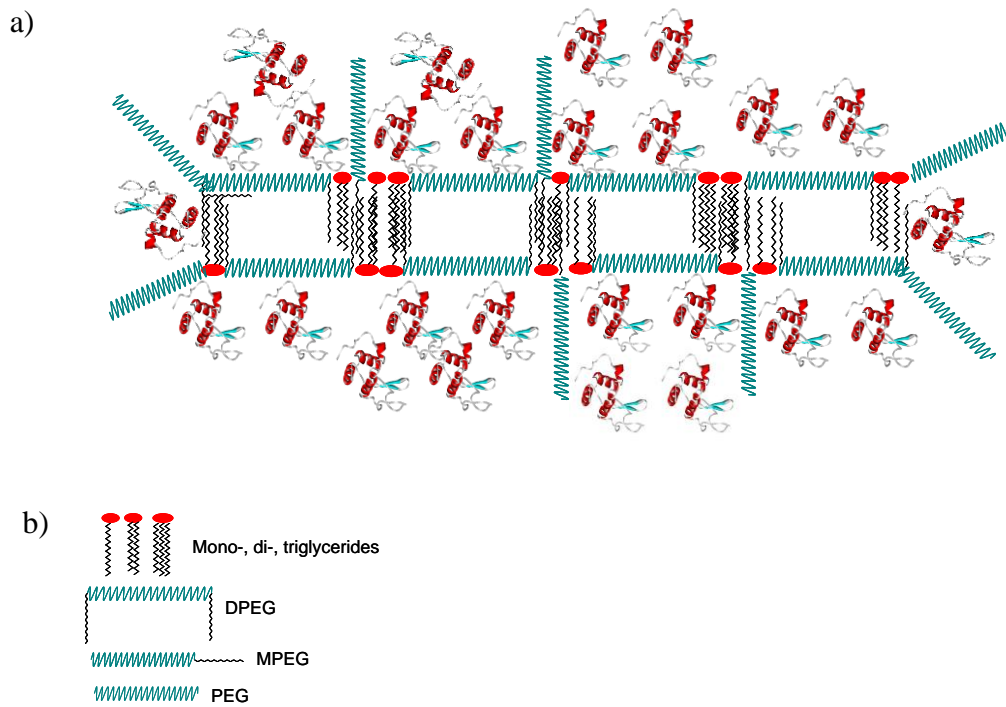


**Figure 6.12** Proposed model of disc-shape nanoparticle with lysozyme molecules encapsulated (a). A legend with the species present in the nanoparticles is also shown (b).

#### 6.4.2.5 Lysozyme activity and retained biological activity (%RBA)

The retained biological activities of lysozyme in different gel nanoparticle formulations were measured using the micrococcus lysodeikticus assay. Figure 6.13 shows the decrease in absorbance with time of the *Micrococcus lysodeikticus* incubated with the lysozyme-loaded nanoparticles formulations. The activity of lysozyme expressed in units/ml of lysozyme and it can be calculated according to Equation 2, or in units/mg of the solid lysozyme according to Equation 3 as described in section 6.3.4.2. Table 6.10 lists the lysozyme activity in units/ml and units/mg of protein of the formulations F2, F3 and F4, the lysozyme solution and the calculated RBA (%).

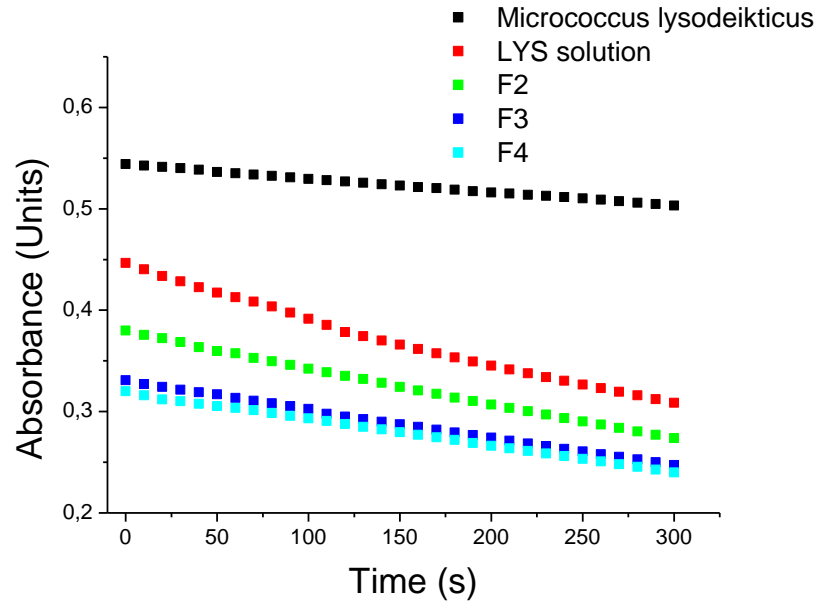


**Figure 6.13** Decrease in absorbance versus time of micrococcus lysodeikticus incubated with lysozyme solution and lysozyme-loaded nanoparticle formulations.

In order to assess the original activity of the lysozyme (as raw material) used in the formulations and the effect of the process of forming the nanoparticles on the activity, the activity of the lysozyme solution was analysed first. According to the assay, the lysozyme solution retains half of the original activity (46%). For the formulation F2, the activity is higher than the lysozyme solution (59%). On the contrary, for in the formulations F3 and F4 (which were prepared from the gels with higher water content) the activity is reduced to ~20%. As reported in section 6.4.2.3, the formulation F2 has the highest lysozyme encapsulation efficiency, the high retained activity in the formulation F2 may indicate that the formulation protects the lysozyme from degradation and helps to retain its activity.

**Table 6.10** Lysozyme activity in units per ml and units per mg of protein.

Formulations	$\Delta A$ Test/min	$\Delta A$ Blank/min	units/ml enzyme	units/mg solid	% RBA
LYZ solution	0.0276	0.0082	194.2	18286	46%
F2+LYZ	0.03204	0.0082	238.6	23765	59%
F3+LYZ	0.01674	0.0082	85.6	8534	21%
F4+LYZ	0.016	0.0082	78.2	7781	19%

#### ***6.4.2.6 Assessment of the structural conformation of the lysozyme by using Circular Dichroism (CD)***

The CD is a widely used technique to study the structural changes of proteins. From a CD spectrum in the far UV region (below 250 nm), the secondary structure of the proteins can be obtained. The CD spectrum in the near UV (between 260-320 nm) provides the tertiary structure fingerprint of the proteins. In the near UV, the spectrum arises from the aromatic amino acids of the proteins, such as Tryptophan (Trp), Tyrosine (Tyr), Phenylalanine (Phe) and disulfides bridges. In general, Trp shows a peak in the region between 290 and 305 nm, the Tyr between 275 and 282 nm and the Phe between 255 and 270 nm [204]. In a lysozyme molecule, the Trp is the most present aromatic amino acid with 6 residues per molecule, while the Tyr and Phe have 3 residues each [133]. The shape and the magnitude of the CD spectrum depend on the number of each amino acid present in the protein, as well as their mobility, the medium and the amino acids present in the surrounding, though the effect from the last factor is minimum.

CD spectra were obtained on the aqueous suspension of lysozyme-loaded F1, F2, F3 and F4 nanoparticles. Aqueous lysozyme solution and unloaded nanoparticles suspensions were also analysed as controls. The concentration of the lysozyme in the nanoparticles suspension and in the aqueous solution was fixed at 0.6 mg/ml. The experiments were carried out at 25 °C by using a quartz cuvette with 10 mm pathlength. Reliable data in the far UV region could not be obtained since the voltage of the instrument exceeded 500 volts, therefore, only spectra in the near UV region were taken into consideration. Although the CD spectra obtained in the near UV cannot provide detailed information regarding the secondary structure of the proteins, it can provide a valuable fingerprint of the tertiary structure, which can be used in comparing the spectra of the proteins in different concentration and environment [204] (in this case, in different nanoparticles formulations). In this work, the CD has been used to assess the changes in the tertiary structure of the lysozyme as a result of the encapsulation by the nanoparticles.

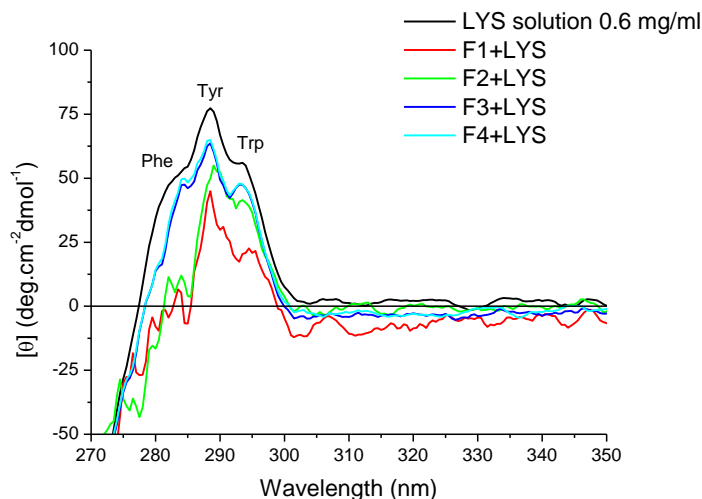


**Figure 6.14** Near UV CD spectra of lysozyme solution and lysozyme-loaded nanoparticles. Lysozyme aqueous solution was prepared at room temperature as control.

Figure 6.14 shows the CD spectra of the lysozyme aqueous solution and lysozyme-loaded nanoparticles formulations (F1, F2, F3 and F4). As it can be seen, the lysozyme retains its tertiary structure in the nanoparticles F3 and F4, which are prepared from gel with higher water content, while difference in structure is noted for formulations F2 and F1. The difference is more evident in the peak associated with the Phe. For the formulations F3 and F4, the peak at 284 nm is more evident and they show a weak peak at 281 nm. In formulations F1 and F2 the peak at 284 nm is less intense, but the peak at 281 nm is more evident. The peak at 290 nm, associated to the Trp residues, is still visible. However, despite the variation in the tertiary structure of the lysozyme, the formulation F2 ensures the retaining of the biological activity of lysozyme in the formulations (section 6.4.2.5).

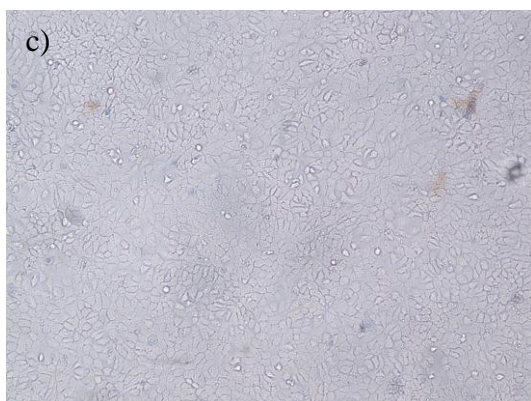
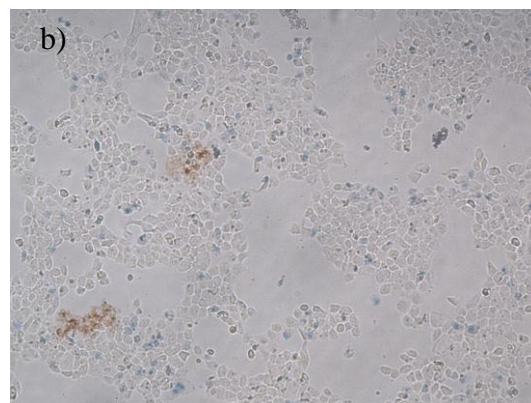
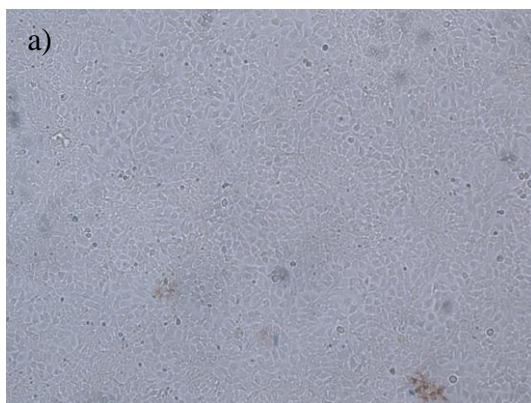
### 6.4.3 In vitro cytotoxicity study

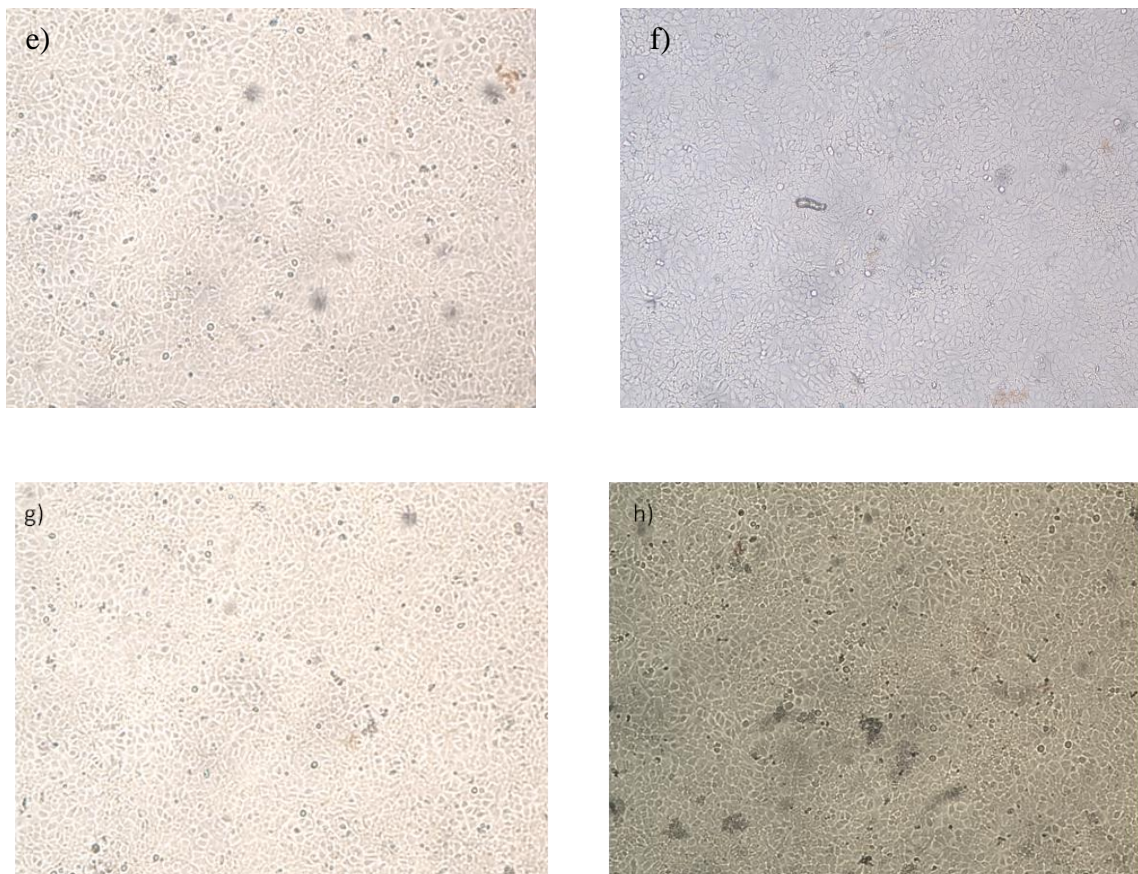
As F2 nanoparticle formulation has many promising properties such as the physical stability, the encapsulation efficiency and high level of retained activity of the lysozyme encapsulated, its potential as carrier for protein delivery was further explored. *In vitro* cytotoxicity of unloaded nanoparticles formulation F2 was tested by using a model human lung epithelial cell line, H292 and human colon epithelial cell line, Caco-2, following the methodology described in section 2.7. The nanoparticles were prepared from the bulk gel with 40% water and the dispersion has a final lipid concentration of 12 mg/ml. A range of dilutions of the formulation F2 was prepared. Table 6.11 lists the final concentration of the dilutions which were used to incubate with the both cells line.

**Table 6.11** Final concentrations of the dilutions of the nanoparticles formulation F2 used in the cytotoxicity study.

<i>Dilutions</i>	<i>Concentration</i> ( $\mu\text{g/ml}$ )
Stock	600
D1	300
D2	200
D3	150
D4	120
D5	100

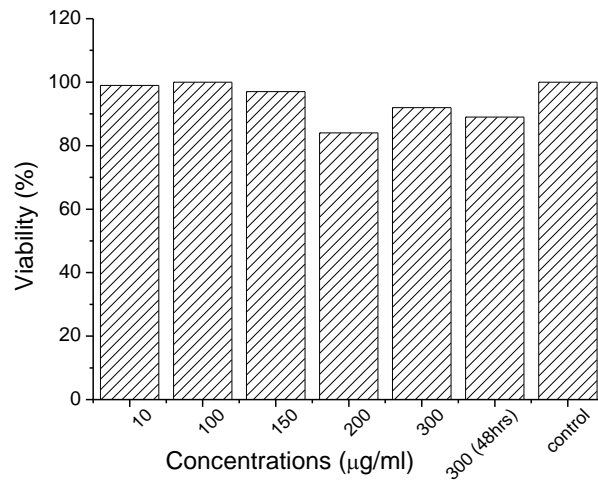
To assess the cytotoxicity of the unloaded F2 formulations for the lung cell line H292, cells were incubated with the dilutions of nanoparticle formulations for 24 h or 48 h at 37 °C. After incubation, agglomerate of particles was floating on the top of the cells. Cell viability was measured by trypan blue, as described in Chapter 2, section 2.7.3. The non-viable cells were stained blue after adding 0.2% of trypan blue solution (Figure 6.15).





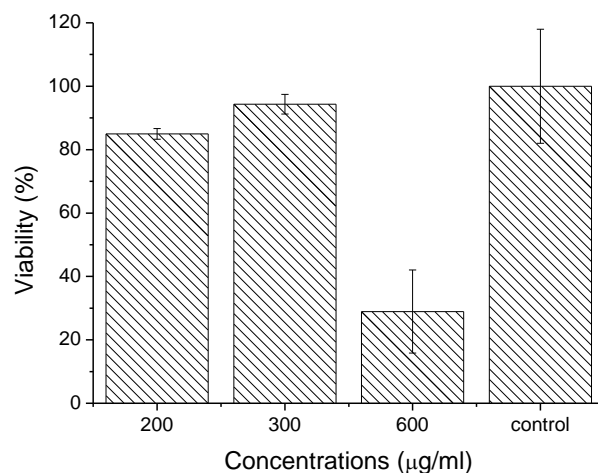
**Figure 6.15** Microscopy images of H292 cells incubated with the dilutions of F2 nanoparticle suspension for 24 hours at 37°C and treated with trypan blue. a) Control (cells without nanoparticles); b) stock solution, 600µg/ml; c) D1; d) D2; e) D3; f) D4; g) D5; h) D3 (after 48hrs incubation).

The results indicate that the nanoparticles with concentration of 600 µg/ml of total Gelucire were toxic (Figure 6.15 b), which caused a significant reduction in the number of adhered cells. The results of the other dilutions (up to 300 µg/ml) of the F2 nanoparticles showed cells with high viability. The viability of the cells versus the concentration of total lipid in each nanoparticle dilution is shown in Figure 6.16.



**Figure 6.16** In vitro cell viability of cells H292 incubated with different concentrations of nanoparticles at 37°C for 24 hours or 48 hours and determined microscopically by counting the blue stained cells (non-viable) by using trypan blue dye.

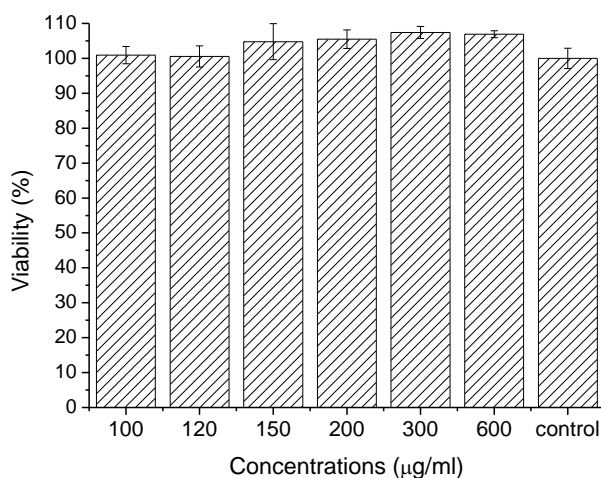
The Cell viability after incubation with the F2 nanoparticles was confirmed by MTS assay. The MTS assay was carried out in a 96-well plate as described in section 2.9.3. Figure 6.17 shows the mean cell viability of different dilutions. Good cell viability can be obtained when the cells were incubated with the nanoparticles dilutions with Gelucire concentrations of 200 and 300 µg/ml (85% and 94%, respectively). The nanoparticle suspension with a total lipid concentration of 600 µg/ml, however, was highly toxic and cell viability was reduced to 29%. The MTS assay results agreed well with the results obtained using trypan blue.



**Figure 6.17** Cell vability (% ± SD) of H292 model cell line determined using MTS assay (n=3).

The effects of the F2 nanoparticle suspension on Caco-2 cell viability was also assessed by MTS assay. The cells were incubated for 24 hours at 37 °C with concentrations of the stock solution and the dilutions D1, D2, D3, D4 and D5. Figure 6.18 shows cell viability after

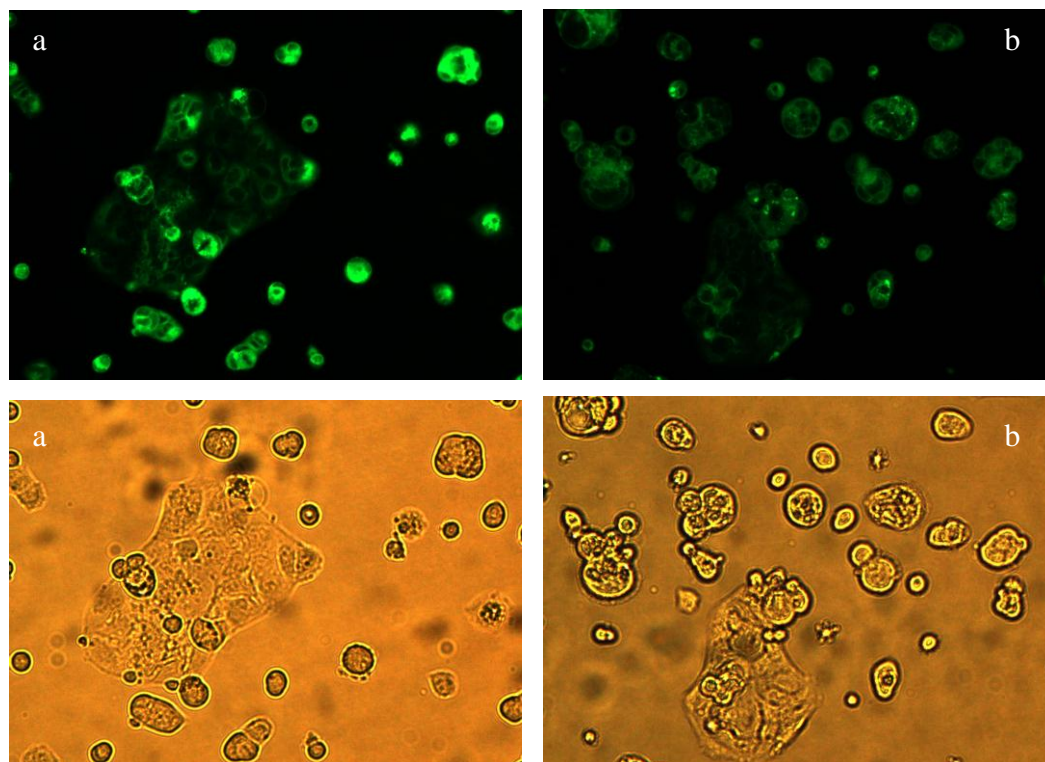
incubation with F2 nanoparticle suspensions. In contrast to the results obtained using H292 cells, the nanoparticles were not toxic for lipid concentrations up to 600  $\mu\text{g/ml}$ .



**Figure 6.18** Cell viability of Caco-2 model cell line incubated with F2 nanoparticle suspensions determined with MTS assay. The percentage was calculated relatively to the control (n=3).

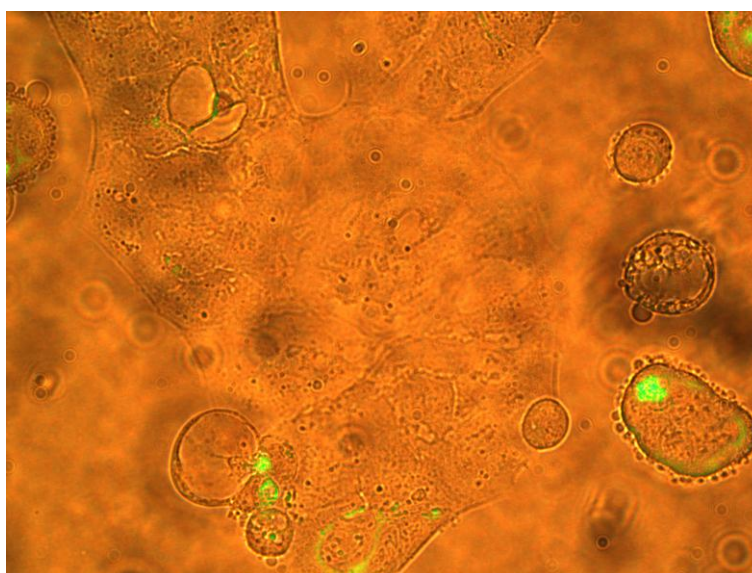
#### 6.4.4 Cellular uptake

The *in vitro* cell uptake of Gelucire 50/13 nanoparticles formulation F2 was investigated using Caco-2 cells. In order to be able to assess the uptake, fluorescently labeled nanoparticles were prepared as described in section 2.3.3. A hydrophobic dye, Coumarin 6 was added to the molten Gelucire during the preparation of the nanoparticles. It can be supposed that the Coumarin 6 is going to interact with the hydrophobic inner part of the nanoparticles. The encapsulation efficiency of Coumarin was assessed by centrifugation as previously described (see section 6.3.3). 100% of encapsulation efficiency of Coumarin 6 was obtained. The F2 nanoparticle dilutions (D1 and D4) with final concentrations of total lipid of 300 and 120  $\mu\text{g/ml}$  were used to incubate the cell monolayer for 15 minutes, after which images were taken with fluorescent and normal light (see Figure 6.19).



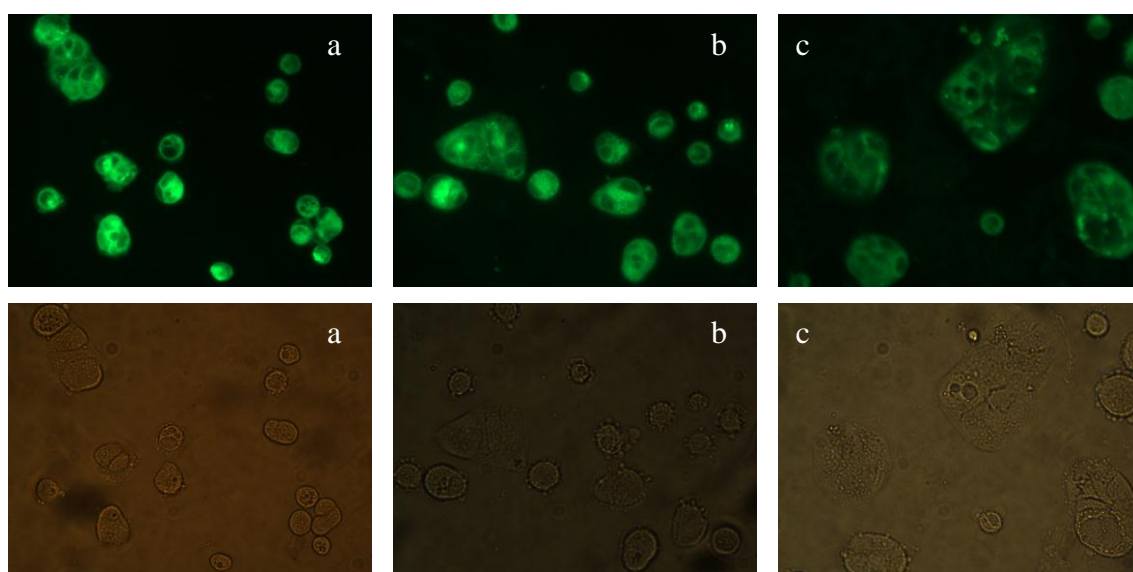
**Figure 6.19** *In vitro* Caco-2 cellular uptake of the F2 nanoparticles from dilutions D1 (a) and D4 (b) after 15 minutes of incubation. The images were taken under fluorescent light (upper row) and normal light (lower row).

Figure 6.19 shows the cellular uptake of the F2 nanoparticles prepared from dilutions D1 and D4 after 15 minutes of incubation. It is evident that the uptake is significant and rapid. No differences were observed after 120 minutes of incubation (Figure 6.20).



**Figure 6.20** *In vitro* Caco-2 cellular uptake of the F2 nanoparticles from dilutions D4 after 120 minutes of incubation (overlay image).

Figure 6.20 shows the uptake of the nanoparticles in the dilution D4 after 120 minutes of incubation. In this image, the fluorescent nanoparticles were overlaid over the cell image, in order to better localise the nanoparticles within the cell. In order to further examine the effect of the incubation time on the cell uptake of the nanoparticles 30, 90, 120, 180, 240 minutes and 24 hours incubations using the dilution D2 of the unloaded F2 nanoparticles (with final concentration of 200  $\mu\text{g/ml}$ ) were applied to the cells at 37 °C. The images were taken at each time point under fluorescent and normal light. Figure 6.21 shows the cellular uptake after 30 minutes, 240 minutes and 24 hours. As previously observed for the dilutions D1 and D4 (Figure 6.19), the uptake of the nanoparticles can be observed after 30 minutes incubation. They are stable over time up to 24 hours in the cells, as seen in Figure 6.21b and c.



**Figure 6.21** *In vitro* Caco-2 cellular uptake of the dilution D2 of the unloaded F2 nanoparticles from dilutions (200  $\mu\text{g/ml}$ ) after 30 minutes (a), 240 minutes (b) and after 24 hours (c) of incubation. The images were taken under fluorescent light (upper row) and normal light (lower row).

The pictures show a rapid and stable uptake of the nanoparticles into the cell compartment, although the mechanism by which the nanoparticles are uptake by the Caco-2 cells remains unknown and further studies will be required. Previous study from Li et al. [266] on the cellular uptake of Coumarin 6-loaded liposomes modified by Pluronic suggests that the Coumarin 6 detected within the cells derives from the interaction between the cells and liposomes. Therefore, it was excluded the possibility that Coumarin 6 diffused within the cells after being released from the liposomes. Similar mechanism may also apply to our case.

## 6.5 Conclusions

This work demonstrated the ability of Gelucire 50/13 gels to directly form stable disc-shaped nanoparticles. The preparation method of nanoparticles is low cost and organic solvent free without addition of any stabilisers. Five nanoparticle formulations were prepared from the bulk gels differing in water contents. The DLS results indicated that the nanoparticle formulations are polydisperse and with two main populations of nanoparticles with diameters of 20 nm and between ~120-200 nm. The size of the small population is consistent in all the formulations, while for the second population the sizes change according to the formulation. However, no particular trend was identified.

The disc-like shape was identified through the imaging techniques, including AFM and cryo-TEM. These techniques also were used to assess the size and dimensions of the nanoparticles. The cryo-TEM confirmed the size calculated with the DLS, but the diameter measured using AFM is smaller. The reason for that may be due to the drying process during the sample preparation. Lysozyme was used as model protein encapsulated into the nanoparticles. The physical stability of the nanoparticles was monitored using DLS. The lysozyme-loaded nanoparticles have larger diameter, but they are less stable than the unloaded nanoparticles. This may be due to the presence of the lysozyme (possibly concentrated at the surface of the disc-shaped nanoparticles) that increases the tendency of aggregation. A good efficiency of encapsulation of the lysozyme was achieved in the formulations F1 and F2, with higher Gelucire content than F3 and F5. These formulations showed bigger diameter, which means a large surface able to accommodate a larger amount of lysozyme. The encapsulation efficiency is close to literature value when lysozyme was incorporated in SLN (59%) [4]. Furthermore, the lysozyme retained its biological activity after loaded into the nanoparticle formulation F2, which proves the ability of the formulation to prevent degradation of the enzyme. Therefore, the formulation F2 was the chosen formulation for further cytotoxicity studies on two cell model lines, lung cell H292 and intestinal cells, Caco-2. The nanoparticles are non-toxic to the H292 cell line with up to 300 µg/ml Gelucire concentration, and they are safe up to 600 µg/ml for the Caco-2 cell line. The ability of the nanoparticles to be uptake by Caco-2 cells also was assessed. The cellular uptake of the nanoparticles by Caco-2 cells is rapid and stable up to 24 hours. Furthermore, the uptake behaviour is not affected by testing different nanoparticle dilutions.

## 7 Conclusions and Future work

This project has attempted to provide the full characterisation of the Gelucire 50/13 gels, which can guide the development of the application of such gels and nanoparticles for protein delivery. The characterisation work led to a better understanding of the structural changes of the gels with altering the formulation (the water content in the gel) and the method of preparation (Chapters 3 and 4). The thorough knowledge on the detailed microstructure of the gels allowed the proposal of using the ordered structure of the Gelucire 50/13 gels and the gel-based nanoparticles as carriers to deliver protein drugs. Finally the *in vitro* performance of the gels (Chapter 5) and the nanoparticles (Chapter 6) were examined and the suitability as delivery systems for proteins was assessed. This Chapter is presented with a primary attempt to summarise the key findings of the project and offer recommendations on the future work in the further development of the pharmaceutical application of the Gelucire 50/13 gels.

Gelucire 50/13 is a complex lipid-based material formed by a mixture of glycerides and PEG. With the presence of a polar and a hydrophobic component it is able to incorporate drugs of different nature. However, its pharmaceutical commercial applications have been mainly limited as excipient in solid formulation, e.g. pellets, tablets and capsules for sustained drug release [118, 131] due to its poor solid-state physical stability [121]. In literature, it has been demonstrated by numerous studies that it can facilitate the enhancement of the bioavailability of poorly soluble drugs [124-127, 267]. However, the multi-component nature of Gelucire 50/13 makes the interpretation and the characterisation of the material and formulations made from Gelucire 50/13 extremely challenging even in solid-state. To our knowledge, up to now there has been no report on the potential of using this compound for protein/peptide delivery. Concerning the lipophilic nature of the material and ability to form gels, we proposed the use of hydrated Gelucire 50/13 (Gelucire 50/13 gels) for protein delivery. This hypothesis was tested during this project.

Due to its complex nature, the involvement of a wide range of analytical techniques was employed to fully characterise the physical and mechanical properties of the Gelucire 50/13 gels. The physicochemical characterisation of Gelucire 50/13-based gels showed the formation of semi-crystalline/liquid crystalline structures. The complexity of the results obtained reflects the multi-component nature of the Gelucire 50/13. The combination of ATR-FTIR, SAXS, DSC and rheometer agreed in the co-existence of multiple ordered structures. The formation of the different structures for the gels was proven to be thermal

history and water content dependent. The degree of hydration of Gelucire 50/13 plays a crucial role in the determination of the structure and the physical properties of the gels. The statistical analyses confirmed that the rheological and mechanical properties of the gels are water dependent. Moreover, increasing the water content in the gels leads to an increase in the mucoadhesive properties of the gels.

These characterisation results all confirmed the importance of water content in influencing the gel structure and performance. Therefore in order to fully explain this water effect, it is necessary to further understand the states of water in the gels. The complex interior structures with networks of pores/channels with different sizes were suggested by the SEM results on the freeze-dried gels. According to the physical states of water in the gels, two groups of gels with different internal structure can be identified. The first group of gels with water content below 40% is characterised by multiple layered interior structure with no water channels. This closed packing leads to no free bulk water identified using DSC. Relaxometry NMR also confirmed that the presence of lipid rich phase and restricted diffusion of water molecules are the common characteristic of this group of gels. This agreed well with the structural analysis results of these gels obtained in Chapter 3, which indicated largely lamellar-dominated structure of the gels. The second group of the gel with water contents above 50% is characterised by the presences of water channels (detected using SEM) and free bulk water (detected using DSC). In these gels two phases, water rich phase (possible water channels and water pockets) and lipid rich phase (lipid bilayers), can be detected by the prompt diffusion with some restrictions using NMR. This also agrees well with the characterisation results on these gels, which revealed a range of highly ordered structure in these gels including hexagonal, diamond cubic and mixed liquid crystalline phases. These detailed structure information reassured the feasibility of using such gel for protein delivery.

Based on the knowledge obtained from the characterisation of the gels, lysozyme (as model protein) was incorporated in the gels with proved optimal physical properties for hosting and delivery proteins. The presence of lysozyme induced some changes in the structure of the gels, but overall it showed little effect on the physicochemical properties of the gels. More interestingly, lysozyme incorporated in the gels prepared by hydration method retained its native conformations. However, when it was incorporated in the gels prepared by heating method, some changes in the conformation were observed. Whether these changes in the lysozyme conformation in the gels can lead to the loss of its biological activity could not be experimentally examined in this project due to the physical form of the gels being not suitable for the activity assay testing. The appropriate setup of activity test for the protein loaded into the gels should be further explored in the future work. Overall, the main effect on

the physicochemical properties of the gels still remains as the water content and the incorporation of lysozyme showed little impact. Similar to the unloaded gels, for the lysozyme-loaded gels, the method of preparation show no significant impact on the properties of the gels. This finding is particularly important for the development of formulations for the delivery of labile macromolecules, such as proteins or peptides. In our work, a relatively stable model protein was used which retained its secondary structure when incorporated in the gels prepared by both hydration and heating methods. However, many proteins/peptide may be thermosensitive. Gelucire 50/13-based gels prepared by hydration showed similar properties to the ones of the gels prepared by heating methods giving the opportunity to successfully incorporate thermolabile macromolecules using these gel formulations. The release of the model protein from the gels can be controlled by altering the water content in the gel formulation. This effect is particularly clear for the gels prepared using heating method. Both sustained (over 10 hour) and immediately release can be achieved by changing the water content in the gel. The changes of release rate with the water content in the gel were also seen in rate of diffusion of lysozyme measured using Franz diffusion cells. It follows the same trend as the dissolution results, the higher the water contents in the gels, the faster the rate of release/diffusion.

The flow tests of the unloaded and lysozyme-loaded Gelucire 50/13 gels indicated the shear thinning behaviour of the gels. The materials with shear-thinning behaviour commonly exhibit good spreadability. This suggests the potential of these gels to be used as topical drug delivery systems. Although, this possible application of Gelucire 50/13-based gels was not fully assessed in this project, some preliminary data was collected which can act as proof-of-concept data for future development of this topical formulation approach. In order to determine the feasibility of using Gelucire 50/13 gels for topical administration, transepidermal water loss (TEWL) test was performed on two gels with 50% and 70% water content prepared by heating. The result of the gel with 70% water content is encouraging and worthwhile in proceeding with further study (Figure 7.1). The transient flux peaks do not refer to the TEWL but are signal from near-surface water. The steady flux is the region of interest and it is where TEWL reaches steady state and is a constant value for the water evaporation across the skin.

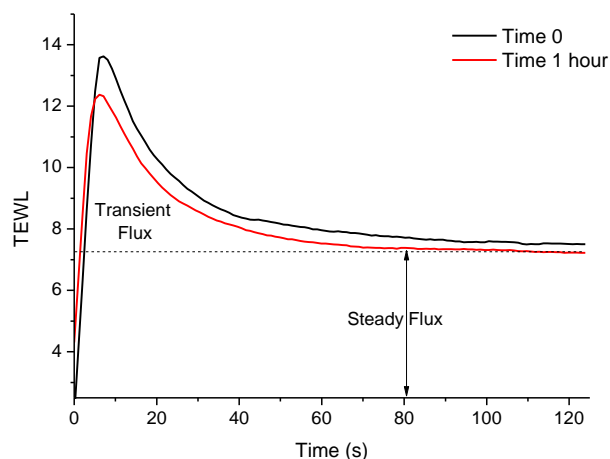


**Figure 7.1** TEWL results for gel with 70% water content prepared by heating at time 0 and after 1 hour of application of the gel on the inner forearm of the volunteer.

Progressing from the Gelucire 50/13-based gel form systems, the formation of disc-shaped nanoparticles from the bulk Gelucire 50/13 gels were demonstrated using high-pressure homogenisation which is an easy to scale up and organic-solvent free method. Unlike most classes of nanoparticles, these Gelucire 50/13 gel nanoparticles require no addition of stabiliser was not required. This is likely to be attributed to the PEG present in the Gelucire 50/13 which coated on the surface of the nanoparticles providing the steric effect for the nanoparticles. The nanoparticles showed good stability up to 4 months when stored at 4 °C. However, due to the time restriction of the project, the stability of the nanoparticles was not assessed after 4 months. Therefore, an evaluation of the full length long-term stability and accelerated stability tests is recommended as a part of the future plan to continue the project. A relatively good encapsulation efficiency of lysozyme (compatible with many other nanoparticulate delivery systems [4, 72]) was achieved especially in F1 and F2 formulations prepared from gels with lower water content (30% and 40%, respectively). After incorporation in F2 formulation, lysozyme retained its tertiary structure and its biological activity, indicating the ability of F2 to protect the lysozyme from degradation. Considering, the good encapsulation efficiency and the retained biological activity of the lysozyme in the formulation F2, further biological studies were performed to assess the uptake efficiency of F2 nanoparticles by model cell lines. Ideally if the nanoparticles can resist the release of protein before uptake by the targeting cells, targeted delivery of the protein drug can be achieved. *In vitro* cytotoxicity of F2 nanoparticles was assessed on H292 and Caco-2 cells line proving the high level of tolerance of such nanoparticles by the model cells (up to 300 µg/ml for H292 and 600 µg/ml for Caco-2). Furthermore, F2 showed a rapid and stable uptake (up to 24 hours) by Caco-2 cells. More experiments need to be conducted in order to accurately localise the nanoparticles within the cell compartments after uptake. Future work

will be required to investigate the uptake mechanism of the Gelucire 50/13-gels nanoparticles.

Although the proof-of-concept study on the use of Gelucire 50/13-gels nanoparticles for protein delivery has been conducted in this project, more *in vitro* and *in vivo* investigations are required in order to develop the full range of applications of these nanoparticles. A preliminary study on developing the possible use of such nanoparticles for inhalation was conducted. Low-density highly porous microparticles can be achieved via spray-freeze-drying the aqueous dispersion of the Gelucire 50/13 gel-based nanoparticles with lactose. Figure 7.2 shows the SEM image of the microparticles obtained after the process.

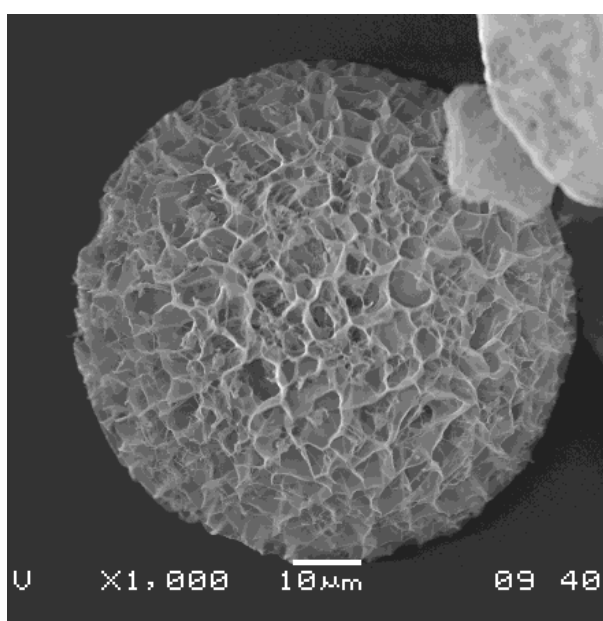


**Figure 7.2** SEM image of spray-freeze dried nanoparticles.

Moreover, the stability studies of the nanoparticles at different physiological pH conditions (such as different regions of the GI tract) have also been assessed. The size changes of the nanoparticles incubated in the media were measured over time using DLS. The results suggest a good stability of the nanoparticles in both gastric and intestinal pH environments (data not shown). Further studies should also involve the assessment of the drug release from the nanoparticles and the evaluation of the possible interaction and penetration of the nanoparticles through mucus layer. It has been reported that some PEG coated nanoparticles with particular size range can penetrate mucus instead of being entrapped by mucus [268]. An attempt to evaluate the potential interaction of the nanoparticles with mucus layer (being muco-penetrating or muco-adhesive) has been performed using Franz diffusion cells. The fluorescent nanoparticles (containing Coumarin 6 as loaded dye) were loaded on the top of scraped intestinal mucus layer stratified on a cellulose membrane and sampling from the

receptor chamber was taken at fixed times. However, the interaction of the nanoparticles with the filter membrane negatively affected the result of the experiment. Therefore, further investigations on the appropriate model membrane suitable for such diffusion experiments should be carried out. Finally, it would be worthwhile studying the effects of molecular dimensions and size of the loaded protein/peptides on the performance of the gel nanoparticles.

In conclusion, the hydrated forms of Gelucire 50/13 are characterised by a complex interior microstructure associated with the formation of various semi-crystalline/liquid crystalline phases depending on the water content and the thermal history of the gels. The complexity of the structures reflects the multi-component nature of the Gelucire 50/13. A model protein, lysozyme, was successfully incorporated and released from the gels proving the potential of these systems to be used for oral protein/peptide delivery. Finally, the stable disc-like nanoparticles made from the Gelucire 50/13-based gels were successfully formed and characterised. The lysozyme encapsulation efficiency was relatively high and compatible with other classes of reported nanoparticles. Lysozyme incorporated in the gel nanoparticles was able to retain its native conformation and biological activity. These findings combined with encouraging *in vitro* cellular uptake results indicate the good potential of such nanoparticles as a new class of safe, low-cost and effective carriers for protein/peptide delivery.

## 8 Appendix

### 8.1 Appendix I: ATR-FTIR

**Table 8.1** Comparison of peaks between Gelucire 50/13 and hydrated forms of Gelucire prepared by heating methods with ultrapure water at room temperature

<i>Gelucire 50/13</i>	<i>PEG</i>	<i>Gel 10%</i>	<i>Gel 20%</i>	<i>Gel 30%</i>	<i>Gel 40%</i>	<i>Gel 50%</i>	<i>Gel 60%</i>	<i>Gel 70%</i>	<i>Gel 80%</i>	<i>Gel 90%</i>	<i>H<sub>2</sub>O</i>
		3448	3421	3407	3389	3384	3372	3362	3351	3340	3323
2916		2916	2915	2916	2917	2918	2919	2919	2919	2920	
2885	2890	2886									
2850		2850	2850	2850	2850	2851	2851	2851	2851	2851	
	2735										
	2695										
				2324							
					2164	2164	2164	2164	2164	2164	2165
				2051	2051	2051	2051	2051	2051	2051	2051
					1981						
1736		1736	1736	1736	1736	1736					
		1647	1644	1645	1643	1642	1641	1640	1639	1638	1636
1466	1466	1467	1468	1468	1467	1467	1467	1468	1468		
	1453										
1359	1359										
1343	1342	1344	1349	1349	1349	1349	1349	1350	1350	1350	
1280	1283	1280	1290	1290	1290	1289	1291				
1241	1240	1242	1251	1253	1252	1253	1253	1253			
1197		1197									
1179		1181									
1147		1146									
1105		1108	1091	1091	1089	1087	1088	1089	1093	1095	
1061	1061										
962	957	963	948	949	949	949	949	949	949		
842	842	843	842	841	841	840					
721		720	720	720	721						
			649		646	644	647				
		630		631				632			
					618					613	
						604			605		605
					580						578
				556		560			565		

**Table 8.2** Comparison of peaks between Gelucire 50/13 and hydrated forms of Gelucire prepared by heating methods with ultrapure water at 37 °C

$H_2O$	Gelucire 50/13	PEG	Gel 10%	Gel 20%	Gel 30%	Gel 40%	Gel 50%	Gel 60%	Gel 70%	Gel 80%	Gel 90%
3342			3491	3421	3410	3395	3386	3379	3381	3363	3352
	2916		2915	2915	2917	2917	2919	2920	2920	2921	2922
	2885	2890									
	2850		2850	2850	2850	2850	2851	2851	2852	2852	
		2735									
		2695									
						2324	2324		2324		
2164								2164		2164	2165
2051					2051	2051	2051	2051	2051	2051	2051
						1981		1981		1981	
	1736		1736	1736	1737	1736	1736				
1637			1642	1644	1643	1647	1642	1640	1640	1639	1637
	1466	1466	1467	1468	1468	1467	1467	1467	1467	1467	
		1453									
	1359	1359									
	1343	1342	1345	1349	1350	1350	1350	1350	1350	1350	
	1280	1283	1282	1290			1292	1291			
	1241	1240	1244	1251	1253	1253	1253	1253	1253		
	1197										
	1179										
	1147										
	1105		1103	1091	1100	1097	1092	1088	1090	1092	1093
	1061	1061									
	962	957	948	948	949	949	949	948	949	948	
	842	842	843	842				839			
	721		719	720							
				649							
					630	631	631	635	631		
										623	
614								605		608	608
											573
					558	559	561		562	565	557

**Table 8.3** Comparison of peaks between Gelucire 50/13 and hydrated form of Gelucire prepared by heating method with D<sub>2</sub>O analysed at room temperature.

<i>Gelucire 50/13</i>	<i>PEG</i>	<i>Gel 10%</i>	<i>Gel 20%</i>	<i>Gel 30%</i>	<i>Gel 40%</i>	<i>Gel 50%</i>	<i>Gel 60%</i>	<i>Gel 70%</i>	<i>Gel 80%</i>	<i>Gel 90%</i>	<i>D<sub>2</sub>O</i>	
								3743				
2916		3462	3444	3442	3427	3430	3397	3392				
2885	2890	2915	2915	2915	2916	2918	2918	2919	2919	2919		
2850		2886										
		2849	2850	2849	2850	2850	2850	2851	2851			
	2735											
	2695											
		2524	2513	2506	2500	2494	2493	2485	2478	2486	2468	
					2051							
				1980	1980	1980			1980			
1736		1735	1737	1737	1736	1736	1737	1737	1737			
											1561	
1466	1466	1466	1467	1467	1467	1467	1467	1467	1468			
	1453											
1359	1359											
1343	1342	1344	1346	1349	1349	1349	1349	1349	1349			
1280	1283	1280	1287	1288	1288	1288						
1241	1240	1242	1244	1245								
		1219										
							1206	1206	1205	1205	1206	1205
1197		1198	1199	1199	1200							
1179		1181		1180								
1147		1146										
1105		1107	1108	1089	1086	1086	1093	1093	1091			
1061	1061											
								1031				
962	957	964	950	949	949	949	949	949	949			
842	842	843	844	842	842	841	843	841	842			
												742
721		720	721	721	721			720	724			
			683	670		700	703					
		659										
		623	631	626		627	631	630		631	623	
					563	569	571		603			
						557			566			
								553	555	554		

**Table 8.4** Comparison of peaks between Gelucire 50/13 and hydrated form of Gelucire prepared by hydration method with D<sub>2</sub>O analysed at room temperature.

<i>D<sub>2</sub>O</i>	<i>H<sub>2</sub>O</i>	<i>Gelucire 50/13</i>	<i>PEO</i>	<i>Gel 10%</i>	<i>Gel 20%</i>	<i>Gel 30%</i>	<i>Gel 40%</i>	<i>Gel 50%</i>	<i>Gel 60%</i>	<i>Gel 70%</i>	<i>Gel 80%</i>	<i>Gel 90%</i>
	3342			3454	3437	3435	3427	3419	3428	3416		
		2916		2915	2915	2915	2915	2915	2916	2915	2916	2915
		2885	2890									
		2850		2849	2850	2850	2850	2850	2850	2850		2849
			2735									
			2695									
				2510	2503	2496	2495	2491	2486	2481		2472
	2164											
	2051				2051	2051	2051					
2468												2476
							1980	1980	1980			
		1736		1736	1736	1736	1736	1736	1736	1736	1736	
	1637											
1561												
		1466	1466	1467	1467	1467	1467	1471	1471	1472	1471	1472
			1453									
		1359	1359									
		1343	1342	1344	1348	1348	1349	1349	1349	1349	1349	
		1280	1283	1281	1287	1286	1288					
		1241	1240	1242	1243							
1205		1197		1199	1200	1201	1202	1202	1203	1203	1204	1204
		1179		1181								
		1147										
		1105		1095	1091	1088	1087	1086	1086	1087	1089	1097
		1061	1061									
		962	957	949	949	948	949	949	949	949	949	949
		842	842	842	842	842	842	841	840	841	840	
742											737	741
		721		720	721		720	718	717	716		
						687	683					
				675	671							
											658	659
623				624	628	624	627					
	614											
								605				
							591	585	594			
					574			575	571		573	571
									561	564	563	560
					558		558	557	554			

**Table 8.5** Comparison between peaks of untreated Gelucire 50/13 and hydrated forms of Gelucire prepared by hydration with D<sub>2</sub>O alone and loaded with lysozyme. The tests were performed at room temperature.

<i>Gelucire</i> 50/13	<i>LYS</i>	<i>LYS-</i> <i>D<sub>2</sub>O</i>	<i>Gel</i> 20%	<i>Gel</i> 20% + <i>LYS</i>	<i>Gel</i> 40%	<i>Gel</i> 40% + <i>LYS</i>	<i>Gel</i> 60%	<i>Gel</i> 60% + <i>LYS</i>	<i>Gel</i> 70%	<i>Gel</i> 70% + <i>LYS</i>
			3437		3427		3428	3400	3416	3402
		3313								
	3285			3297		3297				
	2960									
2916			2915	2915	2915	2918	2916	2915	2915	2915
2885										
2850			2850	2850	2850		2850	2850	2850	2850
			2503	2484	2495		2486	2486	2481	2480
		2470								
	2325									
	2051		2051		2051					
				1980	1980		1980			
1736			1736	1736	1736		1736	1736	1736	1736
		1650								
	1641			1637		1636		1648		1649
				1581		1581				
		1542		1540		1540		1541		1541
	1514									
1466			1467		1467		1471		1472	
	1454	1456		1453		1444		1456		1456
	1389									
1359										
1343			1348	1347	1349	1348	1349	1349	1349	1349
				1306		1308				
1280			1287		1288					
	1233									
1241			1243							
		1204	1200	1201	1202	1203	1203	1202	1203	1203
1197										
1179										
1147										
1105	1102		1091	1091	1087	1088	1086	1087	1087	1088
1061										
962			949	948	949	949	949	949	949	949
842			842	841	842	837	840	840	841	838
	741			737		736				
721			721		720		717		716	
					683					
			671							
		659								
			628		627					
		604								
		595			591		594			
	582	589								
			574							
							571			
	568						561		564	
	557		558		558		554	557		

## 8.2 Appendix II: SAXS

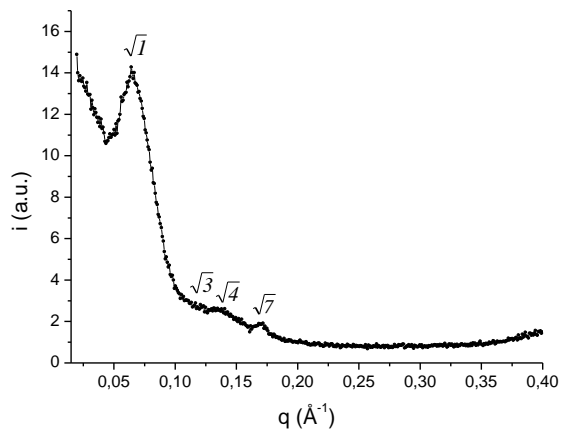


**Figure 8.1** SAXS spectrum of the intensity versus  $q$  ( $\text{\AA}^{-1}$ ) of the lysozyme-loaded gel with 50% water prepared by hydration and corresponding peaks position (25 °C).

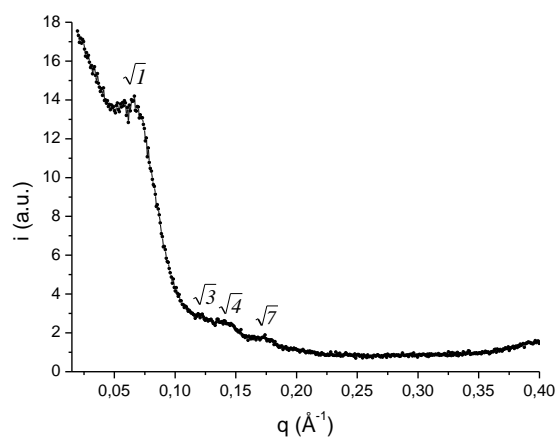


**Figure 8.2** SAXS spectrum of the intensity versus  $q$  ( $\text{\AA}^{-1}$ ) of the lysozyme-loaded gel with 50% water prepared by hydration and corresponding peaks position (30 °C).

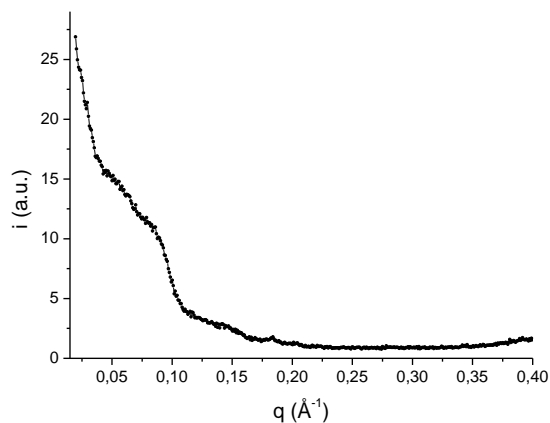


**Figure 8.3** SAXS spectrum of the intensity versus  $q$  ( $\text{\AA}^{-1}$ ) of the lysozyme-loaded gel with 50% water prepared by hydration and corresponding peaks position (35 °C).

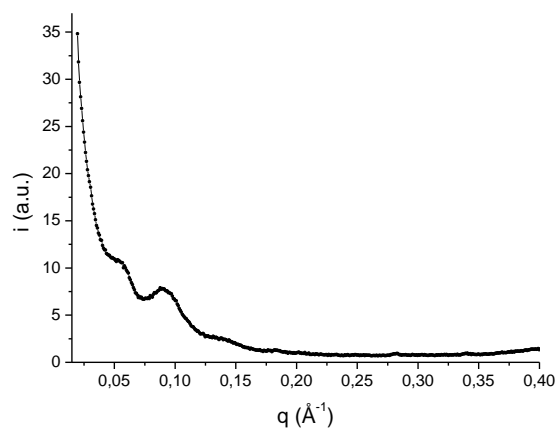


**Figure 8.4** SAXS spectrum of the intensity versus  $q$  ( $\text{\AA}^{-1}$ ) of the lysozyme-loaded gel with 50% water prepared by hydration and corresponding peaks position (37 °C).

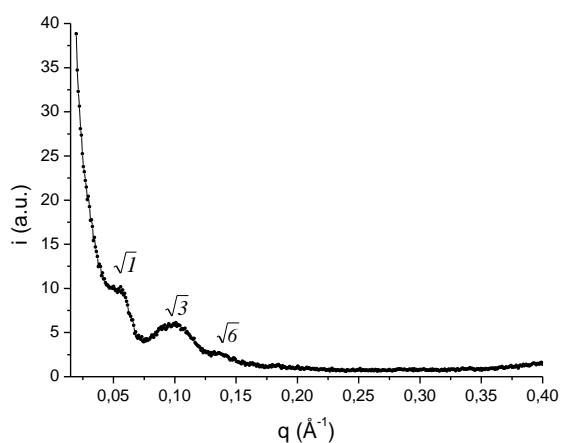


**Figure 8.5** SAXS spectrum of the intensity versus  $q$  ( $\text{\AA}^{-1}$ ) of the lysozyme-loaded gel with 50% water prepared by hydration and corresponding peaks position (35 °C during the cooling cycle).

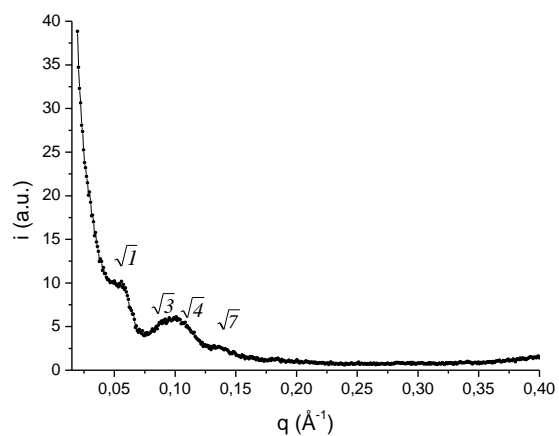


**Figure 8.6** SAXS spectrum of the intensity versus  $q$  ( $\text{\AA}^{-1}$ ) of the lysozyme-loaded gel with 50% water prepared by hydration and corresponding peaks position (30 °C during the cooling cycle).

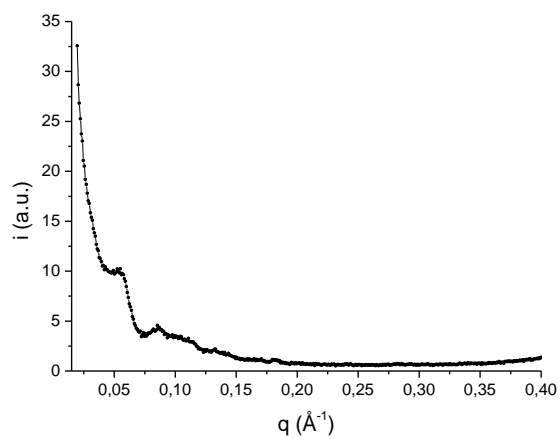


**Figure 8.7** SAXS spectrum of the intensity versus  $q$  ( $\text{\AA}^{-1}$ ) of the lysozyme-loaded gel with 50% water prepared by hydration and corresponding peaks position (25 °C during the cooling cycle).

## 9 References

- [1] Frokjaer, S., Otzen, D.E., Protein drug stability: a formulation challenge, *Nat Rev Drug Discov* 4(2005) 298-306.
- [2] Morishita, M., Peppas, N.A., Is the oral route possible for peptide and protein drug delivery?, *Drug Discov. Today* 11(2006) 905-910.
- [3] Hussain, A., Arnold, J.J., Khan, M.A., Ahsan, F., Absorption enhancers in pulmonary protein delivery, *J. Control. Release* 94(2004) 15-24.
- [4] Almeida, A.n.J., Souto, E., Solid lipid nanoparticles as a drug delivery system for peptides and proteins, *Adv. Drug Del. Rev.* 59(2007) 478-490.
- [5] Uchenna Agu, R., Ikechukwu Ugwoke, M., Armand, M., Kinget, R., Verbeke, N., The lung as a route for systemic delivery of therapeutic proteins and peptides, *Respir. Res.* 2(2001) 198 - 209.
- [6] Park, K., Kwon, I.C., Park, K., Oral protein delivery: Current status and future prospect, *React. Funct. Polym.* 71(2011) 280-287.
- [7] Fasano, A., Novel approaches for oral delivery of macromolecules, *J. Pharm. Sci.* 87(1998) 1351-1356.
- [8] Brayden, D.J., Jepson, M.A., Baird, A.W., Keynote review: Intestinal Peyer's patch M cells and oral vaccine targeting, *Drug Discov. Today* 10(2005) 1145-1157.
- [9] Fasano, A., Innovative strategies for the oral delivery of drugs and peptides, *Trends Biotechnol.* 16(1998) 152-157.
- [10] Pisal, D.S., Kosloski, M.P., Balu-Iyer, S.V., Delivery of Therapeutic Proteins, *J. Pharm. Sci.* 99(2010) 2557-2575.
- [11] Brange, J., Owens, D.R., Kang, S., VÃlund, A., Monomeric Insulins and Their Experimental and Clinical Implications, *Diabetes Care* 13(1990) 923-954.
- [12] Rouquayrol, M., Gaucher, B.r.r., Roche, D., Greiner, J., Vierling, P., Transepithelial Transport of Prodrugs of the HIV Protease Inhibitors Saquinavir, Indinavir, and Nelfinavir Across Caco-2 Cell Monolayers, *Pharm. Res.* 19(2002) 1704-1712.
- [13] Nielsen, C.U., Andersen, R., Brodin, B., Frokjaer, S., Taub, M.E., Steffansen, B., Dipeptide model prodrugs for the intestinal oligopeptide transporter. Affinity for and transport via hPepT1 in the human intestinal Caco-2 cell line, *J. Control. Release* 76(2001) 129-138.
- [14] Pauletti, G.M., Gangwar, S., Siahaan, T.J., Jeffrey, A., T. Borchardt, R., Improvement of oral peptide bioavailability: Peptidomimetics and prodrug strategies, *Adv. Drug Del. Rev.* 27(1997) 235-256.
- [15] Kramer, W., Corsiero, D., Friedrich, M., Girbig, F., Stengelin, S., Weyland, C., Intestinal absorption of bile acids: paradoxical behaviour of the 14 kDa ileal lipid-binding protein in differential photoaffinity labelling, *Biochem J* 333(1998) 335-341.

- 
- [16] Swaan, P.W., Hillgren, K.M., Szoka, F.C., Øie, S., Enhanced Transepithelial Transport of Peptides by Conjugation to Cholic Acid, *Bioconj. Chem.* 8(1997) 520-525.
- [17] Russell-Jones, G.J., Westwood, S.W., Habberfield, A.D., Vitamin B12 Mediated Oral Delivery Systems for Granulocyte-Colony Stimulating Factor and Erythropoietin, *Bioconj. Chem.* 6(1995) 459-465.
- [18] Habberfield, A., Jensen-Pippo, K., Ralph, L., Westwood, S.W., Russell-Jones, G.J., Vitamin B12-mediated uptake of erythropoietin and granulocyte colony stimulating factor in vitro and in vivo, *Int. J. Pharm.* 145(1996) 1-8.
- [19] Kurtzhals, P., Havelund, S., Jonassen, I., Kiehr, B., Larsen, U.D., Ribel, U., Markussen, J., Albumin binding of insulins acylated with fatty acids: characterization of the ligand-protein interaction and correlation between binding affinity and timing of the insulin effect in vivo, *Biochem J* 312 (1995) 725-731.
- [20] Lee, Y.H., Sinko, P.J., Oral delivery of salmon calcitonin, *Adv. Drug Del. Rev.* 42(2000) 225-238.
- [21] Ekrami, H.M., Kennedy, A.R., Shen, W.-C., Water-soluble fatty acid derivatives as acylating agents for reversible lipidization of polypeptides, *FEBS Lett.* 371(1995) 283-286.
- [22] Wang, J., Chow, D., Heiati, H., Shen, W.-C., Reversible lipidization for the oral delivery of salmon calcitonin, *J. Control. Release* 88(2003) 369-380.
- [23] Veronese, F.M., Pasut, G., PEGylation, successful approach to drug delivery, *Drug Discov. Today* 10(2005) 1451-1458.
- [24] Liu, D.-Z., Lecluyse, E.L., Thakker, D.R., Dodecylphosphocholine-mediated enhancement of paracellular permeability and cytotoxicity in Caco-2 cell monolayers, *J. Pharm. Sci.* 88(1999) 1161-1168.
- [25] Obata, Y., Sesumi, T., Takayama, K., Isowa, K., Grosh, S., Wick, S., Sitz, R., Nagai, T., Evaluation of skin damage caused by percutaneous absorption enhancers using fractal analysis, *J. Pharm. Sci.* 89(2000) 556-561.
- [26] Sakai, M., Imai, T., Ohtake, H., Otagiri, M., Biopharmaceutics: Cytotoxicity of Absorption Enhancers in Caco-2 Cell Monolayers, *J. Pharm. Pharmacol.* 50(1998) 1101-1108.
- [27] Yen, W.-C., Lee, V.H.L., Penetration enhancement effect of Pz-peptide, a paracellularly transported peptide, in rabbit intestinal segments and Caco-2 cell monolayers, *J. Control. Release* 36(1995) 25-37.
- [28] Goldberg, M., Gomez-Orellana, I., Challenges for the oral delivery of macromolecules, *Nat Rev Drug Discov* 2(2003) 289-295.
- [29] Philip, A.K., Philip, B., Colon targeted drug delivery systems: a review on primary and novel approaches, *Oman Med. J.* 25(2010) 79-87.
- [30] Agarwal, V., Nazzal, S., Reddy, I.K., Khan, M.A., Transport studies of insulin across rat jejunum in the presence of chicken and duck ovomucoids, *J. Pharm. Pharmacol.* 53(2001) 1131-1138.
- [31] Qiu, Y., Park, K., Environment-sensitive hydrogels for drug delivery, *Adv. Drug Del. Rev.* 53(2001) 321-339.

- 
- [32] Prego, C., Garcia, M., Torres, D., Alonso, M.J., Transmucosal macromolecular drug delivery, *J. Control. Release* 101(2005) 151-162.
- [33] Calceti, P., Salmaso, S., Walker, G., Bernkop-Schnürch, A., Development and in vivo evaluation of an oral insulin-PEG delivery system, *Eur. J. Pharm. Sci.* 22(2004) 315-323.
- [34] Marschütz, M., Caliceti, P., Bernkop-Schnürch, A., Design and In Vivo Evaluation of An Oral Delivery System for Insulin, *Pharm. Res.* 17(2000) 1468-1474.
- [35] Sakuma, S., Sudo, R., Suzuki, N., Kikuchi, H., Akashi, M., Hayashi, M., Mucoadhesion of polystyrene nanoparticles having surface hydrophilic polymeric chains in the gastrointestinal tract, *Int. J. Pharm.* 177(1999) 161-172.
- [36] Bernkop-Schnürch, A., The use of inhibitory agents to overcome the enzymatic barrier to perorally administered therapeutic peptides and proteins, *J. Control. Release* 52(1998) 1-16.
- [37] Mathiowitz, E., Chickering, D.E., Lehr, C.M., *Bioadhesive Drug Delivery Systems: Fundamentals, Novel Approaches, and Development*, Marcel Dekker, New York, 1999.
- [38] Ahuja, A., Khar, R.K., Ali, J., *Mucoadhesive Drug Delivery Systems*, *Drug Dev Ind Pharm* 23(1997) 489-515.
- [39] Tamburic, S., Craig, D.Q.M., A comparison of different in vitro methods for measuring mucoadhesive performance, *Eur J Pharm Biopharm* 44(1997) 159-167.
- [40] Smart, J.D., The basics and underlying mechanisms of mucoadhesion, *Adv. Drug Del. Rev.* 57(2005) 1556-1568.
- [41] Khanvilkar, K., Donovan, M.D., Flanagan, D.R., Drug transfer through mucus, *Adv. Drug Deliv. Rev.* 48(2001) 173-193.
- [42] Bansil, R., Turner, B.S., Mucin structure, aggregation, physiological functions and biomedical applications, *Current Opinion in Colloid & Interface Science* 11(2006) 164-170.
- [43] Norris, D.A., Sinko, P.J., Effect of size, surface charge, and hydrophobicity on the translocation of polystyrene microspheres through gastrointestinal mucin, *J. Appl. Polym. Sci.* 63(1997) 1481-1492.
- [44] Mathiowitz, E., Chickering, D.E.I., Lehr, C.M., *Bioadhesive Drug Delivery Systems: fundamental, novel approaches and development*, Marcel Dekker, New York, 1999.
- [45] Khutoryanskiy, V.V., *Advances in Mucoadhesion and Mucoadhesive Polymers*, *Macromolecular Bioscience* 11(2011) 748-764.
- [46] Duchêne, D., Touchard, F., Peppas, N.A., *Pharmaceutical and Medical Aspects of Bioadhesive Systems for Drug Administration*, *Drug Dev Ind Pharm* 14(1988) 283-318.
- [47] des Rieux, A., Fievez, V., Garinot, M., Schneider, Y.J., Preat, V., Nanoparticles as potential oral delivery systems of proteins and vaccines: A mechanistic approach, *J. Control. Release* 116(2006) 1-27.
- [48] Soppimath, K.S., Aminabhavi, T.M., Kulkarni, A.R., Rudzinski, W.E., Biodegradable polymeric nanoparticles as drug delivery devices, *J. Control. Release* 70(2001) 1-20.
- [49] Kost, J., Langer, R., Responsive polymeric delivery systems, *Adv. Drug Del. Rev.* 64(2012) 327-341.

- 
- [50] Mathot, F., van Beijsterveldt, L., Preat, V., Brewster, M., Arien, A., Intestinal uptake and biodistribution of novel polymeric micelles after oral administration, *J. Control. Release* 111(2006) 47-55.
- [51] Panyam, J., Labhasetwar, V., Biodegradable nanoparticles for drug and gene delivery to cells and tissue, *Adv. Drug Del. Rev.* 55(2003) 329-347.
- [52] Danhier, F., Ansorena, E., Silva, J.M., Coco, R., Le Breton, A., Pr eat, V., PLGA-based nanoparticles: An overview of biomedical applications, *J. Control. Release* 161(2012) 505-522.
- [53] Makadia, H.K., Siegel, S.J., Poly Lactic-co-Glycolic Acid (PLGA) as Biodegradable Controlled Drug Delivery Carrier, *Polymers* 3(2011) 1377-1397.
- [54] Giteau, A., Venier-Julienne, M.C., Marchal, S., Courthaudon, J.L., Sergent, M., Montero-Menei, C., Verdier, J.M., Benoit, J.P., Reversible protein precipitation to ensure stability during encapsulation within PLGA microspheres, *Eur. J. Pharm. Biopharm.* 70(2008) 127-136.
- [55] Desai, M.P., Labhasetwar, V., Walter, E., Levy, R.J., Amidon, G.L., The mechanism of uptake of biodegradable microparticles in Caco-2 cells is size dependent, *Pharm. Res.* 14(1997) 1568-1573.
- [56] Choi, S.H., Park, T.G., G-CSF loaded biodegradable PLGA nanoparticles prepared by a single oil-in-water emulsion method, *Int. J. Pharm.* 311(2006) 223-228.
- [57] Johnson, O.L., Cleland, J.L., Lee, H.J., Charnis, M., Duenas, E., Jaworowicz, W., Shepard, D., Shahzamani, A., Jones, A.J.S., Putney, S.D., A month-long effect from a single injection of microencapsulated human growth hormone, *Nat. Med.* 2(1996) 795-799.
- [58] Martins, S., Sarmiento, B., Ferreira, D.C., Souto, E.B., Lipid-based colloidal carriers for peptide and protein delivery--liposomes versus lipid nanoparticles, *Int J Nanomedicine* 2(2007) 595-607.
- [59] Torchilin, V.P., Recent advances with liposomes as pharmaceutical carriers, *Nat. Rev. Drug. Discov.* 4(2005) 145-160.
- [60] Wright, S., Huang, L., Antibody-Directed Liposomes as Drug-Delivery Vehicles, *Adv. Drug Del. Rev.* 3(1989) 343-390.
- [61] Mastrobattista, E., Koning, G.A., Storm, G., Immunoliposomes for the targeted delivery of antitumor drugs, *Adv. Drug Del. Rev.* 40(1999) 103-127.
- [62] Klibanov, A.L., Maruyama, K., Torchilin, V.P., Huang, L., Amphipathic Polyethyleneglycols Effectively Prolong the Circulation Time of Liposomes, *FEBS Lett.* 268(1990) 235-237.
- [63] Lasic, D.D., Needham, D., The "Stealth" liposome: A prototypical biomaterial, *Chem. Rev.* 95(1995) 2601-2628.
- [64] Woodle, M.C., Controlling liposome blood clearance by surface-grafted polymers, *Adv. Drug Del. Rev.* 32(1998) 139-152.
- [65] Whiteman, K.R., Subr, V., Ulbrich, K., Torchilin, V.P., Poly(HPMA)-coated liposomes demonstrate prolonged circulation in mice, *J. Liposome Res.* 11(2001) 153-164.

- [66] Torchilin, V.P., Levchenko, T.S., Whiteman, K.R., Yaroslavov, A.A., Tsatsakis, A.M., Rizos, A.K., Michailova, E.V., Shtilman, M.I., Amphiphilic poly-N-vinylpyrrolidones:: synthesis, properties and liposome surface modification, *Biomaterials* 22(2001) 3035-3044.
- [67] Metselaar, J.M., Bruin, P., de Boer, L.W.T., de Vringer, T., Snel, C., Oussoren, C., Wauben, M.H.M., Crommelin, D.J.A., Storm, G., Hennink, W.E., A Novel Family of l-Amino Acid-Based Biodegradable Polymer-Lipid Conjugates for the Development of Long-Circulating Liposomes with Effective Drug-Targeting Capacity, *Bioconj. Chem.* 14(2003) 1156-1164.
- [68] Takeuchi, H., Kojima, H., Yamamoto, H., Kawashima, Y., Evaluation of circulation profiles of liposomes coated with hydrophilic polymers having different molecular weights in rats, *J. Control. Release* 75(2001) 83-91.
- [69] Müller, R.H., Mäder, K., Gohla, S., Solid lipid nanoparticles (SLN) for controlled drug delivery - a review of the state of the art, *Eur. J. Pharm. Biopharm.* 50(2000) 161-177.
- [70] Mehnert, W., Mäder, K., Solid lipid nanoparticles: Production, characterization and applications, *Advanced Drug Delivery Reviews* 47(2001) 165-196.
- [71] Gasco, M.R., Method for producing solid lipid microspheres having a narrow size distribution US5250236 A, 1995.
- [72] Almeida, A.J., Runge, S., Müller, R.H., Peptide-loaded solid lipid nanoparticles (SLN): Influence of production parameters, *Int. J. Pharm.* 149(1997) 255-265.
- [73] Müller, R.H., Runge, S., Ravelli, V., Mehnert, W., Thünemann, A.F., Souto, E.B., Oral bioavailability of cyclosporine: Solid lipid nanoparticles (SLN®) versus drug nanocrystals, *Int. J. Pharm.* 317(2006) 82-89.
- [74] Qi, J.P., Lu, Y., Wu, W., Absorption, Disposition and Pharmacokinetics of Solid Lipid Nanoparticles, *Curr. Drug Metab.* 13(2012) 418-428.
- [75] Sek, L., Porter, C.J.H., Kaukonen, A.M., Charman, W.N., Evaluation of the in-vitro digestion profiles of long and medium chain glycerides and the phase behaviour of their lipolytic products, *J. Pharm. Pharmacol.* 54(2002) 29-41.
- [76] Müller, R.H., Keck, C.M., Challenges and solutions for the delivery of biotech drugs - a review of drug nanocrystal technology and lipid nanoparticles, *J. Biotechnol.* 113(2004) 151-170.
- [77] Yoon, G., Park, J.W., Yoon, I.-S., Solid lipid nanoparticles (SLNs) and nanostructured lipid carriers (NLCs): recent advances in drug delivery, *J. Pharm. Invest.* 43(2013) 353-362.
- [78] Shah, J., Sadhale, Y., Chilukuri, D.M., Cubic phase gels as drug delivery systems, *Adv Drug Deliver Rev* 47(2001) 229-250.
- [79] Seddon, J.M., Templer, R.H., Polymorphism of lipid-water systems, *Handbook of Biological Physics, Vol. 1; Structure and dynamics of membranes: From cells to vesicles*, 1995, pp. 97-160.
- [80] Sagalowicz, L., Leser, M.E., Watzke, H.J., Michel, M., Monoglyceride self-assembly structures as delivery vehicles, *Trends Food Sci. Technol.* 17(2006) 204-214.
- [81] Shah, M.H., Paradkar, A., Cubic liquid crystalline glyceryl monooleate matrices for oral delivery of enzyme, *Int J Pharm* 294(2005) 161-171.

- 
- [82] Clogston, J., Caffrey, M., Controlling release from the lipidic cubic phase. *Amino acids, peptides, proteins and nucleic acids, J. Control. Release* 107(2005) 97-111.
- [83] Tanaka, S., Maki, S., Ataka, M., Structural transitions of the mono-olein bicontinuous cubic phase induced by inclusion of protein lysozyme solutions, *Phys. Rev. E* 73(2006).
- [84] Razumas, V., Talaikyte, Z., Barauskasa, J., Larsson, K., Mieziš, Y., Nylander, T., Effects of distearoylphosphatidylglycerol and lysozyme on the structure of the monoolein-water cubic phase: X-ray diffraction and Raman scattering studies, *Chem. Phys. Lipids* 84(1996) 123-138.
- [85] Lynch, M.L., Spicer, P.T., *Bicontinuous liquid crystals*, CRC press, 2005.
- [86] Leslie, S.B., Puvvada, S., Ratna, B.R., Rudolph, A.S., Encapsulation of hemoglobin in a bicontinuous cubic phase lipid, *Biochim. Biophys. Acta* 1285(1996) 246-254.
- [87] Giorgione, J.R., Huang, Z., Eppard, R.M., Increased Activation of Protein Kinase C with Cubic Phase Lipid Compared with Liposomes *Biochemistry* 37(1998) 2384-2392.
- [88] Heberle, J., Büldt, G., Koglin, E., Rosenbusch, J.P., Landau, E.M., Assessing the functionality of a membrane protein in a three-dimensional crystal, *J. Mol. Biol.* 281(1998) 587-592.
- [89] Nollert, P., Royant, A., Pebay-Peyroula, E., Landau, E.M., Detergent-free membrane protein crystallization, *FEBS Lett.* 457(1999) 205-208.
- [90] Sadhale, Y., Shah, J.C., Stabilization of insulin against agitation-induced aggregation by the GMO cubic phase gel, *Int. J. Pharm.* 191(1999) 51-64.
- [91] Sadhale, Y., Shah, J.C., Biological activity of insulin in GMO gels and the effect of agitation, *Int. J. Pharm.* 191(1999) 65-74.
- [92] Nielsen, L.S., Schubert, L., Hansen, J., Bioadhesive drug delivery systems: I. Characterisation of mucoadhesive properties of systems based on glyceryl mono-oleate and glyceryl monolinoleate, *Eur. J. Pharm. Sci.* 6(1998) 231-239.
- [93] Yang, D., Armitage, B., Marder, S.R., Cubic liquid-crystalline nanoparticles, *Angew. Chem. Int. Ed.* 43(2004) 4402-4409.
- [94] Larsson, K., Cubic lipid-water phases: structures and biomembrane aspects, *J Phys Chem* 93(1989) 7304-7314.
- [95] Gustafsson, J., Ljusberg-Wahren, H., Almgren, M., Larsson, K., Cubic Lipid-Water Phase Dispersed into Submicron Particles, *Langmuir* 12(1996) 4611-4613.
- [96] Gustafsson, J., Ljusberg-Wahren, H., Almgren, M., Larsson, K., Submicron particles of reversed lipid phases in water stabilized by a nonionic amphiphilic polymer, *Langmuir* 13(1997) 6964-6971.
- [97] Nakano, M., Teshigawara, T., Sugita, A., Leesajakul, W., Taniguchi, A., Kamo, T., Matsuoka, H., Handa, T., Dispersions of liquid crystalline phases of the monoolein/oleic acid/Pluronic F127 system, *Langmuir* 18(2002) 9283-9288.
- [98] Kim, J.S., Kim, H., Chung, H., Sohn, Y.T., Kwon, I.C., Jeong, S.Y., Drug formulations that form a dispersed cubic phase when mixed with water, *Proc. Int. Symp. Control. Rel. Bioact. Mat.* 27(2000) 1118-1119.

- 
- [99] Engstrom, S., Ericsson, B., Landh, T., A cubosome formulation for intravenous administration of somatostatin, *Proc. Int. Symp. Control. Rel. Bioact. Mat.* 23(1996) 89-90.
- [100] Chung, H., Kim, J., Um, J.Y., Kwon, I.C., Jeong, S.Y., Self-assembled "nanocubicle" as a carrier for peroral insulin delivery, *Diabetologia* 45(2002) 448-451.
- [101] Um, J.Y., Chung, H.S., Kim, K.S., Kwon, I.C., Jeong, S.Y., In vitro cellular interaction and absorption of dispersed cubic particles, *Int. J. Pharm.* 253(2003) 71-80.
- [102] Sutananta, W., Craig, D.Q.M., Newton, J.M., An Evaluation of the Mechanisms of Drug Release from Glyceride Bases, *J. Pharm. Pharmacol.* 47(1995) 182-187.
- [103] Sutananta, W., Craig, D.Q.M., Newton, J.M., An investigation into the effect of preparation conditions on the structure and mechanical properties of pharmaceutical glyceride bases, *Int. J. Pharm.* 110(1994) 75-91.
- [104] Choy, Y.W., Khan, N., Yuen, K.H., Significance of lipid matrix aging on in vitro release and in vivo bioavailability, *Int J Pharm* 299(2005) 55-64.
- [105] Ratsimbazafy, V., Bourret, E., Duclos, R., Brossard, C., Rheological behavior of drug suspensions in Gelucire® mixtures and proxiphylline release from matrix hard gelatin capsules, *Eur. J. Pharm. Biopharm.* 48(1999) 247-252.
- [106] Siepmann, F., Muschert, S., Flament, M.P., Leterme, P., Gayot, A., Siepmann, J., Controlled drug release from Gelucire-based matrix pellets: Experiment and theory, *Int J Pharm* 317(2006) 136-143.
- [107] Qi, S., Marchaud, D., Craig, D.Q.M., An investigation into the mechanism of dissolution rate enhancement of poorly water-soluble drugs from spray chilled Gelucire 50/13 microspheres, *J Pharm Sci* 99(2010) 262-274.
- [108] Gattefossé, Gelucire® 50/13, <http://www.gattefosse.com>.
- [109] Brubach, J.B., Ollivon, M., Jannin, V., Mahler, B., Bourgaux, C., Lesieur, P., Roy, P., Structural and thermal characterization of mono- and diacyl polyoxyethylene glycol by infrared spectroscopy and -ray diffraction coupled to differential calorimetry, *J Phys Chem* 108(2004) 17721-17729.
- [110] Alessi, M.L., Norman, A.I., Knowlton, S.E., Ho, D.L., Greer, S.C., Helical and Coil Conformations of Poly(ethylene glycol) in Isobutyric Acid and Water, *Macromolecules* 38(2005) 9333-9340.
- [111] Gu, F., Bu, H., Zhang, Z., A unique morphology of freeze-dried poly(ethylene oxide) and its transformation, *Polymer* 41(2000) 7605-7609.
- [112] Branca, C., Magazù, S., Maisano, G., Migliardo, P., Romeo, G., Study of Conformational Properties of Poly(ethylene oxide) by SANS and PCS Techniques, *Phys. Scr.* 67(2003) 551-554.
- [113] Jeevanandam, P., Vasudevan, S., Intercalation of Alkali Metal-Polyethylene Oxide Polymer Electrolytes in Layered CdPS3, *Chem. Mater.* 10(1998) 1276-1285.
- [114] Small, D.M., Lateral chain packing in lipids and membranes, *J. Lipid Res.* 25(1984) 1490-1500.
- [115] Larsson, K., Classification of Glyceride Crystal Forms, *Acta Chem. Scand.* 20(1966) 2255-2260.

- 
- [116] Sutananta, W., Craig, D.Q.M., Newton, J.M., The effects of ageing on the thermal behaviour and mechanical properties of pharmaceutical glycerides, *Int J Pharm* 111(1994) 51-62.
- [117] Sutananta, W., Craig, D.Q.M., Newton, J.M., An investigation into the effect of preparation conditions on the structure and mechanical properties of pharmaceutical glyceride bases, *Int J Pharm* 110(1994) 75-91.
- [118] Dennis, A.B., Farr, S.J., Kellaway, I.W., Taylor, G., Davidson, R., In vivo evaluation of rapid release and sustained release Gelucire capsule formulations, *Int. J. Pharm.* 65(1990) 85-100.
- [119] Saito, H., Takatori, T., Higashi, T., Nakamura, Y., Design of Novel Controlled-Release Suppositories Containing Polyglycerol Ester of Fatty Acid, *Chem. Pharm. Bull.* 42(1994) 1506-1509.
- [120] Sutananta, W., Craig, D.Q.M., Newton, J.M., The effects of ageing on the thermal behaviour and mechanical properties of pharmaceutical glycerides, *Int. J. Pharm.* 111(1994) 51-62.
- [121] Khan, N., Craig, D.Q.M., Role of blooming in determining the storage stability of lipid-based dosage forms, *J. Pharm. Sci.* 93(2004) 2962-2971.
- [122] Qi, S., Belton, P., McAuley, W., Codoni, D., Darji, N., Moisture Uptake of Polyoxyethylene Glycol Glycerides Used as Matrices for Drug Delivery: Kinetic Modelling and Practical Implications, *Pharm. Res.* 30(2013) 1123-1136.
- [123] Qi, S., Deutsch, D., Craig, D.Q.M., An investigation into the mechanisms of drug release from taste-masking fatty acid microspheres, *J. Pharm. Sci.* 97(2008) 3842-3854.
- [124] Passerini, N., Perissutti, B., Moneghini, M., Voinovich, D., Albertini, B., Cavallari, C., Rodriguez, L., Characterization of carbamazepine–Gelucire 50/13 microparticles prepared by a spray-congealing process using ultrasounds, *J. Pharm. Sci.* 91(2002) 699-707.
- [125] Cavallari, C., Rodriguez, L., Albertini, B., Passerini, N., Rosetti, F., Fini, A., Thermal and fractal analysis of diclofenac/Gelucire 50/13 microparticles obtained by ultrasound-assisted atomization, *J. Pharm. Sci.* 94(2005) 1124-1134.
- [126] Fini, A., Moyano, J.R., Ginés, J.M., Perez-Martinez, J.I., Rabasco, A.M., Diclofenac salts, II. Solid dispersions in PEG6000 and Gelucire 50/13, *Eur. J. Pharm. Biopharm.* 60(2005) 99-111.
- [127] Passerini, N., Albertini, B., Perissutti, B., Rodriguez, L., Evaluation of melt granulation and ultrasonic spray congealing as techniques to enhance the dissolution of praziquantel, *Int. J. Pharm.* 318(2006) 92-102.
- [128] El-Badry, M., Fetih, G., Fathy, M., Improvement of solubility and dissolution rate of indomethacin by solid dispersions in Gelucire 50/13 and PEG4000, *Saudi Pharm J* 17(2009) 217-225.
- [129] Shimpi, S.L., Chauhan, B., Mahadik, K.R., Paradkar, A., Stabilization and improved in vivo performance of amorphous etoricoxib using Gelucire 50/13, *Pharm. Res.* 22(2005) 1727-1734.
- [130] Fukushima, K., Terasaka, S., Haraya, K., Kodera, S., Seki, Y., Wada, A., Ito, Y., Shibata, N., Sugioka, N., Takada, K., Pharmaceutical Approach to HIV Protease

- Inhibitor Atazanavir for Bioavailability Enhancement Based on Solid Dispersion System, *Biological and Pharmaceutical Bulletin* 30(2007) 733-738.
- [131] Pongjanyakul, T., Medlicott, N.J., Tucker, I.G., Melted glyceryl palmitostearate (GPS) pellets for protein delivery, *Int. J. Pharm.* 271(2004) 53-62.
- [132] Date, A.A., Vador, N., Jagtap, A., Nagarsenker, M.S., Lipid nanocarriers (GeluPearl) containing amphiphilic lipid Gelucire 50/13 as a novel stabilizer: fabrication, characterization and evaluation for oral drug delivery, *Nanotechnology* 22(2011).
- [133] Jollès, P., *Lysozymes: A Chapter of Molecular Biology*, *Angewandte Chemie International Edition in English* 8(1969) 227-239.
- [134] Jollès, P., *Recent Developments in the Study of Lysozymes*, *Angewandte Chemie International Edition in English* 3(1964) 28-36.
- [135] Horn, D.W., Tracy, K., Easley, C.J., Davis, V.A., Lysozyme Dispersed Single-Walled Carbon Nanotubes: Interaction and Activity, *J. Phys. Chem. C* 116(2012) 10341-10348.
- [136] Mishraki, T., Libster, D., Aserin, A., Garti, N., Lysozyme entrapped within reverse hexagonal mesophases: Physical properties and structural behavior, *Colloids Surf. B. Biointerfaces* 75(2010) 47-56.
- [137] Mishraki, T., Libster, D., Aserin, A., Garti, N., Temperature-dependent behavior of lysozyme within the reverse hexagonal mesophases (H-II), *Colloids Surf. B. Biointerfaces* 75(2010) 391-397.
- [138] Hirano, A., Maeda, Y., Akasaka, T., Shiraki, K., Synergistically Enhanced Dispersion of Native Protein-Carbon Nanotube Conjugates by Fluoroalcohols in Aqueous Solution, *Chem. Eur. J.* 15(2009) 9905-9910.
- [139] Horn, D.W., Tracy, K., Easley, C.J., Davis, V.A., Lysozyme Dispersed Single-Walled Carbon Nanotubes: Interaction and Activity, *J. Phys. Chem. C* 116(2012) 10341-10348.
- [140] Canfield, R.E., The amino acid sequence of egg white lysozyme, *J. Biol. Chem.* 238(1963) 2698-2707.
- [141] Jollès, J., Jauregui-Adell, J., Bernier, I., Jollès, P., La structure chimique du lysozyme de blanc d'oeuf de poule: étude détaillée, *Biochim Biophysica Acta* 78(1963) 668-689.
- [142] Blake, C.C.F., Koenig, D.F., Mair, G.A., North, A.C.T., Phillips, D.C., Sarma, V.R., Structure of Hen Egg-White Lysozyme: A Three-dimensional Fourier Synthesis at 2 Å Resolution, *Nature* 206(1965) 757.
- [143] <http://lysozyme.co.uk>,
- [144] Phillips, D.C., The hen egg-white lysozyme molecule, *Proc. Natl. Acad. Sci. USA* 57(1967) 483-495.
- [145] Smith, I., Smith, M.J., Roberts, L., Models for tertiary structures: Myoglobin and lysozyme, *Journal of Chemical Education* 47(1970) 302.
- [146] Nelson, D.L., Cox, M.M., *Lehninger Principles of Biochemistry*, fourth edition, W. H. Freeman.
- [147] Phillips, D.C., The three-dimensional structure of an enzyme molecule, *Sci. Am.* 215(1966) 78-90.
- [148] Vocadlo, D.J., Davies, G.J., Laine, R., Withers, S.G., Catalysis by hen egg-white lysozyme proceeds via a covalent intermediate, *Nature* 412(2001) 835-838.

- 
- [149] Craig, D.Q.M., Reading, M., Thermal analysis of pharmaceuticals, CRC Press, 2007.
- [150] Barnes, H.A., Hutton, J.F., Walters, K., An introduction to rheology, Elsevier, 1989.
- [151] Jones, D.S., Bruschi, M.L., de Freitas, O., Gremião, M.P.D., Lara, E.H.G., Andrews, G.P., Rheological, mechanical and mucoadhesive properties of thermoresponsive, bioadhesive binary mixtures composed of poloxamer 407 and carbopol 974P designed as platforms for implantable drug delivery systems for use in the oral cavity, *Int. J. Pharm.* 372(2009) 49-58.
- [152] Chirila, T.V., Hong, Y., Poly(1-vinyl-2-pyrrolidinone) hydrogels as vitreous substitutes: a rheological study, *Polymer International* 46(1998) 183-195.
- [153] Jones, D.S., Lawlor, M.S., Woolfson, A.D., Examination of the flow rheological and textural properties of polymer gels composed of poly(methylvinylether-co-maleic anhydride) and poly(vinylpyrrolidone): Rheological and mathematical interpretation of textural parameters, *J. Pharm. Sci.* 91(2002) 2090-2101.
- [154] Jones, D.S., Lawlor, M.S., Woolfson, A.D., Rheological and mucoadhesive characterization of polymeric systems composed of poly(methylvinylether-co-maleic anhydride) and poly(vinylpyrrolidone), designed as platforms for topical drug delivery, *J. Pharm. Sci.* 92(2003) 995-1007.
- [155] Barnes, H.A., A handbook of elementary rheology, The University of Wales Institute of Non-Newtonian Fluid, Aberystwyth, 2000.
- [156] Craig, D.Q.M., Reading, M., Thermorheological (dynamic oscillatory) characterisation of pharmaceutical and biomedical polymers, in: C. Press, (Ed), Thermal analysis of pharmaceuticals, 2007.
- [157] Radebaugh, G.W., Simonelli, A.P., Phenomenological viscoelasticity of a heterogeneous pharmaceutical semisolid, *J. Pharm. Sci.* 72(1983) 415-422.
- [158] Kavanagh, G.M., Ross-Murphy, S.B., Rheological characterisation of polymer gels, *Prog. Polym. Sci.* 23(1998) 533-562.
- [159] Mezzenga, R., Meyer, C., Servais, C., Romoscanu, A.I., Sagalowicz, L., Hayward, R.C., Shear Rheology of Lyotropic Liquid Crystals: A Case Study, *Langmuir* 21(2005) 3322-3333.
- [160] Estellé, P., Lanos, C., Mélinge, Y., Servais, C., On the optimisation of a texture analyser in squeeze flow geometry, *Measurement* 39(2006) 771-777.
- [161] Thirawong, N., Nunthanid, J., Puttipatkachorn, S., Sriamornsak, P., Mucoadhesive properties of various pectins on gastrointestinal mucosa: An in vitro evaluation using texture analyzer, *Eur. J. Pharm. Biopharm.* 67(2006) 132-140.
- [162] Jones, D.S., Woolfson, D.A., Brown, A.F., Textural, viscoelastic and mucoadhesive properties of pharmaceutical gels composed of cellulose polymers, *Int. J. Pharm.* 151(1997) 223-233.
- [163] Jones, D.S., Woolfson, D.A., Djokic, J., Texture profile analysis of bioadhesive polymeric semisolids: mechanical characterization and investigation of interactions between formulation components, *J. Appl. Polym. Sci.* 61(1996) 2229-2234.
- [164] Rosenthal, A.J., Texture profile analysis-how important are the parameters?, *J. Texture Stud.* 41(2010) 672-684.

- 
- [165] Jones, D.S., Woolfson, A.D., Brown, A.F., Textural analysis and flow rheometry of novel, bioadhesive antimicrobial oral gels, *Pharm. Res.* 14(1997) 450-457.
- [166] Jones, D.S., Woolfson, A.D., Djokic, J., Coulter, W.A., Development and mechanical characterization of bioadhesive semi-solid, polymeric systems containing tetracycline for the treatment of periodontal diseases, *Pharm. Res.* 13(1996) 1734-1738.
- [167] Wong, C.F., Yuen, K.H., Peh, K.K., An in-vitro method for buccal adhesion studies: importance of instrument variables, *Int. J. Pharm.* 180(1999) 47-57.
- [168] Ahuja, A., Khar, R.K., Ali, J., Mucoadhesive Drug Delivery Systems, *Drug Dev. Ind. Pharm.* 23(1997) 489-515.
- [169] Xu, R., Particle characterisation: light scattering methods, Kluwer Academic Publisher, 2002.
- [170] Berne, B.J., Pecora, R., Dynamic Light Scattering with Applications to chemistry, Biology and Physics, John Wiley, 1976.
- [171] van de Hulst, H.C., Light scattering by small particles, Dover Publications, Inc., 1981.
- [172] Pecora, R., Dynamic light scattering: applications of photon correlation spectroscopy, Plenum press, New York, 1985.
- [173] De Jaeger, N., Demeyere, H., Finsy, R., Sneyers, R., Vanderdeelen, J., van der Meeren, P., van Laethem, M., Particle Sizing by Photon Correlation Spectroscopy Part I: Monodisperse latices: Influence of scattering angle and concentration of dispersed material, *Part Part Syst Charact* 8(1991) 179-186.
- [174] Xu, R., Shear Plane and Hydrodynamic Diameter of Microspheres in Suspension, *Langmuir* 14(1998) 2593-2597.
- [175] Svergun, D.I., Koch, M.H.J., Small-angle scattering studies of biological macromolecules in solution, *Rep. Prog. Phys.* 66(2003) 1735.
- [176] Glatter, O., Kratky, O., Small angle x-ray scattering, Academic Press, 1982.
- [177] Koch, M.H.J., Vachette, P., Svergun, D.I., Small-angle scattering: a view on the properties, structures and structural changes of biological macromolecules in solution, *Q. Rev. Biophys.* 36(2003) 147-227.
- [178] Putnam, C.D., Hammel, M., Hura, G.L., Tainer, J.A., X-ray solution scattering (SAXS) combined with crystallography and computation: defining accurate macromolecular structures, conformations and assemblies in solution, *Q. Rev. Biophys.* 40(2007) 191-285.
- [179] Garti, N., Somasundaran, P., Mezzenga, R., Self-Assembled Supramolecular Architectures: Lyotropic Liquid Crystals, Wiley, John & Sons, Incorporated, 2012.
- [180] Venugopal, E., Bhat, S.K., Vallooran, J.J., Mezzenga, R., Phase Behavior of Lipid-Based Lyotropic Liquid Crystals in Presence of Colloidal Nanoparticles, *Langmuir* 27(2011) 9792-9800.
- [181] Garstecki, P., HoÅ,yst, R., Scattering Patterns of Self-Assembled Cubic Phases. 2. Analysis of the Experimental Spectra, *Langmuir* 18(2002) 2529-2537.
- [182] Hyde, S.T., Identification of lyotropic liquid crystalline mesophases, in: K. Holmberg, (Ed), Handbook of Applied Surface and Colloid Chemistry, John Wiles & Sons, Ltd, 2002.

- 
- [183] Bras, W., Ryan, A.J., Sample environments and techniques combined with Small Angle X-ray Scattering, *Adv. Colloid Interface Sci.* 75(1998) 1-43.
- [184] Hornak, J.P., The Basics of NMR, <http://www.cis.rit.edu/htbooks/nmr/bnmr.htm>, 1996-2011
- [185] Cohen, Y., Avram, L., Frish, L., Diffusion NMR Spectroscopy in Supramolecular and Combinatorial Chemistry: An Old Parameter—New Insights, *Angew. Chem. Int. Ed.* 44(2005) 520-554.
- [186] Evans, J.N.S., *Biomolecular NMR Spectroscopy*, Oxford University Press, 1995.
- [187] Lambert, J.B., Mazzola, E.P., *Nuclear Magnetic Resonance Spectroscopy: an introduction to principles, applications and experimental methods*, Pearson Education 2003.
- [188] Callaghan, P.T., *Principles of Nuclear Magnetic Resonance Spectroscopy*, Oxford University Press, 1991.
- [189] Callaghan, P.T., Pulsed-Gradient Spin-Echo NMR for Planar, Cylindrical, and Spherical Pores under Conditions of Wall Relaxation, *J. Magn. Reson. A* 113(1995) 53-59.
- [190] Codd, S.L., Callaghan, P.T., Spin Echo Analysis of Restricted Diffusion under Generalized Gradient Waveforms: Planar, Cylindrical, and Spherical Pores with Wall Relaxivity, *J. Magn. Reson.* 137(1999) 358-372.
- [191] Callaghan, P.T., Godefroy, S., Ryland, B.N., Diffusion-relaxation correlation in simple pore structures, *J. Magn. Reson.* 162(2003) 320-327.
- [192] Busignies, V., Porion, P., Leclerc, B., Evesque, P., Tchoreloff, P., Application of PGSTE-NMR technique to characterize the porous structure of pharmaceutical tablets, *Eur. J. Pharm. Biopharm.* 69(2008) 1160-1170.
- [193] Stuart, B., *Infrared spectroscopy: fundamentals and applications*, John Wiley, 2004.
- [194] Luo, S.Q., Huang, C.Y.F., McClelland, J.F., Graves, D.J., A Study of Protein Secondary Structure by Fourier Transform Infrared/Photoacoustic Spectroscopy and Its Application for Recombinant Proteins, *Anal Biochem* 216(1994) 67-76.
- [195] Surewicz, W.K., Mantsch, H.H., Chapman, D., Determination of protein secondary structure by Fourier transform infrared spectroscopy: A critical assessment, *Biochem* 32(1993) 389-394.
- [196] Grdadolnik, J., A FTIR investigation of protein conformation, *Bull Chem Technol Macedonia* 21(2002) 23-34.
- [197] Susi, H., Byler, D.M., Resolution-enhanced fourier transform infrared spectroscopy of enzymes, *Methods Enzymol* 130(1986) 290-311.
- [198] Byler, D.M., Susi, H., Examination of the secondary structure of proteins by deconvolved FTIR spectra, *Biopolymers* 25(1986) 469-487.
- [199] Oberg, K., Chrnyk, B.A., Wetzel, R., Fink, A.L., Native-like Secondary Structure in Interleukin-1.β. Inclusion Bodies by Attenuated Total Reflectance FTIR, *Biochem* 33(1994) 2628-2634.
- [200] Chittur, K.K., FTIR/ATR for protein adsorption to biomaterial surfaces, *Biomaterials* 19(1998) 357-369.

- 
- [201] Wang, Y., Boysen, R.I., Wood, B.R., Kansiz, M., McNaughton, D., Hearn, M.T.W., Determination of the secondary structure of proteins in different environments by FTIR-ATR spectroscopy and PLS regression, *Biopolymers* 89(2008) 895-905.
- [202] Hajime, T., Mitsuo, T., Model calculations on the amide-I infrared bands of globular proteins, *J Chem Phys* 96(1992) 3379-3387.
- [203] Greenfield, N.J., Using circular dichroism collected as a function of temperature to determine the thermodynamics of protein unfolding and binding interactions, *Nat. Protoc.* 1(2006) 2876-2890.
- [204] Kelly, S.M., Jess, T.J., Price, N.C., How to study proteins by circular dichroism, *Biochim. Biophys. Acta Proteins Proteomics* 1751(2005) 119-139.
- [205] Johnson, W.C.J., Secondary Structure of Proteins Through Circular Dichroism Spectroscopy, *Annu. Rev. Biophys. Biophys. Chem.* 17(1988) 145-166.
- [206] Kelly, S.M., Price, N.C., The Use of Circular Dichroism in the Investigation of Protein Structure and Function, *Curr. Protein Pept. Sci.* 1(2000) 349-384.
- [207] Nabok, A., Organic and inorganic nanostructure, Artech house, 2005.
- [208] Kaminskyj, S.G.W., Dahms, T.E.S., High spatial resolution surface imaging and analysis of fungal cells using SEM and AFM, *Micron* 39(2008) 349-361.
- [209] Hafner, J.H., Cheung, C.L., Woolley, A.T., Lieber, C.M., Structural and functional imaging with carbon nanotube AFM probes, *Progress in Biophysics and Molecular Biology* 77(2001) 73-110.
- [210] Neto, C., Aloisi, G., Baglioni, P., Larsson, K., Imaging soft matter with the atomic force microscope: cubosomes and hexosomes, *J Phys Chem B* 103(1999) 3896-3899.
- [211] Almgren, M., Edwards, K., Karlsson, G., Cryo transmission electron microscopy of liposomes and related structures, *Colloids Surf., A* 174(2000) 3-21.
- [212] Johansson, E., Lundquist, A., Zuo, S., Edwards, K., Nanosized bilayer disks: Attractive model membranes for drug partition studies, *Biochimica et Biophysica Acta (BBA) - Biomembranes* 1768(2007) 1518-1525.
- [213] Dressman, J., Amidon, G., Reppas, C., Shah, V., Dissolution Testing as a Prognostic Tool for Oral Drug Absorption: Immediate Release Dosage Forms, *Pharm. Res.* 15(1998) 11-22.
- [214] Aranda, P., Ruiz-Hitzky, E., Poly(ethylene oxide)-silicate intercalation materials, *Chem. Mater.* 4(1992) 1395-1403.
- [215] Wang, H., Zhang, G., Du, Z., Li, Q., Wang, W., Liu, D., Zhang, X., Effect of temperature on dynamic rheological behavior of discontinuous cubic liquid crystal, *J. Colloid Interface Sci.* 300(2006) 348-353.
- [216] Montalvo, G., Valiente, M., Rodenas, E., Rheological Properties of the L Phase and the Hexagonal, Lamellar, and Cubic Liquid Crystals of the CTAB/Benzyl Alcohol/Water System, *Langmuir* 12(1996) 5202-5208.
- [217] Radiman, S., Toprakcioglu, C., McLeish, T., Rheological study of ternary cubic phases, *Langmuir* 10(1994) 61-67.
- [218] Ferry, J.D., Viscoelastic properties of polymers, John Wiley & Sons, New York, 1980.

- [219] Jones, D.S., Brown, A.F., Woolfson, A.D., Rheological characterization of bioadhesive, antimicrobial, semisolids designed for the treatment of periodontal diseases: Transient and dynamic viscoelastic and continuous shear analysis, *J. Pharm. Sci.* 90(2001) 1978-1990.
- [220] Teng, L.Y., Chin, N.L., Yusof, Y.A., Rheological and textural studies of fresh and freeze-thawed native sago starch-sugar gels. II. Comparisons with other starch sources and reheating effects, *Food Hydrocolloids* 31(2013) 156-165.
- [221] Gilbert, L., Picard, C., Savary, G., Grisel, M., Rheological and textural characterization of cosmetic emulsions containing natural and synthetic polymers: relationships between both data, *Colloids and Surfaces A: Physicochem. Eng. Aspects* 421(2013) 150-163.
- [222] Smart, J.D., An *in vitro* assessment of some mucosa-adhesive dosage forms, *Int. J. Pharm.* 73(1991) 69-74.
- [223] Ponchel, G., Touchard, F.d.r., Duchêne, D., Peppas, N.A., Bioadhesive analysis of controlled-release systems. I. Fracture and interpenetration analysis in poly(acrylic acid)-containing systems, *J. Control. Release* 5(1987) 129-141.
- [224] Chen, W.-G., Hwang, G.C.-C., Adhesive and *in vitro* release characteristics of propranolol bioadhesive disc system, *Int. J. Pharm.* 82(1992) 61-66.
- [225] Tobyn M, J., Johnson J, R., Dettmar P, W., Factors affecting *in vitro* gastric mucoadhesion. I: Test conditions and instrumental parameters, *Eur. J. Pharm. Biopharm.* 41(1995) 235-241.
- [226] Lai, S.K., Wang, Y.-Y., Wirtz, D., Hanes, J., Micro- and macrorheology of mucus, *Adv. Drug Deliv. Rev.* 61(2009) 86-100.
- [227] Mortazavi, S.A., Smart, J.D., An investigation of some factors influencing the *in vitro* assessment of mucoadhesion, *Int. J. Pharm.* 116(1995) 223-230.
- [228] Sigurdsson, H.H., Loftsson, T., Lehr, C.-M., Assessment of mucoadhesion by a resonant mirror biosensor, *Int. J. Pharm.* 325(2006) 75-81.
- [229] Khutoryanskaya, O.V., Potgieter, M., Khutoryanskiy, V.V., Multilayered hydrogel coatings covalently-linked to glass surfaces showing a potential to mimic mucosal tissues, *Soft Matter* 6(2010) 551-557.
- [230] Blanco-Fuente, H., Vila-Dorrio, B., Anguiano-Igea, S., Otero-Espinar, F.J., Blanco-Méndez, J., Tanned leather: A good model for determining hydrogels bioadhesion, *Int. J. Pharm.* 138(1996) 103-112.
- [231] Brovchenko, I., Oleinikova, A., Multiple Phases of Liquid Water, *ChemPhysChem* 9(2008) 2660-2675.
- [232] Schulz, P., DSC analysis of the state of water in surfactant-based microstructures, *Journal of Thermal Analysis and Calorimetry* 51(1998) 135-149.
- [233] Garti, N., Aserin, A., Ezrahi, S., Tiunova, I., Berkovic, G., Water Behavior in Nonionic Surfactant Systems I: Subzero Temperature Behavior of Water in Nonionic Microemulsions Studied by DSC, *Journal of Colloid and Interface Science* 178(1996) 60-68.
- [234] Stillinger, F.H., Thermal Properties of Water in Restrictive Geometries, *Water in Polymers*, ACS Symposium Series 127, American Chemical Society, 1980, pp. 11-21.

- [235] Maran Ultra User-Manual, Resonance Instrument, 2003.
- [236] Price, W.S., Pulsed-field gradient nuclear magnetic resonance as a tool for studying translational diffusion: Part 1. Basic theory, *Concepts Magn. Reson.* 9(1997) 299-336.
- [237] Matthews, K.H., Freeze-drying of shaped pharmaceutical dosage forms, *European Industrial Pharmacy*(2009).
- [238] Quinn, F.X., Kampff, E., Smyth, G., McBrierty, V.J., Water in hydrogels. 1. A study of water in poly(N-vinyl-2-pyrrolidone/methyl methacrylate) copolymer, *Macromolecules* 21(1988) 3191-3198.
- [239] LaTorraca, G.A., Dunn, K.J., Webber, P.R., Carlson, R.M., Low-field NMR determinations of the properties of heavy oils and water-in-oil emulsions, *Magn. Reson. Imaging* 16(1998) 659-662.
- [240] Hills, B.P., Manoj, P., Destruel, C., NMR Q-space microscopy of concentrated oil-in-water emulsions, *Magn. Reson. Imaging* 18(2000) 319-333.
- [241] Hills, B., Benamira, S., Marigheto, N., Wright, K., T 1-T 2 correlation analysis of complex foods, *Appl. Magn. Reson.* 26(2004) 543-560.
- [242] Marigheto, N., Venturi, L., Hibberd, D., Wright, K.M., Ferrante, G., Hills, B.P., Methods for peak assignment in low-resolution multidimensional NMR cross-correlation relaxometry, *J. Magn. Reson.* 187(2007) 327-342.
- [243] Belton, P.S., NMR studies of hydration in low water content biopolymer systems, *Magn. Reson. Chem.* 49(2011) S127-S132.
- [244] Stejskal, E.O., Tanner, J.E., Spin Diffusion Measurements: Spin Echoes in the Presence of a Time-Dependent Field Gradient, *J. Chem. Phys.* 42(1965) 288-292.
- [245] Zhang, J., Yan, Y.-B., Probing conformational changes of proteins by quantitative second-derivative infrared spectroscopy, *Anal Biochem* 340(2005) 89-98.
- [246] Costa, P., Sousa Lobo, J.M., Modeling and comparison of dissolution profiles, *Eur. J. Pharm. Sci.* 13(2001) 123-133.
- [247] Higuchi, T., Mechanism of sustained-action medication. Theoretical analysis of rate of release of solid drugs dispersed in solid matrices, *J. Pharm. Sci.* 52(1963) 1145-1149.
- [248] Gao, Z., Mathematical modeling of variables involved in dissolution testing, *J. Pharm. Sci.* 100(2011) 4934-4942.
- [249] Niebergall, P.J., Milosovich, G., Goyan, J.E., Dissolution rate studies II. Dissolution of particles under conditions of rapid agitation, *J. Pharm. Sci.* 52(1963) 236-241.
- [250] Korsmeyer, R.W., Gurny, R., Doelker, E., Buri, P., Peppas, N.A., Mechanisms of solute release from porous hydrophilic polymers, *Int. J. Pharm.* 15(1983) 25-35.
- [251] Ritger, P.L., Peppas, N.A., A simple equation for description of solute release II. Fickian and anomalous release from swellable devices, *J. Controlled Release* 5(1987) 37-42.
- [252] Kumosinski, T.F., Unruh, J.J., Quantitation of the global secondary structure of globular proteins by FTIR spectroscopy: Comparison with X-ray crystallographic structure, *Talanta* 43(1996) 199-219.
- [253] Dong, A., Huang, P., Caughey, W.S., Protein secondary structures in water from second-derivative amide I infrared spectra, *Biochemistry* 29(1990) 3303-3308.

- 
- [254] Levitt, M., Greer, J., Automatic Identification of Secondary Structure in Globular Proteins, *J. Mol. Biol.* 114(1977) 181-239.
- [255] Chen, Y.-H., Yang, J.T., Martinez, H.M., Determination of the secondary structures of proteins by circular dichroism and optical rotatory dispersion, *Biochemistry* 11(1972) 4120-4131.
- [256] Hennessey, J.P., Johnson, W.C., Information-Content in the Circular-Dichroism of Proteins, *Biochemistry* 20(1981) 1085-1094.
- [257] Provencher, S.W., Glockner, J., Estimation of Globular Protein Secondary Structure from Circular-Dichroism, *Biochemistry* 20(1981) 33-37.
- [258] Chang, C.T., Wu, C.S.C., Yang, J.T., Circular Dichroic Analysis of Protein Conformation - Inclusion of Beta-Turns, *Anal. Biochem.* 91(1978) 13-31.
- [259] Brahms, S., Brahms, J., Determination of Protein Secondary Structure in Solution by Vacuum Ultraviolet Circular-Dichroism, *J. Mol. Biol.* 138(1980) 149-178.
- [260] Manavalan, P., Johnson, W.C., Variable Selection Method Improves the Prediction of Protein Secondary Structure from Circular-Dichroism Spectra, *Anal. Biochem.* 167(1987) 76-85.
- [261] Greenfield, N., Fasman, G.D., Computed Circular Dichroism Spectra for Evaluation of Protein Conformation, *Biochemistry* 8(1969) 4108-4116.
- [262] Spicer, P.T., Hayden, K.L., Lynch, M.L., Ofori-Boateng, A., Burns, J.L., Novel process for producing cubic liquid crystalline nanoparticles (cubosomes), *Langmuir* 17(2001) 5748-5756.
- [263] Date, A.A., Vador, N., Jagtap, A., Nagarsenker, M.S., Lipid nanocarriers (GeluPearl) containing amphiphilic lipid Gelucire 50/13 as a novel stabilizer: fabrication, characterization and evaluation for oral drug delivery, *Nanotechnology* 22(2011) 275102.
- [264] Shugar, D., The measurement of lysozyme activity and the ultra-violet inactivation of lysozyme, *Biochim. Biophys. Acta* 8(1952) 302-309.
- [265] Zetterberg, M.M., Reijmar, K., Pr anting, M., Engstr om,  ., Andersson, D.I., Edwards, K., PEG-stabilized lipid disks as carriers for amphiphilic antimicrobial peptides, *J. Controlled Release* 156(2011) 323-328.
- [266] Li, X., Chen, D., Le, C., Zhu, C., Gan, Y., Hovgaard, L., Yang, M., Novel mucus-penetrating liposomes as a potential oral drug delivery system: preparation, in vitro characterization, and enhanced cellular uptake, *Int J Nanomedicine* 6(2011) 3151-3162.
- [267] Chauhan, B., Shimpi, S., Paradkar, A., Preparation and evaluation of glibenclamide-polyglycolized glycerides solid dispersions with silicon dioxide by spray drying technique, *Eur. J. Pharm. Sci.* 26(2005) 219-230.
- [268] Lai, S.K., Wang, Y.-Y., Hanes, J., Mucus-penetrating nanoparticles for drug and gene delivery to mucosal tissues, *Advanced Drug Delivery Reviews* 61(2009) 158-171.